

AD-A018 184

**IMPROVED NOZZLE TESTING TECHNIQUES IN TRANSONIC FLOW**

**A. Ferri**

**Advisory Group for Aerospace Research and Development**

**Prepared for:**

**North Atlantic Treaty Organization**

**October 1975**

**DISTRIBUTED BY:**

**NTIS**

**National Technical Information Service  
U. S. DEPARTMENT OF COMMERCE**

346092

dc

0

AGARD-AG-208

AGARD-AG-208

# AGARD

ADVISORY GROUP FOR AEROSPACE RESEARCH & DEVELOPMENT

7 RUE ANCELLE 92200 NEUILLY SUR SEINE FRANCE

AGARDograph No.208

on

## Improved Nozzle Testing Techniques in Transonic Flow

Edited by  
A.Ferri

**DISTRIBUTION STATEMENT A**

Approved for public release;  
Distribution Unlimited

DDC  
RECEIVED  
DEC 8 1975  
A

NORTH ATLANTIC TREATY ORGANIZATION



Reproduced by  
NATIONAL TECHNICAL  
INFORMATION SERVICE  
US Department of Commerce  
Springfield, VA. 22151

**DISTRIBUTION AND AVAILABILITY  
ON BACK COVER**

ADA018184

**NORTH ATLANTIC TREATY ORGANIZATION**  
**ADVISORY GROUP FOR AEROSPACE RESEARCH AND DEVELOPMENT**

---

**ORGANISATION DU TRAITE DE L'ATLANTIQUE NORD**  
**GROUPE CONSULTATIF POUR LA RECHERCHE ET LE DEVELOPPEMENT AEROSPATIAL**

**AGARDograph No.208**

**IMPROVED NOZZLE TESTING TECHNIQUES IN**  
**TRANSONIC FLOW**

**Edited by**

**A.Ferri**

**Director, Aerospace and Energetics Laboratory**  
**New York University, Westbury, Long Island, New York**

**DISTRIBUTION STATEMENT A**

**Approved for public release;**  
**Distribution Unlimited**

DEC 8 1975

Report of a Study organized by the AGARD Propulsion and Energetics Panel with the collaboration of the Fluid Dynamics Panel and including papers and discussions from the special session on this topic held at the 35th Fluid Dynamics Panel Meeting in Rome, Italy, 4-10 Sept. 1974.

## **THE MISSION OF AGARD**

The mission of AGARD is to bring together the leading personalities of the NATO nations in the fields of science and technology relating to aerospace for the following purposes:

- Exchanging of scientific and technical information;
- Continuously stimulating advances in the aerospace sciences relevant to strengthening the common defence posture;
- Improving the co-operation among member nations in aerospace research and development;
- Providing scientific and technical advice and assistance to the North Atlantic Military Committee in the field of aerospace research and development;
- Rendering scientific and technical assistance, as requested, to other NATO bodies and to member nations in connection with research and development problems in the aerospace field;
- Providing assistance to member nations for the purpose of increasing their scientific and technical potential;
- Recommending effective ways for the member nations to use their research and development capabilities for the common benefit of the NATO community.

The highest authority within AGARD is the National Delegates Board consisting of officially appointed senior representatives from each member nation. The mission of AGARD is carried out through the Panels which are composed of experts appointed by the National Delegates, the Consultant and Exchange Program and the Aerospace Applications Studies Program. The results of AGARD work are reported to the member nations and the NATO Authorities through the AGARD series of publications of which this is one.

Participation in AGARD activities is by invitation only and is normally limited to citizens of the NATO nations.

Part of the material in this publication has been reproduced directly from copy supplied by AGARD or the authors; the remainder has been set by Technical Editing and Reproduction Ltd.

Published October 1975

Copyright © AGARD 1975

533.6.011.35:533.697.4

**National Technical Information Service is authorized to reproduce and sell this report.**



*Set and printed by Technical Editing and Reproduction Ltd  
Harford House, 7-9 Charlotte St, London. W1P 1HD*



## MEMBERS OF THE STUDY GROUP

**Professor A.Ferri (Study Group Leader)**  
Director, Aerospace and Energetics Laboratory  
New York University  
Westbury, Long Island, New York, USA

**Dipl. Ing. F.Aulehla**  
Messerschmitt-Bölkow-Blohm GmbH  
Munich, W.Germany

**Dipl. Ing. H.Dissen**  
DFVLR,  
Braunschweig Flughafen, W.Germany

**Mr C.C.Groothoff**  
National Aerospace Laboratory (NLR)  
Amsterdam, Netherlands

**Dr H.Hardegan**  
DFVLR,  
Braunschweig, W.Germany

**Mr J.M.Hardy**  
SNECMA, Villaroche  
Moissy-Cramayel, France

**Mr L.R.Harper**  
Rolls-Royce (1971) Ltd.  
Bristol, England

**Mr F.Jaarsma**  
National Aerospace Laboratory  
Amsterdam, Netherlands

**Mr E.Johnson**  
Aerospace Research Laboratory  
Wright-Patterson AFB, Ohio, USA

**Mr W.J.Leynaert**  
ONERA  
Chatillon, France

**Mr W.J.Lewis**  
Rolls-Royce (1971) Ltd.  
Bristol, England

**Mr B.M.Mechin**  
ONERA  
Chatillon, France

**Mr G.Richey**  
Air Force Flight Dynamics Laboratory  
Wright-Patterson AFB, Ohio, USA

**Dr D.Zonars**  
Air Force Flight Dynamics Laboratory  
Wright-Patterson AFB, Ohio, USA

Other contributors to the study include the following personnel:

**Besigk, G**  
**Bowers, D.L.**  
**Compton, W.B.III**  
**Derksen, W.B.G.**  
**Emunds, H.**  
**Galigher, L.L.**  
  
**Jackson, F.M.**  
**Laughrey, J.A.**  
**Poisson-Quinton, M.Ph.**  
**Reidel, H.**  
**Robinson, C.M.**  
**Rozendal, D.**  
**Runckel, J.F.**  
**Schwantes, E.**  
**Zacharias, A.**

**MBB GmbH, Germany**  
**AFFDL, W-PAFB, Ohio, USA**  
**NASA Langley, USA**  
**NLR, Netherlands**  
**DFVLR, Germany**  
**Arnold Engineering Development**  
**Center, Tennessee, USA**  
**AEDC, Tennessee, USA**  
**AFFDL, W-PAFB, Ohio, USA**  
**ONERA, France**  
**DFVLR, Germany**  
**AEDC, Tennessee, USA**  
**NLR, Netherlands**  
**NASA Langley, USA**  
**DFVLR, Germany**  
**DFVLR, Germany**

## CONTENTS

### INTRODUCTION

by A.Ferri

Page

vi

Reference

### PART I: DESCRIPTION OF TESTS AND PRELIMINARY RESULTS

#### ONERA: ETUDE EXPERIMENTALE DE LA TUYERE ETALON AGARD "15°" EN ECOULEMENTS SUBSONIQUE ET TRANSSONIQUE

par N.Mechin

A

#### DESCRIPTION OF TESTS CARRIED OUT AT ROLLS-ROYCE (1971) LTD BRISTOL ENGINE DIVISION

by L.R.Harper

B

#### DFVLR BRAUNSCHWEIG: AN EXPERIMENTAL STUDY OF THE INFLUENCE OF THE JET PARAMETERS ON THE AFTERBODY DRAG OF A JET ENGINE NACELLE SCALE MODEL

by H.Dissen and A.Zacharias

C

#### CONTRIBUTION OF THE INSTITUT FUR ANGEWANDTE GASDYNAMIC OF THE DFVLR, PORZ-WAHN

by H.Emunds and H.Riedel

D

#### RESULTS OF NLR CONTRIBUTION TO AGARD AD HOC STUDY

by D.Rozendal, C.C.Groothoff and W.B.G.Derksen

E

#### AFFDL WRIGHT-PATTERSON AFB: EFFECTS OF VARYING REYNOLDS NUMBER AND BOUNDARY LAYER DISPLACEMENT THICKNESS ON THE EXTERNAL FLOW OVER NOZZLE BOATTAILS (*This paper includes both a description of the AFDDL test, and an analysis of the effects of parameters appropriate to Part II below*)

by D.Zonars, J.A.Laughrey and D.' Bowers

F

#### DESCRIPTION OF THE AGARD NOZZLE AFTERBODY EXPERIMENTS CONDUCTED BY AEDC. TENNESSEE

by L.L.Galigher, F.M.Jackson and C.E.Robinson

G

#### CONTRIBUTION OF NASA LANGLEY RESEARCH CENTER

by W.B.Compton III and J.F.Runckel

H

### PART II: CRITICAL ANALYSIS OF EFFECTS OF PARAMETERS

#### THE INFLUENCE OF MODEL EXTERNAL GEOMETRY

by L.R.Harper and W.J.Lewis

A

#### INFLUENCE DU TAUX DE DETEMTE DU JET SUR LES COEFFICIENTS DE PERFORMANCE D'UN ARRIERE-CORPS MONOFLUX AGARD DE MACH 0,60 A MACH 0,95

par Bernard Mechin et Jean-Marie Hardy

B

#### INFLUENCE OF JET P/ RAMETERS: NOZZLE THRUST AND DISCHARGE COEFFICIENTS

by C.C.Groothoff

C

#### INFLUENCE OF JET PARAMETERS: BOATTAIL PRESSURE DISTRIBUTION AND PRESSURE DRAG

by H.Dissen, H.Emunds, H.Riedel and A.Zacharias

D

#### DATA VARIANCE DUE TO DIFFERENT TESTING TECHNIQUES

by J.A.Laughrey, G.K.Richey and A.Ferri

E

**FORE- AND AFTERBODY FLOW FIELD INTERACTION WITH CONSIDERATION OF  
REYNOLDS NUMBER EFFECTS**

by F.Aulehla and G.Besigk

F

**CONCLUDING REMARKS**

by A.Ferri

Con

## INTRODUCTION

by

Antonio Ferri

The determination of engine inlet, and nozzle performance at transonic speed is one of the most difficult experimental tasks encountered by aerodynamicists. The characteristics of the engine installation (inlet and nozzle) depend on an interaction of the engine flow and the external flow. The pressure rise near the trailing edge of the nozzle can produce local boundary layer separation. The local separation depends substantially on the properties of the internal flow field, the external surface flow field and their interaction in the plume downstream of the nozzle. The problem becomes more complex in three-dimensional flow when the separation is not uniformly distributed and the flow is extremely sensitive to small variations of pressure distribution and cross flow pressure gradients. Duplication in small scale experiments of all the important parameters involved in the problem is practically impossible, since it would require representation of the actual boundary layer in the external flow, as well as accurate geometrical and aerodynamic model simulation. In addition, it would require exact simulation of the internal flow, and heat transfer from the engine to the nozzle. This cannot be obtained in present experimental facilities. At transonic conditions small variations of the initial flow properties approaching the boattail can produce significant effects that are difficult to predict and evaluate.

In addition to difficulties of accurate simulation are all the difficulties related to transonic testing techniques. The presence of a model mounting system, proximity of the tunnel walls, the method and amount of flow removal at the walls, and slight variations in tunnel conditions can produce significant effects on the external flow over the boattail. The importance of such effects is well appreciated by the experimenters; however, a detailed evaluation of their influence on the experimental results does not exist. A detailed evaluation of such influences can be performed only by means of a program involving large scale research facilities, substantial time and funds, beyond those usually available to the experimental groups involved in this type of research.

In view of the importance and wide interest in the problems of nozzle testing techniques in transonic flow, a special effort under an Ad Hoc Group was organized by the Propulsion and Energetics Panel of AGARD in May 1972, with the support and cooperation of the Fluid Dynamics Panel, directed to two main goals:

- (1) Development of an international program of research directed to demonstrating the influence of the experimental apparatus on the results, even for the case of a relatively simple axially symmetric nozzle boattail.
- (2) Determination of the importance of the various parameters investigated on the results.

An important by-product of this effort has been the demonstration of the possibility of performing, through AGARD, research efforts in fields where the utilization of different research groups and facilities can be effective in solving problems of common interest which are beyond the resources available to individual research organizations.

The experiments and analysis reported here have involved the following research groups:

ONERA - France

Rolls-Royce Ltd. (Bristol Division) - United Kingdom

DFVLR and Messerschmitt-Bölkow-Blohm GmbH - Germany

National Aerospace Lab (NLR) - The Netherlands

Air Force Flight Dynamics Laboratory, WPAFB, Ohio - USA

Air Force Arnold Engineering Development Center, Tennessee - USA

NASA Langley Research Center, Virginia - USA

Each nation participating in the program has committed a significant effort to the project, generating a large body of information which makes it possible to begin to reach an understanding of transonic nozzle flow phenomena and test techniques. Many of the nozzle flow parameters were investigated by more than one group in various facilities. Thus the results not only provide insight to the effect of the parameters investigated, they can be used to study the effects of the various experimental test techniques used. Each investigation used one or more of the three nozzle designs selected by the group, described in detail in the next section.

Each of the nozzles has a circular body upstream of the boattail with a smooth fairing between the forebody and aftbody. All three nozzles have the same area ratio between the cylindrical section and the nozzle exit, but differ in the length of the external convergent section; the long nozzle (10° boattail mean chord angle) would be expected to minimize flow separation at the end, while the shortest (25° boattail mean chord angle) was selected to invite a substantial region of boundary layer separation.

The presentation of the results in this report has been organized into two parts. The first part includes a detailed description of the experimental technique used, of the parameters investigated, and sample data from the tests conducted in each facility. This part of the report has been prepared by the research group that performed the experiments. The second part of the report contains a critical analysis of the effects of the various parameters investigated, utilizing all the data available on a particular parameter from the entire study. Included as a subsection is a discussion of the effects of the experimental techniques on the nozzle external flow. It discusses the effects of the correct representation of the forebody configuration on the boattail flow, and presents a detailed comparison and analysis of results obtained under supposedly equivalent conditions by different investigators to give insight to the effects that varying test techniques and wind tunnel/model interaction can have on the results.

As will be discussed in more detail in the text of this report and in the conclusions, the efforts presented here should be considered only as the first step of an overall investigation. It is strongly recommended that AGARD find an organizational structure to continue and expand this investigation.

It can be of interest to note that the total experimental effort, which includes several large scale programs, has been obtained at a small fraction of the total cost to each single nation, and has been organized without additional funds requested specifically for this effort. The work performed has been obtained mainly by modifying already planned and authorized programs.

**PART I**

**DESCRIPTION OF TESTS  
AND PRELIMINARY RESULTS**



## ETUDE EXPERIMENTALE DE LA TUYERE ETALON AGARD "15°" EN ECOULEMENTS SUBSONIQUE ET TRANSSONIQUE

par

B.Mechin

Office National d'Etudes et de Recherches Aérospatiales  
Direction de l'Aérodynamique  
29, Avenue de la Division Leclerc, 92320 Châtillon

(Onera Rapport Technique No 26/2621 AN)

### INTRODUCTION

Parmi les 3 tuyères étalon proposées par le "Groupe d'Etudes sur les techniques d'essai d'arrière-corps en écoulement transsonique", l'ONERA n'a retenu que la configuration dite "15°" et a réalisé avec cette tuyère un programme d'essais permettant d'étudier l'influence des divers paramètres : obstruction de la veine d'essais, nature de la couche limite (naturelle ou soufflée), taux de détente, nombre de Mach de l'écoulement extérieur. Les principaux résultats obtenus concernent les performances (coefficients de poussée) de cette tuyère au point fixe et avec écoulement externe, la caractérisation du flux interne (sondages en pression statique, pression et température totales) et les répartitions de pression statique à la surface extérieure de la tuyère.

Ce document rassemble donc :

- la description de l'installation d'essai utilisée.
- la définition du montage d'essai d'arrière-corps.
- les résultats des essais effectués dans le cadre de cette étude.

### NOTATIONS

$M_0$	=	Mach dit "infini amont" de l'écoulement dans la veine
$M_p$	=	Mach local
$P_j$	=	pression génératrice moyenne de l'écoulement interne déterminée à partir du débit, de la température génératrice moyenne au col, et de l'aire critique $A_{j^*}$
$P_i$	=	pression génératrice locale de l'écoulement interne mesurée par une sonde Pitot
$P_t$	=	pression génératrice du jet de soufflage de couche limite
$p$	=	pression statique
$p_0$	=	pression statique dans la veine
$T_{j1}$	=	température génératrice mesurée par l'anneau de thermocouples en amont de la tôle perforée.
$T_{j2}$	=	température génératrice en aval de la grille calculée à partir de $P_j$ et $T_{j1}$ par un effet de Joule-Thomson.
$T_i$	=	température génératrice locale mesurée par la sonde thermocouple
$A_m$	=	aire de la section du maître couple
$A_j$	=	aire géométrique du col de la tuyère
$A_{j^*}$	=	aire critique de l'écoulement au plan de sortie (au col de la tuyère)
$C_D$	=	coefficient de débit $C_D = A_j/A_{j^*}$
$K_p$	=	coefficient de pression $K_p = \frac{p - p_0}{\frac{\gamma}{2} p_0 M_0^2}$

$D_p$  = trainée de pression  $D_p = \int_{A_m}^{A_j} K_p dA$

$D_{FR}$  = trainée de frottement

$C_{DP}$  = coefficient de trainée  $C_{DP} = D_p / \frac{\gamma}{2} p_0 M_0^2 A_m$

$X_{GA_i}$  = poussée absolue de l'écoulement interne (dynamie de sortie)

$K_{TA_i}$  = coefficient de poussée absolue interne  $K_{TA_i} = X_{GA_i} / P_j A_j \star$

$K_{Ti}$  = coefficient de poussée interne  $K_{Ti} = K_{TA_i} - \frac{p_0 A_j}{P_j A_j \star}$

$K'_T$  = coefficient de poussée sans frottement  $K'_T = K_{Ti} - D_p / P_j A_j \star$

$K_T$  = coefficient de poussée  $K_T = K'_T - D_{FR} / P_j A_j \star$

## 1. MONTAGE D'ESSAIS D'ARRIERE-CORPS

### 1.1 Caractéristiques générales de la soufflerie S3 Ch (CHALAIS-MEUDON)

Le schéma général de la soufflerie est donné sur la Planche 1 ; les caractéristiques essentielles en sont les suivantes :

- Le domaine de nombre de Mach est compris entre  $M_0 = 0,1$  et  $M_0 = 0,95$  en fonctionnement continu (avec reprise de veine No.2) et s'étend jusqu'à  $M_0 = 1,10$  (avec reprise de veine No.1) en fonctionnement par rafales de 1 minute.
- La pression génératrice est voisine de la pression atmosphérique.
- La température génératrice est croissante en fonction du nombre de Mach depuis la température ambiante jusqu'à  $340^\circ K$ .
- Le nombre de Reynolds rapporté au maître couple de la maquette ( $\varnothing 80$ ) varie de  
 $0,88 \times 10^6$  à  $M_0 = 0,60$   
à  
 $1,01 \times 10^6$  à  $M_0 = 0,95$
- Une section quasi-octogonale de  $0,66 m^2$  (diamètre du cercle circonscrit = 1 mètre),
- Une longueur totale de 1,75 m ; la longueur utile correspond aux dimensions des hublots : 0,60 m,
- Des parois haute et basse légèrement divergentes ( $0,5^\circ$ ) et perforées (perméabilité 24%),
- Des parois latérales pleines et parallèles (hublots)
- Le nombre de Mach dans la veine est calculé à partir du rapport de la pression  $p_0$ , pression statique mesurée dans les "plenum chamber", à la pression génératrice  $p_{i0}$  mesurée par 3 tubes Pitot dans la chambre de tranquillisation.

### 1.2 Montage de base (Planches 1 et 2)

Le montage d'essais d'arrière-corps utilisé depuis plusieurs années a été conçu sur le principe du dard amont, où la maquette à étudier est fixée à l'aval d'une canne axiale (dard "mont") qui sert à amener les flux d'air comprimé et les tubes de mesure des pressions.

La balance utilisée est une balance à une composante (poussée axiale) et comporte un barreau dynamométrique équipé de jauges de contrainte.

La canne est solidaire d'un ensemble balance-bloc d'alimentation des flux situé dans le collecteur de la soufflerie.

Cet ensemble est caréné par un capotage cylindrique de révolution (diamètre 372 mm) comportant une ogive à l'amont et se raccordant au dard portemaquette par un cône de révolution.

L'alimentation de la balance se fait perpendiculairement à l'axe, la liaison entre partie pesée et partie non pesée étant assurée par des membranes en caoutchouc (Planche 2).

L'ensemble est disposé dans la soufflerie par l'intermédiaire :

- d'une contre-fiche axiale prenant appui sur le filtre situé en amont de la chambre de tranquillisation,
- d'un système de haubans profilés accrochés sur le collecteur de la soufflerie,
- d'un mât vertical profilé comprenant les canalisations d'air comprimé et autres liaisons de servitudes, et disposé à l'entrée du collecteur.

### 1.3 Dispositif de soufflage tangentiel de la couche-limite

Le développement de la couche limite naturelle le long de la canne conduit à des épaisseurs caractéristiques de couche limite généralement trop importantes par rapport au cas de l'avion en vol. Afin de réduire cette couche limite, un dispositif de soufflage tangentiel sur la canne a été aménagé.

Le dispositif est représenté sur la Planche 3. La fente de soufflage est située à 5 diamètres (400 mm) en amont du plan de joint "maquette". La première partie de la canne, en amont de la fente a un diamètre de 84 mm et la seconde partie, en aval, de 80 mm ce qui donne une épaisseur de sortie de fente de 1,8 mm compte-tenu de l'épaisseur de bord de fuite de 0,2 mm.

### 1.4 Banc de striction

Cette installation annexe permet d'évaluer l'aire critique d'une tuyère alimentée par un écoulement permanent de conditions génératrices uniformes

### 1.5 Moyens de mesure

Toutes les mesures sont effectuées à l'aide de capteurs produisant un signal électrique :

- Pressions : capteurs à jauges
- Températures : thermocouples Chromel-Alumel
- Efforts : barreau dynamométrique à jauges de contrainte.

Les signaux électriques sont acquis et traités par la chaîne automatique de la soufflerie. Les mesures sortent sous forme de ruban perforé qui peut être dépouillé en temps différé court par le Centre de Calcul de l'ONERA.

## 2. DESCRIPTION DE LA TUYERE ETALON AGARD - 15°

### 2.1 Caractéristiques générales

La tuyère étalon définie par l'AGARD est une tuyère monoflux, à convergent tronconique de demi-angle 7° et dont le profil extérieur est donné par points. Parmi les 3 tuyères proposées, seule la tuyère dont la longueur du rétreint est équivalente est celle d'un cône de demi-angle au sommet de 15°, a été retenue, les deux autres ayant respectivement des angles de 10° et 25°.

Le maître couple de base choisi pour les essais à l'ONERA est de 80 mm ce qui correspond à une obstruction géométrique globale de 0,75 %. Pour répondre aux besoins du programme d'essais envisagé, un certain nombre de maquettes ont été étudiées et fabriquées par les soins de l'ONERA.

### 2.2 Maquette "Point fixe" AGARD PF 80 (Planche 4)

Cette maquette ne reproduit que la géométrie interne et permet :

- de déterminer, au banc de striction en fonction du taux de détente, l'aire critique d'éjection qui détermine le coefficient de débit  $C_D$ .
- de déterminer les performances au point fixe ( $M_0 = 0$ ) de la tuyère.
- de sonder l'écoulement interne.
  - (a) en pression et température totales (P, T) à l'aide de sonde interchangeables (sonde Pitot ou sonde thermocouple) montées sur un explorateur situé à l'extérieur de la maquette.
  - (b) en pression statique à la paroi, en l'absence du dispositif de sondage précédent.

### 2.3 Maquette Ø 80 pour sondage de la couche limite : AGARD AV-CL80

Représentée sur la Planche 5, cette maquette dispose d'un explorateur de couche limite permettant de sonder la couche limite à 7 mm en aval du plan de joint. Son profil externe est celui de la tuyère étalon AGARD. Un essai préliminaire a permis de vérifier que le sondage sur une génératrice n'était pas affecté par la forme du capotage situé sur la génératrice opposée.

## 2.4 Maquette $\phi$ 80 AGARD AV-80 MOD (Planches 6 et 7)

Cette maquette dont les profils extérieur et intérieur sont conformes aux tableaux de cotes officiels est équipée de 17 prises de pression statique disposées en hélice et d'une prise de pression statique interne destinée à caractériser le taux de détente.

## 2.5 Maquettes AGARD AV-100 et AGARD AV-120 (Planches 8 et 9)

Pour compléter le programme initialement prévu et pour étudier l'influence de l'obstruction de la veine, une extension du montage à des diamètres de 100 et 120 mm a été réalisée. Les maquettes correspondantes AV 100 et AV 120, dont le profil extérieur correspond à un tableau de cotes légèrement retouché vers l'extrémité (suppression du point d'inflexion du tableau de cotes officiel) sont équipées de prises de pressions statiques externes.

## 3. ESSAIS

Les paragraphes suivants décrivent les essais qui ont été réalisés conformément au programme établi au cours des réunions préparatoires.

### 3.1 Contrôle de la couche limitée par soufflage tangentiel

Au cours d'une campagne d'essais préliminaires, une configuration géométrique a été choisie pour le dispositif de soufflage. Le débit et la pression du jet et de soufflage ont été choisis de manière à restituer au niveau de la maquette un profil de vitesses dans la couche limite aussi régulier que possible.

### 3.2 Définition des sondages de couche limite

Ces sondages sont effectués :

- à 7 mm en aval du plan de joint soit  $0.276 D$  en amont du plan de sortie
- selon les 4 orientations  $\varphi = 0^\circ, 90^\circ, 180^\circ, 270^\circ$
- avec et sans soufflage tangentiel.

### 3.3 Programme des essais au banc de striction

Ces essais conduisent à la détermination de l'aire sonique aérodynamique  $A_{j^*}$  et du coefficient de débit  $C_D$  de la tuyère AV-80 MOD. Le taux de détente  $P_j/p_0$  a varié de 1,15 à 5,0.

### 3.4 Sondages en pression et température de l'écoulement interne

Ces sondages ont été réalisés avec la maquette PF-80 pour des taux de détente de 1,50 à 4,07. Ils ont pour objet de préciser la distorsion en pression et en température totales du flux interne ainsi que la répartition de pression statique à la paroi interne de la tuyère en l'absence du dispositif interne de sondage.

### 3.5 Programme des essais

- A Mach nul, l'essai de la tuyère PF 80 a permis la détermination du coefficient de poussée absolue interne  $KTA_j$ .
- Chacune des tuyères AV-80 MOD, AV-100 et AV-120 a été essayée pour des nombres de Mach de 0.60, 0.80, 0.85, 0.90 et 0.95 et pour des taux de détente variant de 1 (pas de jet interne) à 5.

Seule la tuyère AV-80 MOD a été essayée avec et sans soufflage tangentiel. Sur toutes les maquettes, les pressions statiques externes ont été relevées. Pour la maquette AV-80 MOD, l'effort axial (poussée) a été mesuré pour chaque point d'essai.

## 4. RESULTATS

### 4.1 Profils de couche-limite

Les profils de couche-limite obtenus avec et sans soufflage tangentiel sont représentés de la Planche 10 à la Planche 13.

Les sondages effectués sans soufflage sur les quatre génératrices de la maquette montrent une dissymétrie de la couche limite qui n'est pas résorbée par le soufflage.

## 4.2 Striction

Sur la planche 14 sont représentées les variations de l'aire sonique aérodynamique  $A_{j^*}$  et du coefficient de débit  $C_D$  de la tuyère AGARD 15° - AV 80 MOD. Le taux de détente de blocage est alors déterminé par la valeur à partir de laquelle l'aire  $A_{j^*}$  devient constante quel que soit le taux de détente.

## 4.3 Distorsions de l'écoulement interne

Les tracés des sondages de pression et température totales du flux interne, sur les figures 15 et 16 déterminent la valeur des coefficients de distorsion en pression.

$$C_p = \frac{P_{iMAX} - P_{iMIN}}{P_j} < 3\%$$

en température

$$C_T = \frac{T_{iMAX} - T_{iMIN}}{T_{j2}} < 0,4\%$$

## 4.4 Pressions statiques internes

La répartition de pression statique à la paroi interne de la tuyère, rapportée à  $P_j$ , est donnée sur la figure 17 pour des taux de détente allant de 1,5 à 4,0. Elle est également graduée en nombre de Mach local  $M_1$ .

## 4.5 Pressions statiques externes

Les répartitions du coefficient de pression  $K_p$  sur les différentes tuyères sont montrées sur les figures 18 à 27 pour la tuyère AV-80 MOD (avec et sans soufflage), 28 à 32 pour la tuyère AV-100 et 33 à 37 pour la tuyère AV-120.

Ces répartitions mettent en évidence le choc et le décollement de couche limite qui s'ensuit à l'extrémité du rétreint.

La graduation en nombre de Mach local  $M_d$  permet de localiser les zones d'écoulement supersonique à partir de  $M_0 = 0.85$ .

Une comparaison des coefficients de pression pour les tuyères AV-80 MOD, AV-100 et AV-120 est montrée sur les figures 38 à 40.

De légères différences apparaissent au niveau du choc, mais le nombre de prises de pression dans cette région est insuffisant pour préciser les phénomènes.

## 4.6 Coefficient de traînée de pression

Obtenu par intégration du coefficient de pression  $K_p$  sur le rétreint, ce coefficient est représenté, en fonction du taux de détente  $P_j/p_0$ , sur la figure 41 pour les nombres de Mach 0.80, 0.90 et 0.95. A  $M_0 = 0.80$ , la soufflage de couche limite n'a pratiquement pas d'influence, tandis qu'à  $M_0 = 0.95$  la traînée de pression est sensiblement augmentée.

L'accroissement de la traînée de pression avec le nombre de Mach résulte principalement de l'extension d'un décollement sur le rétreint.

L'évolution de l'écoulement est décrite de façon plus approfondie référence 1.

## 4.7 Performances de la tuyère AV-80 MOD

Les performances de la tuyère AV-80 MOD sont concrétisées par les coefficients de poussée suivants :

- Le coefficient de poussée absolue interne  $K_{TAi}$ , défini par le rapport de la poussée absolue interne  $X_{GAi}$  à la grandeur  $P_j A_{j^*}$ . Les variations de ce coefficient en fonction du taux de détente sont représentées sur la planche 42. Ce coefficient est constant dès que le taux de détente de blocage est atteint ( $P_j/p_0 = 2.2$ ). Sa valeur mesurée, au blocage,  $K_{TAi} = 1,2724$  est très proche de la valeur théorique  $K_{TAi} = 1,2740$  déterminée avec la méthode exposée réf 2.
- Le coefficient de poussée interne  $K_{Ti}$ , qui représente le précédent exprimé en pressions relatives :

$$K_{Ti} = K_{TAi} = \frac{P_0 A_j}{P_j A_{j^*}}$$

- (c) Le coefficient de poussée sans frottement  $K'_T$  obtenu en soustrayant de la poussée interne la traînée de pression du rétreint,  $D_p$

$$K'_T = K_{T_I} - \frac{D_p}{P_I A_{j^*}}$$

- (d) Le coefficient de poussée  $K_T$  déduit globalement de la pesée, et qui représente la poussée nette, poussée interne diminuée des traînées de pression  $D_p$  et de frottement  $D_{FR}$  de l'arrière-corps.

Les variations de ces coefficients en fonction du taux de détente et pour les nombres de Mach  $M_0 = 0.60, 0.80, 0.90$  et  $0.95$  sont représentées sur les planches 43 à 46.

En fait, les valeurs de  $\frac{D_{FR}}{P_I A_{j^*}}$  mises ainsi en évidence par des différences ne sont pas très précises en valeurs relatives, étant donné leur faible niveau, et l'imprécision sur les valeurs de  $D_p$  notamment, obtenues par intégration à partir d'un nombre rétreint de prises de pression.

## 5. CONCLUSION

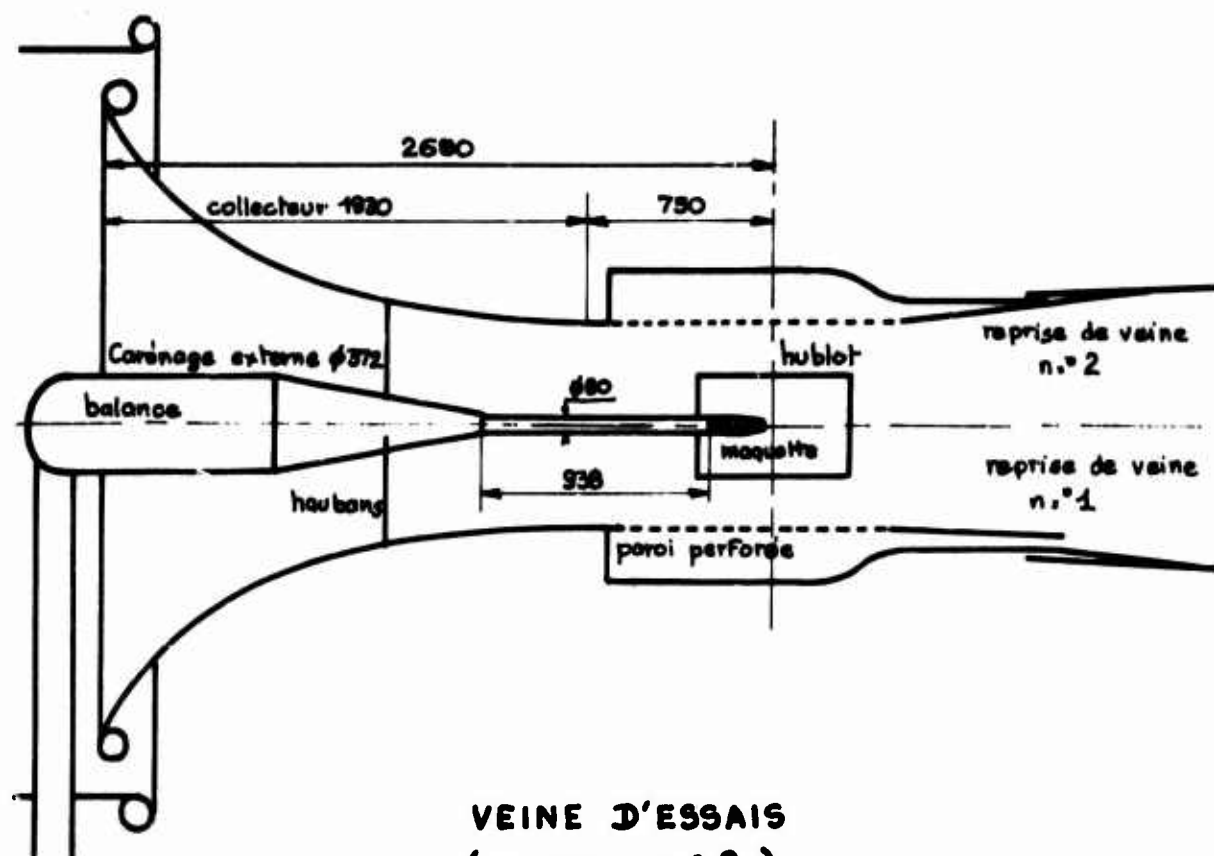
Un ensemble de mesures concernant la tuyère étalon AGARD dite "15°" a été présenté : sondages en pression et température de l'écoulement interne, coefficient de striction de la tuyère, répartitions des pressions externes pour deux valeurs de l'épaisseur initiale de la couche limite, traînées de pression du rétreint, poussées du jet et poussées nettes.

Les résultats de ces mesures pourront être comparés à ceux obtenus sur la même maquette dans d'autres souffleries, dans le cadre de l'étude de validité des essais d'arrière-corps organisée par l'AGARD.

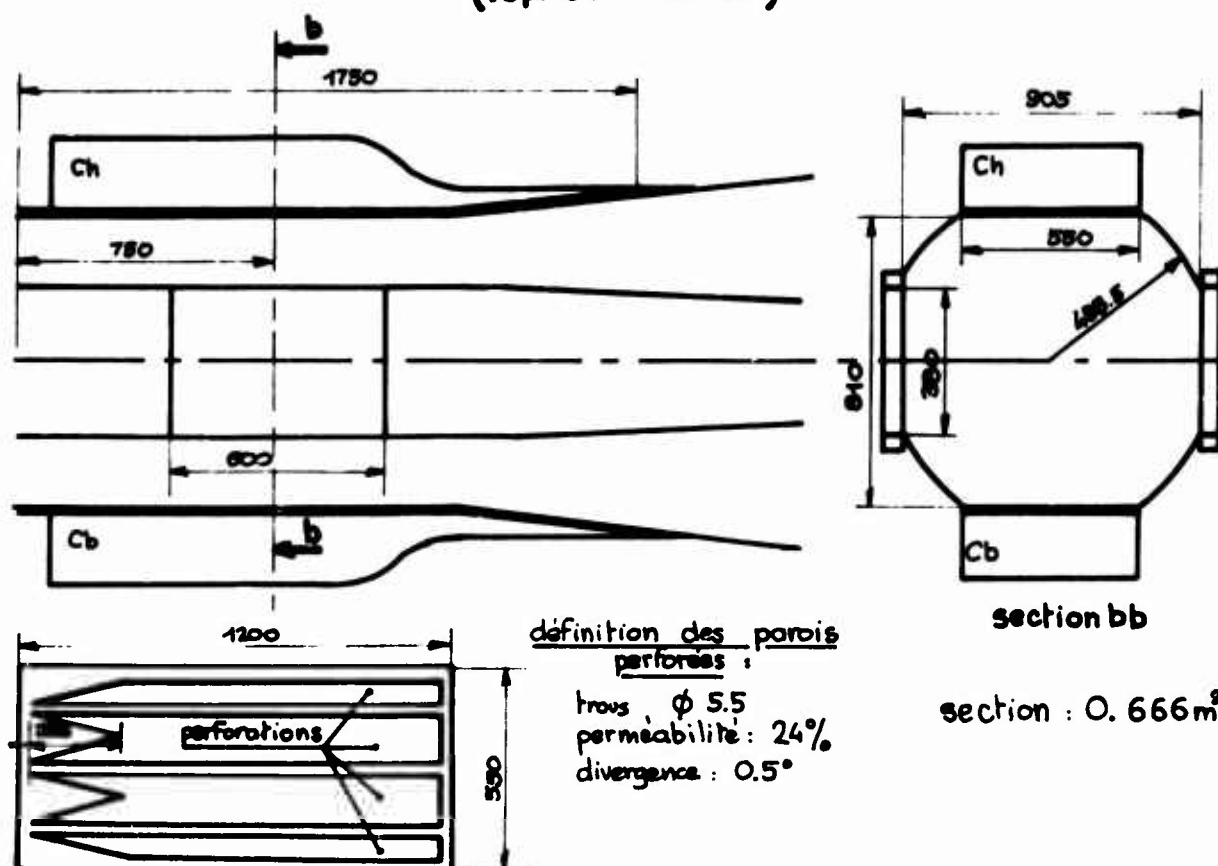
## 6. REFERENCES

1. Hardy, J.M.      *Influence du taux de détente du jet sur les coefficients de performance d'un arrière-corps monoflux AGARD de Mach 0,60 à Mach 0,95. Communication au Congrès AGARD de Rome, 3.6 September 1974.*  
Mechin, B.
2. Masure, B.      *Problèmes de mesure sur maquette de la poussée d'un arrière-corps d'avion supersonique. Tuyères de référence. AGARDograph CP - 91, 1971.*

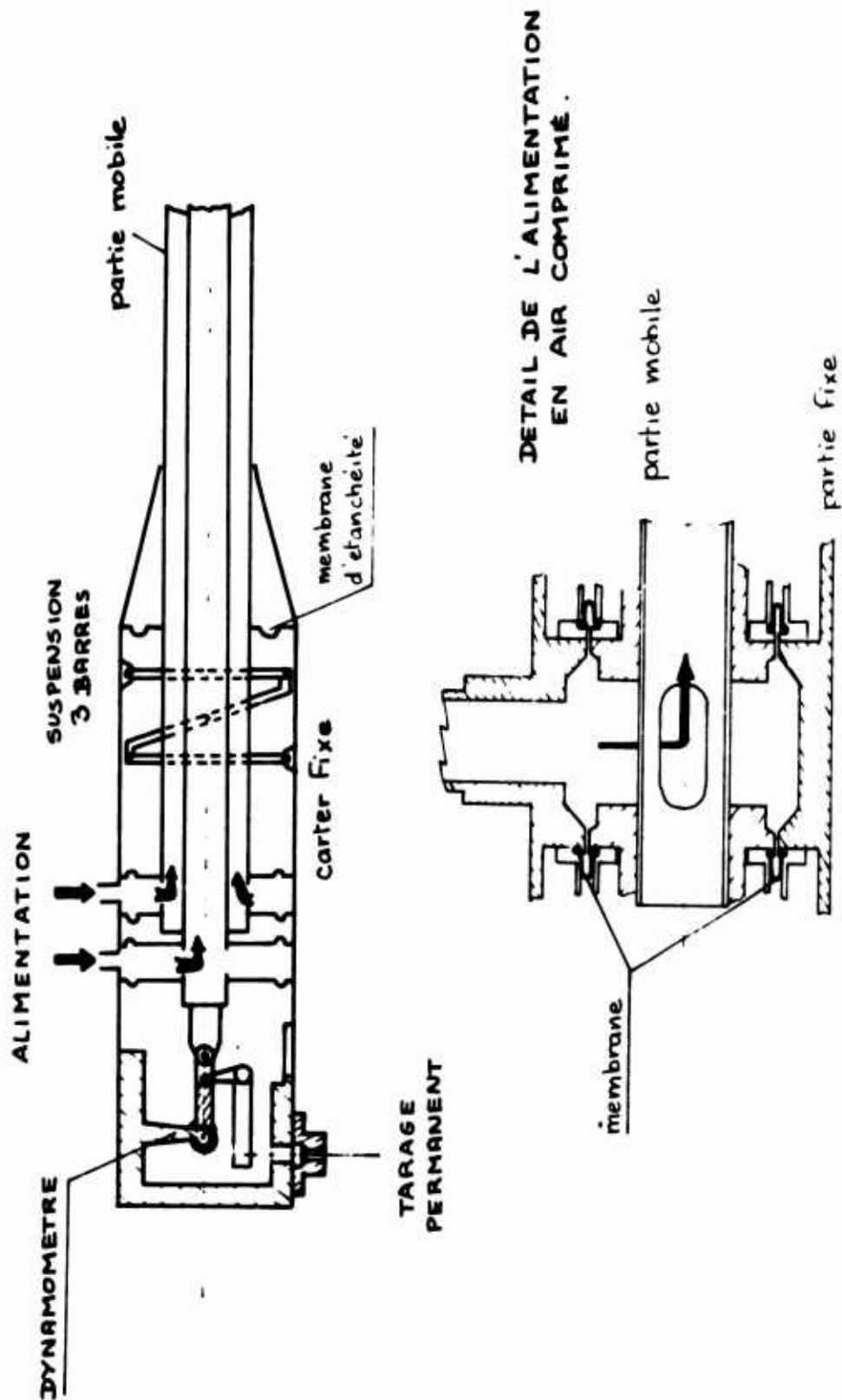




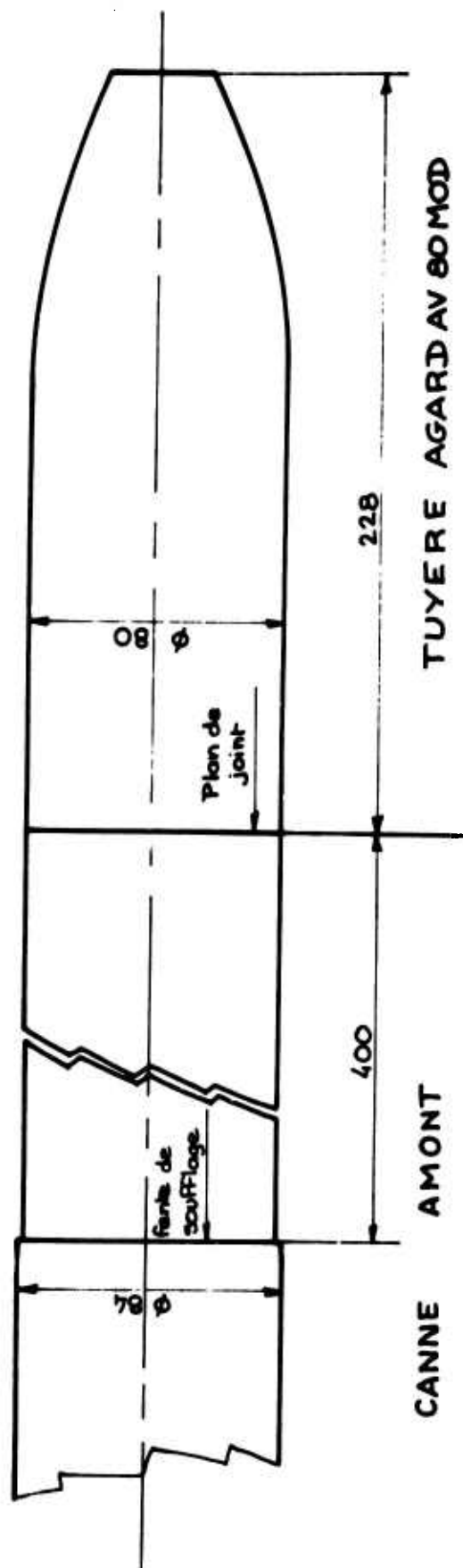
### VEINE D'ESSAIS (reprise n.° 2)



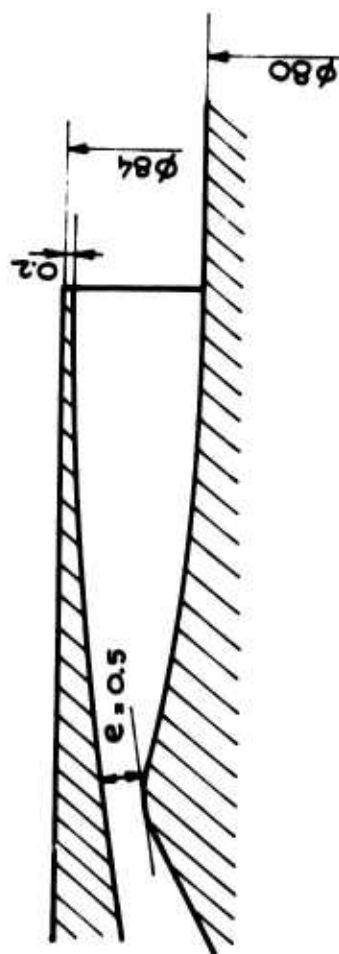
Pl.1 Montage de pesées d'arrière-corps à S3Ch — Veine d'essais



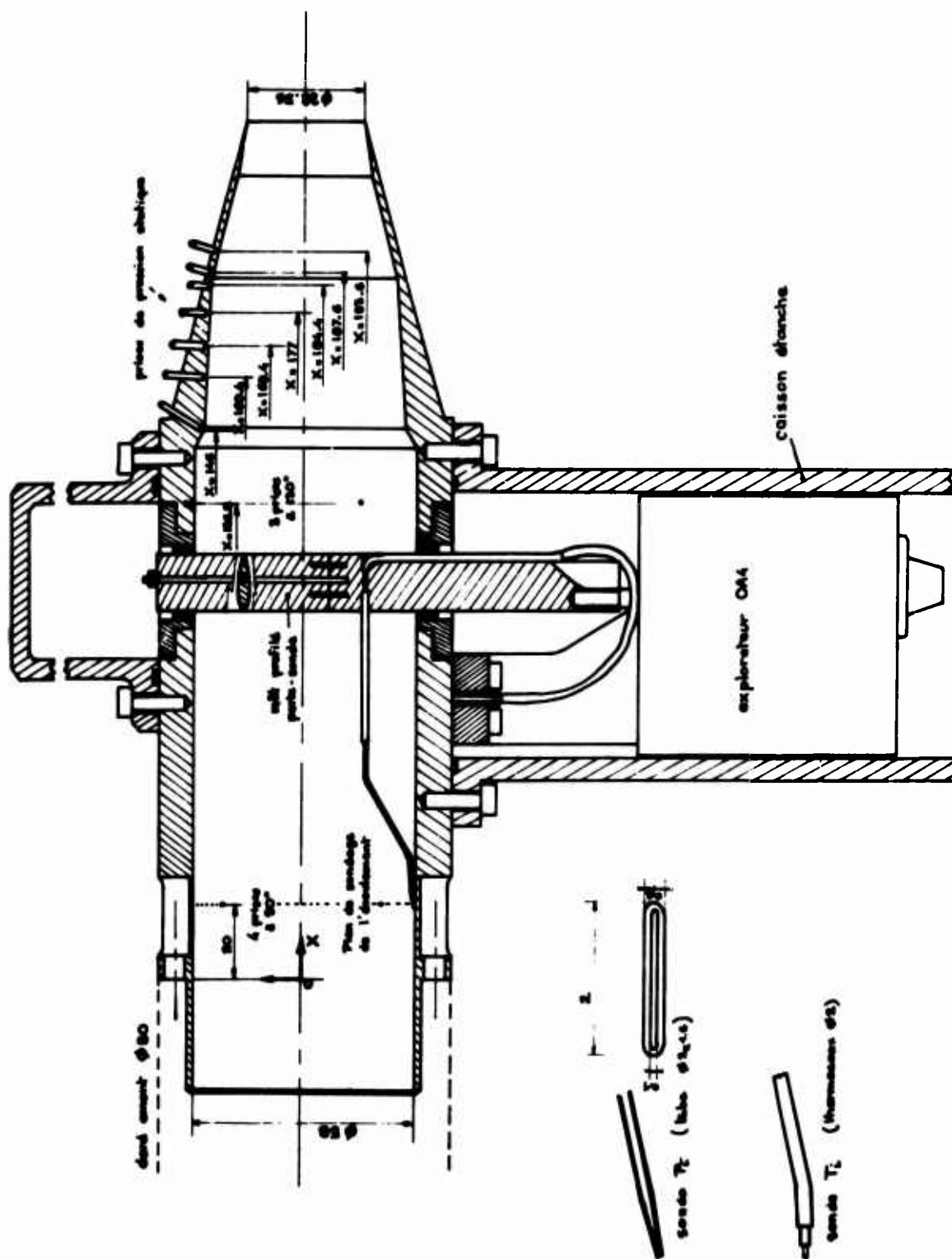
Pl.2 Schéma de la balance de poussée à S3Ch



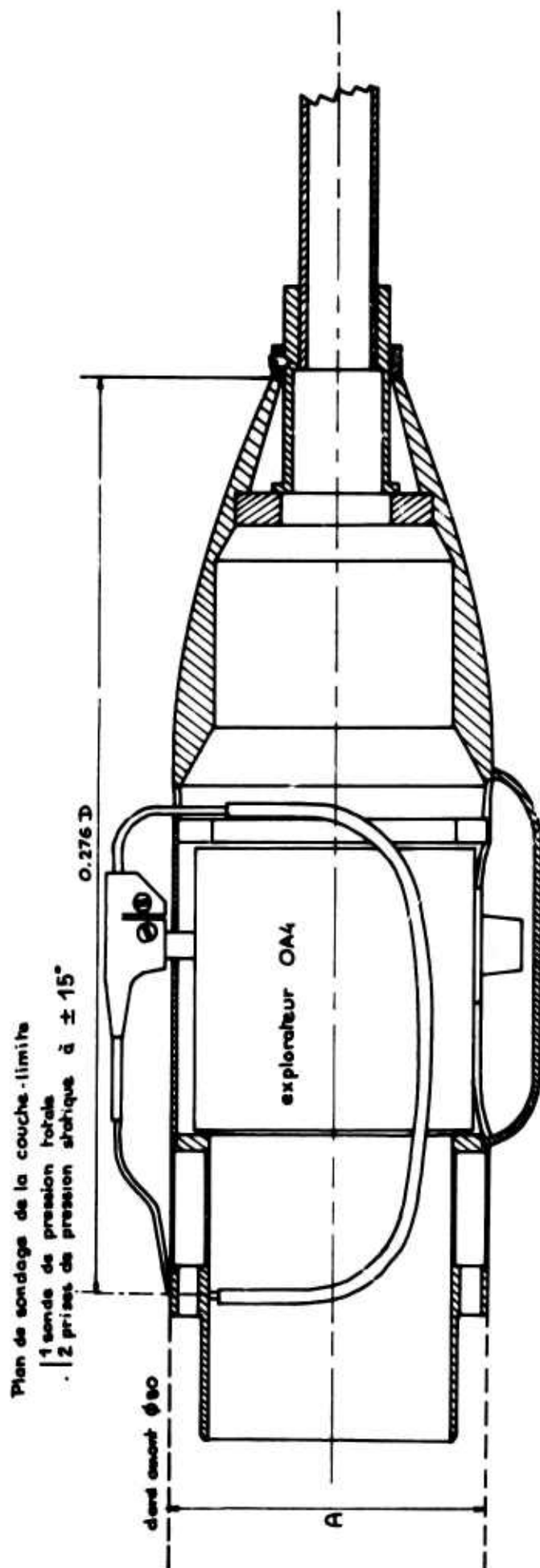
## DETAIL DE LA FENTE DE SOUFFLAGE



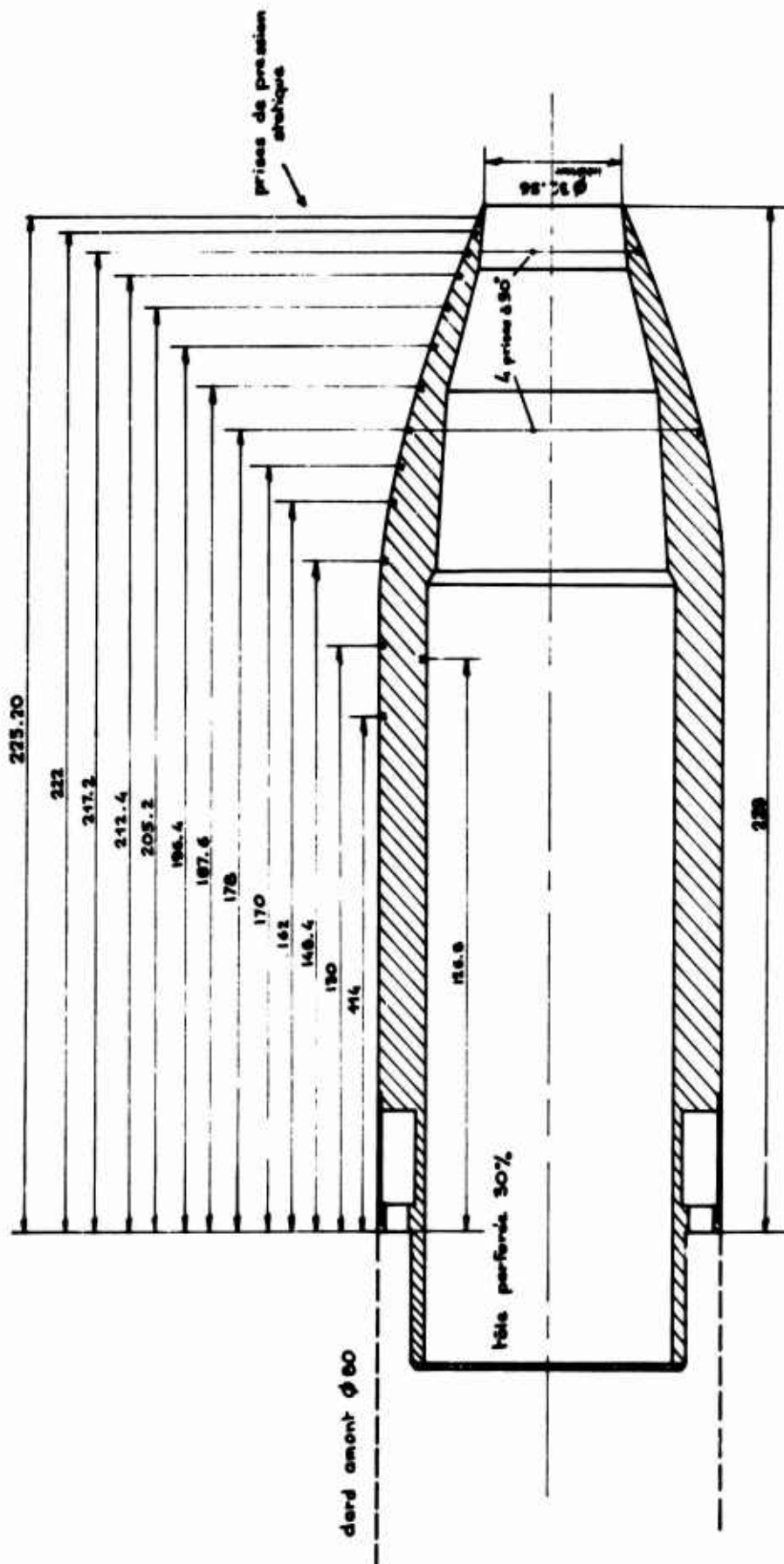
Pl.3 Tuyère AGARD AV-80-MOD — Montage avec soufflage de la couche limite



#### P1.4 Tuyère AGARD PF – 80

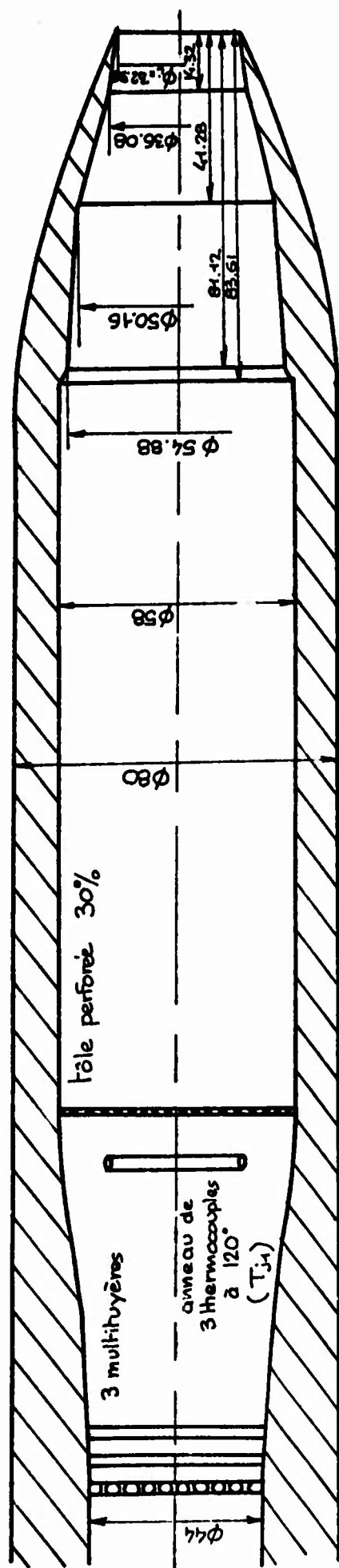


Pl.5 Tuyère AGARD VCL-80

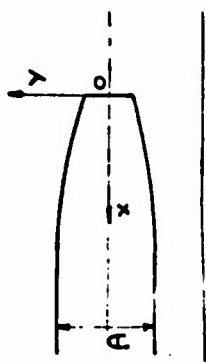


### P1.6 Tuyère AGARD AV-80-MOD

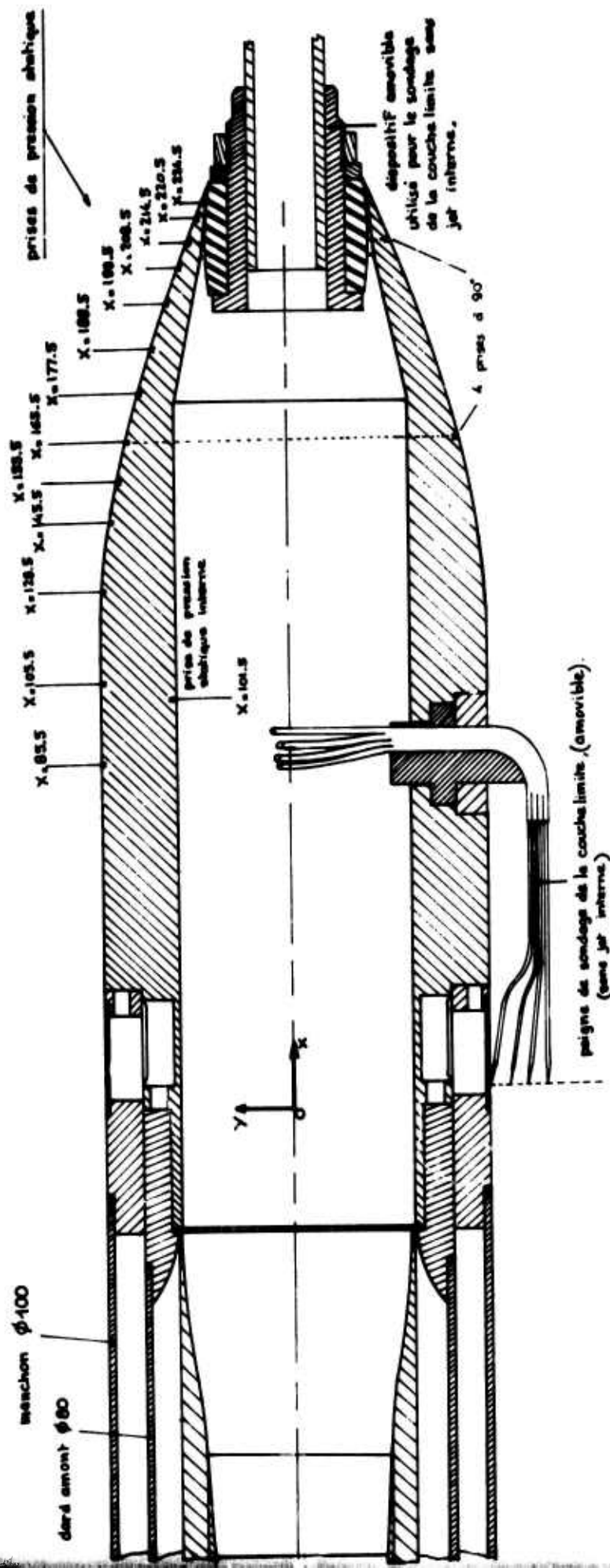




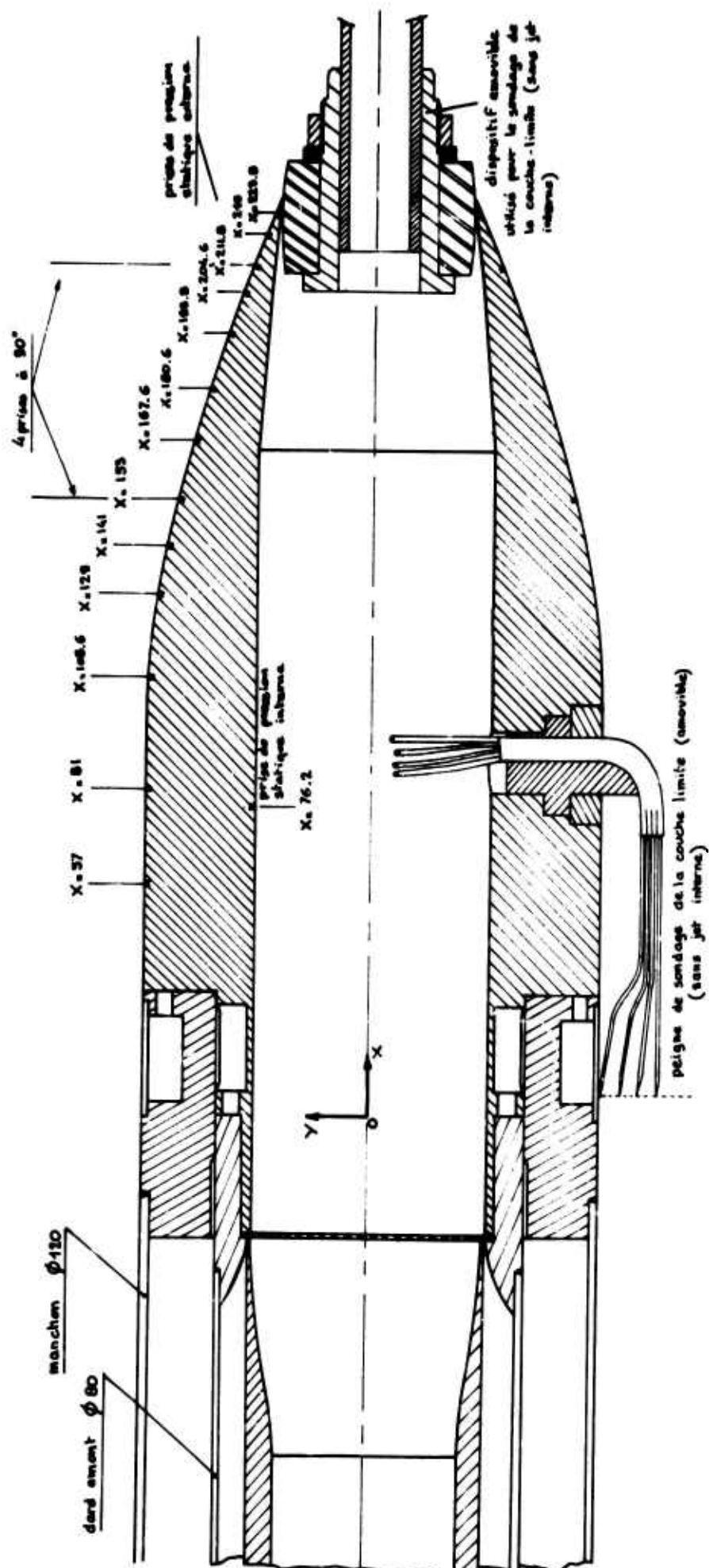
$x/D$	$X_{min}$	$Y/D$	$Y_{min}$	$X/D$	$X_{min}$	$Y/D$	$Y_{min}$
0.000	0	0.2035	16.28	0.525	42	0.4033	32.264
0.000	0	0.2075	16.60	0.550	44	0.4108	32.864
0.025	2	0.2155	17.24	0.575	46	0.4178	33.424
0.050	4	0.2245	17.96	0.600	48	0.4248	33.984
0.075	6	0.2347	18.78	0.625	50	0.4317	34.504
0.100	8	0.2457	19.66	0.650	52	0.4375	35.00
0.125	10	0.2568	20.544	0.675	54	0.4435	35.48
0.150	12	0.2678	21.424	0.700	56	0.4490	35.92
0.175	14	0.2788	22.304	0.725	58	0.4543	36.344
0.200	16	0.2888	23.104	0.750	60	0.4595	36.76
0.225	18	0.2998	23.904	0.775	62	0.4645	37.16
0.250	20	0.3085	24.680	0.800	64	0.4695	37.56
0.275	22	0.3180	25.44	0.825	66	0.4743	37.944
0.300	24	0.3275	26.20	0.850	68	0.4788	38.304
0.325	26	0.3368	26.944	0.875	70	0.4828	38.624
0.350	28	0.3458	27.664	0.900	72	0.4863	38.904
0.375	30	0.3545	28.360	0.925	74	0.4898	39.184
0.400	32	0.3630	29.04	0.950	76	0.4928	39.424
0.425	34	0.3718	29.744	0.975	78	0.4953	39.624
0.450	36	0.3800	30.40	1.000	80	0.4978	39.824
0.475	38	0.3880	31.04	1.025	82	0.4990	39.920
0.500	40	0.3958	31.664	1.050	84	0.5000	40.000



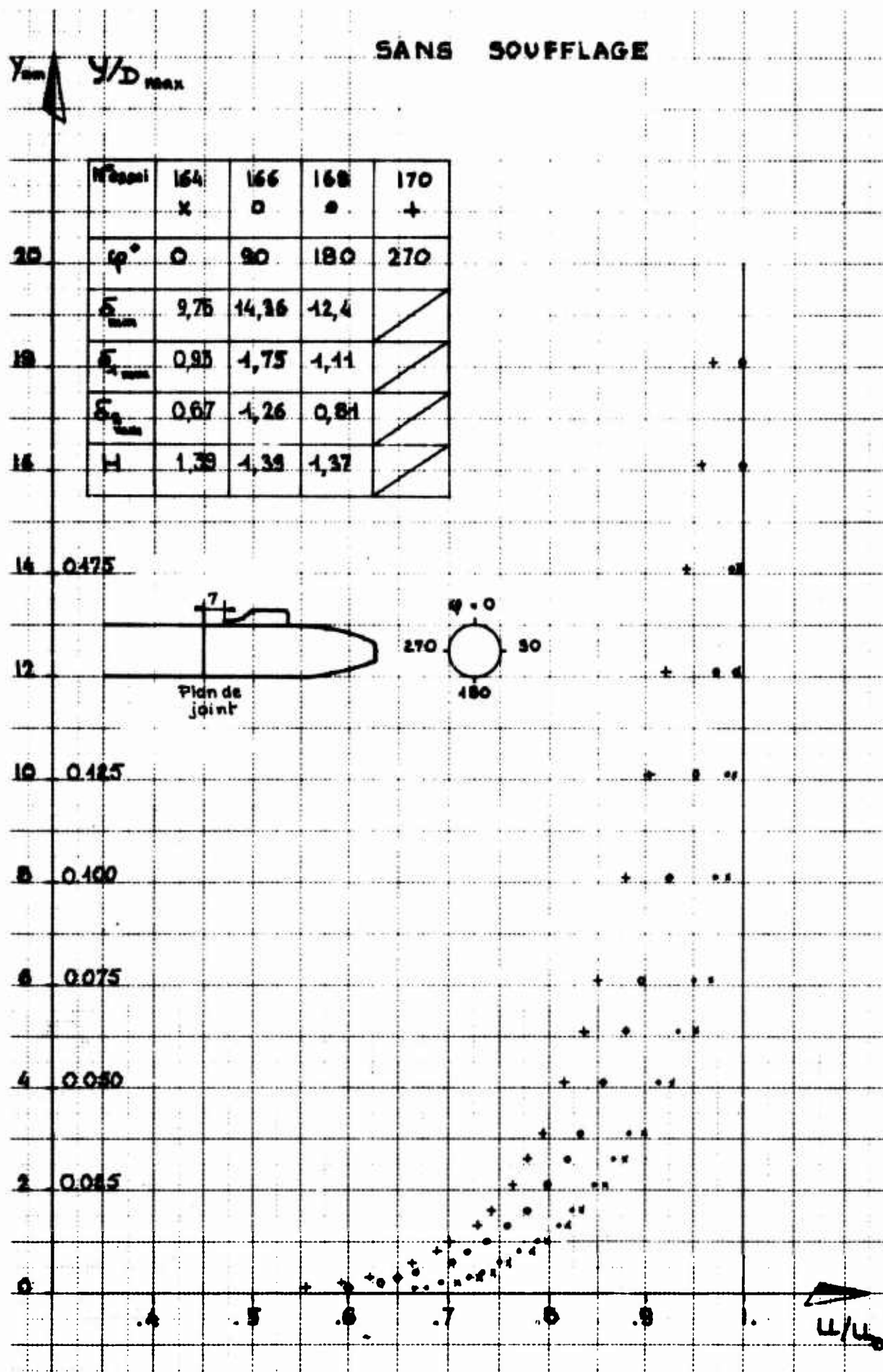
Pl.7 Tuyère AGARD AV-80-MOD - Canal interne



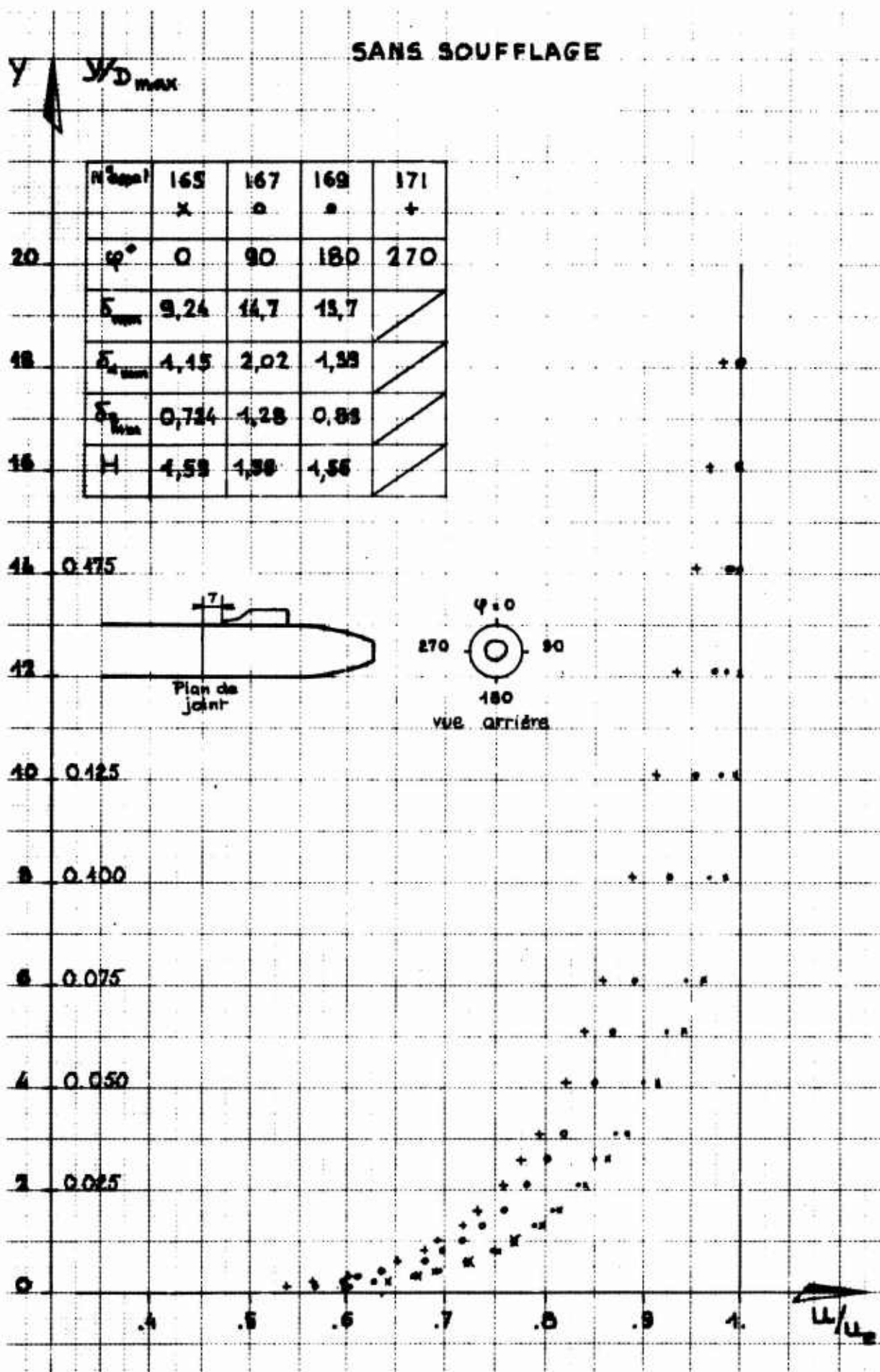
Pl.8 Tuyère AGARD AV-100

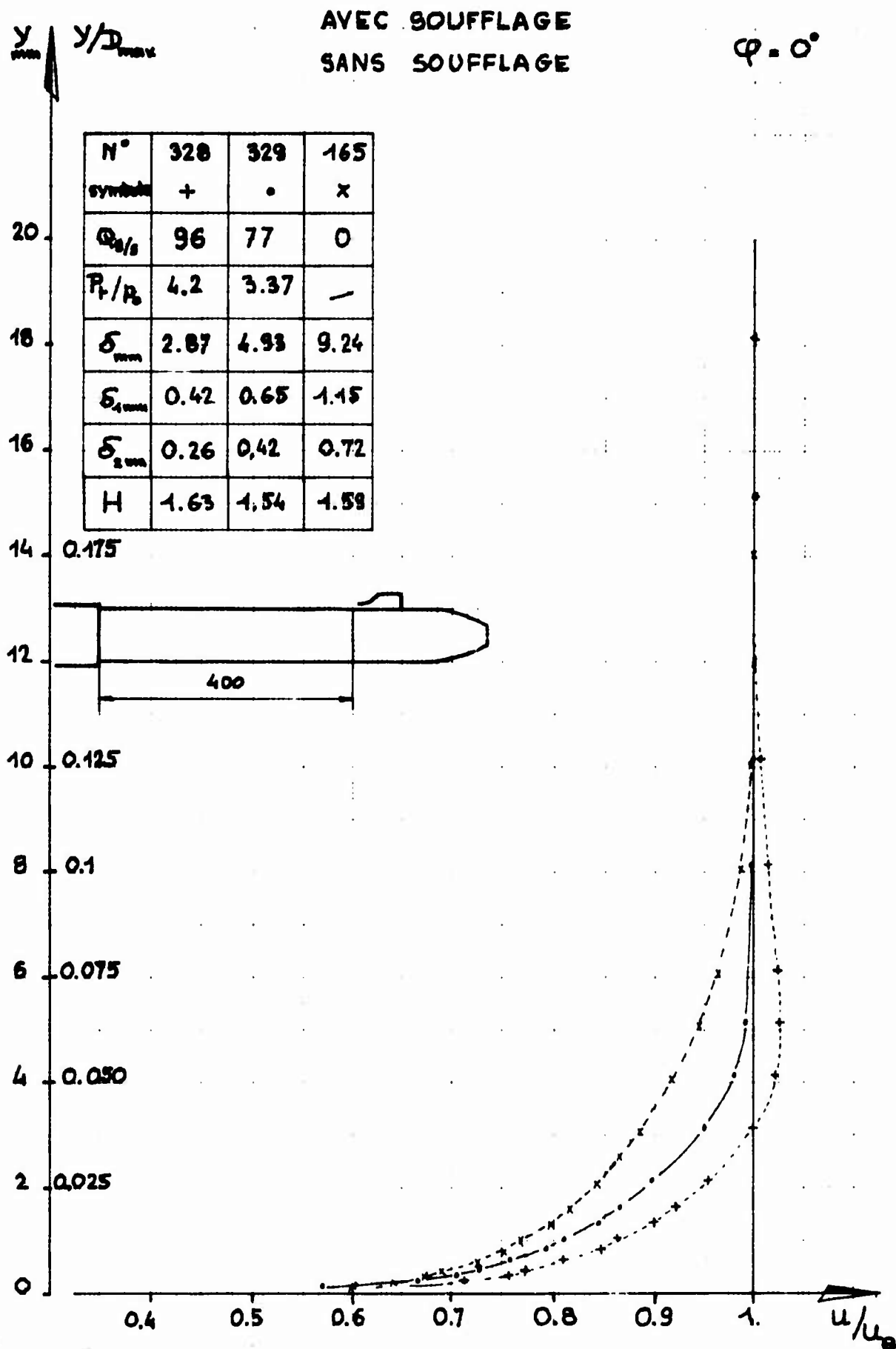


Pl.9 Tuyère AGARD AV-120

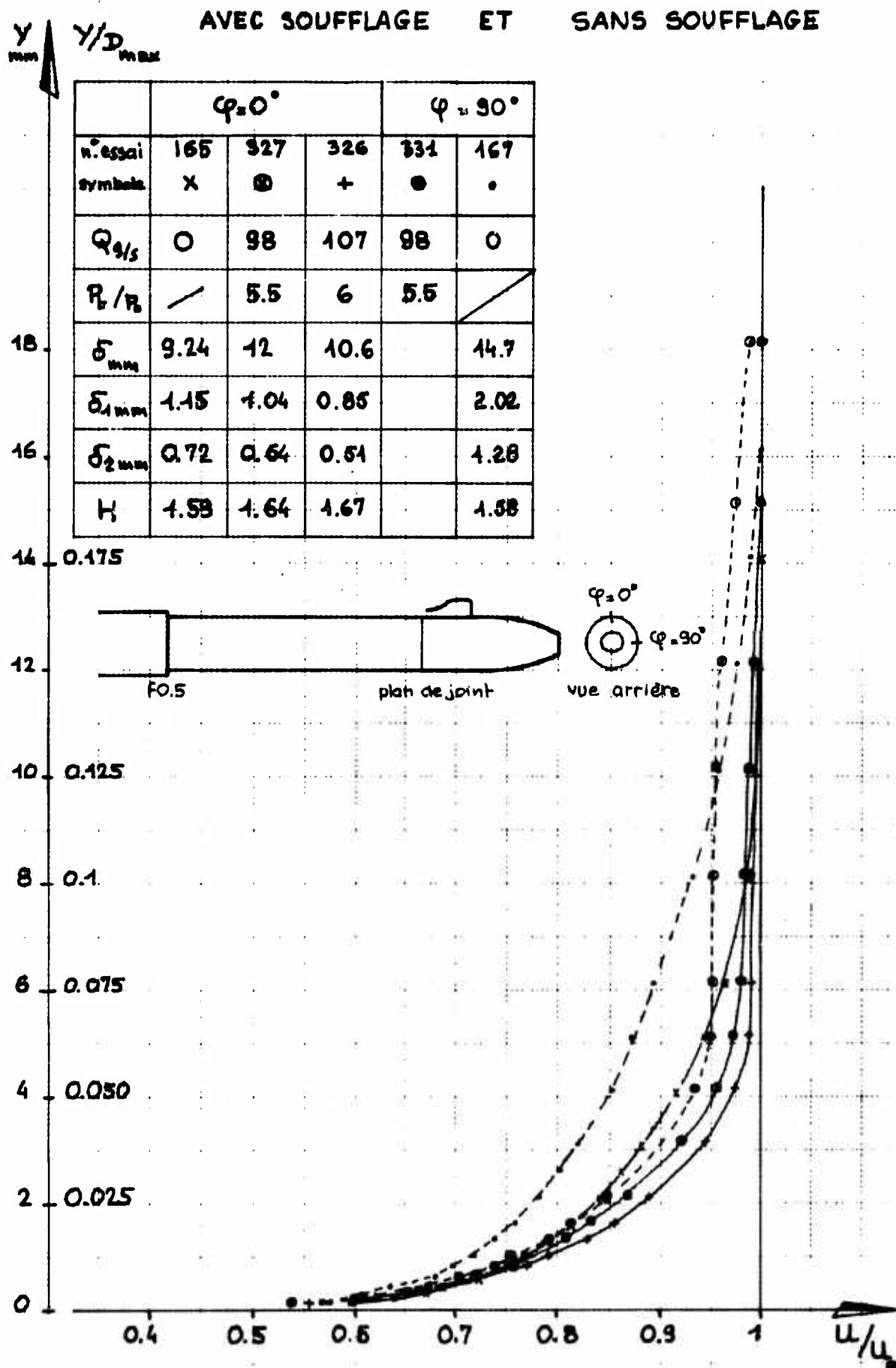
Pl.10 Couche limite sur la canne  $\phi$  80 à  $M_0 = 0,6$  - sans soufflage

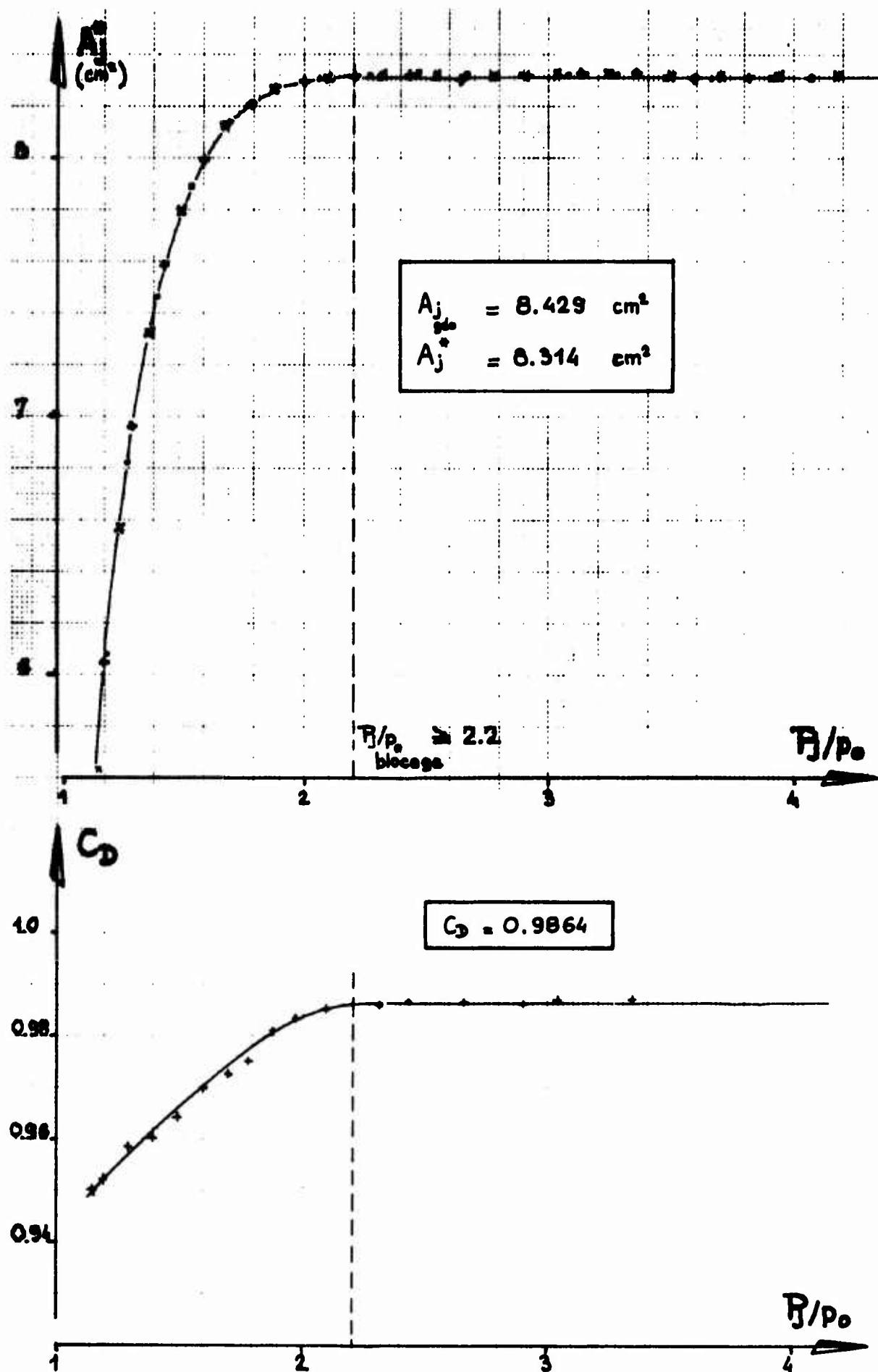
## SANS SOUFFLAGE

Pl.11 Couche limite sur la canne  $\phi 80$  à  $M_0 = 0,9$  -- sans soufflage

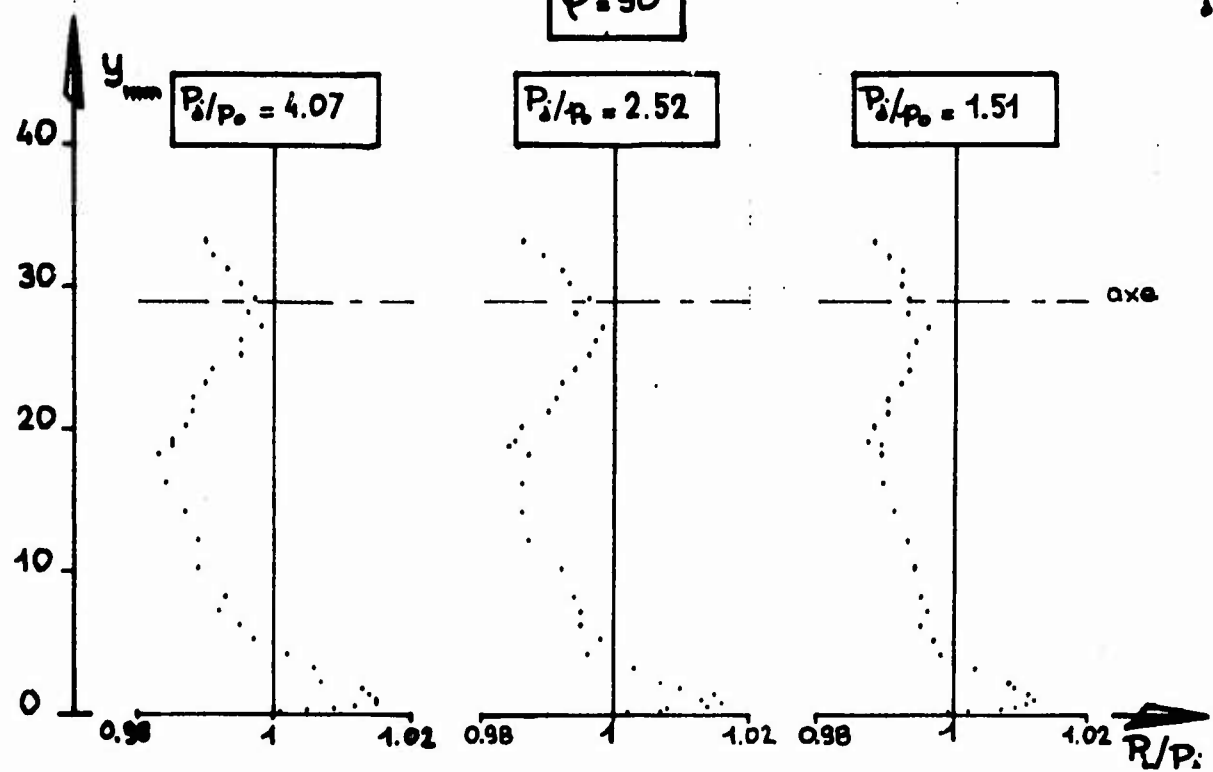
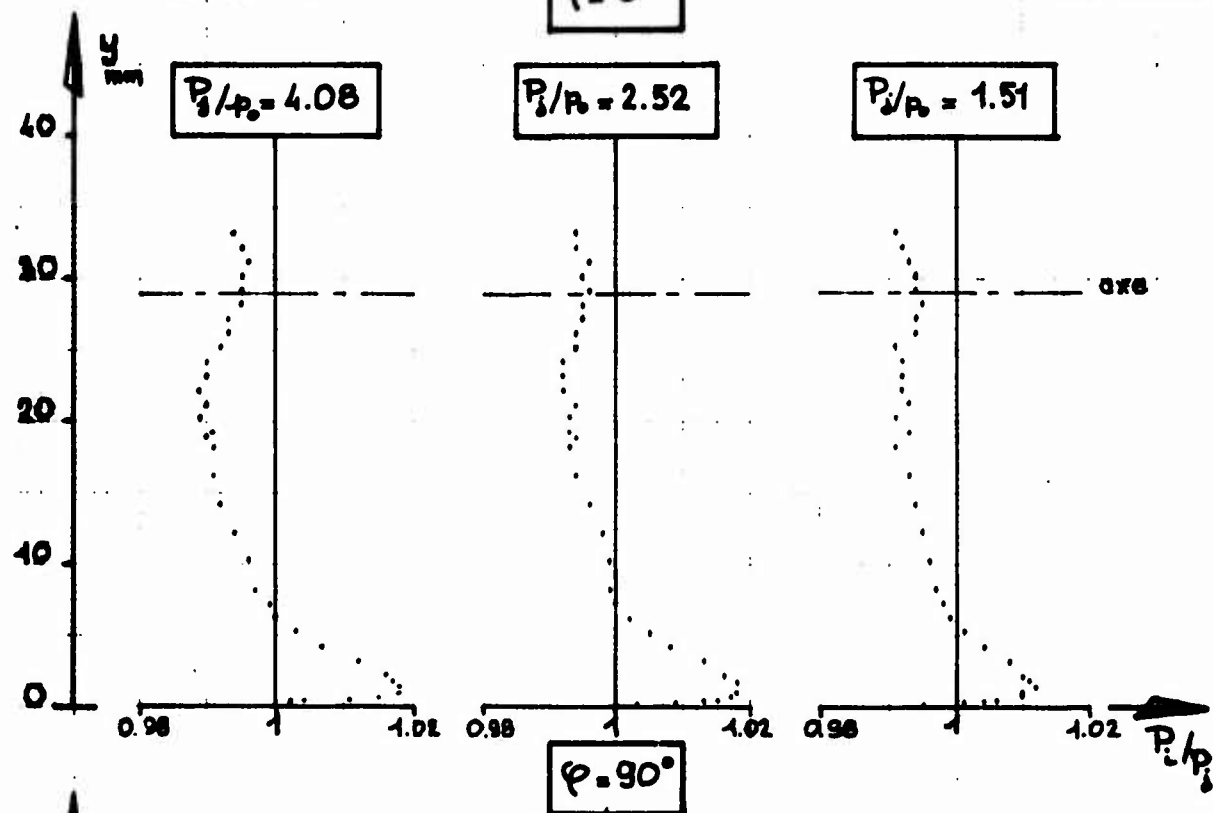
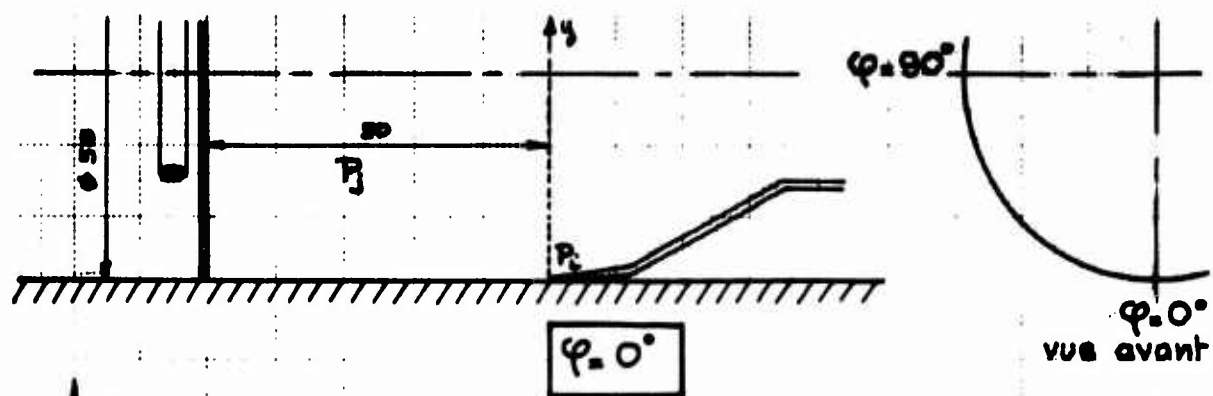
Pl.12 Couche limite sur la canne  $\phi 80$  à  $M_0 = 0,6$  et  $\varphi = 0^\circ$



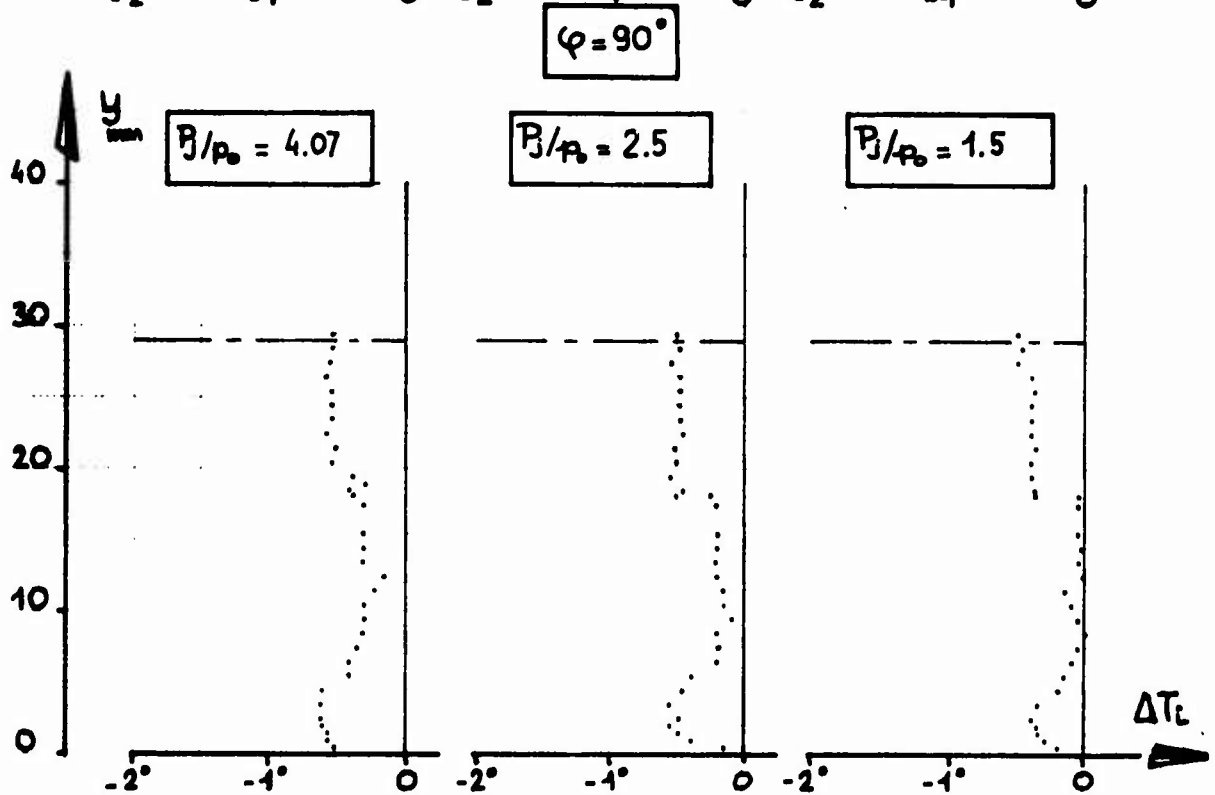
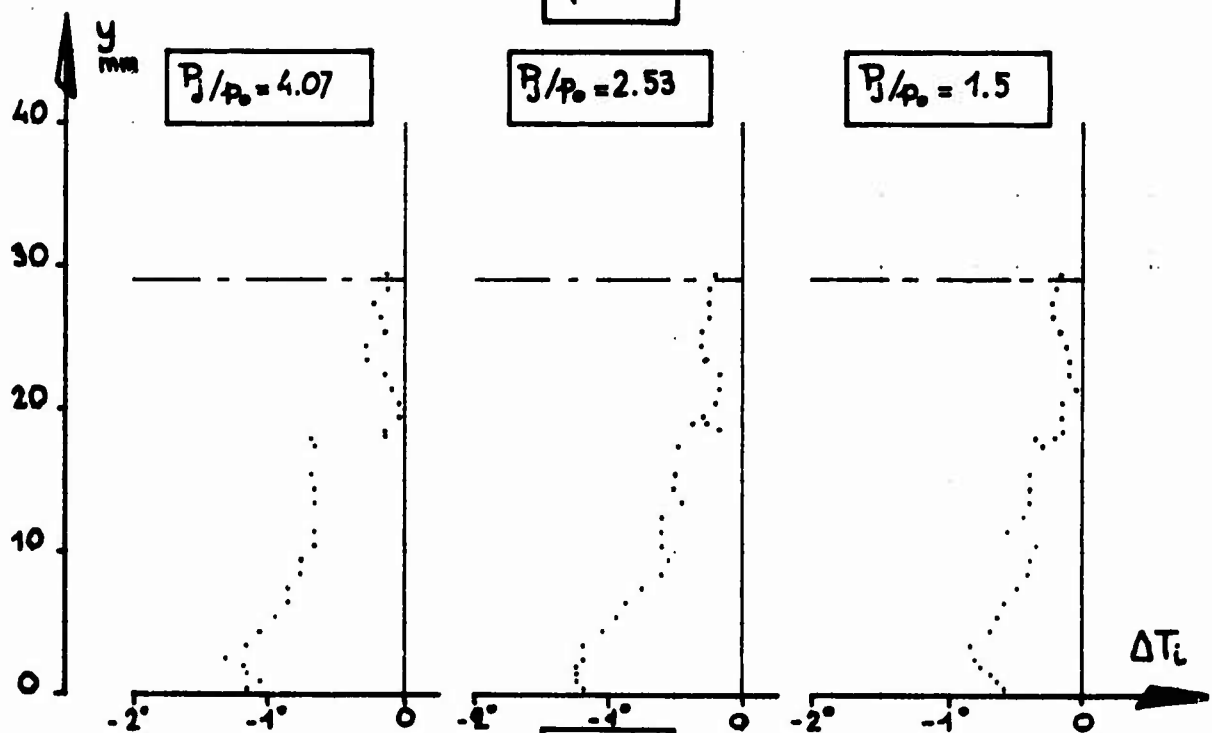
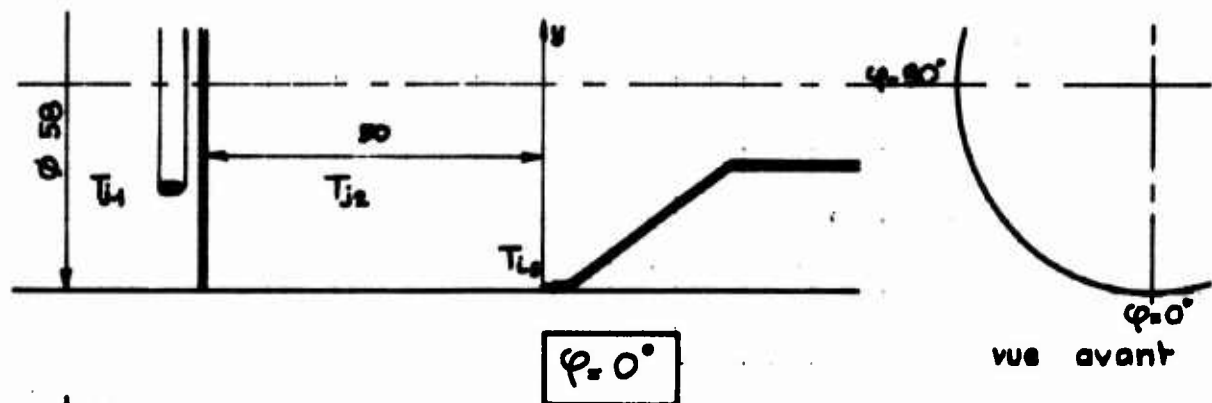
Pl.13 Couche limite sur la canne  $\phi 80$  à  $M_0 = 0,90$  et  $\varphi = 0^\circ$  et  $90^\circ$



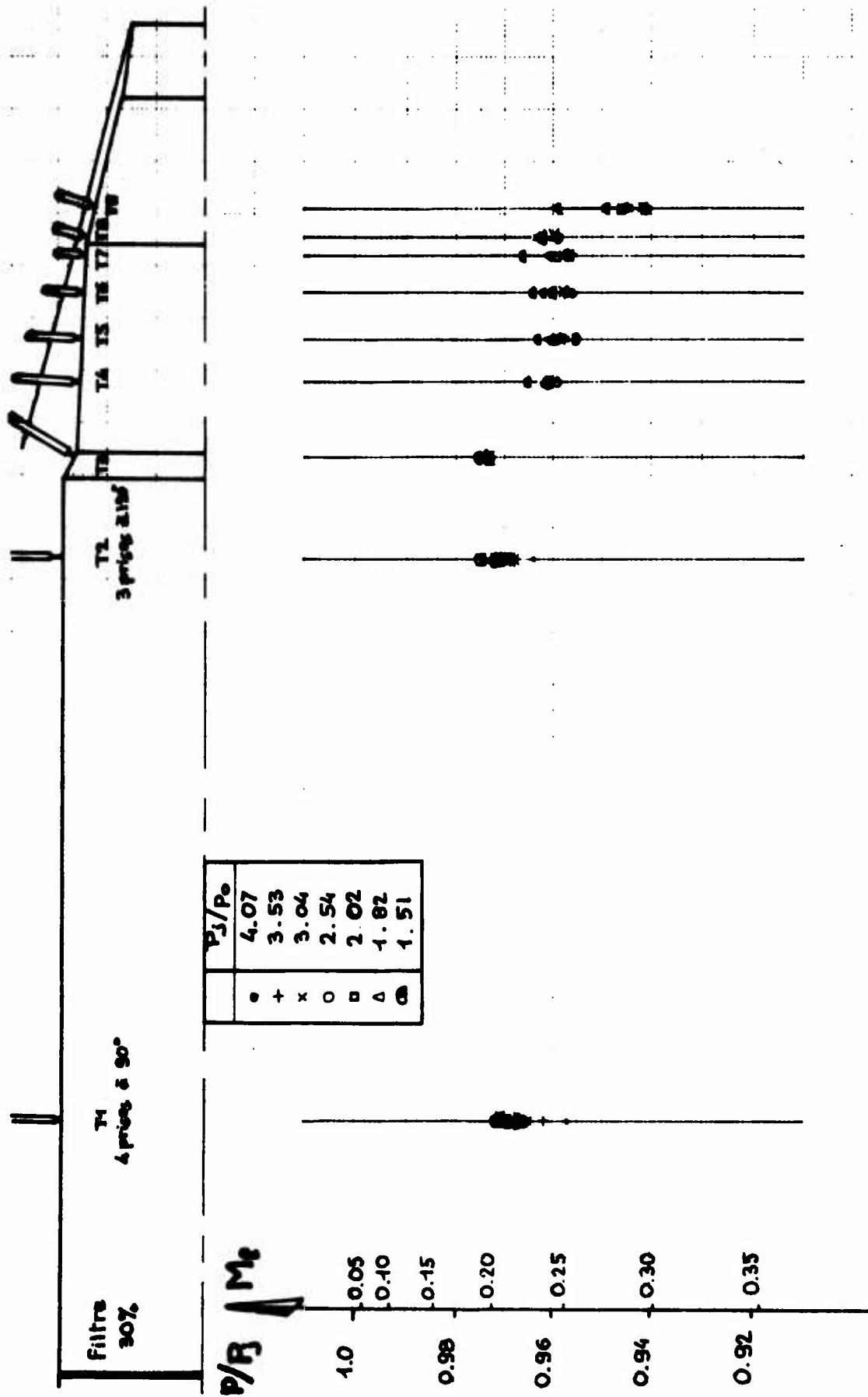
Pl.14 Tuyère AGARD AV-80-MOD – Striction



Pl.15 Sondages en pression totale du flux interne



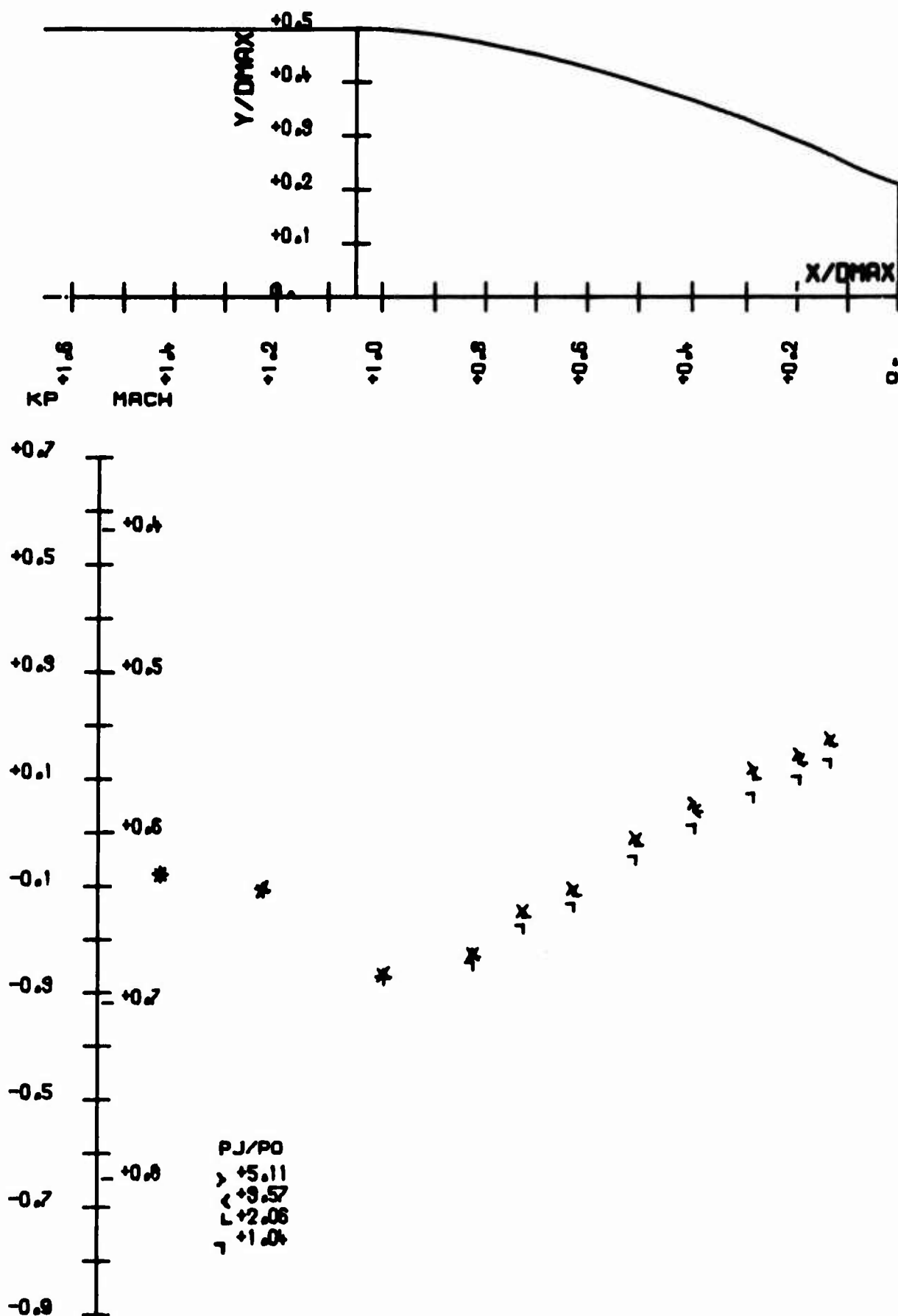
Pl.16 Sondages en température totale du flux interne



Pl.17 AGARD PF-80 — Pressions statiques internes

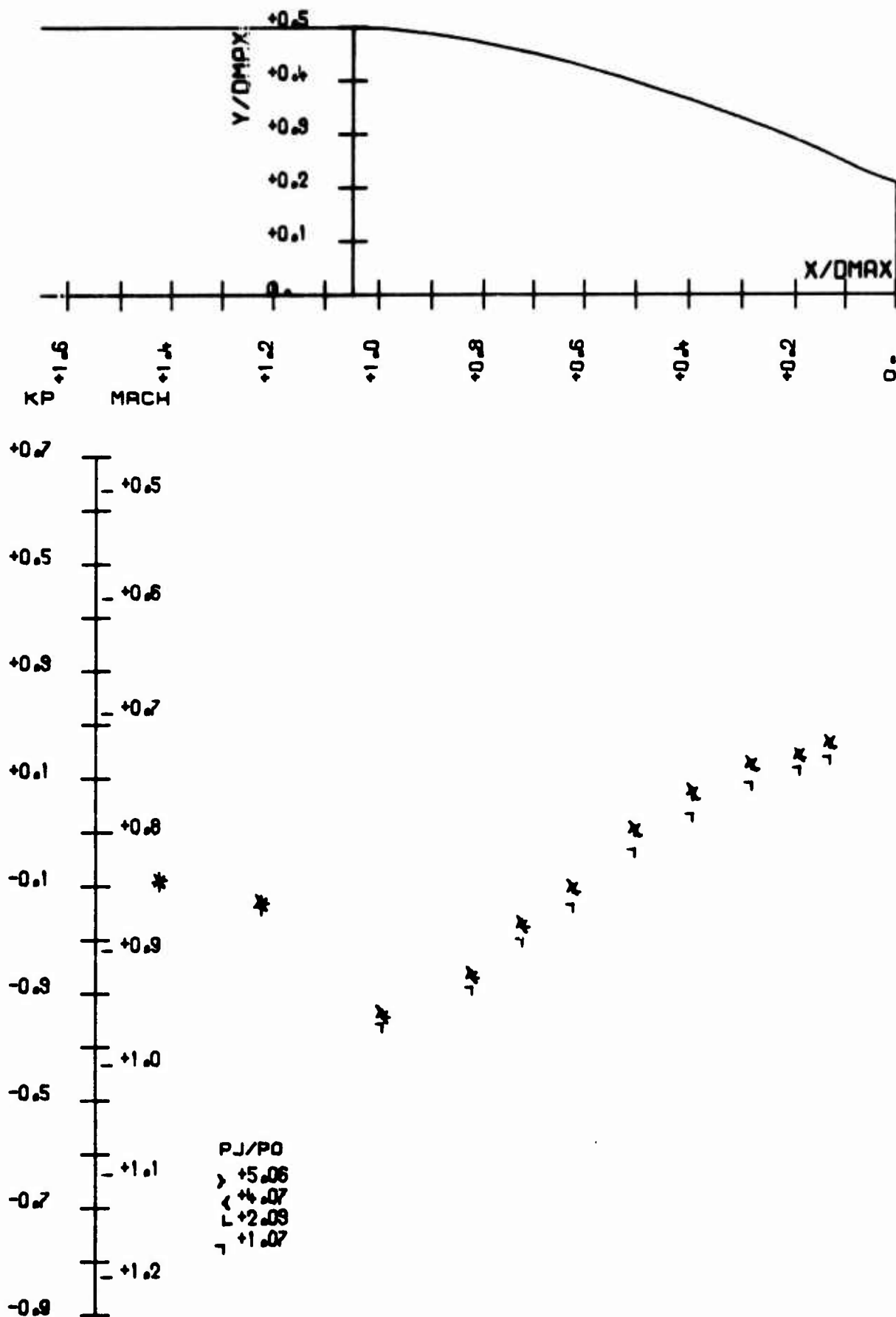
ESSAI NO 284

SANS SOUFFLAGE

Pl.18 Tuyère AGARD  $\phi$  80 MOD - sans soufflage -  $M_0 = 0,60$

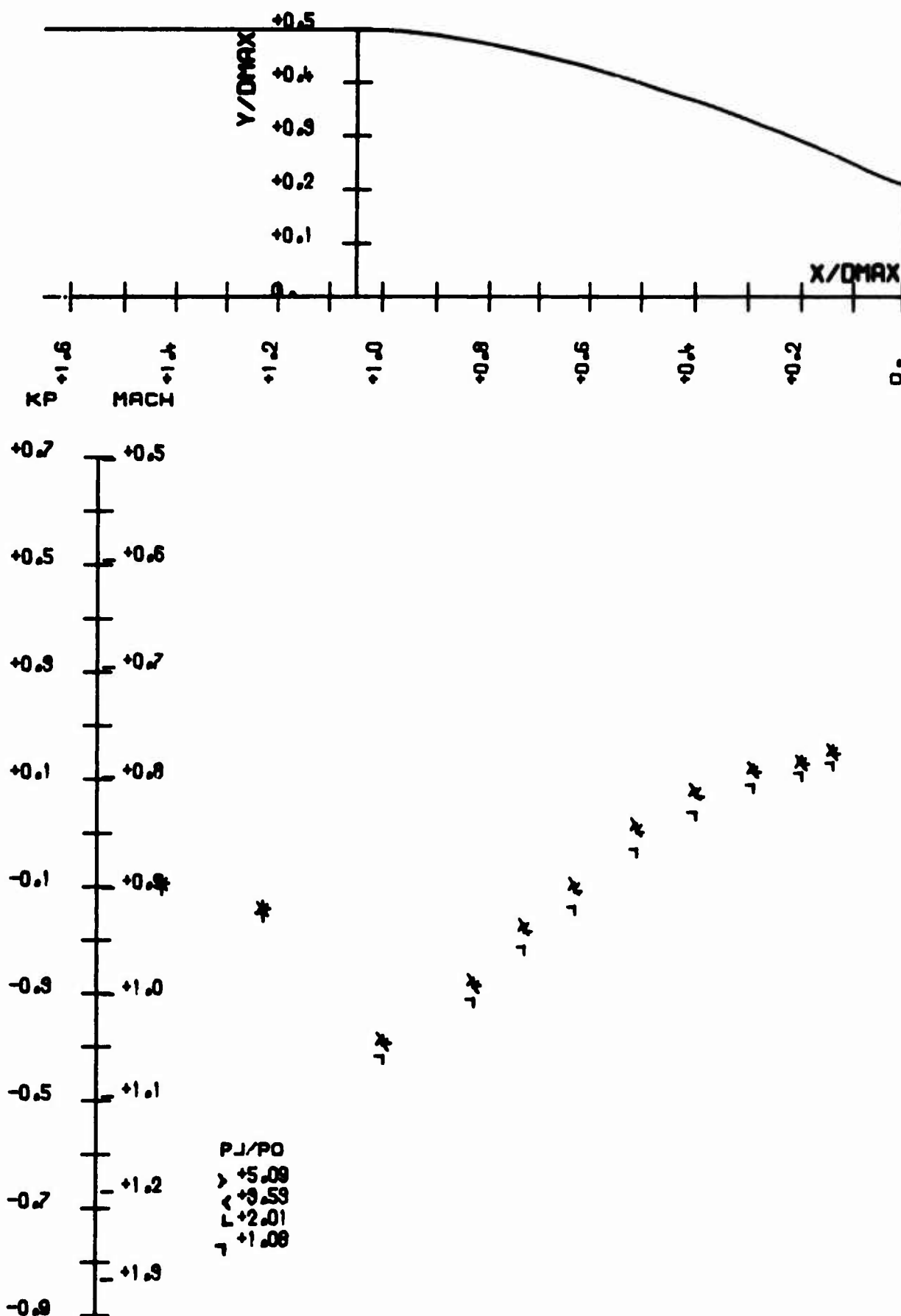
ESSAI NO 295

SANS SOUFFLAGE

Pl.19 Tuyère AGARD  $\phi$  80 MOD - sans soufflage -  $M_0 = 0,80$

ESSAI NO 298

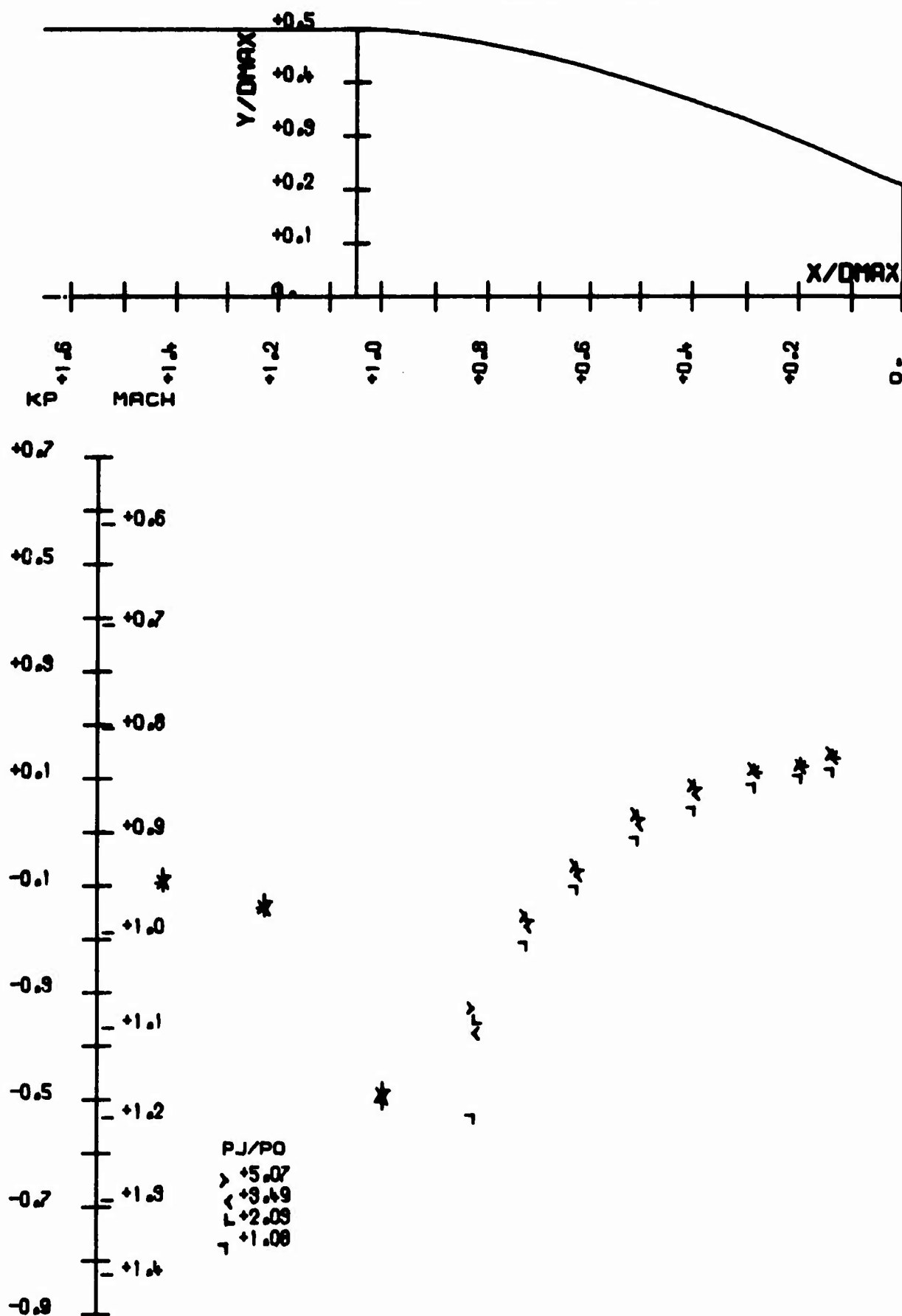
SANS SOUFFLAGE

Pl.20 Tuyère AGARD  $\phi$  80 MOD — sans soufflage —  $M_0 = 0,85$



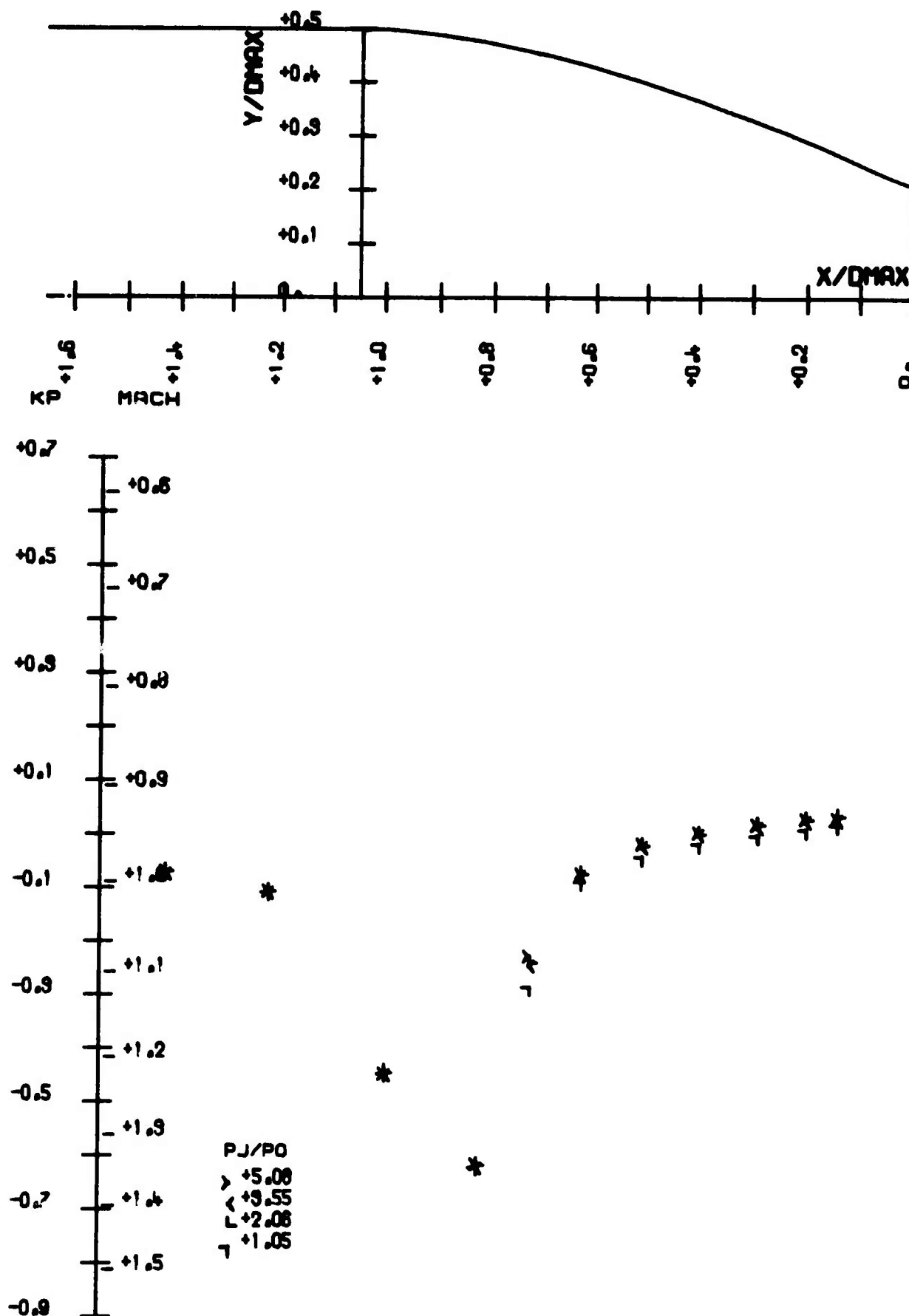
ESSAI NO 287

SANS SOUFFLAGE

Pl.21 Tuyère AGARD  $\phi$  80 MOD — sans soufflage —  $M_0 = 0.90$

ESSAI NO 280

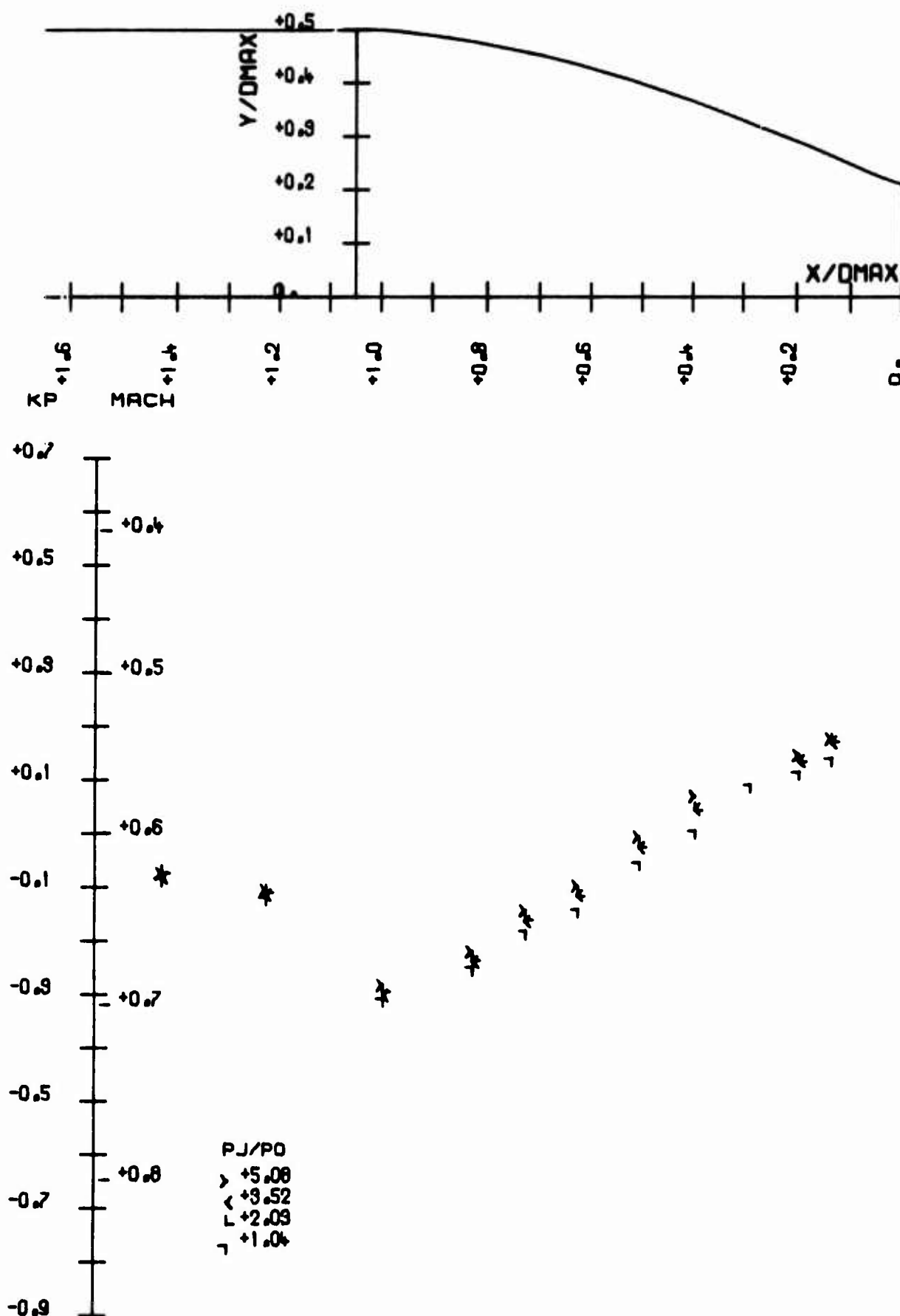
SANS SOUFFLAGE

Pl.22 Tuyère AGARD  $\phi$  80 MOD - sans soufflage -  $M_0 = 0,95$

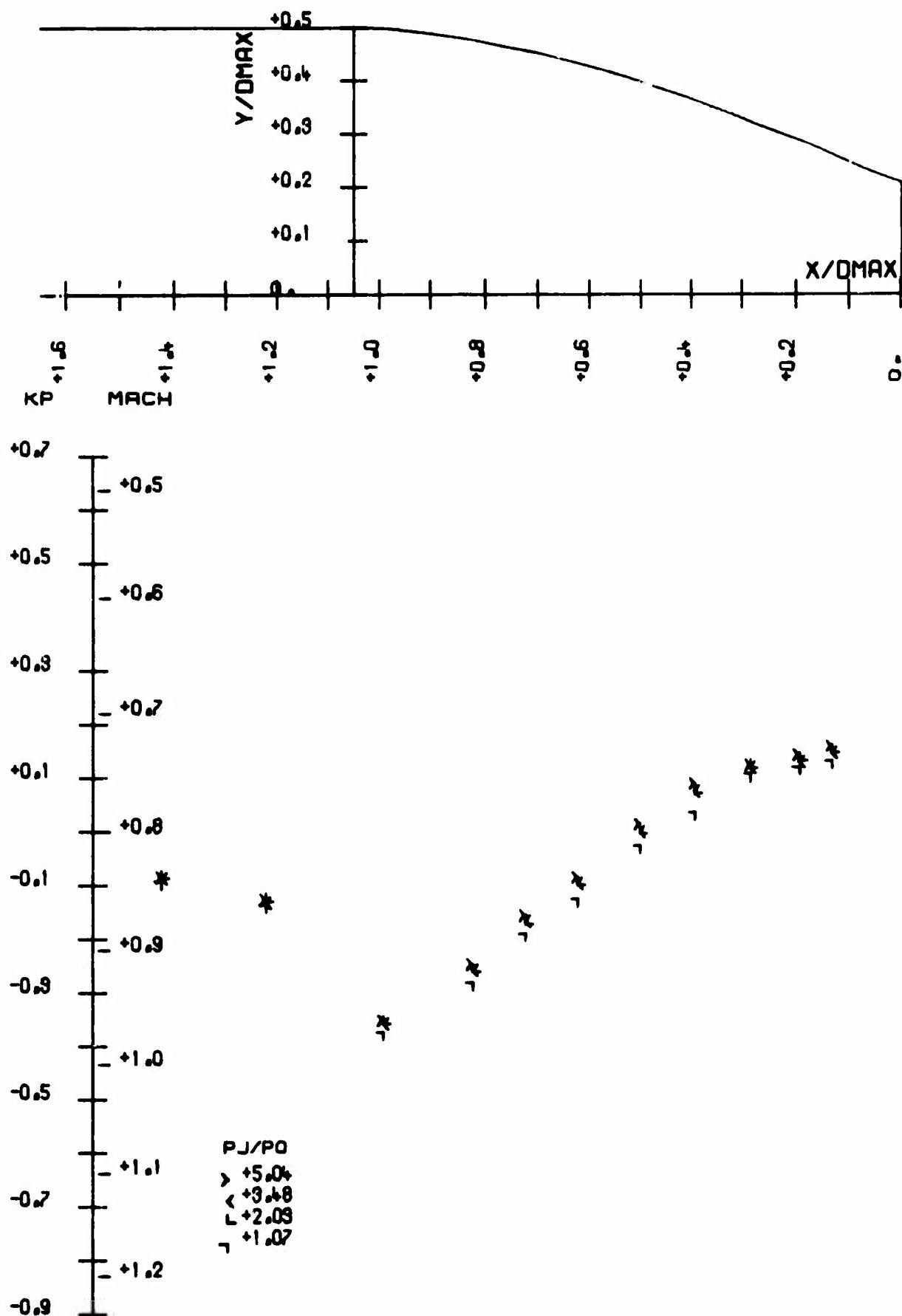
ESSAI NO 33

AVEC SOUFFLAGE

$$P_b/P_0 = 3.5$$

Pl.23 Tuyère AGARD Ø 80 MOD — avec soufflage —  $M_0 = 0,60$

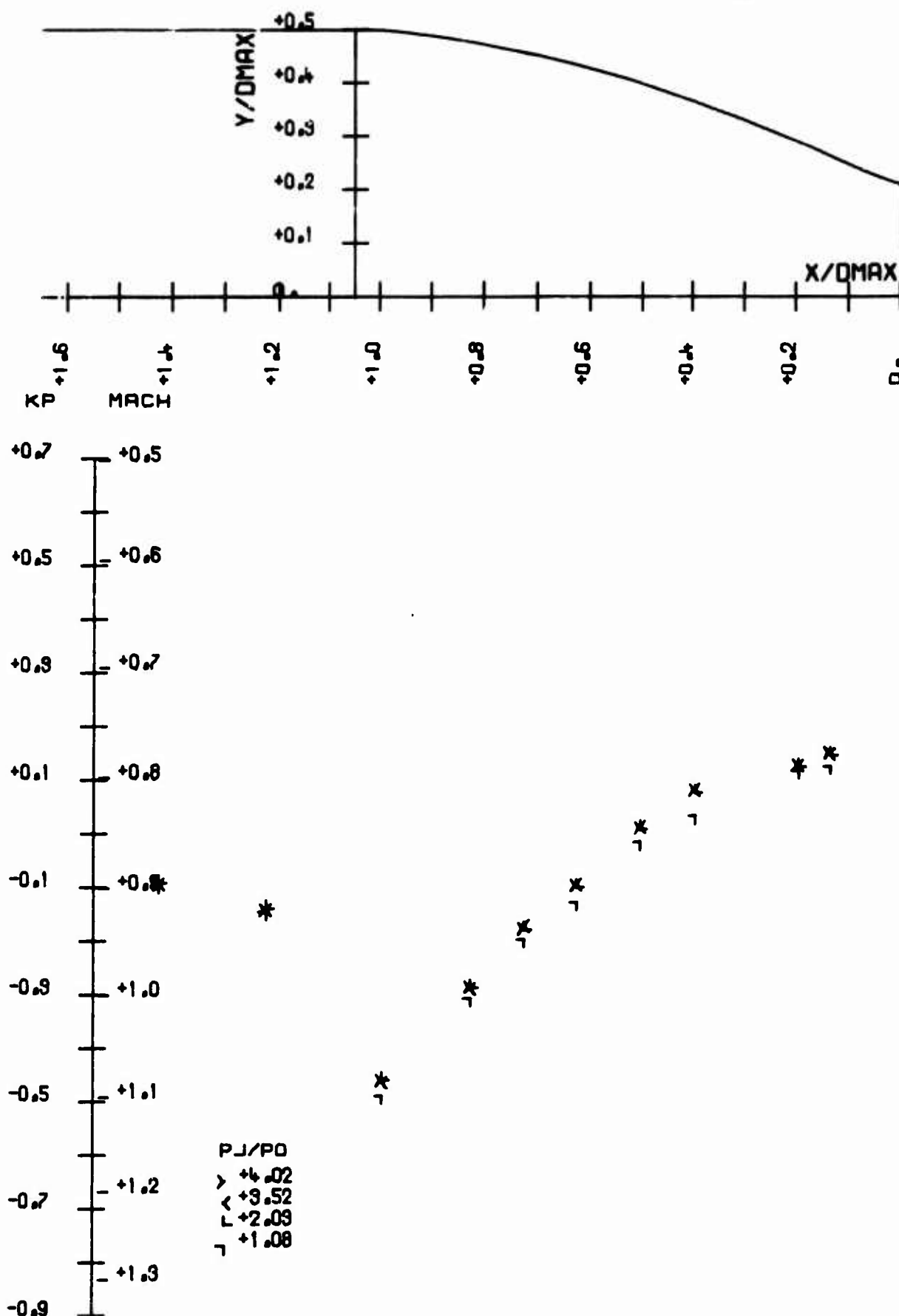
ESSAI NO 998

AVEC SOUFFLAGE  $P_t/p_o = 4.2$ Pl.24 Tuyère AGARD  $\phi$  80 MOD — avec soufflage —  $M_o = 0.80$

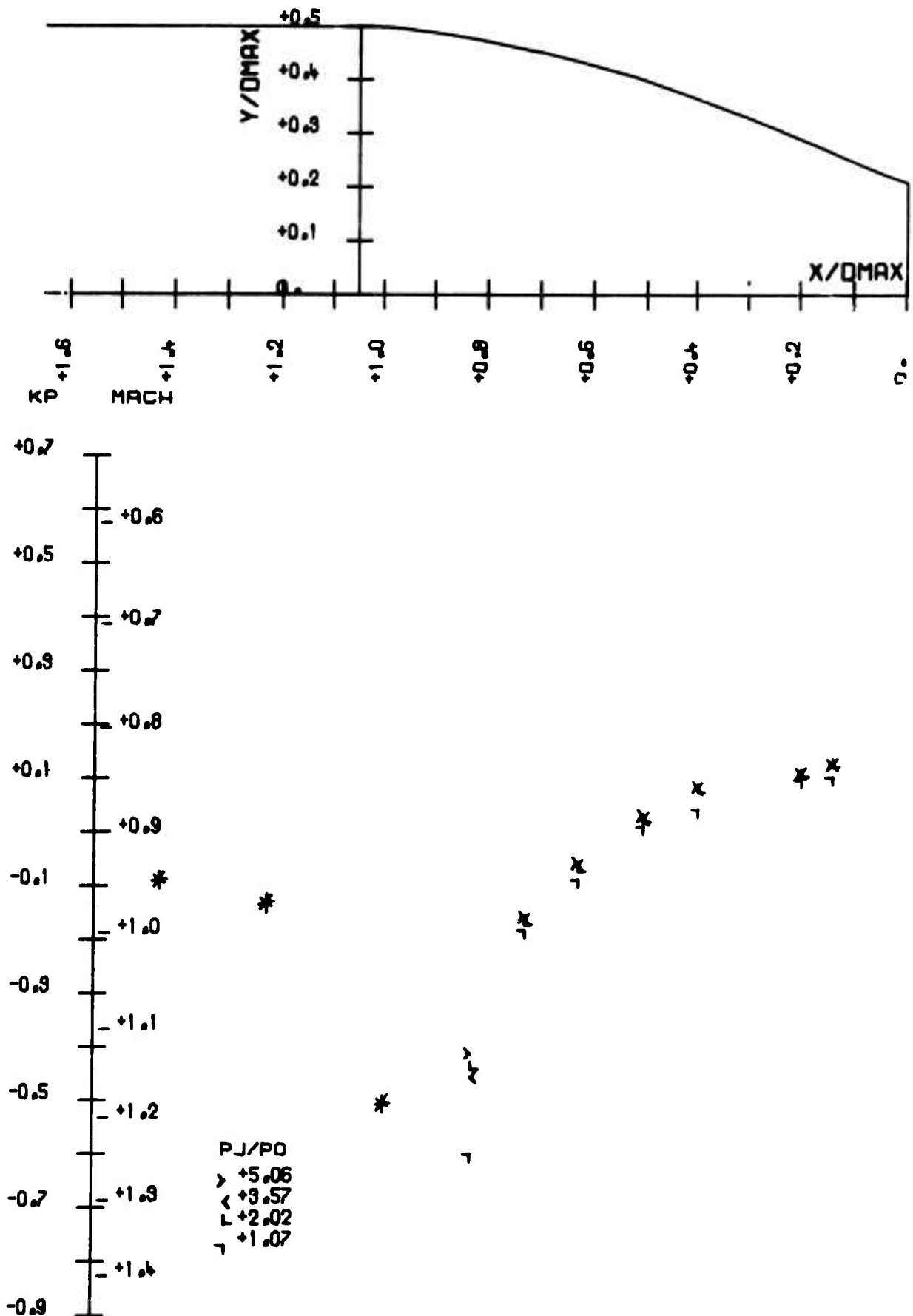
ESSAI NO 997

AVEC SOUFFLAGE

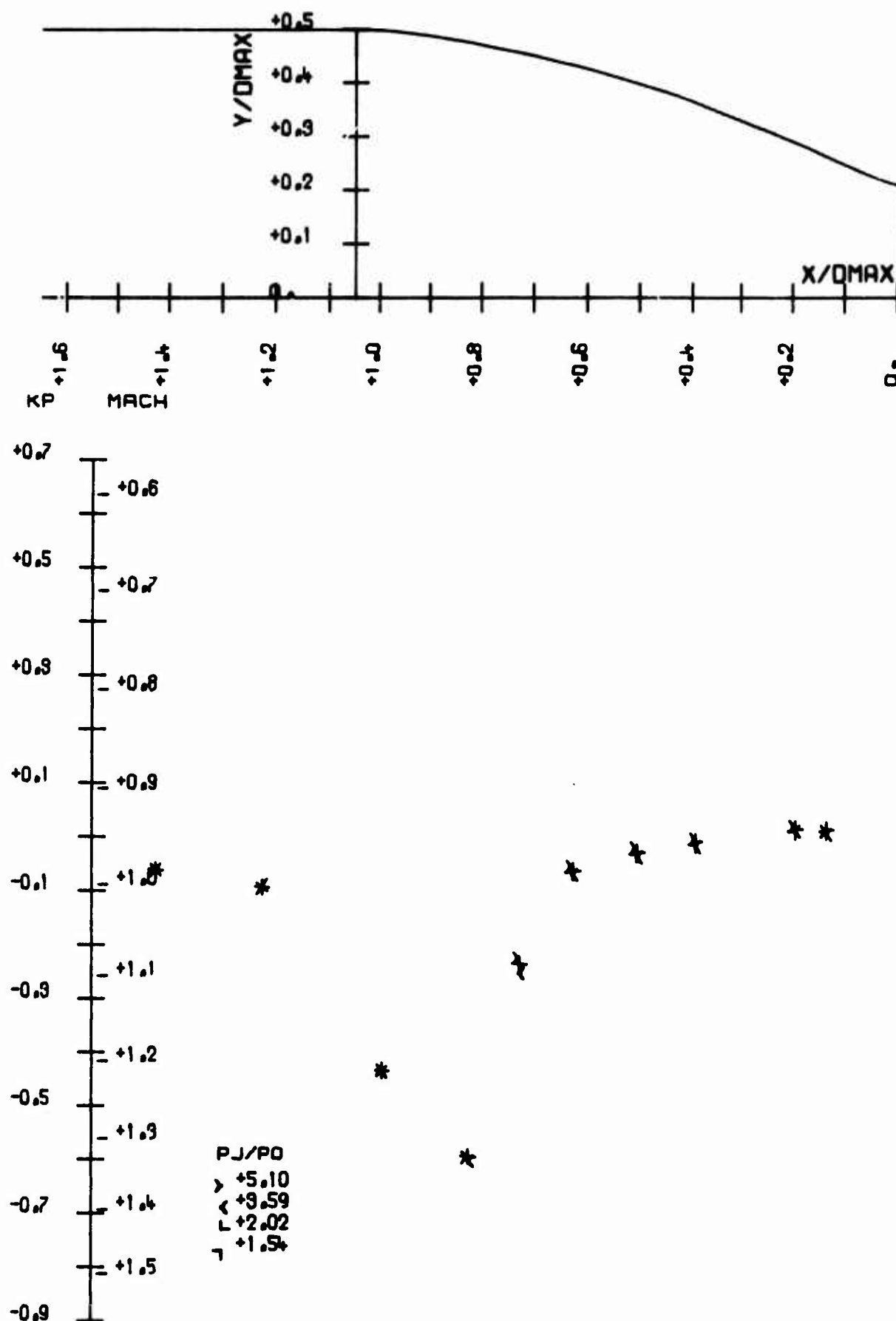
$$P_t/p_o = 6.1$$

Pl.25 Tuyère AGARD  $\phi$  80 MOD – avec soufflage –  $M_0 = 0,85$

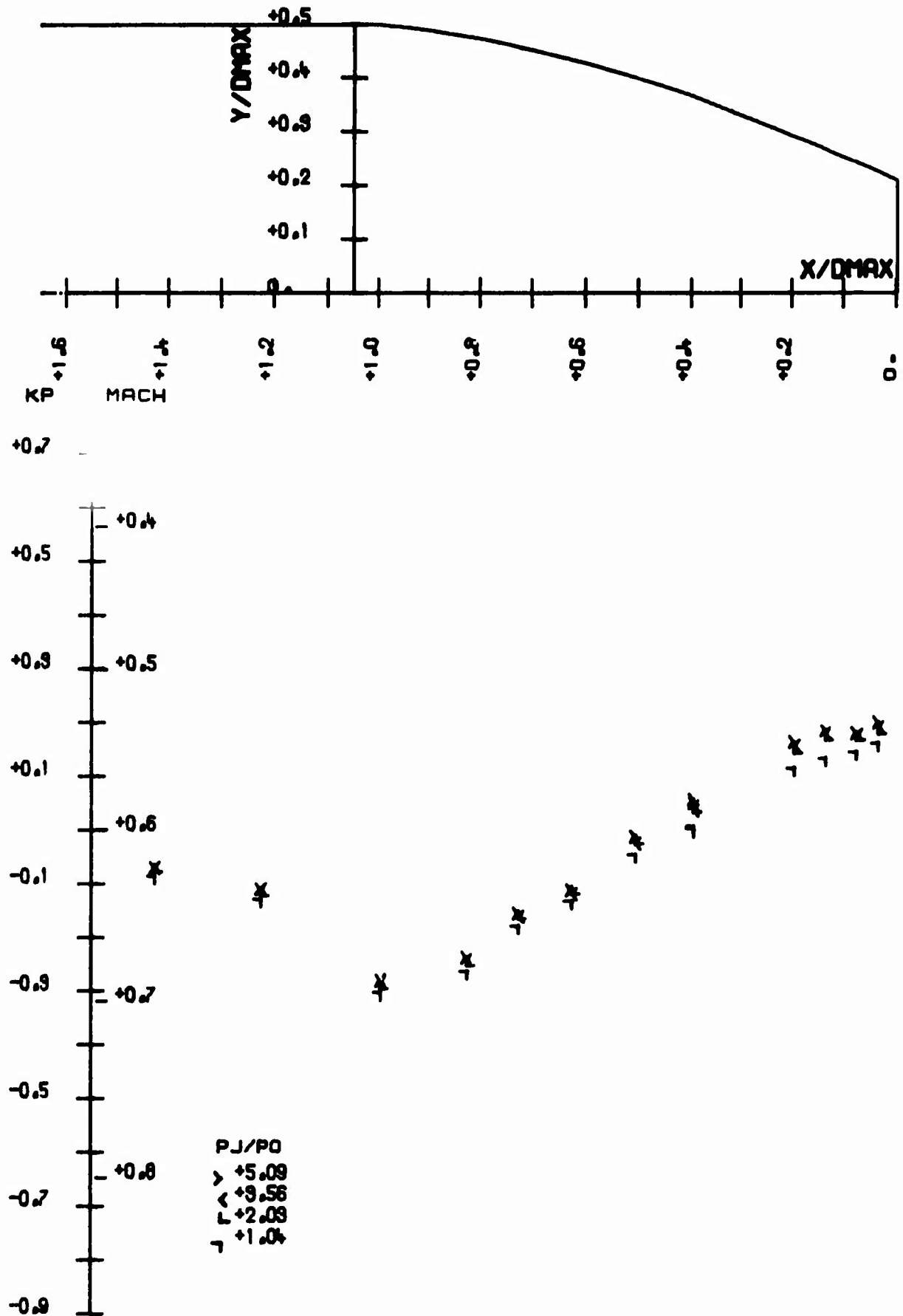
ESSAI NO 998

AVEC SOUFFLAGE  $P_t/p_0 = 5.6$ Pl.26 Tuyère AGARD  $\phi$  80 MOD — avec soufflage —  $M_0 = 0.90$

ESSAI NO 995

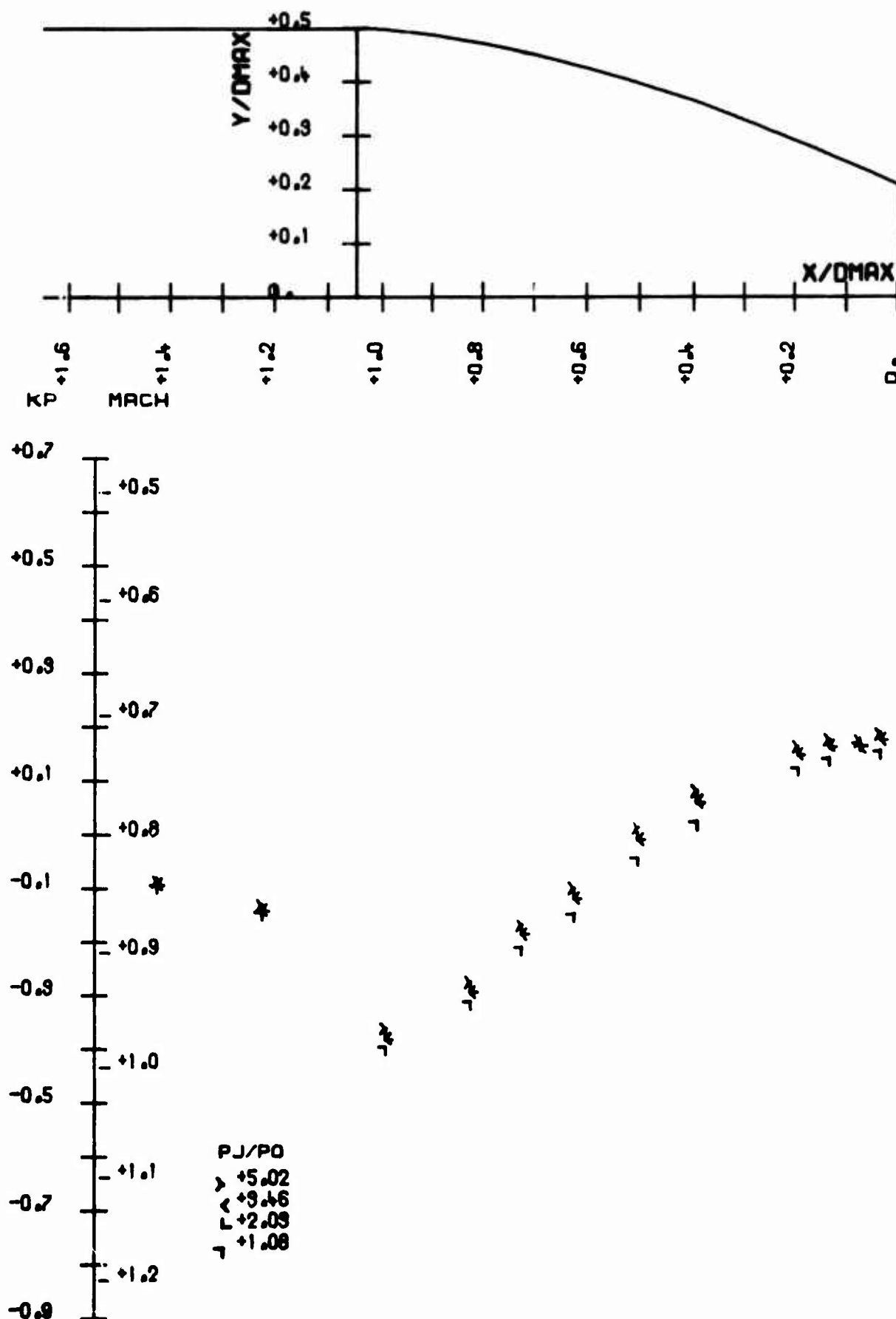
AVEC SOUFFLAGE  $P_t/p_o = 5.3$ Pl.27 Tuyère AGARD  $\phi$  80 MOD - avec soufflage -  $M_o = 0,95$

## ESSAI NO 200

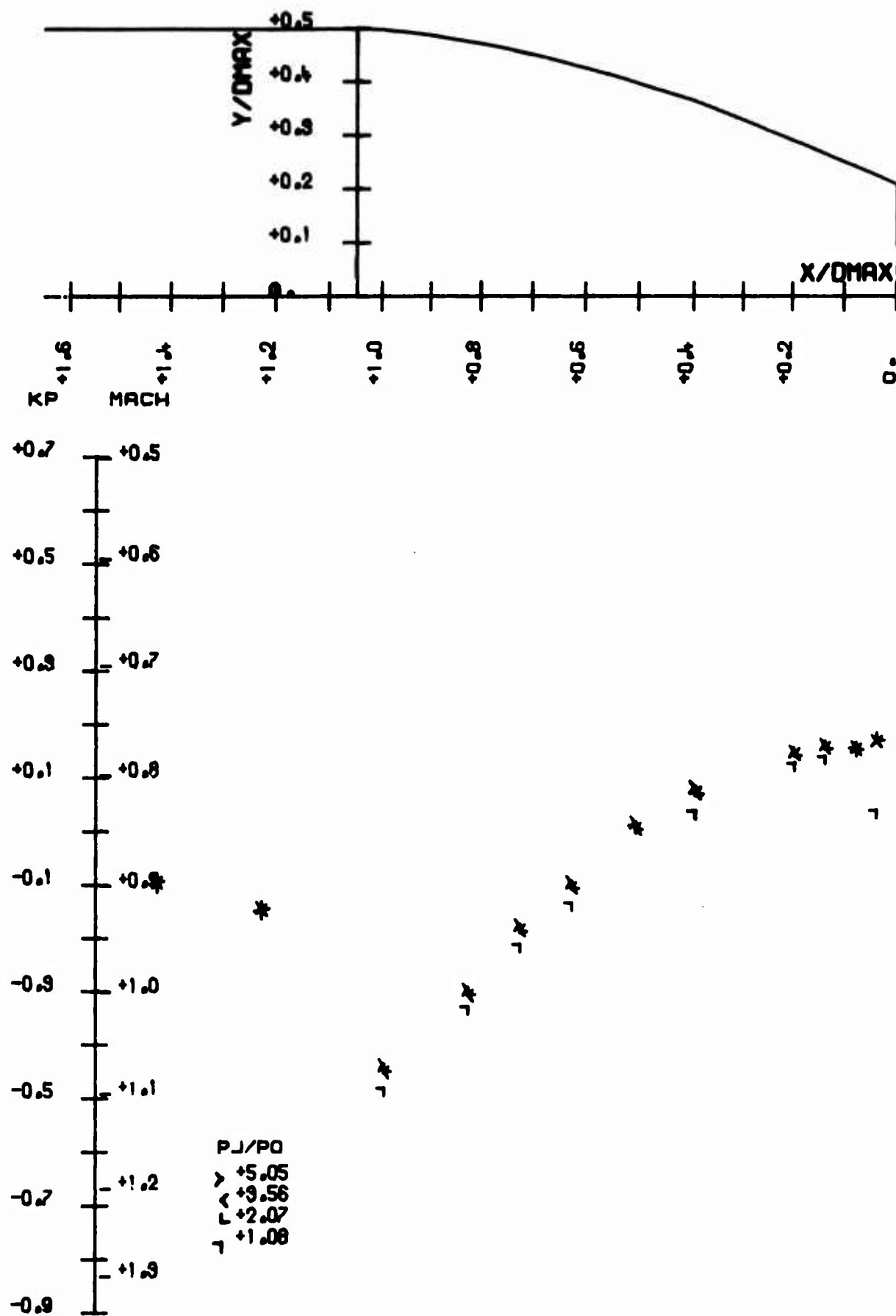
Pl.28 Tuyère AGARD  $\phi$  100  $M_0 = 0,60$



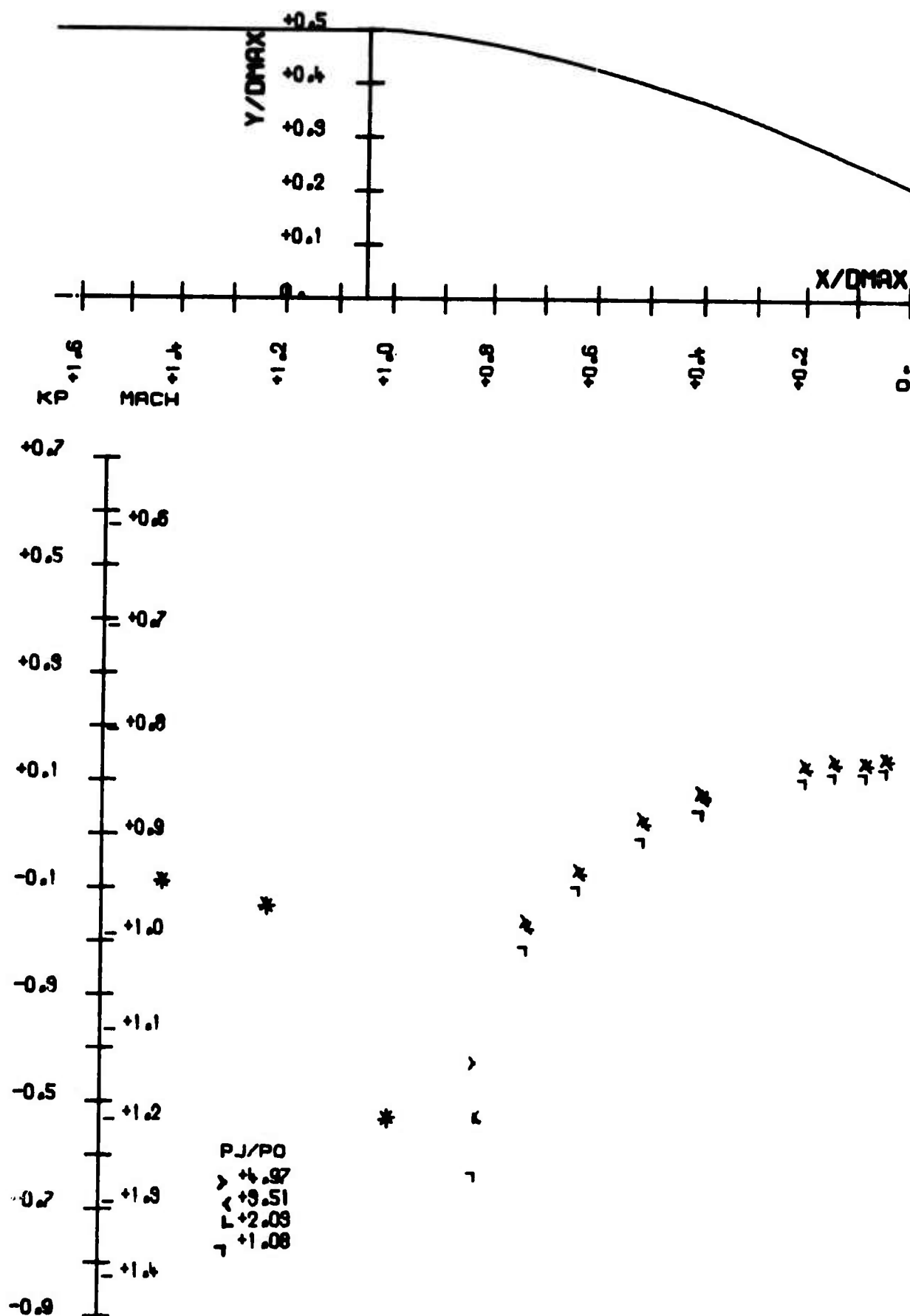
ESSAI NO 290

Pl.29 Tuyère AGARD  $\phi$  100  $M_0 = 0.80$

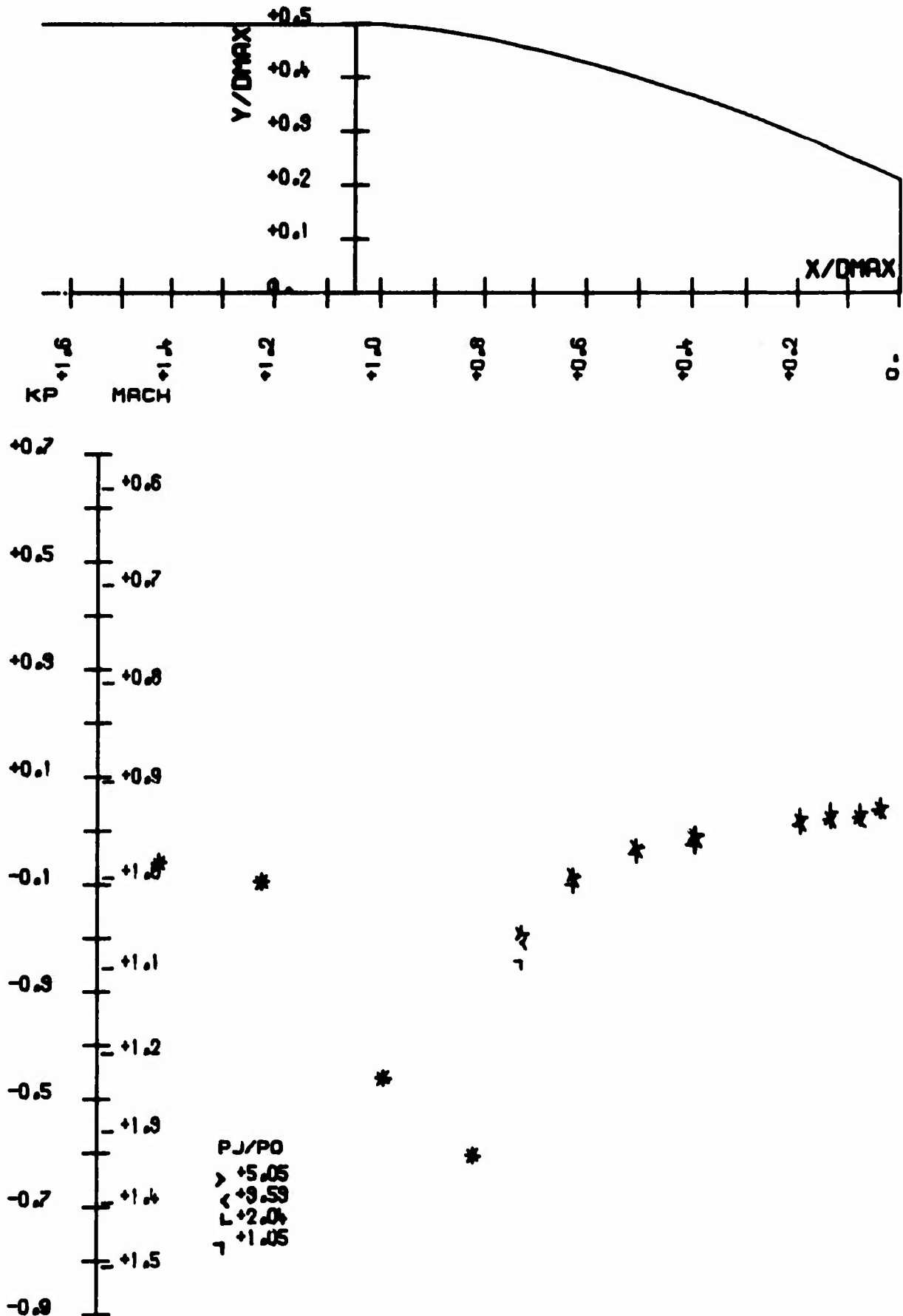
ESSAI NO 291

Pl.30 Tuyère AGARD  $\phi$  100  $M_0 = 0.85$

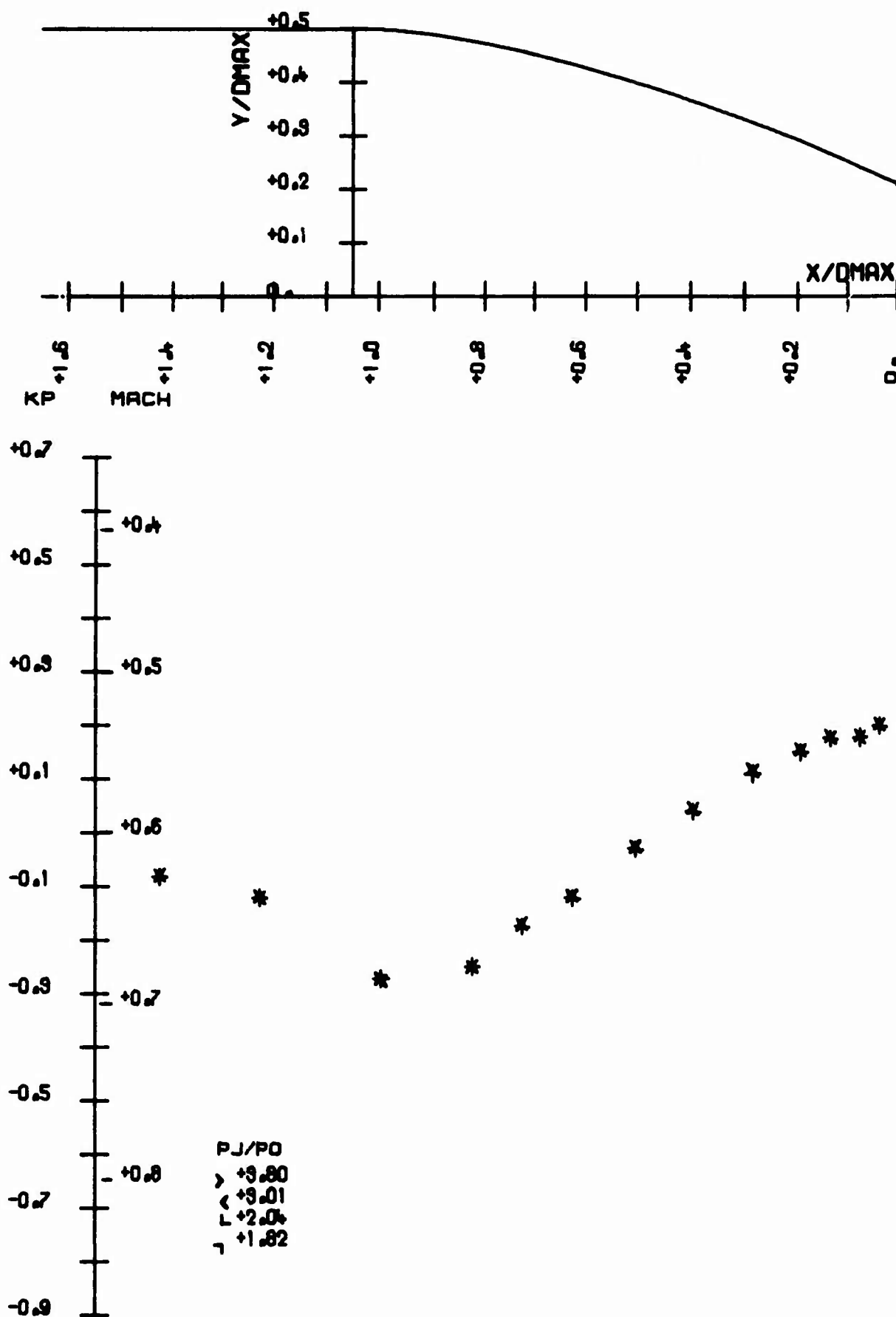
ESSAI NO 292

Pl.31 Tuyère AGARD  $\phi$  100  $M_0 = 0,90$

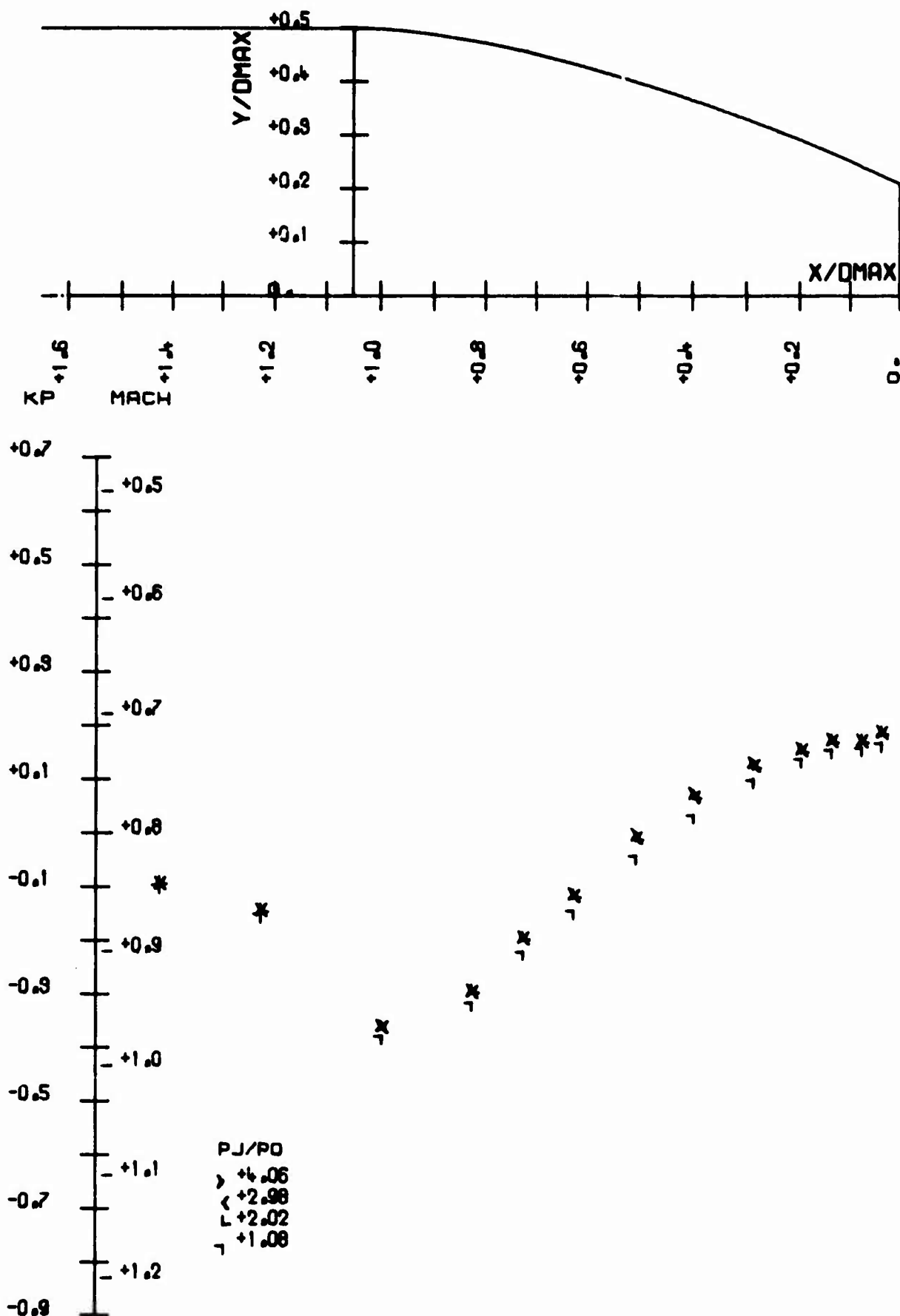
ESPA1 NO 289

Pl.32 Tuyère AGARD  $\phi$  100  $M_0 = 0.95$

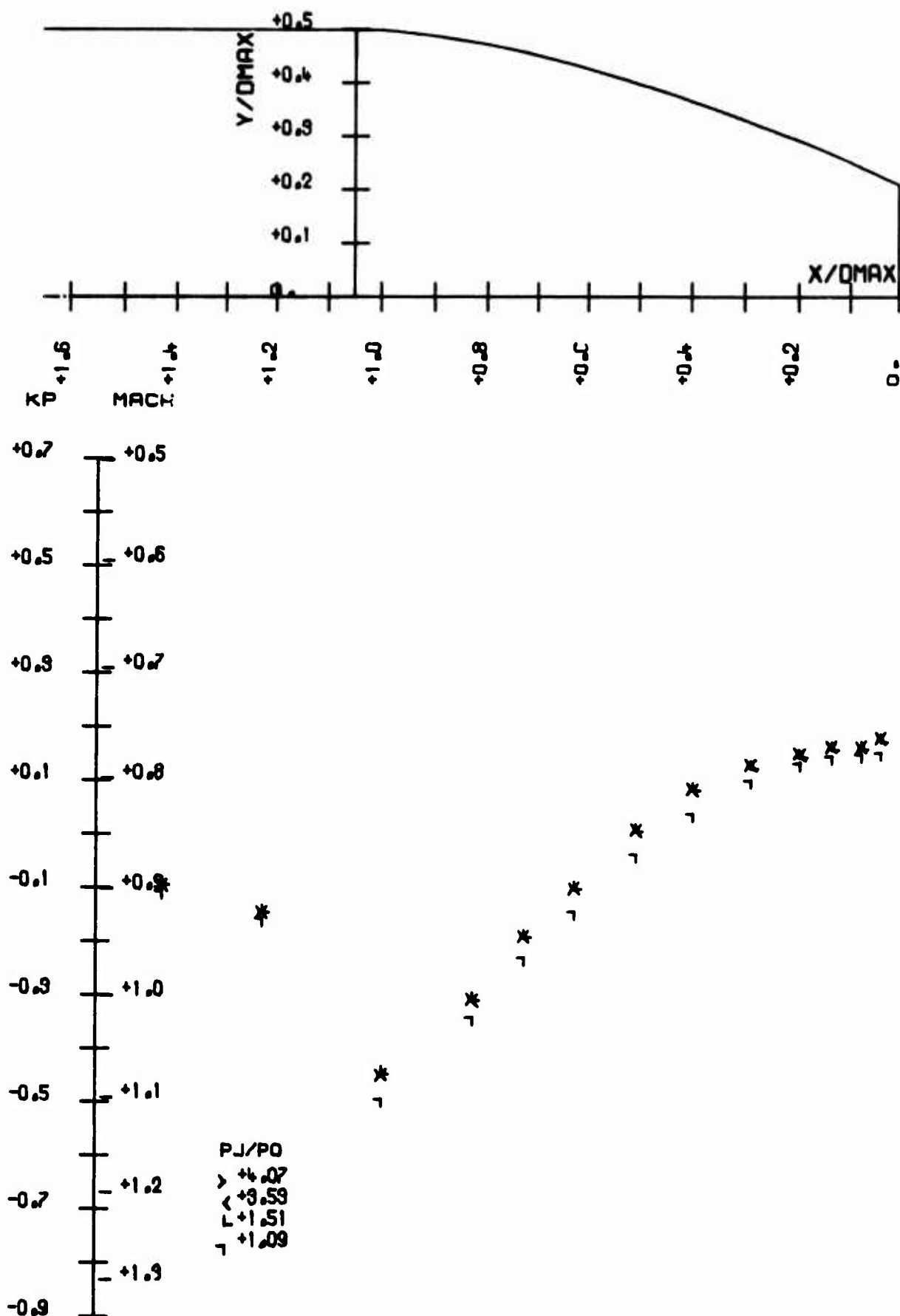
ESSAI NO 900

Pl.33 Tuyère AGARD  $\phi$  120  $M_0 = 0.60$

ESSAI NO 901

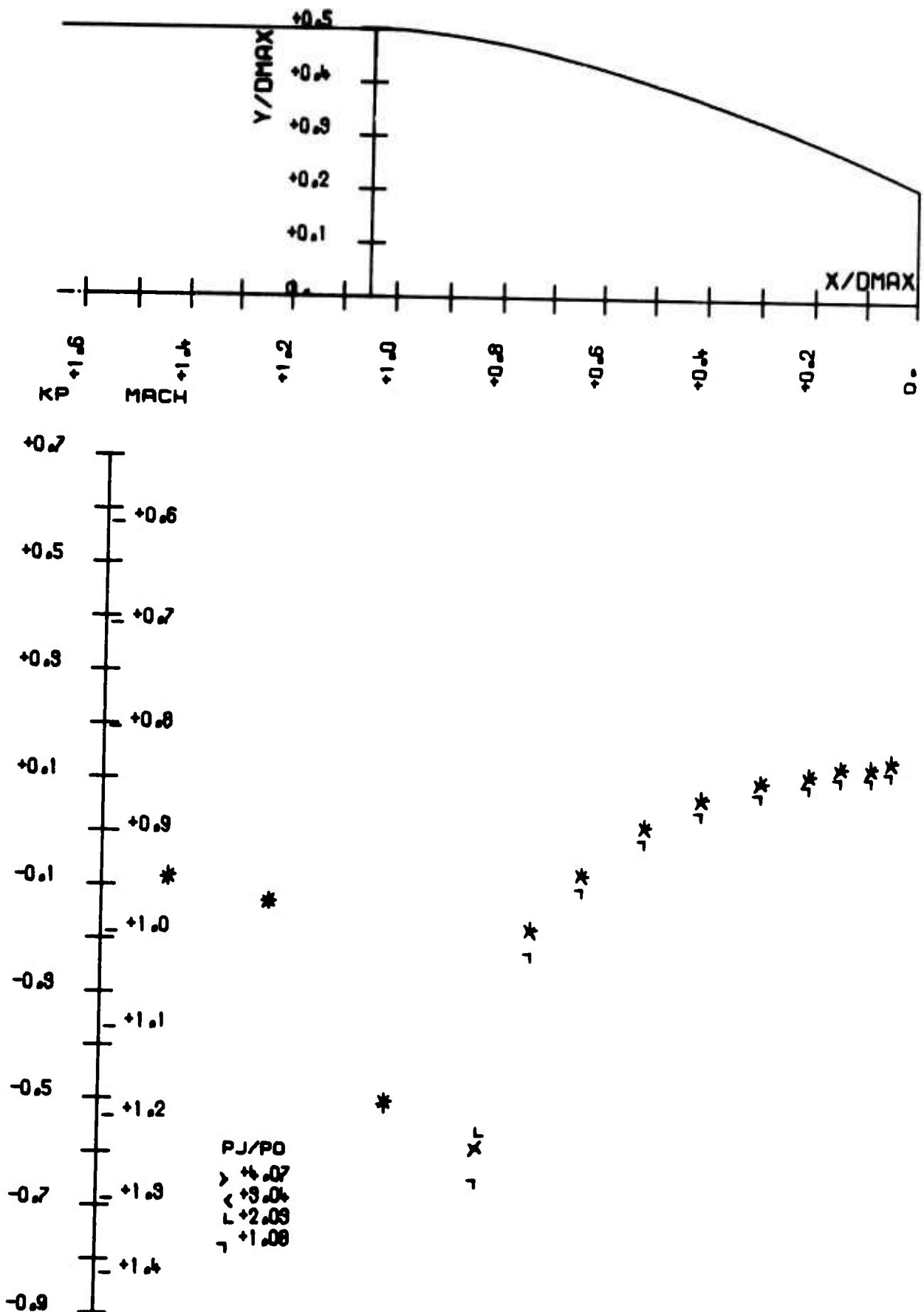
P134. Tuyère AGARD  $\phi$  120  $M_0 = 0.80$

ESSAI NO 902



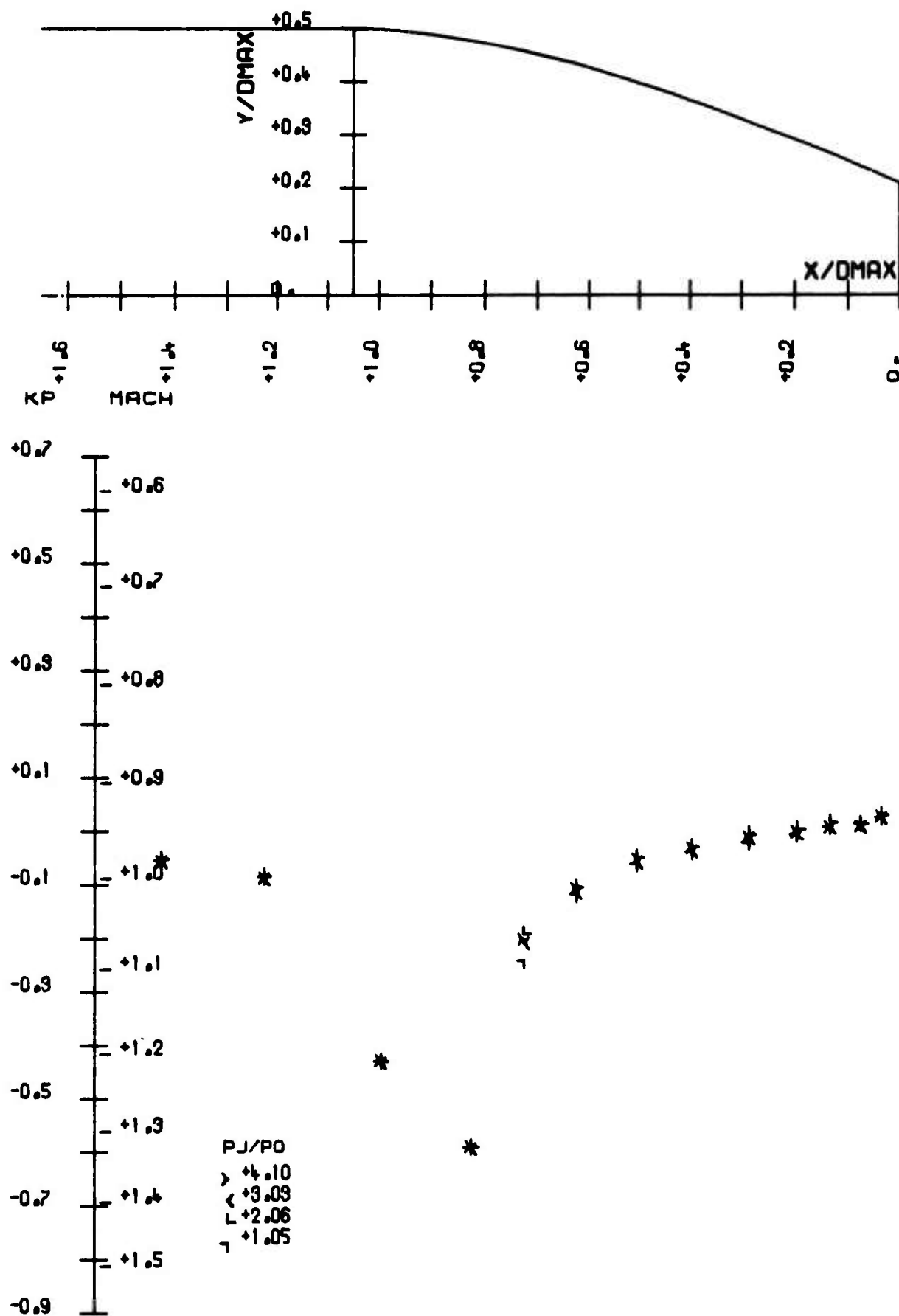
Pl.35 Tuyère AGARD Ø 120  $M_0 = 0.85$

ESSAI NO 309

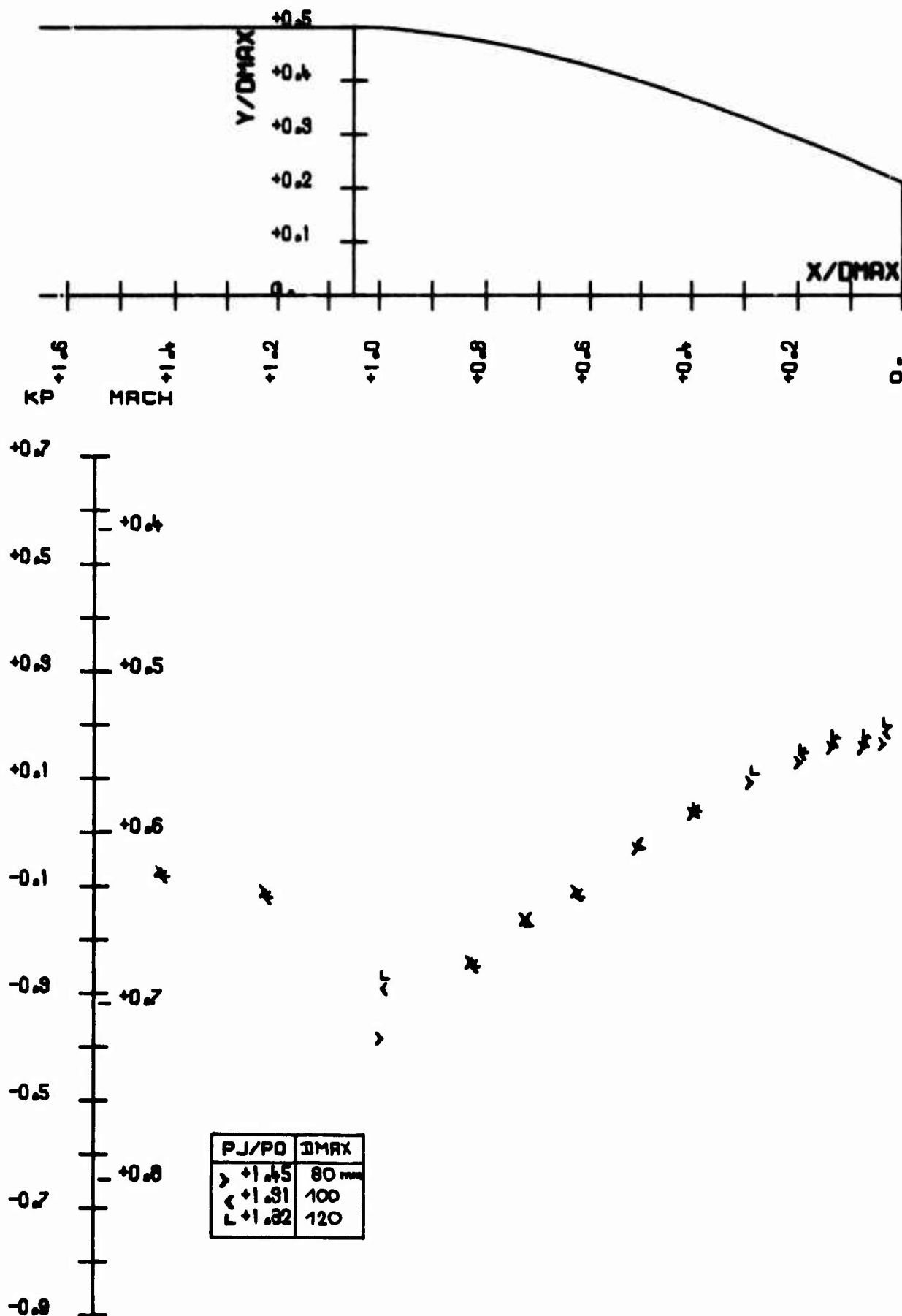
Pl.36 Tuyère AGARD Ø 120  $M_0 = 0.90$



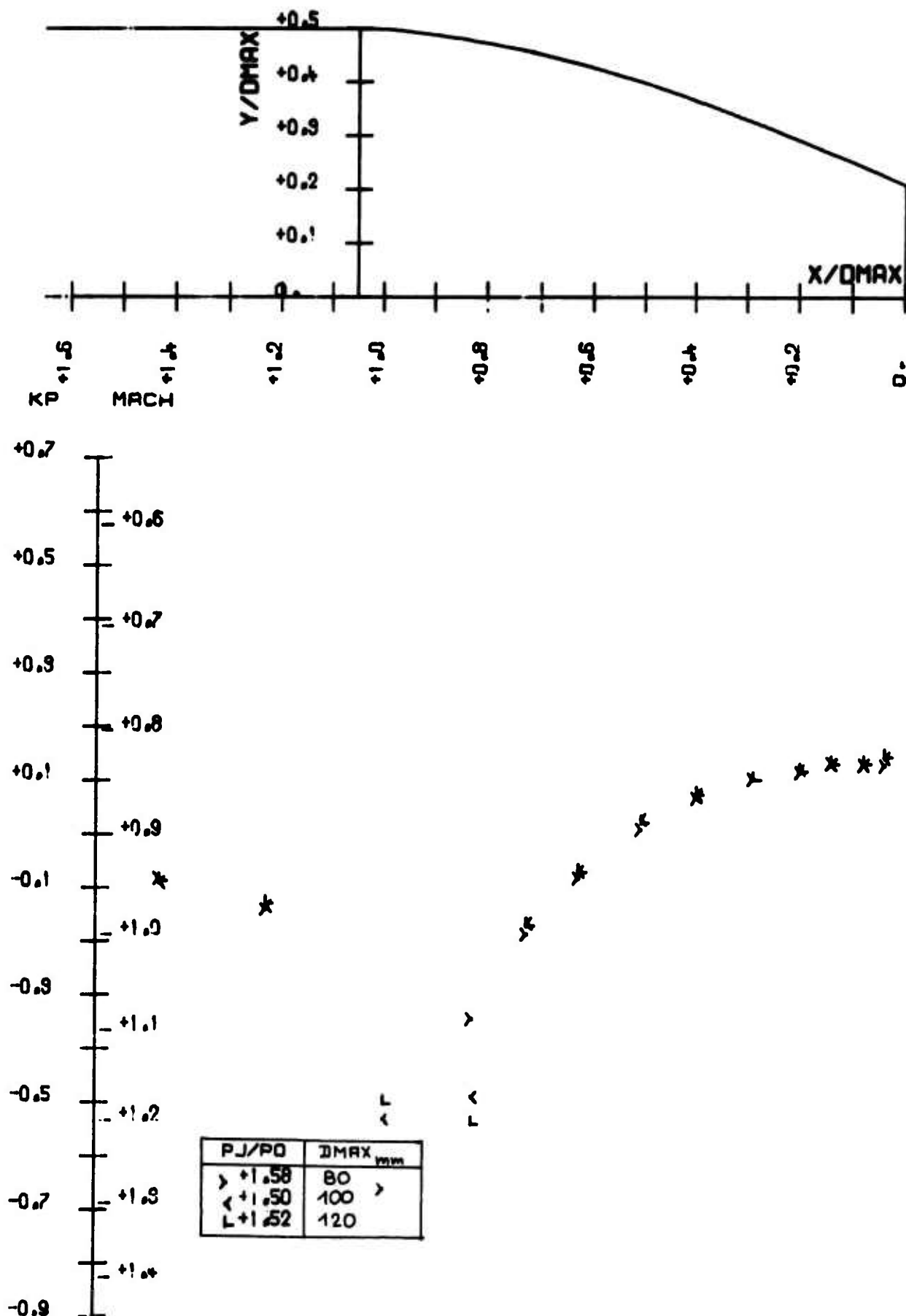
ESSAI NO 904

Pl.37 Tuyère AGARD  $\phi$  120  $M_0 = 0.95$

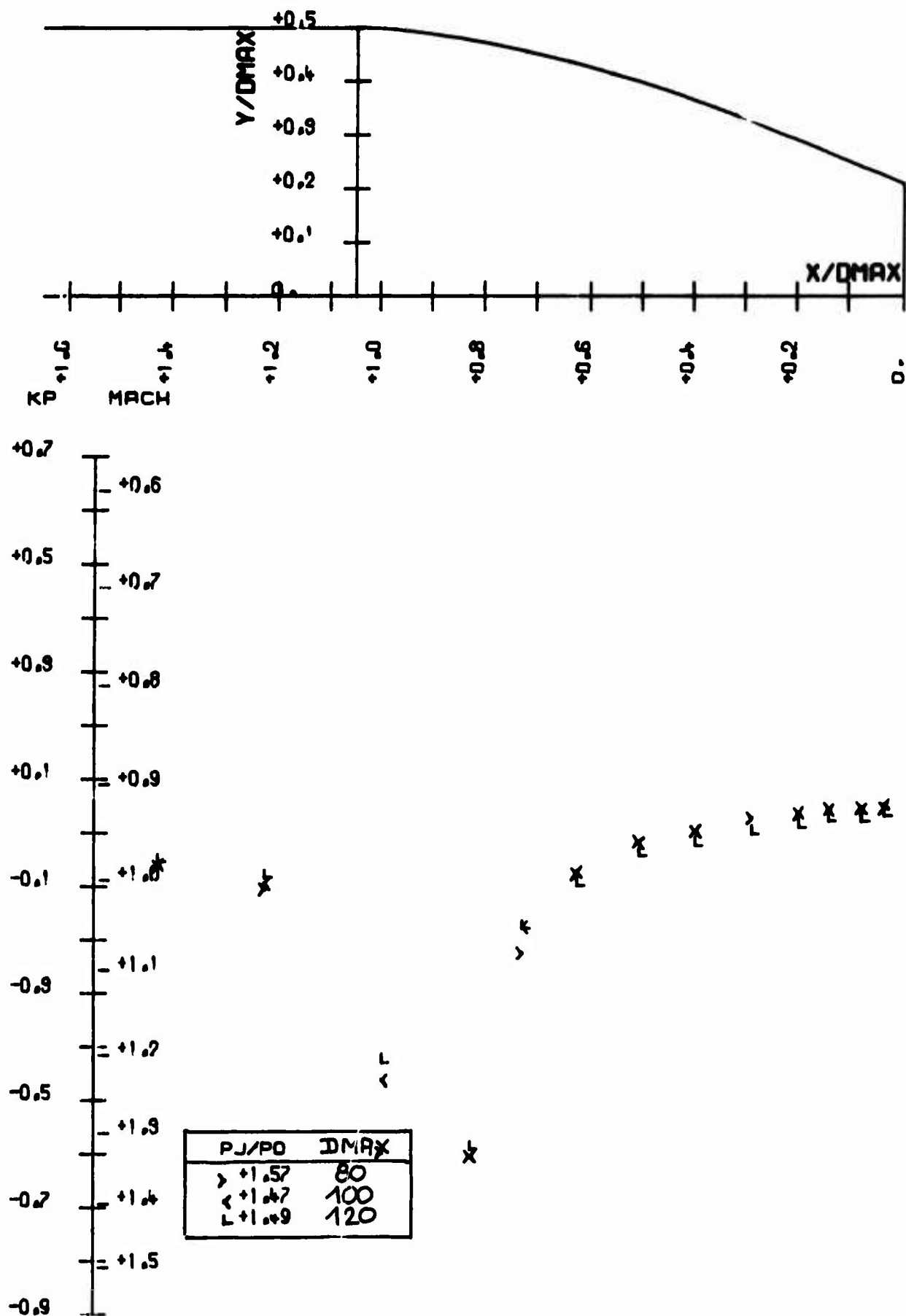
## INFLUENCE DU DIAMETRE

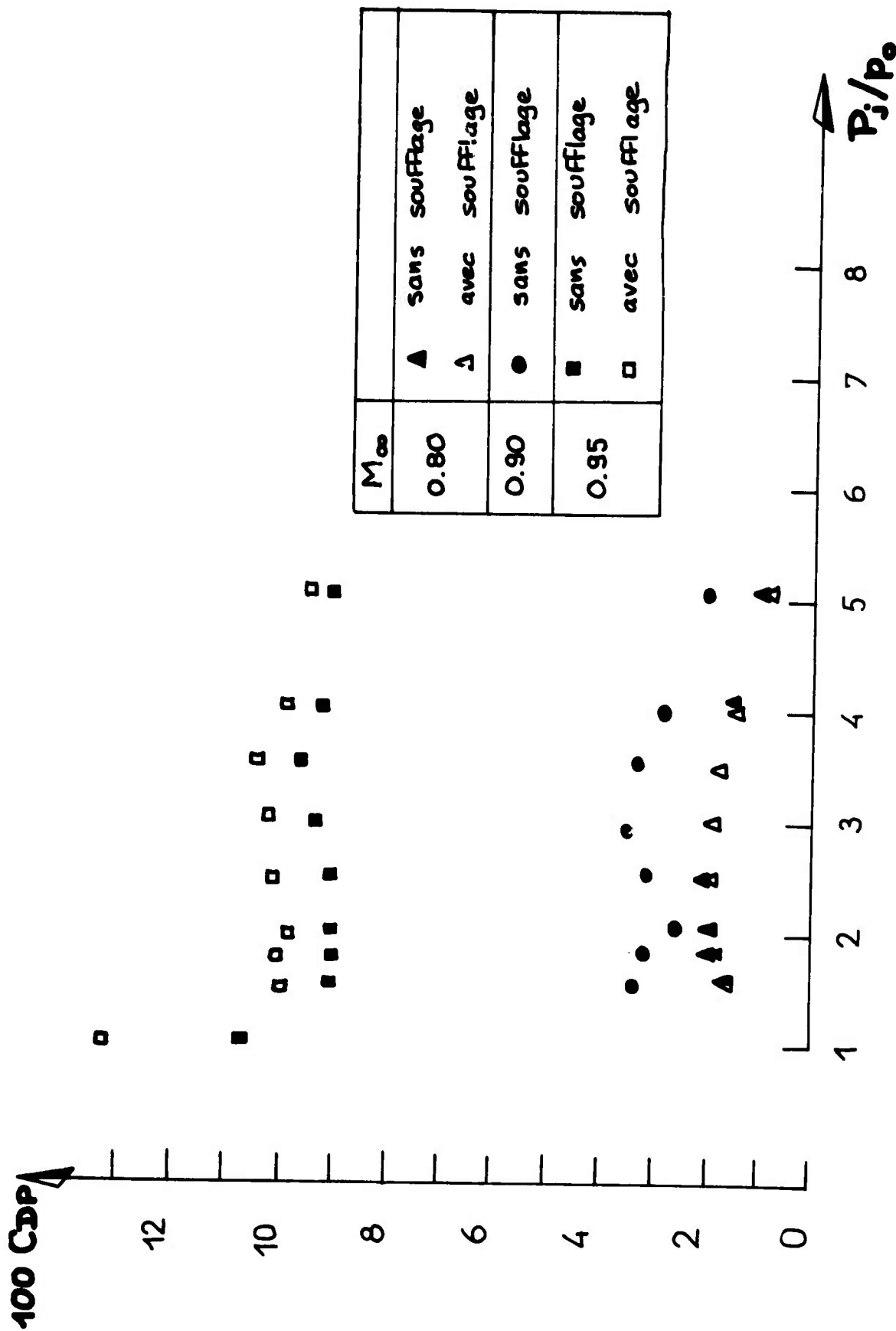
Pl.38 Tuyère AGARD — Influence du diamètre  $M_0 = 0,60$

## INFLUENCE DU DIAMETRE

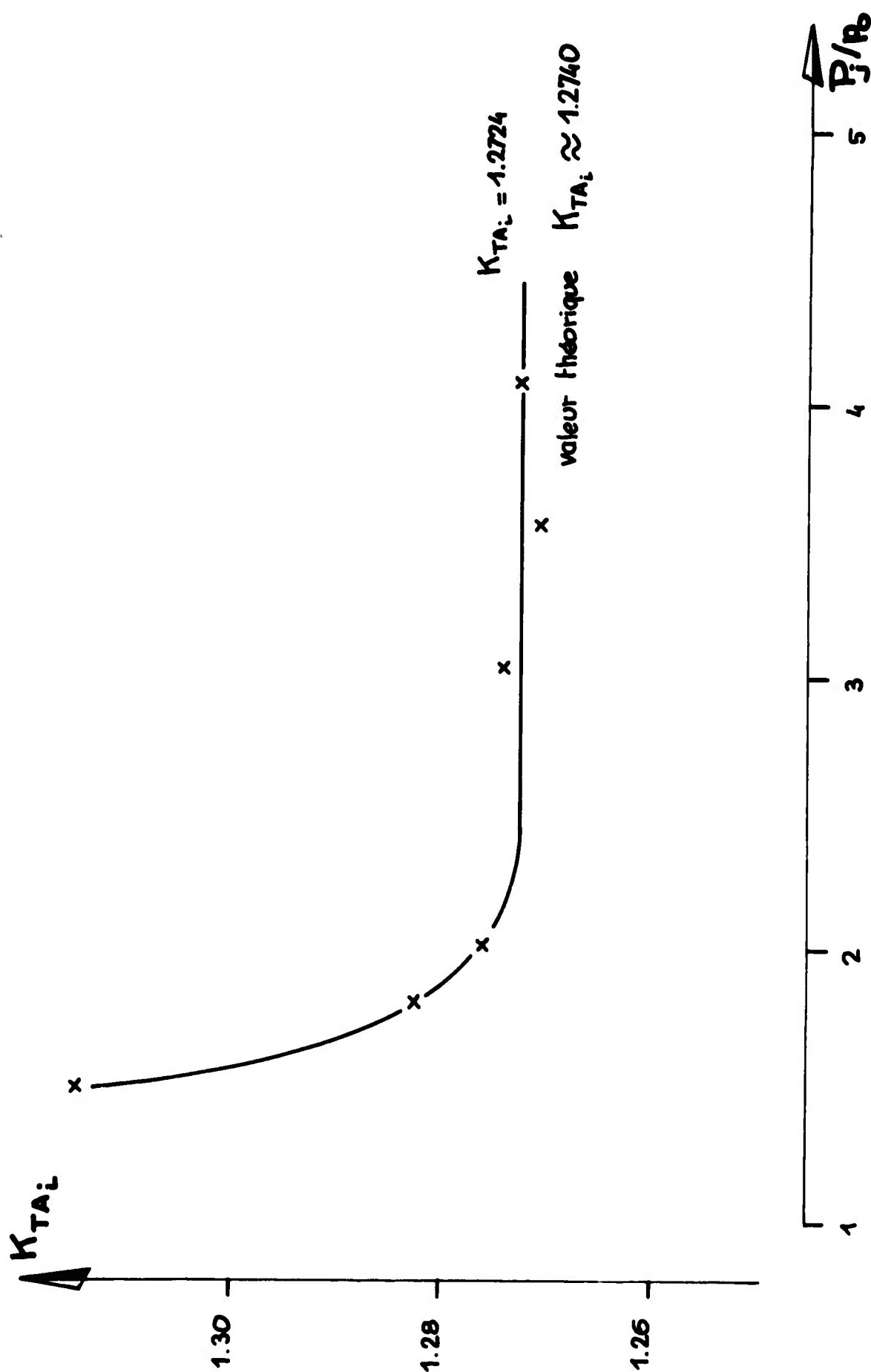
Pl.39 Tuyère AGARD - Influence du diamètre  $M_0 = 0.90$

## INFLUENCE DU DIAMETRE

Pl.40 Tuyère AGARD - Influence du diamètre  $M_0 = 0,95$

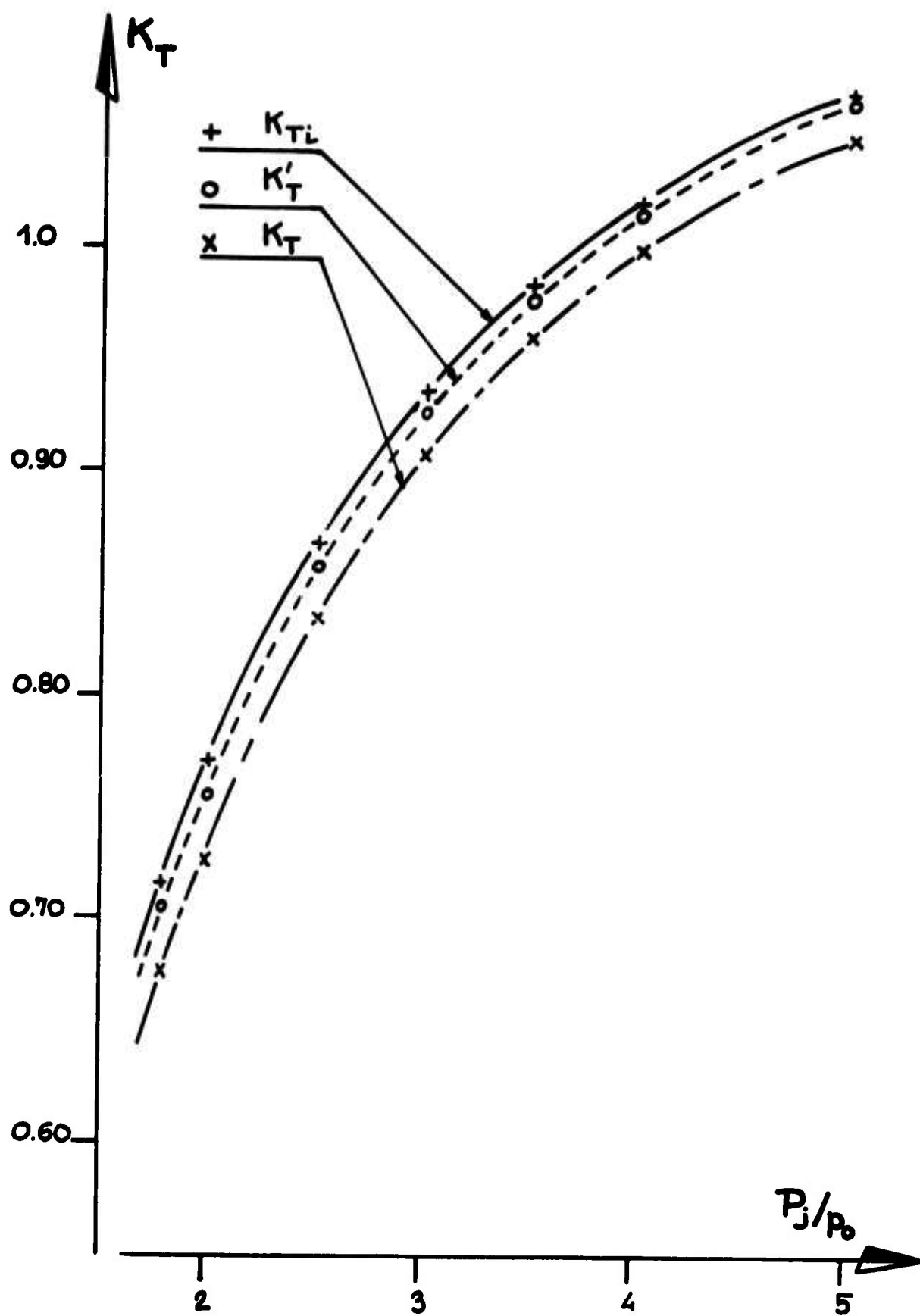


Pl.41 Tuyère AGARD 15° – Coefficient de traînée

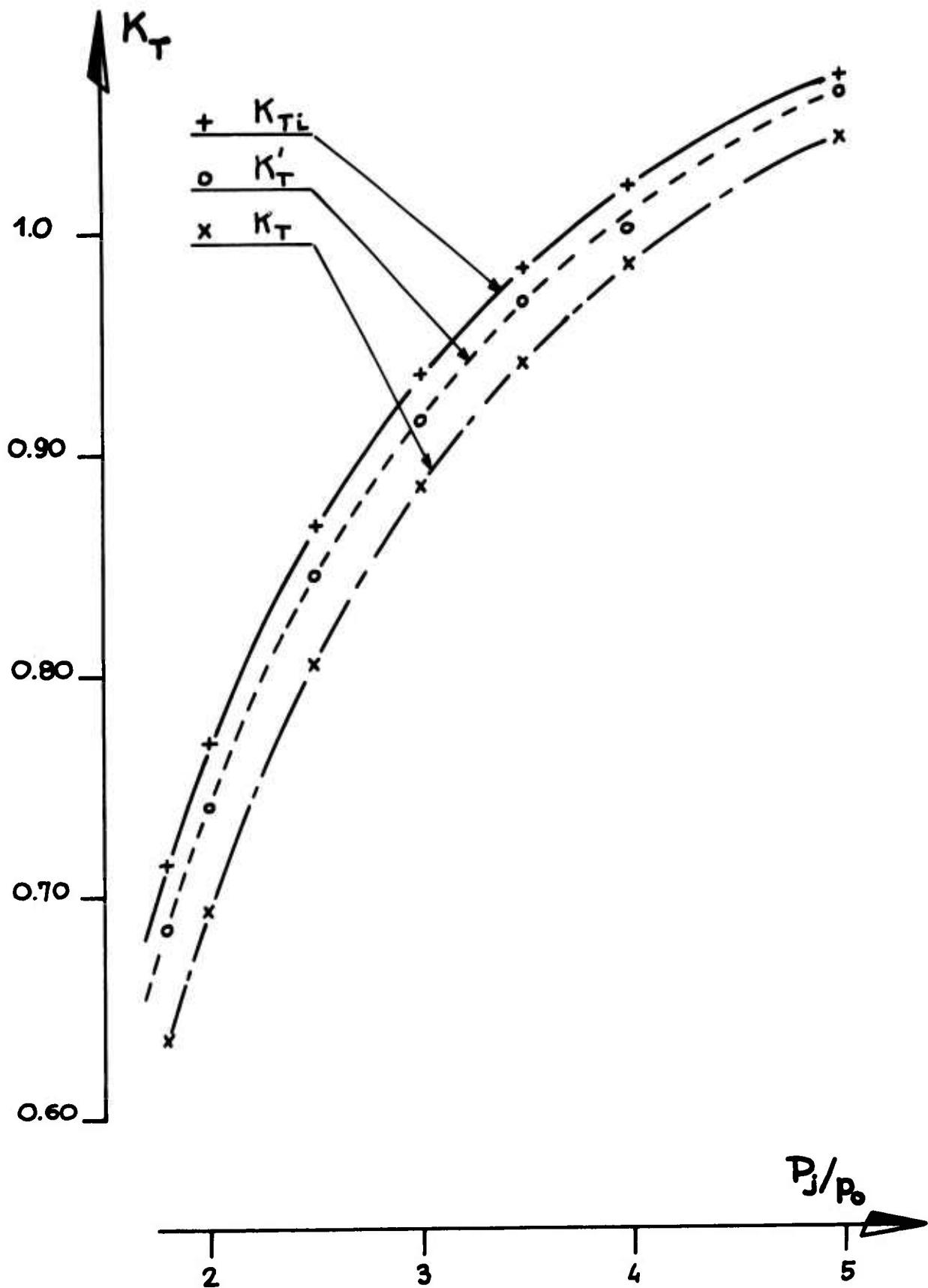


P1.42 Tuyère AGARD 15° - Performances au point fixe

## SANS SOUFFLAGE DE COUCHE-LIMITE

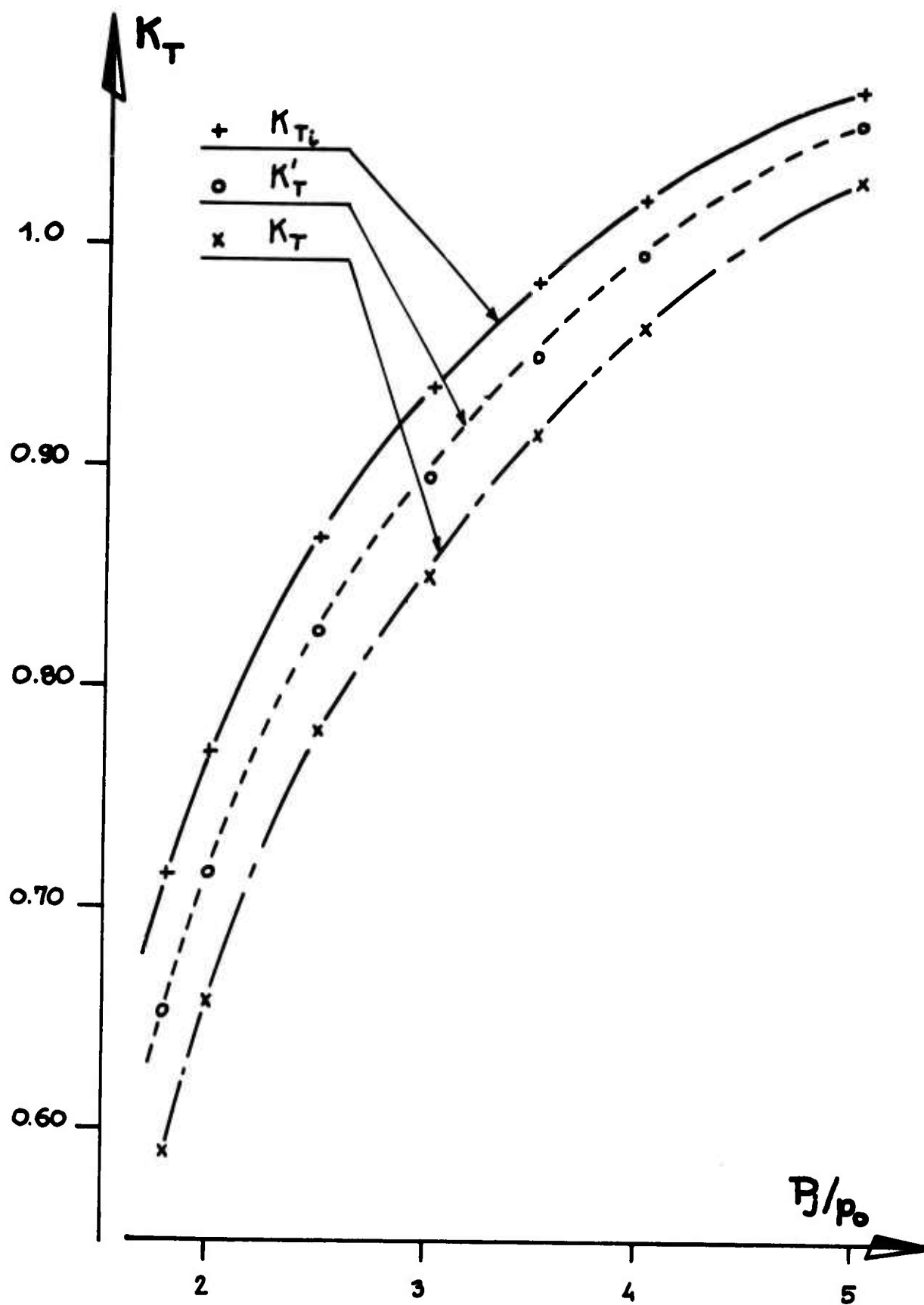
Pl.43 Performances de la tuyère AGARD AV-80-MOD  $M_0 = 0,60$

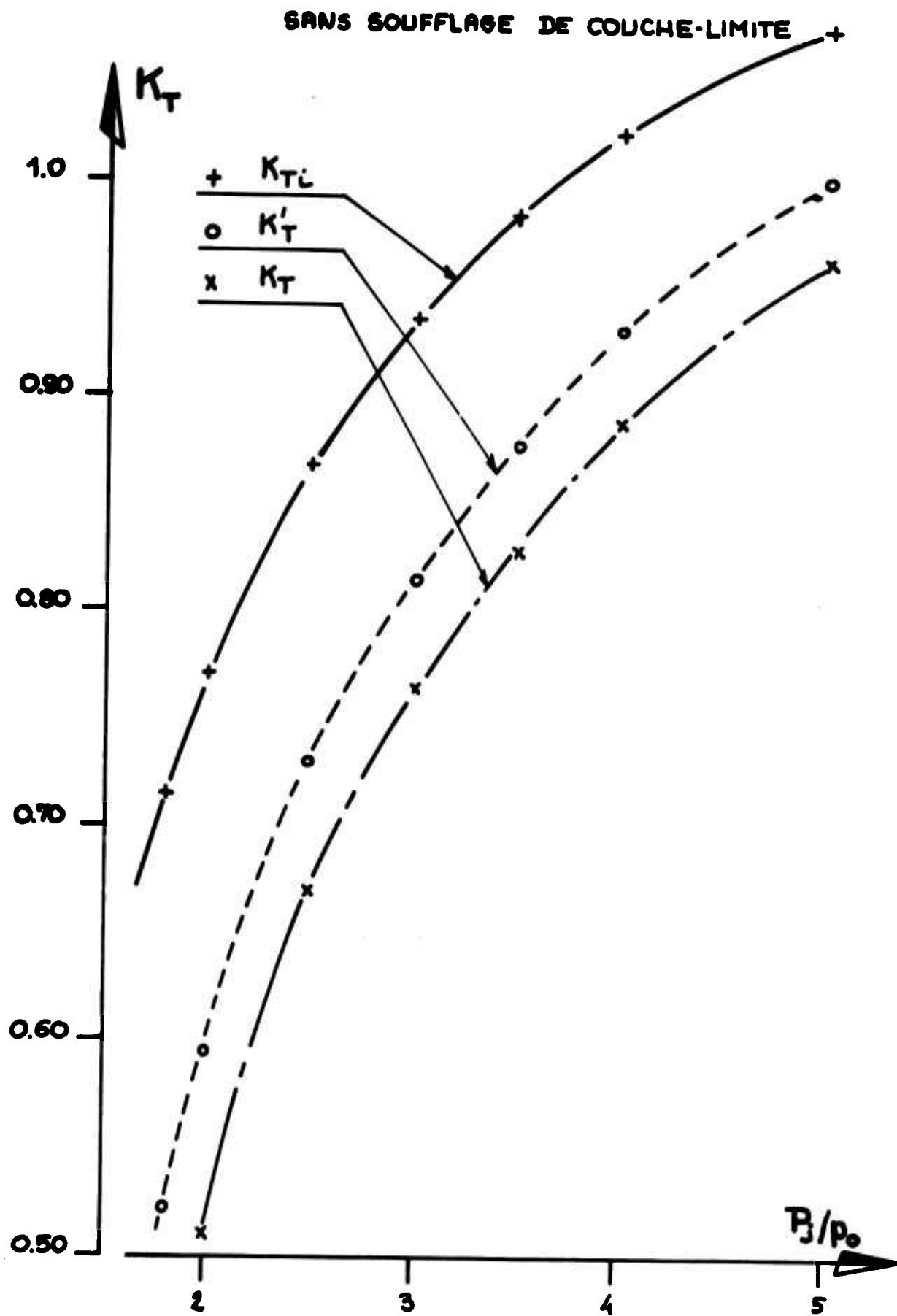
## SANS SOUFFLAGE DE COUCHE-LIMITE

Pl.44 Performances de la tuyère AGARD AV-80-MOD  $M_0 = 0,80$



## SANS SOUFFLAGE DE COUCHE-LIMITE

Pl.45 Performances de la tuyère AGARD AV-80-MOD  $M_0 = 0,90$



Pl.46 Performances de la tuyère AGARD AV-80-MOD  $M_0 = 0,95$

# DESCRIPTION OF TESTS CARRIED OUT AT ROLLS-ROYCE (1971) LTD BRISTOL ENGINE DIVISION

by

L.R. Harper

## SUMMARY

Three nozzle afterbody models were tested in the Rolls-Royce (1971) Ltd. Transonic Wind Tunnel at Bristol using a model support sting which provided means for boundary layer thickness variation by blowing.

The tests covered the Mach number range 0.75 to 0.95 and nozzle pressure ratios were in the range 1.7 to 4.7:1.

The model surface static pressure distributions were measured and integrated to obtain pressure drag coefficients. Measurements are also presented of model internal pressures, boundary layer profiles and tunnel wall static pressure distributions.

## LIST OF SYMBOLS

$C_{Dp}$	boattail pressure drag coefficient
$C_p$	pressure coefficient, $\frac{p - p_{TS}}{\frac{1}{2} \gamma p_{TS} M_0^2}$
$D_{max}$	model maximum diameter
$d_b$	diameter at end of boattail
$d_e$	nozzle exit diameter
$l$	length of boattail
$M_0$	tunnel free stream Mach number
$P_B$	blowing slot delivery pressure
$P_j$	nozzle total pressure
$P_{JP}$	jet pipe local total pressure
$P_{JC}$	jet pipe centre-line total pressure
$P_a$	ambient pressure
$P_{JL}$	jet pipe static pressure
$P_{TS}$	tunnel reference static pressure
$u$	velocity
$u_\infty$	free stream velocity
$x$	axial distance, measured from nozzle exit plane
$x_T$	axial location of jet pipe static tapping
$x_\beta$	afterbody axial coordinate
$y_{JP}$	radial location of jet pipe pitot probe
$y_\beta$	afterbody radial coordinate
$y_{BL}$	height in boundary layer from model surface

$\beta$	boattail final angle
$\delta_{0.95}$	height in boundary layer where $u/u_\infty = 0.95$
$\theta$	boattail chord angle

## 1. INTRODUCTION

As part of the AGARD coordinated investigation into improved Nozzle Testing Techniques three afterbody models of the agreed geometries were tested at Bristol towards the end of 1973. This work was funded by a United Kingdom Ministry of Defence research contract.

A major objective of these tests was to examine the way in which afterbody pressure distribution and pressure drag varied with boundary layer thickness. In this facility, as in many others, the boundary layer on the model is two to three times as thick as the equivalent flight value. Techniques are available for thinning the boundary layer but they involve a substantial increase in the complexity of the model support system and so would only be used if a clear need was demonstrated. In these tests measurements were made both with a thick "natural" sting boundary layer and with a thinner layer, similar to the flight value, obtained by blowing.

## 2. TEST FACILITY

The tests were carried out in the open circuit ejector driven wind tunnel at Rolls-Royce (1971) Ltd., Bristol Engine Division. The working section is octagonal (534 mm across the flats) with slotted walls as illustrated in Figure 1. The slot geometry is based on Shape II of Reference 1, and the porosity is approximately 11%.

The model was mounted on a circular sting of 101.6 mm diameter, giving a geometric blockage of 3.4%. The sting was supported in an air bearing located ahead of the entry plane of the tunnel bellmouth. Air bearing and nozzle airflows were supplied perpendicularly to the sting axis through the air bearing support legs. The general arrangement of the model support sting is sketched in Figure 2.

Model boundary layer thickness reduction was achieved by blowing high pressure air parallel to the sting surface. The blowing slot location and geometry is sketched in Figure 3.

The nozzle and blowing slot were supplied with dry compressed air at a temperature approximately 3°C higher than ambient. The tunnel air flow was induced from the atmosphere and its humidity was therefore variable. Condensing water vapour could be seen in the tunnel flow at Mach numbers above about 0.9.

## 3. DESCRIPTION OF THE MODELS

The three afterbody models were fitted to a common nozzle and jet pipe. The internal dimensions of the nozzle are detailed in Figure 4 and the external geometries of the afterbodies are specified in Figure 5.

## 4. INSTRUMENTATION

The three afterbodies were each provided with approximately 60 surface pressure tappings distributed axially and circumferentially as tabulated in Figure 6.

Nozzle airflow was measured using a calibrated venturi mounted within the upstream end of the model support sting and the jet pipe total pressure was derived from this measured flow and the jet pipe static pressure at the datum plane, ( $x_T/D_m = 1.515$ , Figure 4) using the geometric area at this plane.

Internal tappings were provided to measure the jet pipe static pressure distribution and a static test was carried out in which a rake of nineteen pitot probes was fitted to measure the jet pipe total pressure profile. The locations of these tappings are shown in Figure 4.

The external boundary layer profile was measured, and the blowing system calibrated, with the afterbody model replaced by a cylindrical body fitted with three rakes of nineteen pitots at the model attachment plane (Fig.3).

Twenty static pressure tappings were distributed along the centre-line of one of the working section wall plates at axial locations indicated in Figure 2.

All pressures were sampled using Scanivalves and recorded automatically.

## 5. TUNNEL MACH NUMBER AND STATIC PRESSURE DISTRIBUTION

The tunnel air stream total pressure is uniform, out of the wall and sting boundary layers, and equal to the ambient pressure ahead of the tunnel bellmouth. The free stream Mach number is calculated from the ratio of this total pressure to the tunnel reference static pressure.

Typical tunnel wall static pressure distributions are plotted in Figure 7. These show that the model afterbody flow field caused significant perturbation of the static pressure at the wall near the axial location of the model. Therefore the reference static pressure, which is used to calculate Mach number and against which pressure coefficients are referred, is taken as the mean of the pressures at tappings numbers 4, 5 and 6 (as indicated in Figures 2 and 7) which are considered to be upstream of the afterbody field but downstream of the influence of the tunnel entry field.

As part of the tunnel commissioning a calibration of the tunnel was carried out to determine the correct value of wall static pressure to use. This calibration was made by determining the drag of a faired body independently by a wake traverse and by direct force measurement. These two measurements are each dependent on stream static pressure which could therefore be derived by cross plotting. This derived "correct" value of static pressure was then compared with the measured wall static pressures to determine which static tappings should be used to define stream static pressure in subsequent tests.

## 6. TEST RESULTS AND DISCUSSION

### 6.1 Boundary Layer Profiles

A preliminary series of tests was carried out to establish the blowing pressures to provide a thin boundary layer. At any Mach number, for a given slot geometry and position, there is a unique blowing pressure which provides a minimum thickness boundary layer of realistic profile. If the slot is blown at too low a pressure the boundary layer is inadequately thinned while if the pressure is too high a wall jet type of profile persists at the measurement plane. Typical profiles without blowing and at the optimum blowing pressure are shown in Figure 8. The development of the blowing technique has been described in Reference 2 which also contains more comprehensive boundary layer profiles.

Blowing can be seen to have been very effective in re-energising the more significant part of the boundary layer near the body surface but a plateau of velocity slightly below the free stream value was left at the top of the layer. Since this plateau probably does not greatly influence the flow over the afterbody the boundary layer thickness has been referred to the height at which the velocity is 95% of the free stream value. On this basis the thickness,  $\delta_{0.95}/D_m$ , was 0.027 with blowing and 0.10 without blowing. These values are quite representative of typical flight and model test conditions respectively.

### 6.2 Jet Pipe Static and Total Pressure Measurements

The axial variation of jet pipe static pressure is plotted in Figure 9 and total pressure profiles are plotted in Figure 10. These profiles show a somewhat distorted form as a result of the large amount of diffusion in the delivery duct, as sketched in Figure 3.

### 6.3 Afterbody Pressure Distribution and Drag

Representative pressure coefficient distributions for the three geometries at various test conditions are plotted in Figures 11 to 14. These distributions have been integrated over the boattail projected area to obtain pressure drag coefficients which are plotted as functions of nozzle pressure ratio and Mach number in Figures 15, 16, 17. Finally these plots have been interpolated to give the variation of drag with Mach number at a nozzle pressure ratio of 3.0:1. This is plotted for the three afterbodies in Figure 18.

The significance of these results is discussed with respect to the influence of model geometry and boundary layer thickness in later papers.

The results of these tests have been presented more completely in Reference 3 and the influence of boundary layer thickness has been examined in Reference 4.

## 7. CONCLUSIONS

Three afterbody models corresponding to the AGARD 10°, 15° and 25° geometries have been tested over a range of Mach numbers and nozzle pressure ratios in the Rolls-Royce (1972) Ltd. Transonic Wind Tunnel at Bristol.

Blowing air from a slot on the model support sting upstream of the model attachment plane has proved to be a successful technique for reducing the boundary layer on the model to a thickness similar to a typical equivalent flight value.

Reduction of boundary layer thickness has been shown to have a significant effect on afterbody pressure distribution and at higher Mach numbers a substantial change of pressure drag results.

## 8. REFERENCES

1. Wright, R.H.  
Ritchie, V.S.  
Pearson, A.O.      *Characteristics of the Langley 8-foot Transonic Tunnel with Slotted Test Section.*  
NACA Report 1389, 1958.
2. Deer, D.J.      *Model Sting Boundary Layer Control by Blowing.* Rolls-Royce (1971) Ltd., BED  
Report PD.1785. 25th September, 1972.
3. Deer, D.J.      *Results of Tests on Single Afterbody Nozzles Defined by AGARD.* Rolls-Royce (1971)  
Ltd., BED Report PPE.67. March 1974.
4. Harper, L.R.      *The Influence of Boundary Layer Thickness on Nozzle Afterbody Pressure Drag.*  
Rolls-Royce (1971), Ltd., BED Report PPE.69. April 1974.

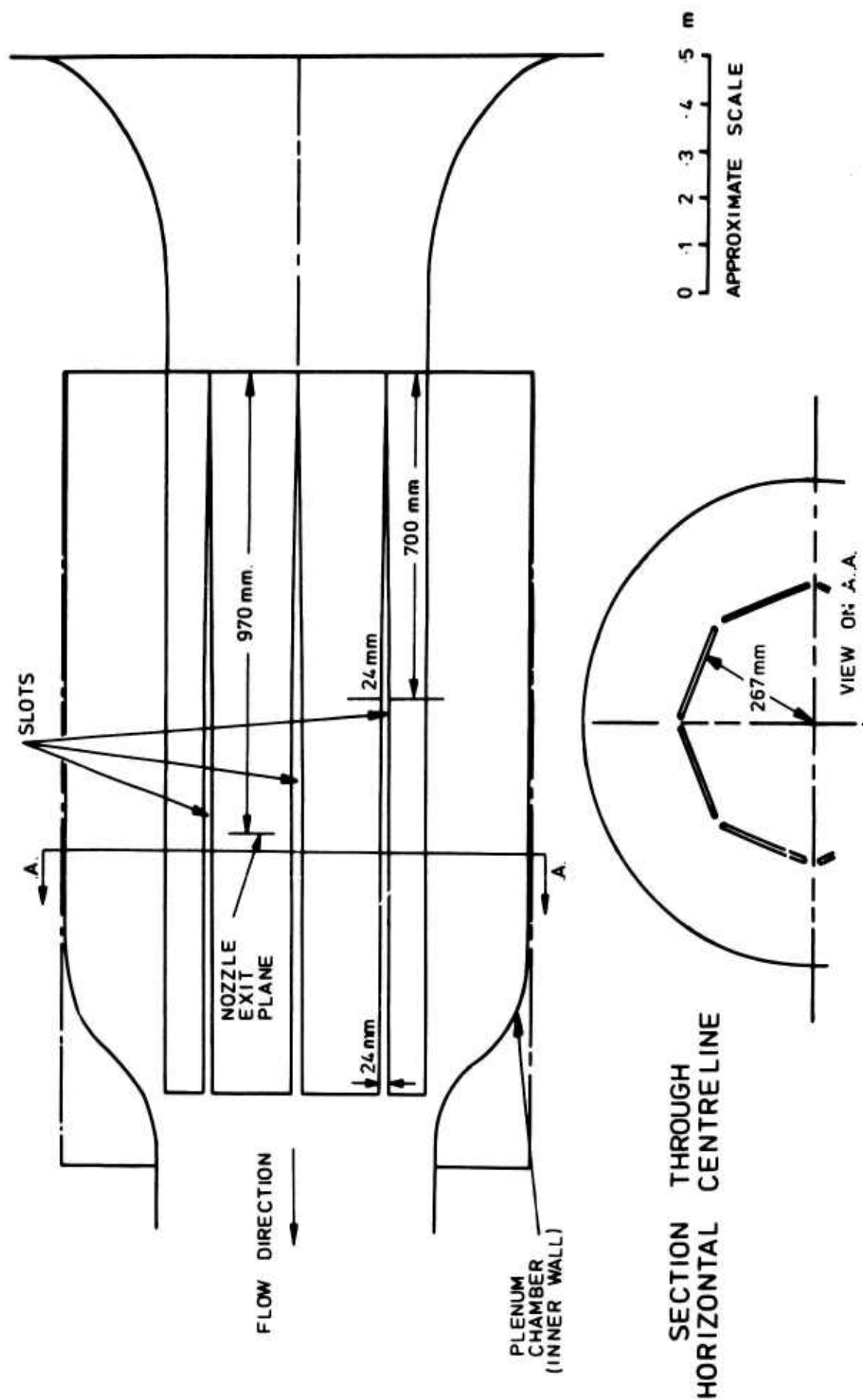


Fig.1 Diagram of transonic tunnel working section

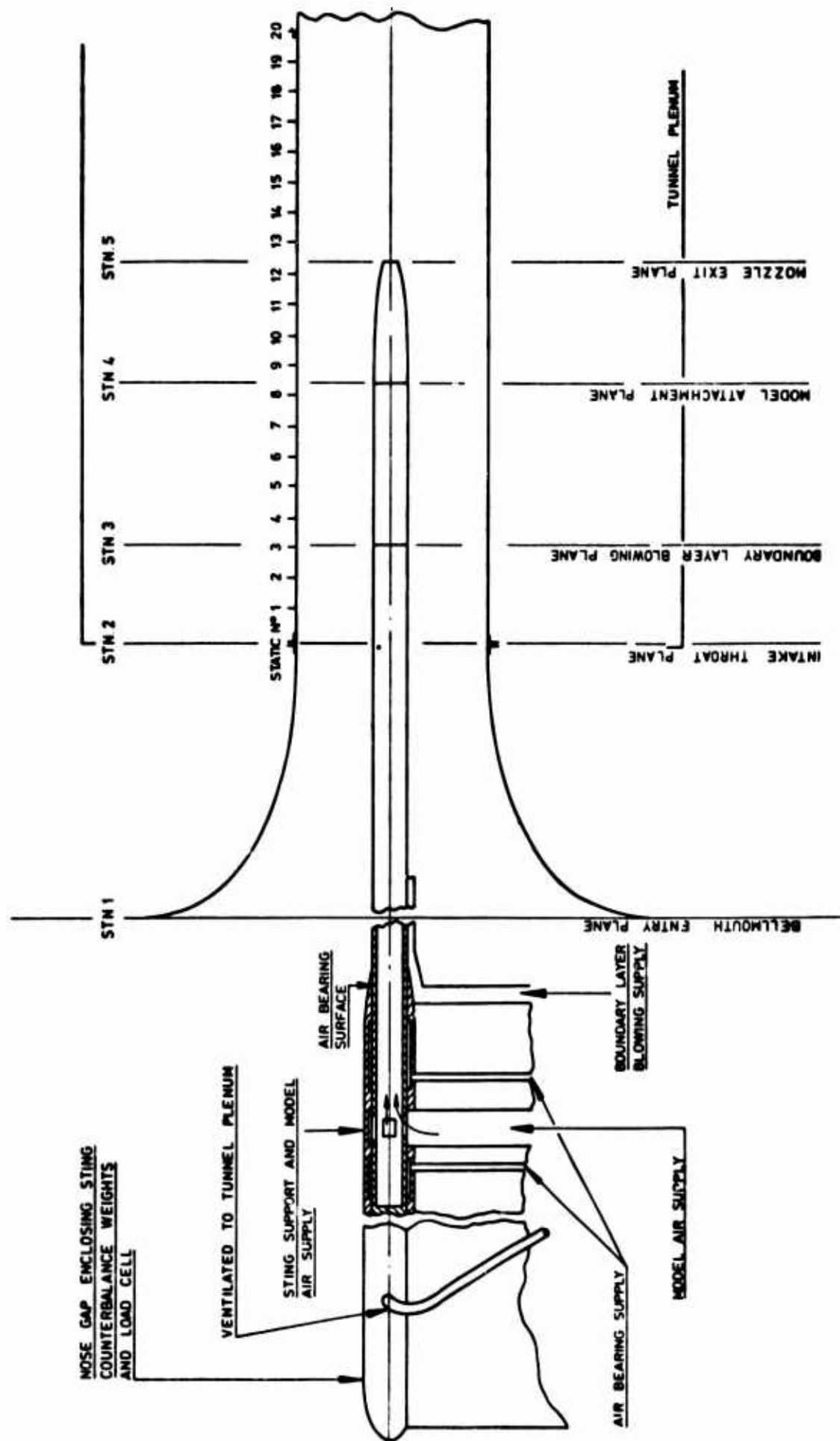


Fig.2 Sketch of transonic wind tunnel layout



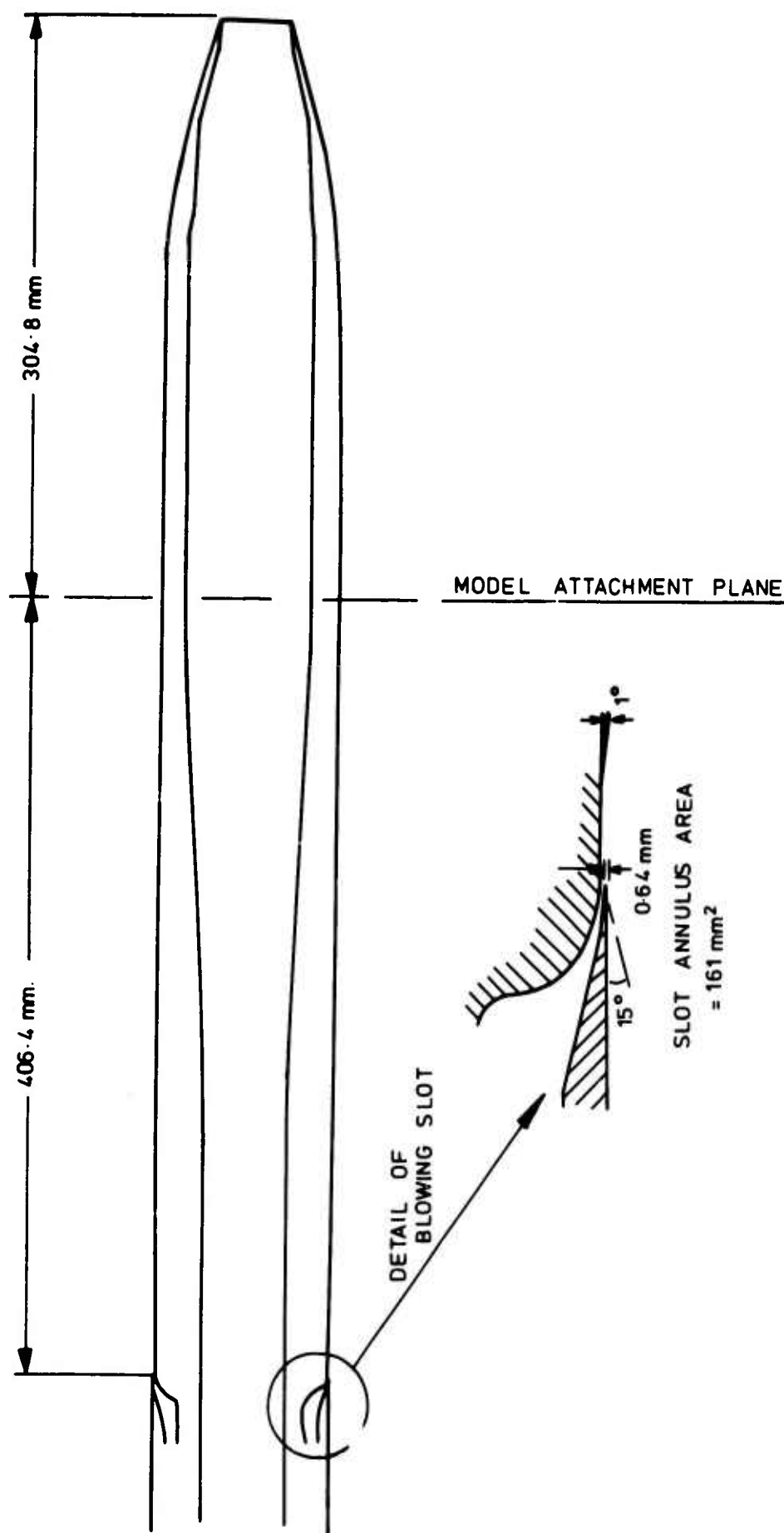
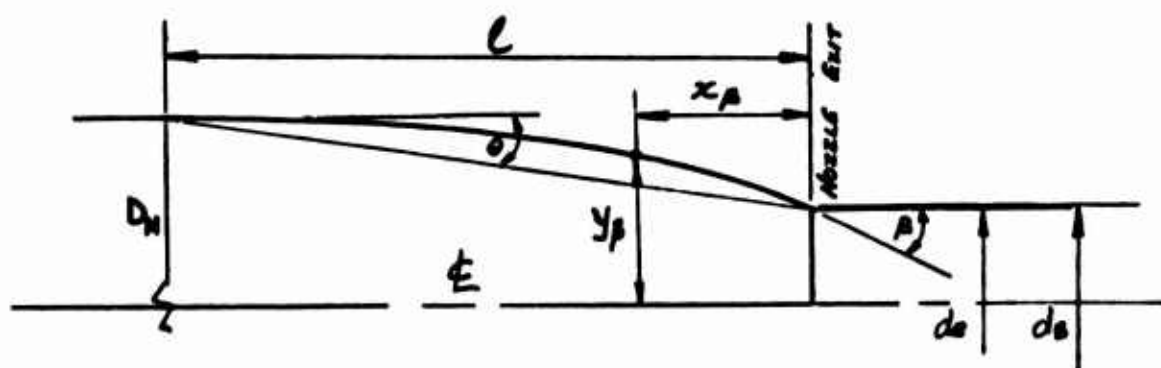


Fig.3 Transonic wind tunnel sting boundary layer blowing system





CONFIGURATION 1 , AGARD 10°					
$x_p/D_M$	$y_p/D_M$	$x_p/D_M$	$y_p/D_M$	$x_p/D_M$	$y_p/D_M$
0	0.20750	0.60	0.39625	1.20	0.48005
0.05	0.22440	0.65	0.40503	1.25	0.48495
0.10	0.24520	0.70	0.41323	1.30	0.48902
0.15	0.26640	0.75	0.42109	1.35	0.49209
0.20	0.28622	0.80	0.42867	1.40	0.49433
0.25	0.30446	0.85	0.43594	1.45	0.49596
0.30	0.32127	0.90	0.44301	1.50	0.49722
0.35	0.33671	0.95	0.44985	1.55	0.49821
0.40	0.35111	1.00	0.45647	1.60	0.49897
0.45	0.36405	1.05	0.46283	1.65	0.49950
0.50	0.37585	1.10	0.46889	1.70	0.49984
0.55	0.38656	1.15	0.47465	1.775	0.50000
CONFIGURATION 2 , AGARD 15°					
0	0.20750	0.40	0.36311	0.80	0.46956
0.05	0.22450	0.45	0.37985	0.85	0.47875
0.10	0.24568	0.50	0.39574	0.90	0.48634
0.15	0.26783	0.55	0.41072	0.95	0.49267
0.20	0.28881	0.60	0.42473	1.00	0.49756
0.25	0.30846	0.65	0.43761	1.05	0.49966
0.30	0.32737	0.70	0.44906	1.15	0.50000
0.35	0.34559	0.75	0.45958		
CONFIGURATION 3 , AGARD 25°					
0	0.20750	0.25	0.32400	0.50	0.44818
0.05	0.23080	0.30	0.34741	0.55	0.47358
0.10	0.25410	0.35	0.37169	0.60	0.49269
0.15	0.27740	0.40	0.39688	0.65	0.49981
0.20	0.30070	0.45	0.42247	0.725	0.50000

GEOMETRIC PARAMETERS					
CONFIGURATION	$l/D_M$	$de/D_M$	$de/D_M$	$\theta$ , DEG.	$\beta$ , DEG.
1	1.775	0.407	0.415	9.4	18.7
2	1.150	0.407	0.415	14.3	18.7
3	0.725	0.407	0.415	22.0	25.0

Fig.5 Afterbody ordinates

$\frac{x_T}{D_m}$	$\phi$ ~ Angle Orientation ~ Deg.					
	0	45	90	135	180	270
.035	1 2 3	1 2 3	1 2 3	1 2 3	1 2 3	1 2 3
.075	1 2 3		1 2 3		1 2 3	1 2 3
.135	1 2 3	1 2 3	1 2 3	1 2 3	1 2 3	1 2 3
.195	1 2 3		1 2 3		1 2 3	1 2 3
.285	1 2 3	1 2 3	1 2 3	1 2 3	1 2 3	1 2 3
.395	1 2 3		1 2 3		1 2 3	1 2 3
.505	1 2 3		1 2 3		1 2 3	1 2 3
.550	3		3		3	3
.575	3	3	3	3	3	3
.600	3	3	3	3	3	3
.625	1 2 3	1 2 3	1 2 3	1 2 3	1 2 3	1 2 3
.725	1 2 3		1 2 3	3	1 2 3	1 2 3
.825	1 2 3				1 2 3	
.995	1 2				1 2	
1.175	1 2		1 2		1 2	1 2
1.425	1 2				1 2	
1.805	1		1		1	1

Fig.6 Afterbody surface static tapping locations. The numbers 1, 2, 3, refer to the three afterbodies, as specified in Figure 5, and signify that a tapping is fitted to the afterbody indicated at the particular location

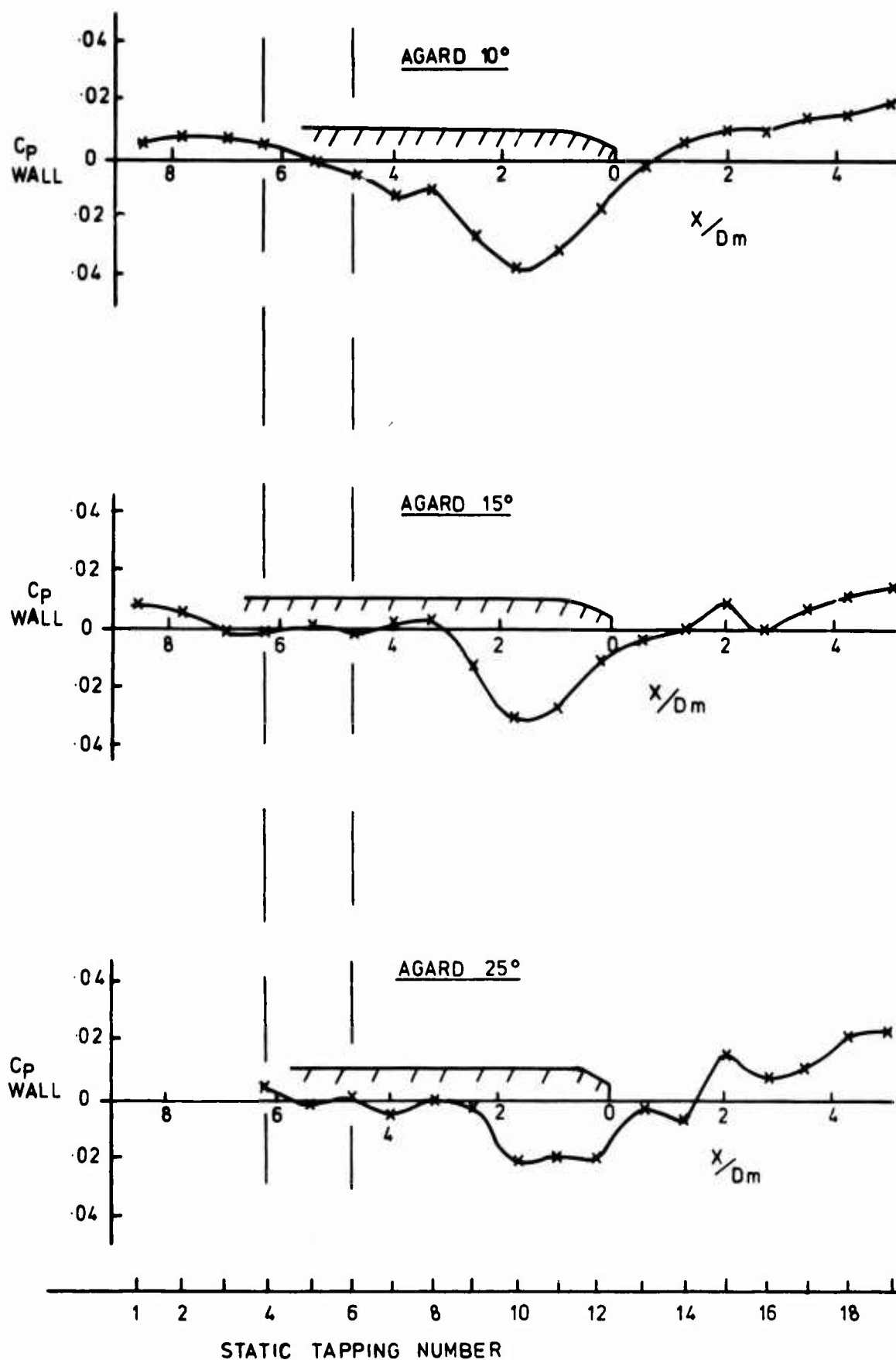


Fig.7 Tunnel wall static pressure distributions  $M_0 \sim 0.8$ ,  $P_j/P_{TS} \sim 3$

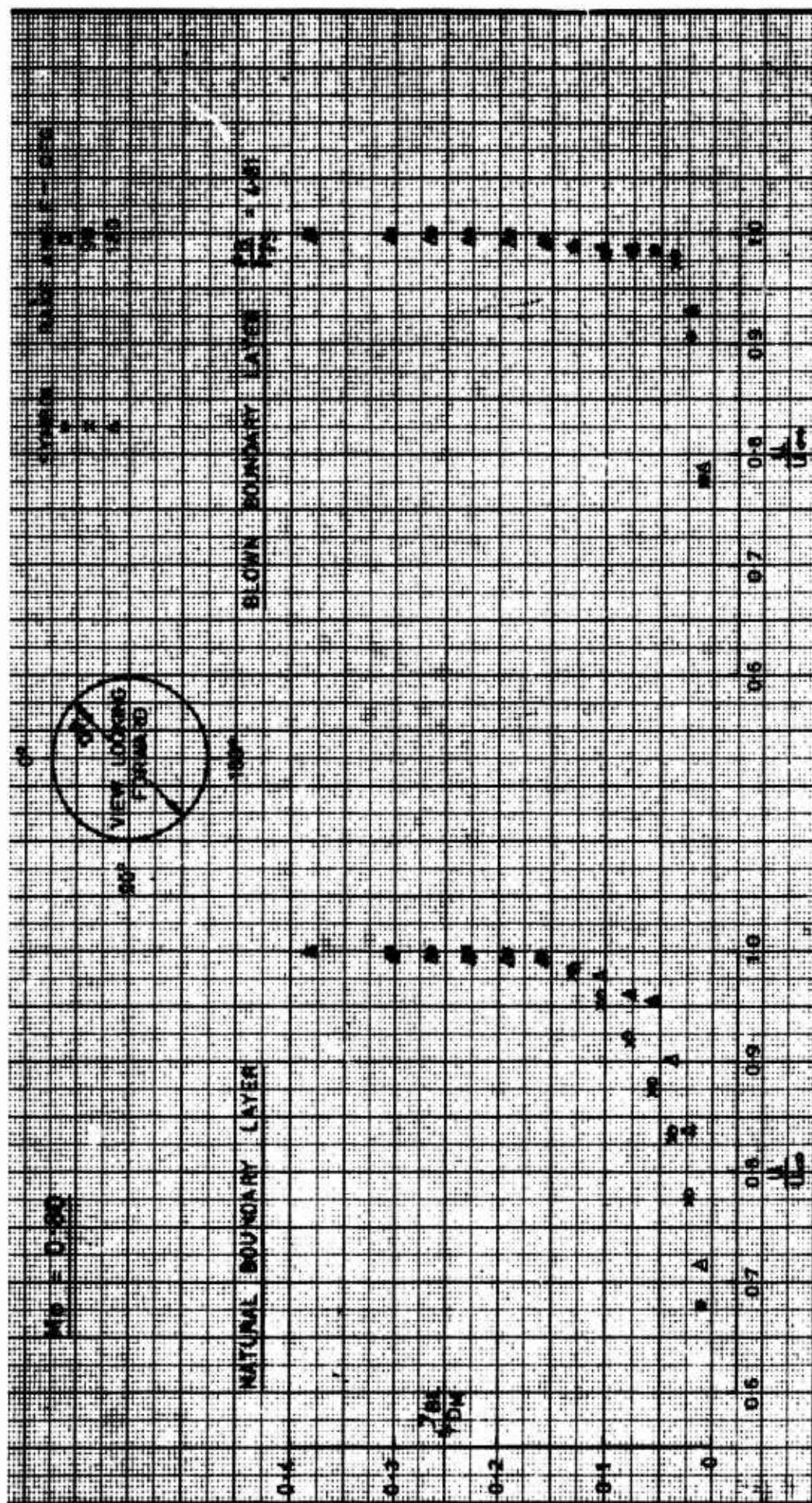


Fig.8 Sting boundary layer profiles with and without blowing

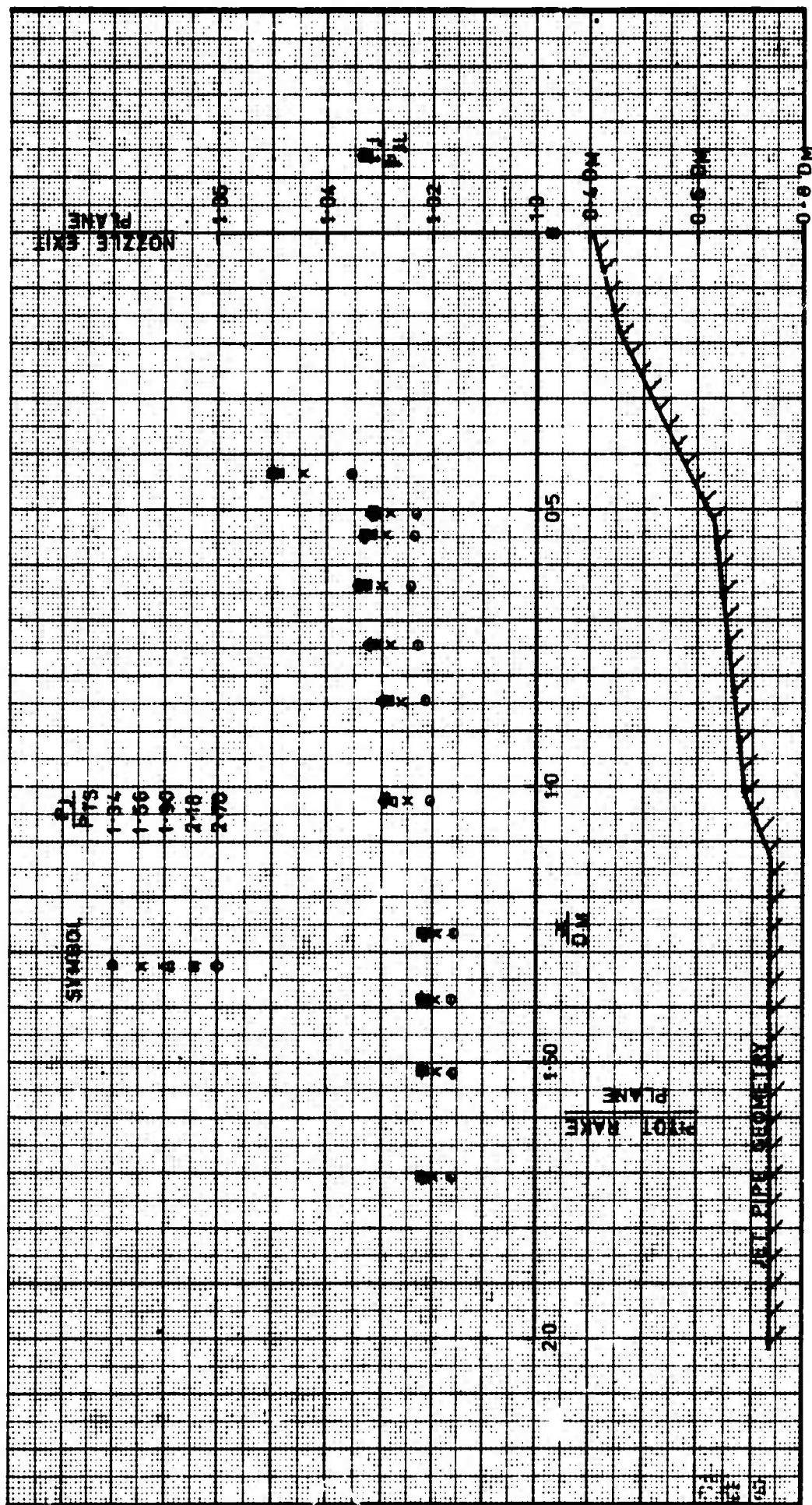


Fig.9 Jet pipe static pressure distribution



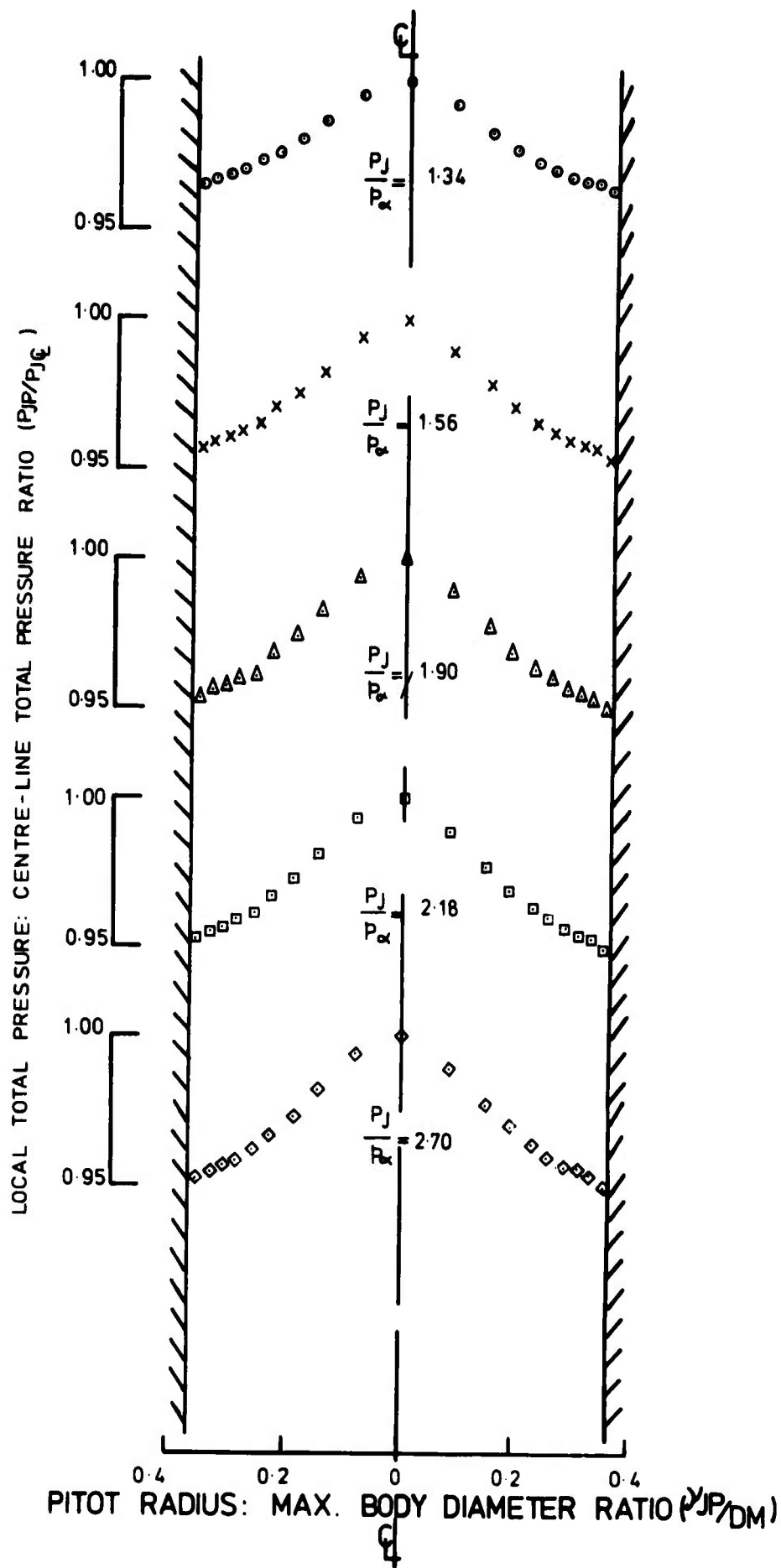


Fig.10 Jet pipe total pressure profiles



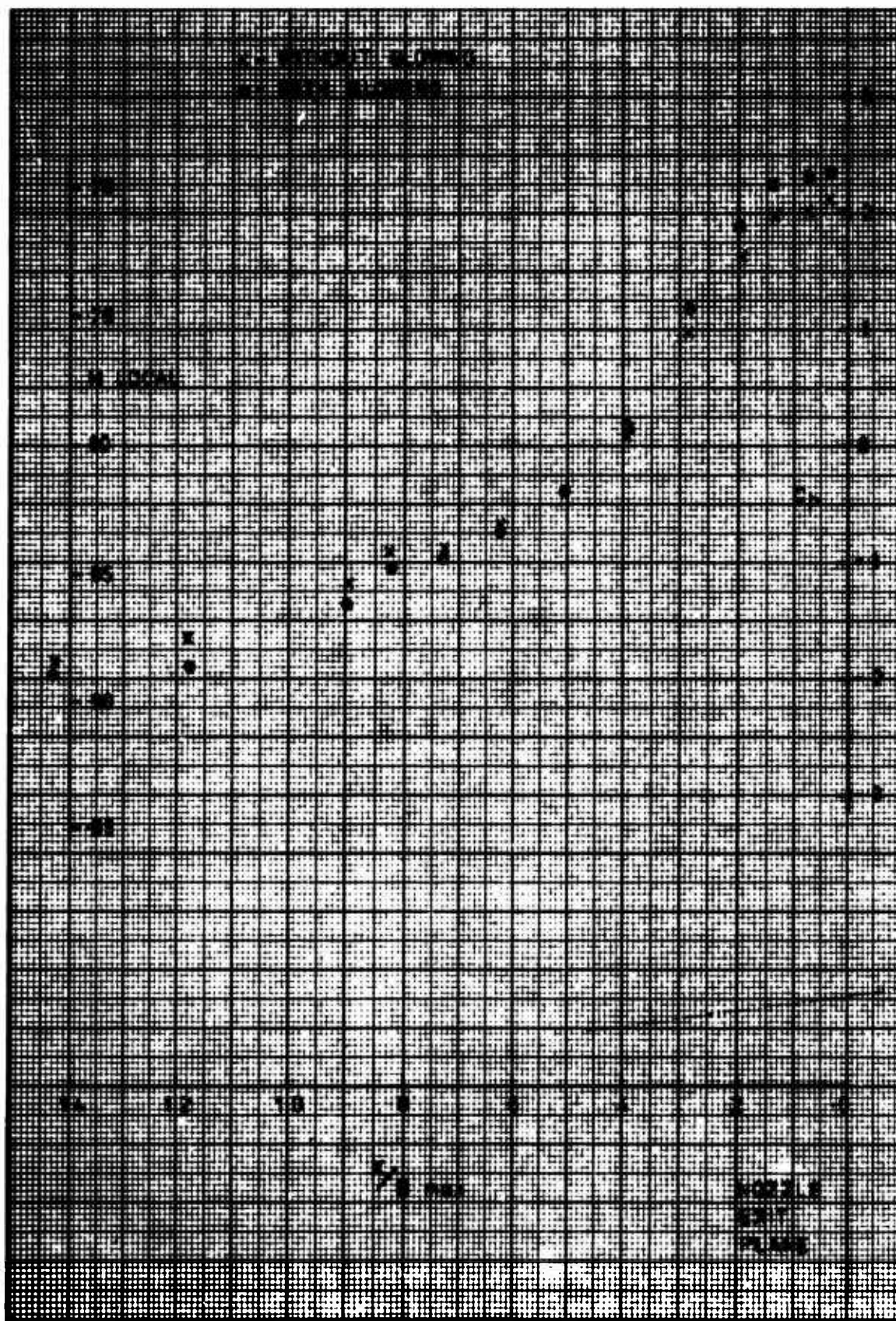


Fig.11 Effect of boundary layer blowing Rolls-Royce tests of AGARD 10° boattail  $M_0 = 0.80$ ,  $P_j/P_{TS} = 4.1$

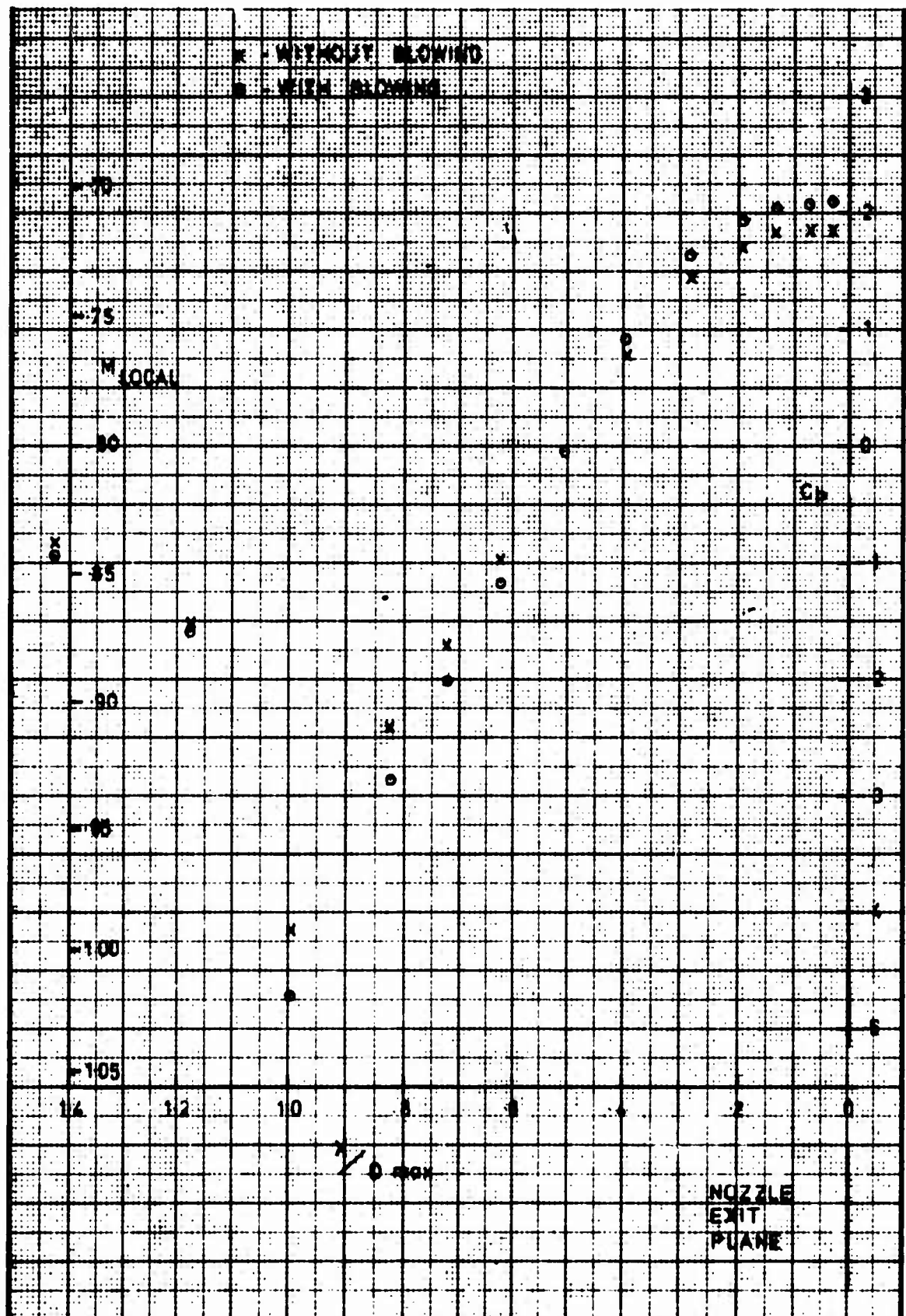


Fig.12 Effect of boundary layer blowing Rolls-Royce tests of AGARD 15° boattail  $M_0 = 0.80$ ,  $P_j/P_{TS} = 3.9$

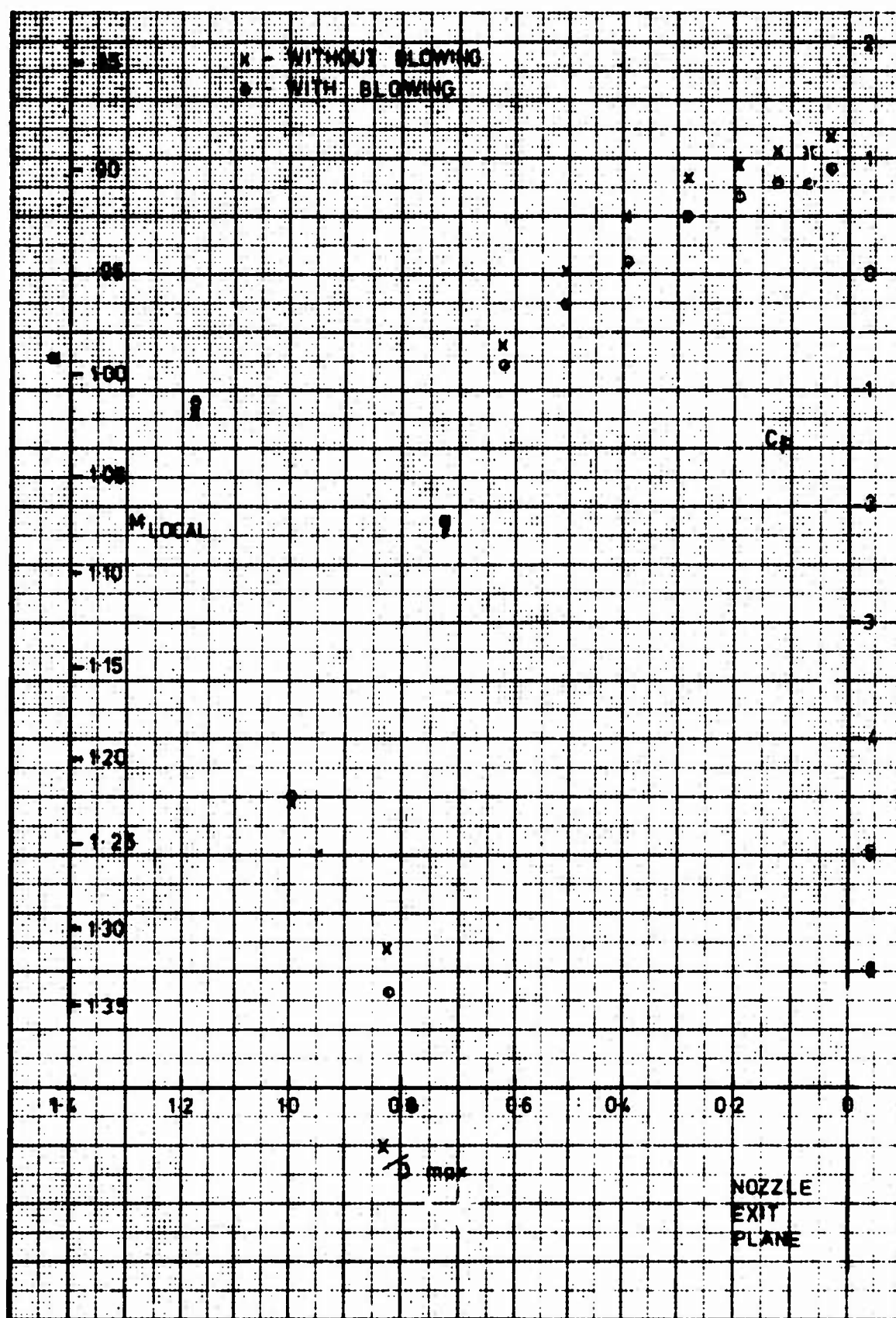


Fig.13 Effect of boundary layer blowing Rolls-Royce tests of AGARD 15° boattail  $M_0 = 0.95$ ,  $P_j/P_{TS} = 5.1$

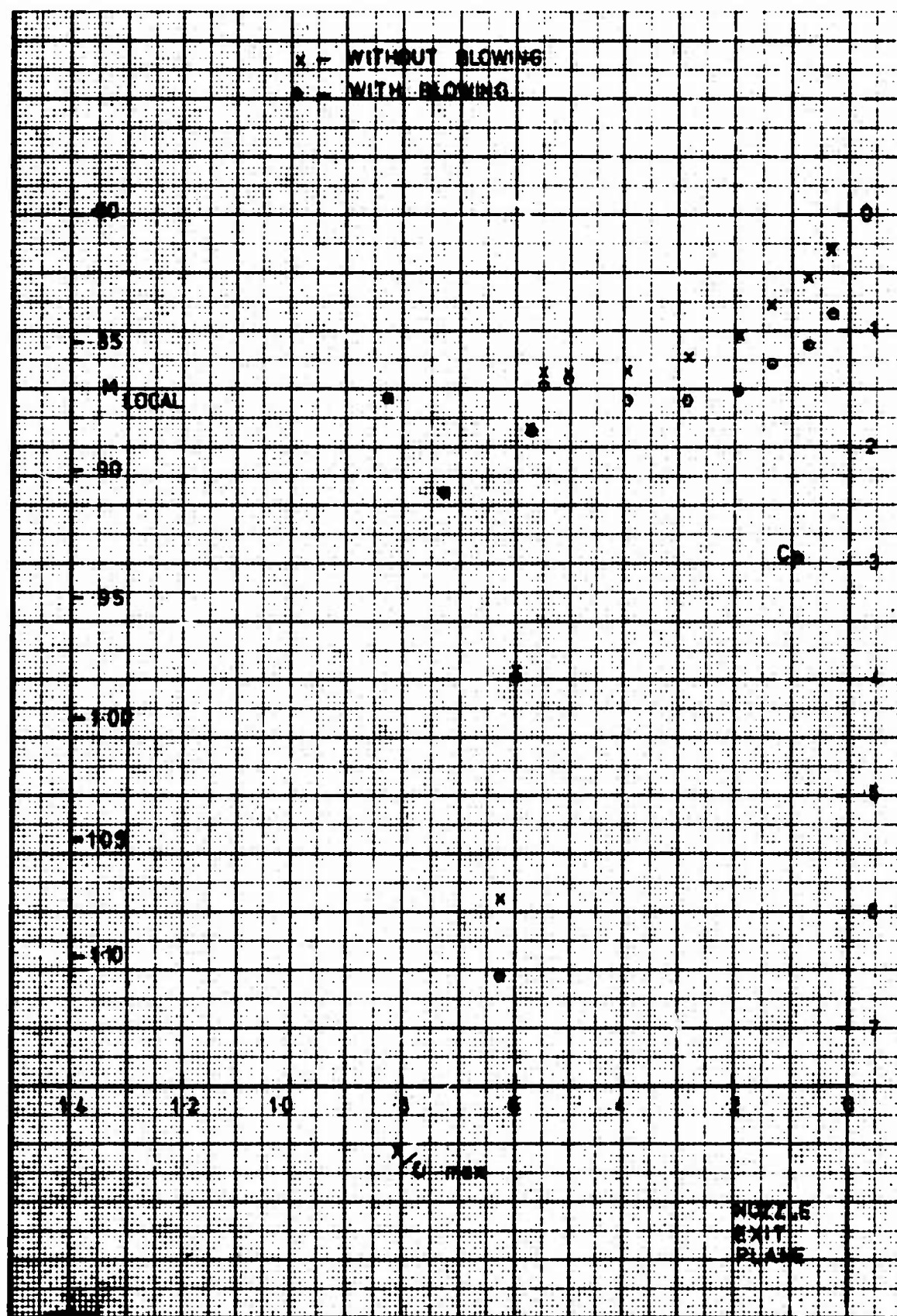


Fig.14 Effect of boundary layer blowing Rolls-Royce tests of AGARD 25° boattail  $M_0 = 0.80$ ,  $P_j/P_{TS} = 3.9$

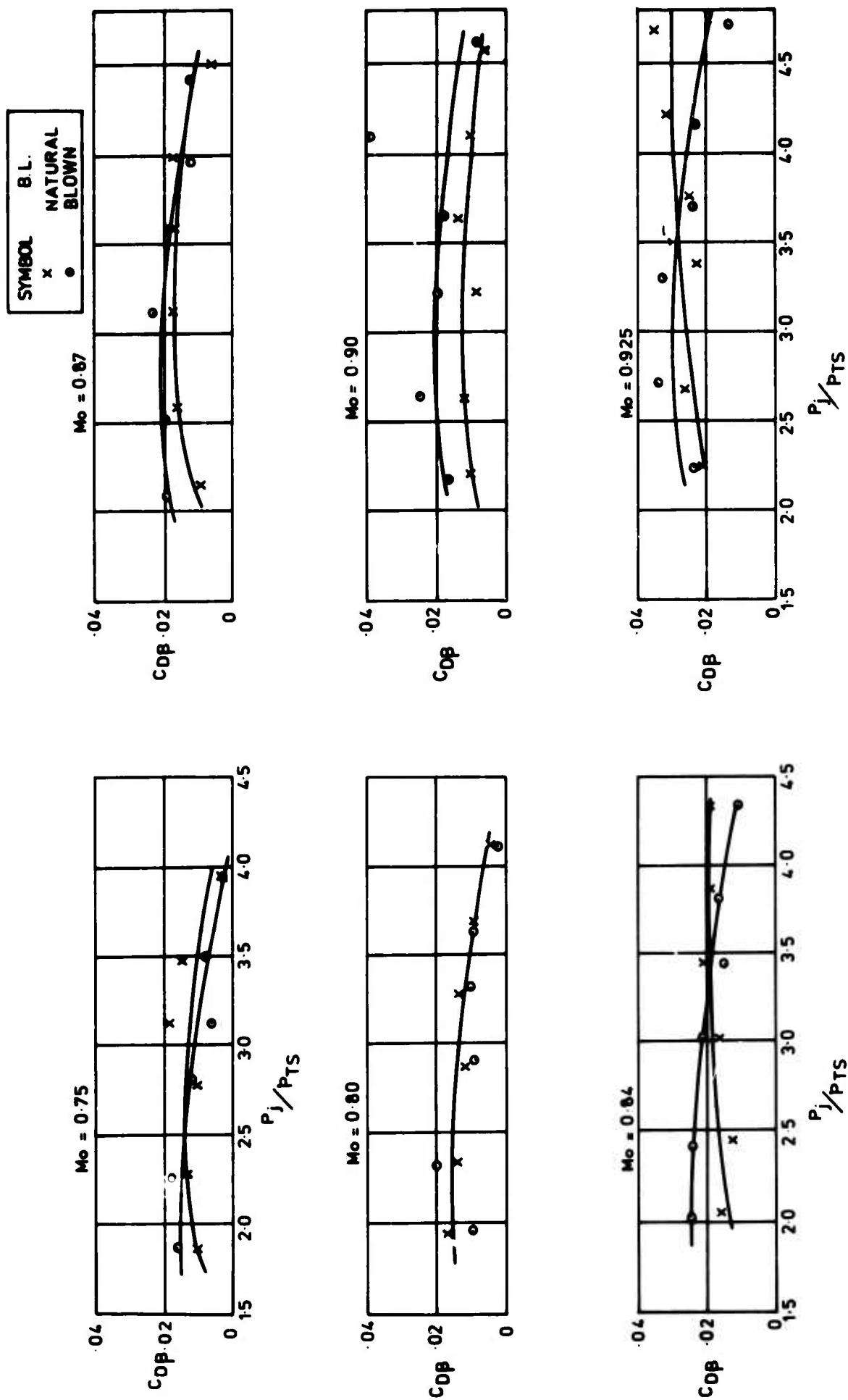


Fig.15 Boattail pressure drag coefficient configuration 1



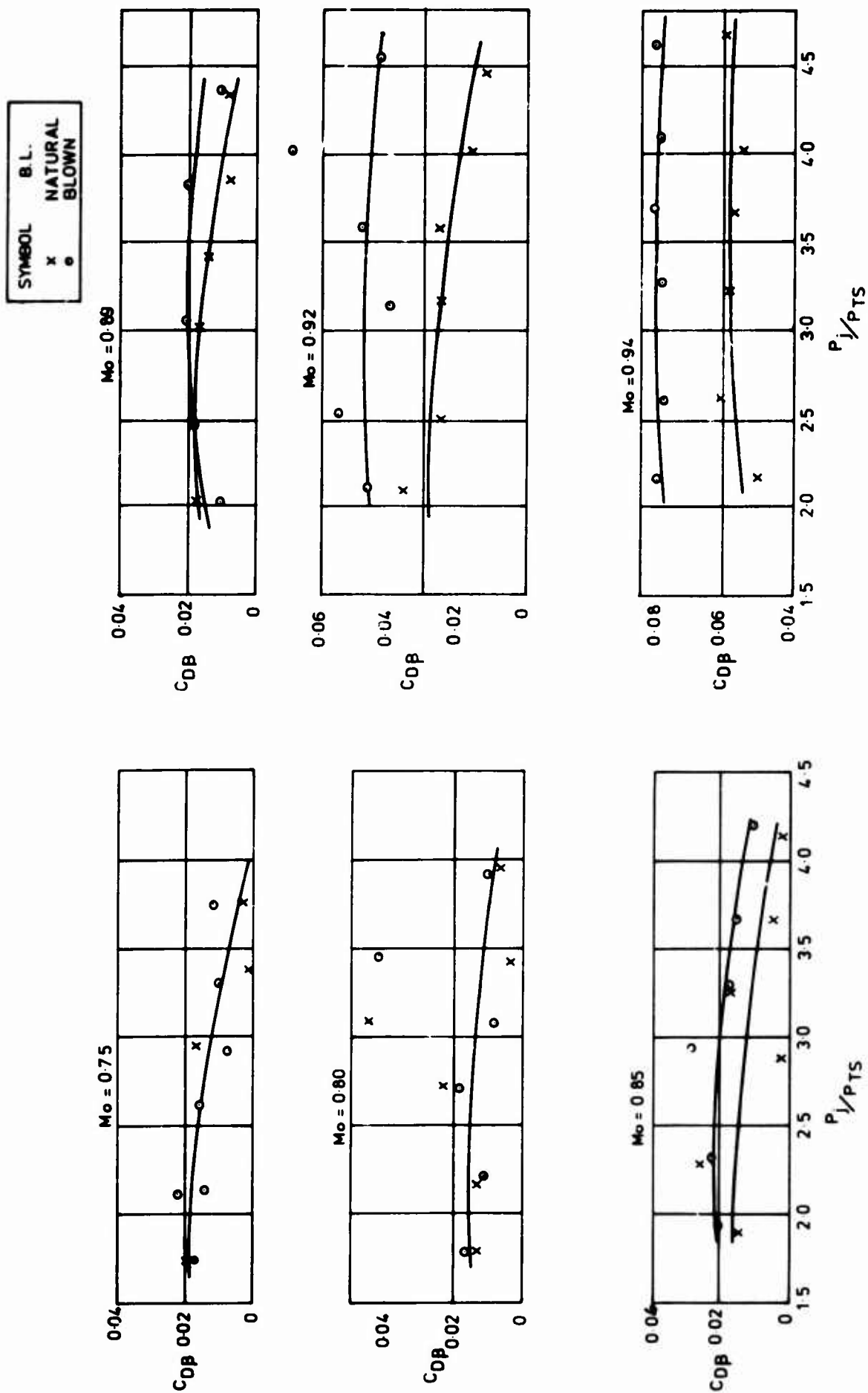


Fig.16 Boattail pressure drag coefficient configuration 2

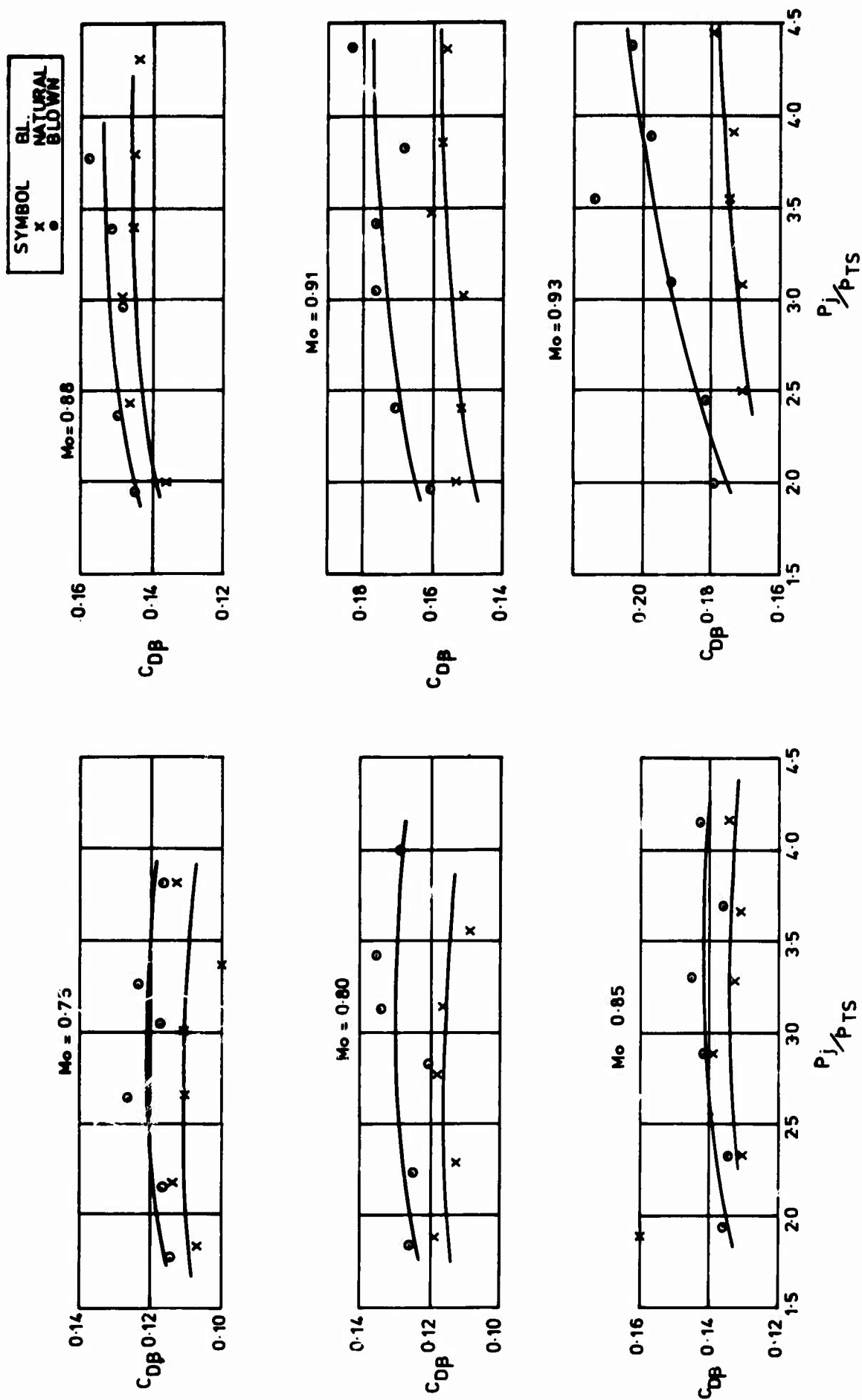


Fig.17 Boattail pressure drag coefficient configuration 3

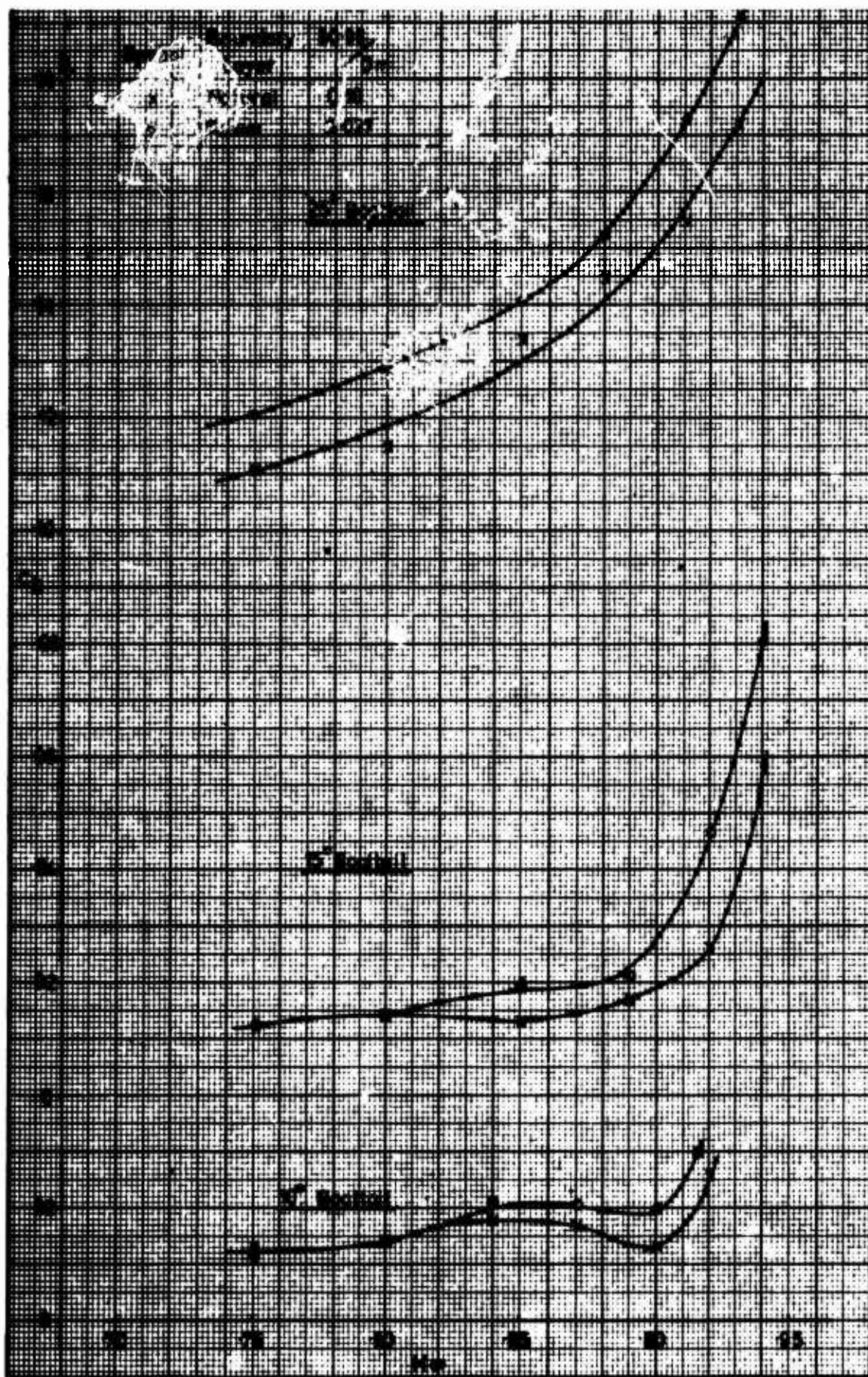


Fig.18 Variation of pressure drag with boundary layer thickness  $P_j/p_{Ts} = 3.0$



# AN EXPERIMENTAL STUDY OF THE INFLUENCE OF THE JET PARAMETERS ON THE AFTERBODY DRAG OF A JET ENGINE NACELLE SCALE MODEL

by

H. Dissen, A. Zacharias

DFVLR-Institut für Antriebssysteme, Braunschweig, Flughafen

## SUMMARY

Numerous experimental tests with an engine nacelle scale model were made to investigate the influence of engine jet parameters on the pressure distribution of the engine nacelle and therefore on the boattail pressure drag. Regarding the planned flight tests on the HFB 320 Hansa Jet at the end of 1975, the experimental work was done with a model of the GE CJ 610 engine nozzle, including its nacelle. The influence of jet pressure ratio and jet temperature on the boattail pressure distribution at different flight Mach numbers are shown. The effect of boundary layer control and the influence of changing the internal nozzle geometry on the pressure drag is also investigated.

## SYMBOLS

A	area, $m^2$
$A_{MAX}$	maximum cross-sectional area of model, $m^2$
$C_{DP}$	pressure drag coefficient, $D_p / (q_\infty \cdot A_{MAX})$
$C_p$	pressure coefficient, $(p - p_\infty) / q_\infty$
$c_p$	specific heat at constant pressure, $kJ/kgK$
$D_p$	pressure drag, N
L	length, m
M	Mach number
$\dot{m}$	massflow, $kg/s$
p	pressure, $N/m^2$
q	dynamic pressure, $N/m^2$
R	gas constant, $kJ/kgK$
Re	Reynolds number
$Re_{DMAX}$	free stream Reynolds number based on maximum model diameter
r	radial distance from model center line, m
$r^*$	recovery factor (specially determined for the used thermocouples)
t	temperature $^{\circ}C$
T	temperature, K
U	velocity in x-direction, $m/s$
x	axial coordinate
y	radial coordinate
$\beta$	afterbody boattail angle
$\kappa$	ratio of specific heats
$\rho$	density, $kg/m^3$

I-C2

NPR nozzle pressure ratio,  $NPR = p_t/p_\infty$

$\epsilon$  compressibility factor,  $\frac{\kappa-1}{\kappa} (p_t/p_s - 1) / ((p_t/p_s)^{(\kappa-1)/\kappa} - 1)$

### Subscripts

B.L. boundary layer

e exit

j jet

M measuring

MAX maximum

s static

t total

$\infty$  free stream

## 1. EXPERIMENTAL TEST SETUP

### 1.1 Wind Tunnel

The arrangement of the wind tunnel is shown in Figure 1. The test facility consists of 4 elements:

- the turbojet engine J65, which is only shown with its bellmouth,
- the transition unit between the test section and the jet engine inlet,
- the test section with air inlet and rake displacement device and
- the model support unit including the hot gas generator.

The engine massflow of the J65 turbojet was directly used to simulate the flight velocity by sucking the air from the surrounding atmosphere through the test section and transition unit into the engine inlet. Flight Mach number can be changed by controlling the engine speed. The model is coaxially situated in the test section.

The turbojet engine J65 (1) has a 13-stage axial flow compressor with a pressure ratio of about 6.4. The maximum engine speed is 8,300 revolutions per minute (RPM) and the engine airflow is 52 kg/s. The test section was built corresponding to these data.

The transition unit (2) consists in its first version of two cylindrical steel pipes one fitted into the other, of 795 mm diameter. In order to simulate higher Mach numbers a modified version of this stage is planned and will be built as a conical diffuser to reduce total pressure loss.

The test section (3) is cylindrical with 505 mm diameter, and has a length of 2,000 mm. In a slot on the bottom side of the test section the rake (5) for measuring the total pressure and temperature distribution of the jet and the freestream velocity profile can be displaced downstream in an axial direction. The rake (6) for determining the boundary layer profile is also installed in the test section. The static pressure distribution can be measured by several static pressure probes placed in 6 areas on the wall of the test section (Fig.2). The area blockage due to the model is about 4%.

### 1.2. Model

The model, which is not insulated, is in its internal and external geometry a 1/7.3 scale model of the HFB 320 CJ 610 jet engine nacelle. At its maximum diameter a slot for blowing air is fitted to the model to influence the boundary layer (Fig.3). The model consists of two halfshells and incorporates 28 static taps and 10 thermocouples. The model contour is described in Figure 4. The model is flanged to a cylindrical pipe connecting the model with the hot gas generator. This hot gas generator heats up compressed air in a combustion chamber and is installed on a movable lifting device. This makes it possible to position the model in the desired place of the test section (Fig.1(4)). The connecting pipe consists of two coaxial arranged pipes, the internal one for the hot gas, the outer one to supply air to the slots for boundary layer control.

### 1.3 Instrumentation

The ordinates describing the static taps and the position of the thermocouples on the nacelle are listed on

Figure 4. The jet rake consists of 40 pitot probes and 40 NiCr-Ni thermocouples. The boundary layer rake has only 4 pitot probes and 4 NiCr-Ni thermocouples. The disposition of both rakes is illustrated on Figure 1 and Figure 2. Static taps and thermocouples in the connection pipe in front of the nozzle are used to determine the nozzle airflow. Twenty-four static tapings were distributed axially along the test section wall on six measuring planes. The disposition of these tapings is shown in Figure 2. Tunnel Mach number was evaluated from the total pressure of the rake in the jet exit area outside the jet and the static pressure in the measuring plane "2". All data (pressures and temperatures) were recovered automatically on paper tapes and evaluated with a computer program.

In subsonic flow the measured dynamic pressure is

$$q = \frac{\rho}{2} \cdot U^2 \cdot \epsilon.$$

With the density  $\rho$  and the measured temperature  $T_M$

$$\rho = \frac{P_s}{R \cdot T_s}; \quad T_M = T_s + \frac{U^2}{2 \cdot c_p} \cdot r^*$$

the tunnel Mach number

$$M = U / \sqrt{\kappa R T_s}$$

is defined by the Mach number found for the tunnel flow in the jet exit area. The influence of the test section length and of area blockage on the velocity profile respectively on static pressure distribution on the wall is shown in Figure 5 and Figure 6. It is indicated that tunnel length has no significant effect on these parameters at several RPM's.

The pressure coefficient  $C_p = (p - p_\infty)/q_\infty$  is calculated using the difference between the measured static pressure on the nacelle and the static pressure measured in plane "2" of the test section wall. (The jet exit area is located between the measuring planes "2" and "3".) The dynamic pressure is determined by the pitot pressure and the static pressure on the wall in plane "2". The pitot pressure is measured in the freestream outside the jet with the rake (5). The pressure drag coefficient  $C_{DP} = D_p/q_\infty A_{max}$  is derived from the boattail pressure drag  $D_p = \int_A$

$\Delta p \sin \varphi \, dA$ .  $\sin \varphi \cdot dA$  is the finite area element of the boattail surface projected vertical to the model axis. It is assumed that there is a symmetrical pressure distribution on the boattail surface.

## 2. TEST PARAMETERS

Due to the windtunnel capability the investigations were made for flight Mach numbers of  $M_\infty = 0.2, 0.45, 0.6$ . Regarding these flight velocities the Reynolds numbers are  $Re_{D_{MAX}} \cdot 10^{-6} = 0.4822, 1.0194$  and  $1.2108$ . The Reynolds numbers are related to the maximum diameter of the model. Three different nozzle pressure ratios  $NPR = 1.7, 2.2$  and  $3.0$  and, for each, two jet temperatures of  $T_j = 290K$  and  $790K$  are chosen for the above mentioned flight Mach numbers. The boundary layer was influenced by a secondary airstream ejected through a slot on the model surface. For the three Mach numbers the massflow of this secondary airstream was constant with  $m_{B.L.} = 0.8 \text{ kg/s}$ . The massflow rate limited by the pressure air supply unit could influence the boundary layer up to  $M_\infty < 0.45$  sufficiently. The boundary layer could not be completely corrected by the massflow at  $M_\infty = 0.6$ . Distortion of the jet velocity distribution was produced in controlling the air supply for secondary airflow at the nozzle exit (Fig.3). Moreover to  $M_\infty = 0.45$  the slot for the jet exit bypass stream was closed. The following table describes the different test parameters in summary.

$M_\infty$	$Re_{D_{MAX}}$	NPR	$T_j$	B.L.	Distortion	Configuration Boattail/Nozzle
0.2	$0.4822 \cdot 10^6$	1.7,2.2,3.0	290	natural	no	HFB/HFB
			790	blown	yes	
0.45	$1.0194 \cdot 10^6$	1.7,2.2,3.0	290	natural	no	HFB/HFB
			790	blown	yes	HFB/AGARD
0.6	$1.2108 \cdot 10^6$	1.7,2.2,3.0	290	natural	no	HFB/HFB
			790	blown	yes	

### 3. RESULTS AND DISCUSSION

Figure 7a shows the boundary layer velocity and temperature profiles at the maximum diameter of the HFB 320 CJ 610 jet engine model with natural and blown boundary layer at  $M_\infty = 0.45$  for a cold jet. At this Mach number it was possible to almost eliminate the boundary layer. Figure 7b shows the boundary layer profiles at the same Mach number for cold and hot jets without blowing. With the above mentioned measurements it is evident that, as a result of the heat conduction within the model for the hot jet condition, the surface temperature of the model exceeded the static temperature, entailing a heat transfer from the model to the free stream. This gives rise to a more turbulent shape of the velocity profiles; the influence is equivalent to the effect produced by boundary layer blowing. Figure 7c shows the natural and blown boundary layer profiles at  $M = 0.6$ . At this Mach number the influence of blowing is not significant.

Surface temperature distributions of the model at  $M_\infty = 0.45$  and  $0.6$  are presented in Figure 8. For the hot jet the wavy trend of the curves is caused by the structural layout of the model of the engine nacelle. At the attachment points between the nacelle and the jet pipe the heat flux to the outer surface is intensified in comparison with the more insulated intermediate portions of the nacelle. The slight streamwise rise in the surface temperature is also a result of the heat conduction within the model, if the jet is hot. In Figures 9 and 10 the influence of jet temperature on the pressure distribution on the boattail is shown. These data are plotted for  $M_\infty = 0.45$  and  $0.6$ , a nozzle pressure ratio of 3.0, and for natural and blown boundary layer. It is confirmed that for both Mach numbers at least up to NPR (nozzle pressure ratio  $p_t/p_\infty$ ) = 3.0 the hot jet is more penalized than the cold jet, for the natural boundary layer as well as for the blown one. Only at  $M_\infty = 0.6$  and blown boundary layer (Fig. 10b) the difference between the hot and cold jet is not so clear, but this will be evident when estimating the drag. Up to this nozzle pressure ratio the flow curvature of the jet is concave and the jet plume effect, which favours the recompression on the boattail is not so intensified. Here the jet entrainment, favoured by the faster decay of the hot jet<sup>1</sup> compared to the cold jet, dominates. So the recompression is hindered and the pressure distribution is more penalized. Concerning the hot jet the shape of the boundary layer velocity profiles is comparable to that of a blown boundary layer due to the heat transfer from the model to the free stream. So it cannot be said that the difference between the pressure distributions is only based on the intensified hot jet entrainment. Planned investigations with an insulated model surface will give more distinctive explanation. Figure 11 shows the influence of the nozzle pressure ratio for a cold and hot jet on the boattail pressure distribution. There is hardly a difference between the pressure distributions at various NPRs ( $1.7 < \text{NPR} < 3.0$ ). Investigations at the same conditions without a jet show a significant difference between the pressure distributions. This confirms the jet plume effect, which favours the recompression.

The influence of the boundary layer on the pressure distribution at  $M_\infty = 0.45$  with cold and hot jet is shown in Figure 12. At this Mach number the boundary layer could almost be corrected completely. It is evident that (Fig. 12a) an improvement of the pressure distribution for a cold jet is caused by blowing. For the hot jet a similar statement can be made, although in this case the difference is not clear enough. By estimating the drag this can be seen quite clearly. Figure 13 shows the boattail surface static pressure distribution on the model for a cold and hot jet at  $M_\infty = 0.6$ . They indicate that a distortion of the jet velocity profile produces no significant effect on the static pressure distribution. The effect of the internal nozzle configuration on the pressure distribution at  $M_\infty = 0.45$  for a cold jet and  $\text{NPR} = 1.89$  is shown in Figure 14. Two different nozzle contours incorporating the same boattail shape were used to investigate this effect. It can be seen that there is no difference between the boattail pressure distributions obtained with the AGARD and HFB 320 nozzles.

In Figure 15 the pressure drag coefficient for a cold and hot jet is shown for  $\text{NPR} = 3.0$  at  $M_\infty = 0.2, 0.45$  and  $0.6$ . Corresponding to the pressure distributions, the pressure drag coefficient for hot jets is higher than for cold jets. By increasing the flight Mach number from 0.2 to 0.45, the pressure drag coefficient decreases and remains nearly constant from  $M_\infty = 0.45$  to  $M_\infty = 0.6$ .

### 4. CONCLUSION

Experimental tests were made to investigate the influence of the jet temperature and jet pressure ratio on the static pressure distribution of the engine nacelle and therefore on the boattail pressure drag. Moreover the effect on boundary layer control of changing the inner nozzle contour and of distortion of the jet velocity profile is included.

In the Mach numbers range  $0.2 < M_\infty < 0.6$  hot jet causes a penalized static pressure distribution on the nacelle and therefore a higher boattail pressure drag. These results have to be proved by further tests with an insulated nozzle to eliminate the heat flux from the nozzle to the nacelle. Nozzle pressure ratios in the range of  $1.7 < \text{NPR} < 3.0$  do not effect the pressure distribution to a measurable degree.

The influence of the boundary layer on the boattail static pressure distribution can only be stated for  $M_\infty = 0.45$ . Boundary layer control favours the pressure drag for the cold jet, but for the hot jet this effect cannot be shown clearly.

Changing the inner nozzle contour or distorting the jet did not act upon the static pressure distribution in this investigation.

#### REFERENCES

1. Schwantes, E. *Das Rezirkulationsströmungsfeld eines VTOL-Hubtriebwerks*; DLR-FB 72-50.

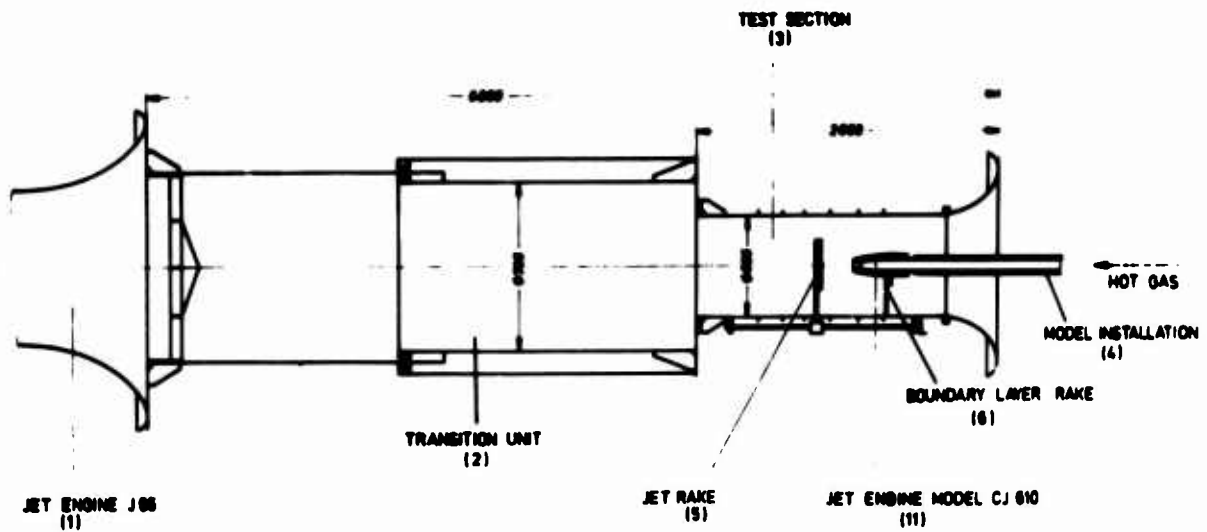


Fig.1 Test setup

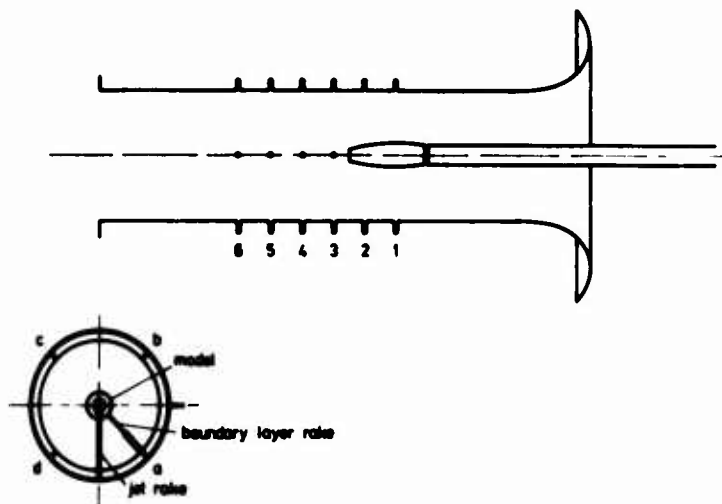


Fig.2 Measuring planes with pressure taps on the wind tunnel wall

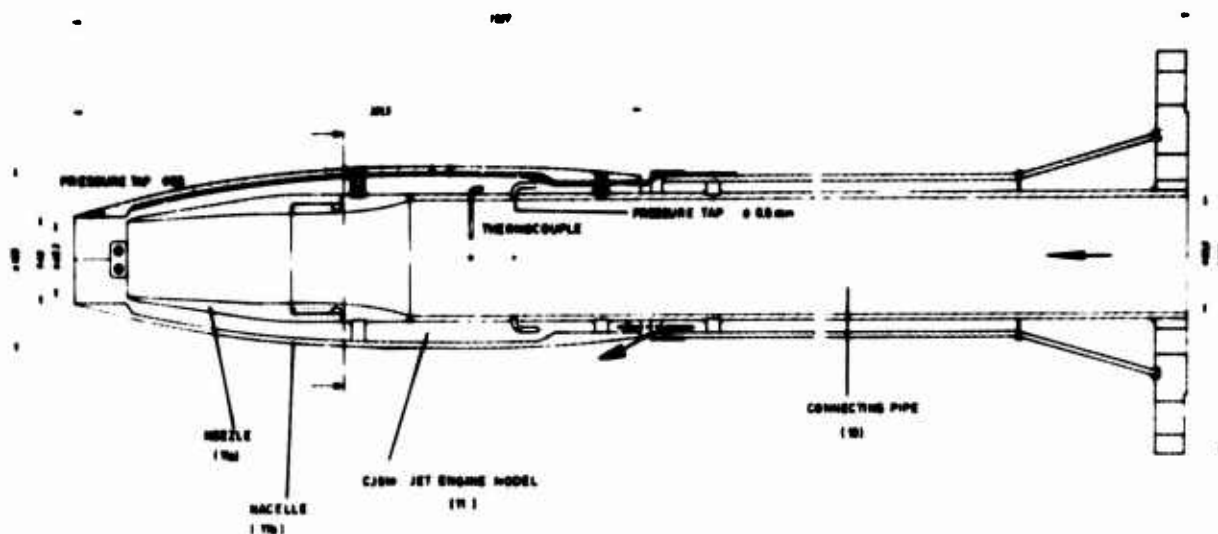


Fig.3 HFB 320 CJ 610 Model assembly

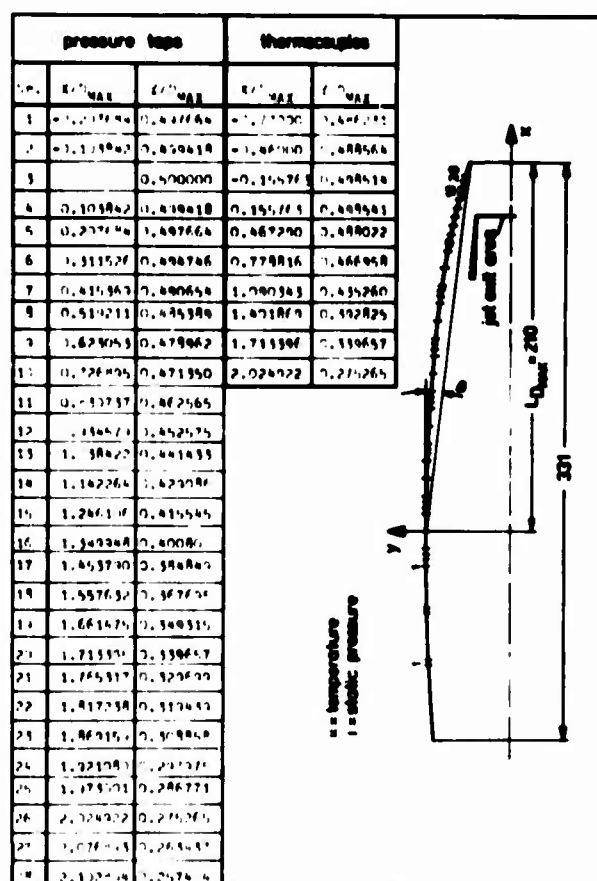


Fig.4 Location of pressure taps and thermocouples

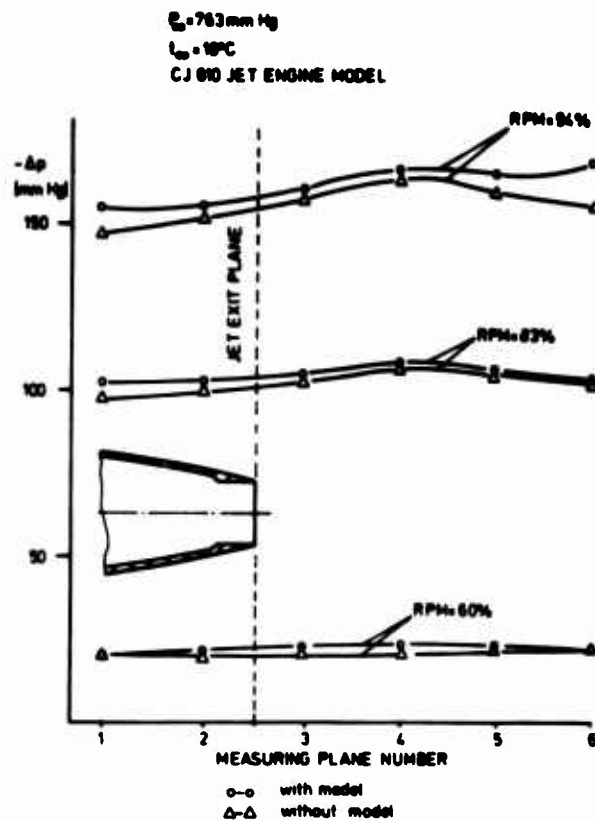


Fig.5 Pressure distribution on the wind tunnel wall with and without model ( $\Delta p = p_{\text{wall}} - p_{\infty}$ )

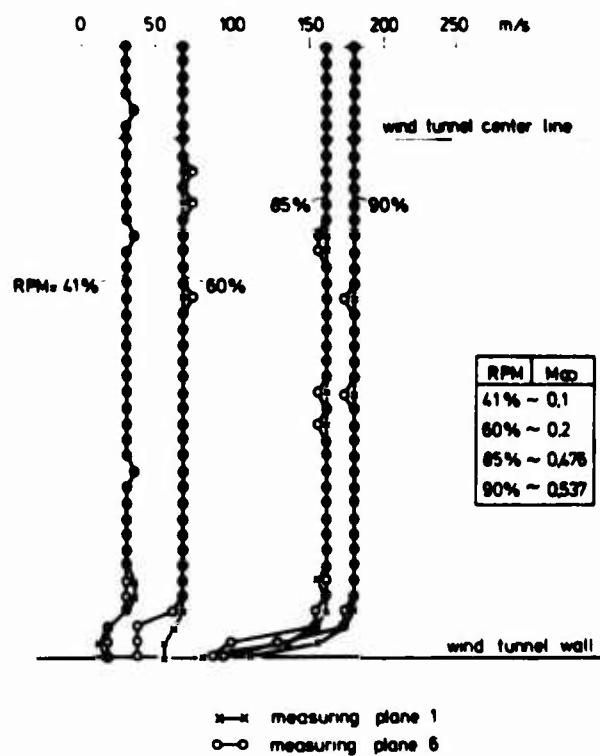


Fig.6 Wind tunnel velocity profiles without model



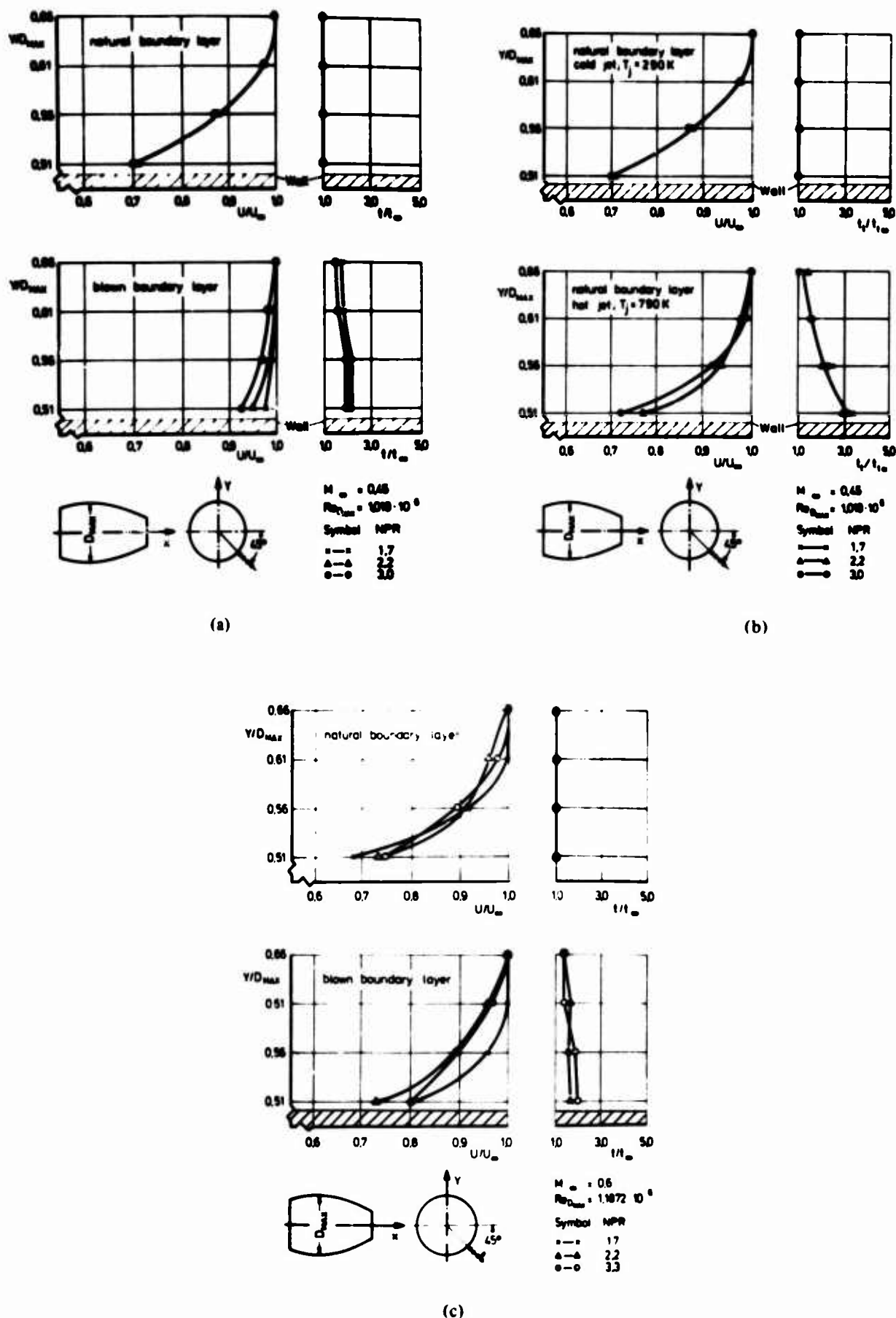
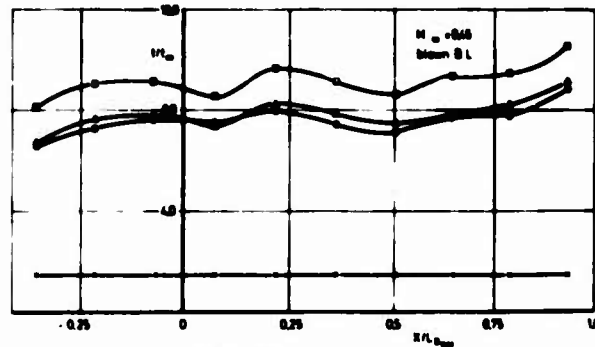
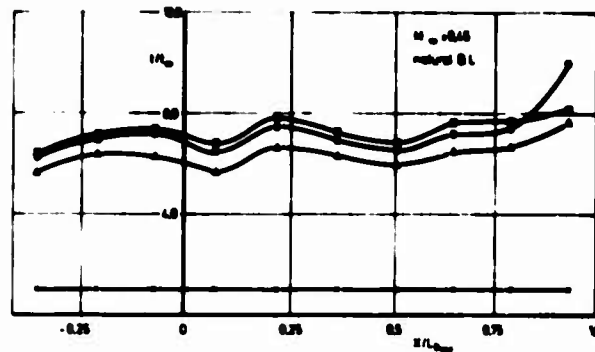


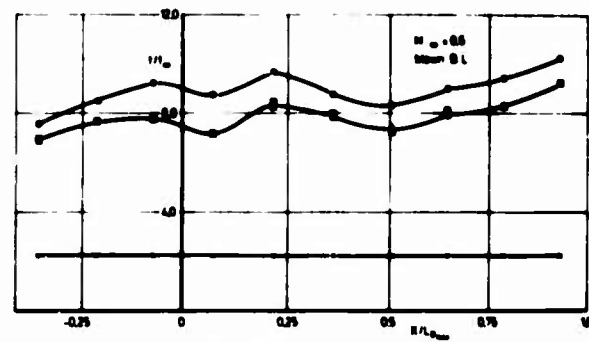
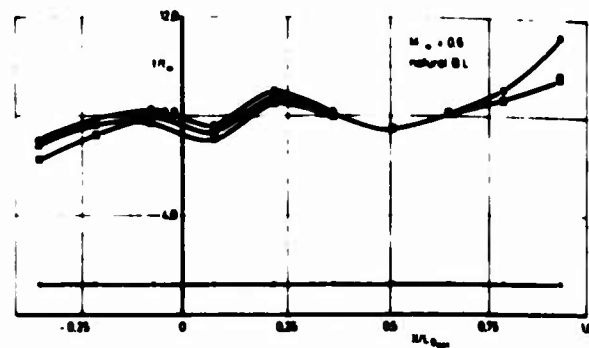
Fig. 7 Boundary layer velocity and total temperature profiles at the maximum diameter of HFB 320 engine nacelle model for cold and hot jets and for natural and blown boundary layer



Symbol	jet	jet
□	1.7	2.2
△	17	2.2
○	22	3.0
●	30	3.0

cold jet      hot jet

(a)

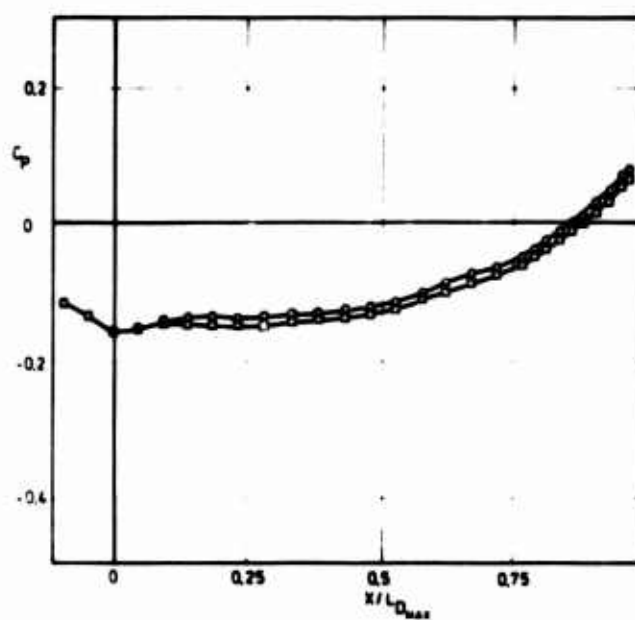


Symbol	jet	jet
□	1.7	2.2
△	17	2.2
○	22	3.0
●	30	3.0

cold jet      hot jet

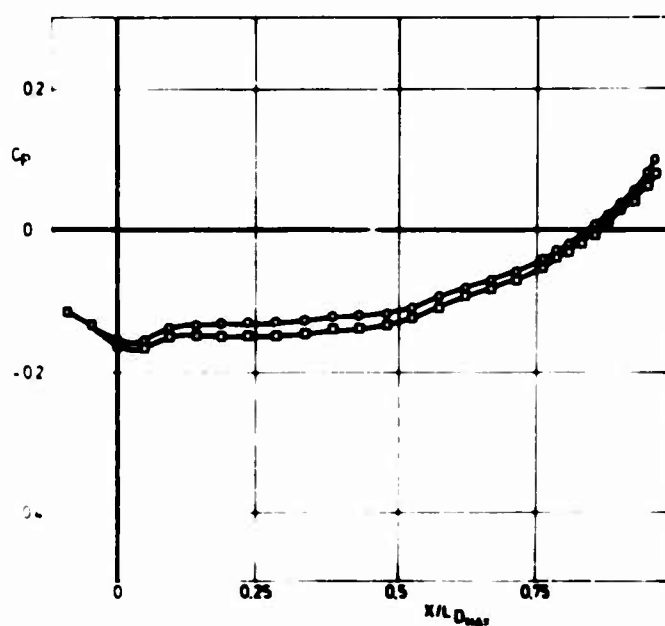
(b)

Fig.8 Static temperature distribution on the boattail of HFB 320 CJ 610 jet engine nacelle model for cold and hot jets and natural and blown boundary layers at  $M_{\infty} = 0.45$



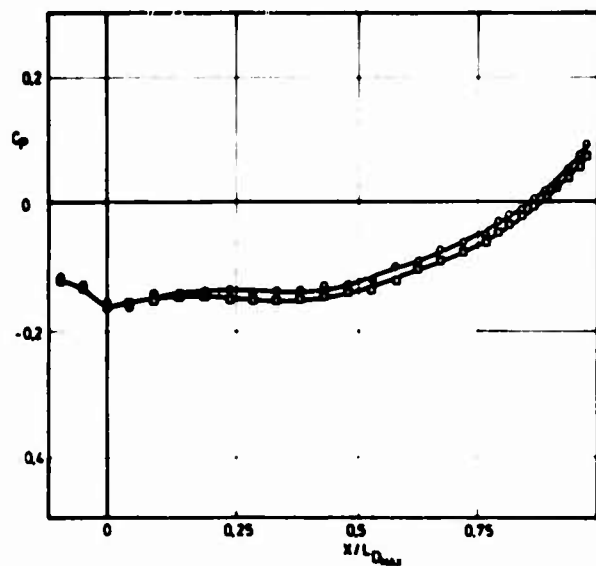
(a)

290K ○ — ○  
790K □ — □

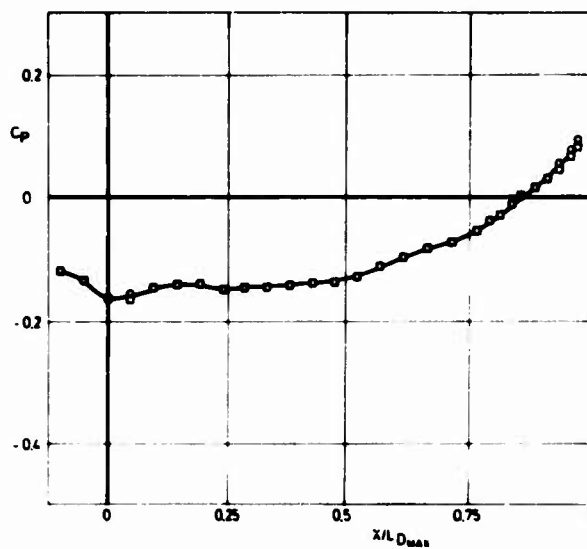


(b)

Fig.9 Boattail pressure distribution on the HFB 320 CJ 610 jet engine nacelle model: cold and hot jet at  $M_\infty = 0.45$ ,  $NPR = 3.0$ , for natural (9a) and blown (9b) boundary layer



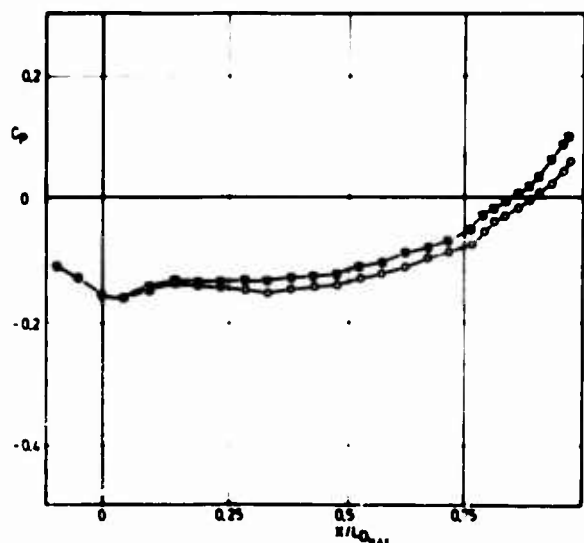
(a)



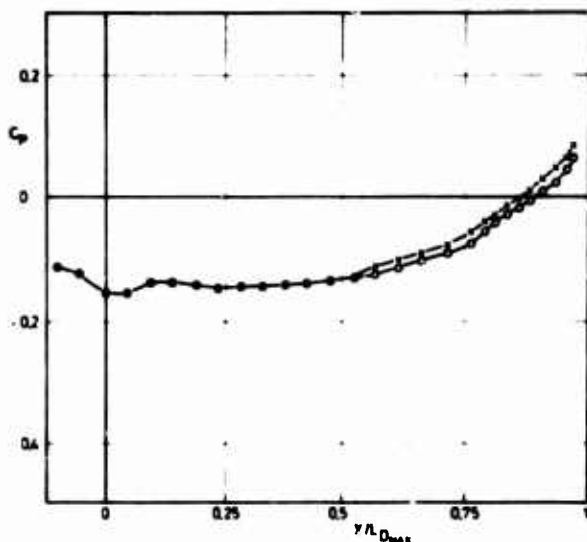
(b)

290K ○ — ○  
790K □ — □

Fig.10 Boattail pressure distribution on the HFB 320 CJ 610 jet engine nacelle model; cold and hot jet at  $M_{\infty} = 0.6$ ,  $NPR = 3.0$  for natural (10a) and blown (10b) boundary layer



(a)



(b)

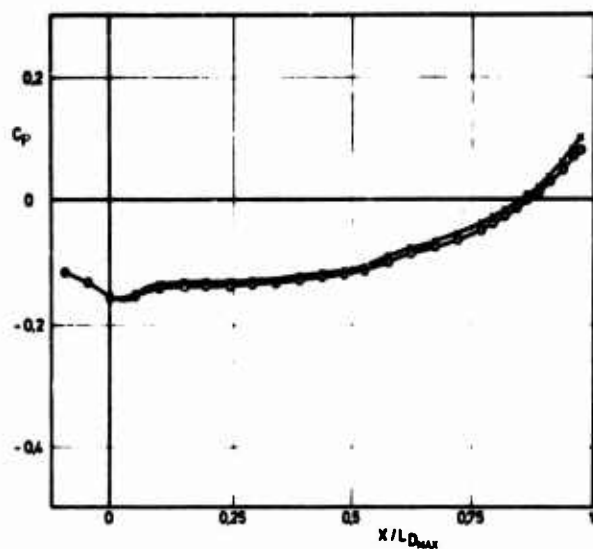
$NPR = 1.0$  (jet off)

1.7  
2.2  
3.0

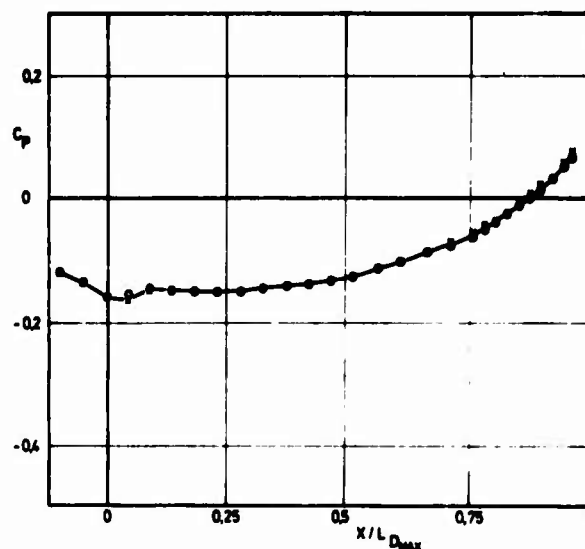
○ — ○  
□ — □  
△ — △

× — ×  
× — ×  
× — ×

Fig.11 Boattail pressure distribution on the HFB 320 CJ 610 jet engine nacelle model at  $M_{\infty} = 0.6$  and various  $NPR$  and for cold (11a) and hot (11b) jet



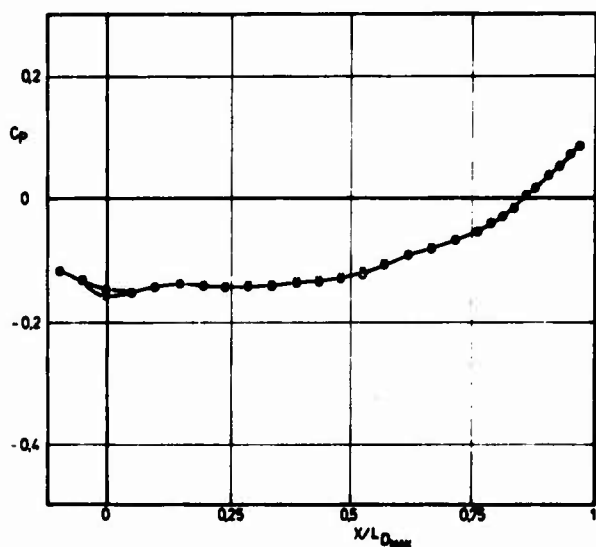
(a)



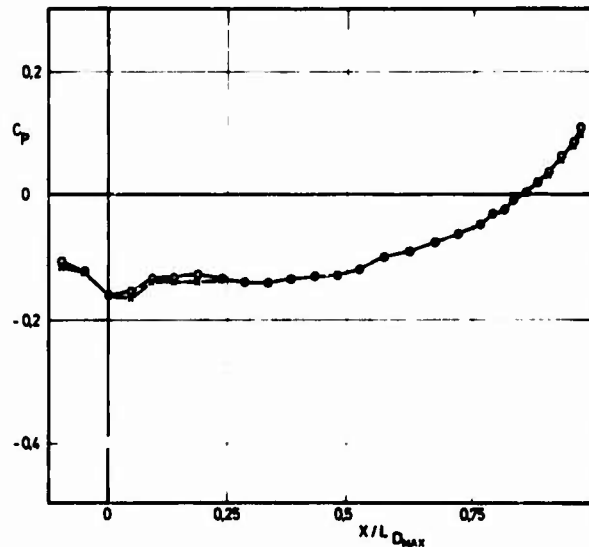
(b)

$\dot{m}_{B.L.} = 0.0 \text{ kg/s}$  ○ — ○  
 $\dot{m}_{B.L.} = 0.8 \text{ kg/s}$  x — x

Fig.12 Boattail pressure distribution on the HFB 320 CJ 610 jet engine nacelle model with and without blown boundary layer at  $M_\infty = 0.45$  and  $NPR = 3.0$ ; cold jet (12a) and hot jet (12b)



(a)



(b)

Fig.13 Boattail pressure distribution on the HFB 320 CJ 610 jet engine nacelle model at  $NPR = 3.0$ ,  $M_\infty = 0.45$  (13a) and  $0.6$  (13b) for cold jet ( $T_j = 290K$ ). Comparison of no distorted (○ — ○) and distorted (x — x) jet

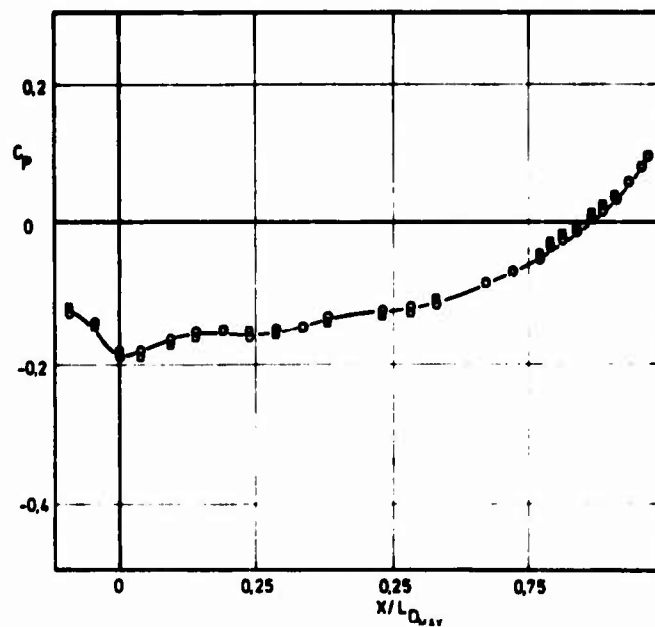


Fig.14 Boattail pressure distribution on the HFB 320 CJ 610 jet engine nacelle model at various nozzle innercontours at  $M_\infty = 0.45$

HFB-nozzle ○—○  
AGARD-nozzle □—□

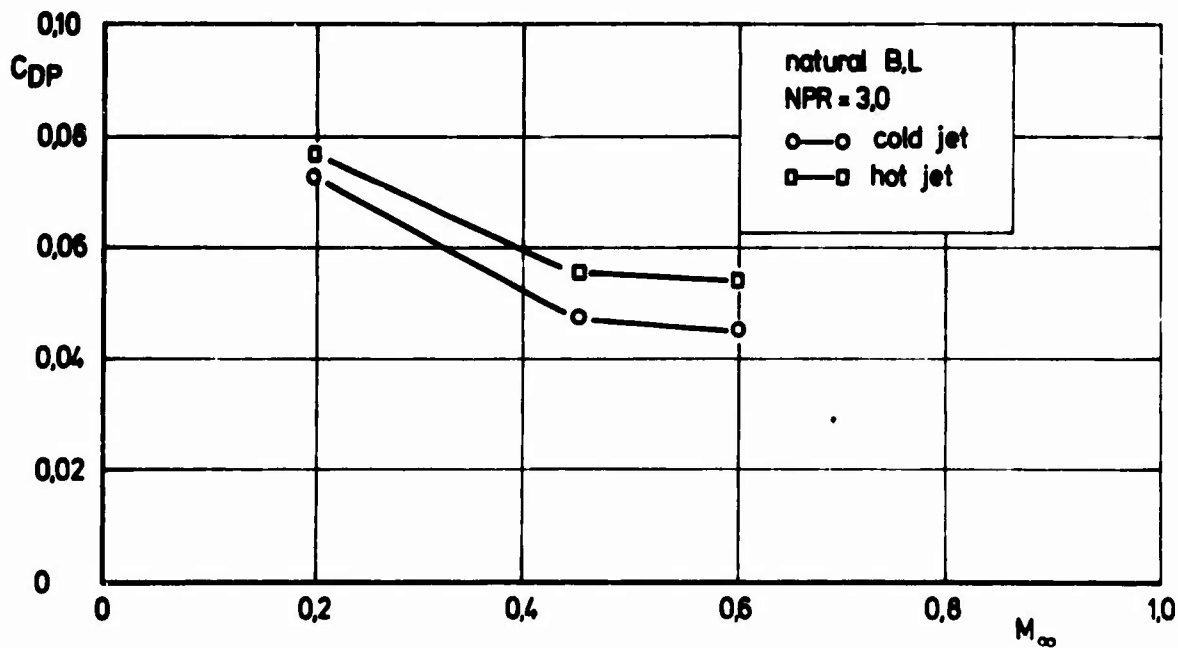


Fig.15 Boattail drag coefficient as a function of  $M_\infty$  for cold and hot jet and natural boundary layer at different NPR

# CONTRIBUTION OF THE INSTITUT FÜR ANGEWANDTE GASDYNAMIK OF THE DFVLR, PORZ-WAHN

by

H.Emunds and H.Riedel  
Deutsche Forschungs- und Versuchsanstalt für Luft-  
und Raumfahrt E.V., Porz-Wahn

## SUMMARY

The results presented relate to the AGARD models with 10° and 15° boattail chord angle. They cover the static pressure distributions on the afterbody and wall of the propulsive nozzle as well as the total pressure distributions in the nozzle flow and in the external flow field. The latter was only investigated for the model with 10° boattail. From the surface static pressure distributions on the afterbody of the models the boattail pressure drag coefficient was deduced. A cold propulsive jet of air was used, the nozzle total pressure ratio ranging from 1.0 to 6.63. The free stream Mach numbers covered the regime  $0.5 < M_{\infty} < 0.96$ .

## LIST OF SYMBOLS

(See also Figures 1 and 5.)

$A_{MAX} = \frac{\pi D^2}{4}$	maximum cross-sectional area
$C_{DP} = \frac{D_p}{q_{\infty} A_{MAX}}$	boattail pressure drag coefficient
$C_p = \frac{p - p_{\infty}}{q_{\infty}}$	boattail surface static pressure coefficient
$D$	maximum model diameter
$D_p$	boattail pressure drag
$l$	boattail length
$M$	Mach number
$NPR = p_{ij}/p_{\infty}$	nozzle pressure ratio
$p_t$	total pressure
$q_{\infty} = \frac{\gamma}{2} M_{\infty}^2 p_{\infty}$	free stream dynamic pressure
$r$	radius
$Re_{\infty} = \frac{\rho_{\infty} U_{\infty} D}{\mu_{\infty}}$	free stream Reynolds number based on maximum model diameter
$U$	velocity in X-direction
$X, Y$	Cartesian co-ordinate system at model nose (Fig.1)
$\bar{X}, \bar{Y}$	Cartesian co-ordinate system at nozzle exit (Fig.8)
$x, y$	Cartesian co-ordinate system with y-axis parallel to Y-axis (Fig.5)
$x', y'$	Cartesian co-ordinate system with y'-axis along the local surface normal (Fig.5)
$\beta$	boattail chord angle

$\rho$	density
$\mu$	coefficient of molecular viscosity

### Subscripts

j	jet at nozzle exit ( $X/D = 14.725$ , $Y/D = 0$ )
$\infty$	free stream (i.e. tunnel flow)
R	reference ( $X/D = 1.7164$ , $Y/D = 0$ )

## 1. EXPERIMENTAL SET-UP

### 1.1 Wind Tunnel

The investigation was carried out in the 340 mm diameter vertical free jet test section of the 30 x 30 cm<sup>2</sup> supersonic blowdown tunnel of the Institut für Angewandte Gasdynamik of the DFVLR in Porz-Wahn. The model support was in the form of a sting. Figure 2 shows the test section and the rig for the model support. The dimensions in this figure are in mm.

### 1.2 Models

A survey of the different AGARD-Models, including some constructional details, is given in Figure 6. The models designated A1, A2, and A3 correspond to 10°, 15°, and 25° boattail chord angles, respectively. All dimensions in Figure 6 are in mm. Geometric details of the boattail and nozzle contours of the models are presented on Figure 7. The contour of the curved section of the boattails is a circular arc.

### 1.3 Instrumentation

#### 1.3.1 Wind Tunnel Instrumentation

The basic instrumentation of the wind tunnel consisted of a total and a static pressure probe for the measurement of the wind tunnel reference conditions. These probes (Items (4.1) and (4.2) in Figure 3) were positioned in the exit plane of the wind tunnel nozzle, as indicated in Figure 3. The tunnel reference temperature was measured upstream of the model support with a Fe-Constantan thermocouple.

#### 1.3.2 Flow Field Traverse Gear

The traverse gear for the investigation of the flow field (Item (1) in Figure 3) comprised a rotatable probe holder support (1.1), a total temperature probe (1.2), and a total pressure probe (1.3). The total temperature probe consisted of a NiCr-Ni thermocouple. The positioning of the traverse gear at any point in the flow field was controlled by servomotors. Details of the probes of the traverse gear are displayed in Figure 4, all dimensions on this figure being in mm.

The main traverse directions of the total pressure probe of the traverse gear were as indicated in Figure 5, the plane of measurement coinciding with that of the static pressure on the boattail of the respective model (Item (5) in Figure 3). The plane of traverse of the total temperature probe was parallel to this at a distance of 2.5 mm. In the region of the boattail ( $13.067 < X/D < 14.725$  for model A1) two different traverse directions were chosen for a particular  $X/D = \text{const}$ . In one case this was the y-direction, which is parallel to the Y-axis, and in the other case the traverse took place in the y'-direction which is the outward normal to the surface at the same  $X/D$ . As indicated on Figure 5, the origins of the systems of axes  $x, y$  and  $x', y'$  are at a distance of half a total pressure tube external diameter  $= 0.5 \text{ mm} = 0.00747 D$  from the model surface along the directions of  $y$  and  $y'$ , respectively. On the cylindrical part of the model afterbody the traverse took place in the y-direction. Downstream of the model base the flow field was traversed from the centre line in the direction of the positive Y-axis.

#### 1.3.3 Model Instrumentation

The model instrumentation comprised taps for the static pressure on the model afterbody and on the internal nozzle wall, a total pressure rake inside the nozzle, and a total temperature probe for the internal nozzle flow. With reference to Figure 8, at the taps numbered (1)–(10) the internal static pressure was measured. The probes of the internal total pressure rake cover the positions (11)–(17). The total pressure measured with probe (11), which coincides with the model centre line, was taken as total pressure reference ( $p_{TR}$ ) for the nozzle flow. The afterbody static pressure was measured at pressure taps (18)–(31) in the case of AGARD models A1 and A2 and at pressure taps (18)–(36) for Model A3. All pressures, like those of the wind tunnel instrumentation, were recorded automatically using transducers and scanivalves. The internal total temperature was measured at the probe location marked (T) using a Chromel-Alumel (NiCr-Ni) thermocouple. Table I displays the axial positions of the pressure taps and



of the probes of the internal total pressure and temperature. For the total pressure rake the Y-coordinates of the probes are also given.

## 1.4 Wind Tunnel Calibration

The wind tunnel free stream Mach number  $M_\infty$  was determined from the measurements of the wind tunnel reference total pressure  $p_{t\infty}$  (Probe (4.1) in Figure 3) and the reference static pressure  $p_\infty$  (Probe (4.2) in Figure 3) on the basis of the assumption that the wind tunnel air is a perfect gas and flow is isentropic. The expression for the free stream Mach number is

$$M_\infty = \left[ \frac{2}{\gamma - 1} \left( \left( \frac{p_{t\infty}}{p_\infty} \right)^{(\gamma-1)/\gamma} - 1 \right) \right]^{1/2}$$

The free stream dynamic pressure is given by the relation

$$q_\infty = \frac{\gamma}{2} M_\infty^2 p_\infty.$$

As yet no static pressure traverses have been carried out in the test section of the free jet wind tunnel. Thus, the results of Figures 9-16 show the total pressure distributions in the test section with Model A1 installed and the propulsive jet in the off-condition. The exit plane of the wind tunnel nozzle corresponds to  $X/D = 8.495$  and its inner edge to  $y/D = 2.04$  and  $Y/D = 2.54$ , respectively. The results indicate that, when a model is installed in the test section, the uniform core of the wind tunnel free jet ceases to exist for  $X/D > 19.200$  approximately.

## 2. TEST PARAMETERS

Up to the present two of the three AGARD-Models have been subjected to tests. These are the models A1 and A2. The test conditions were the following

- (1) Cold propulsive jet:  $277 \text{ K} < T_{tj} < 288 \text{ K}$ .  
 $M_j = 0, 0.5, 0.75$ , and  $M_j = 1.00$  at  $p_j/p_\infty = 1.00$ .  
 The effect of underexpansion of the propulsive jet was investigated for  $p_j/p_\infty = 1.5, 2.5$ , and  $3.5$ . The relation between the nozzle pressure ratio  $\text{NPR} = p_{tj}/p_\infty$  and the nozzle exit flow conditions expressed by  $M_j$  and  $p_j/p_\infty$  is shown in Figure 17.
- (2) Natural boundary layer flow: i.e. No boundary layer suction or blowing was applied. Thus, slot (2), see Figures 2 and 6, was closed.
- (3) No turbulence generator was installed in the air supply duct leading to the nozzle (see Item (4) of Figure 6).
- (4) External flow: Free stream Mach numbers of  $M_\infty = 0.5, 0.6, 0.7, 0.8, 0.9$ , and  $0.96$ ,  $T_{t\infty} = 280 \text{ K}$  and  $p_\infty = \text{atmospheric}$  were the conditions of the external flow.

The scope of the investigation comprised the measurement of:

- (a) Static pressure distributions on the afterbody of the models and inside the nozzle at the wall.
- (b) Total pressure distributions in the external flow field and inside the nozzle at the position of the internal total pressure rake. Up to the present the total pressure distribution in the external flow field has been investigated for model A1 only.

The free stream Mach number  $M_\infty$  could not be varied independently of the Reynolds number  $Re_\infty$  based on the free stream conditions and the maximum model diameter  $D$ . Similarly, the nozzle pressure ratio  $\text{NPR}$  could not be altered independently of the jet Reynolds number  $Re_j$  based on the nozzle exit conditions and the nozzle exit diameter  $D_j$ . Table II shows the relation between  $M_\infty$  and  $Re_\infty$  and between  $\text{NPR}$  and  $Re_j$ , respectively. The nozzle exit flow conditions expressed by  $M_j$  and  $p_j/p_\infty$  are also shown.

## 3. RESULTS AND DISCUSSION

### 3.1 Static Pressure Distributions

#### 3.1.1 Static Pressure Distributions on the Afterbody

The results, which are expressed by  $C_p = (p - p_\infty)/q_\infty = f(x/l)$ , where  $l$  is the boattail length, are displayed in Figures 18-24 for model A1 and in Figures 25-31 for model A2. Each figure corresponds to a particular nozzle flow condition. The origin of  $x$  coincides with the junction of the cylindrical and boattail portions of the afterbody.

Table III contains the relevant information concerning the symbols on these diagrams and the associated free stream Mach number  $M_\infty$  and the Reynolds number  $Re_\infty$ .

In the following the effect of NPR on the static pressure distributions will be discussed by referring to two representative free stream Mach numbers, i.e.  $M_\infty = 0.80$  and  $M_\infty = 0.95$ . Considering model A1 first, for this the flow field is marked by an absence of any significant flow separation on the model. Results obtained using the oil flow technique indicate that, for example, at  $M_\infty = 0.95$  and  $NPR = 1$  (jet-off condition) no flow separation exists despite of the fact that the local supersonic flow at the shoulder of the model afterbody is terminated by a shock wave. At  $NPR = 6.63$  the shock strength associated with the jet plume had increased sufficiently to cause flow detachment at  $x/l = 0.96$ . Generally, in regions where the streamlines are convex in the outward direction to the model there exists a suction on the model (negative values of  $C_p$ ), a typical example being the shoulder of the model afterbody. Towards the aft end of the model the stream lines assume a concave curvature in the outward direction to the model as the flow external to the wake or jet respectively is turned into the free stream direction. This leads to positive values of  $C_p$  on the model in the region concerned. The difference between the cases of jet-off and jet-on makes itself felt in the following way. When the jet is turned on the elimination of the wake and the displacement of the external flow by the presence of the jet results in an increased concave curvature of the flow in the vicinity of the aft end of the model. Thus, in this region  $C_p$  grows. This is evident in Figure 32 ( $M_\infty = 0.80$ ) by comparison of the static pressure distributions for  $NPR = 1.0$  and  $NPR = 1.19$ . On increasing the NPR from 1.19 to 2.84 no further significant changes in the  $C_p$ -distribution are observed. The underlying reason is that the jet pluming present at  $NPR > 1.89$  is still small and consequently no marked change in the displacement effect exerted by the jet on the external flow occurs. From this observation it can be deduced that no significant alteration of the flow entrainment by the jet arises when NPR is varied, since an increase of the entrainment, for example, would be indicated by decreasing values of  $C_p$ . For  $NPR > 3.0$  the jet pluming becomes important and therefore with increasing NPR the static pressure coefficient at the aft end of the model grows. This trend of the variation of the static pressure coefficient with NPR on the rear part of the model is essentially maintained for  $M_\infty = 0.95$  (Fig.33). Compared with the case of  $M_\infty = 0.80$ , however, the strong expansion at the shoulder of the afterbody leads to a significant rise in the suction peak.

The flow field of model A2 is characterized by a pronounced flow separation for the free stream Mach number range investigated. Thus, using the oil flow technique, for  $M_\infty = 0.5$  separation occurred at  $\frac{x}{l} \approx 0.85$  and for  $M_\infty = 0.95$  at  $\frac{x}{l} \approx 0.4$ , irrespective of the jet nozzle flow conditions. For  $M_\infty = 0.80$  separation was observed to take place at  $\frac{x}{l} \approx 0.725$ . The static pressure distributions for model A2, which are displayed in Figures 34 and 35 for  $M_\infty = 0.80$  and 0.95 respectively, reflect the flow detachment by a plateau pressure distribution, starting approximately at the position of the flow separation. The flow separation entails a reduction of concave curvature of the streamlines of the flow in the rear portion of the model and consequently also a decrease of the magnitude of  $C_p$ . At  $M_\infty = 0.80$  the effect of NPR on the static pressure distribution is essentially the same as that observed for model A1 at the same free stream Mach number. One difference arises in that for model A2, as result of the extensive flow separation at the rear end, the displacement effect exerted by the jet plume in the case of underexpansion of the jet can make itself felt only at higher values of NPR. Thus, while for model A1 the displacement effect by the jet pluming occurred at  $NPR > 3.0$ , for model A2 it becomes significant for  $NPR > 5$  approximately. At  $M_\infty = 0.95$  flow separation on model A2 coincides with the position of the shock wave terminating the region of local supersonic flow of the external flow field at the shoulder of the afterbody. In contrast to the case of  $M_\infty = 0.80$  now at  $M_\infty = 0.95$  there exists a wide wake of separated external flow which is affected by the property of the jet to entrain fluid from its surroundings in addition to the displacement effect exerted by the jet on the external flow. Thus, at the aft end of model A2 the static pressure coefficient arises from the negative value associated with the wake flow in the jet-off condition to a positive value as the jet is turned on. This is exemplified by the case  $M_j = 0.50$  ( $NPR = 1.19$ ) in Figure 35. However, on increasing  $M_j$  the magnitude of  $C_p$  is reduced, since the entrainment of flow from the wake becomes the dominant factor. This trend continues until NPR has increased to  $NPR = 4.74$  approximately, corresponding to  $M_j = 1.0$  and  $p_j/p_\infty = 2.50$ . For values of  $NPR > 4.74$  approximately the displacement effect due to the jet pluming, which sets in at  $NPR \approx 2.84$  ( $M_j = 0$ ,  $p_j/p_\infty = 1.5$ ) begins to counterbalance the entrainment effect and finally dominates, so that  $C_p$  rises again. This is demonstrated by comparison of the cases  $NPR = 4.74$  and 6.63, the latter corresponding to  $M_j = 1.0$  and  $p_j/p_\infty = 3.5$ .

### 3.1.2 Static Pressure Distributions on the Nozzle Wall

Typical examples of the static pressure distributions on the nozzle wall are shown for model A1 and A2 in Figures 35 and 36, respectively. In these figures the local static pressure is related to the nozzle reference total pressure  $p_{tR}$ , which is the total pressure measured with probe (11) (Fig.8). The static pressures were measured at taps (1)-(10). In those cases where a nozzle flow exists ( $M_j > 0$ ), because of the flow contraction towards the nozzle exit and the associated acceleration of the flow, a static pressure reduction is observed as the nozzle flow proceeds towards the nozzle exit. At any particular station  $X/D = \text{const.}$  the static pressure decreases as the nozzle Mach number is raised until the nozzle flow becomes choked ( $M_j = 1.0$ ).

## 3.2 Total Pressure Distributions

### 3.2.1 Total Pressure Distributions in the Flow Field of the Propulsive Jet Without External Flow

The data for model A1 are displayed in Figures 38–48 as plots of  $p_t/p_{tj} = f(Y/D)$  for  $X/D = \text{const.}$ , where  $p_{tj} = p_{tR}$  is the jet reference total pressure and  $p_t$  is the total pressure measured with probe (1.3) of the flow field traverse gear (Fig.3). For sonic nozzle flow and  $p_j/p_\infty = 1.0$  within the limits of the measuring accuracy no difference existed between  $p_{tR}$  and  $p_t$  measured in the nozzle exit plane on the model centre line ( $X/D = 14.725$ ,  $Y/D = 0$ ).

The results show that for sonic nozzle flow and  $p_j/p_\infty = 1.0$  the effect of the flow mixing of the jet with the surrounding medium at rest reaches the centre line of the jet at approximately  $X/D = 16.965$ . For  $p_j/p_\infty > 1.0$  the jet flow becomes underexpanded and within the jet core not affected by the flow mixing supersonic flow is established. The ratio of  $p_t/p_{tj}$  on  $Y/D = 0$  at any particular  $X/D = \text{const.}$  is reduced compared with the corresponding value for  $p_j/p_\infty = 1.0$  on account of the total pressure loss across the normal shock wave that is presented upstream of the total pressure probe of the flow field traverse gear. Across internal shocks of the jet flow field an additional total pressure loss occurs due to the entropy rise associated with the presence of a shock wave.

### 3.2.2 Total Pressure Distributions in the Flow Field Without Propulsive Jet

Reference is again made to model A1. For the region of the flow field upstream of the aft end of the model ( $X/D < 14.725$ ) the data are plotted as  $p_t/p_{t\infty} = f(y/D)$  or  $f(y'/D)$  with the free stream Mach number  $M_\infty$  as parameter. The co-ordinate systems used are explained in Figure 5. These results are presented on Figures 9–12. The free boundary of the external flow (wind tunnel free jet) is at a distance of approximately  $y/D = 2.0$  from the model surface. The reduction of total pressure of the free stream in the vicinity of the model ( $y/D$  or  $y'/D < 0.4$ ) is due to the effect of the skin friction and is an indication of the boundary layer flow established. Details of the total pressure distribution across the boundary layer are presented in Figures 49–55. The boundary layer thickness, defined by  $y/D$  or  $y'/D$  where  $p_t/p_{t\infty} = 0.99$ , increases from 0.1 at  $X/D = 10.250$  to 0.3 at  $X/D = 14.725$  (aft end of the model). For  $X/D \geq 14.725$  the results are plotted as  $p_t/p_{t\infty} = f(Y/D)$  on Figures 13–16. The region of the flow field where  $p_t/p_{t\infty} < 1.0$  in the vicinity of  $Y/D = 0$  represents the wake of the model. As already indicated when discussing the wind tunnel calibration the effect of the mixing of the free jet of the wind tunnel with the surrounding medium penetrates into the wake flow at approximately  $X/D > 19.2$  (Fig.15).

### 3.2.3 Total Pressure Distributions in the Flow Field with Propulsive Jet

It was observed that for model A1 in the presence of an external flow ( $M_\infty > 0$ ) the propulsive jet had no effect on the total pressure distributions in the region of the flow field upstream of the nozzle exit. The total pressure distributions at the nozzle exit and downstream of it are displayed in Figures 56–75. A comparison with the case where the surrounding medium is at rest (Figures 38–48) leads to the conclusion that the presence of the external flow introduces no significant change in the rate of the mixing of the jet with its surrounding medium when this is in motion. Otherwise the flow features observed when discussing the flow field of the propulsive jet in the absence of an external flow (Section 3.2.1) are essentially retained.

### 3.2.4 Total Pressure Distributions at the Internal Rake

Figures 76 and 77 show two typical examples of the total pressure distributions measured with the internal total pressure rake in the pipe supplying the air for the jet simulation to the nozzle. The results are expressed by  $p_t/p_{tR} = f(Y/D)$ , where  $p_{tR}$  is the total pressure measured with probe (11) of the rake (Fig.8). Differences in the total pressure distributions for models A1 and A2 at a given NPR reflect the measuring accuracy, since the set-up for testing both models incorporated one and the same air supply system, including the air supply pipe to the model and the internal total pressure rake. These differences amount to 0.2% of  $p_{tR}$  at the maximum.

## 3.3 Pressure Drag Coefficient

### 3.3.1 Effect of NPR

The pressure drag coefficient was obtained by integration of the static pressure-area distributions on the boattail. The results reflect the flow features already observed when discussing the static pressure distributions. With reference to model A1 the influence of NPR is displayed in Figure 78. Turning the jet on eliminates the wake flow at the base of the model and displaces the external flow, so that the associated static pressure rise at the aft end of the model creates a thrust force and thereby reduces the  $C_{DP}$  value in comparison with the jet-off case. For  $1.5 < \text{NPR} < 3.0$  on the whole the displacement effect of the jet is relatively unaltered like the rate of flow entrainment by the jet, so that  $C_{DP}$  remains effectively constant. However, the slight growth of  $C_{DP}$  for the lowest free stream Mach number ( $M_\infty < 0.7$  approximately) investigated seems to indicate that the flow entrainment effect outweighs the displacement effect of the jet with growing NPR. The opposite appears to be true for the highest free stream Mach numbers covered in the investigation ( $M_\infty > 0.9$ ). For  $\text{NPR} > 3.0$  with growing NPR the jet pluming becomes the dominant factor and the accompanying static pressure rise at the model aft end results in an increasing thrust and thus a reduction of  $C_{DP}$ .

For model A2 flow separation is present already at  $M_\infty = 0.5$  irrespective of the nozzle flow conditions, so that the displacement effect exerted on the external flow by the jet when this is turned on is generally smaller in comparison with that experienced for model A1. Depending on the free stream Mach number, two different trends of  $C_{DP}$  with NPR are observed for model A2. For  $M_\infty < 0.8$ , there exists only a relatively slight flow separation, the separation lying within the range  $0.725 < x/l < 1.0$ . The wake of the model is comparatively narrow, so that when the jet is turned on the effect of NPR on  $C_{DP}$  is similar to that observed in the case of model A1. For  $M_\infty > 0.8$  flow separation becomes pronounced, separation progressing upstream from  $x/l = 0.725$  at  $M_\infty = 0.8$  to  $x/l = 0.41$  at  $M_\infty = 0.95$ . Under these conditions the wake of the model is wide, and, consequently, the displacement effect of the jet is relatively unimportant for the NPR range  $1.25 < NPR < 3$  in comparison with the entrainment effect. The latter leads to a reduction of the static pressure on the boattail in the vicinity of the nozzle exit and thereby entails a rise in  $C_{DP}$  with NPR. Decreasing NPR from  $NPR = 1.25$  to 1.0 (jet-off condition) involves flow conditions where the velocity difference between the wake flow and the jet flow is reduced to such an extent that there is practically no significant entrainment effect of the jet, and the initial decline of  $C_{DP}$  with NPR from the jet-off condition is the result of the jet displacing the wake flow from the base of the model when the jet is turned on. Thus, there exists a depression or valley at  $NPR = 1.25$  in the plot of  $C_{DP}$  against NPR. For  $NPR > 3.0$ , approximately, the displacement effect exerted by the jet begins to outweigh the contribution stemming from the entrainment effect, so that  $C_{DP}$  declines again with NPR.

### 3.3.2 Effect of Free Stream Mach Number

The variation of the pressure drag coefficient with the free stream Mach number is plotted in Figures 79 and 81 for the models A1 and A2 respectively. The Mach number drag rise is found to be more pronounced in the case of model A2 than for model A1. This is largely due to the extensive shock induced flow separation associated with the large boattail angle of model A2. No further analysis of the results plotted in Figures 79 and 81 is attempted at this stage, because, as already indicated, during testing the free stream Mach number could not be varied independently of the Reynolds number. The relation between  $M_\infty$  and the free stream Reynolds number is given in Table II.

## 4. CONCLUSIONS

Concerning the various factors influencing the boattail pressure drag coefficient the following conclusions can be drawn:

### (a) Effect of Boattail Geometry expressed by Boattail Chord Angle $\beta$ and the Effect of Free Stream Mach Number

For small boattail chord angles  $\beta$  of the order of  $10^\circ$  (Model A1) the external flow is fully attached except at high subsonic Mach numbers and relatively strong underexpansion of the propulsive jet. If flow separation occurs, this is comparatively weak. Thus, flow recompression at the aft end of the model is under all circumstances effective in keeping the pressure drag coefficient small. Drag rise with free stream Mach number is moderate. In contrast, for boattail chord angles  $\beta$  of the order of  $15^\circ$  (Model A2) flow separation exists even at low free stream Mach numbers ( $M_\infty = 0.5$ ). The level of the pressure drag coefficient is therefore raised. At higher values of  $M_\infty$  ( $M_\infty > 0.8$ ) shock wave induced flow separation is responsible for a wide wake and the drag rise in this free stream Mach number range is large.

### (b) Effect of NPR

For slender boattails ( $\beta < 10^\circ$ ) the displacement effect of the propulsive jet is the dominant factor and this causes a decrease of the boattail pressure drag coefficient because of the associated stronger recompression of the external flow at the aft end of the model. Turning the propulsive jet on leads to a rapid decrease of  $C_{DP}$ . For  $1.5 < NPR < 3.0$  no significant changes in the displacement and entrainment effects of the jet occur so that the boattail pressure drag coefficient remains at a plateau level. On raising the nozzle total pressure ratio above  $NPR = 3.0$  the jet pluming results in a predominance of the displacement effect of the jet over the entrainment effect and  $C_{DP}$  consequently falls with NPR.

For large boattail angles ( $\beta > 15^\circ$ ), where flow separation is already present at low free stream Mach numbers, the influence of the jet on the fluid of the wake is of importance. This leads to an increase in  $C_{DP}$ . Only for very low values of the nozzle total pressure ratio ( $NPR < 1.25$ ), where the velocity difference between the propulsive jet and the external flow does not cause a significant flow entrainment, and at high values of NPR ( $NPR > 3$ ), where the jet pluming begins to be pronounced, does the displacement effect of the jet predominate. Increasing NPR from the jet-off condition the boattail pressure drag coefficient falls initially to climb between  $NPR = 1.25$  and 2.0 to a plateau value. The level of the plateau is comparable to the magnitude of the boattail pressure drag coefficient at the jet-off condition. For  $NPR > 3.0$  there is a general decline of  $C_{DP}$  with NPR, since as a result of the jet pluming the displacement effect of the jet becomes the dominant factor.

TABLE I

Position of Static Pressure Taps and of Internal Probes for Models A1 and A2 ( $D = 67 \text{ mm}$ )

Static pressure tap or probe location (Fig.8)	$X$ (mm)	$X/D$	$Y$ (mm)	$Y/D$
1	21	0.3135		
2	24	0.3582		
3	39	0.5821		
4	44	0.6567		
5	52	0.7761		
6	57	0.8507		
7	70	1.0448		
8	93	1.3881		
9	102	1.5224		
10	115	1.7164		
11	115	1.7164	0	0
12	115	1.7164	-6	-0.0896
13	115	1.7164	-11	-0.1642
14	115	1.7164	-15	-0.2239
15	115	1.7164	-18	-0.2687
16	115	1.7164	-21	-0.3134
17	115	1.7164	-23	-0.3433
18	202.3	3.0194		
19	170.9	2.5507		
20	121.3	1.8104		
21	95.8	1.4299		
22	79.0	1.1791		
23	67.0	1.0000		
24	55.3	0.8254		
25	48.6	0.7254		
26	41.9	0.6254		
27	33.8	0.5045		
28	26.5	0.3955		
29	19.1	0.2837		
30	13.0	0.1940		
31	9.0	0.1343		
T	115	1.7164		

TABLE II

Relation Between  $M_\infty$  and  $Re_\infty$  and Between  
NPR and  $Re_j$ , Respectively

$M_\infty$	$Re_\infty 10^{-6}$	NPR	$Re_j 10^{-6}$	$M_j$	$p_j/p_\infty$
0.5	0.86	1.19	0.33	0.50	1.0
0.6	1.05	1.45	0.53	0.75	1.0
0.7	1.31	1.89	0.81	1.00	1.0
0.8	1.53	2.84	1.22	1.00	1.5
0.9	1.79	4.74	2.02	1.00	2.5
0.96	1.95	6.63	2.84	1.00	3.5

TABLE III

Symbols Associated with the Results Plotted in Figures 18-31

Symbol	$M_\infty$	$Re_\infty 10^{-6}$
○	0.5	0.86
□	0.6	1.05
◇	0.7	1.31
△	0.8	1.53
▽	0.9	1.79
▷	0.96	1.95

- ① MODEL WITH EXCHANGEABLE TAIL PORTION
- ② SUPPORT STRUT WITH AIR SUPPLY PIPE FOR JET SIMULATION

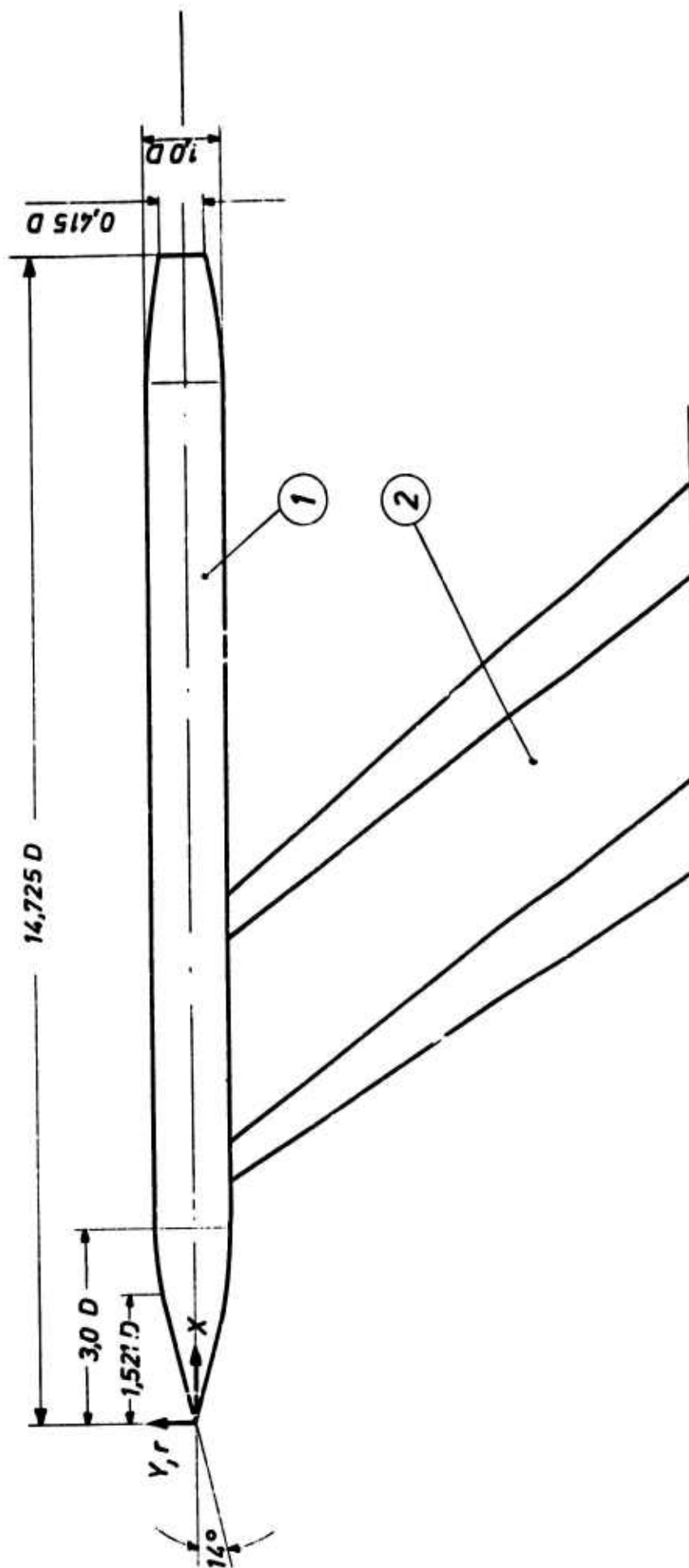
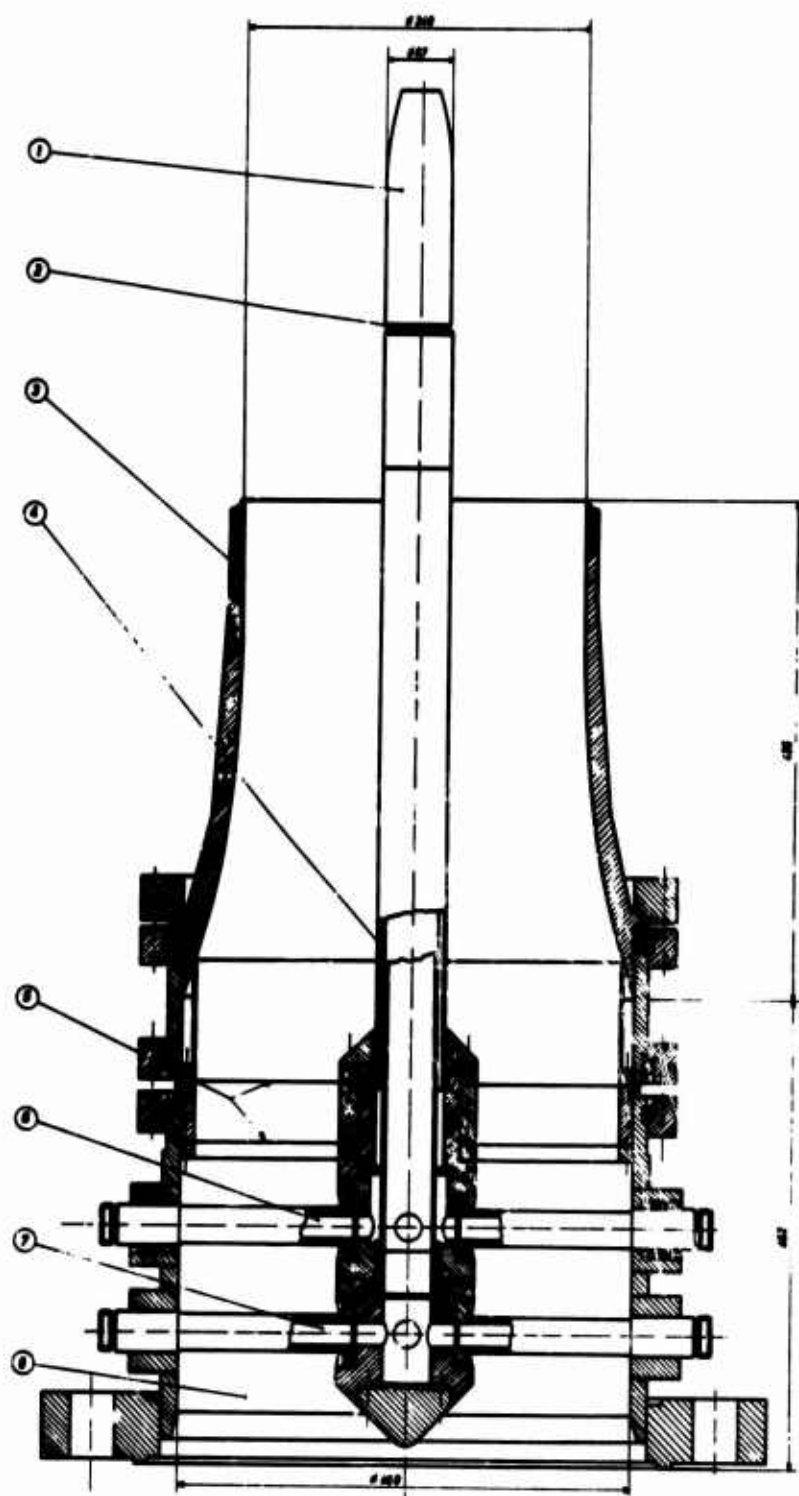


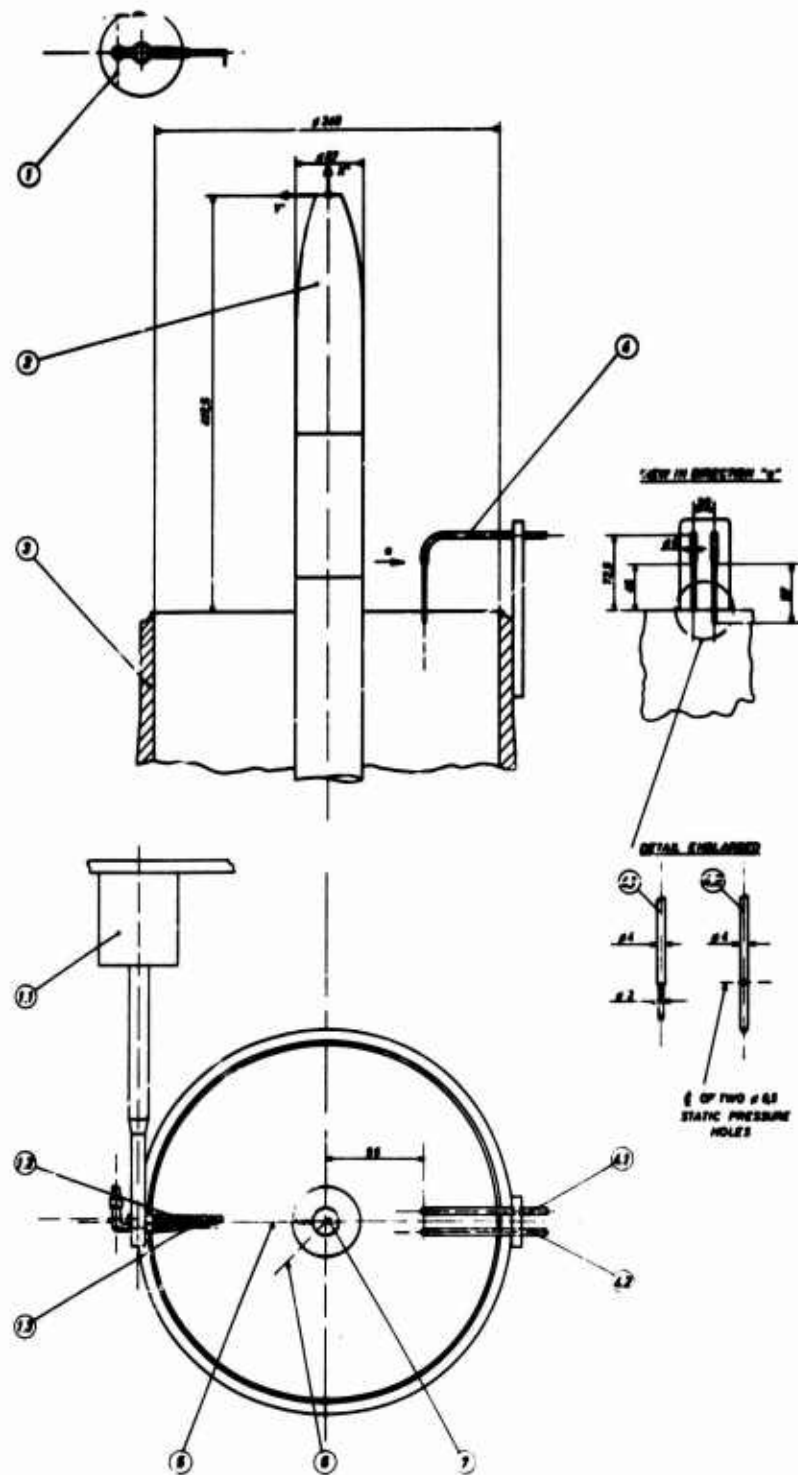
Fig.1 AGARD-model for correct testing techniques of nozzles in transonic flow



- ① AGARD-MODEL
- ② SLOT FOR BOUNDARY LAYER BLOWING OR SUCTION
- ③ FREE JET WIND TUNNEL NOZZLE
- ④ DUCT FOR PRESSURE TUBING, MEASURING LEADS, AND FOR BOUNDARY LAYER CONTROL BY BLOWING AND SUCTION RESPECTIVELY
- ⑤ WIRE SCREENS
- ⑥ CONDUIT FOR PRESSURE TUBING, MEASURING LEADS AND FOR BOUNDARY LAYER CONTROL BY BLOWING AND SUCTION RESPECTIVELY
- ⑦ SUPPLY PIPE FOR COLD AIR AND HOT COMBUSTION GASES FOR SIMULATION OF PROPULSIVE JET
- ⑧ AIR SUPPLY FOR FREE JET WIND TUNNEL

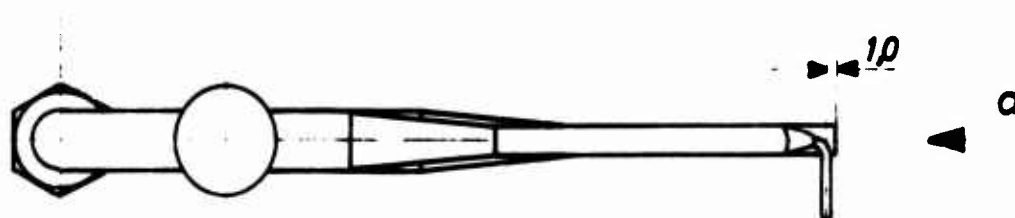
**Fig.2 Test set-up in the 340 mm diameter, free jet wind tunnel**



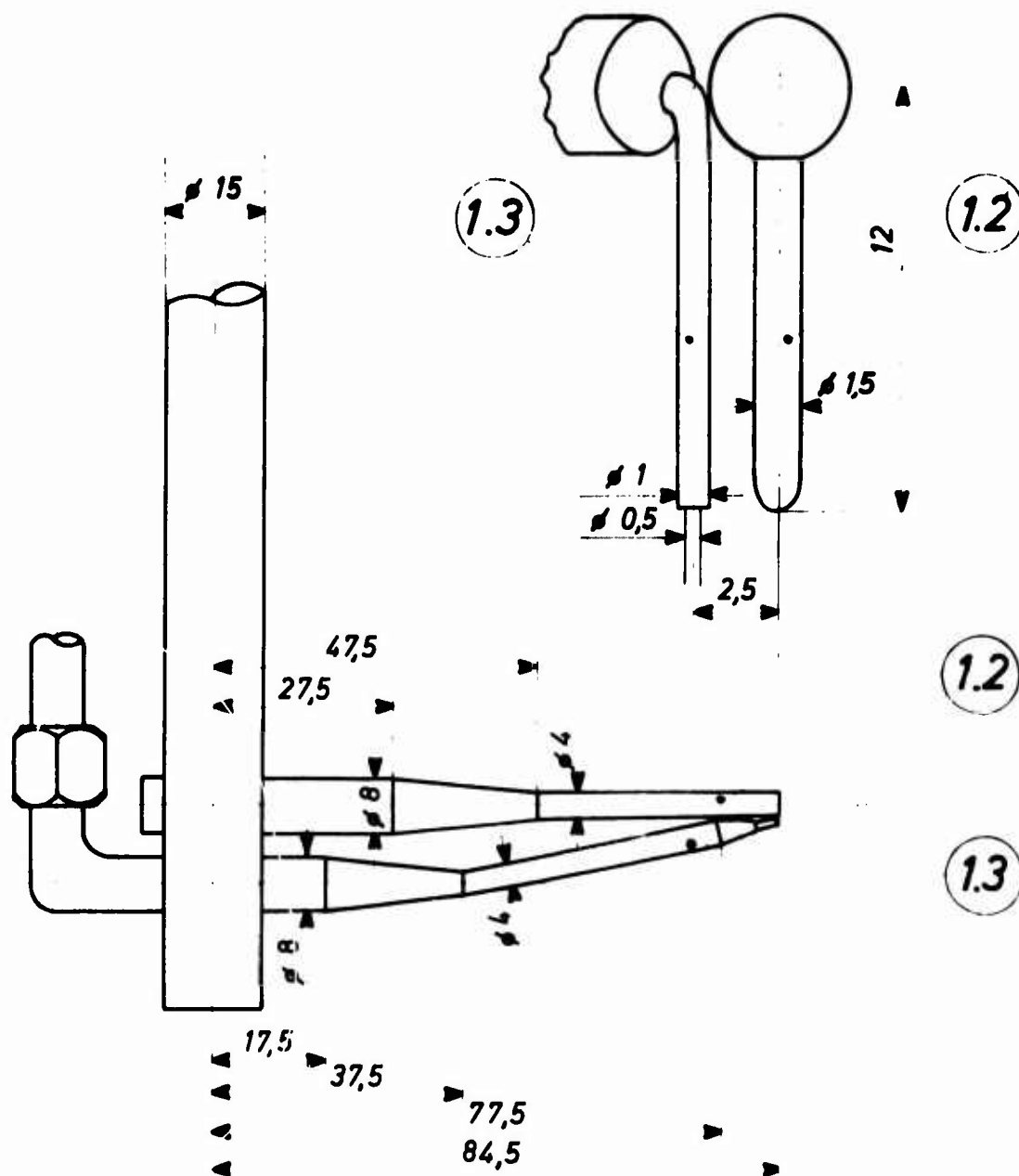


- |   |   |
|---|---|
| ① FLOW FIELD TRAVERSE GEAR                    | ④.1 TOTAL PRESSURE PROBE  |
| ①.1 ROTATABLE PROBE HOLDER SUPPORT            | ④.2 STATIC PRESSURE PROBE   |
| ①.2 TOTAL TEMPERATURE PROBE                   | ⑤ PLANE OF MEASUREMENT OF MODEL SURFACE STATIC PRESSURE           |
| ①.3 TOTAL PRESSURE PROBE                      | ⑥ PLANE OF MEASUREMENT OF STATIC PRESSURE OF INTERNAL NOZZLE FLOW |
| ② AGARD MODEL                                 | ⑦ INTERNAL TOTAL PRESSURE RAKE                                    |
| ③ FREE JET WIND TUNNEL NOZZLE                 |   |
| ④ PROBES FOR WIND TUNNEL REFERENCE CONDITIONS |   |

Fig.3 Basic instrumentation of wind tunnel and for flow field investigation



VIEW IN DIRECTION "a" (Enlarged)



(1.2) TOTAL TEMPERATURE PROBE

(1.3) TOTAL PRESSURE PROBE

Fig.4 Probes of the flow field traverse gear

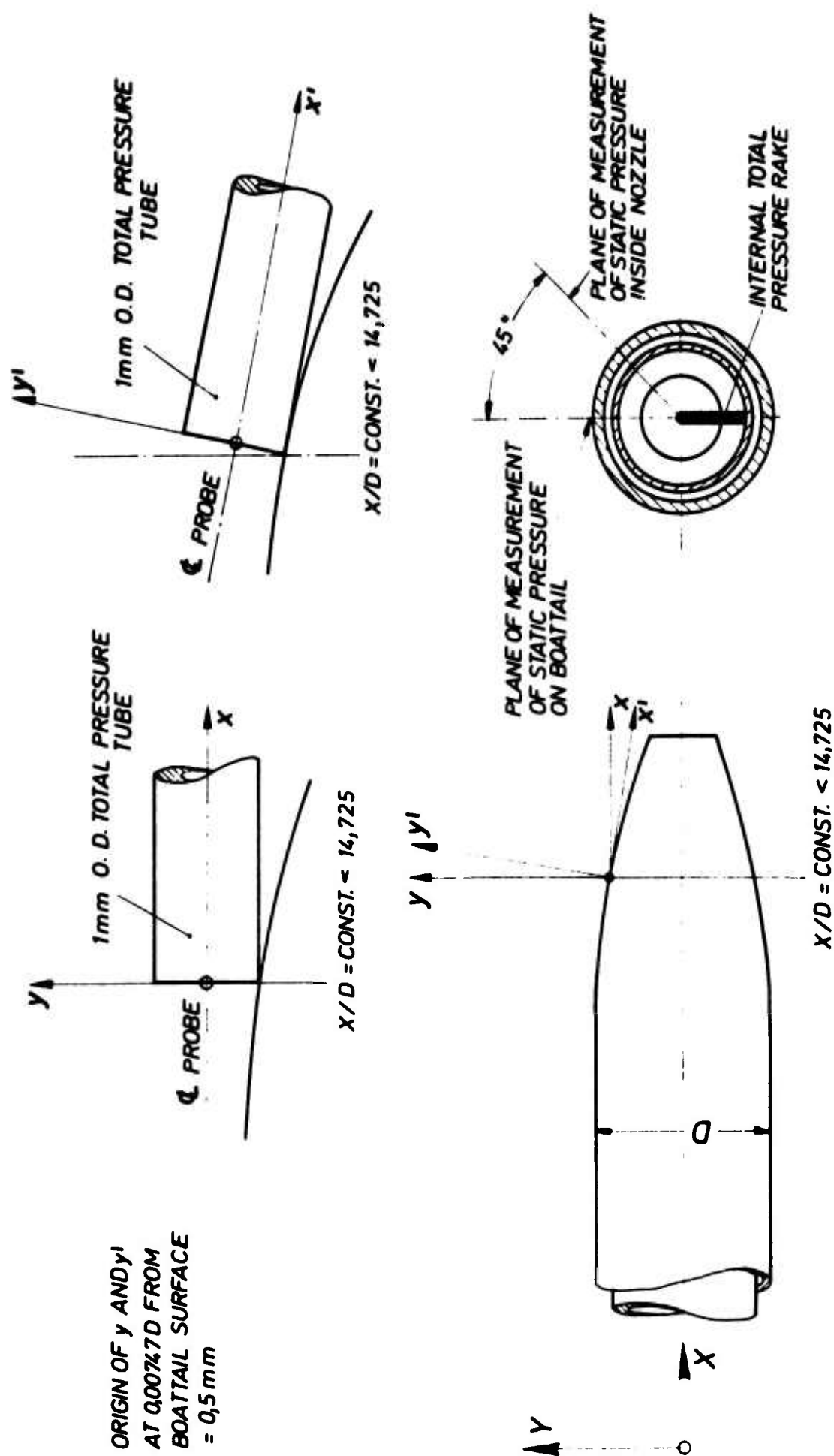


Fig.5 Directions of total pressure traverse and planes of measurement of static pressure on the boattail and inside the nozzle

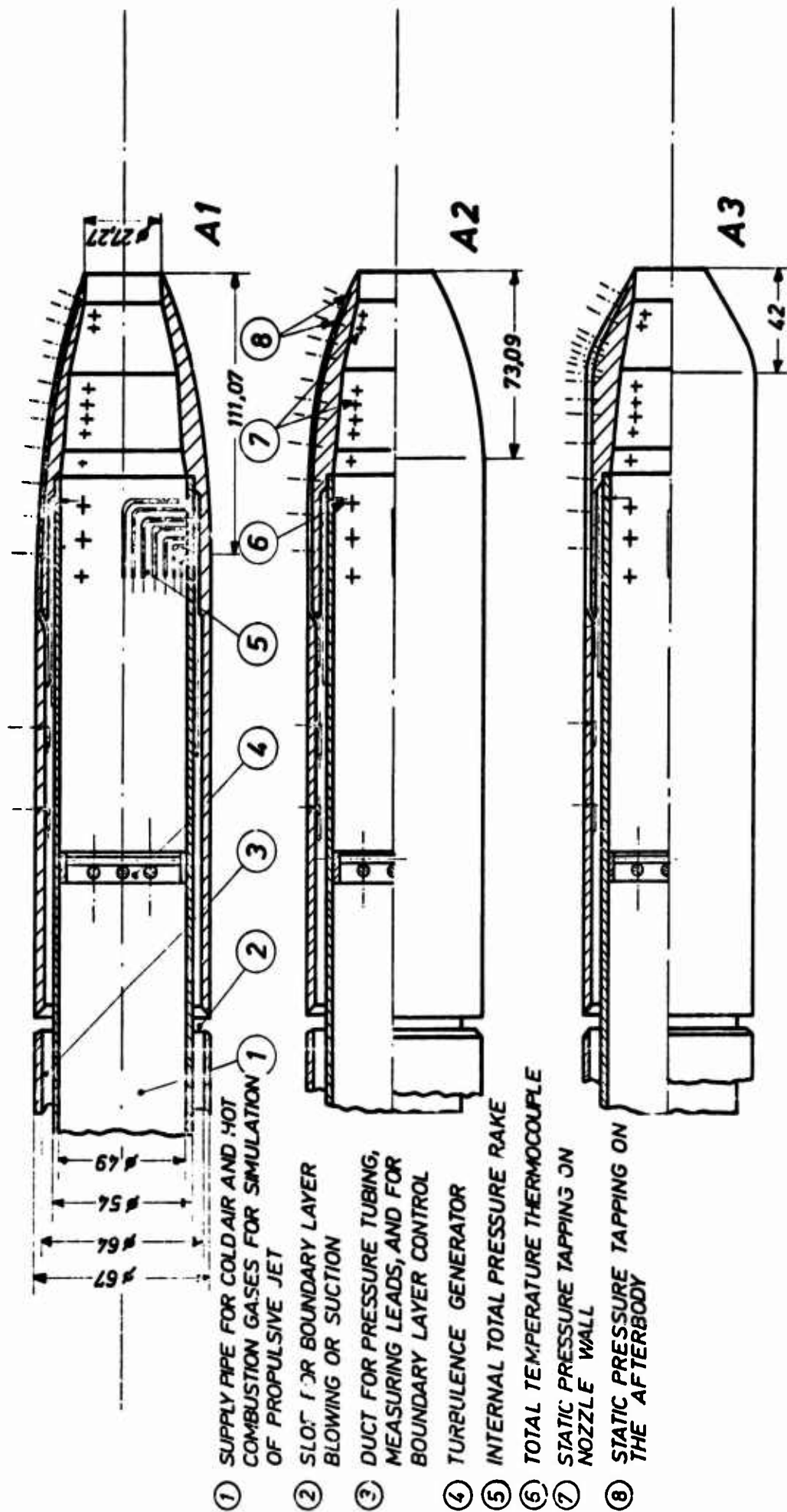


Fig.6 Survey of the different AGARD-models

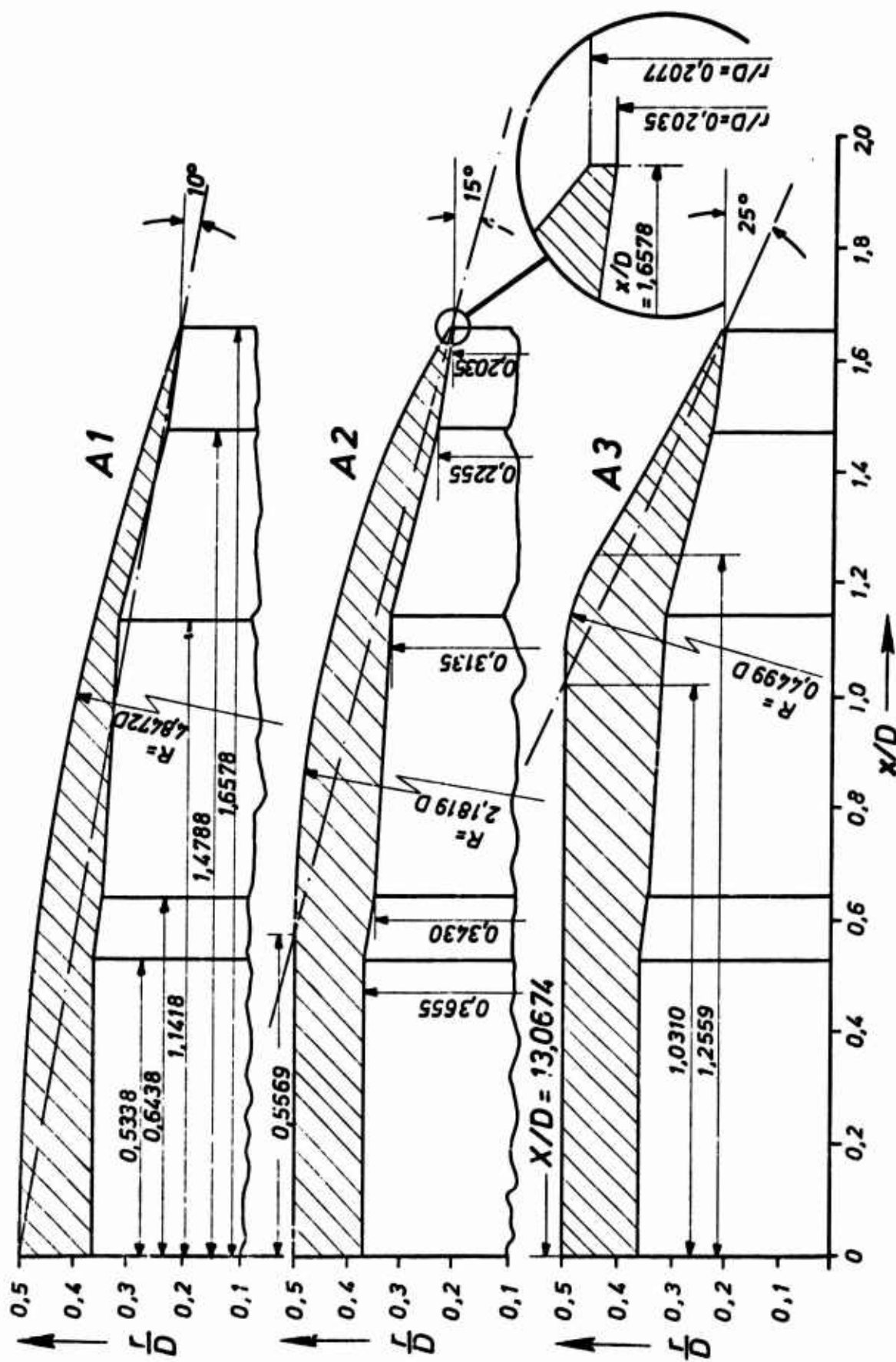


Fig.7 Geometric details of the boattail and nozzle contours of the AGARD-models

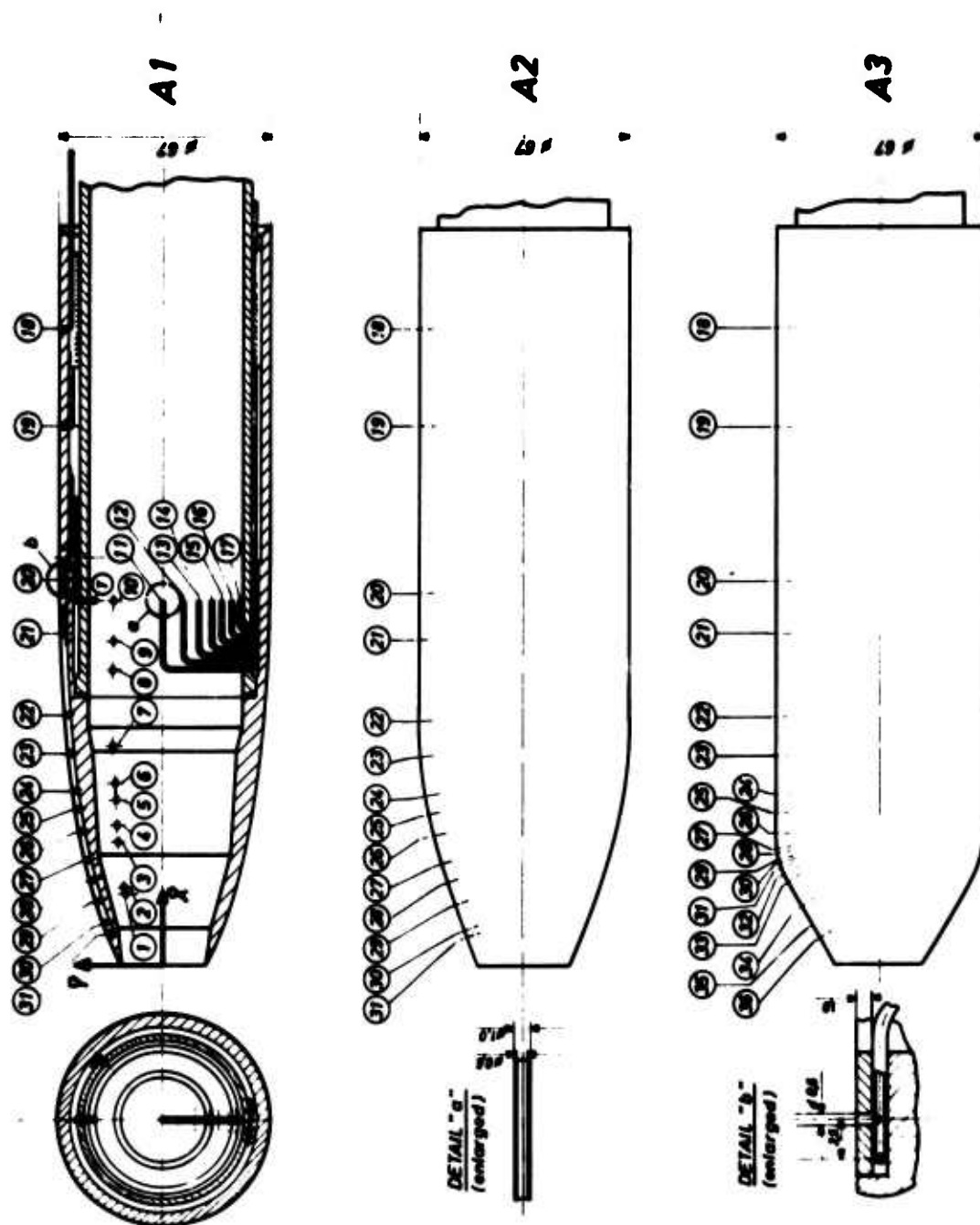


Fig.8 Details of the model instrumentation

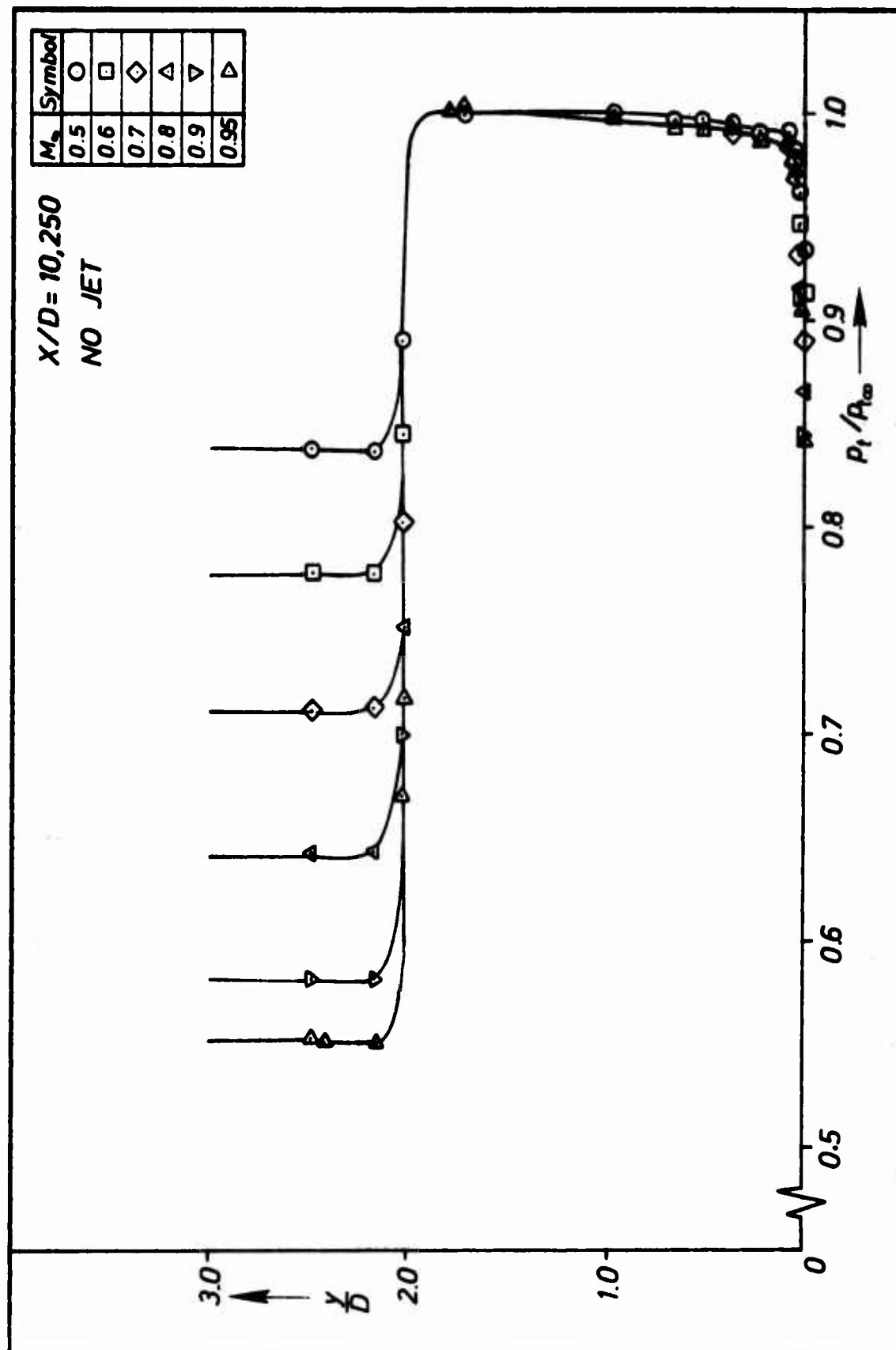


Fig.9 Total pressure distribution in the test section with Model A1 installed:  
propulsive jet off,  $X/D = 10.250$

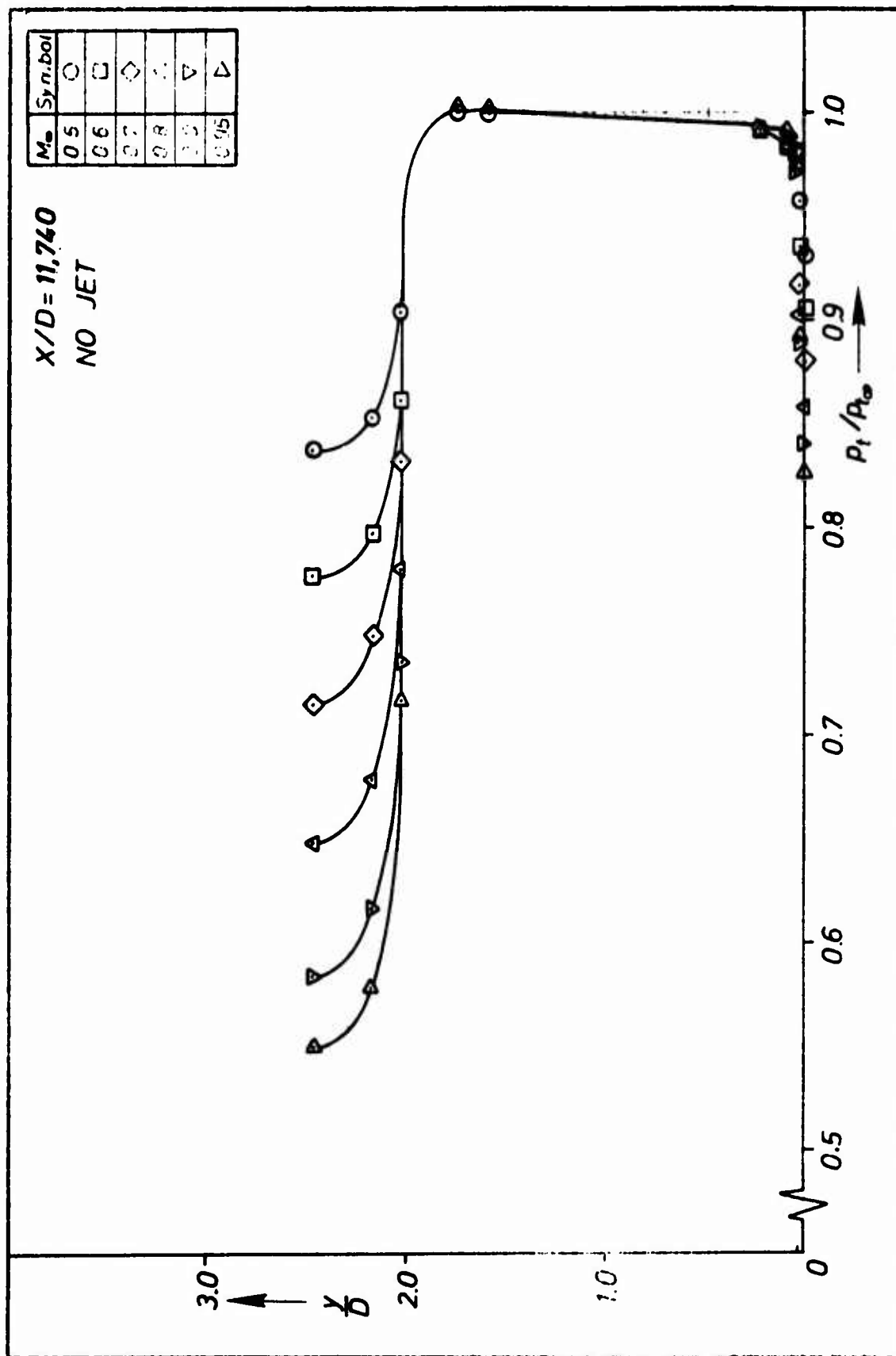


Fig.10 Total pressure distribution in the test section with Model A1 installed:  
propulsive jet off,  $X/D = 11.740$



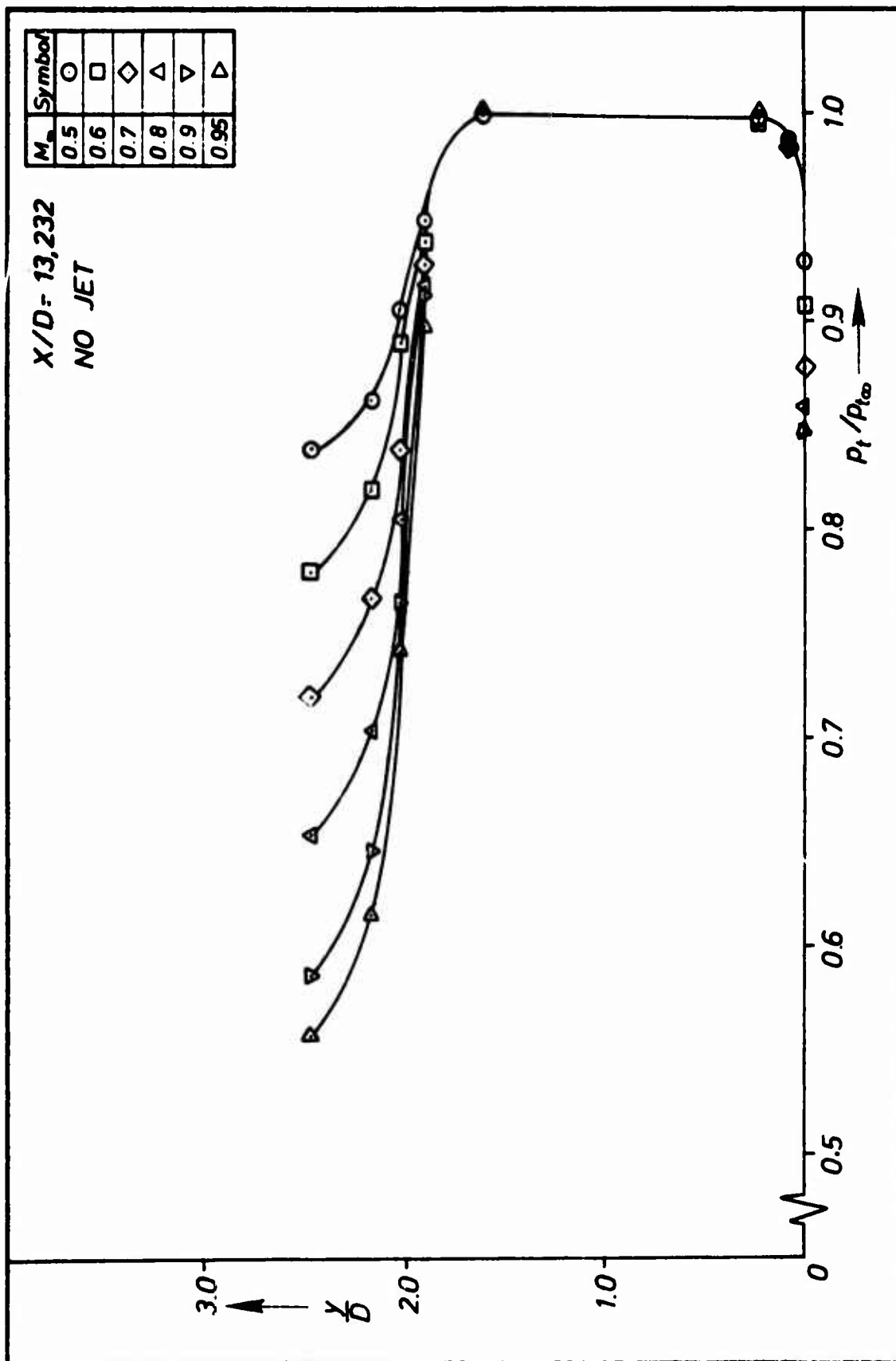


Fig.11 Total pressure distribution in the test section with Model A1 installed:  
propulsive jet off,  $X/D = 13,232$

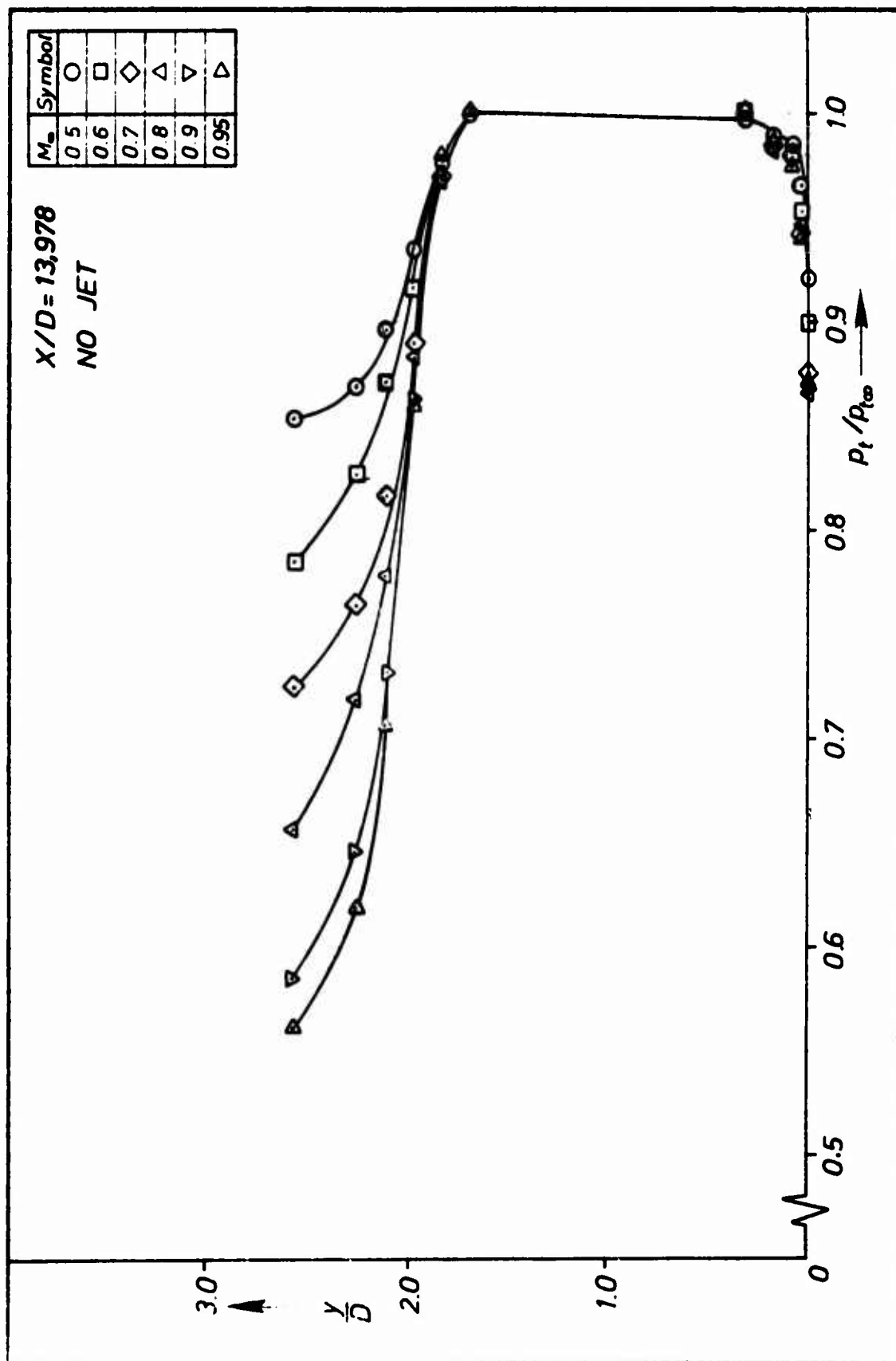


Fig.12 Total pressure distribution in the test section with Model A1 installed:  
propulsive jet off,  $X/D = 13,978$

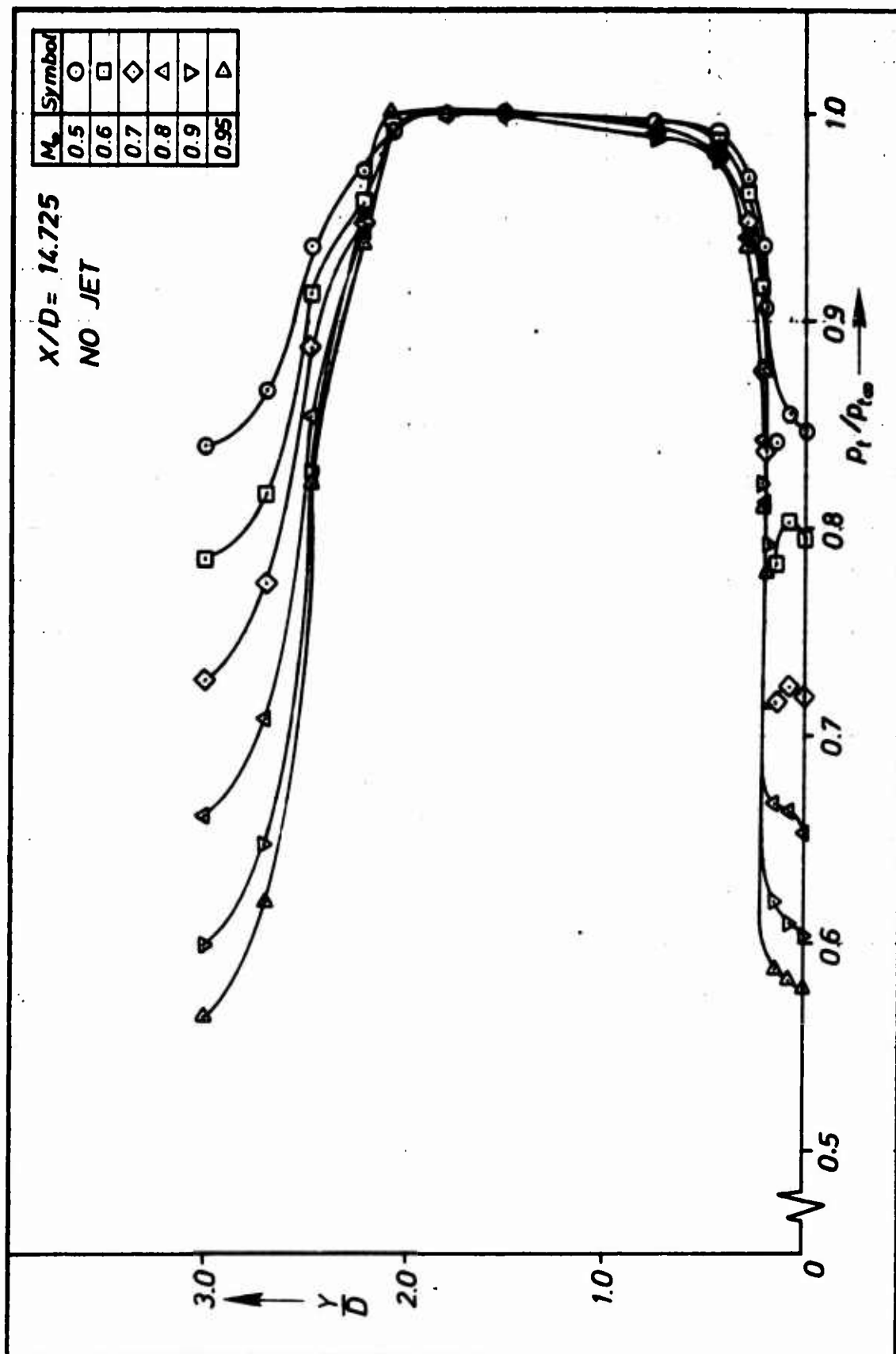


Fig.13 Total pressure distribution in the test section with Model A1 installed:  
propulsive jet off,  $X/D = 14.725$

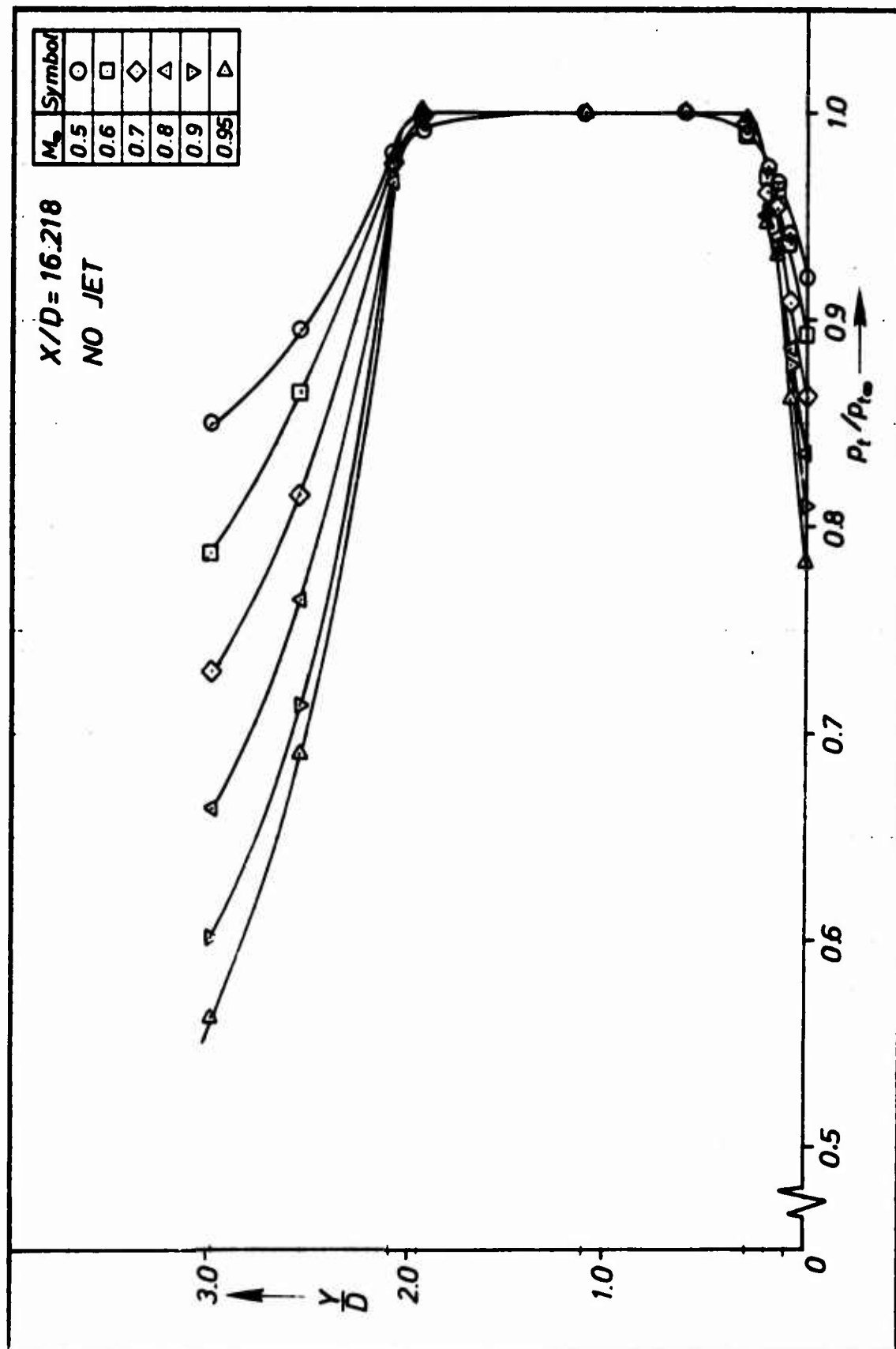


Fig. 14 Total pressure distribution in the test section with Model A1 installed:  
propulsive jet off,  $X/D = 16.218$

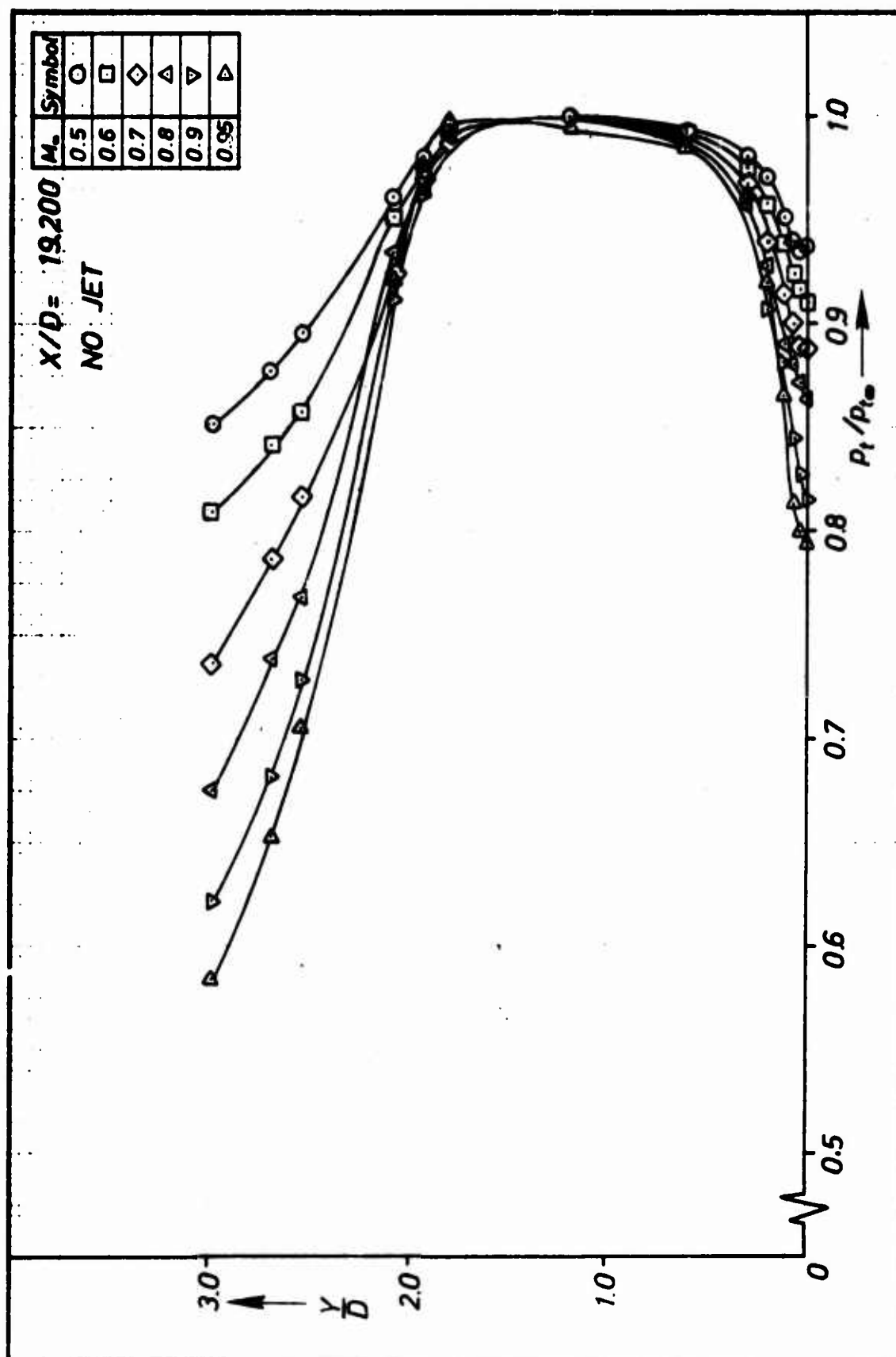


Fig.15 Total pressure distribution in the test section with Model A1 installed:  
propulsive jet off,  $X/D = 19.200$

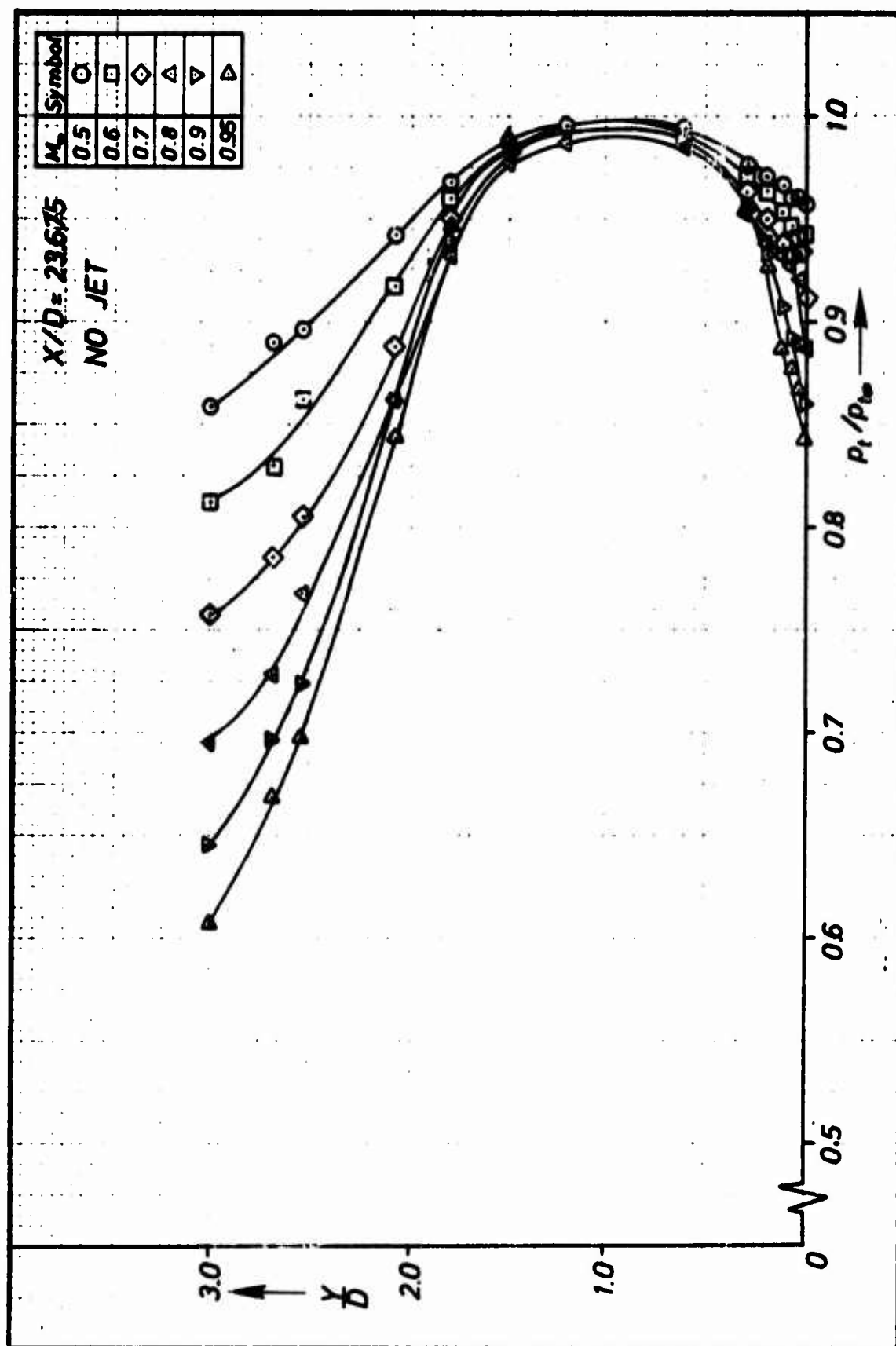


Fig.16 Total pressure distribution in the test section with Model A1 installed:  
propulsive jet off,  $X/D = 23.675$

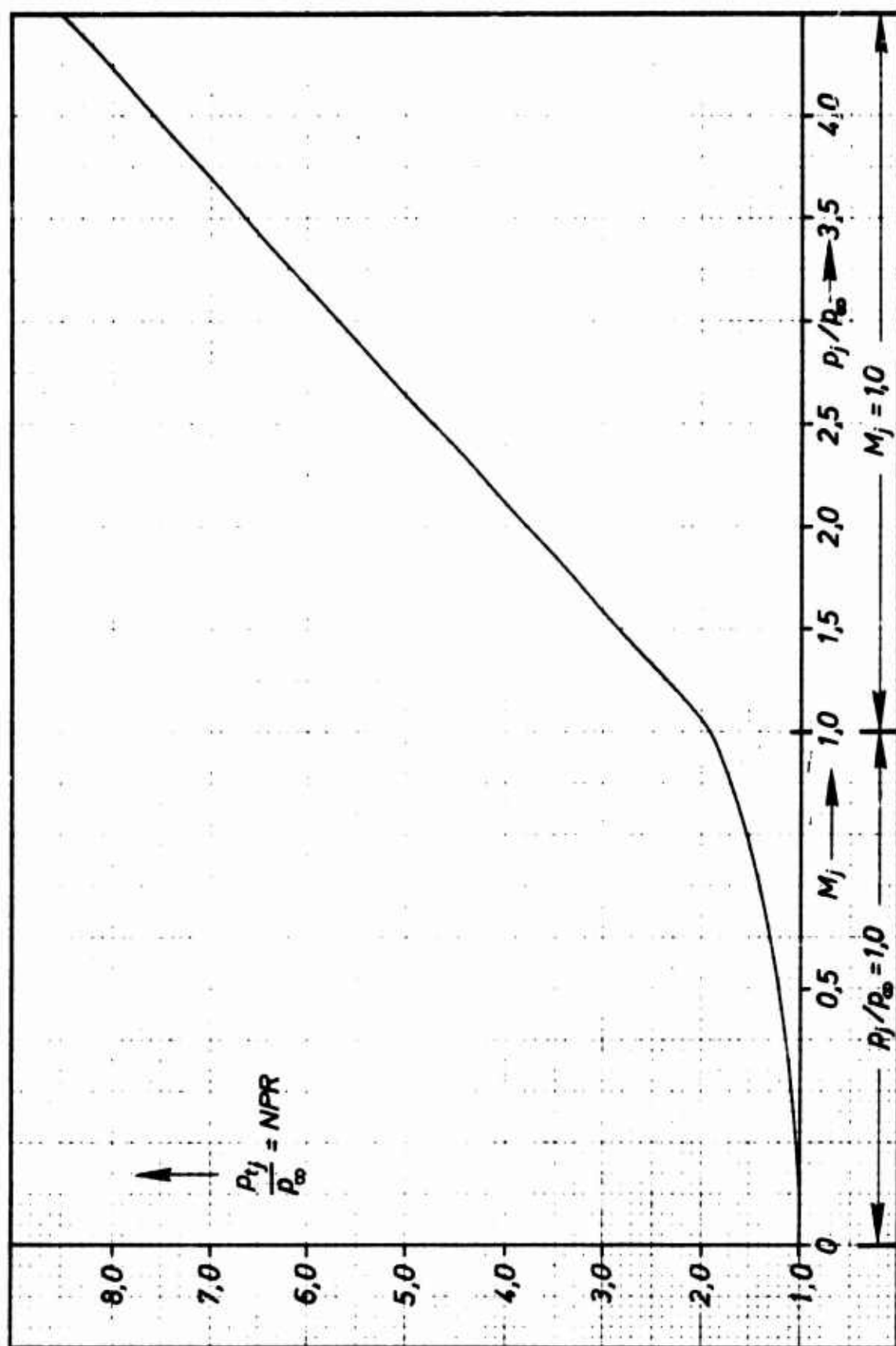


Fig.17 Relation between nozzle pressure ratio  $\text{NPR} = P_{tj}/P_\infty$  and the nozzle exit flow conditions  $M_j$  and  $P_j/P_\infty$

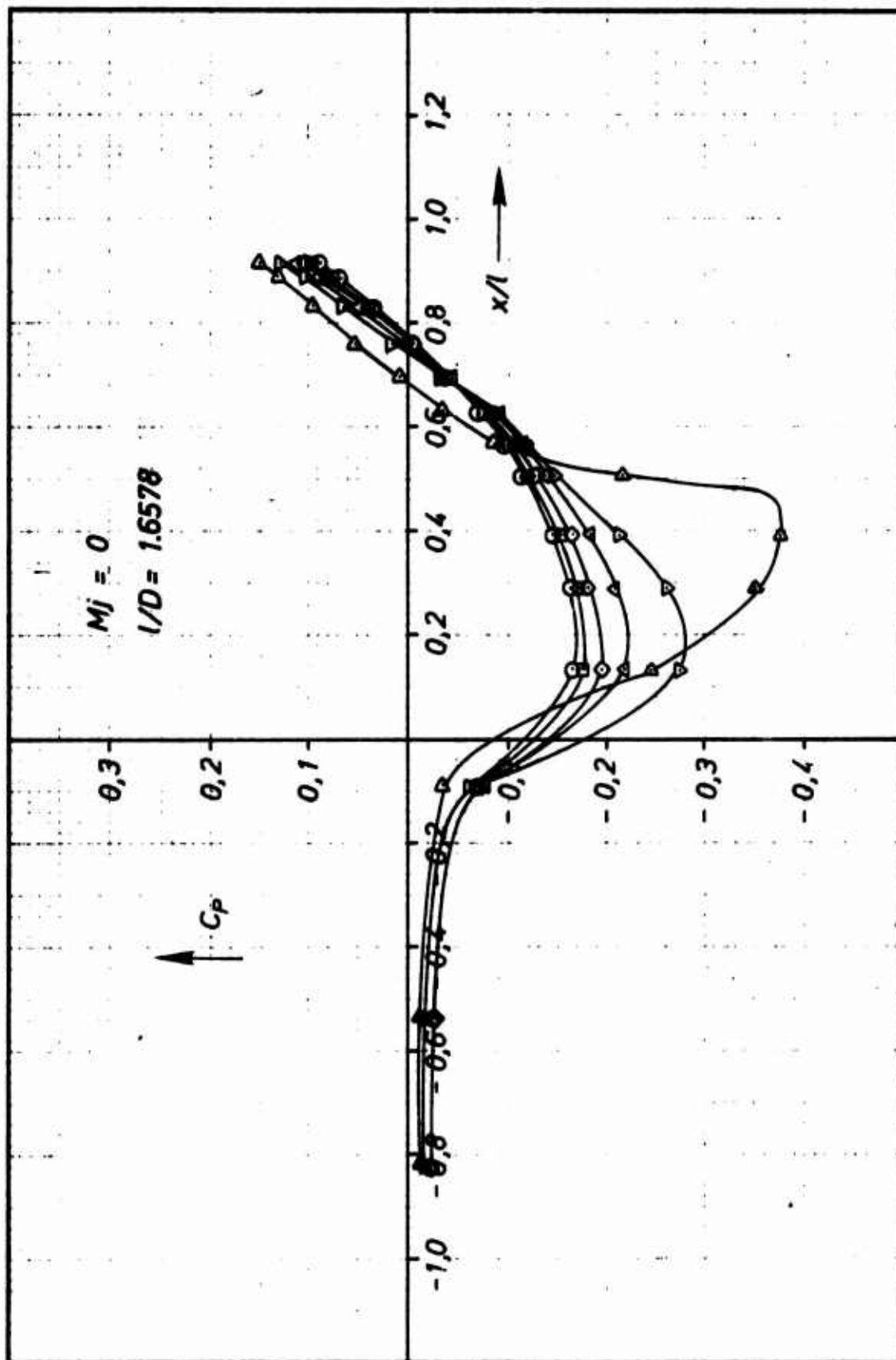


Fig.18 Static pressure distributions on the afterbody of Model A1:  
 $C_p = f(x/l)$  for  $M_j = 0$



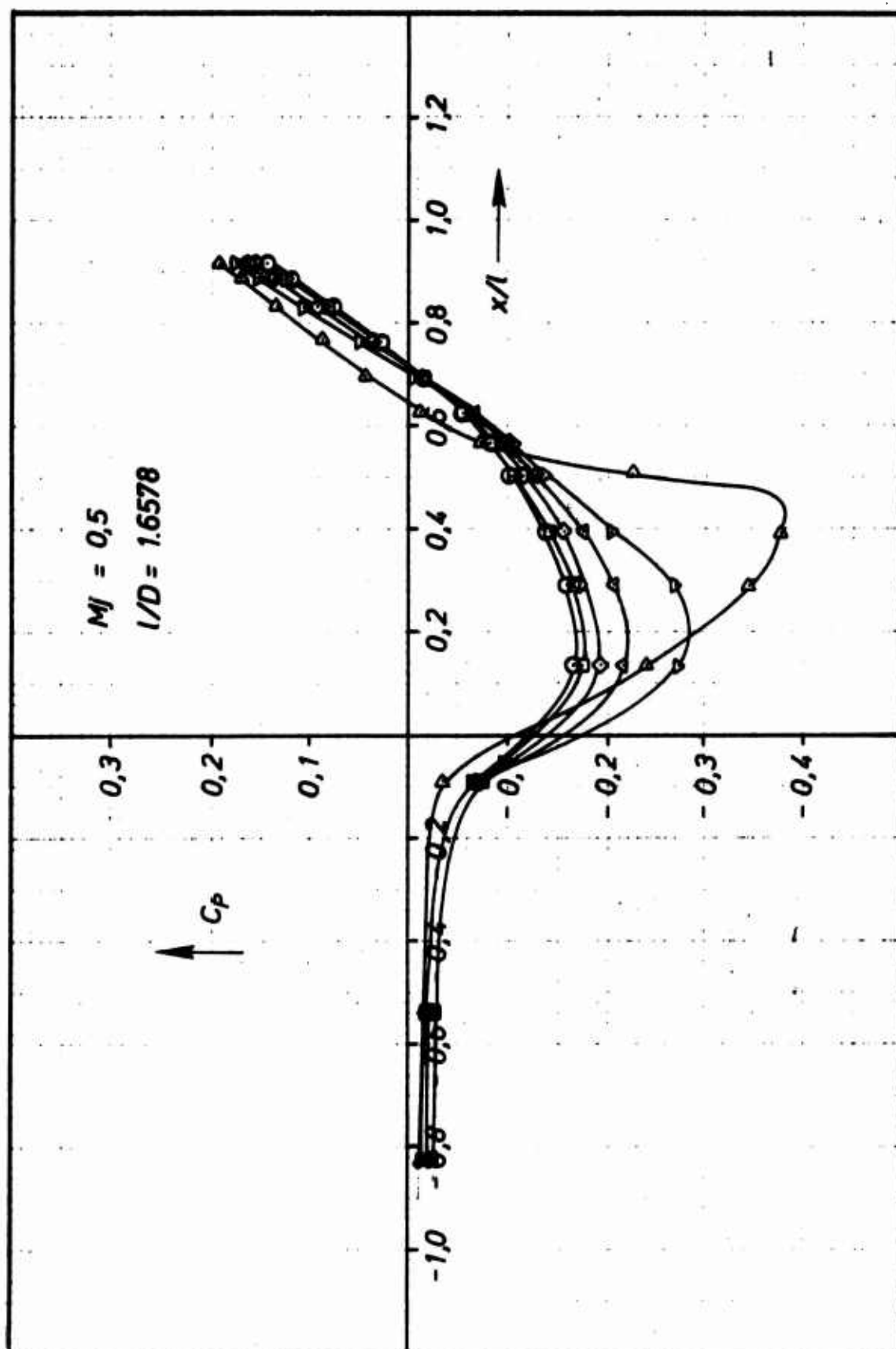


Fig.19 Static pressure distributions on the afterbody of Model A1:  
 $C_p = f(x/l)$  for  $M_j = 0.50$

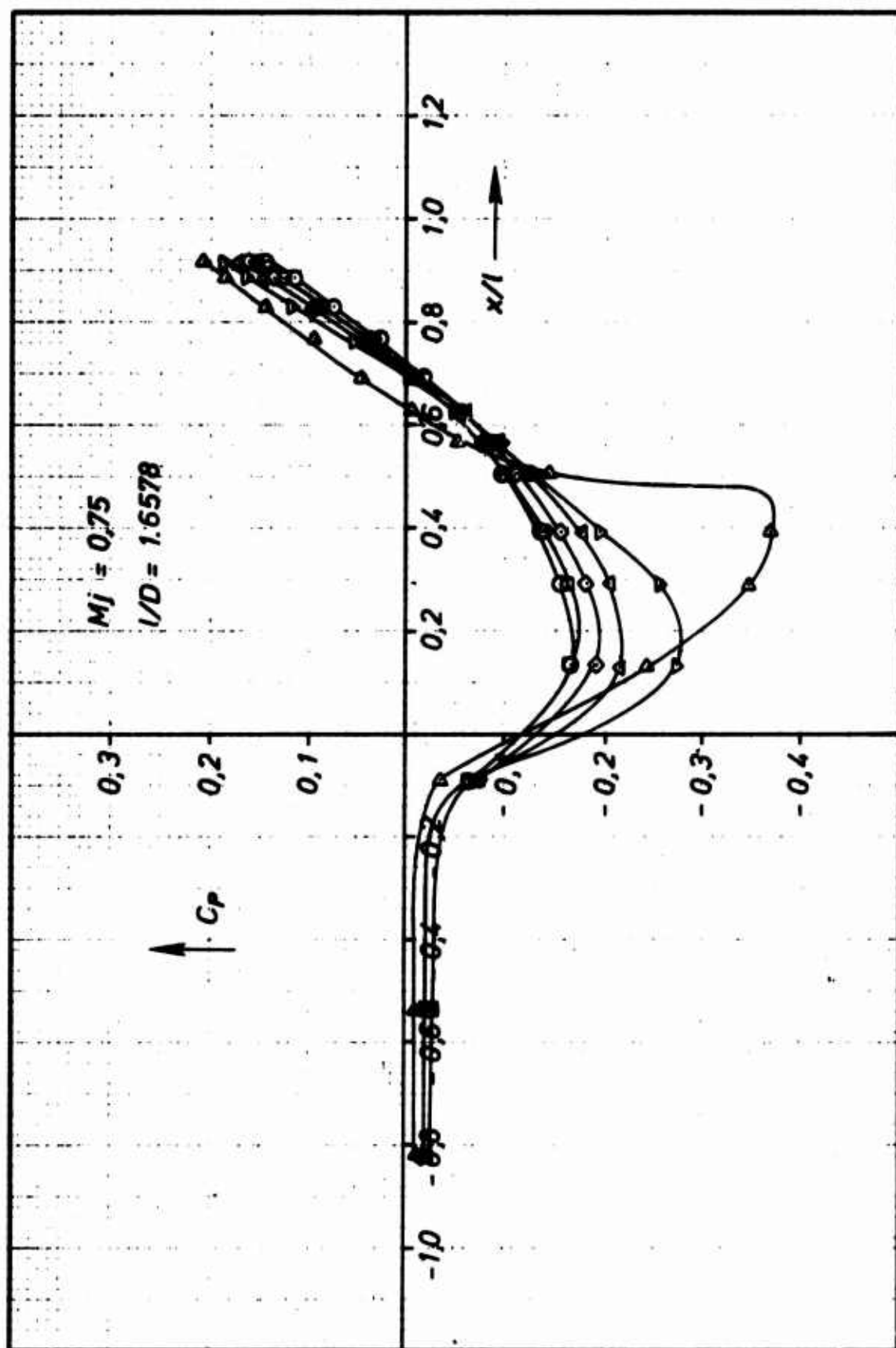


Fig.20 Static pressure distributions on the afterbody of Model A1:  
 $C_p = f(x/l)$  for  $M_j = 0.75$

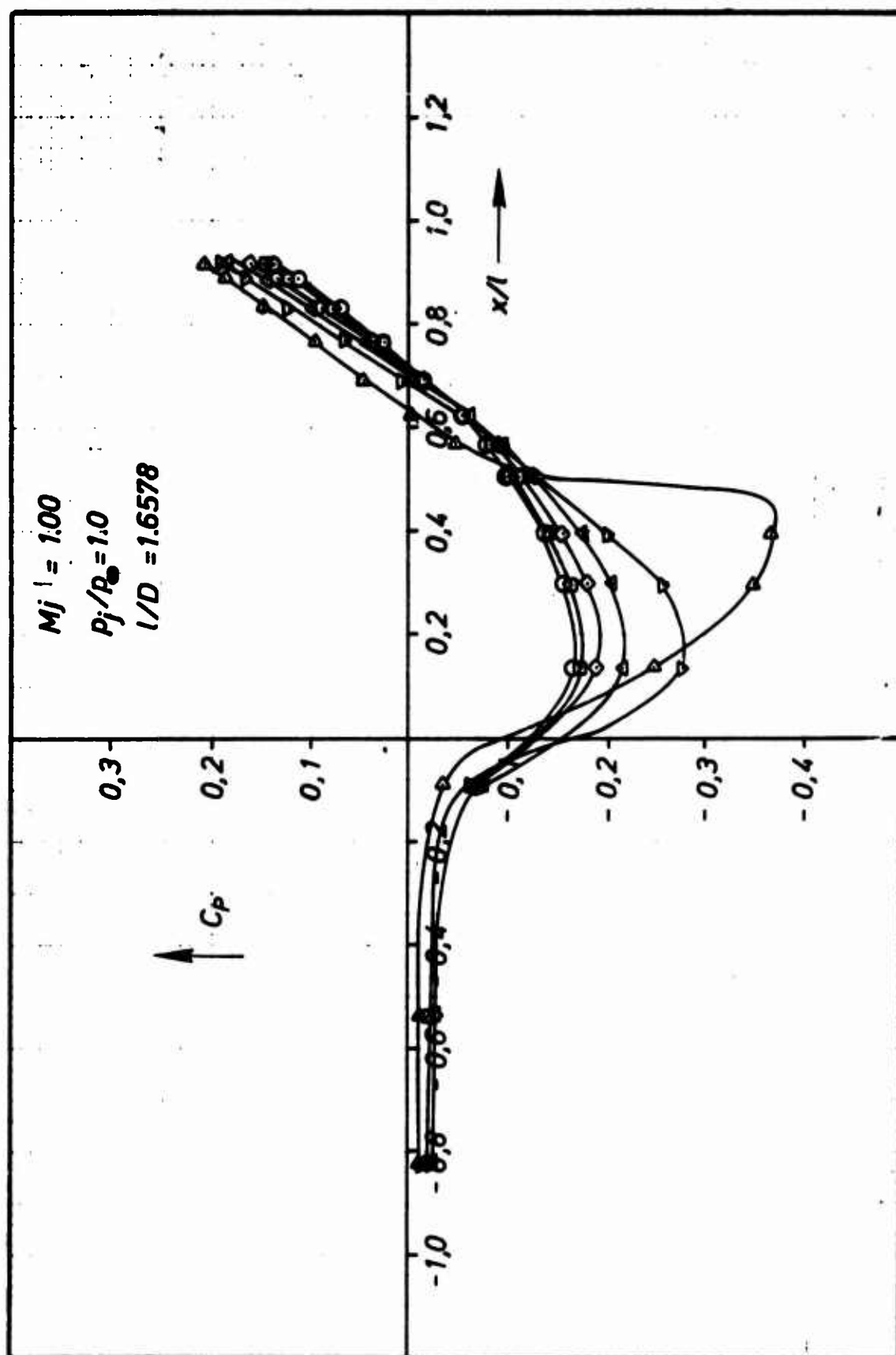


Fig.21 Static pressure distributions on the afterbody of Model A1:  
 $C_p = f(x/l)$  for  $M_j = 1.00$  and  $p_j/p_\infty = 1.0$

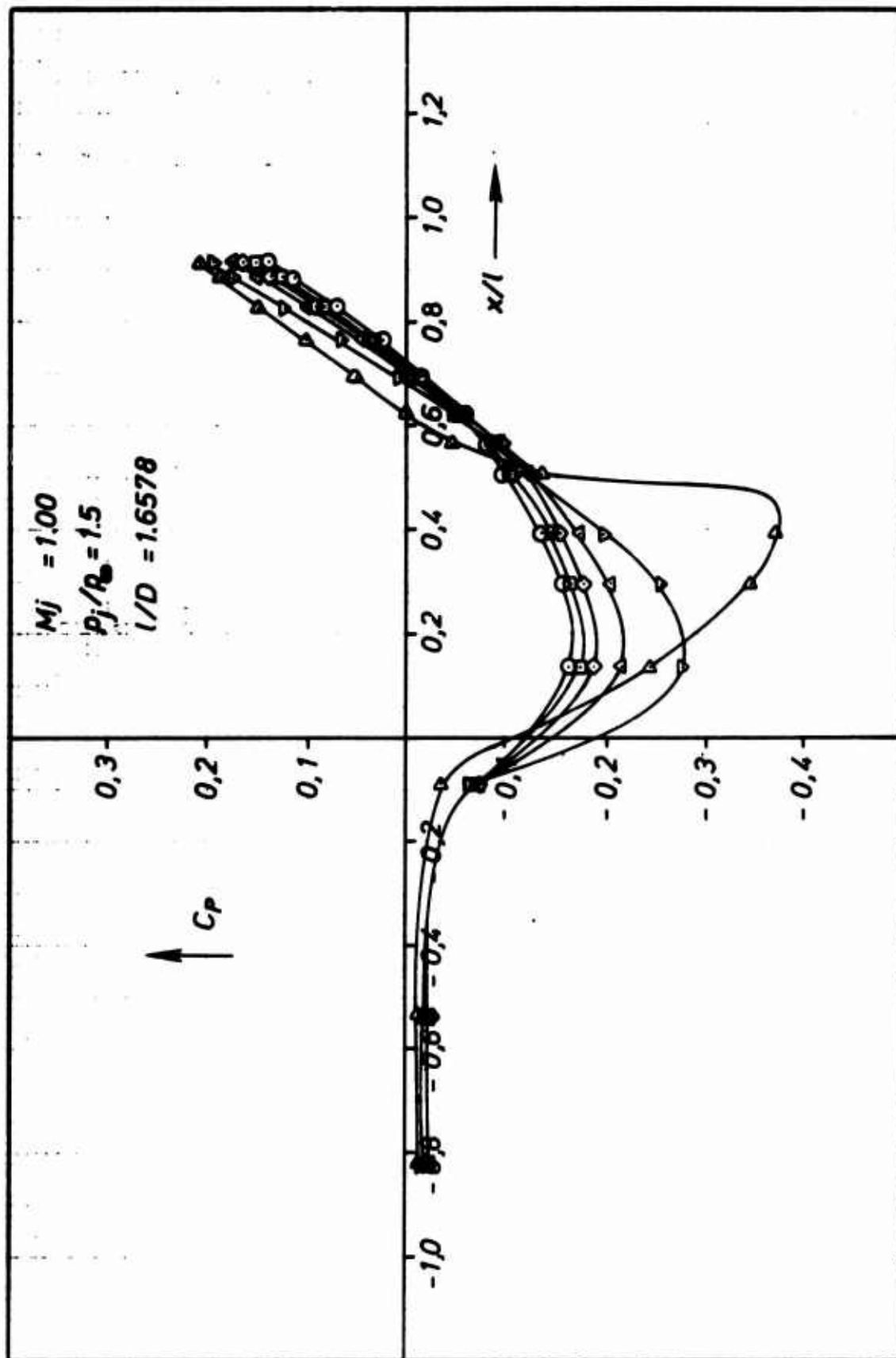


Fig.22 Static pressure distributions on the afterbody of Model A1:  
 $C_p = f(x/l)$  for  $M_j = 1.00$  and  $p_j/p_\infty = 1.5$

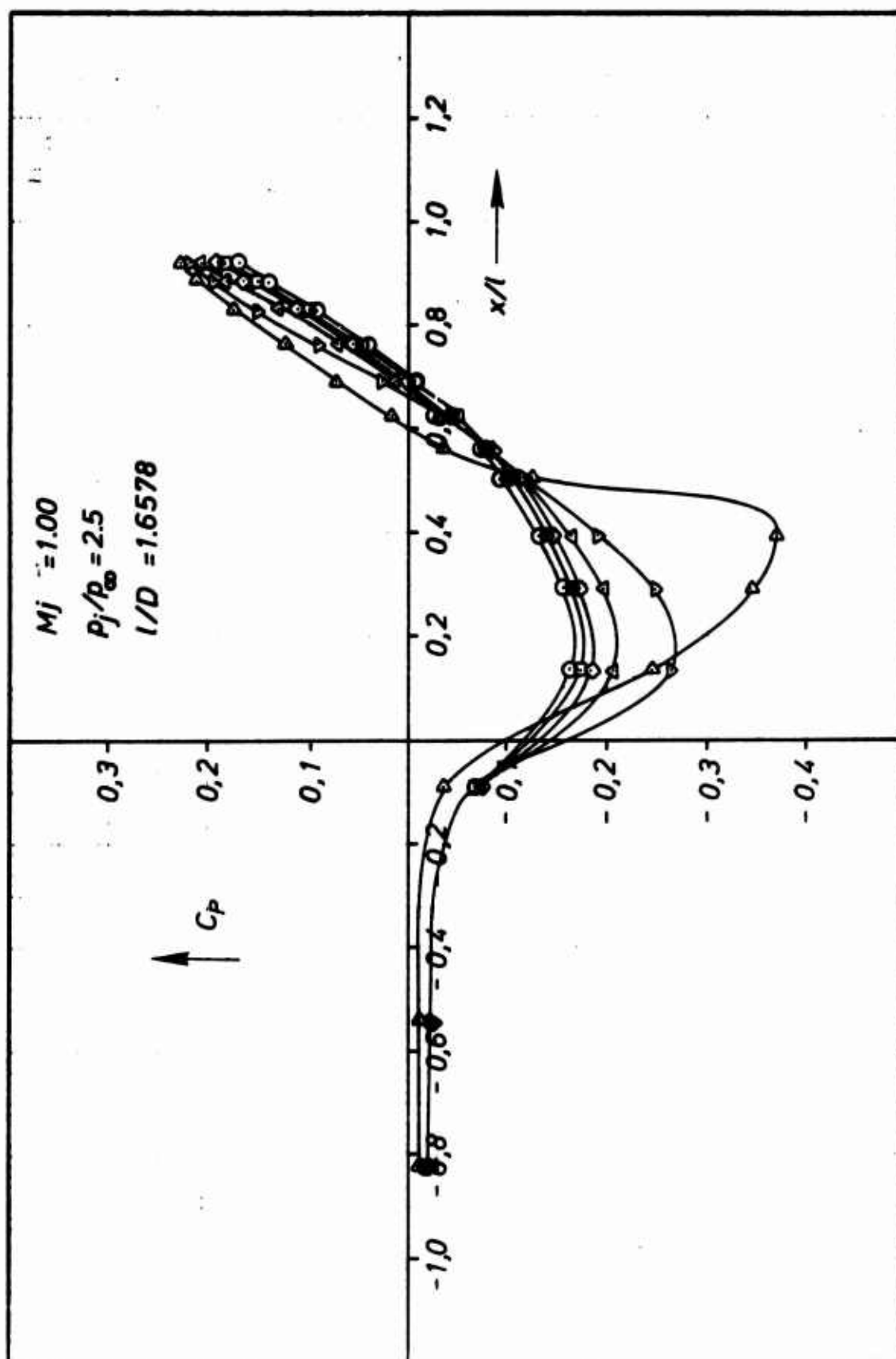


Fig. 23 Static pressure distributions on the afterbody of Model A1:  
 $C_p = f(x/l)$  for  $M_j = 1.00$  and  $p_j/p_\infty = 2.5$

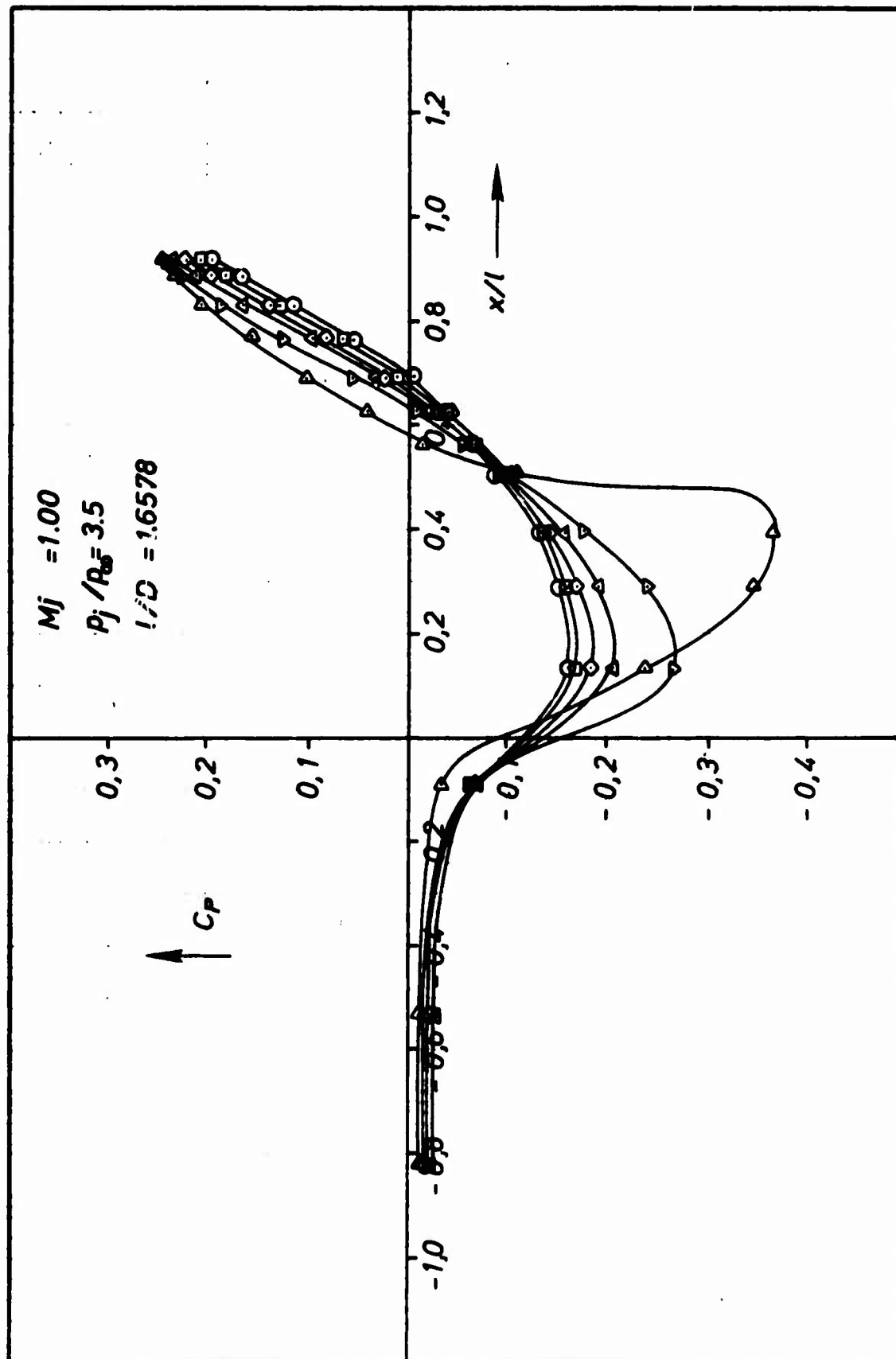


Fig. 24 Static pressure distributions on the afterbody of Model A1:  
 $C_p = f(x/l)$  for  $M_j = 1.00$  and  $p_j/p_\infty = 3.5$

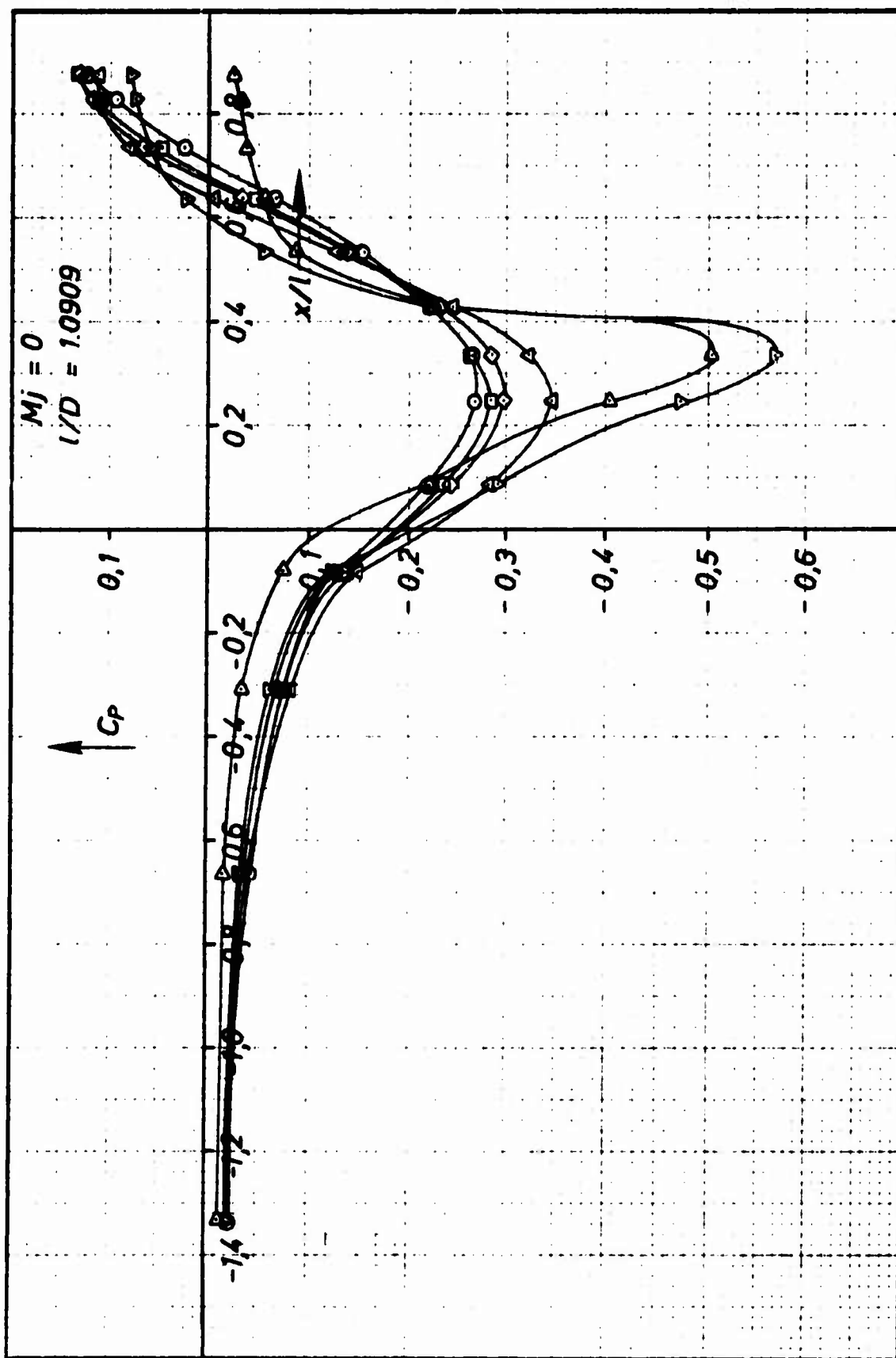


Fig.25 Static pressure distributions on the afterbody of Model A2:  
 $C_p = f(x/l)$  for  $M_j = 0$

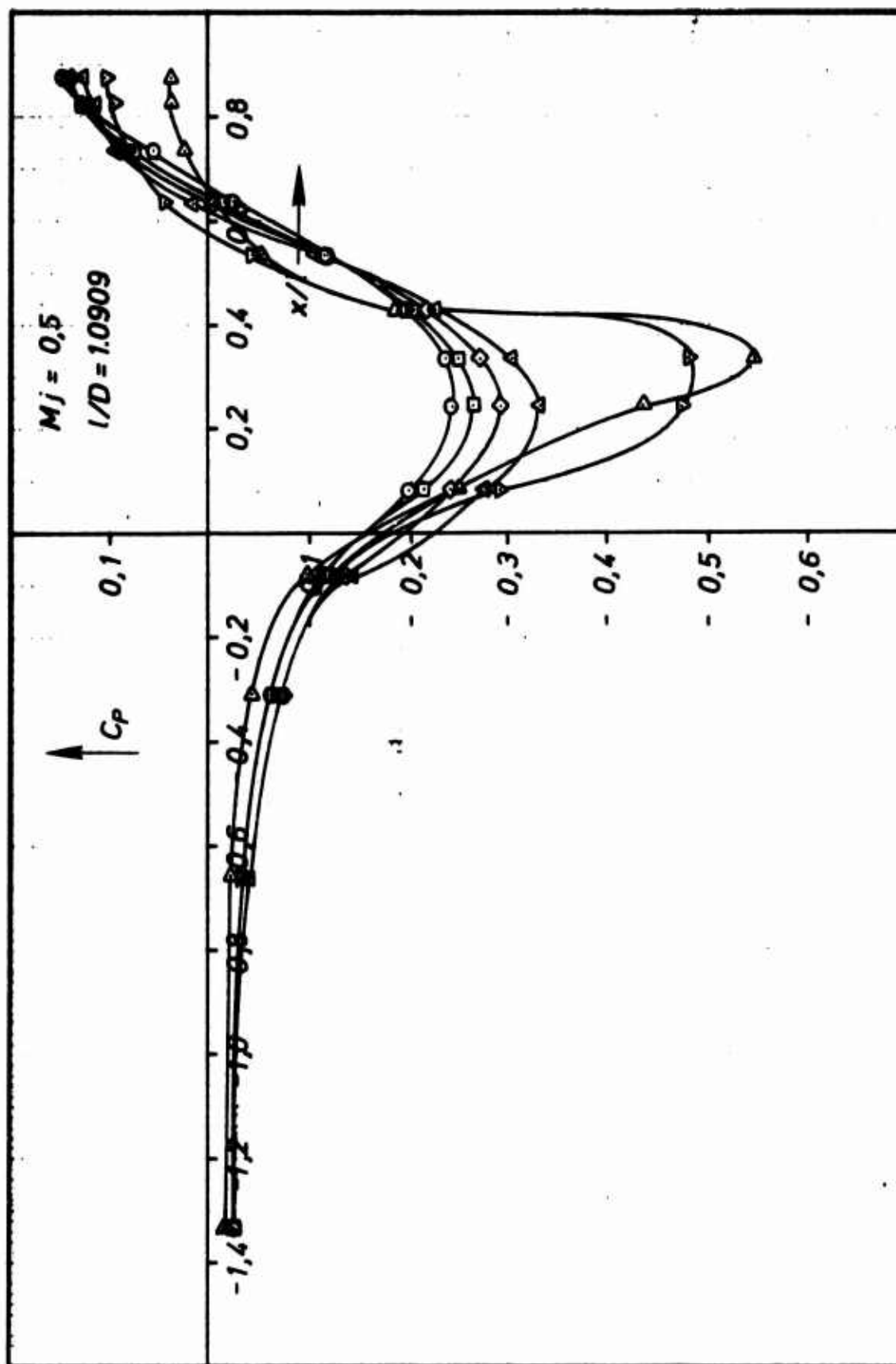


Fig.26 Static pressure distributions on the afterbody of Model A2:  
 $C_p = f(x/l)$  for  $M_j = 0.50$



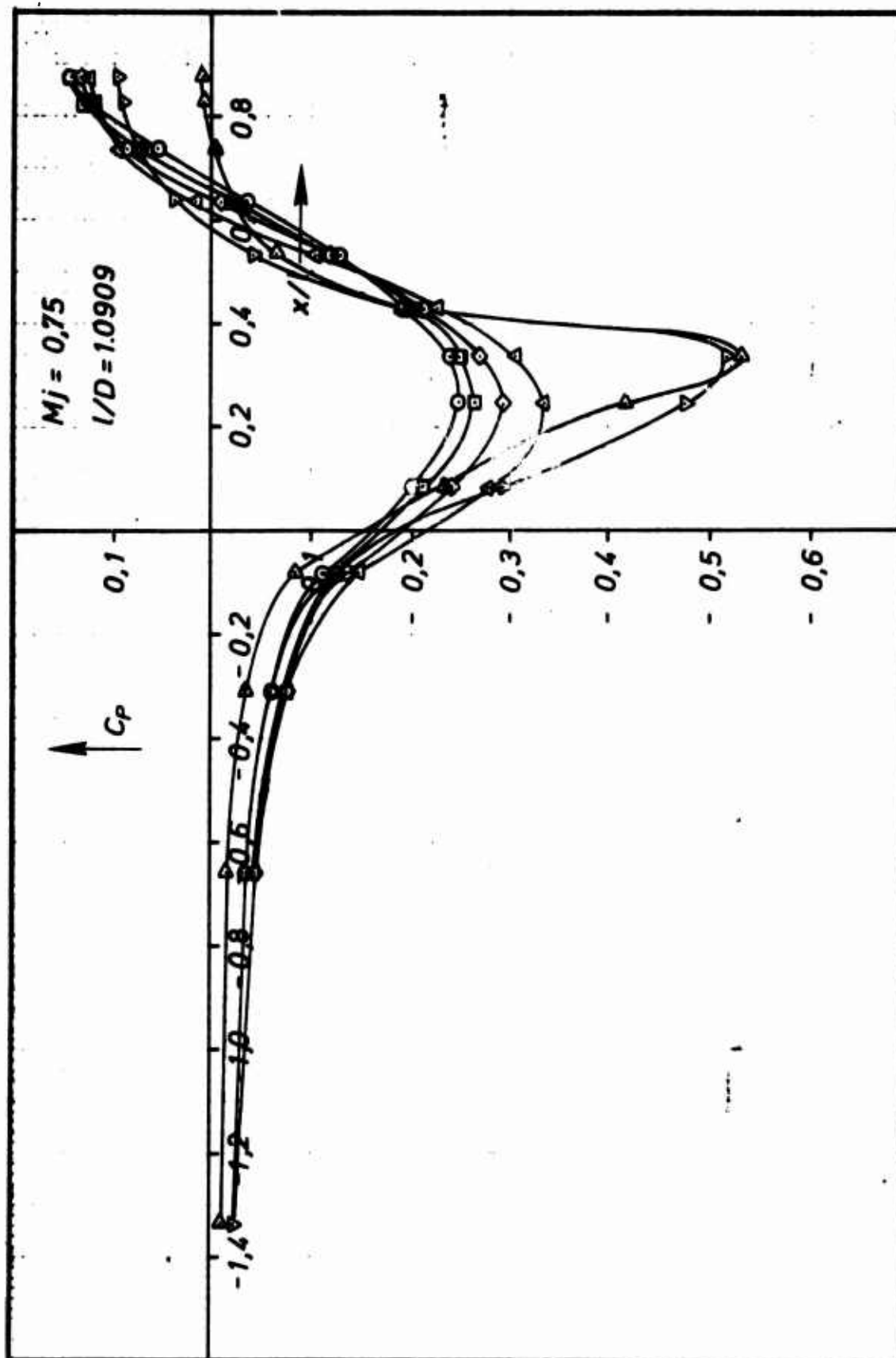


Fig. 27 Static pressure distributions on the afterbody of Model A2:  
 $C_p = f(x/l)$  for  $M_j = 0.75$

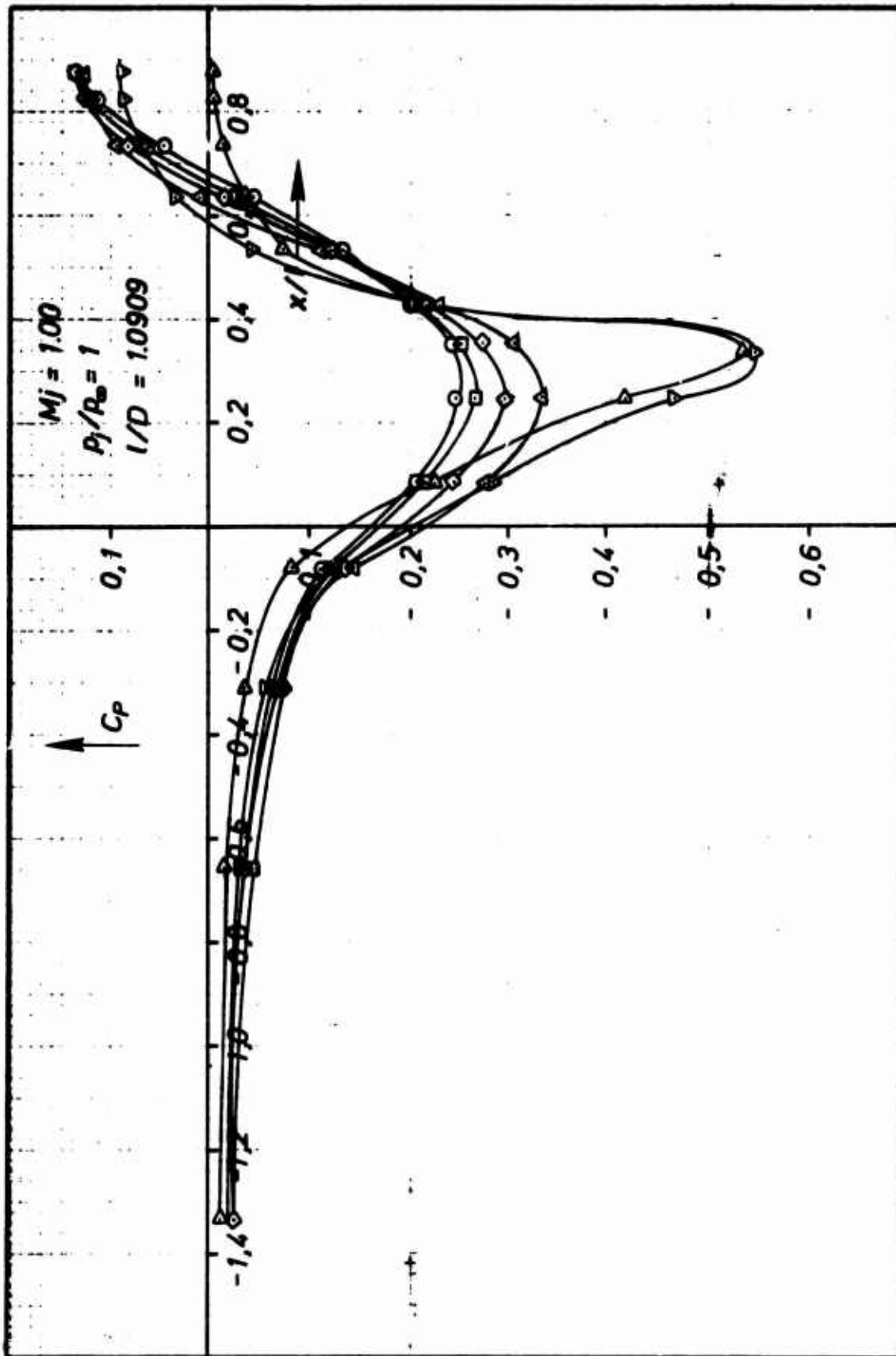


Fig.28 Static pressure distributions on the afterbody of Model A2:  
 $C_p = f(x/l)$  for  $M_j = 1.00$  and  $p_i/p_\infty = 1.0$

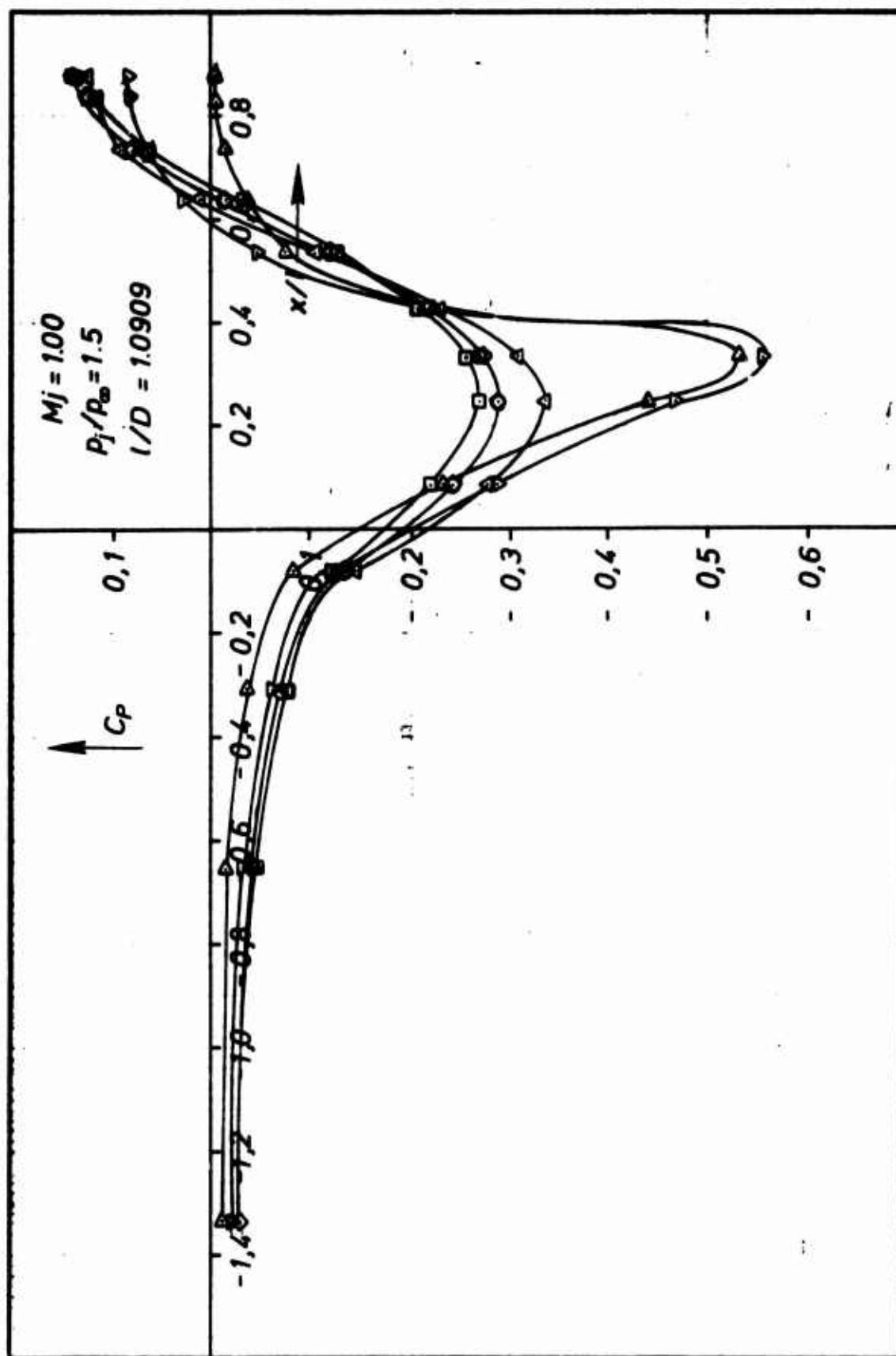


Fig.29 Static pressure distributions on the afterbody of Model A2:  
 $C_p = f(x/l)$  for  $M_j = 1.00$  and  $p_j/p_\infty = 1.5$

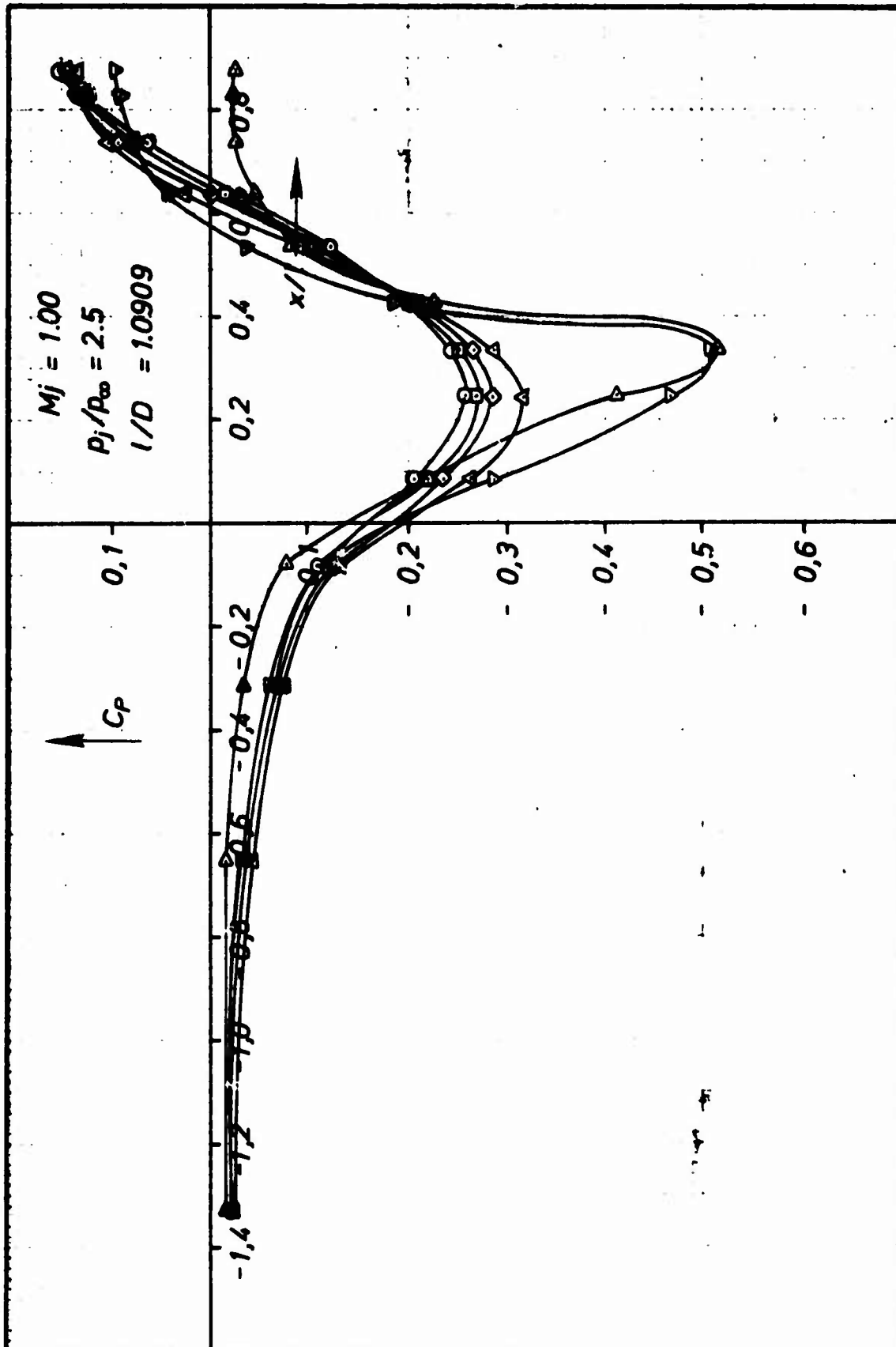


Fig.30 Static pressure distributions on the afterbody of Model A2:  
 $C_p = f(x/l)$  for  $M_j = 1.00$  and  $p_j/p_\infty = 2.5$

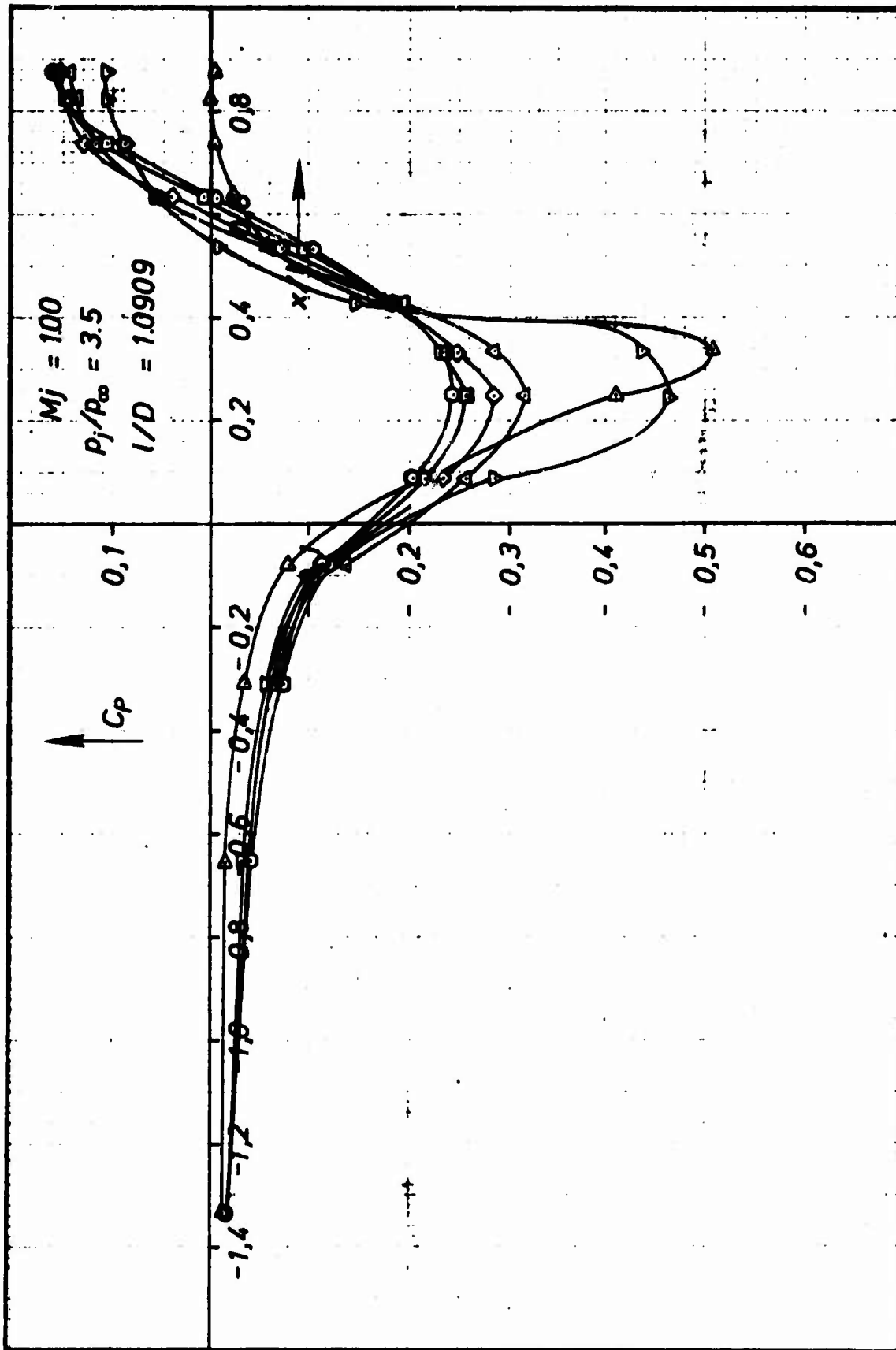


Fig.31 Static pressure distributions on the afterbody of Model A2:  
 $C_p = f(x/l)$  for  $M_j = 1.00$  and  $p_i/p_\infty = 3.5$

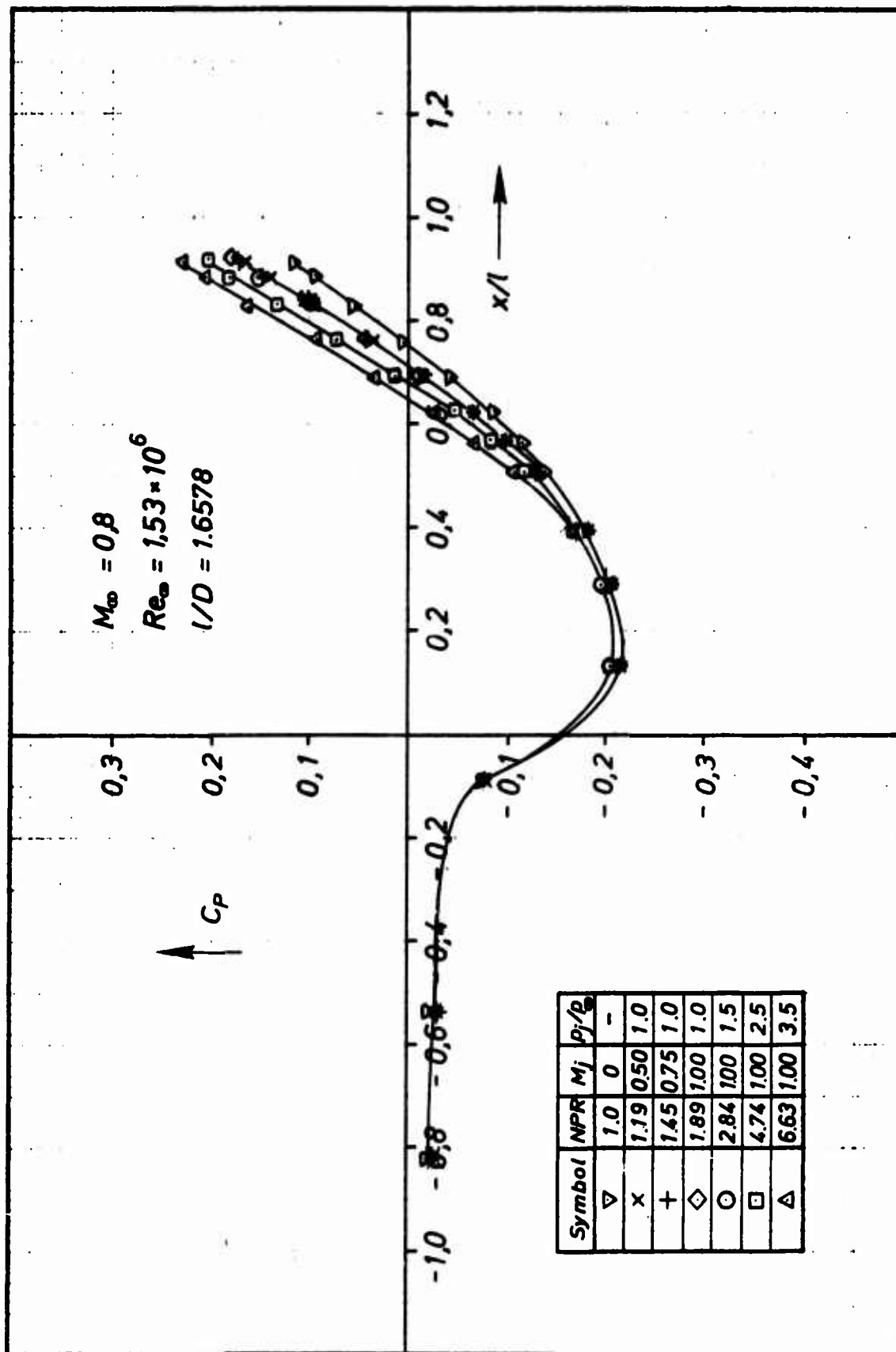
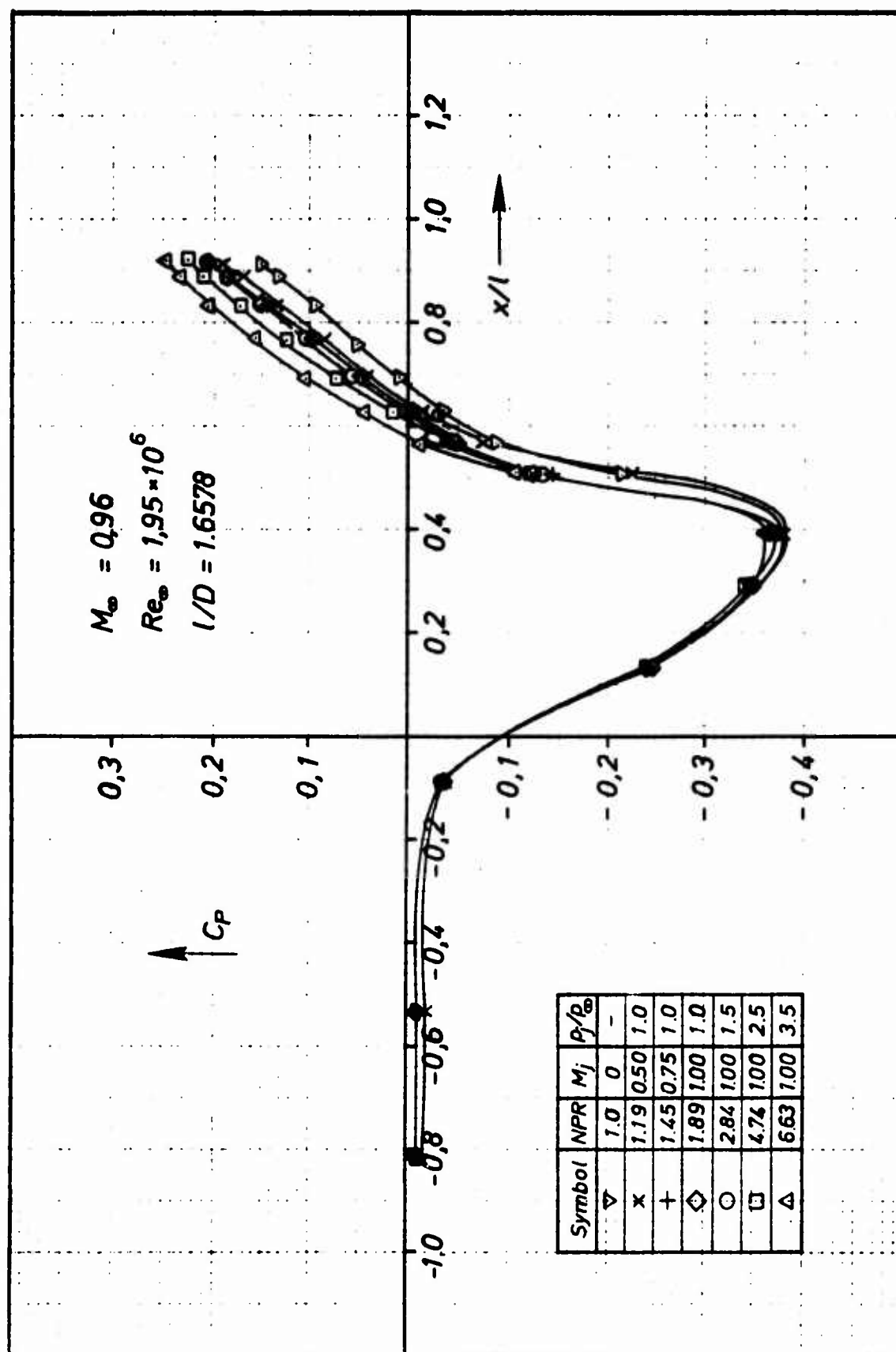
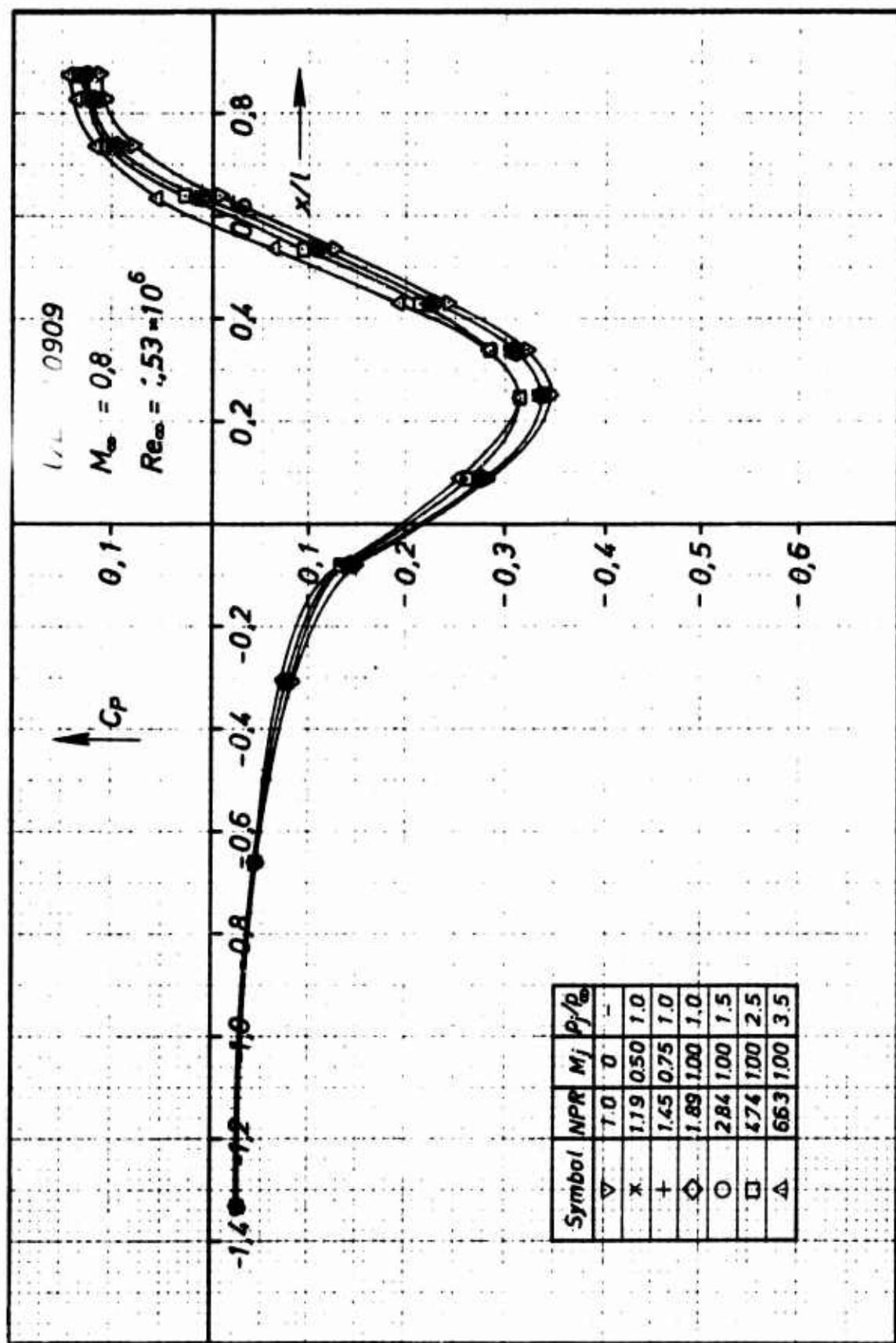
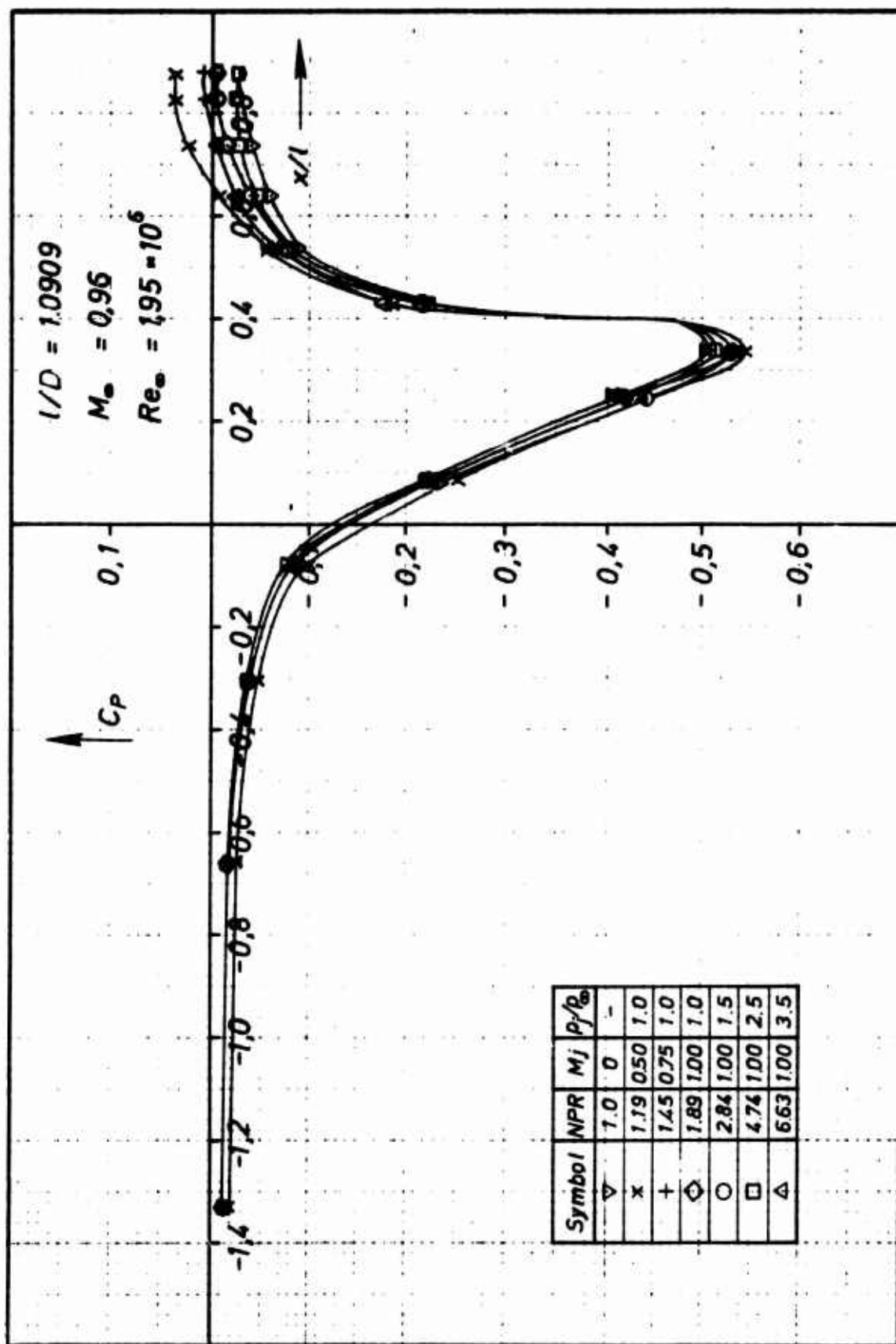


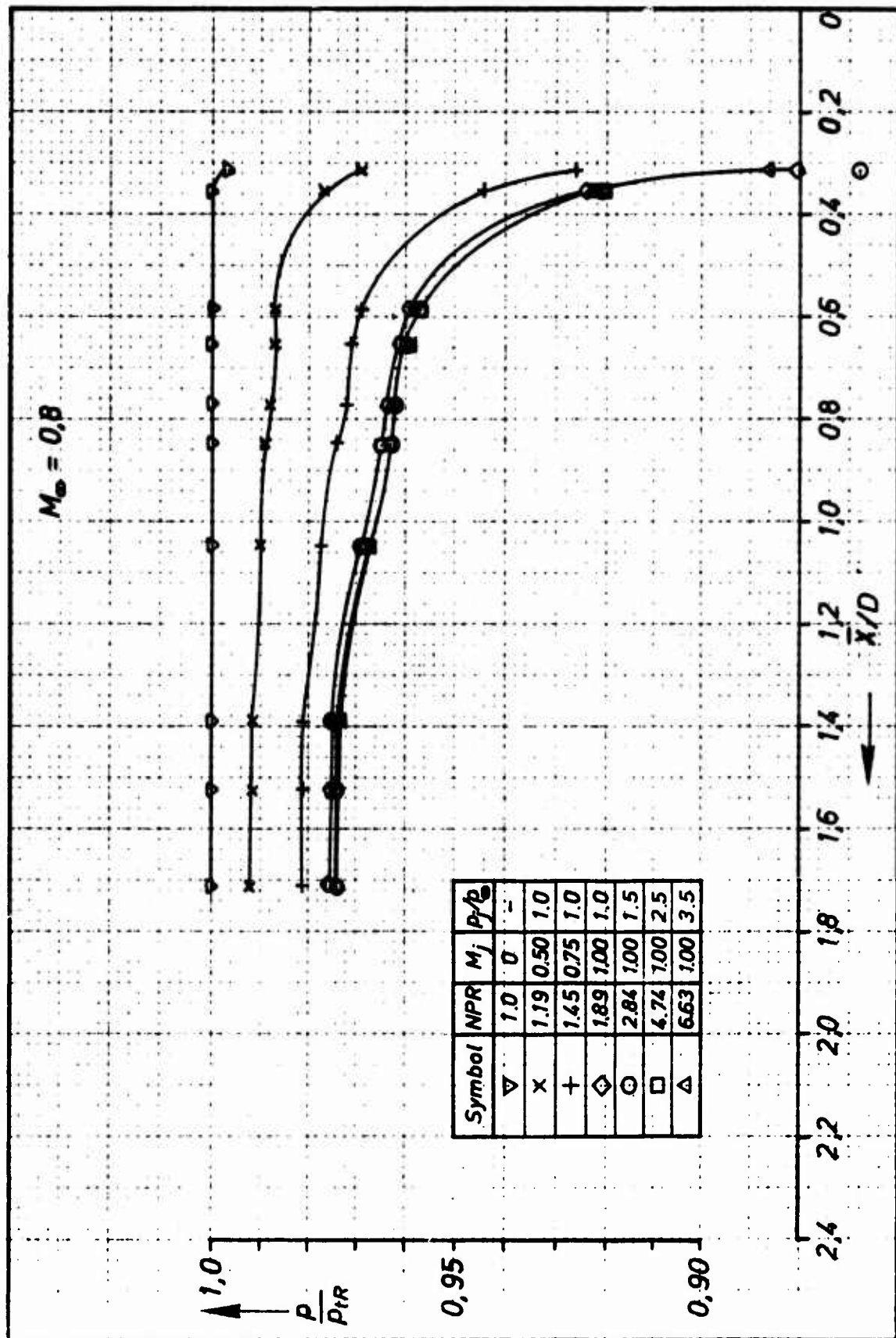
Fig.32 Static pressure distributions on the afterbody of Model A1 for  $M_\infty = 0.8$

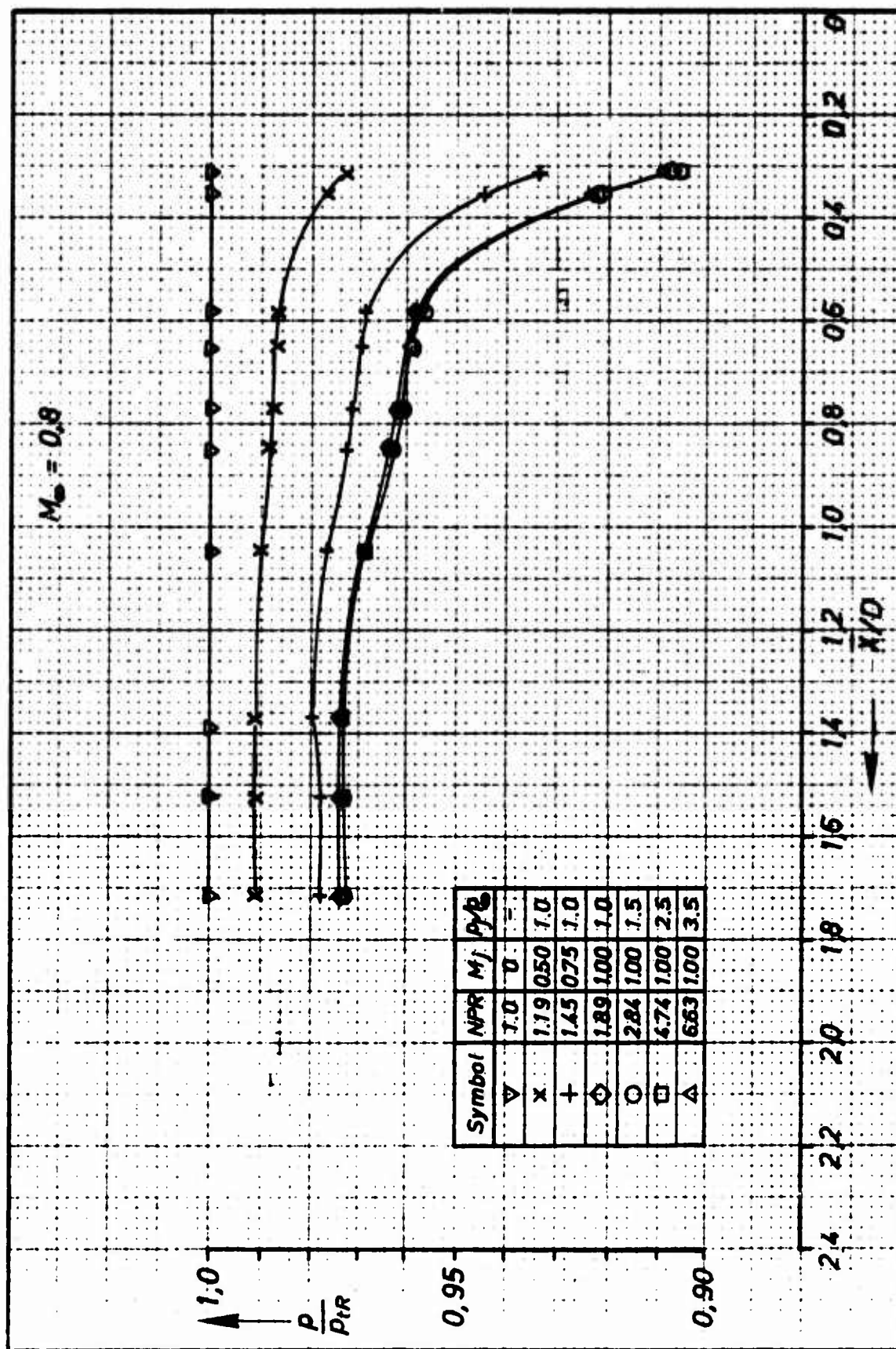
Fig.33 Static pressure distributions on the afterbody of Model A1 for  $M_\infty = 0.96$

Fig.34 Static pressure distributions on the afterbody of Model A2 for  $M_\infty = 0.8$



Fig.35 Static pressure distributions on the afterbody of Model A2 for  $M_\infty = 0.96$

Fig.36 Static pressure distributions on the nozzle wall of Model A1 for  $M_\infty = 0.8$

Fig.37 Static pressure distributions on the nozzle wall of Model A2 for  $M_\infty = 0.8$

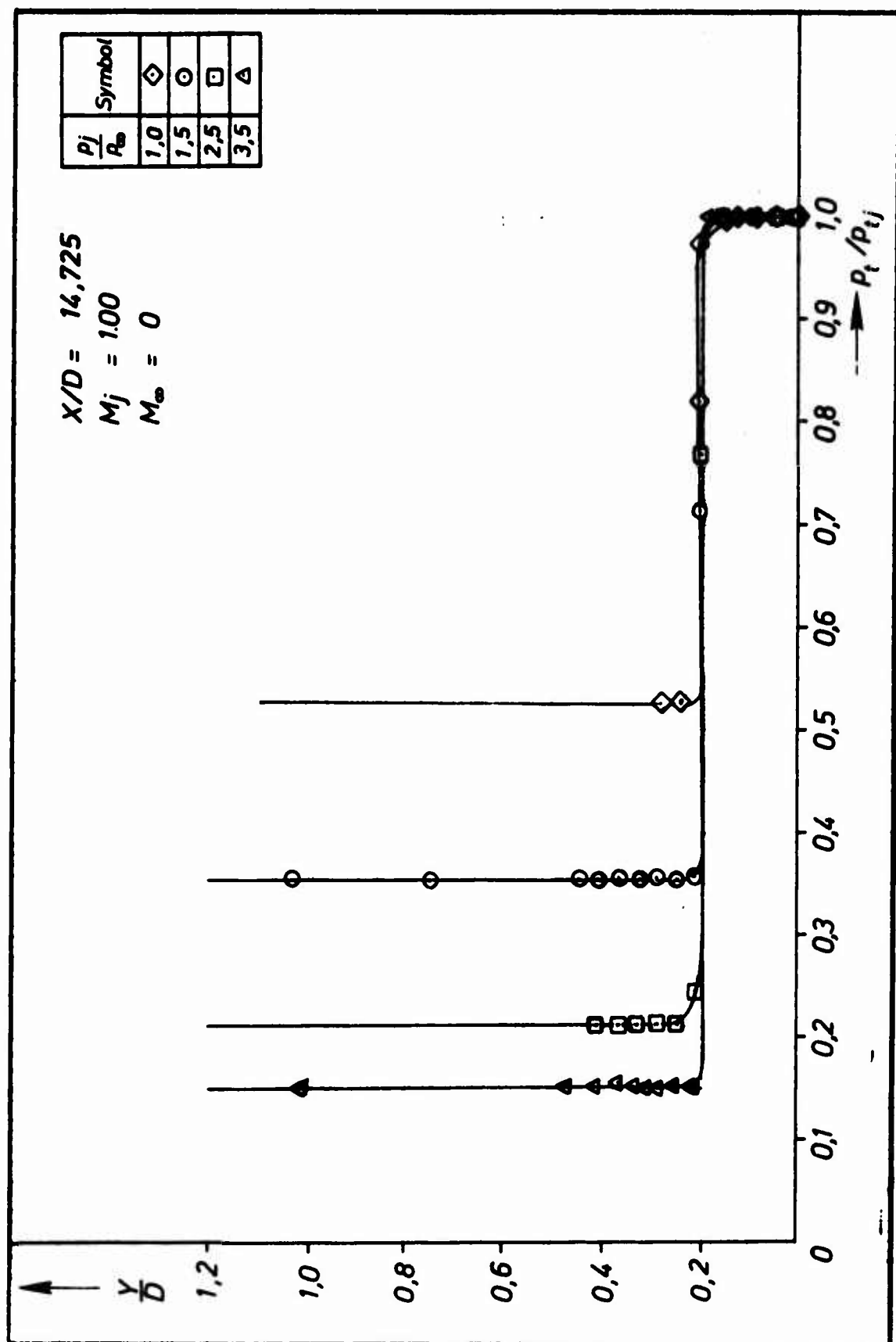


Fig.38 Total pressure distributions in the flow field of the propulsive jet without external flow ( $M_\infty = 0$ ) for Model A1.  
 $X/D = 14,725$ ;  $M_j = 1,0$ ;  $1 < p_j/p_\infty < 3,5$

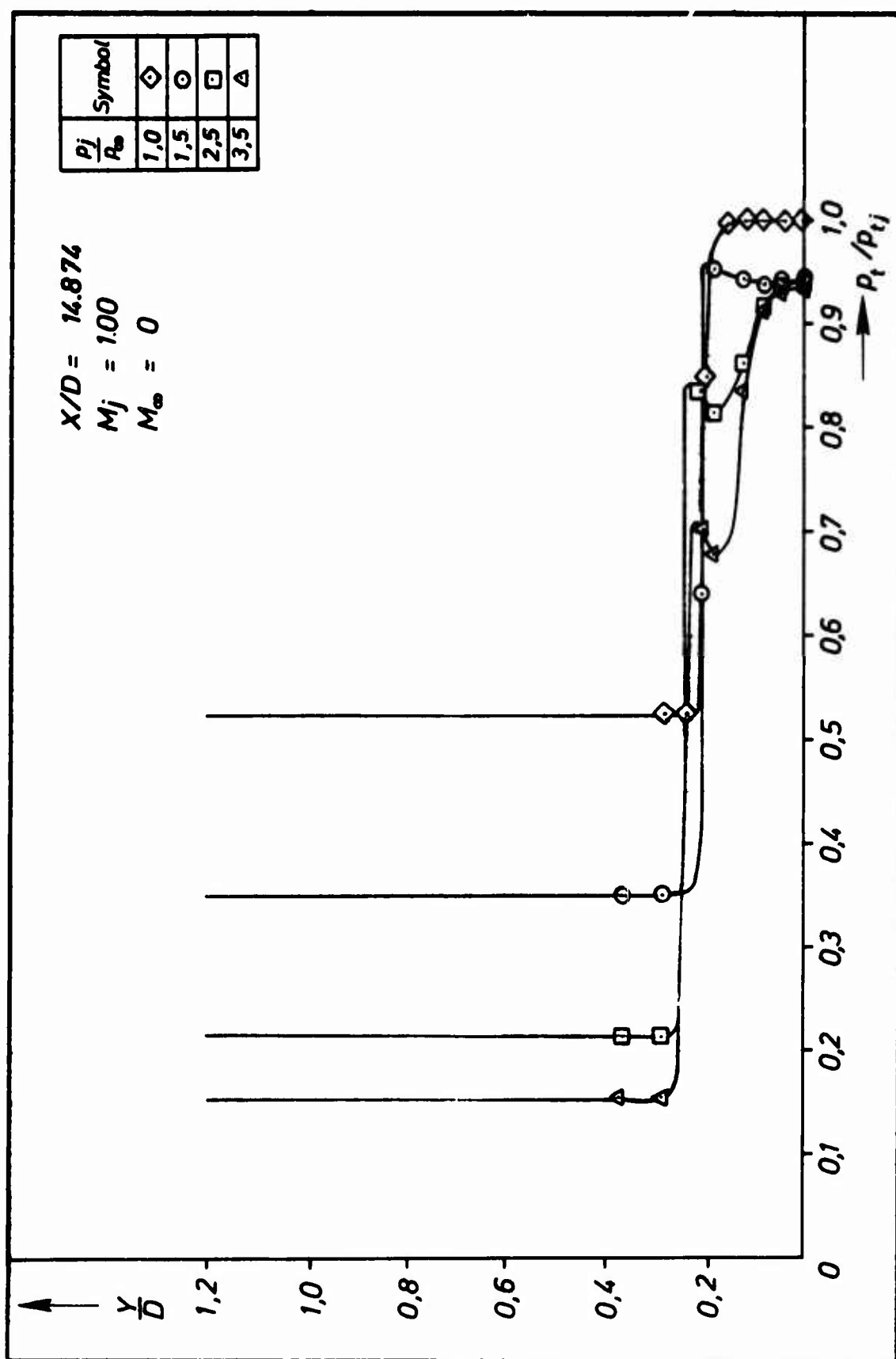


Fig.39 Total pressure distributions in the flow field of the propulsive jet without external flow ( $M_\infty = 0$ ) for Model A1.  $X/D = 14.874$

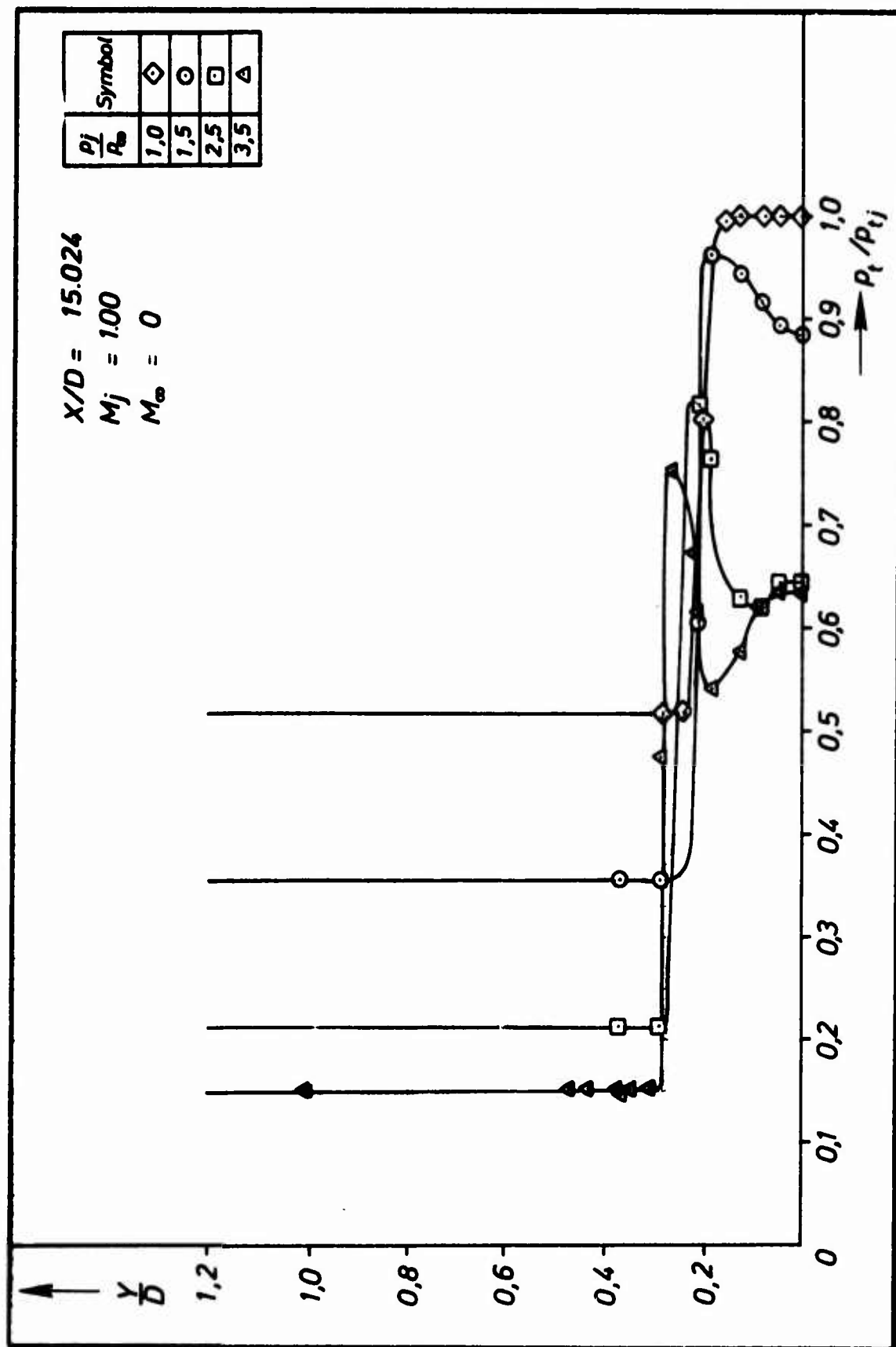


Fig.40 Total pressure distributions in the flow field of the propulsive jet without external flow ( $M_\infty = 0$ ) for Model A1.  $X/D = 15.024$

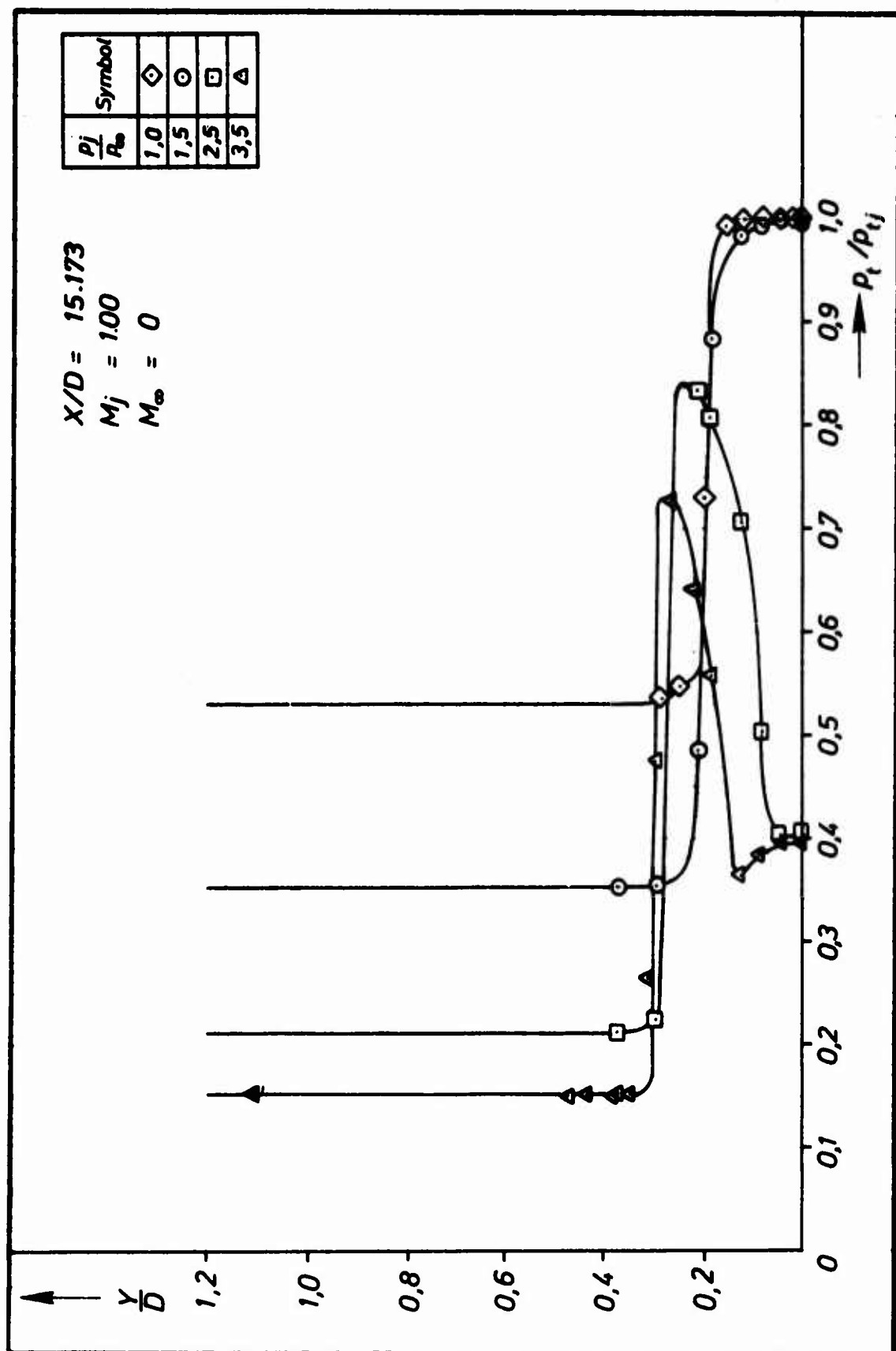


Fig.41 Total pressure distributions in the flow field of the propulsive jet without external flow ( $M_\infty = 0$ ) for Model A1.  $X/D = 15.173$

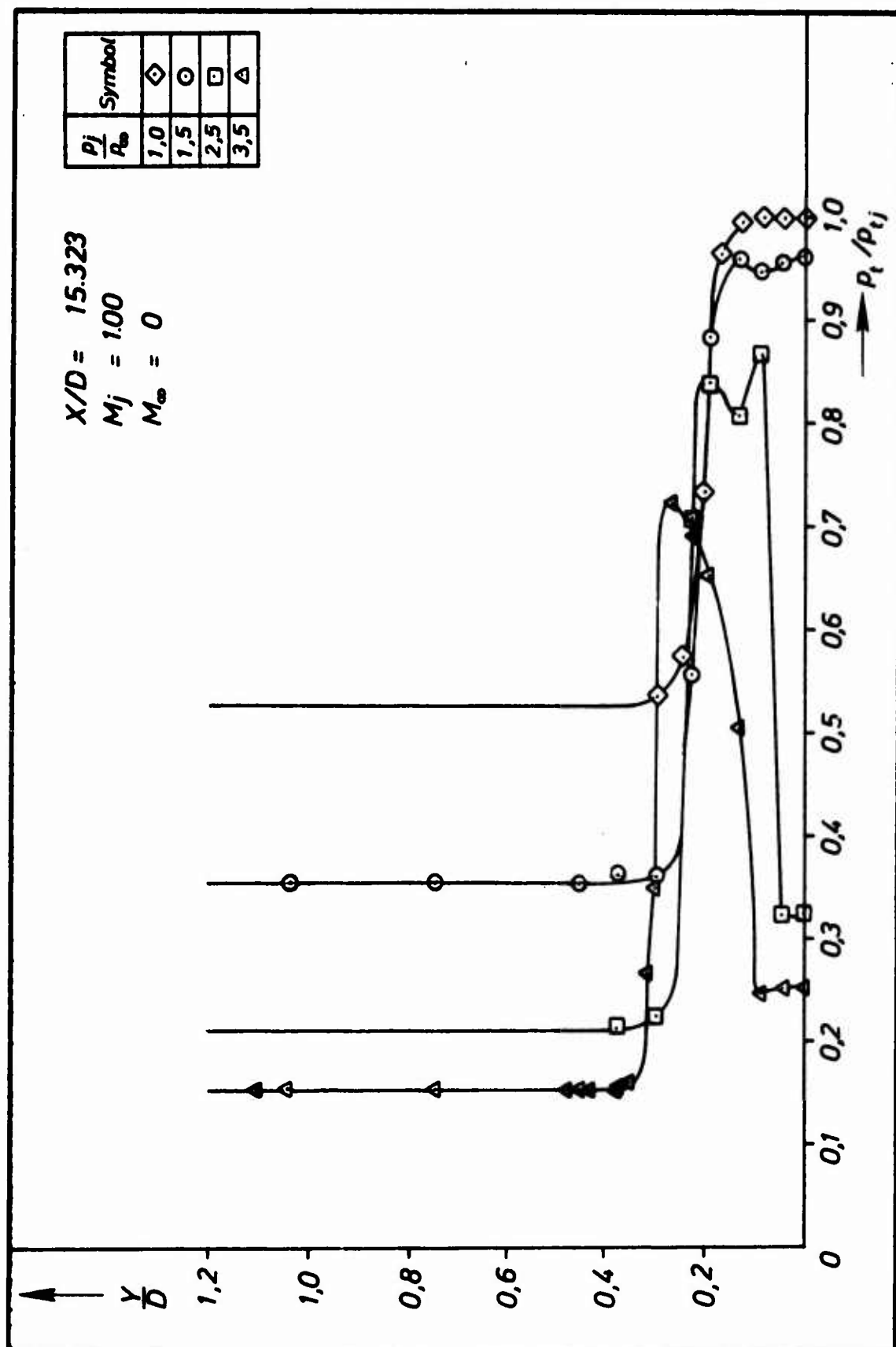


Fig.42 Total pressure distributions in the flow field of the propulsive jet without external flow ( $M_\infty = 0$ ) for Model A1.  $X/D = 15.323$



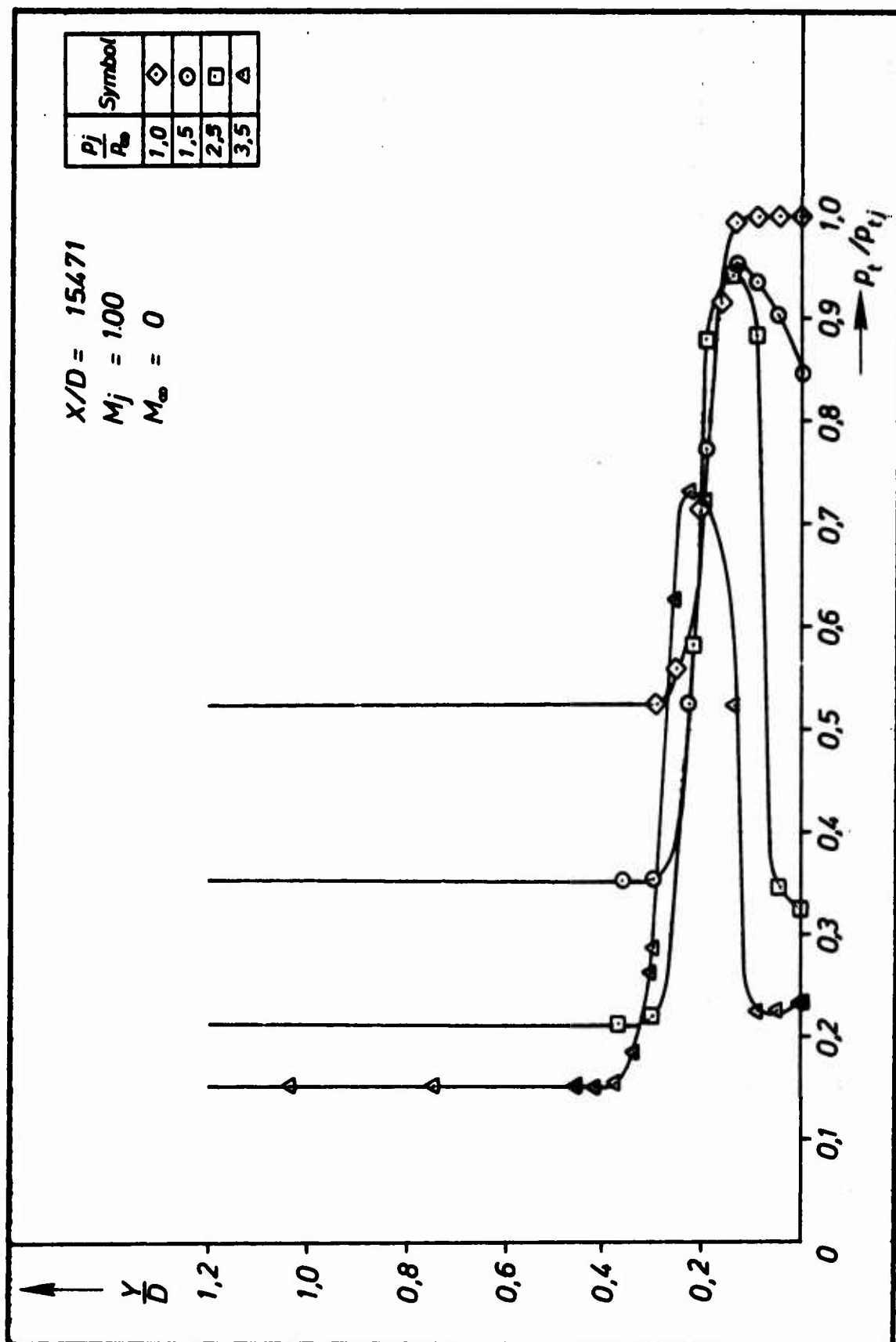


Fig.43 Total pressure distributions in the flow field of the propulsive jet without external flow ( $M_\infty = 0$ ) for Model A1.  $X/D = 15.471$

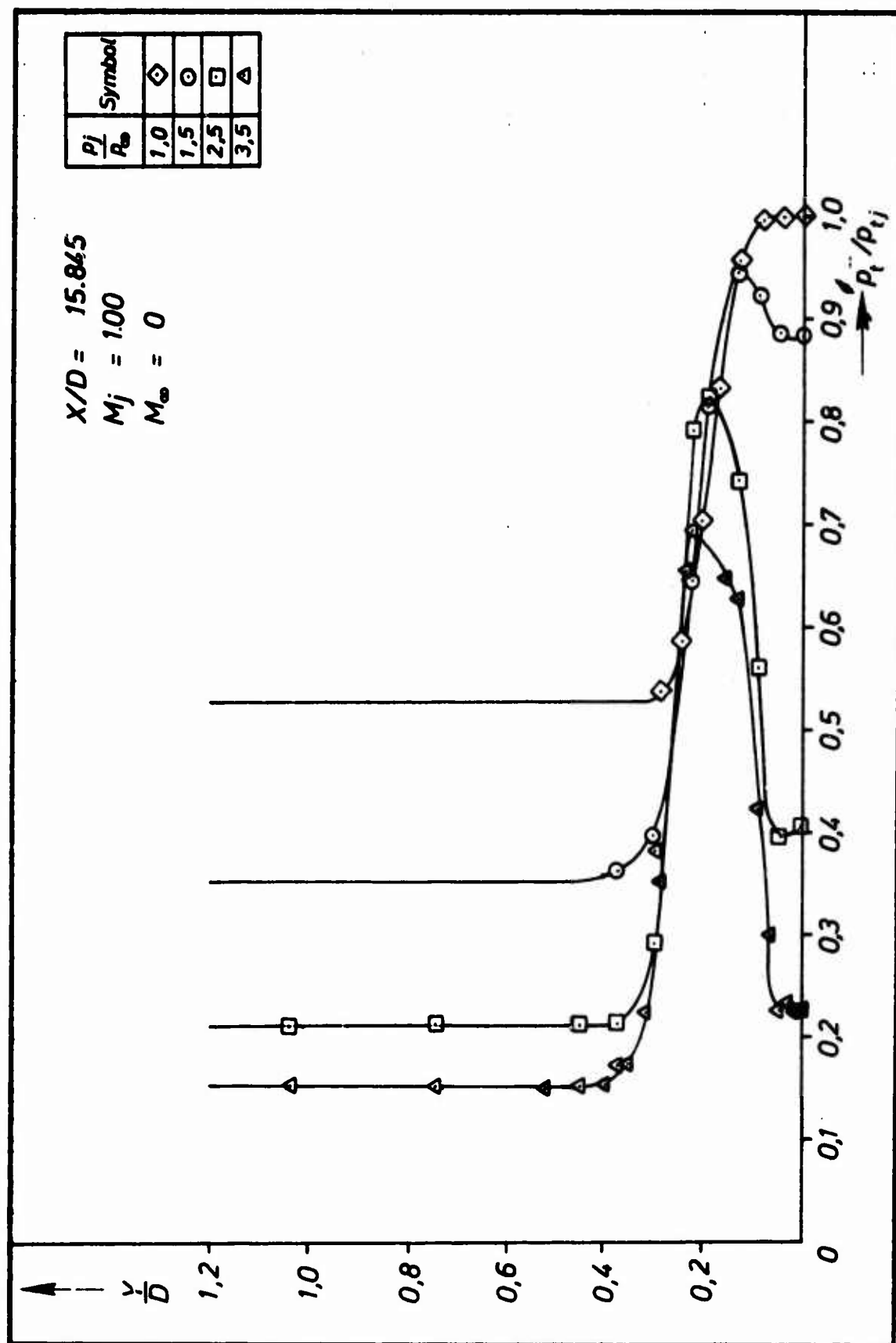


Fig.44 Total pressure distributions in the flow field of the propulsive jet without external flow ( $M_\infty = 0$ ) for Model A1.  $X/D = 15.845$

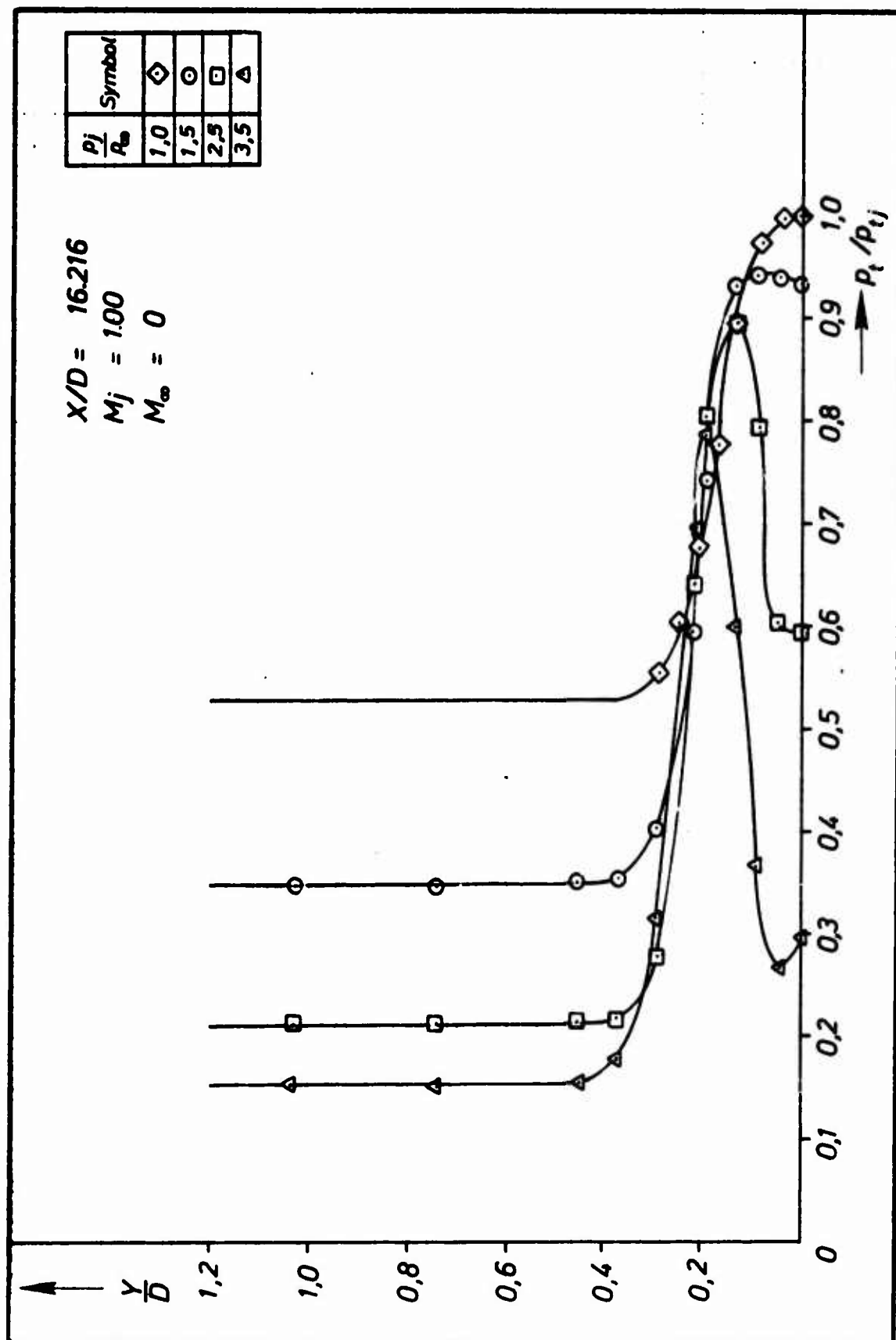


Fig.45 Total pressure distributions in the flow field of the propulsive jet without external flow ( $M_\infty = 0$ ) for Model A.1.  $X/D = 16.216$

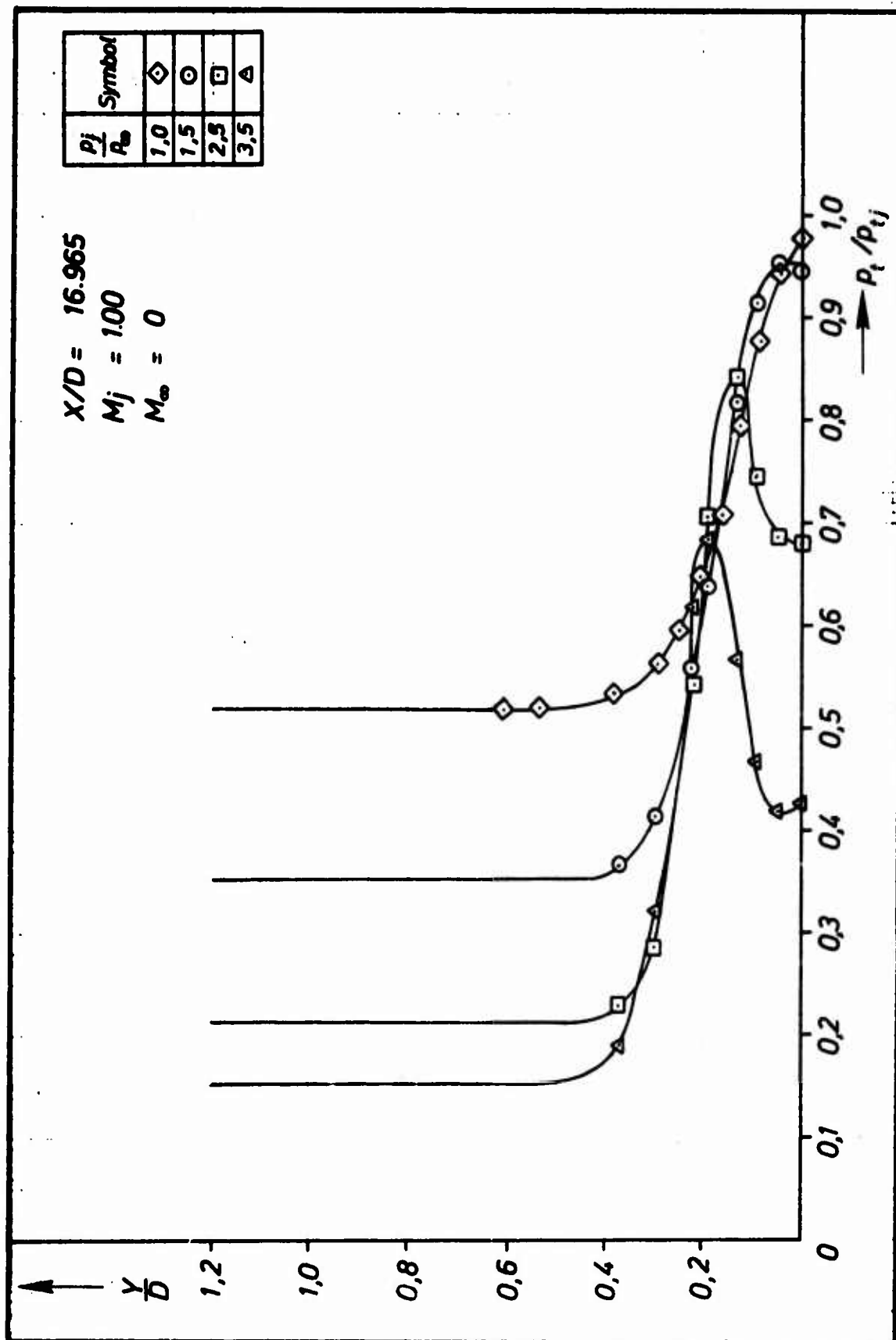


Fig.46 Total pressure distributions in the flow field of the propulsive jet without external flow ( $M_\infty = 0$ ) for Model A1.  $X/D = 16.965$

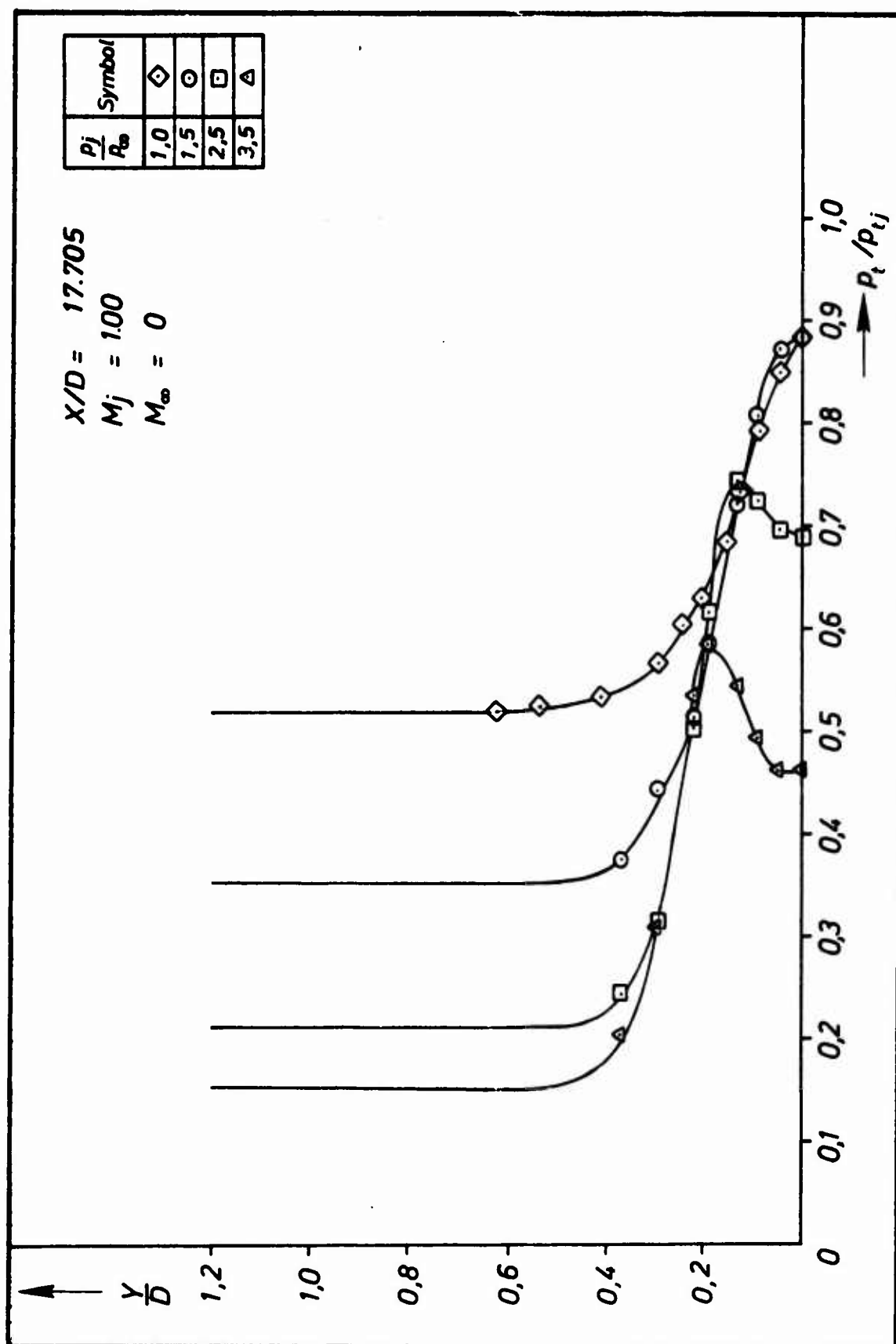


Fig.47 Total pressure distributions in the flow field of the propulsive jet without external flow ( $M_\infty = 0$ ) for Model A1.  $X/D = 17.705$

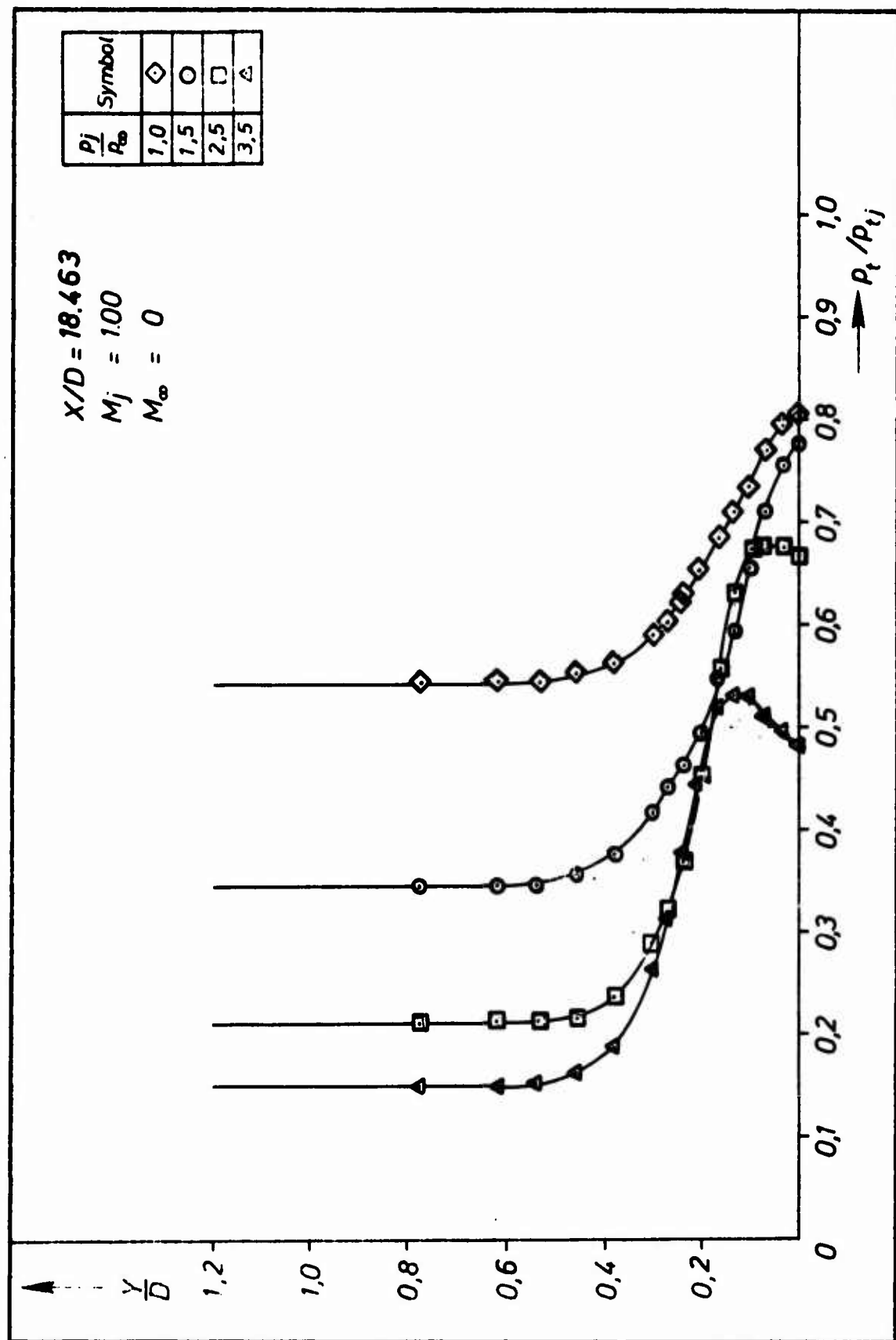


Fig.48 Total pressure distributions in the flow field of the propulsive jet without external flow ( $M_\infty = 0$ ) for Model A1.  $X/D = 18.463$

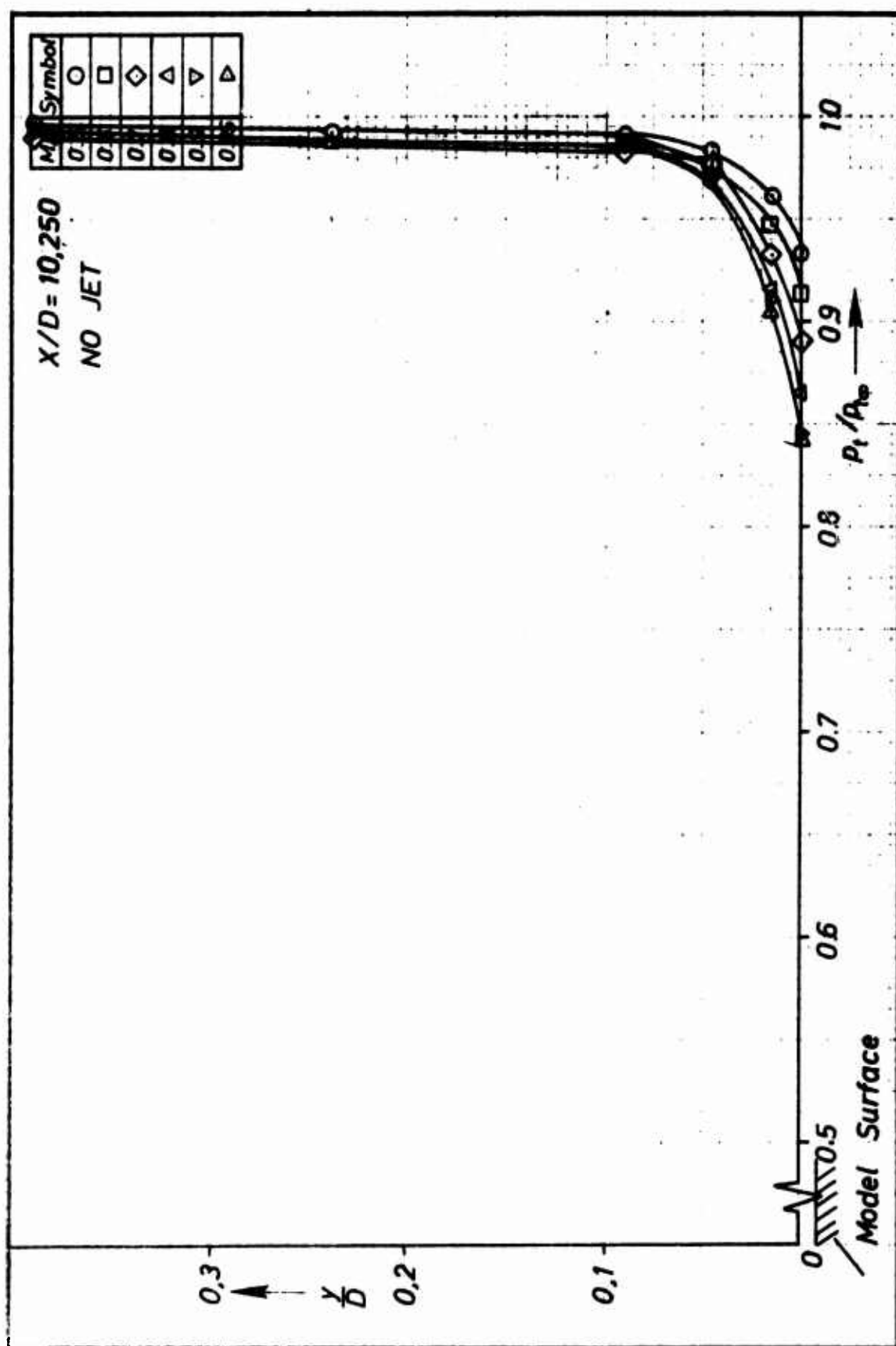


Fig.49 Total pressure distribution across the boundary layer of model A1:  
 $M_j = 0$ ,  $X/D = 10.250$

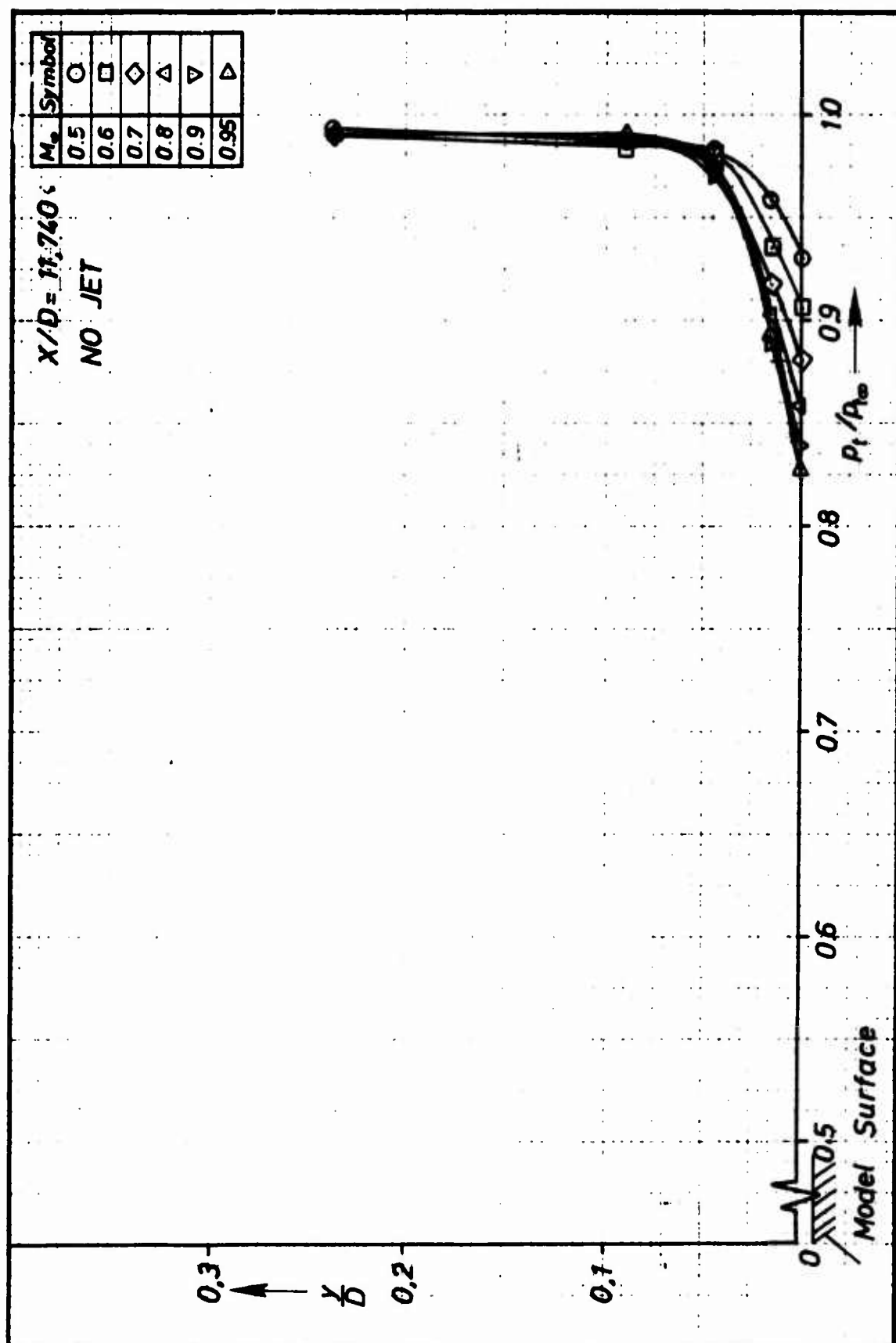


Fig. 50 Total pressure distribution across the boundary layer of Model A1:  
 $M_j = 0$ ,  $X/D = 11.70$



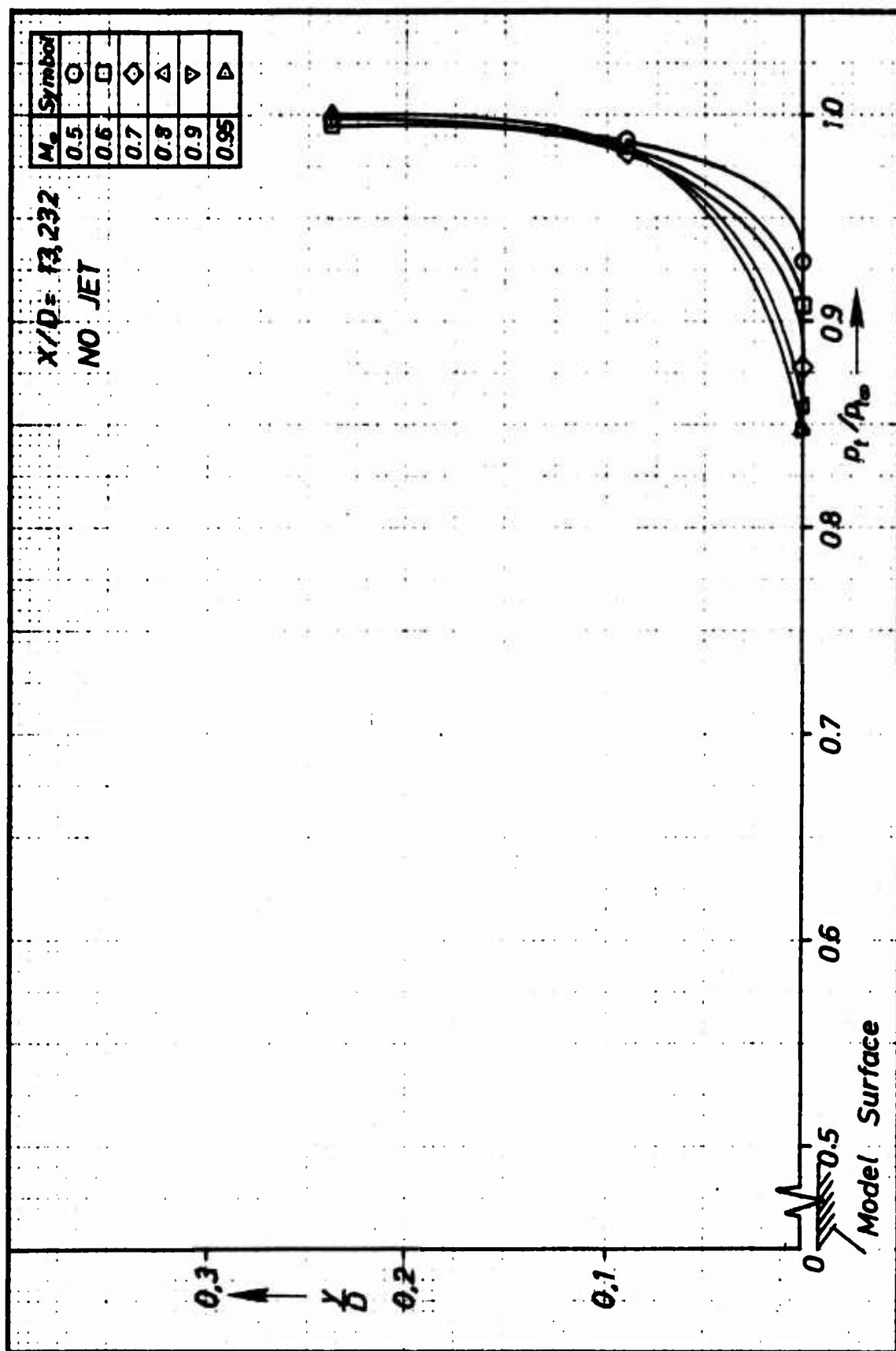


Fig. 51 Total pressure distribution across the boundary layer of Model A1:  
 $M_j = 0$ ,  $X/D = 13.323$

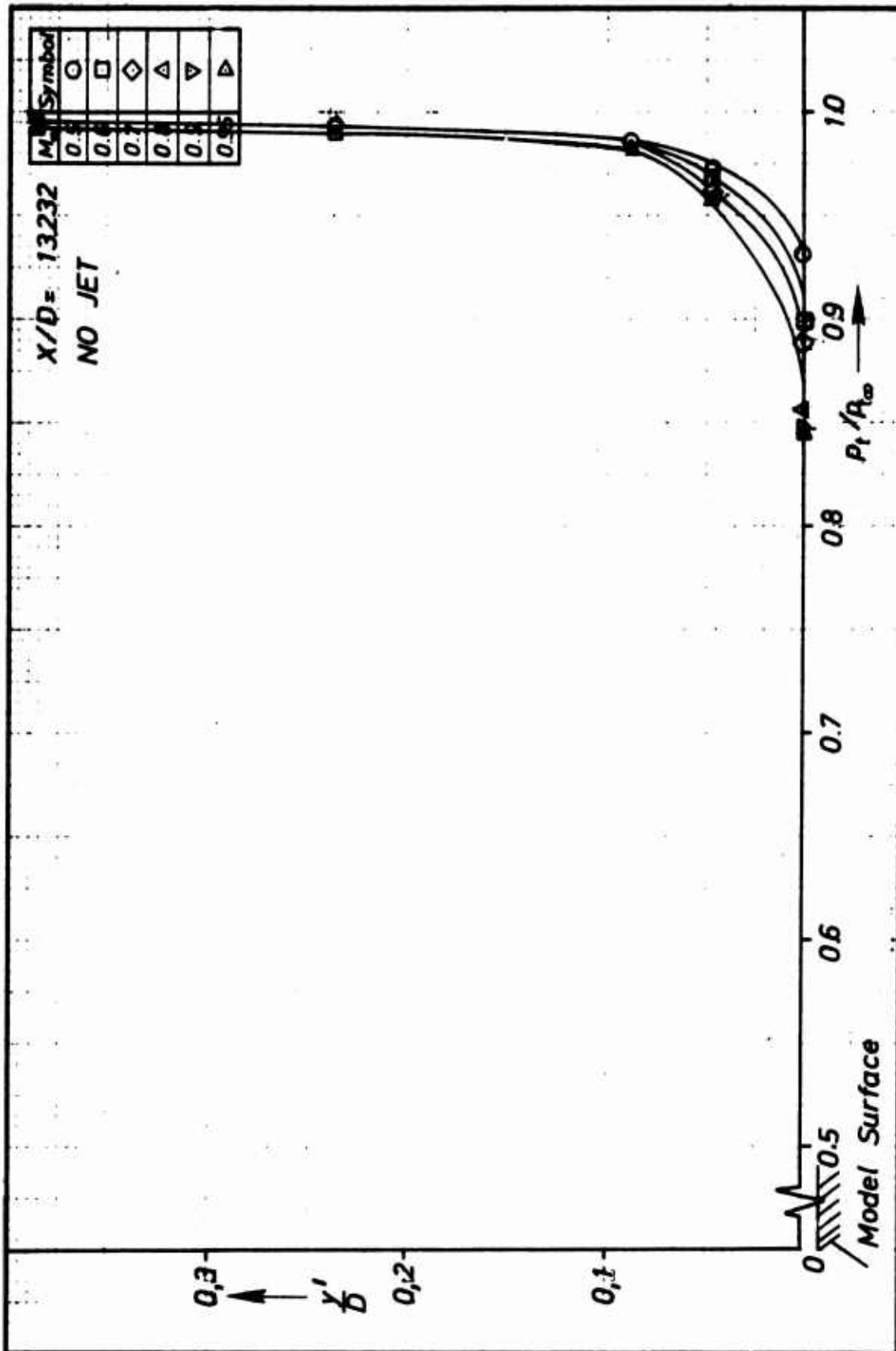


Fig. 52 Total pressure distribution across the boundary layer of Model A1:  
 $M_j = 0$ ,  $X/D = 13.323$

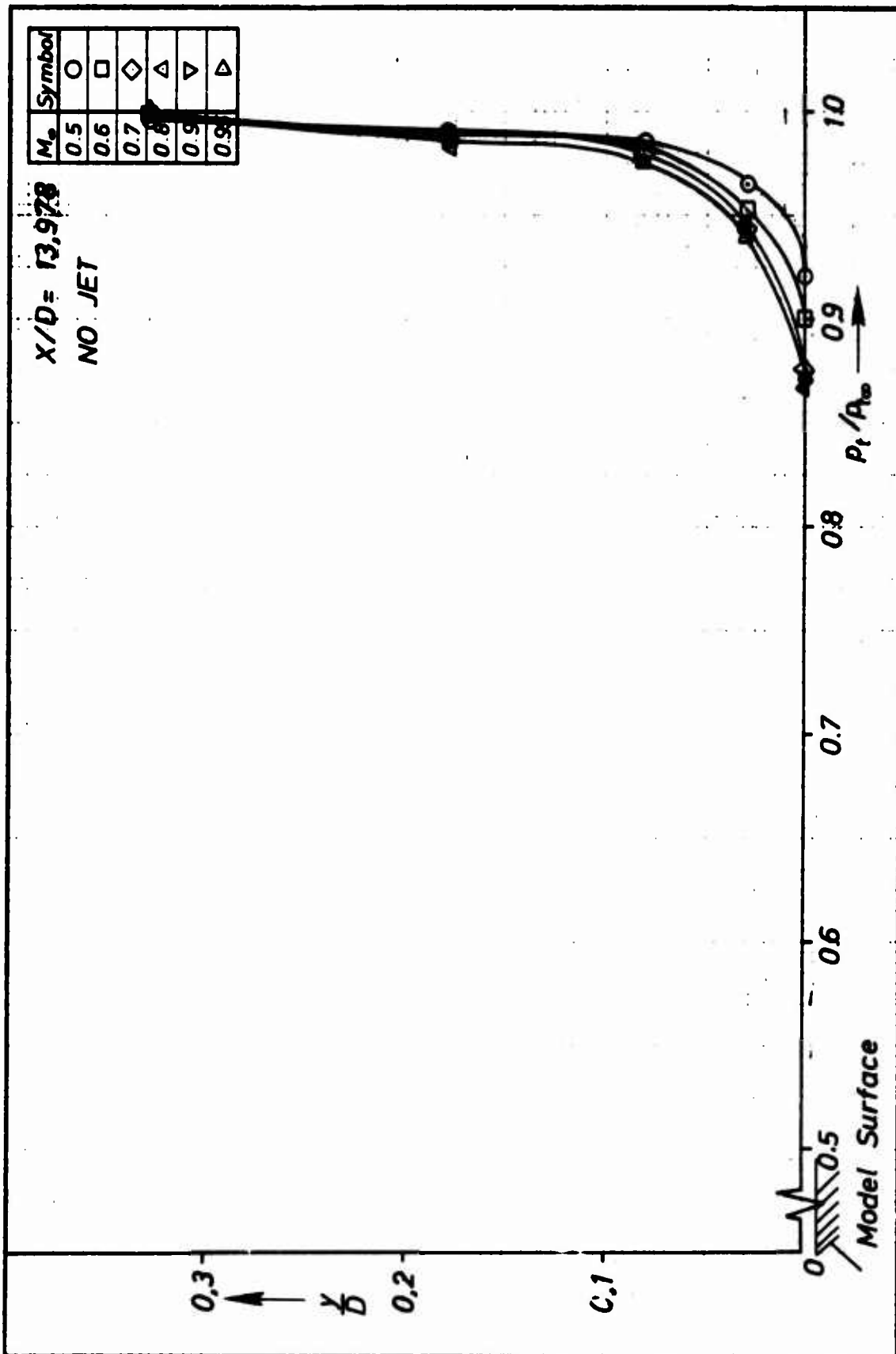


Fig.53 Total pressure distribution across the boundary layer of Model A1:  
 $M_j = 0$ ,  $X/D = 13.978$

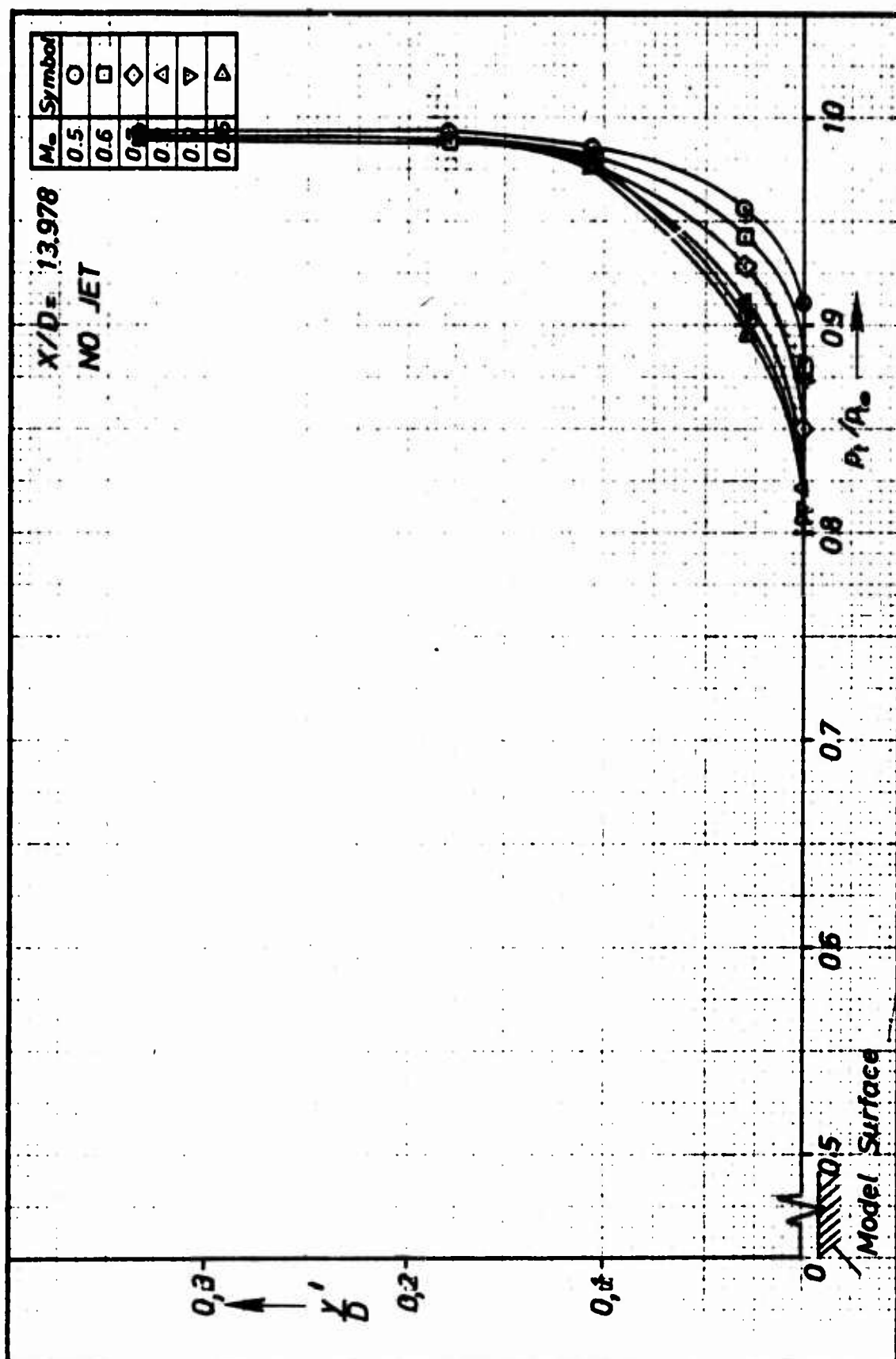


Fig.54 Total pressure distribution across the boundary layer of Model A1:  
 $M_j = 0$ ,  $X/D = 13.978$

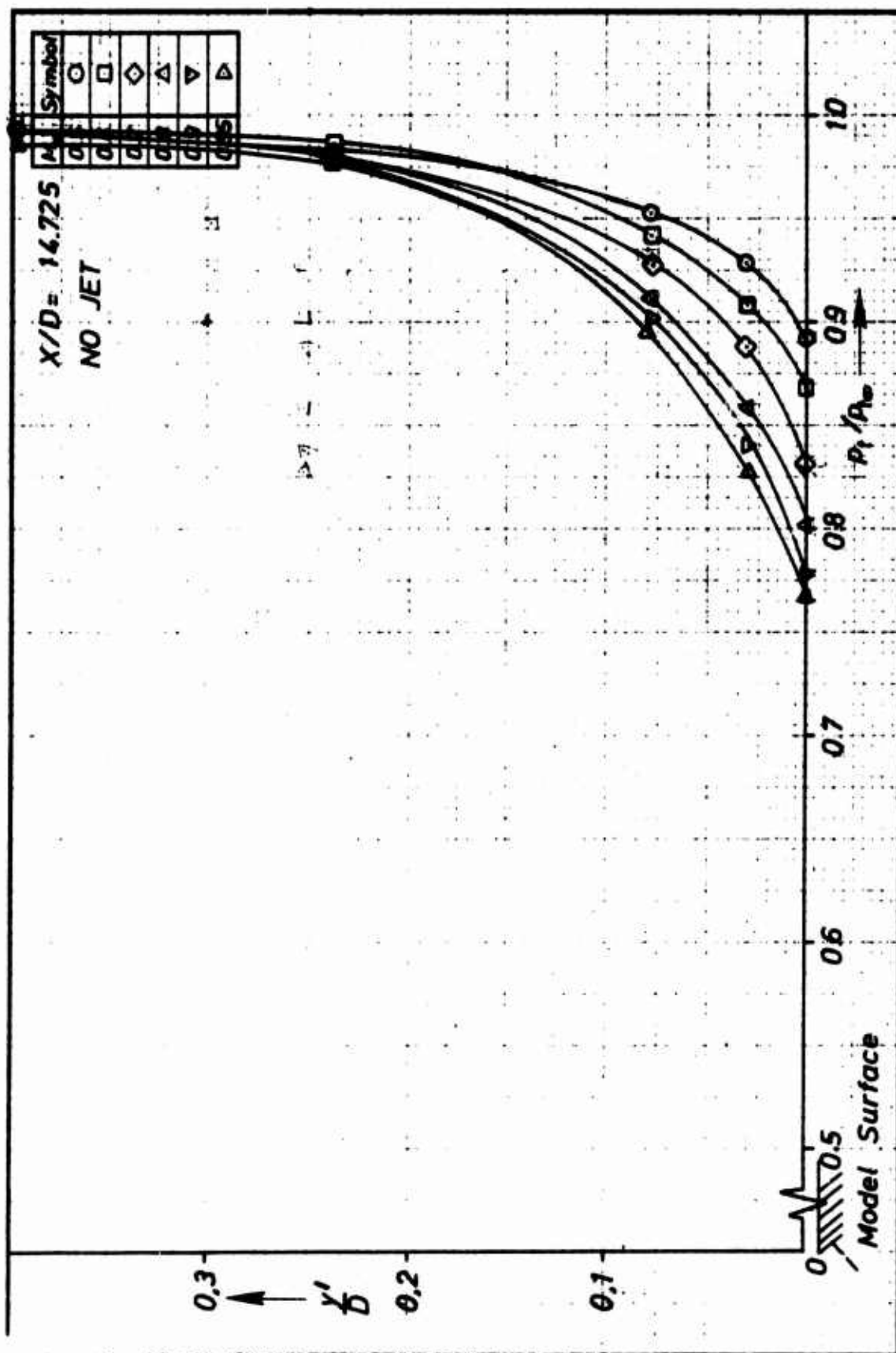


Fig.55 Total pressure distribution across the boundary layer of Model A1:  
 $M_j = 0$ ,  $X/D = 14.725$

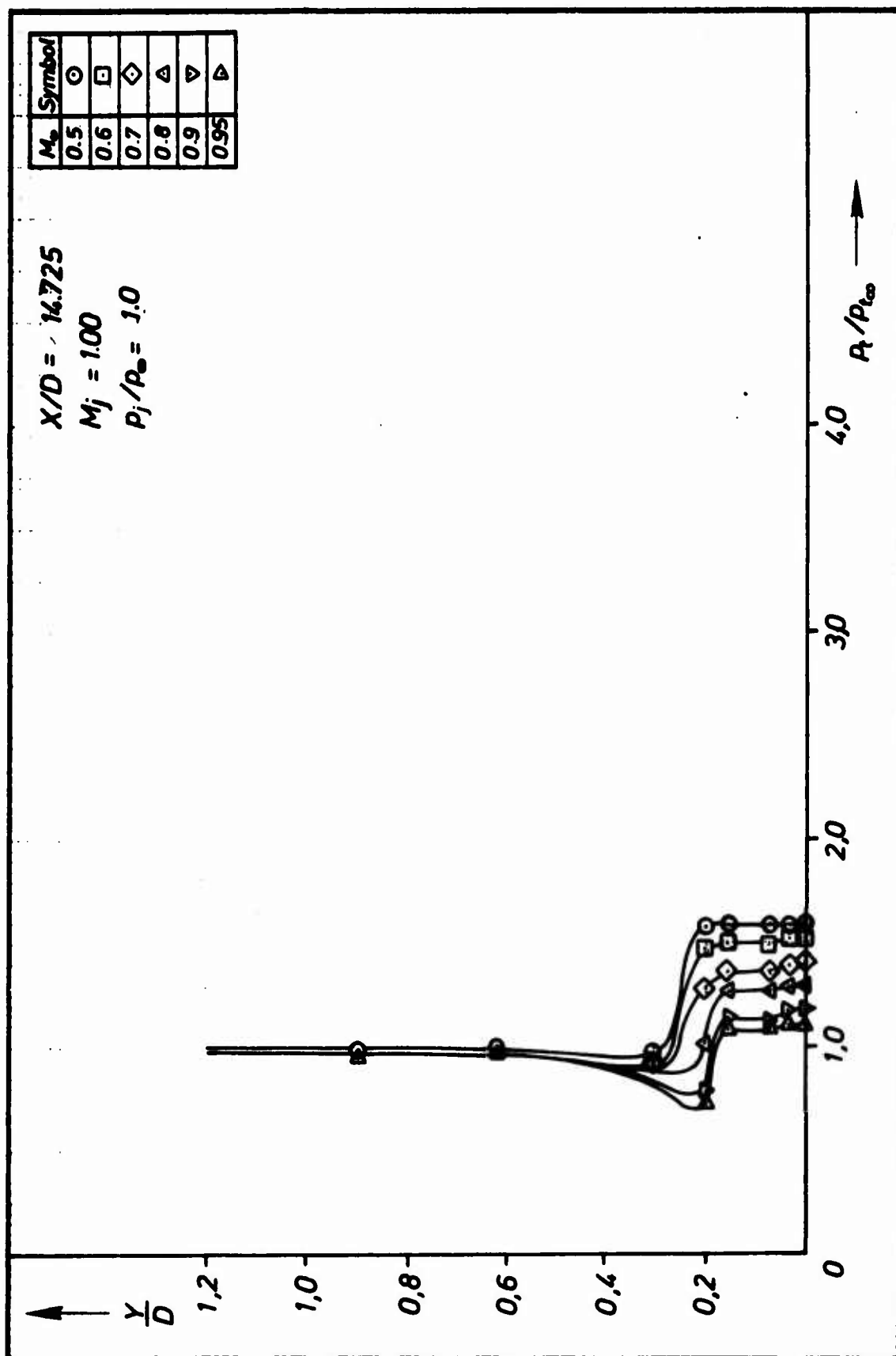


Fig.56 Total pressure distributions in the flow field with propulsive jet for Model A1:  
 $X/D = 14.725$ ;  $M_j = 1.0$ ;  $p_j/p_\infty = 1.0$

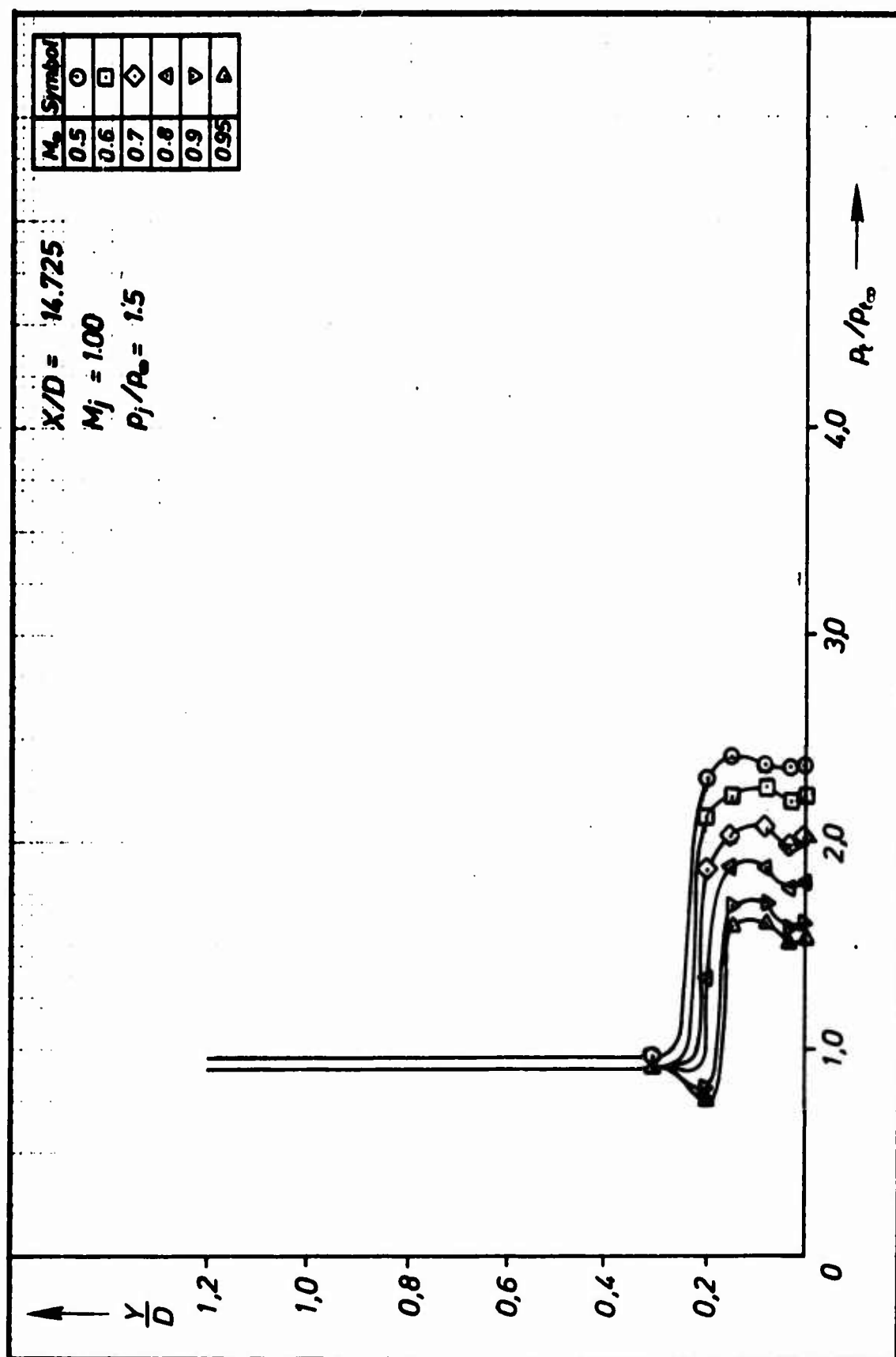


Fig.57 Total pressure distributions in the flow field with propulsive jet for Model A1:  
 $X/D = 14.725$ ;  $M_j = 1.0$ ;  $P_j/P_\infty = 1.5$

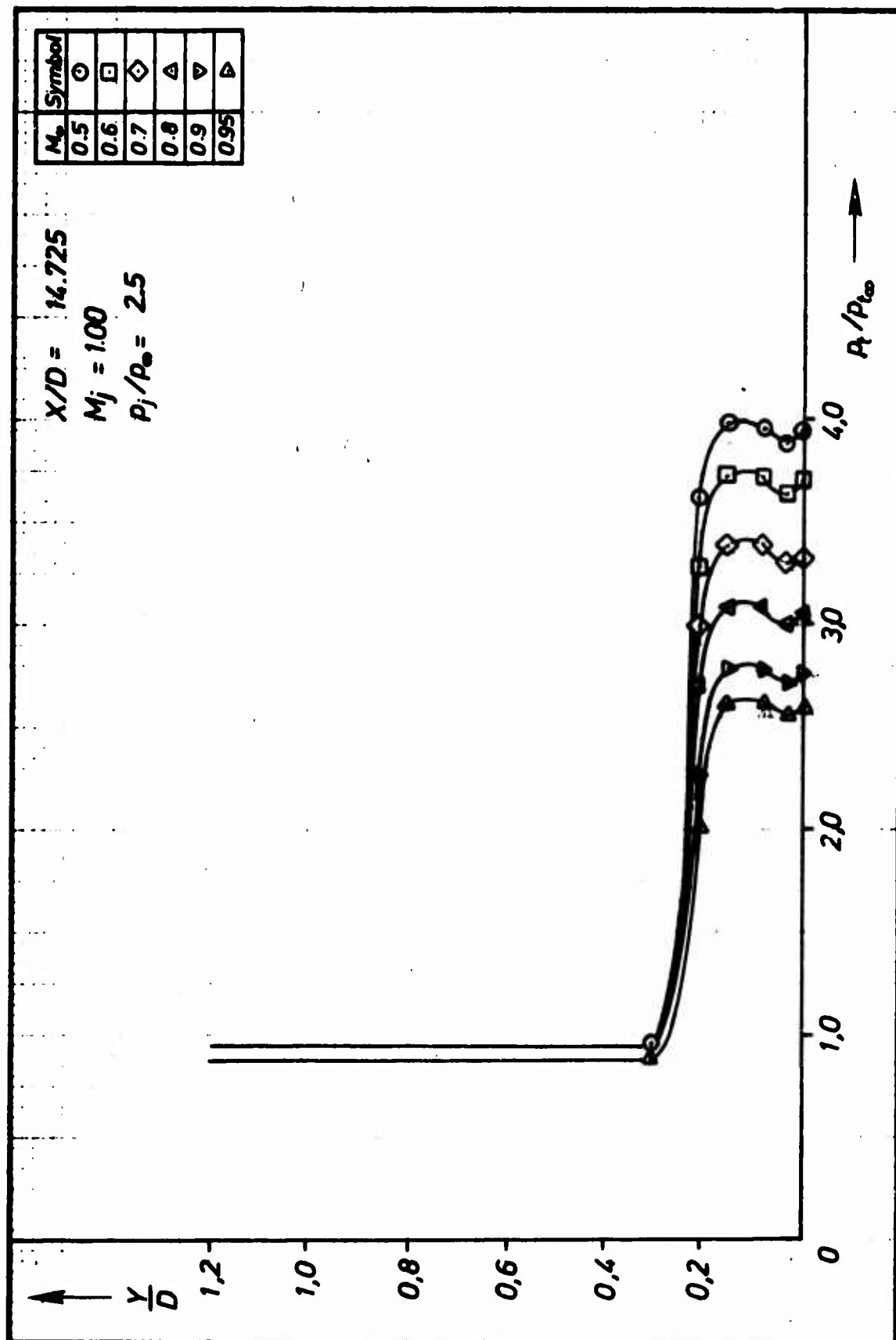


Fig.58 Total pressure distributions in the flow field with propulsive jet for Model A1:  
 $X/D = 14.725$ ;  $M_j = 1.0$ ;  $p_j/p_\infty = 2.5$



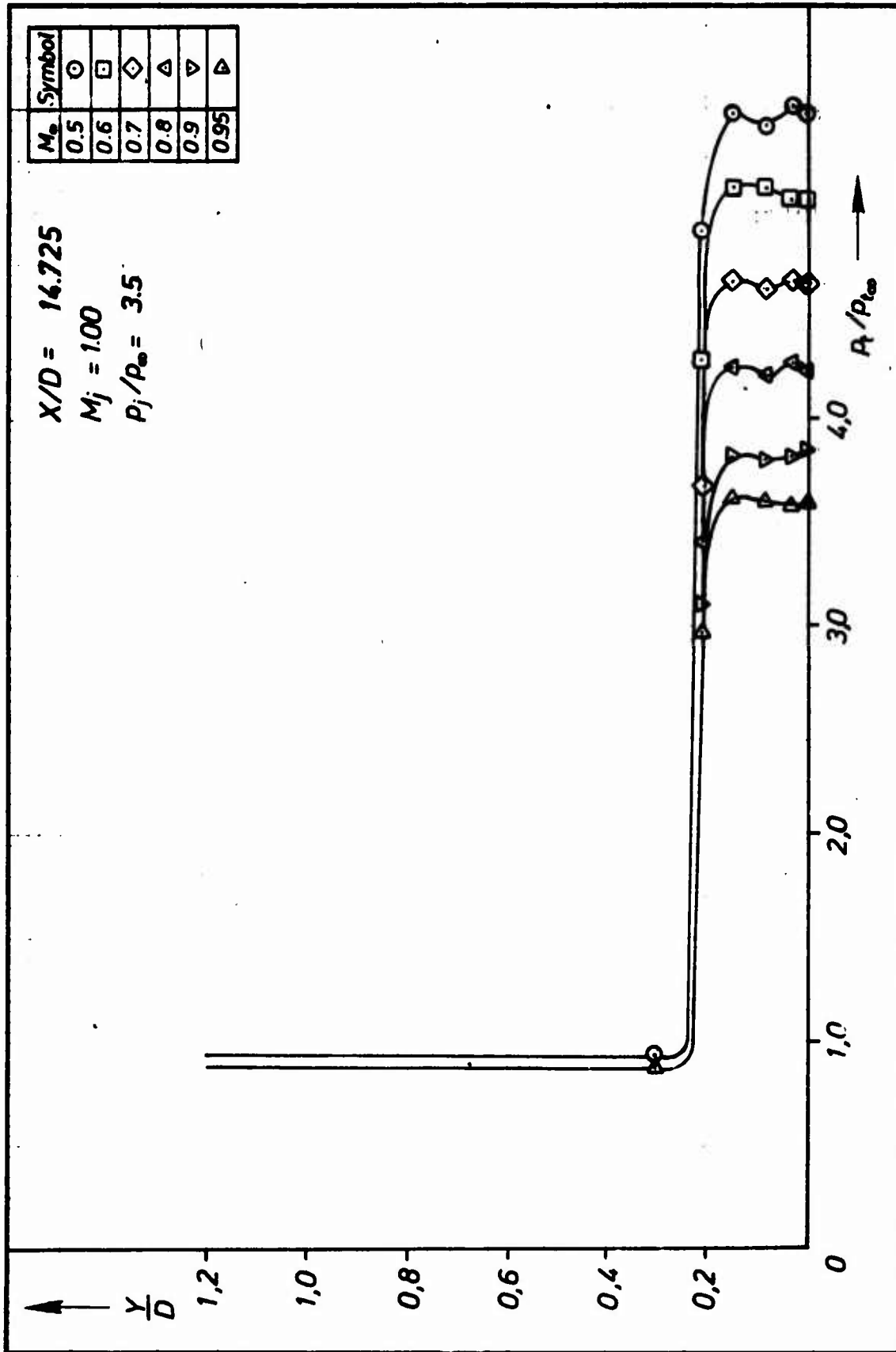


Fig.59 Total pressure distributions in the flow field with propulsive jet for Model A1:  
 $X/D = 14.725$ ;  $M_j = 1.0$ ;  $p_j/p_\infty = 3.5$

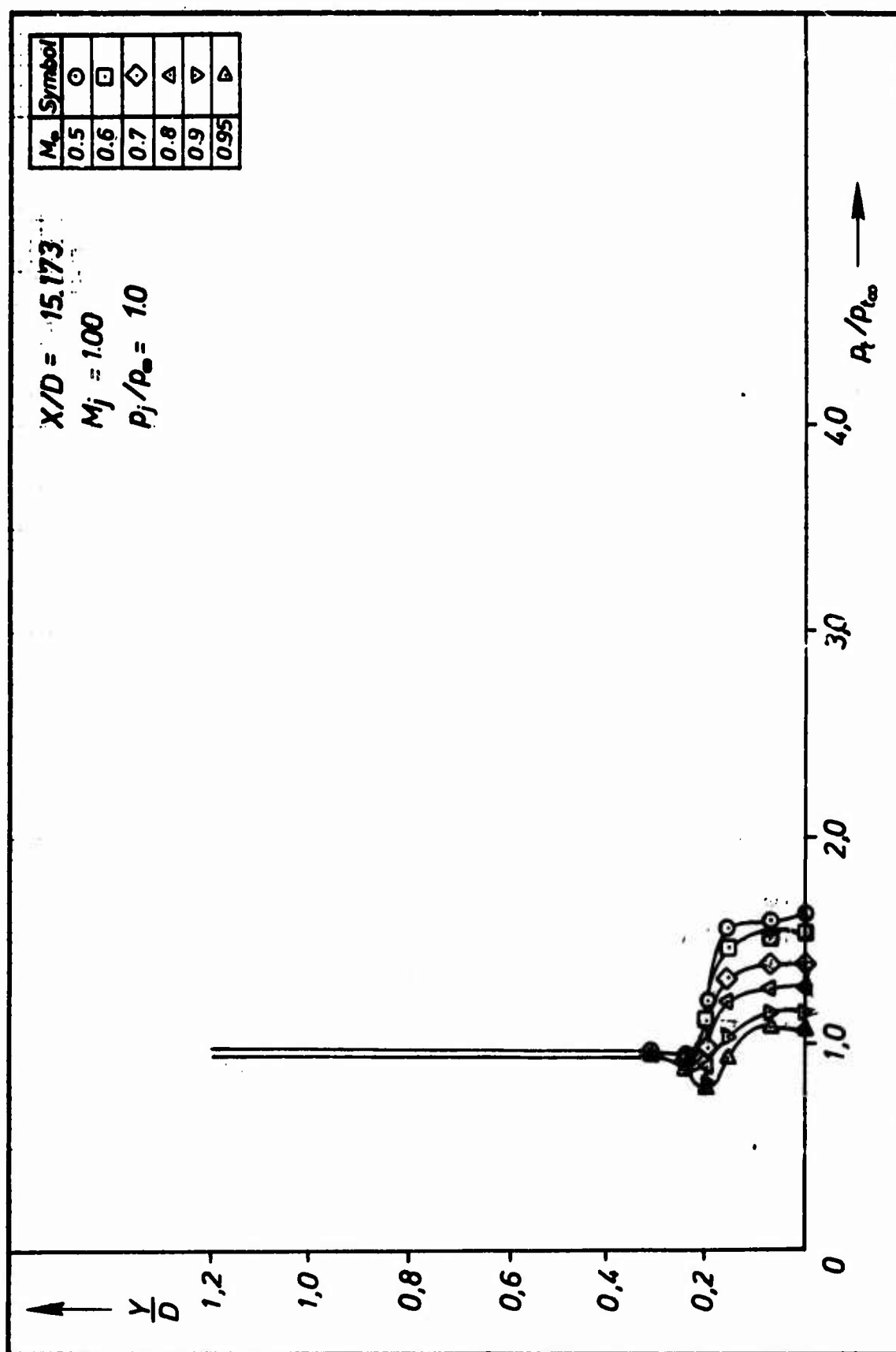


Fig. 60 Total pressure distributions in the flow field with propulsive jet for Model A1:  
 $X/D = 15.173$ ,  $M_j = 1.0$ ;  $p_j/p_\infty = 1.0$

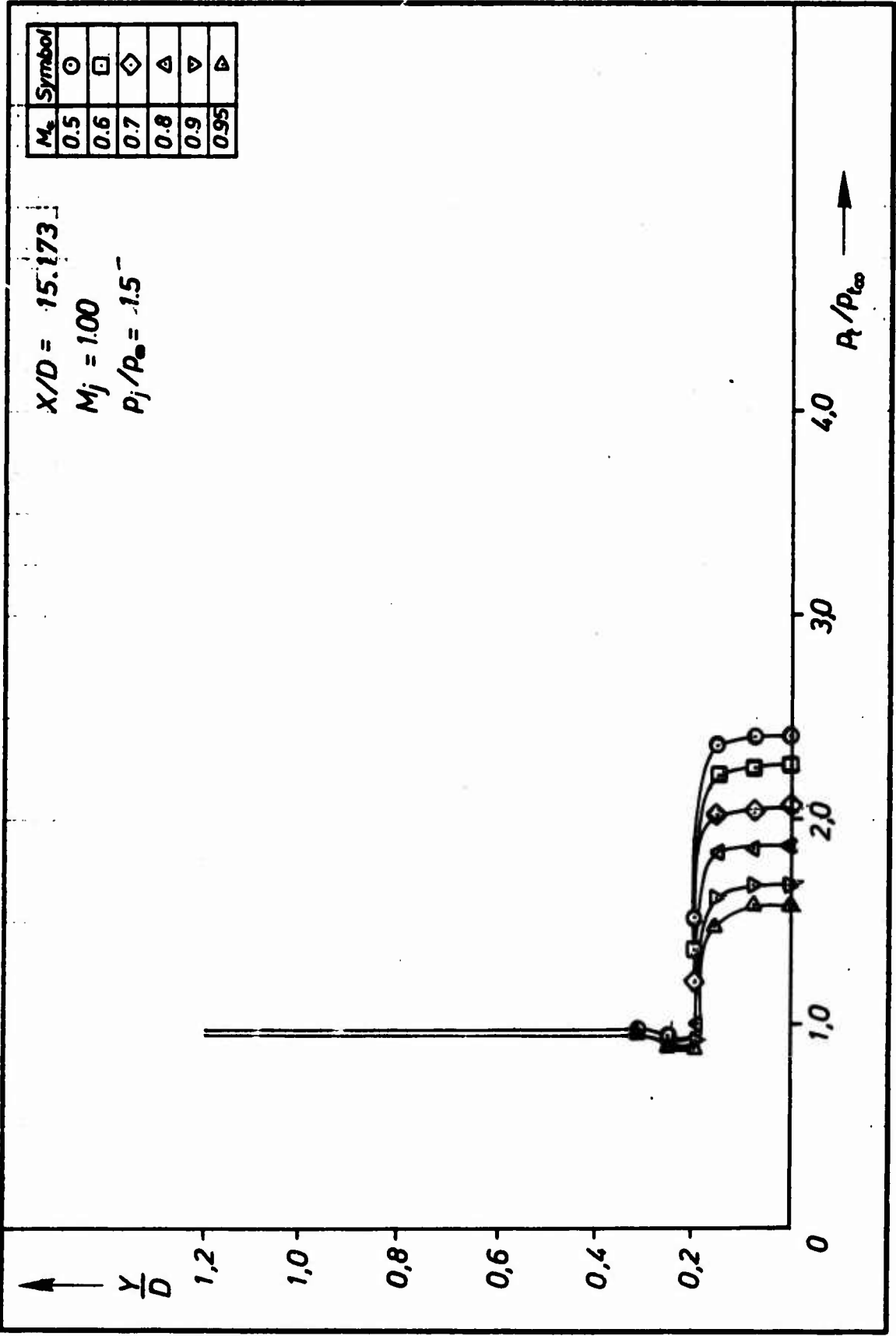


Fig.61 Total pressure distributions in the flow field with propulsive jet for Model A1:  
 $X/D = 15.173$ ,  $M_j = 1.0$ ;  $P_j/P_\infty = 1.5$

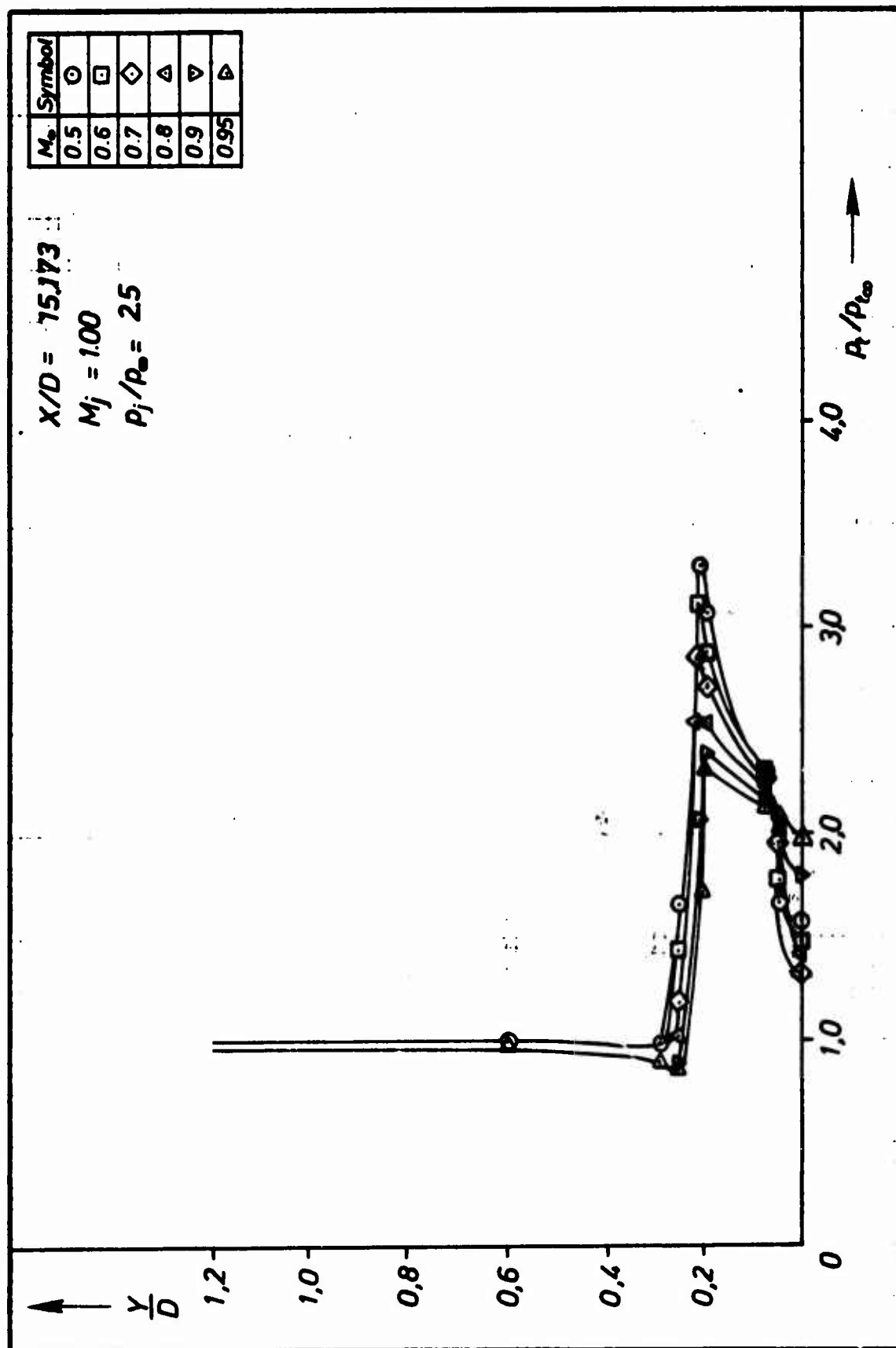


Fig.62 Total pressure distributions in the flow field with propulsive jet for Model A1:  
 $X/D = 15.173$ ,  $M_j = 1.0$ ;  $P_j/P_\infty = 2.5$

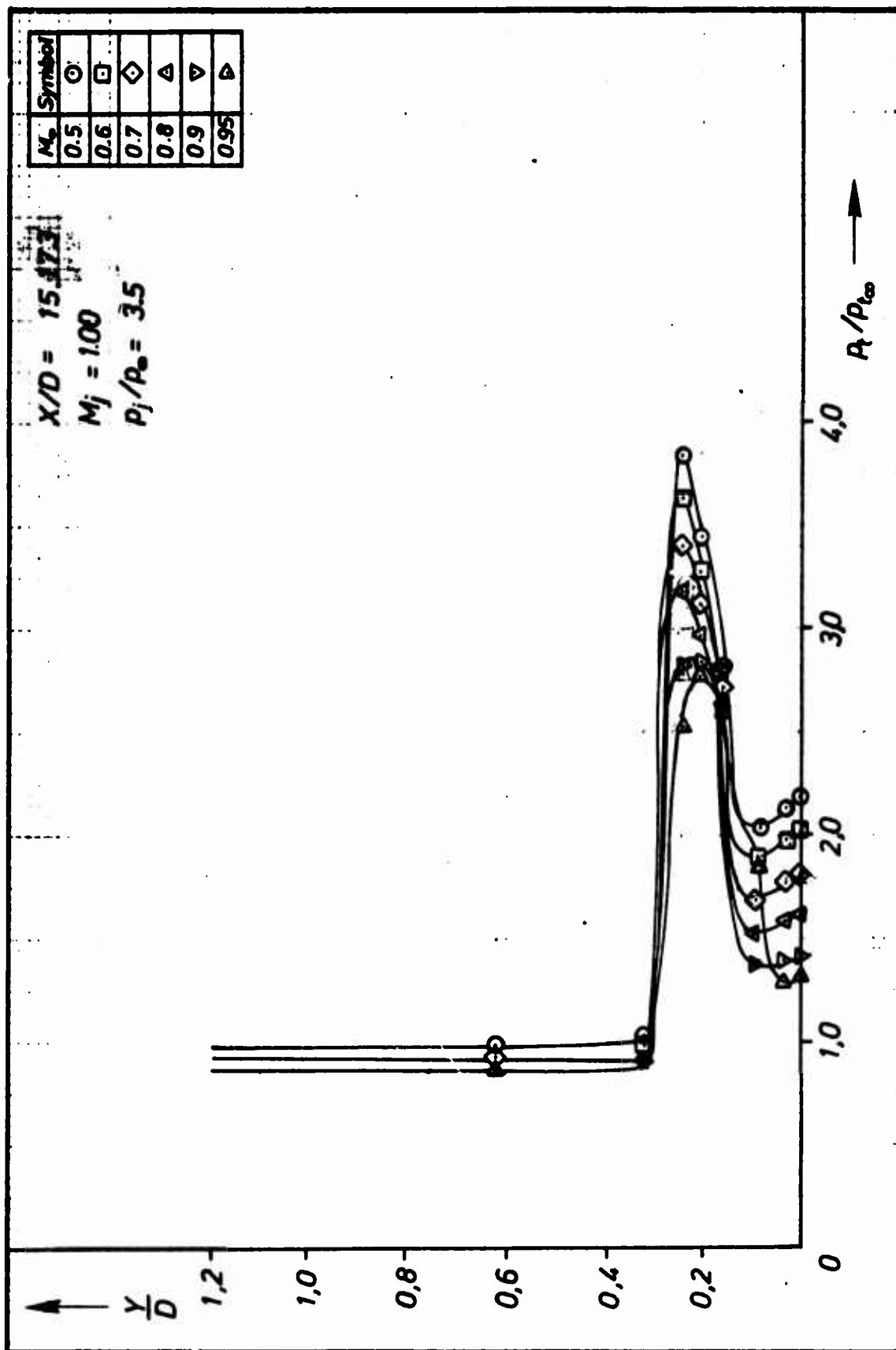


Fig.63 Total pressure distributions in the flow field with propulsive jet for Model A1:  
 $X/D = 15.173$ ,  $M_j = 1.0$ ;  $p_j/p_\infty = 3.5$

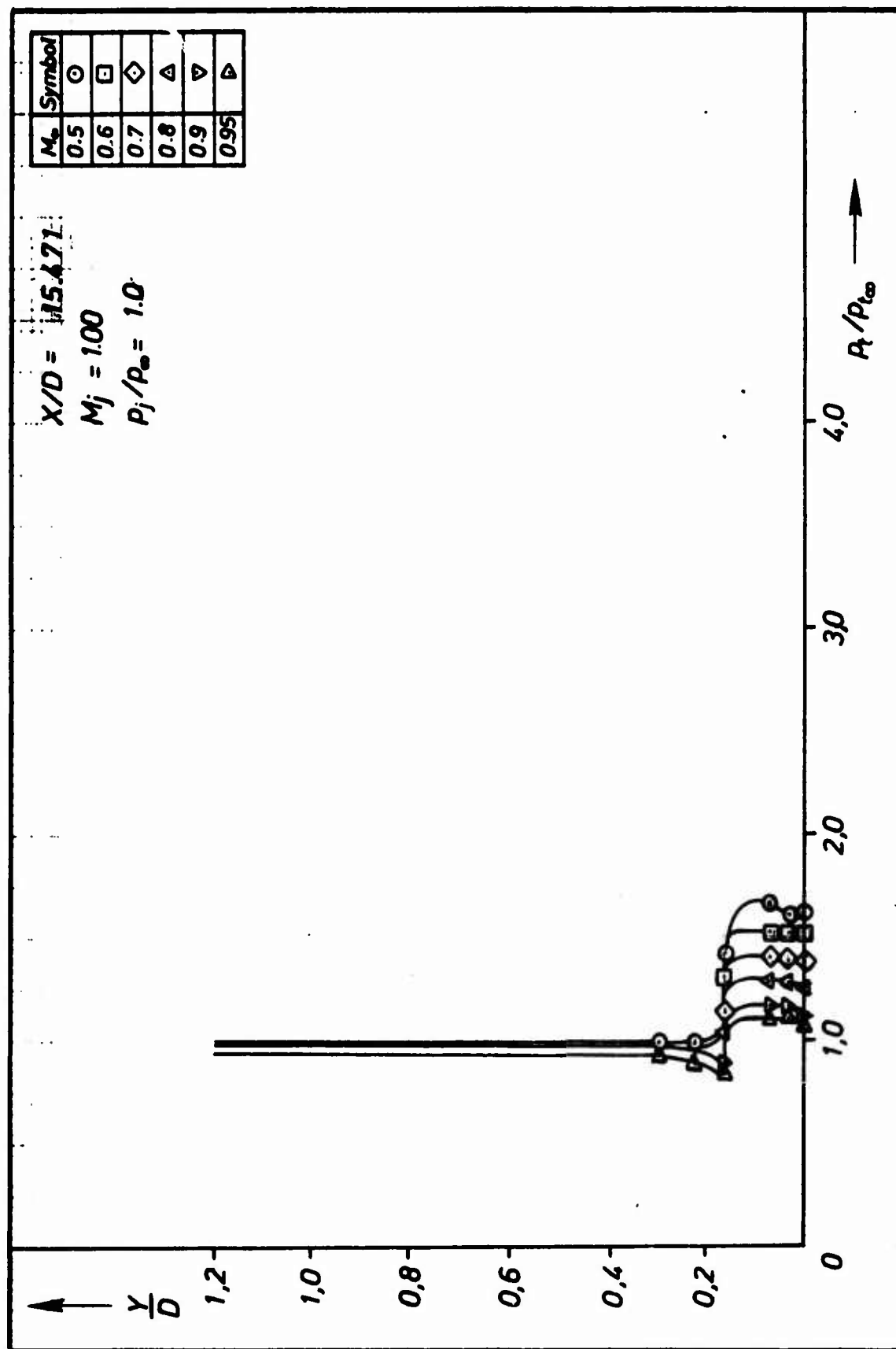


Fig. 64 Total pressure distributions in the flow field with propulsive jet for Model A1:  
 $X/D = 15.471$ ,  $M_j = 1.0$ ;  $p_j/p_\infty = 1.0$

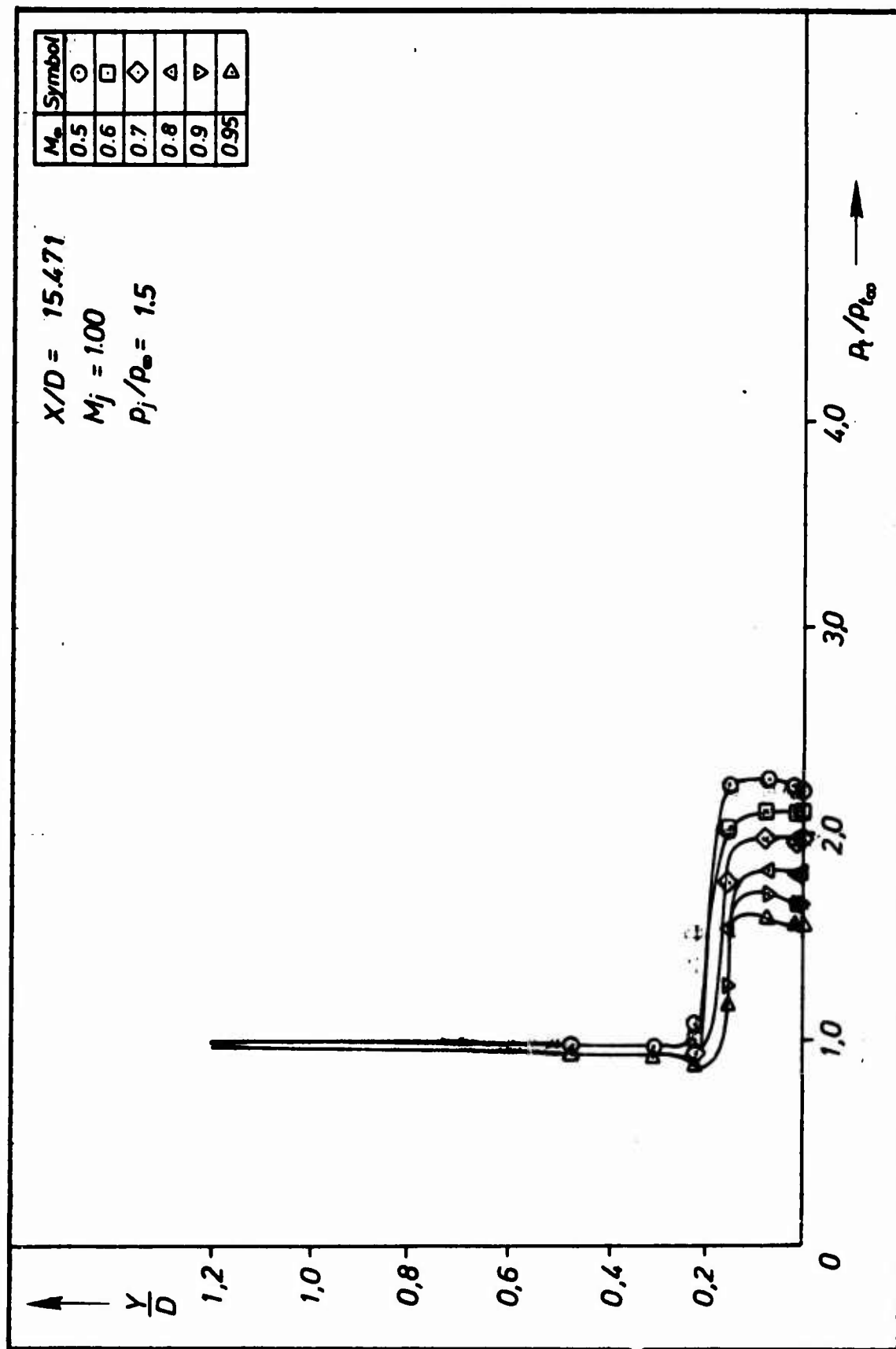


Fig.65 Total pressure distributions in the flow field with propulsive jet for Model A1:  
 $X/D = 15.471$ ,  $M_j = 1.0$ ;  $p_j/p_\infty = 1.5$

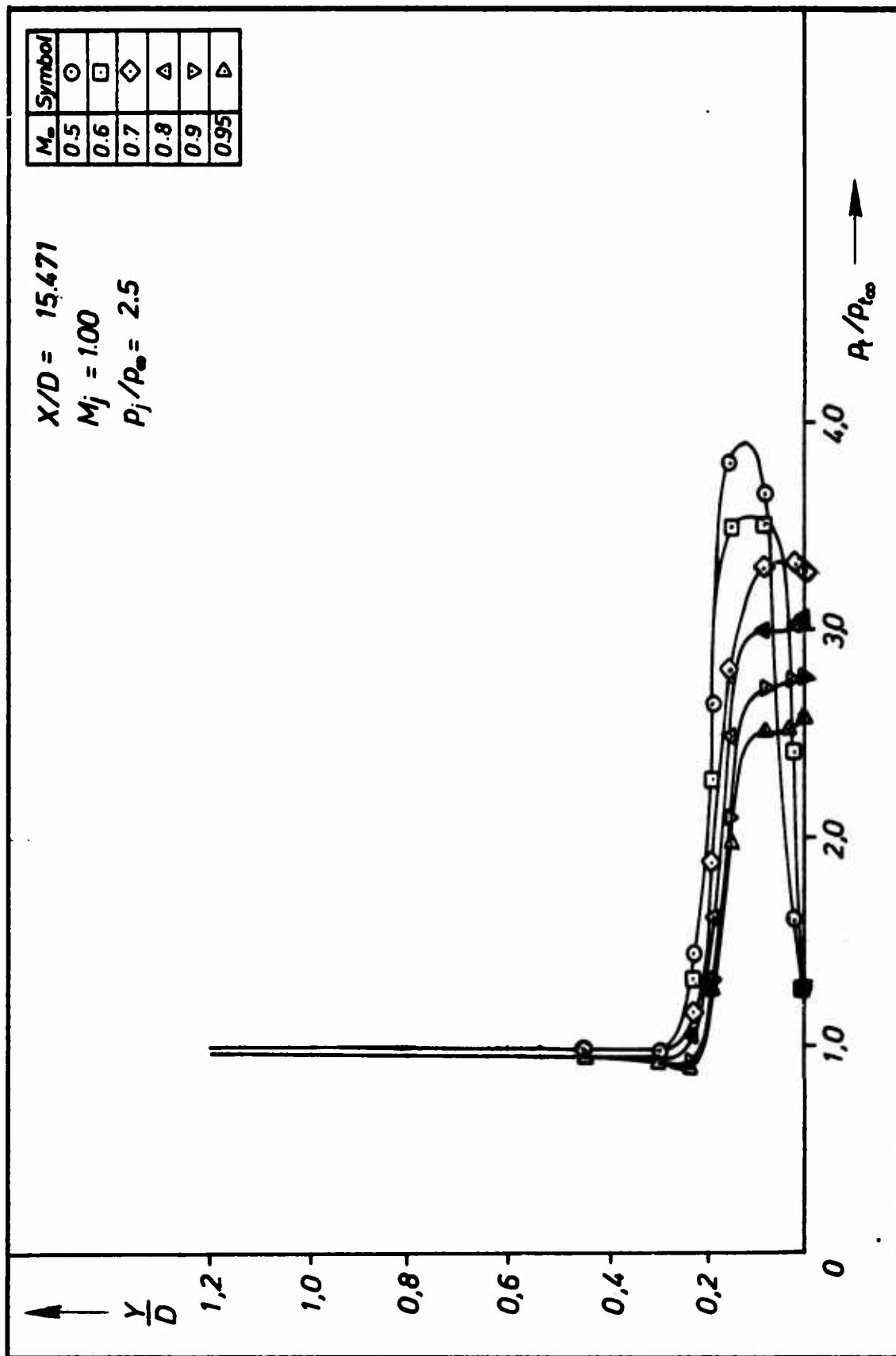


Fig. 66 Total pressure distributions in the flow field with propulsive jet for Model A1:  
 $X/D = 15.471$ ,  $M_j = 1.0$ ;  $p_j/p_\infty = 2.5$



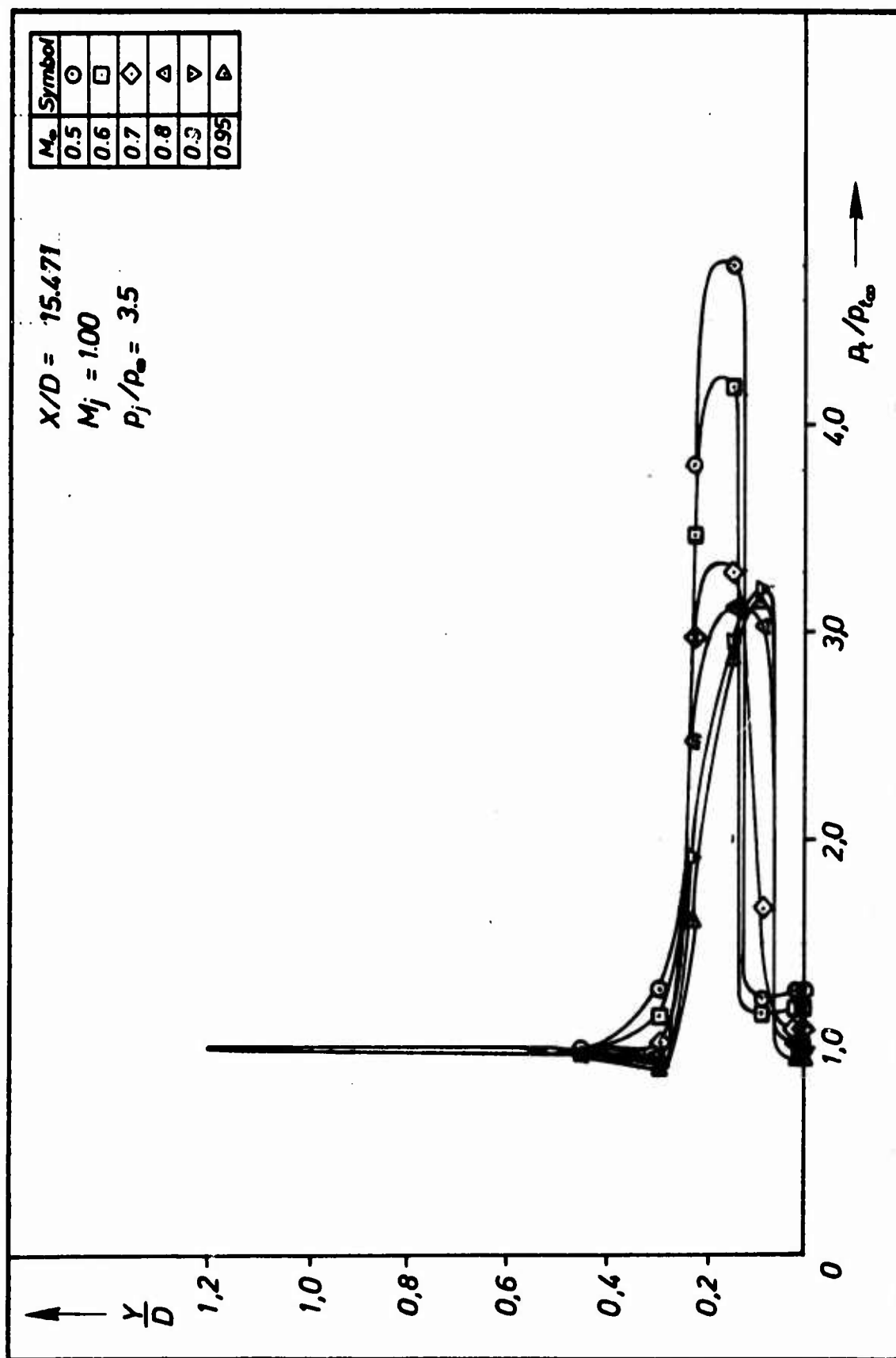


Fig. 67 Total pressure distributions in the flow field with propulsive jet for Model A1:  
 $X/D = 15.471$ ,  $M_j = 1.0$ ;  $p_j/p_\infty = 3.5$

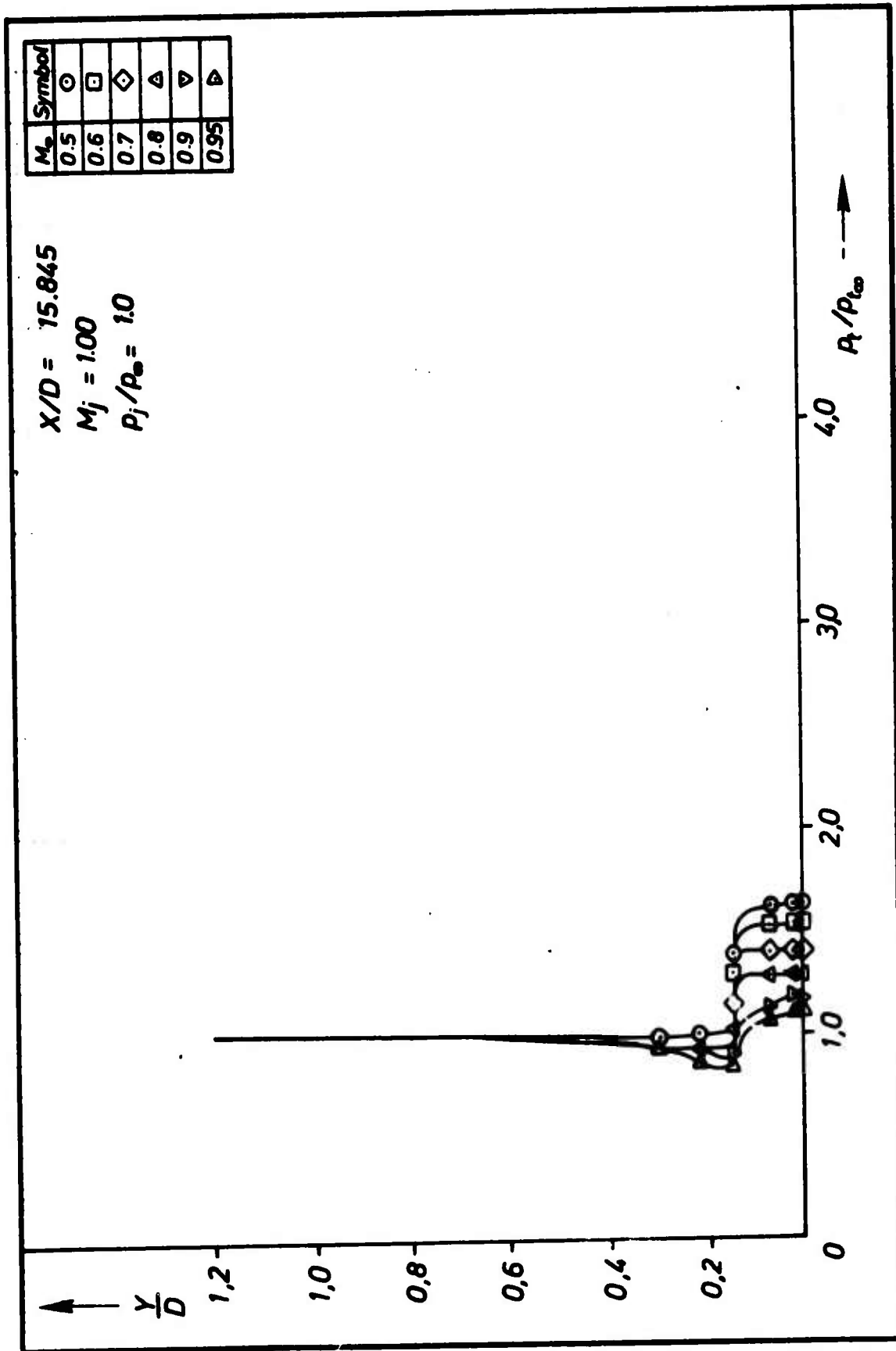


Fig.68 Total pressure distributions in the flow field with propulsive jet for Model A1:  
 $X/D = 15.845$ ,  $M_j = 1.0$ ;  $p_j/p_\infty = 1.0$

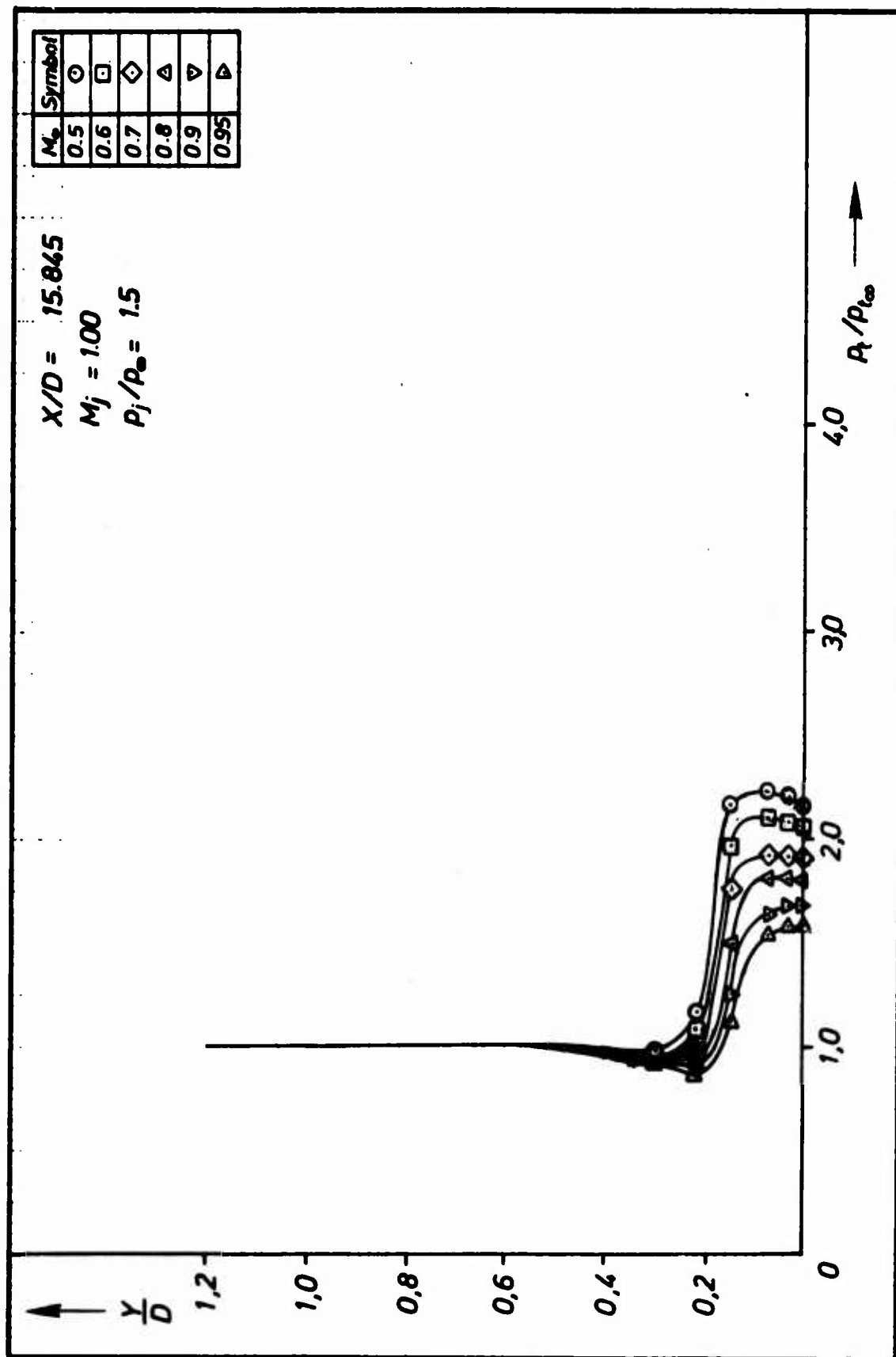


Fig. 69 Total pressure distributions in the flow field with propulsive jet for Model A1:  
 $X/D = 15.845$ ,  $M_j = 1.0$ ;  $p_j/p_\infty = 1.5$

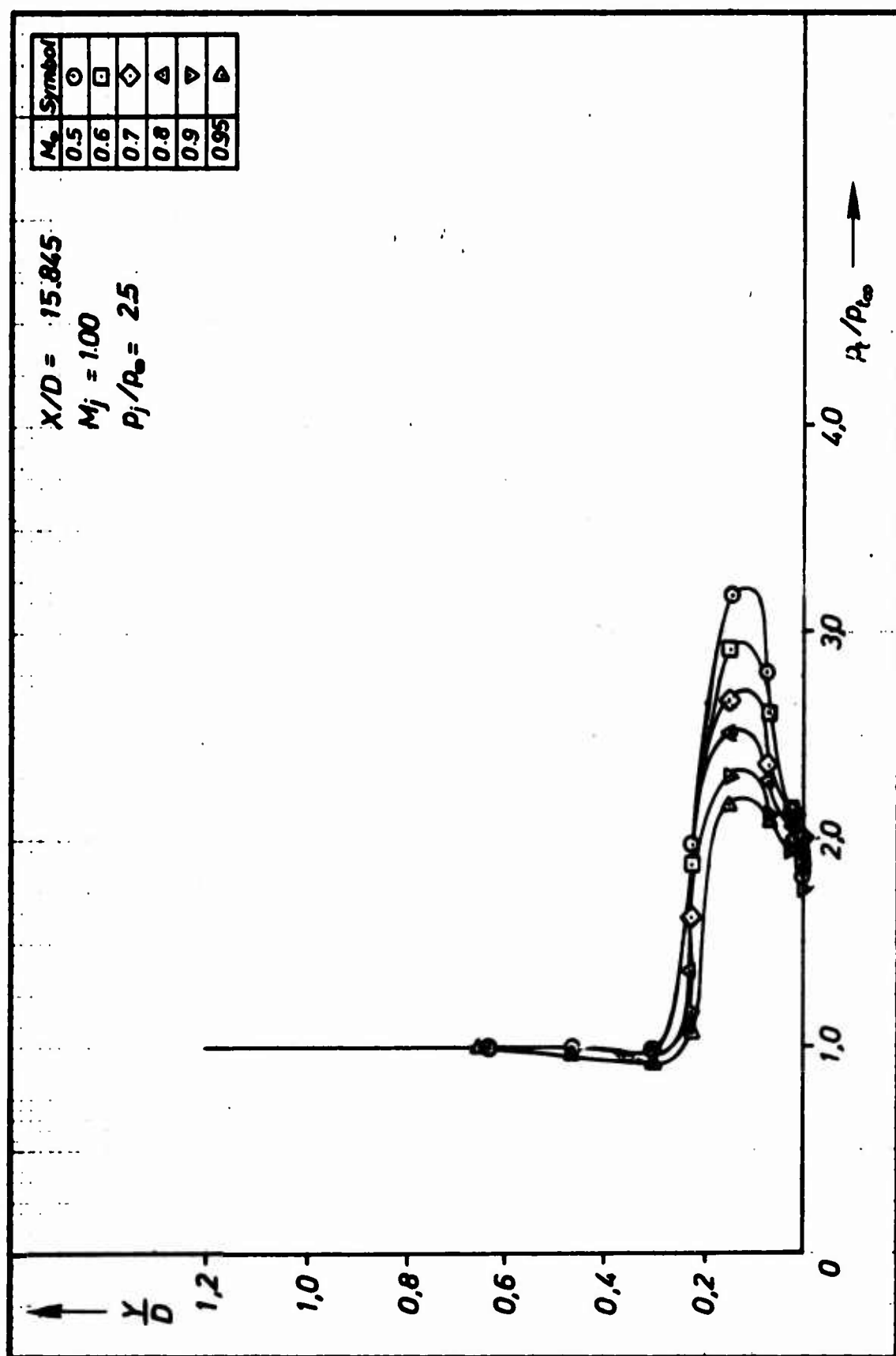


Fig.70 Total pressure distributions in the flow field with propulsive jet for Model A1:  
 $X/D = 15.845$ ,  $M_j = 1.0$ ;  $p_j/p_\infty = 2.5$

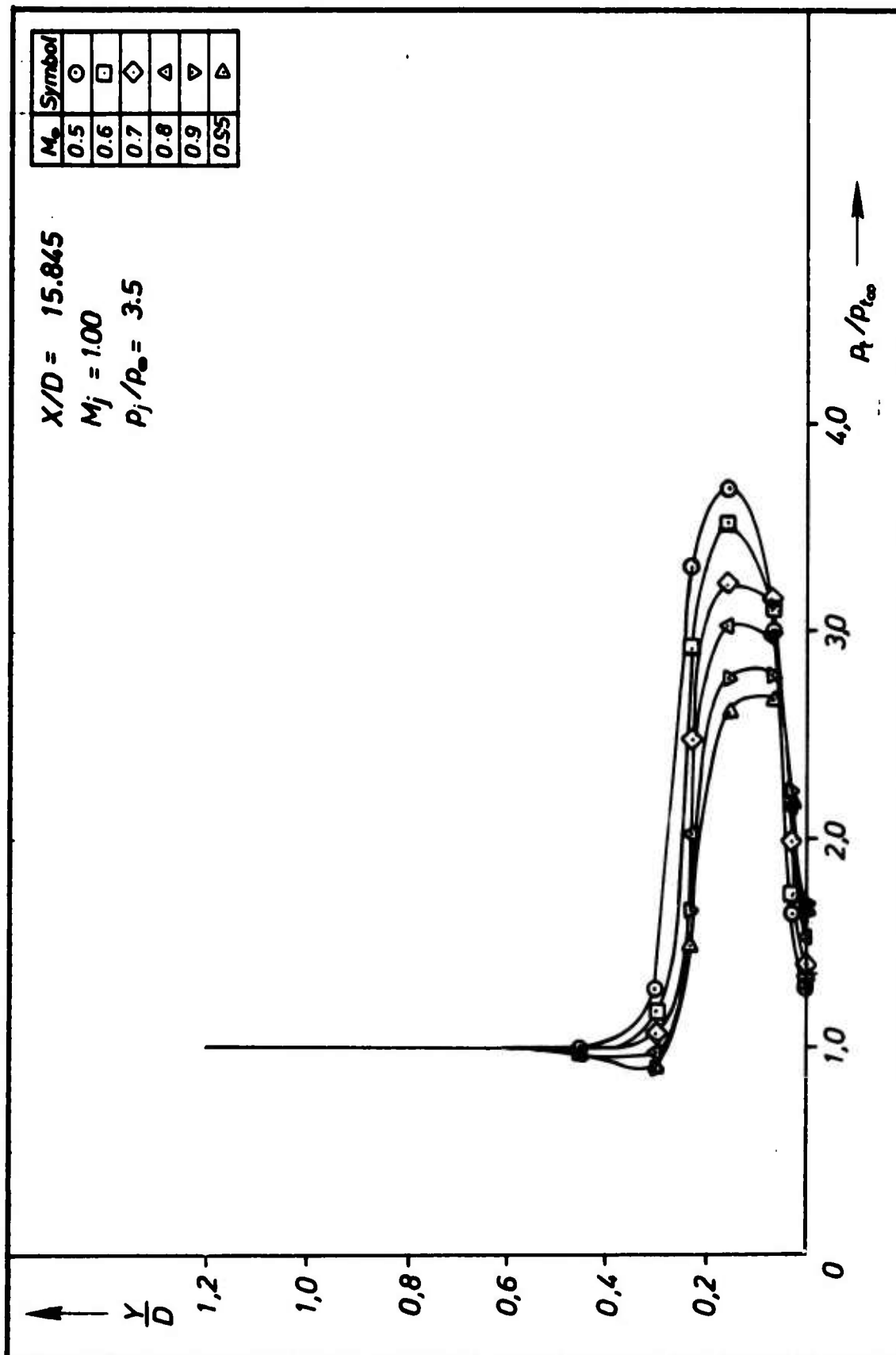


Fig.71 Total pressure distributions in the flow field with propulsive jet for Model A1:  
 $X/D = 15.845$ ,  $M_j = 1.0$ ;  $p_j/p_\infty = 3.5$

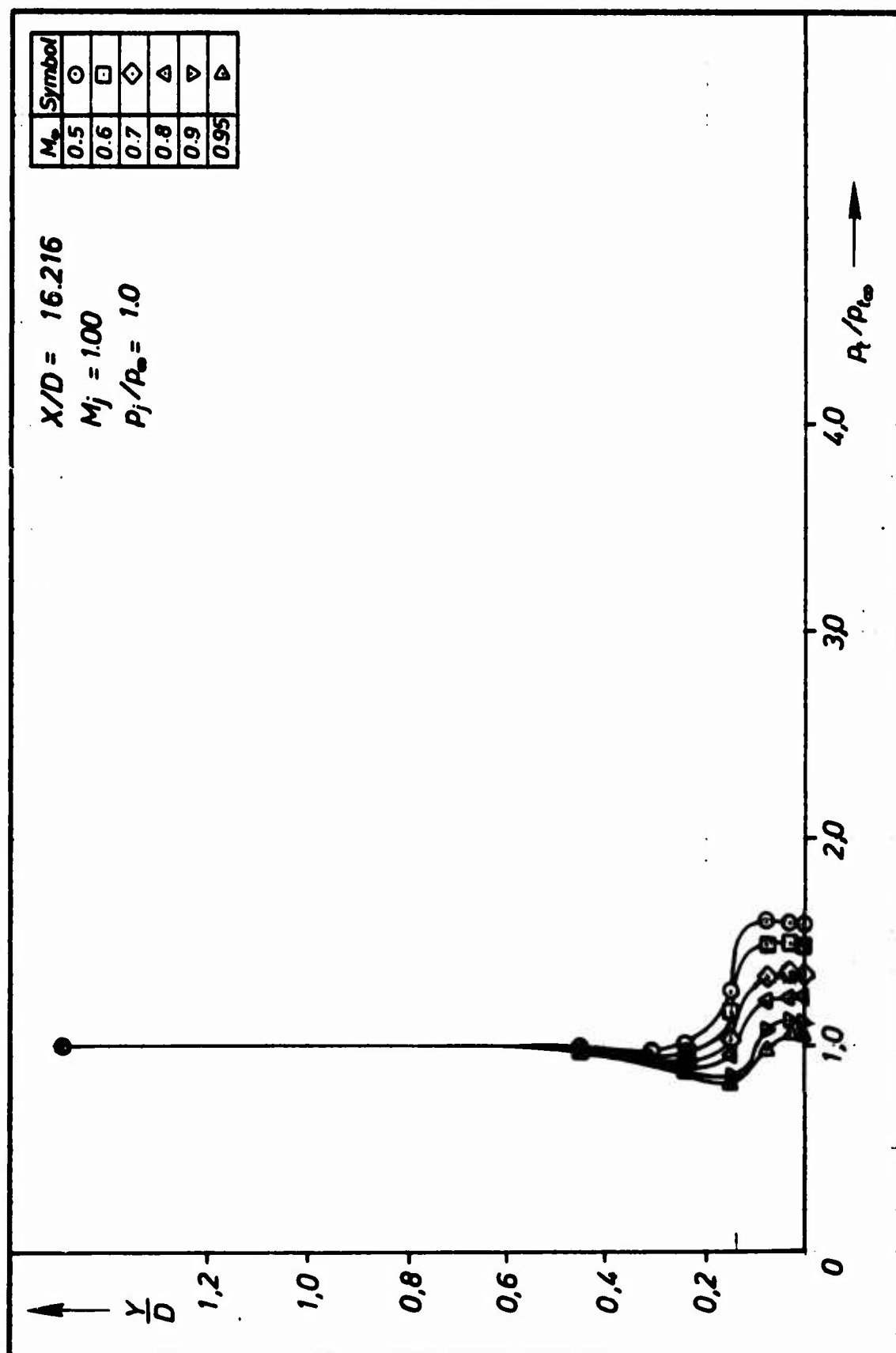


Fig. 72 Total pressure distributions in the flow field with propulsive jet for Model A1:  
 $X/D = 16.216$ ,  $M_j = 1.0$ ;  $p_j/p_\infty = 1.0$

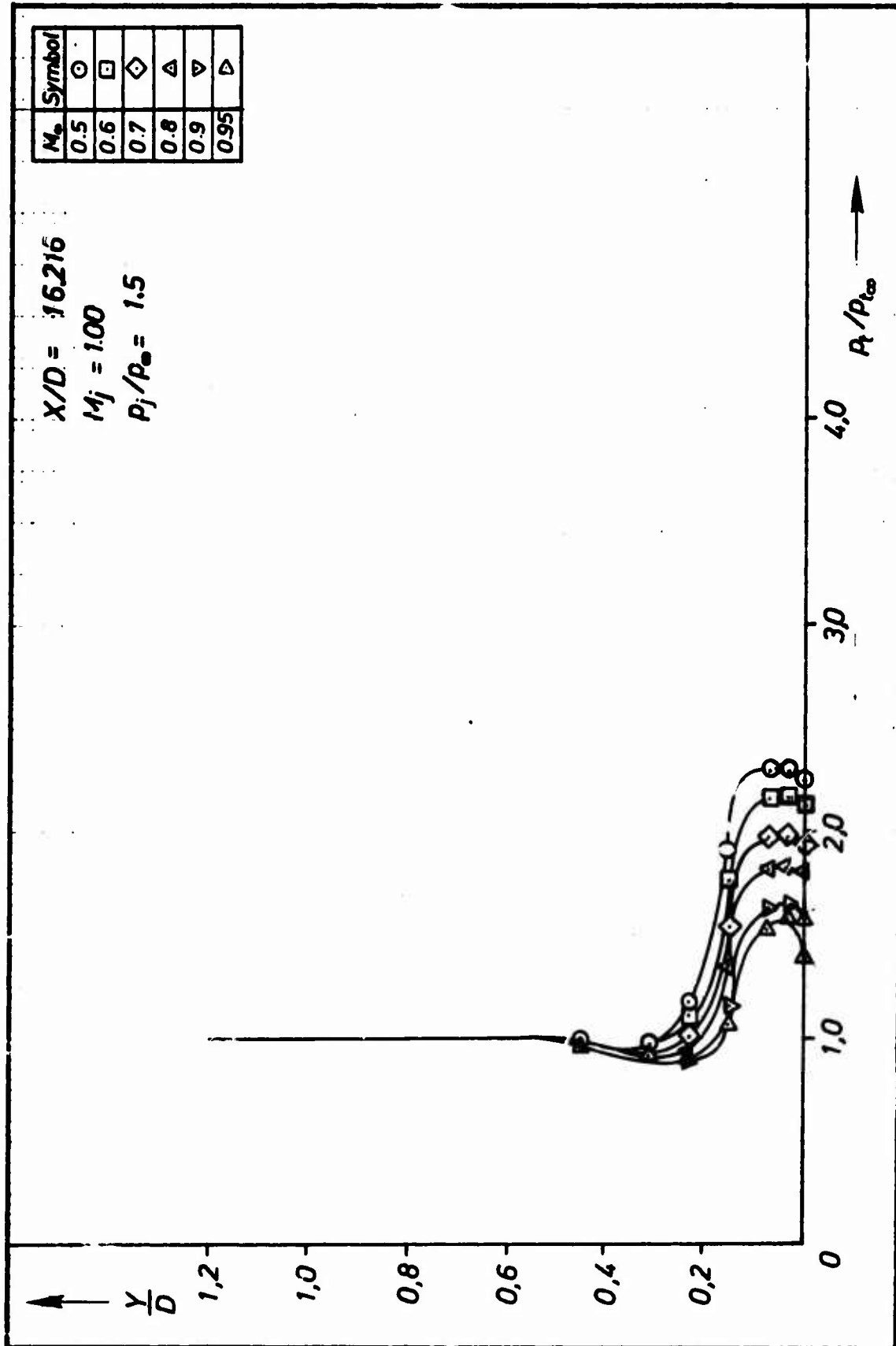


Fig.73 Total pressure distributions in the flow field with propulsive jet for Model A1:  
 $X/D = 16.216$ ,  $M_j = 1.0$ ;  $p_j/p_\infty = 1.5$

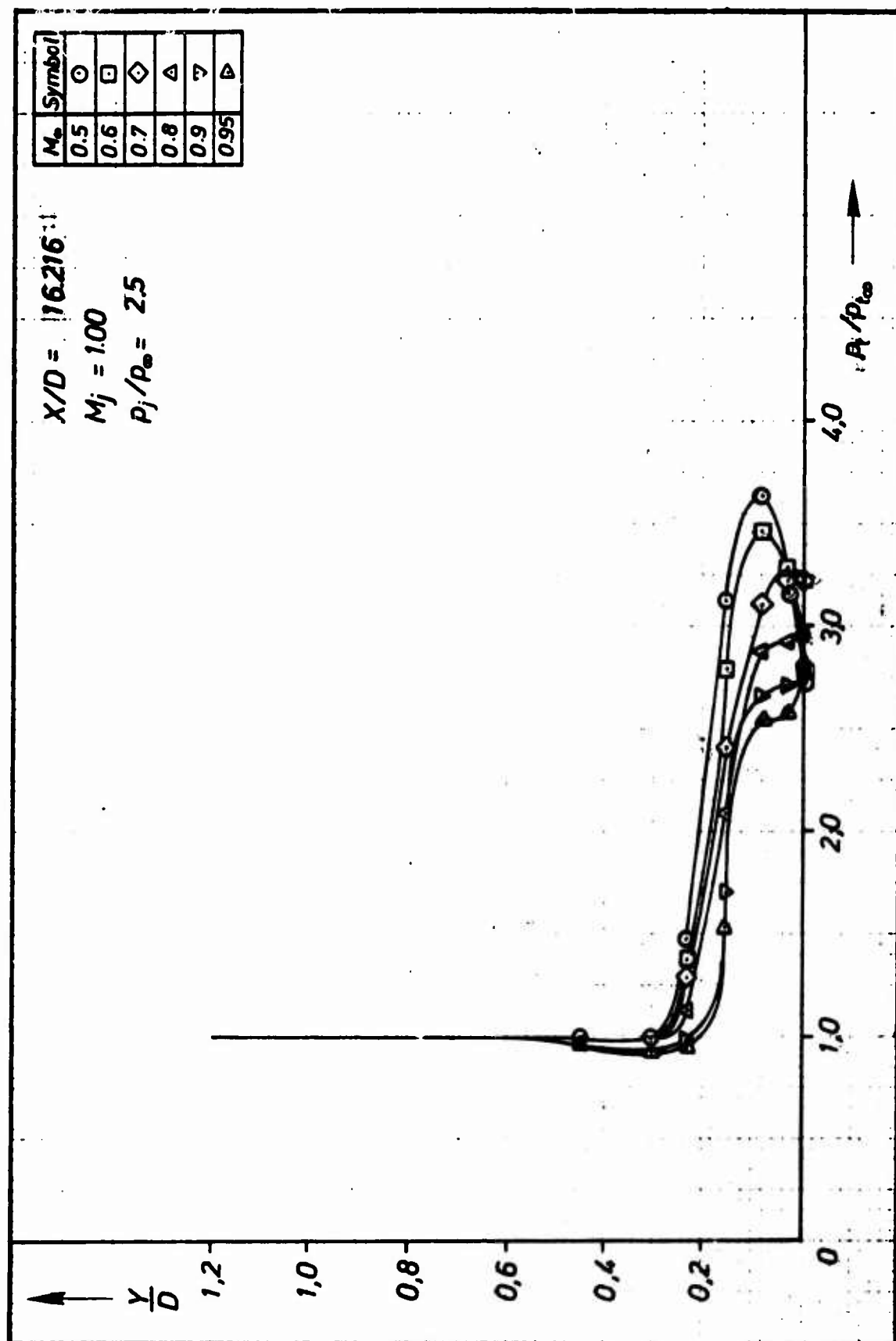


Fig. 74 Total pressure distributions in the flow field with propulsive jet for Model A1:  
 $X/D = 16.216$ ,  $M_j = 1.0$ ;  $P_j/P_\infty = 2.5$



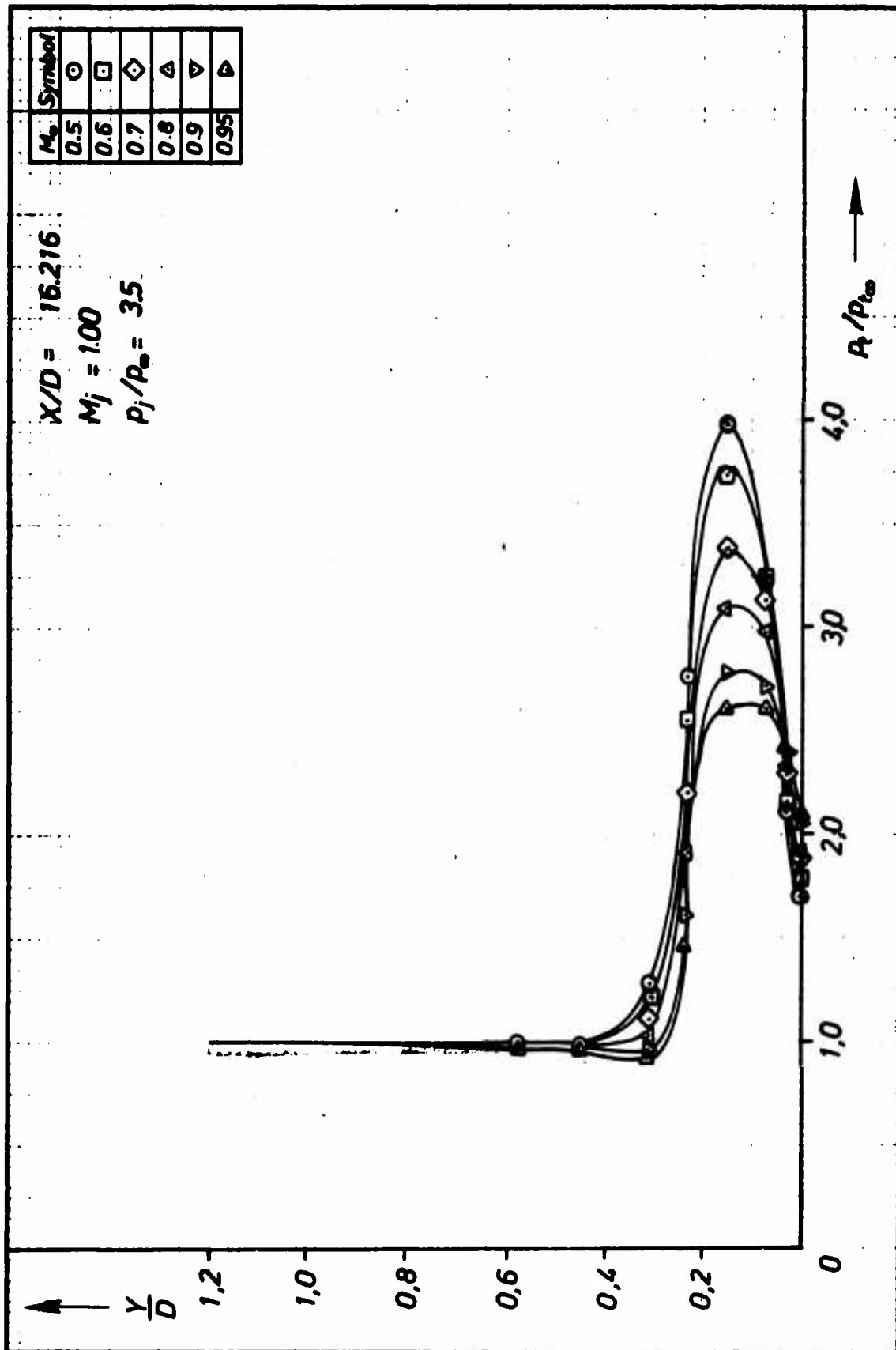
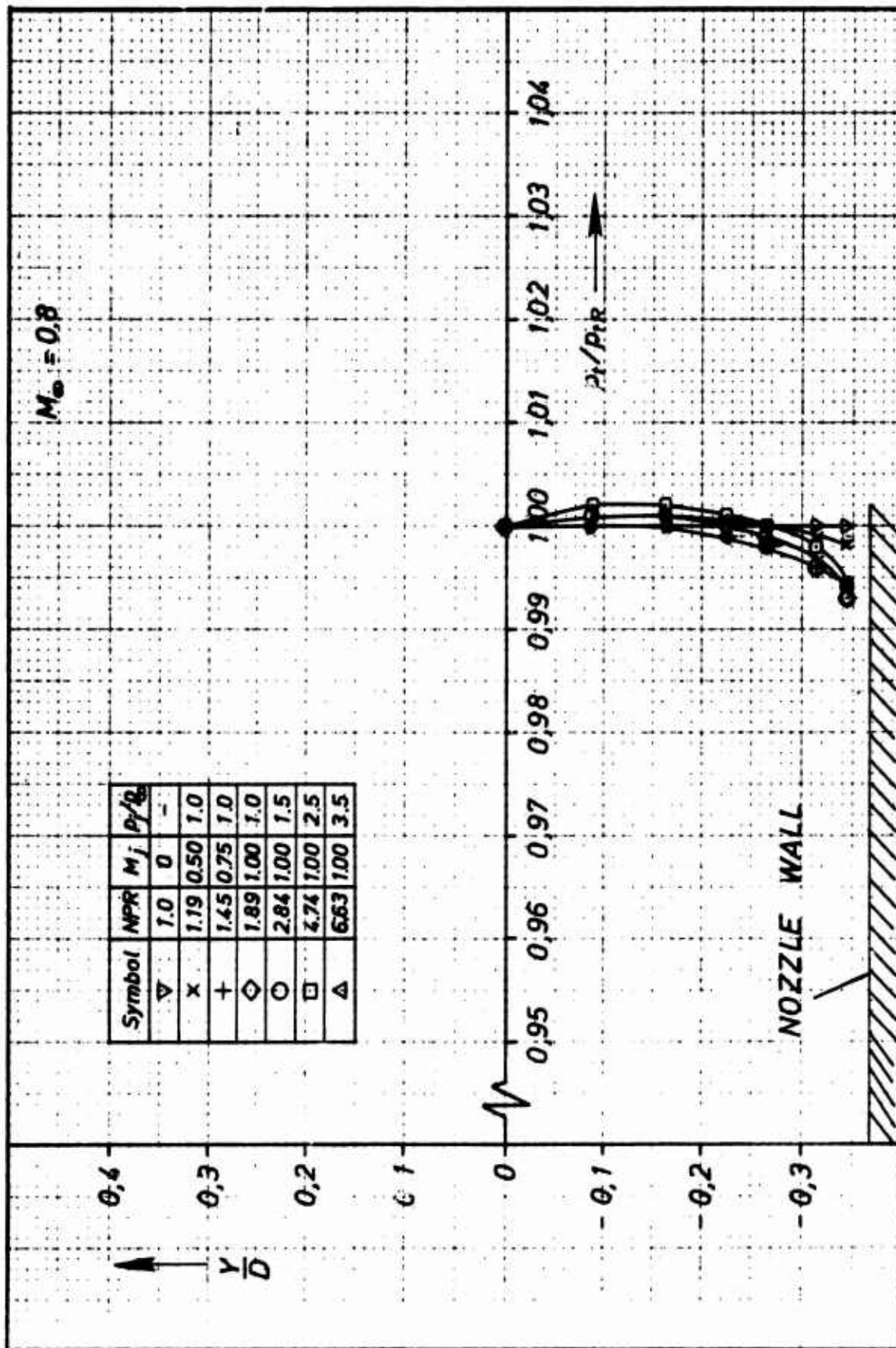
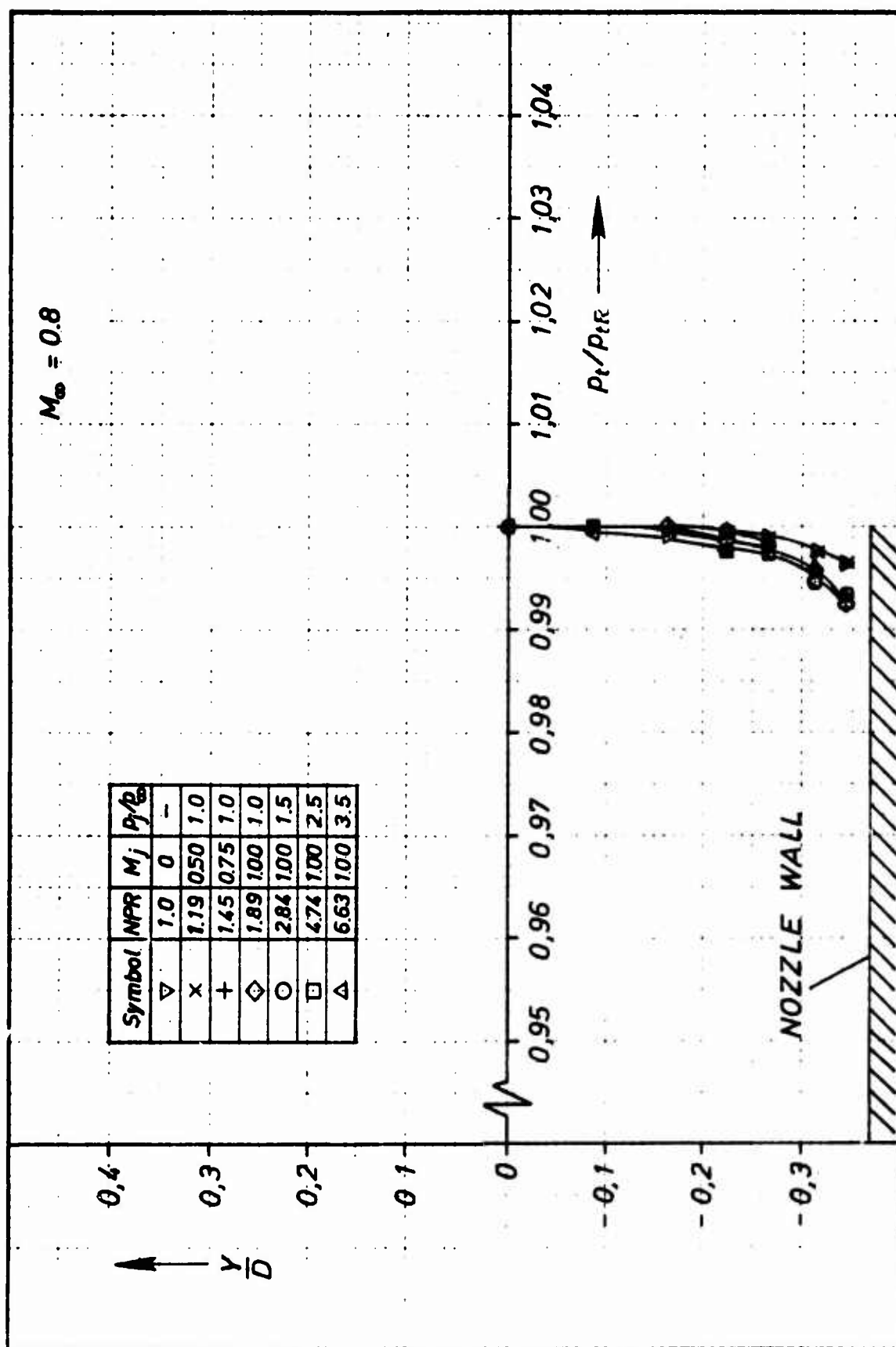


Fig. 75 Total pressure distributions in the flow field with propulsive jet for Model A1:  
 $X/D = 16.216$ ,  $M_j = 1.0$ ;  $p_j/p_\infty = 3.5$

Fig. 76 Total pressure distributions at the internal rake of Model A1 for  $M = 0.8$

Fig.77 Total pressure distributions at the internal rake of Model A2 for  $M_\infty = 0.8$

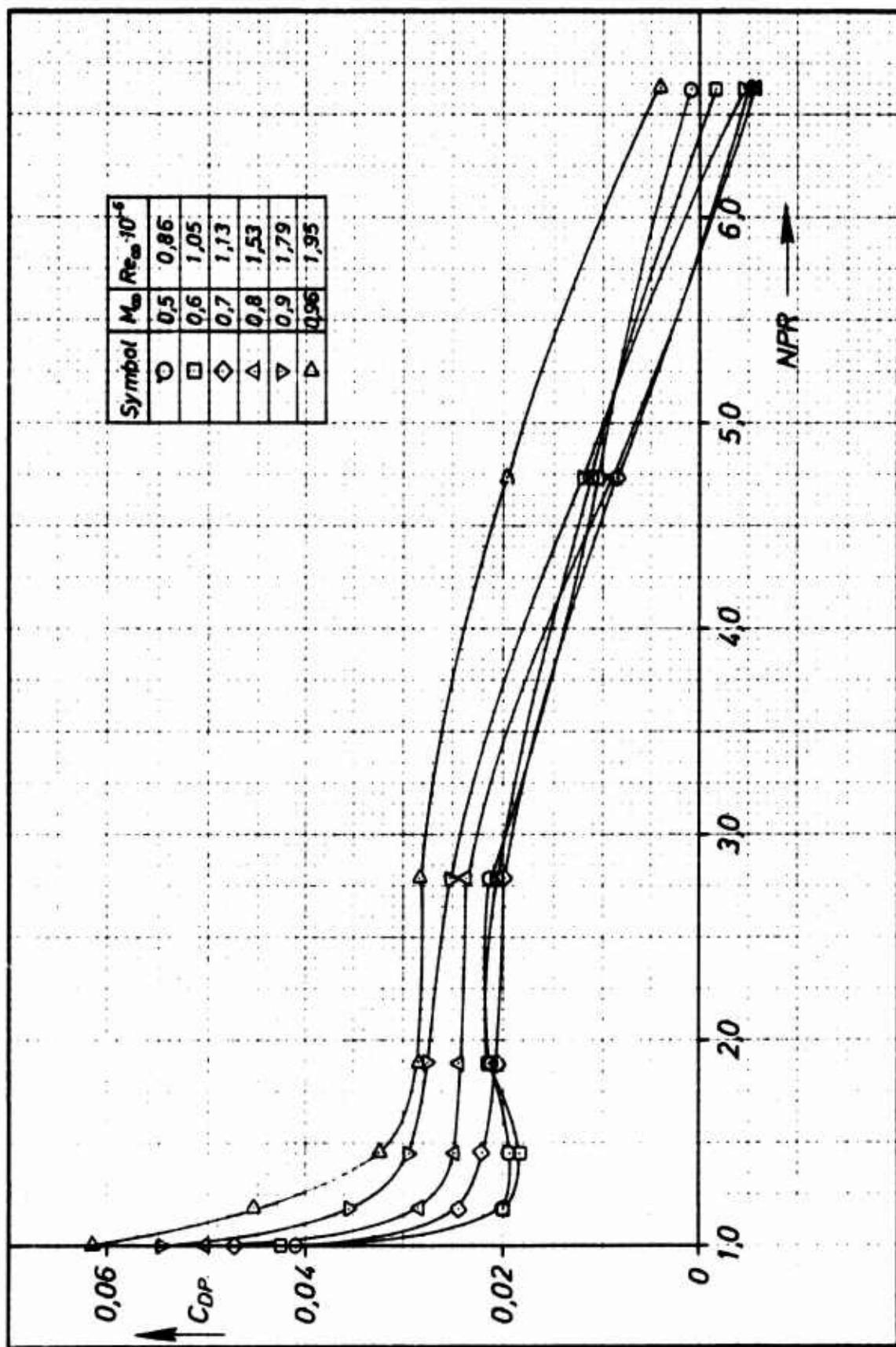


Fig. 78 Pressure drag coefficient of Model A1 as function of NPR

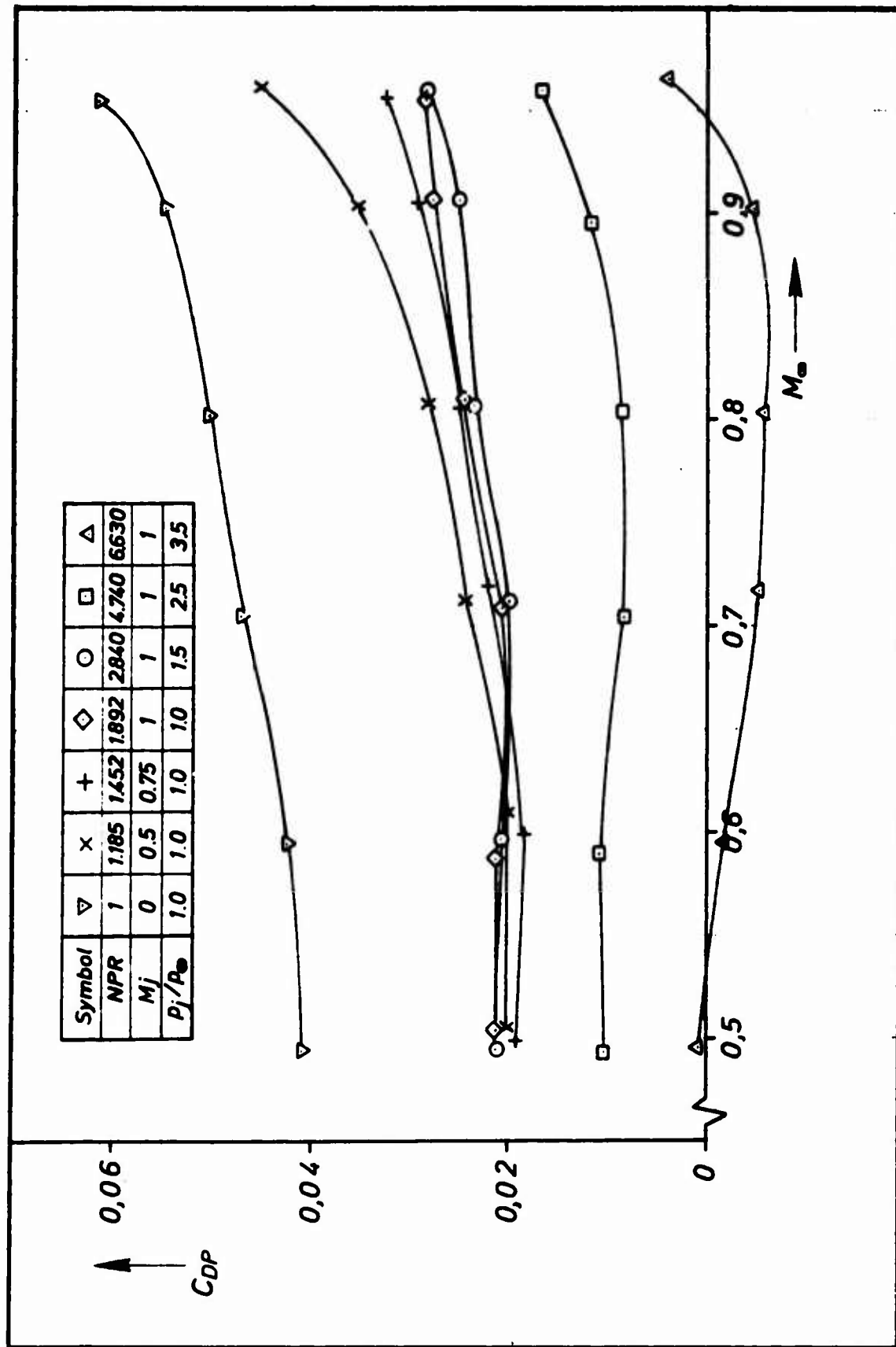


Fig.79 Pressure drag coefficient of Model A1 as function of  $M_\infty$

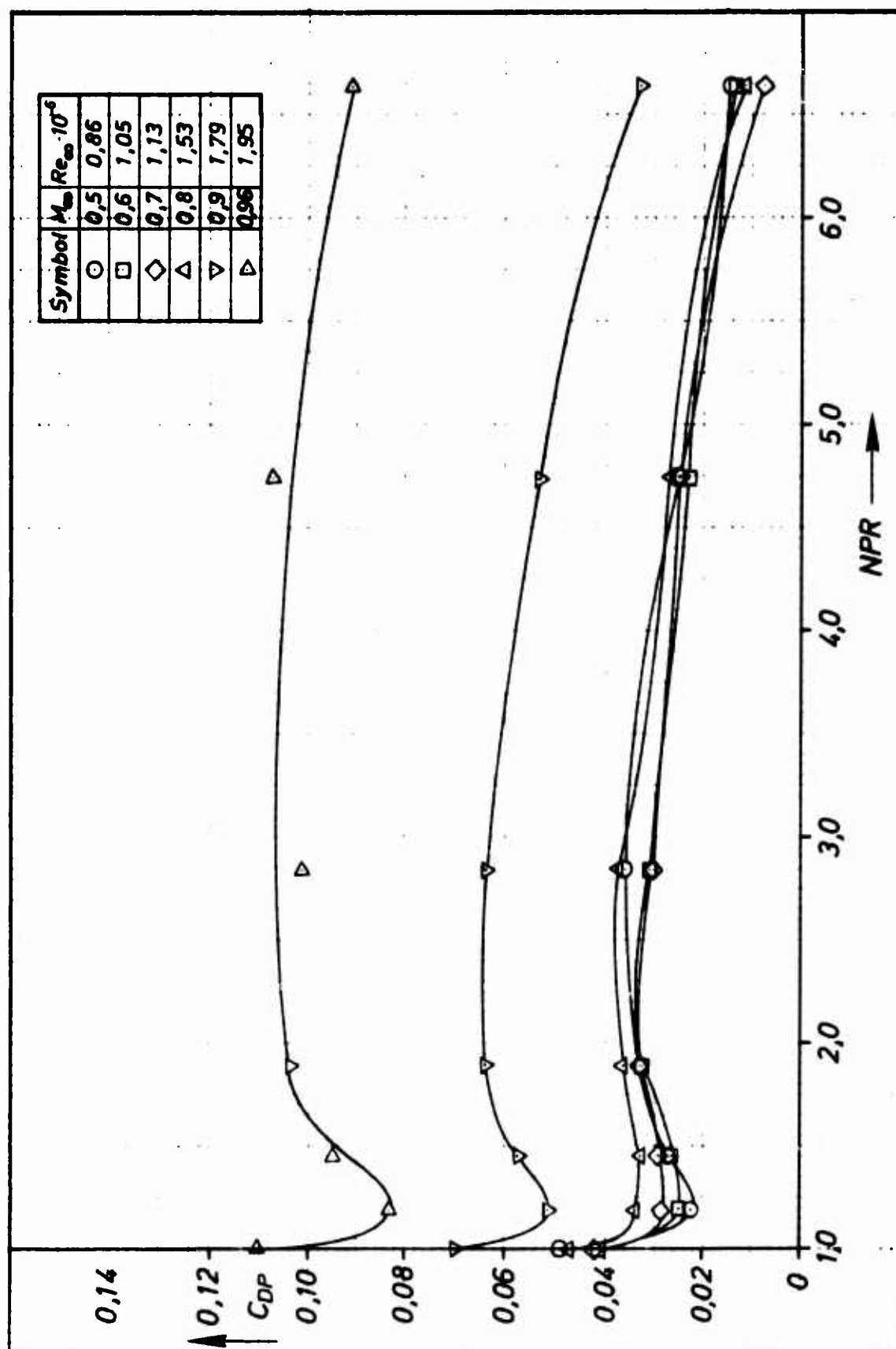
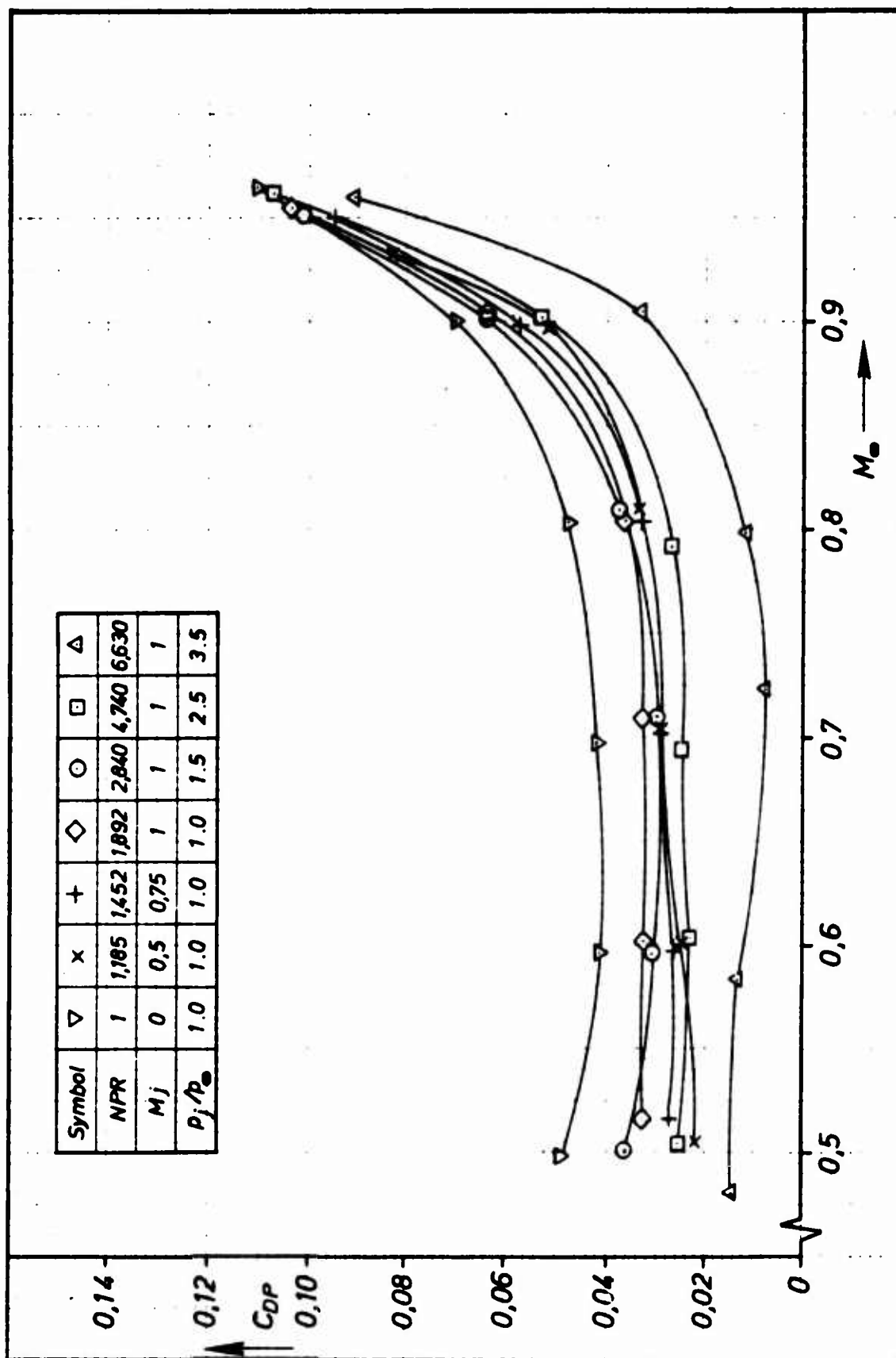


Fig.80 Pressure drag coefficient of Model A2 as function of NPR

Fig.81 Pressure drag coefficient of Model A2 as function of  $M_\infty$

## RESULTS OF NLR CONTRIBUTION TO AGARD AD HOC STUDY

by

D.Rozendal, C.C.Groothoff, W.B.G.Derksen  
National Aerospace Laboratory, NLR, The Netherlands

### SUMMARY

A description is given of a series of experiments in order to assess the influence of jet exhaust parameters – total pressure distortion, nozzle pressure ratio, jet temperature (ratio of specific heats) – at transonic Mach numbers in the range of .8 to .96 on the nozzle thrust and discharge coefficients, on the afterbody pressure distribution and on the afterbody pressure drag.

A model of .08 m diameter was tested in the .27 x .27 m<sup>2</sup> transonic test section of a continuous blow-down wind tunnel. The 15° boattailed afterbody configuration as proposed by AGARD was supplemented by an afterbody with a twice as large nozzle area. The fuselage boundary layer thickness was varied by increasing the forebody length.

A method was developed to define a valid total pressure, based on a mass flow averaging procedure, for a distorted jet pipe flow. The results for the AGARD nozzle, contraction ratio 3.24, show that in the investigated range of NPR's there is only a small effect due to the jet pipe total pressure distortion, while for the larger nozzle with a contraction ratio of 1.62 the "hollow" velocity profile, compared to a flat profile, significantly lowered the nozzle discharge coefficient (3.2%), raised the specific thrust + 2.1% and changed the afterbody pressure distribution at  $M_\infty = .8$ . Effects on afterbody pressure distribution and pressure drag due to different NPR and  $M_\infty$  were evident, while an influence due to fuselage boundary layer thickness is indicated. Furthermore it was found that boattail surface temperature significantly affects the boattail pressure distribution. For the hot jet tests the jet temperature effects on the nozzle characteristics were of minor importance, while the jet temperature effects on the boattail pressures could not be separated from the surface temperature effect.

### LIST OF SYMBOLS

A	area, m <sup>2</sup>
A <sub>n</sub>	geometric exhaust area, corrected for nozzle wall temperature, m <sup>2</sup>
A <sub>ref</sub>	reference area, $\frac{\pi}{4} D_{\max}^2$ , m <sup>2</sup>
C <sub>p</sub>	static pressure coefficient $\frac{p - p_\infty}{q_\infty}$
C <sub>DP</sub>	boattail pressure drag coefficient
C <sub>F</sub>	friction drag coefficient, friction drag/q <sub>∞</sub> A <sub>ref</sub>
C <sub>d</sub>	nozzle discharge coefficient
CT	nozzle thrust coefficient
C*	specific velocity, m/s
D <sub>max</sub>	maximum model diameter, m
i	number of i <sup>th</sup> concentric jet pipe area
L	model length, m
M <sub>∞</sub>	free stream Mach number



I-E2

$\dot{m}$	mass flow, kg/s
NPR	nozzle pressure ratio $p_{tj}/p_{\infty}$
$p$	pressure, N/m <sup>2</sup>
$p_t$	total pressure, N/m <sup>2</sup>
$p_{\infty}$	tunnel / free stream static pressure, N/m <sup>2</sup>
$p_{tj}$	jet total pressure, N/m <sup>2</sup>
$q_{\infty}$	free stream dynamic pressure $\frac{1}{2} \gamma p_{\infty} M_{\infty}^2$ , N/m <sup>2</sup>
$R$	gas constant $\frac{m^2}{s^2 K}$
$r$	distance from model centreline, mm
$Re_{D_{max}}$	free stream Reynolds number based on maximum model diameter
$T$	temperature, K
$t$	temperature, °C
$U$	velocity, m/s
$x$	distance from exit plane of nozzle A, upstream is positive, m
$y$	distance from model wall surface, mm
$\gamma$	ratio of specific heats
$\delta^*$	boundary layer displacement thickness, mm
$\theta$	boundary layer momentum thickness, mm
$\rho$	density, kg/m <sup>3</sup>
$\varphi$	angle, degrees, see Figure 1

#### Subscripts

av	average
e	edge
ex	external near nozzle exit plane, average of values at $x/D_{max} = .056$ (nozzle A) respectively at $\frac{x}{D_{max}} = .27$ (nozzle B)
i	index number of $i^{th}$ concentric jet pipe area
id	ideal
$\infty$	free stream, reference orifice on model at Stn. 16, $\varphi = 0$
j	jet
jp	jet pipe
l	internal near nozzle lip at $\frac{x}{D_{max}} = .063$ (nozzle A) $.264$ (nozzle B)
meas	measured
n	nozzle
t	total
1, 2, 3	different definitions of C <sub>T</sub> coefficients
l	also used in T1, the external total temperature of the boattail, measured at $\frac{x}{D_{max}} = .056$

## LIST OF DEFINITIONS

$$C_d \quad \text{nozzle discharge coefficient} = \frac{\dot{m}}{\dot{m}_{id}}$$

$$\text{For supercritical pressure ratios } C_d = \frac{c^* \cdot \dot{m}}{p_{tj} \cdot A_n} \quad \text{where the specific velocity}$$

$$c^* = \frac{1}{\gamma} \sqrt{\frac{\gamma R T_{tj}}{\left(\frac{2}{\gamma+1}\right)^{(\gamma+1)/(\gamma-1)}}}$$

$$\text{For subcritical pressure ratios } C_d = \frac{\dot{m}}{p_{\infty} A_n} \sqrt{\frac{\gamma-1}{2\gamma} \frac{R T_{tj}}{\left(\frac{p_{tj}}{p_{\infty}}\right)^{(\gamma-1)/\gamma} \left[\left(\frac{p_{tj}}{p_{\infty}}\right)^{(\gamma-1)/\gamma} - 1\right]}}$$

$$\left. \begin{matrix} CT_1 \\ CT_2 \\ CT_3 \end{matrix} \right\} \quad \text{Thrust coefficients} = \frac{F_{\text{meas}}}{F_{id(1,2 \text{ or } 3)}}; \quad F_{id(1,2 \text{ or } 3)}, \text{ the ideal thrust, is based on:}$$

suffix 1: actual  $p_{tj}$  and  $A_n$ , derived  $\dot{m}_{id}$

suffix 2: actual  $p_{tj}$  and  $\dot{m}$ , derived  $A_n \times C_d$

suffix 3: actual  $\dot{m}$  and  $A_n$ , derived  $p_{tj}$  with suffixes 1, 2 or 3 omitted, the used equation is

$$F_{id} = \dot{m} \sqrt{\frac{2\gamma}{\gamma-1} R T_{tj} \left[ 1 - \left(\frac{p_{\infty}}{p_{tj}}\right)^{(\gamma-1)/\gamma} \right]}$$

$$\text{It may be noted that } F_{id1} = \frac{1}{C_d} \times F_{id2}, \text{ and } CT_1 = CT_2 \times C_d$$

$F_{\text{meas}}$  measured thrust force = measured balance force - pressure drag - friction drag - gap pressure correction. (Upstream force is positive.)

nozzle A exhaust nozzle defined by AGARD coordinates, contraction ratio 3.24, see Table II

nozzle B exhaust nozzle with contraction ratio 1.62, see Table II

## 1. INTRODUCTION

Within the Propulsion and Energetics Panel of AGARD an ad hoc study group was formed with the object to initiate a research program to better understand the relevant parameters and their effects on nozzle and afterbody performance at transonic speeds. This study, known as PEP/WG 04 "Improved Nozzle Testing Techniques at Transonic Speeds" was directed by Prof. A. Ferri. Its aim is to compare the results of analogous experiments from different institutes, which yields a common reference base. In addition each group could concentrate on one or more special topics, by preference likewise incorporating equal boattail and nozzle geometries.

In evaluating the performance of jet nozzles, it is known that jet parameters as nozzle pressure ratio, jet temperature and ratio of specific heats may have a marked influence both on the flow field outside the nozzle and on the characteristics of the nozzle flow itself. In real jet engines the jet pipe flow mostly shows some distortion in the total pressure profile, some swirl and turbulence, particularly at afterburning. This may also be the case with turbofan engines. Because to this date the influence of these parameters seems not to have been investigated to the same extent as the other mentioned jet parameters, this topic was emphasized at NLR.

In preliminary tests, which will not be described here, changing swirl or turbulence by means of vanes resp. screens caused also the total pressure profile to change somewhat. By comparison of these preliminary results it was concluded that the total pressure distortion was the prime parameter. Therefore it was decided to study this effect in particular, and not to investigate jet turbulence and swirl.

The best indication of possible effects due to the change of parameters is given if the other test conditions are practically kept constant. Therefore the design of the model for these experiments incorporated a distortion device that could be operated during a run, changing the jet flow total pressure profile.

Apart of the nozzle as specified by AGARD, which can be considered as representative for the nozzle of a non-afterburning jet engine, the investigation included also tests with a nozzle with a twice as large exit area, corresponding to a typical afterburning nozzle or, regarding the contraction ratio, to a fan engine nozzle.

The parameters that were varied, were

- during a run                      - distortion/no distortion
- from run to run                -  $M_\infty$
- NPR
- after a series of runs        -  $RT_j(\gamma)$                       (2 values)
- $A_n$                               (2 values)
- boundary layer thickness (2 values)
- more or less inadvertently   - tunnel wall configuration (2)
- model wall temperature

Before the powered model was tested in the wind tunnel a test series was performed at a static test stand to investigate the jet flow total pressure profiles and to determine a proper definition for the mean jet total pressure.

This report describes the facilities, models and experiments and gives a survey of the results.

## 2. EXPERIMENTAL SET-UP

### 2.1 General

The wind tunnel that was available for the investigation was the NLR-CSST tunnel with a  $.27 \times .27 \text{ m}^2$  test section (Fig.1). Due to the limited size of the test section the model must necessarily be small. In order to be able to perform simultaneously afterbody pressure and nozzle thrust measurements, the hydrogen peroxide catalytic decomposition technique was used. This technique allows small dimensions of the supply tubes and a compact nozzle which the liquid  $\text{H}_2\text{O}_2$  flow causes minimum interaction. The existing thrust balance that was envisaged for the model required a minimum model diameter of about .08 m. This dimension was considered to be tolerable in the wind tunnel as far as blockage was concerned. It was realized however that due to the resulting blockage of 7-10% the experiments yield relative rather than absolute results, at least concerning phenomena that depend on the flow field outside the nozzle.

For the hydrogen peroxide a concentration of 75% was chosen. After decomposition in a catalyst pack this yields hot gases of about 630 K, with  $RT_j$  and  $\gamma$  typical for the jet gases of a non-afterburning turbojet (Ref.1).

To provide a reference base with the investigations of the other study groups also measurements with cold air as jet medium were envisaged. No balance was used in that case.

### 2.2 Wind Tunnel

The transonic test section of the continuous blow down supersonic wind tunnel CSST was provided with closed side walls and with slotted top and bottom walls. Some dimensions are given in Figure 1. The first series of experiments in the wind tunnel was performed while two slats were removed from the test section bottom wall to allow attachment of the stepping mechanism of a total pressure probe for boundary layer measurements. In later test series this probe was removed and the bottom wall slats were replaced. For the wind tunnel test at  $M_\infty = 0$  the transonic test section was removed.

The test section static pressure was adjusted to about 1 atmosphere to provide approximately equal conditions as at the static tests outside the wind tunnel. The adjustment of tunnel free stream conditions was performed by controlling the total pressure and the diffuser throat area. Since this procedure was not standard practice for the wind tunnel, the actual achieved Mach numbers differed slightly from the desired values.

For the present tests a reference Mach number has been determined from the tunnel total pressure and the static pressure at model station 16 (orifice at  $\varphi = 0 \text{ deg.}$ ) on the cylindrical part of the model.

In this test set-up (model blockage of 7%, partially open test section at the downstream end of the model, see Figure 1) it was not possible to find the relation between this Mach number and the free-stream Mach number, that would be obtained with the same model in a much larger test section. It may be added here, that for small models, having a blockage ratio of 1% or less, the free-stream Mach number is usually determined from the plenum pressure and the settling chamber pressure. In most cases a further small correction is required due to a difference between the plenum pressure and the free-stream static pressure. This correction is obtained from tunnel calibration.

Because the relation between measured Mach number and free-stream Mach number is not known in the present tests the pressure coefficients and the pressure drag coefficients may be affected by small systematic errors which depend on Mach number. Here consequently the pressure coefficient at station 16 is zero, which may not be the case if the model were placed in an infinitely free stream. In Section 3.2 the possible errors due to this procedure are further analyzed.

### 2.3 Model

The wind tunnel model consisted of an earthed forebody and a metric afterbody (Figures 1, 2 and 3). The model is basically cylindrical with a maximum diameter of .080 and a maximum length of 1.200 meter.

The model was mounted on two side struts 12 mm thick in which the tubes for  $H_2O_2$ , air, cooling water and pressure measurements and the other instrumentation wires were incorporated. Furthermore it was braced to the top and bottom tunnel wall by two steel wires just upstream of the split line between afterbody and forebody. To prevent choking of the tunnel near the struts the forebody was shaped such that the model cross-sectional area including the struts gradually increased to the maximum model area downstream of the struts.

The fuselage could be lengthened by addition of a cylindrical part to the forebody in order to thicken the natural boundary layer on the afterbody.

The shape of the afterbody with the smaller nozzle (nozzle A), as well as the location of the static pressure and temperature instrumentation followed the coordinates as proposed by the AGARD group (Table I). The afterbody contour was manufactured according to the ordinates as supplied by Rolls Royce.

The larger nozzle configuration (nozzle B) was obtained by "cutting off" an appropriate part of afterbody A and fairing the exhaust nozzle inner contour with a straight cone into the jet pipe. This resulted in a nozzle inside convergence half-angle of  $4^\circ$  vs  $7^\circ$  for the original AGARD nozzle.

The single component thrust balance which was used in the hot jet tests was designed for a maximum force of 800 N. It consisted of a cart wheel sensing element with two solid beams with strain gauges and four hollow spokes. These spokes connected the anulus, where  $H_2O_2$  was supplied through two tubes, with the balance sting, through which the  $H_2O_2$  flowed to the silver screen catalyst pack. At the downstream end the sting was supported by spring beams. Water cooling and a Ferobestos shield prohibited the heat of the catalyst pack to flow to the balance.

The balance was calibrated, including the stiffening effect of the pressure measurement tubing, thermocouple wires, water tubes and air supply tubes to the distortion valve. The calibration tests examined the effects of mass flow, supply pressure, actuation pressure and temperature of  $H_2O_2$  and of the balance parts. These parameters were measured also during the test runs. The correction for temperature and pressure of the liquid  $H_2O_2$  proved to be most important, amounting together to about 1.5 N. The effect of the mass flow was smaller, approximately .5 N. It is estimated that after the corrections are made the error in the balance readings is of the order of the average of the corrections that were applied due to the zero shift of the balance before and after a run, i.e. 1 N.

The difference in axial elongation between the inner and outer structure of the metric afterbody assembly due to temperature effects was compensated internally, assuring that the gap at the splitline location between metric and non metric fore-body remained constant.

The  $H_2O_2$  supply was controlled with high precision by manually adjusting a micrometer which was connected to the movable conical spindle of a cavitating venturi outside the model. For the test series with air as jet medium, the thrust balance and catalyst pack were removed and replaced by an airduct. The air flow was adjusted by an electrically operated plug valve in the supply line from the same pressure vessel that supplied air to the tunnel itself.

For reasons mentioned in the Introduction the configurations that were used in this program were provided with a specially developed distortion device. It consisted of a sleeve valve which could admit or cut off the flow of the jet medium to the centre part (50%) of an orifice plate. Hence the gas flow could either be forced through the outside part of the orifice plate or homogeneously distributed over the cross section area. In the first case a "hollow" velocity profile was created in the jet pipe, in the second case a flat profile resulted. Downstream of the orifice plate four screens smoothened the flow. The sleeve valve could be actuated by one of two small pneumatic cylinders, fed by 40 atm. supply air through thin stainless steel tubes. During a run this air pressure was kept on the actuating cylinder to fix the position of the valve. The air mass that leaked into the valve was measured and was taken into account in the calculations. The influence of the pressurized supply tubes on the thrust balance proved to be nihil. The pressure in the valve housing was measured to monitor the functioning, showing about twice as large a value in the case of "distortion" compared to "no distortion". In Figure 2, showing the wind tunnel model, this distortion valve is schematically drawn.

In a preliminary test series the total pressure profile in the jet pipe was determined. It was preferred not to install a total pressure rake in the wind tunnel model because the construction would become complicated. Moreover it had been proposed by the AGARD group that the jet total pressure would be derived from measurements of the jet pipe static pressure, jet mass flow and temperature.

This preliminary test series was therefore carried out at a static test stand with separate nozzle models which did incorporate the total pressure rake and moreover a cross rake in the exit plane. Two configurations, one with the AGARD nozzle (nozzle A) and one with the larger nozzle (nozzle B) were used in these tests. The latter nozzle could be partially blocked by a stepped plug (.01, .02 and .03 m dia.). These nozzles had arbitrarily shaped outside contours.

The total pressure profile was only determined with  $H_2O_2$  (hot jet tests). These tests have not been performed with cold air as jet medium, because the high pressure air facility was not available at the test stand due to other priorities.

## 2.4 Instrumentation

For the test series to investigate the jet flow total pressure profiles and to define a valid mean jet total pressure, the 10-tube rake as specified by the AGARD group was mounted in the jet pipes, 9 tubes measuring the total pressures while the 10<sup>th</sup> tube on the centreline was modified to measure the static pressure. Besides in the jet pipe the gas temperature was measured. The wall static pressures were measured at 8 locations. In the exit plane the total pressures were surveyed by a cross rake with 20 probes for nozzle A, 24 probes for nozzle B.

During the wind tunnel test the pressures were measured by pressure transducers mostly incorporated in Scanni valves, temperatures by chromel-alumel thermocouples, the balance force by strain gauges. The mass flows of air to the distortion device and  $H_2O_2$  to the gas generator were determined by turbine flow meters. A sharp edge orifice flow meter was used to measure the air flow for the cold air tests.

Recordings were made automatically after conversion into digital values. An U.V. multi-channel recorder was run parallel to provide a quick look capability. In early tests a boundary layer probe was mounted in the wind tunnel between the slats in the tunnel bottom wall. This probe could be stepped every .25 millimetres taking a total pressure survey for a distance of 40 millimetres from the model wall.

The following accuracies (90% probability levels) must be considered, derived from instrument and digitizing characteristics.

Pressure coefficients	$C_p \pm .005$
Pressure drag coefficients	$C_{DP} \pm .003$
Free stream Mach number (see Section 3.2)	$M_\infty \pm .005$
Nozzle discharge coefficients	$C_d$
no distortion, low/high flow	$\pm .7/.5\%$
distortion, low/high flow	$\pm 1.0/.8\%$
Nozzle thrust coefficients	
no distortion, low/high flow at $M_\infty = 0$ (due to scatter at $M_\infty \neq 0$ , 3% more)	$CT \pm 1.4/.6\%$
distortion, low/high flow	$CT \pm 1.7/.9\%$
Nozzle pressure ratio	
no distortion/distortion	$NPR \pm .4/.7\%$

## 2.5 Test Sequence

In Table II a survey is given of the range of parameters that are encompassed in the test series. Series 1 is the forementioned preliminary test series.

During a test run in the wind tunnel at each of the following test conditions, a measurement was taken, if necessary after readjustment of the Mach number:

- tunnel off,
- tunnel started, jet off,
- tunnel on, jet on, no distortion,
- tunnel on, jet on, distortion,
- tunnel on, jet off,
- tunnel off.

## 3. RESULTS AND DISCUSSION

### 3.1 Nozzle Characteristics

#### 3.1.1 Definition and Calibration of Jet Total Pressure

The jet total pressure is of paramount importance in the calculation of the nozzle discharge and thrust coefficients. It had been proposed by the AGARD group that during the research program the jet total pressure if possible be determined from the measured mass flow, the jet temperature and the static pressure in the jet pipe. In a jet flow with a total pressure profile distortion however, the determination of a valid mean jet total pressure from these parameters poses some special problems.

The averaged  $p_{tj}$  that must be determined will have to be a characteristic property of the jet flow, i.e. must be independent of the axial location where the measurements are made. It must not change its value, except due to viscous losses if the cross sectional area of the jet pipe is changed.

The area averaged jet total pressure will not satisfy this requirement. During expansion the cross section area of a stream tube with a higher total pressure will decrease less than that of a stream tube with a lower total pressure. This means that the area averaged total pressure of a distorted flow will increase in a contraction. However the mass flow and the total pressure remain the same per stream tube in a contraction. Hence the total pressure mass averaged over all stream tubes, will remain constant and might therefore be a proper means of averaging, at least superior to area averaging.

For the determination of the mass flow averaged total pressure it is necessary to know everywhere in the cross section of the jet pipe the local total pressure and mass flow, or the local static pressure, temperature and mass flow. Compressible flow relations yield

$$d\dot{m} = \frac{p \, dA}{\sqrt{RT_{tj}}} \sqrt{\frac{2\gamma}{\gamma-1} \left[ \left( \frac{p_t}{p} \right)^{(\gamma-1)/\gamma} - 1 \right] \left( \frac{p_t}{p} \right)^{(\gamma-1)/\gamma}} \quad (1)$$

Solving this equation a value for the local total pressure  $p_t$  can be derived if the mass flow distribution, static pressure and total temperature are known. The mass flow averaged total pressure then is

$$p_{tj} = \int \frac{p_t \, d\dot{m}}{\dot{m}} \quad (2)$$

In order to determine  $p_{tj}$  in the wind tunnel model from static pressures and mass flow, it was therefore necessary to have knowledge of the local static pressure and mass flow in the jet pipe. The  $H_2O_2$  was decomposed just upstream of the measuring station, so the total temperature could be assumed to be constant over the cross section.

During the calibration tests the static pressure distribution in the jet pipe at the location of the total pressure rake was determined by four pressure orifices in the wall and one on the centreline. These all measured essentially equal pressures so it was assumed that the static pressure in the plane of the rake was constant and equal to the average value. It was also established that the pressures measured by the neighbouring orifices in axial direction, were not significantly different from this average static pressure.

The jet pipe cross section was divided into 9 equal areas, defined by the total pressure rake. The mass flow distribution  $\left( \frac{d\dot{m}}{\dot{m}} \right)_i$  over these 9 equal areas  $\Delta A$  can be calculated from Equation (1), if the average static pressure  $p_{jp}$  and the measured total pressure distribution  $p_{ti}$  are known.

Taking  $RT_{tj}$ ,  $\gamma$  and  $\Delta A$  constant and dividing by  $\dot{m}$ , Equation (1) yields

$$\left( \frac{\Delta\dot{m}}{\dot{m}} \right)_i = \frac{\sqrt{\left[ \left( \frac{p_{ti}}{p_{jp}} \right)^{(\gamma-1)/\gamma} - 1 \right] \left( \frac{p_{ti}}{p_{jp}} \right)^{(\gamma-1)/\gamma}}}{\sum_{i=1}^9 \sqrt{\left[ \left( \frac{p_{ti}}{p_{jp}} \right)^{(\gamma-1)/\gamma} - 1 \right] \left( \frac{p_{ti}}{p_{jp}} \right)^{(\gamma-1)/\gamma}}} \quad (3)$$

It was found that this mass flow distribution was insensitive to the total mass flow, pressure level or contraction ratio of the nozzle. For all nozzle configurations for both "distortion" and "no distortion", the difference between the measured and average mass flow distribution was

$$\left| \left( \frac{\Delta\dot{m}}{\dot{m}} \right)_{i_{meas}} - \left( \frac{\Delta\dot{m}}{\dot{m}} \right)_{i_{av}} \right| \leq .01$$

so it could be established with confidence that a standardized mass flow distribution can be assume (Fig.4). Based on the consistency of this standardized mass flow distribution, together with  $\dot{m}_{meas}$ ,  $p_{jpav}$  and  $T_{meas}$ , the mass flow averaged total pressure in the jet pipe can be calculated without knowledge of local total pressures. Solving Equation (1) for  $d\dot{m} = \Delta\dot{m}$  and  $dA = A_{jp}/9$

$$p_{ti} = p_{jp} \left\{ \frac{1}{2} + \frac{1}{2} \sqrt{1 + \left( \frac{\Delta\dot{m}}{\dot{m}} \right)_i^2 \frac{\dot{m}^2 RT_{tj} 2(\gamma-1)}{\left( \frac{A_{jp}}{9} \right)^2 p_{jp}^2 \gamma}} \right\}^{\gamma/(\gamma-1)} \quad (4)$$

and

$$p_{tj} = \sum_{i=1}^2 p_{ti} \left( \frac{\Delta \dot{m}}{\dot{m}} \right)_i \quad (5)$$

The jet total temperature  $T_{tj}$  was (iteratively) calculated from

$$T_{tj} = T_{\text{meas}} \frac{\left( \frac{p_{t2}}{p_{jp}} \right)^{(\gamma-1)/\gamma}}{.87 \left[ \left( \frac{p_{t2}}{p_{jp}} \right)^{(\gamma-1)/\gamma} - 1 \right] + 1} \quad (6)$$

where .87 is the measured recovery factor of the thermocouple. It may be noted that  $\frac{p_{t2}}{p_{jp}}$ , the pressure ratio of the 2nd concentric area, was taken because the jet temperature was measured in the 2nd concentric ring.

If the standardized mass flow averaged total pressure  $p_{tj}$  is compared with the total pressure that was directly derived from the actual measured mass flow distribution in the jet pipe, for 29 runs it was found that  $p_{tj} = p_{tj\text{meas}} \pm .4\%$ , the tolerance indicating the standard deviation.

In the exhaust plane it is not possible to determine along the same method the mass flow averaged total pressure because of radial variations in the static pressure due to sonic line curvature. The total pressures as measured from the cross rake may be used however to calculate an approximate mass flow averaged total pressure. Realizing that at the throat of a nozzle, the flow is near sonic ( $M_j = 1.0 \pm 10\%$ ), and therefore the local mass flow is about proportional to the total pressure ( $\rho v = \text{constant} \times p_t \pm 1\%$ ). With  $\Delta \dot{m} = \rho v \Delta A$ , Equation (5) can be written approximately

$$p_{tj} = \frac{\sum_{i=1}^2 p_{ti}^2 \Delta A}{\sum_{i=1}^2 p_{ti} \Delta A} \quad (7)$$

Illustrating the foregoing, the following examples are given, taken from test series 1, for jet flows with distorted total pressure profiles. The total pressures in  $\text{N/m}^2$ , as determined by the various methods, were for

Nozzle A	in the jet pipe	in the exit plane
standardized mass flow average	$2.335 \times 10^5$	—
measured mass flow average	$2.336 \times 10^5$	$2.335 \times 10^5$ approx.
area average	$2.307 \times 10^5$	$2.335 \times 10^5$
Nozzle B		
standardized mass flow average	$3.069 \times 10^5$	—
measured mass flow average	$3.068 \times 10^5$	$3.095 \times 10^5$ approx.
area average	$2.926 \times 10^5$	$3.053 \times 10^5$

The measured total pressure profiles for these examples are shown in Figures 5a and 5b.

It may be seen from these examples, that the area averaged total pressures increase towards the exit for both nozzles, and that the difference between the area averaged and mass flow averaged values in the jet pipe are considerable for the large nozzle B, but also still clearly evident for nozzle A.

It may be concluded that the method to determine the total pressure from the standardized mass flow yields reliable results.

In the following section this method is applied to calculate the jet total pressures and the derived nozzle thrust and discharge coefficients.

### 3.1.2 Characteristics of Nozzle A

The equations for the discharge and thrust coefficients are given in the list of definitions.

The calculated discharge coefficients for the hot test series 2 and 5 are shown vs the nozzle pressure ratio in Figures 6 and 7 for  $M_\infty = 0$  and  $M_\infty \neq 0$  respectively.

The choked nozzle pressure ratio for this axisymmetric nozzle with a half angle of  $7^\circ$  was expected to be slightly higher than 2.4 (Ref.2). From the test results this cannot be confirmed with certainty, a somewhat lower value would also be possible. To determine the average choked nozzle discharge coefficients the runs with  $\text{NPR} > 2.2$  were used.

The average choked discharge coefficients for both  $M_\infty = 0$  and  $M_\infty \neq 0$  are:

$$\begin{array}{ll} \text{series 2 + 5, 36 runs} & \text{no distortion } C_d = .988 \pm .004 \\ & \text{distortion } C_d = .986 \pm .005 \end{array}$$

the tolerances indicating the standard deviations.

The effect of distortion could not be detected with good confidence. For all runs with  $\text{NPR} > 2.2$ :  $C_d(\text{dist.}) - C_d(\text{no dist.}) = \Delta C_d = -.002 \pm .004$ . This result is not surprising if it is remembered (Fig.5a) that with distortion the total pressure profile is still rather uniform both in the tail pipe and in the exit plane. Neither does the static pressure at the inner nozzle lip show any evidence of being affected by distortion as will be shown later. In these test series 2 and 5 very few tests were performed at unchoked  $\text{NPR}$ , so the effect of ambient airflow on  $C_d$  cannot be shown in detail in these series.

Figure 8 shows the  $C_d$  values for cold air series 3 "no distortion". Here more runs have been performed at unchoked  $\text{NPR}$ , so that the influence of the ambient air stream on  $C_d$  may be shown in more detail than in series 2 and 5.

As will be shown in Section 3.4, for  $M_\infty = .8, .85$  and  $.9$  the pressure at the external nozzle lip is higher than the free stream static pressure,  $C_{p_{\text{ex}}} \approx +.15$ , while at  $M_\infty = .95$  this overpressure has almost disappeared. Hence at the lower Mach numbers the effective nozzle pressure ratio will be lower than the standard  $\text{NPR}$ , which will be reflected in the relation of  $C_d$  vs standard  $\text{NPR}$ . The dashed line in Figure 8 represents the data for  $M_\infty = .8$  to  $.9$ .

The average value and the standard deviation for the choked discharge coefficient, as determined from 21 runs with  $\text{NPR} > 2.2$  is

$$C_d = .986 \pm .004$$

so it may be concluded that the jet medium ( $\text{H}_2\text{O}_2$  decomposition products for test series 2 and 5, and cold air for series 3) did not significantly influence the discharge coefficient of this high contraction ratio nozzle. The value of the determined discharge coefficients for this nozzle for "no distortion" agrees well with the data of Reference 2, which show that a value of approximately .987 would have been expected.

The static pressure distribution along the jet pipe wall of test series 2 and 5 is shown in Figure 9. The difference between "no distortion" and "distortion" has disappeared in the downstream part of the jet pipe due to the high contraction ratio of the nozzle.

For lower  $\text{NPR}$  the results of test series 3 give more details. The ratio of the static pressure in the jet pipe at  $x/D_{\text{max}} = .063$  (nearest to the exit plane) to the jet total pressure is shown in Figure 10. Also shown are the data points with  $\text{NPR} > 2.2$ , where a correction on the  $\text{NPR}$  is applied by replacing  $p_\infty$  by the external boattail overpressure  $p_{\text{ex}}$  near the exit plane. Apparently the corrected nozzle pressure ratio correlates the data points better for the cases with and without external flow.

The thrust coefficients  $CT_1$  and  $CT_2$  vs  $\text{NPR}$  are shown in Figure 11 for the runs of test series 2 and 5 where  $M_\infty = 0$ . The thrust coefficient  $CT_2$  is most practical for engine cycle assessment, because it is related to the actual delivered mass flow and actual jet total pressure.  $CT_1 (= CT_2 \times C_d)$ , sometimes used in relevant literature) is used for reference purpose. No evident difference is seen between "distortion" and "no distortion".

$$\begin{array}{l} \text{For 11 runs } CT_1(\text{dist.}) - CT_1(\text{no dist.}) = \Delta CT_1 = -.003 \pm .007 \\ CT_2(\text{dist.}) - CT_2(\text{no dist.}) = \Delta CT_2 = +.002 \pm .005 \end{array}$$

This result may be due to the fact that these thrust coefficients take into account the measured jet total pressure, which itself is influenced by the distortion profile.

An influence of distortion might better be shown by the change of the reference thrust coefficient  $CT_3$ . This coefficient does not depend on  $p_{t_{\text{meas}}}$  or consequently on  $C_d$ , which themselves are related to the distortion profile.

$$CT_3(\text{dist.}) - CT_3(\text{no dist.}) = \Delta CT_3 = +.005 \pm .003$$

This means that a small increase in thrust may be expected if a nozzle exhausts a certain mass flow with a distorted total pressure profile vs. a flat profile.



It would have been expected that for  $NPR \approx 1.9$  thrust coefficient  $CT_1$  would have been approximately 1.005 (Reference 2,  $\eta_{abs} \equiv CT_1$  for  $NPR \approx 1.9$ ). The high values of  $CT_1$  and  $CT_2$  could not be explained since the measured thrust forces are determined sufficiently accurate to preclude the influence of scatter on the trend of the average thrust coefficients. The balance was calibrated including all known secondary effects.

For the thrust coefficients at  $M_\infty \neq 0$  the actual thrust force had to be derived from a force balance equation incorporating the measured thrust balance force, the integrated boattail pressure drag, the friction drag and the correction force due to the pressure inside the gap between forebody and afterbody. For the friction drag the values as derived from Reference 3 were adapted amounting to a friction drag coefficient, related to  $A_{ref}$ , of  $C_F = .0425$ . These values agreed with the average values obtained from force measurements of test series 2 at "jet off", particularly at the larger Mach numbers. Figure 12 shows the thrust coefficient  $CT_2$  vs.  $NPR$  for  $M_\infty \neq 0$ . The large scatter in the results can be attributed to the inaccuracies introduced by the pressure force corrections, particularly the gap force correction. The same trend however as for  $M_\infty = 0$  is indicated. The possible effects of distortion for  $M_\infty \neq 0$  are seen to submerge in the scatter:

$$\begin{aligned}\Delta CT_1 &= -.003 \pm .010 \\ \Delta CT_2 &= +.000 \pm .008 \\ \Delta CT_3 &= +.001 \pm .008\end{aligned}$$

For this large contraction ratio nozzle it appears that the effects of the jet total pressure distortion on the nozzle characteristics are of minor importance under the condition that the proper mass flow averaged total jet pressure is used.

### 3.1.3 Characteristics of Nozzle B

The larger nozzle B has only been tested with the hot decomposition products of  $H_2O_2$ . Figure 13 shows for  $M_\infty = 0$  and  $M_\infty \neq 0$  the discharge coefficients vs.  $NPR$ . Apart from the effect of the external flow at low nozzle pressure ratios the influence of distortion is clearly shown. The average values of the discharge coefficients of 12 runs for  $NPR > 2.1$  (approximately the choked pressure ratio for undistorted flow) are

$$\begin{aligned}\text{no distortion } C_d &= .978 \pm .002 \\ \text{distortion } C_d &= .946 \pm .010 \\ C_d(\text{dist.}) - C_d(\text{no dist.}) = \Delta C_d &= -.032 \pm .008\end{aligned}$$

For this nozzle with a low contraction ratio the effect of distortion is considerable. This tendency may be ascribed to the increased curvature of the sonic line at the nozzle exit due to the "hollow" velocity profile.

For a nozzle with a convergence half angle of  $4^\circ$  and a contraction ratio of 1.62 the discharge coefficient for non-distorted flow would have been expected to be slightly lower than .99 (Ref.2). The calculated discharge coefficients of nozzle B however average about one per cent lower, which may be caused by the slight amount of hollow distortion that still exists in the mass flow distribution for the "no distortion" condition and by the influence of the step in the duct wall on the internal boundary layer. It must be remarked that the results of a part of the test runs (about 12 runs with  $1.6 < NPR < 2.2$ ) show a slightly different level from the other data points. During this part of the tests the distortion valve functioned erratically due to a silver deposit from the catalyst pack. No effect on the pressure in the valve housing however could be detected. After repolishing the valve the other data points were obtained, which correlated better with results of test series 1. Figure 14 shows the ratio of the static pressure in the jet pipe close to the nozzle lip to the jet total pressure. The difference between "no distortion" and "distortion" is still clearly present.

Figures 15 and 16 show the values of  $CT_1$  and  $CT_2$  vs.  $NPR$  for both "distortion" and "no distortion" for  $M_\infty = 0$  and  $\neq 0$  respectively. Due to erratic output of the gap pressure as mentioned in the previous section, at  $M_\infty \neq 0$  rather a large scatter appears in the results. The difference in thrust coefficients, due to distortion, is

$$\begin{array}{lll}\text{for } M_\infty = 0 & \Delta CT_1 = -.036 \pm .023 & \text{and for } M_\infty \neq 0 \Delta CT_1 = -.049 \pm .009 \\ (12 \text{ runs}) & \Delta CT_2 = -.002 \pm .013 & (11 \text{ runs}) \quad \Delta CT_2 = -.010 \pm .007 \\ & \Delta CT_3 = +.024 \pm .007 & \Delta CT_3 = +.021 \pm .005\end{array}$$

the tolerance again indicating the standard deviations.

It is obvious that  $CT_1$  will show a marked influence from distortion due to the considerable change in  $C_d$  and the direct coupling with this coefficient. For comparison Figure 15 shows the reference line for  $CT_1(\text{dist.})$ , obtained from the line for  $CT_2$  (the same for both distortion and no distortion) multiplied by  $C_d(\text{dist.}, M_\infty = 0)$  from Figure 13.

$CT_3$  increases markedly if the jet flow total pressure profile is distorted. This was clearly shown on the balance readings when the distortion valve was actuated.

It is indicated that the thrust coefficient  $CT_2$  has the least tendency to change due to distortion, and hence may be used as the most characteristic coefficient for nozzle performance evaluations.

## 3.2 Mach Number Measurement

### 3.2.1 General

As mentioned in Section 2.2, an analysis of the reference Mach numbers is required. Because these Mach numbers are derived from the static pressure at the cylindrical part of the fuselage at model station 16 ( $x/D_{\max} = 3.017$ ) the possible effects of jet parameters, tunnel configuration and forebody length on this pressure will be discussed.

### 3.2.2 Effect of Jet Parameters

An analysis of the pressure distribution on the cylindrical part of the model shows that the upstream influence due to variation of jet parameters does not affect model station 14 and stations further upstream (Fig. 17). With the used method of Mach number adjustment (variation of diffuser throat) there might have been a possibility that throat area variations – necessary to allow for the additional mass flow of the jet – would counteract the upstream influences. Therefore some additional tests have been made with solid simulated jet plumes which did not require the Mach number readjustments as necessary for the real jets. Results of these tests are also presented in Figure 17.

Although the plotted points show some scatter there are no systematic variations. It is concluded therefrom that variation of jet parameters does not affect the reference Mach number.

### 3.2.3 Effect of Tunnel Configuration

The partially open transonic test section had closed side walls. The top wall had an open ratio of 11.1%. The open ratio of the bottom wall has been changed after the first test series from 40.7% (further referred to as test section I) to 11.1% (test section II). Figure 18 shows that this variation of bottom wall open ratio has a considerable effect on the axial pressure distribution on the model. Circumferential pressure distributions show that the flow on the model is essentially axisymmetric for both test sections. Therefore the changes of the axial pressure distribution are attributed to changing wall interference effects. This means that the reference Mach numbers from the two test sections are not comparable. Therefore mainly test results obtained in test section II have been presented. Only the test results presenting the influence of boundary layer thickness (Section 3.5) have been obtained with test section I.

### 3.2.4 Effect of Forebody Length

Figure 19 shows axial pressure distributions on the cylindrical part of the model for the two forebody lengths as used in the tests. This figure illustrates that variation of forebody length causes a small change of the pressure at model station 18. This pressure change indicates that the reference Mach number depends slightly on forebody length.

## 3.3 Jet-Off Boattail Pressure Measurements

### 3.3.1 Effect of Mach number

Figure 20 shows the effect of Mach number on the boattail pressure distributions (nozzle A). Schlieren photographs of the flow are presented in Figure 21. At  $M_{\infty} = .85$  weak shocklets appear just downstream of the boattail shoulder indicating the presence of a small region of sonic flow. At higher Mach numbers a shock wave occurs causing the steep pressure rise at  $x/D_{\max} \approx .8$  (Fig. 20). Furthermore the Schlieren photographs indicate that boundary layer separation occurs on the rear part of the boattail at  $M_{\infty} = .90$  and  $M_{\infty} = .95$ .

A comparison of pressure distributions on nozzle A and nozzle B is presented in Figure 22 showing that the differences are very small. The general trends are the same for both nozzles.

Boattail pressure drag as function of Mach number is given in Figure 23 for both nozzles, the bands enclosing 95% of all data points.

### 3.3.2 Effect of Boattail Surface Temperature

A comparison of jet-off pressure distributions obtained during the hot jet test series and the cold jet test series reveals that for nozzle A the boattail surface temperature systematically affects the recompression on the rear part of the boattail. Typical examples of this effect are shown in Figures 24 and 25. Increasing surface temperature causes the boattail pressures to decrease which might be explained by decreasing boundary layer stability.

It should be noticed that the "hot model" results have been measured a few seconds after a hot jet measurement. This means that the model temperature gradually decreases during the jet off measurement due to natural cooling. Moreover the model temperature has been measured at only one position on the model ( $x/D_{\max} = .056$ ) and only at the end of the measurement. Therefore a quantitative analysis of this effect has not been possible in the present test series. It can only be concluded that the rather limited increase of the measured surface temperature already causes a clearly different boattail pressure distribution. Therefore a more detailed study of this temperature effect is required.

### 3.4 Jet-On Boattail Pressure Measurements

#### 3.4.1 Effect of Nozzle Pressure Ratio

Figures 26 through 29 show the effect of nozzle pressure ratio on boattail pressure distribution for  $M_{\infty} = .80$ ,  $M_{\infty} = .85$ ,  $M_{\infty} = .90$  and  $M_{\infty} = .96$  respectively. These data have been obtained with hot jets and nozzle A. All figures show the same trends, i.e. increasing boattail pressures with increasing nozzle pressure ratio. These trends are also found with cold jets (e.g. Figure 30). These test results indicate that jet displacement (increasing surface pressures with increasing nozzle pressure ratio due to increasing jet plume angle) is dominating jet entrainment in the range of the present measurements.

The effect of nozzle pressure ratio on boattail pressure distribution as measured with nozzle B is presented in Figures 31 and 32 for  $M_{\infty} = .79$  and  $M_{\infty} = .89$  respectively. The trends observed from these figures are the same as for nozzle A, except that for the larger nozzle the influence of NPR is more pronounced.

It should be noticed that the jet effects are limited to the rear part of the model at  $M_{\infty} = .89$  due to the region of supersonic flow near the boattail shoulder. At  $M_{\infty} = .79$  no such supersonic flow exists and jet effects are felt further upstream.

The effect of nozzle pressure ratio on boattail pressure drag is presented in Figures 33 through 35.

#### 3.4.2 Effect of Jet Distortion

The effect of jet distortion on boattail pressure drag is illustrated in Figures 36 and 37 for nozzle A and nozzle B respectively. Figure 36 shows that for nozzle A no significant effects of distortion are found. This result is not surprising, however, because distortion is not very pronounced with nozzle A (see Figure 5a).

With nozzle B the distortion is more effective (Fig. 5b). In this case it appears that the boattail pressure drag is affected by jet distortion at  $M_{\infty} = .80$  (Fig. 37) only. At  $M_{\infty} = .90$  and  $M_{\infty} = .95$  no effect is found. It is rather surprising that the separated boundary layers as occur at the higher two Mach numbers are not affected by a variation of jet entrainment (due to jet distortion) whereas at  $M_{\infty} = .8$  when no separation seems to occur (cf. Section 3.3.1), the effect is significant for all nozzle pressure ratios tested (Fig. 38), except for the lowest NPR ( $= 1.67$ ). In this case the outer part of the distorted exhaust flow is subcritical vs. supercritical for the other cases. This effect of distortion is also indicated by the external pressures, Figure 39. At  $M_{\infty} = .90$  the pressure distribution is unaffected by distortion, Figure 40.

#### 3.4.3 Effects of Jet Temperature

A comparison of boattail pressure distributions for hot and cold jets is presented in Figures 41 and 42. Both figures show that the pressure distributions on the boattail differ markedly for hot and cold jets. Generally these changes of boattail pressure distribution are considered to be caused by two phenomena:

- change of jet displacement,
- change of jet entrainment.

A simple prediction based on isentropic Prandtl/Meyer expansion suggests that jet plume angle (jet displacement) is larger for the hot jet due to the lower value of  $\gamma$ . This is confirmed by Schlieren photographs of the jets.

The jet entrainment, itself being of less importance than the plume shape effect, would be expected to be lower for the hot jets than for the cold jets (Ref. 4). Because both increasing jet displacement and decreasing jet entrainment tend to cause a pressure rise on the boattail one would expect that for the hot jets boattail pressures would be higher than for the cold jets, giving lower drag. This expected trend is only partly supported by the measured pressure distribution (Figures 41 and 42) which show that just downstream of the boattail shoulder the pressures are higher for the hot jets. However, at the downstream end of the boattail the pressures for the hot jets are about equal or even lower than the pressures for the cold jets. This might be explained by the effect of boattail surface temperature as described in Section 3.3.2. Because during hot jet measurements the boattail surface temperature is considerably higher ( $T_1 \approx 500$  K) than during the measurements described in Section 3.3.2, a marked decrease of boattail pressures may be expected due to this surface temperature effect.

The resulting boattail pressure drag for the hot jets is compared with boattail pressure drag for cold jets in Figures 43 and 44 for  $NPR \approx 3$  and  $NPR \approx 4$  respectively.

With  $NPR \approx 4$  boattail pressure drag is about equal for hot and cold jets indicating that the jet temperature effect (decreasing drag) is compensated by the opposite boattail temperature effect (Fig. 44). With  $NPR \approx 3$  it appears from Figure 43 that the boattail temperature effect is even stronger than the jet temperature effect at  $M_{\infty} = .85$  and  $M_{\infty} = .9$  which may be due to earlier flow separation on the hot boattail (for jet off conditions flow separation starts at  $M_{\infty} = .9$ , cf. Section 3.3.1). From these results it is concluded that the present measurements are not suitable to make a quantitative analysis of jet temperature effects.

### 3.5 Boundary Layer Effects

In the present test series boundary layer effects have been studied by varying forebody length. Figure 45 shows the measured boundary layer velocity profiles for both the short ( $L/D_{\max} = 10.63$ ) and long models ( $L/D_{\max} = 15$ ).

Some characteristic data of the boundary layer are summarized in Table III. It should be noted that the boundary layer profiles have been measured on a cold model and without a jet. Because during hot jet measurements model surface temperature rises approximately 60 deg C at the model station where the profiles have been measured, one should be careful when using the presented boundary layer data for an analysis of hot jet test results.

The influence of forebody length on boattail pressure drag is illustrated in Figure 46 both for jet-off conditions and for a nozzle pressure ratio of approximately 2 (hot jet). This figure shows that in both cases an increase of forebody length causes the pressure drag to decrease at  $M_{\infty} = .9$  and at  $M_{\infty} = .96$  whereas at  $M_{\infty} = .85$  no significant effect is found. Typical examples of boattail pressure distribution for long and short forebodies are shown in Figures 47 and 48.

### 3.6 Tunnel Wall Interference

As indicated in Section 3.2 measured reference Mach numbers cannot be related to free stream conditions due to the relatively large model blockage. Because of the large model length the corrections required to obtain interference-free data (solid blockage and wake blockage correction, e.g. Reference 5) do not merely consist of a Mach number correction. Further correction terms are necessary which vary in axial direction.

Although it has been demonstrated in Section 3.2.1 that variation of jet parameters (wake blockage) had no effect on the forebody it is possible that the wake blockage effects on the boattail are changing.

To get some more information on these wall interference effects, pressures have been measured on a solid tunnel side wall during the cold jet test series. Some typical examples of wall pressure distribution are presented in Figures 49 and 50.

Figure 49 shows that tunnel wall pressures are very sensitive to Mach number which consequently indicates that blockage effects depend also on Mach number.

Figure 50 presents the effect of nozzle pressure ratio on tunnel wall pressure distribution indicating that wake blockage effects will also depend slightly on nozzle pressure ratio. Both figures show that the pressure variations measured on the tunnel wall are much smaller than the variation measured on the model. Because wall pressures are induced by model pressures, this indicates that flow field disturbances at the model are damped out rapidly when moving away from the model. Because the blockage effects on the model are in an analogous way related to the tunnel wall pressures, it seems reasonable to assume that pressure changes on the model due to varying blockage effects are again much smaller than the wall pressure variations. This would mean that the measured trends of Mach and jet effects on the boattail pressure distribution are valid. However these data cannot be used as absolute due to wall interference.

## 4. CONCLUSIONS

- A method using a standardized mass flow distribution was developed to determine the mass flow averaged jet total pressure from mass flow, static pressure and temperature in the jet pipe. The results of this method agreed with values derived from total pressure rake measurements.
- For nozzle A with a contraction ratio of 3.24 the following characteristics were determined, the tolerances indicating the standard deviations:

The choked discharge coefficient for a hot jet consisting of decomposed  $H_2O_2$ , without distortion

$$C_d = .988 \pm .004$$

For a hollow distorted total pressure profile in the jet pipe the discharge coefficient decreased

$$.002 \text{ to } C_d = .986 \pm .005$$

For cold air, no distortion,

$$C_d = .986 \pm .004$$

These results show that for this nozzle the influence of jet medium and distortion on the discharge coefficient was small.

The effect of ambient airstream on the discharge coefficient resulted in lower values for  $C_d$  in the case of unchoked nozzle pressure ratios.

The thrust coefficients were found to be higher than expected, and no clear difference was found between values for jet pipe flows with and without distorted total pressure profiles.

- The characteristics of nozzle B with a contraction ratio of 1.62 were more clearly influenced by distortion

$$C_d (\text{no dist.}) = .978 \pm .002$$

$$C_d (\text{dist.}) = .946 \pm .010$$

Ambient airflow lowered the discharge coefficients for unchoked nozzle pressure ratios.

The net thrust forces for the same mass flow were higher for the distorted flow, resulting in higher values of the reference thrust coefficient  $CT_j$ , for "no distortion" and "distortion". The thrust coefficient  $CT_j$  was found to be least sensitive to distortion.

- The obtained data for the boattail pressures cannot be used as absolute, due to the relatively large blockage ratio of the used model/test section combination. It is argued however that the measured trends are valid.
- The defined Mach number was found to depend slightly on test section configuration and model forebody length, but was not influenced by the nozzle pressure ratio.
- For both afterbodies it was found that increasing the Mach number changed the afterbody pressure distribution, resulting in higher pressure drag coefficients. Increasing the nozzle pressure ratio decreased the afterbody pressure drag, nozzle B being more sensitive than nozzle A.
- For "jet off" higher model temperatures were found to decrease the pressures on the rear part of the boat-tail, causing increasing pressure drag.
- For nozzle A the use of hot or cold jet medium caused a rather small difference in afterbody pressure distribution due to the opposing effects of the jet temperature and the model surface temperature. A further investigation of this effect is recommended.
- The influence of distortion on the boattail pressure distribution was not significant for nozzle A, for nozzle B at  $M_\infty = .8$  the hollow distortion decreased the pressure on the rear part of the boattail, resulting in pressure drag.
- Thickening the fuselage boundary layer by increasing the forebody length for the model with nozzle A decreased the pressure drag.

## 5. REFERENCES

1. Jaarsma, F. *Experimental Determination of Nozzle Characteristics and Nozzle Airframe Interference*. AGARD-LS-53, 1972.
2. Hardy, J.M.  
Dutouquet, L. *Etude de l'écoulement dans un éjecteur transonique*, l'Aéronautique et l'Astronautique No.47, 1974.
3. Smith, K.G. *Methods and Charts for Estimating Skin Friction Drag in Wind Tunnel Tests with Zero Heat Transfer*, A.R.C. C.P. 824, 1956.
4. Compton, W.B. *An Experimental Study of Jet Exhaust Simulation*, AGARD Conference Pre-Print No.150, 1974.
5. Garner, H.C.  
et al. *Subsonic Wind Tunnel Wall Corrections*, AGARDograph 109, 1966.

TABLE I

Co-ordinates of Boattail Contour and Position of Pressure Orifices and Thermocouples

## 1a 15° Boattail Ordinates

$x/D_{\max}$	$r/D_{\max}$
0	.2075
.025	.2155
.050	.2245
.075	.23475
.100	.24575
.125	.2568
.150	.2678
.175	.2788
.200	.2888
.212	end of nozzle B
.225	.2988
.250	.3085
.275	.3180
.300	.3275
.325	.3368
.350	.3458
.400	.3630
.425	.3718
.450	.3500
.475	.3580
.500	.3958

$x/D_{\max}$	$r/D_{\max}$
.525	.4033
.550	.4108
.575	.4178
.600	.4248
.625	.4313
.650	.4375
.675	.4435
.700	.4499
.725	.4543
.750	.4595
.775	.4645
.800	.4695
.825	.4743
.850	.4788
.875	.4828
.900	.4863
.925	.4898
.950	.4928
.975	.4953
1.000	.4978

$x/D_{\max}$	$r/D_{\max}$
1.025	.4990
1.050	.5000
3.000	.5000

## 1b Internal Geometry of Nozzles

	Nozzle A	Nozzle B
$x/D_{\max}$	$r/D_{\max}$	$r/D_{\max}$
1.513	.366	.366
1.124	.366	.366
1.014	.343	.343
.516	.314	.314
.212		.287
.179	.226	
0	.204	



## Id Internal Model Pressures

$x/D_{\max}$	$\varphi$
.063	270
.125	270
.154	270
.204	270
.435	45
.505	45
.545	45
.635	45
.745	45
.845	45
1.025	45
1.265	45
1.385	45
1.515	45
1.515	135
1.515	225
1.515	315

## Ie Thermocouples

$x/D_{\max}$	$\varphi$	
.056	225	external
.997	225	external
3.017	225	external
1.490	60	internal

If

total pressure rake in jet pipe at  $\frac{x}{D_{\max}} = 1.515$  ,  
dividing the cross section in 9 equal areas



TABLE II

## Survey of Test Series

Series	1	2	3	4	5
$M_\infty$	0	0, 0.8 - 0.95	0, 0.8 - 0.95	0, 0.8 - 0.95	0, 0.8 - 0.95
jet medium, $T_t$ , K	$H_2O_2$ , 630	$H_2O_2$ , 630	Air, 290	$H_2O_2$ , 630	$H_2O_2$ , 630
$R$ , $\frac{m^2}{s^2 K}$	390	390	287	390	390
$\gamma$	1.30	1.30	1.40	1.30	1.30
NPR	1.8 - 4.6	0, 1.9 - 4.6	0, 1.1 - 4.4	0, 1.3 - 3.3	0, 1.7 - 4.5
contr. ratio $A_{jp}/A_n$	1.62 - 3.24	3.24 (A)	3.24 (A)	1.62 (B)	3.24 (A)
body length	—	short + long	short	short	short
tunnel bottom wall, % open	—	40.7	11.1	11.1	11.1
$Re_{D_{max}}$ ( $\times 10^6$ )	—	1.6 - 2.1	1.6 - 2.1	1.6 - 2.1	1.6 - 2.1
balance thrust range N	90 - 300	100 - 400	—	100 - 500	100 - 400

TABLE III

Summary of Boundary Layer Characteristics at  $x/D_{max} = 2.91$ 

$M_\infty$ (—)	$Re_D$ (—)	$\delta^*$ (mm)	$\theta$ (mm)	
.806	$1.74 \times 10^6$	.97	.61	short fuselage $L/D_{max} = 10.63$
.854	$1.89 \times 10^6$	.99	.60	
.915	$1.91 \times 10^6$	1.09	.64	
.943	$2.09 \times 10^6$	1.14	.66	
.804	$1.63 \times 10^6$	1.25	.79	long fuselage $L/D_{max} = 15$
.857	$1.90 \times 10^6$	1.25	.78	
.907	$2.00 \times 10^6$	1.29	.78	
.963	$2.09 \times 10^6$	1.36	.80	

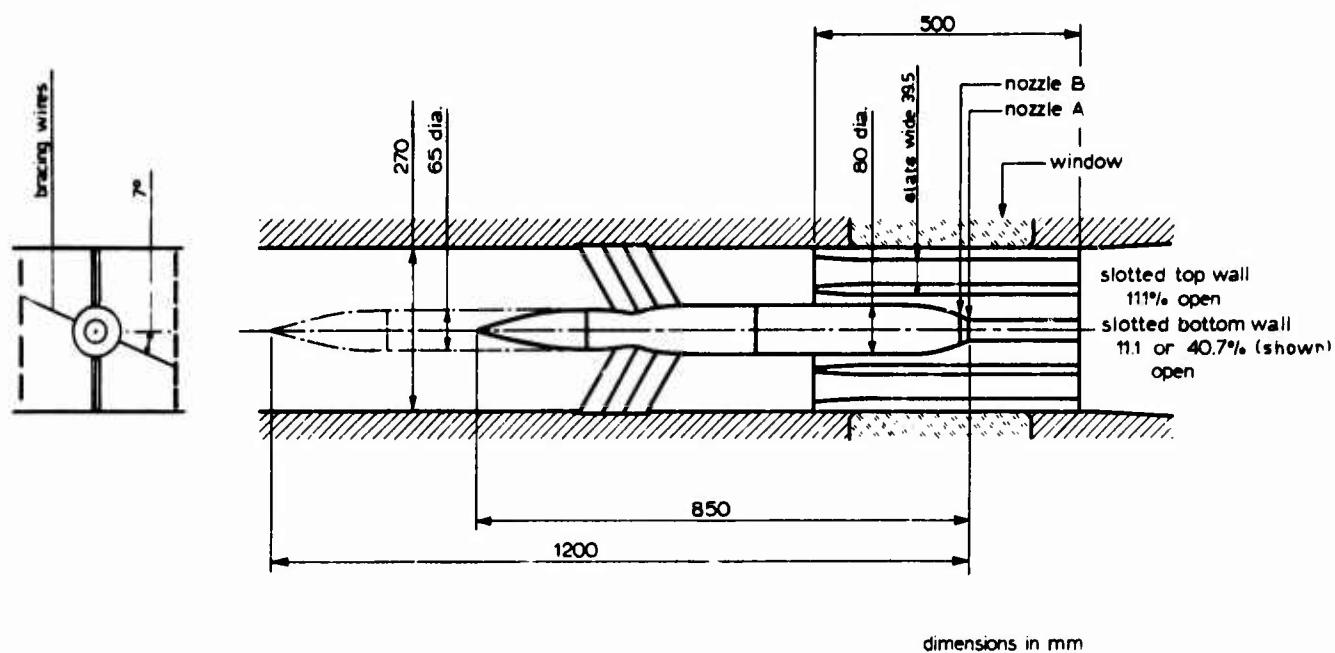


Fig.1 Sketch of the model in the wind tunnel

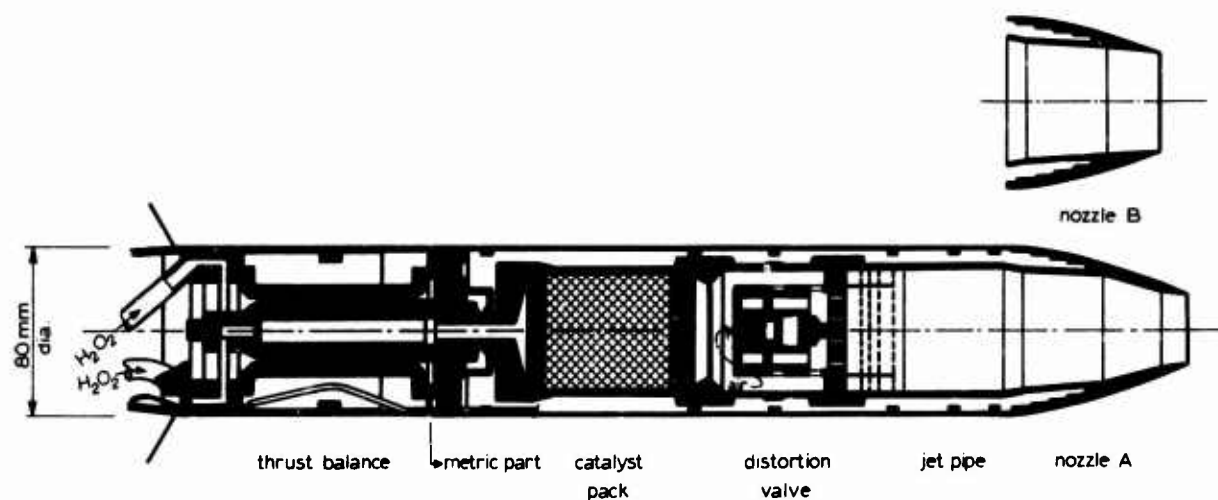


Fig.2 Main features of model

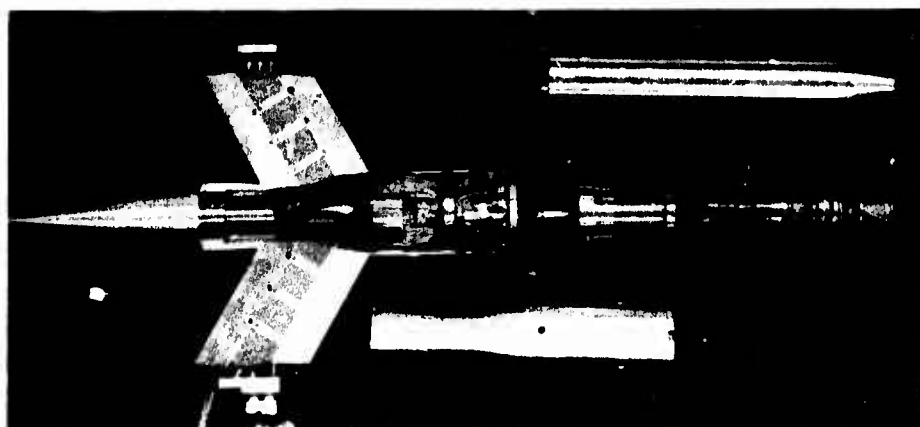


Fig.3 Exploded view of model with afterbody A

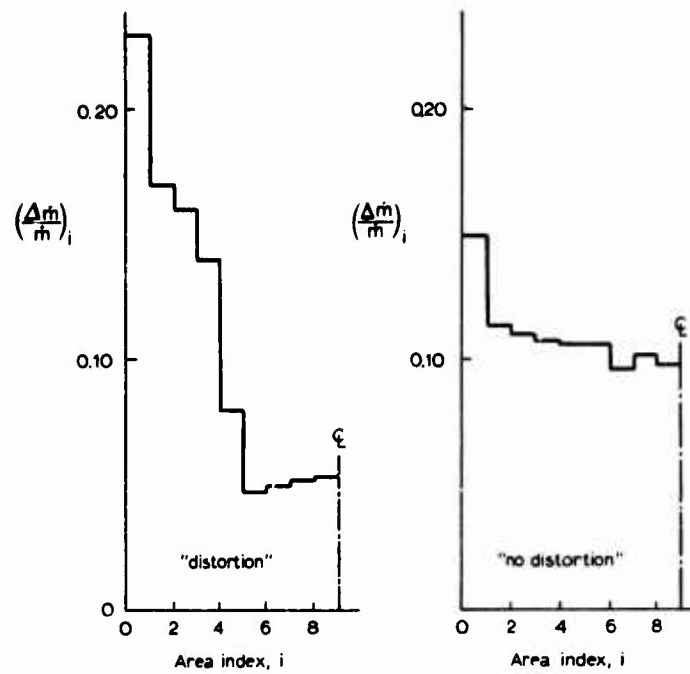
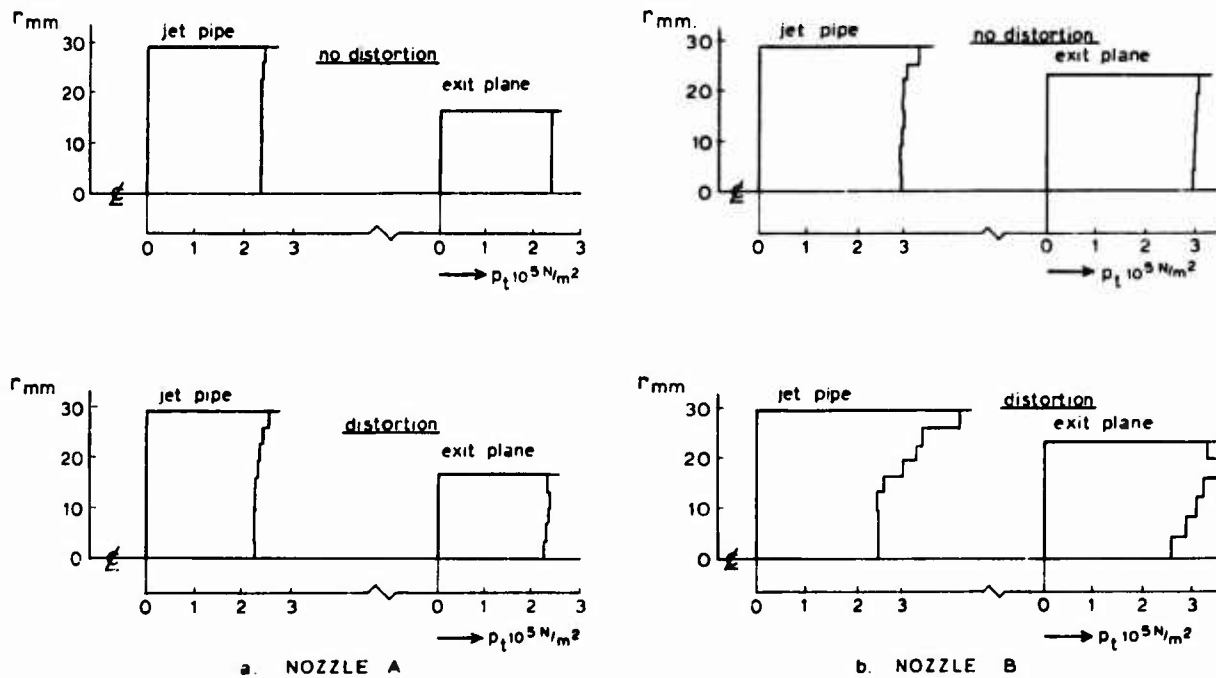


Fig.4 Standardized mass flow distribution in the jet pipe

Fig.5 Examples of the total pressure profiles in the jet pipe at  $x/D_{\max} = 1.515$  and in the exit plane

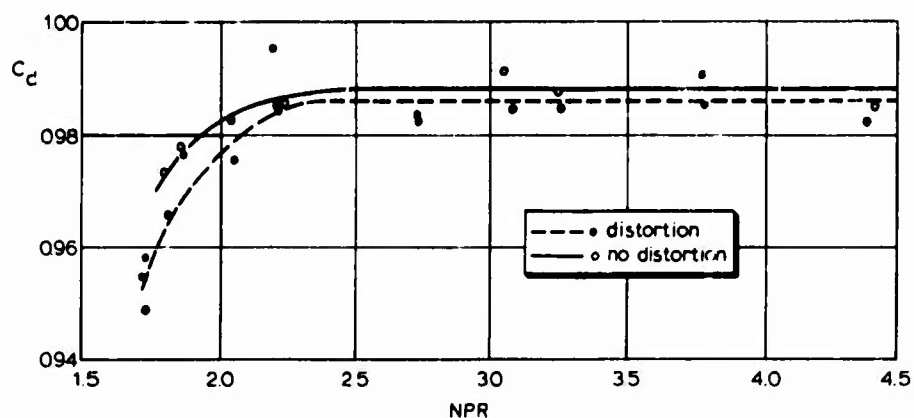


Fig.6 Discharge coefficient vs. NPR at  $M_{\infty} = 0$ , hot jet, nozzle A, series 2 and 5

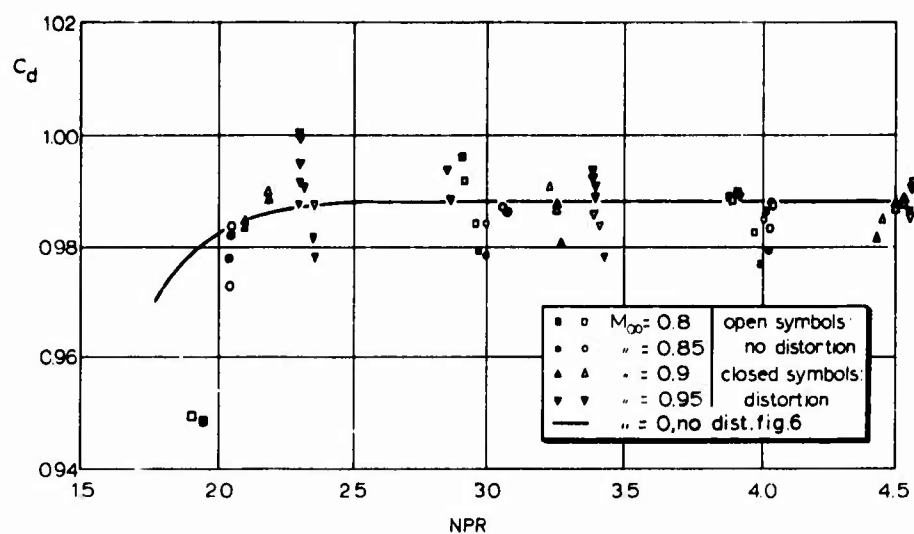


Fig.7 Discharge coefficient vs. NPR for nozzle A at  $M_{\infty} \neq 0$  for long and short forebody, hot jet, series 2 and 5

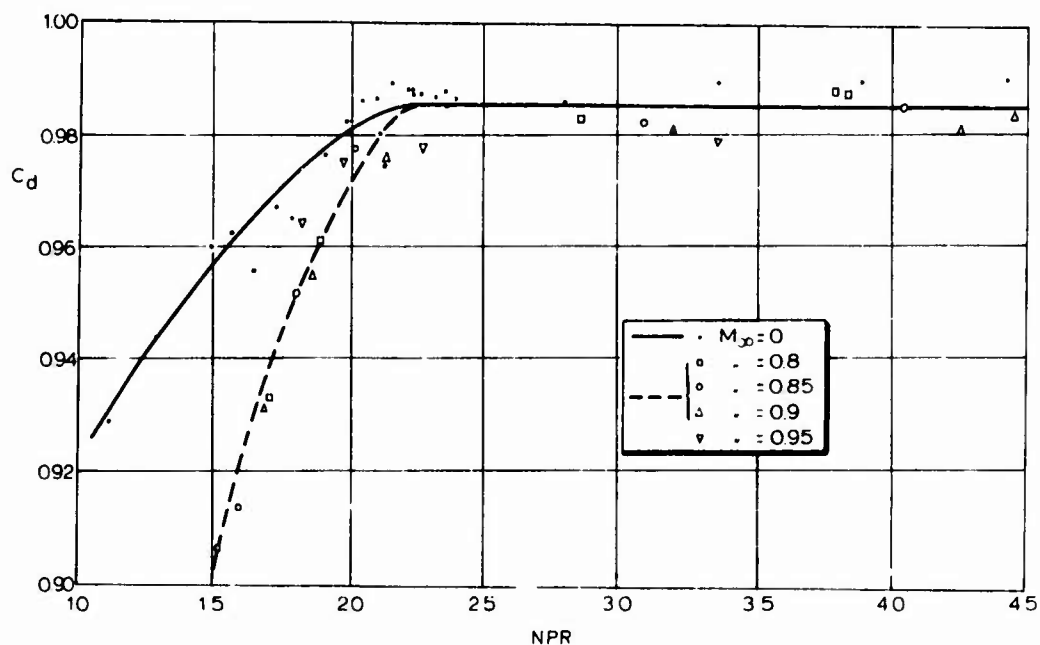


Fig.8 Nozzle discharge coefficient vs. NPR for cold air tests, no distortion, nozzle A

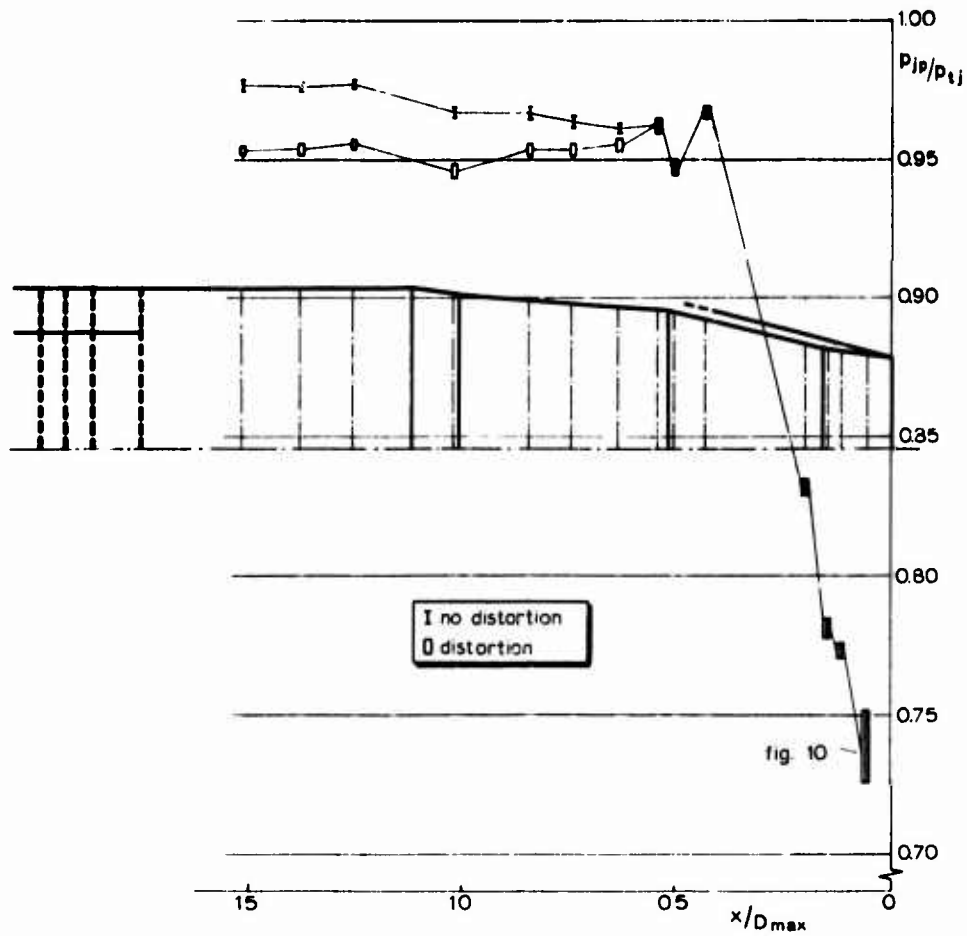


Fig.9 Jet pipe static pressure distribution for NPR's  $> \sim 2$ , nozzle A, series 2 and 5

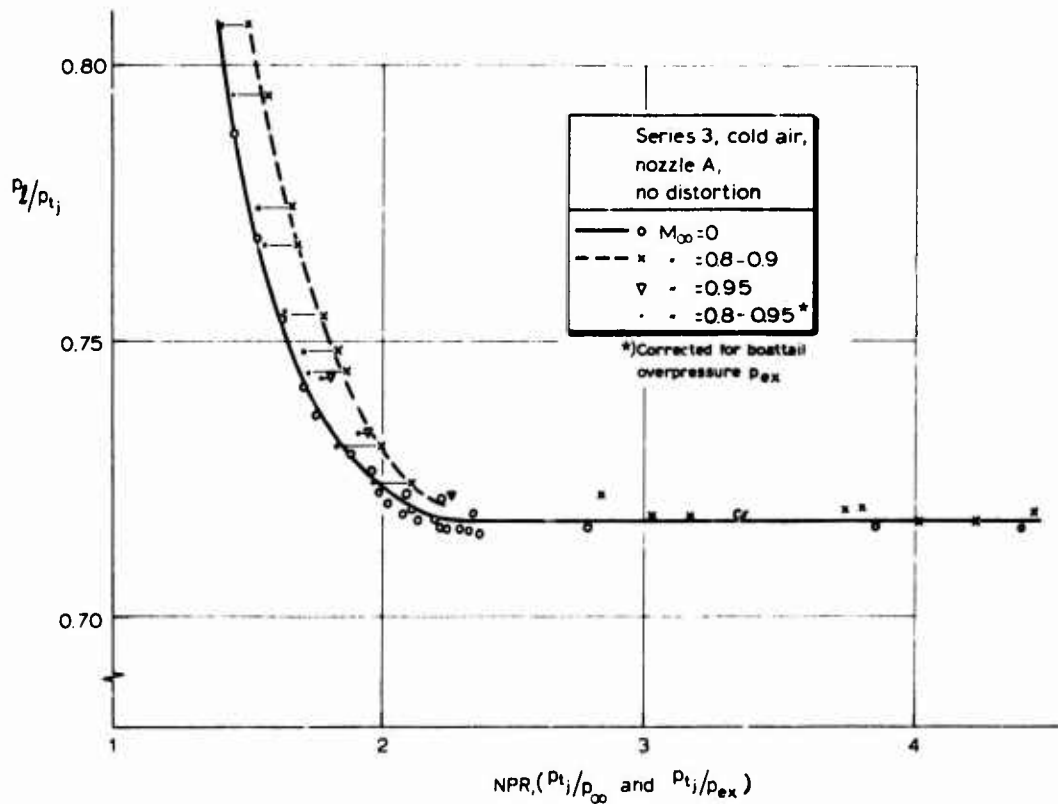
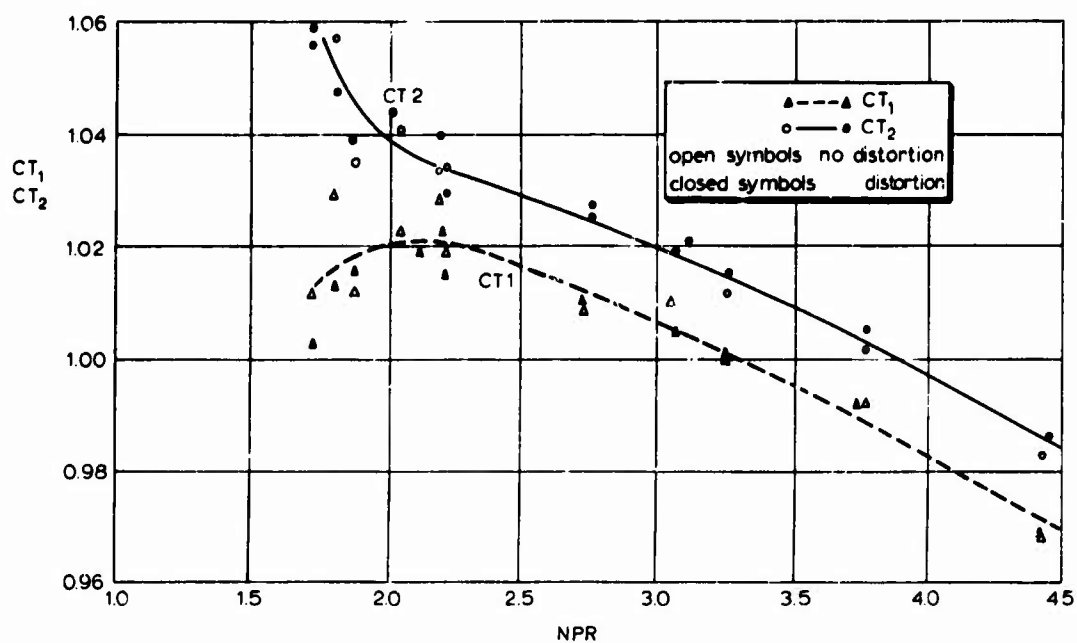
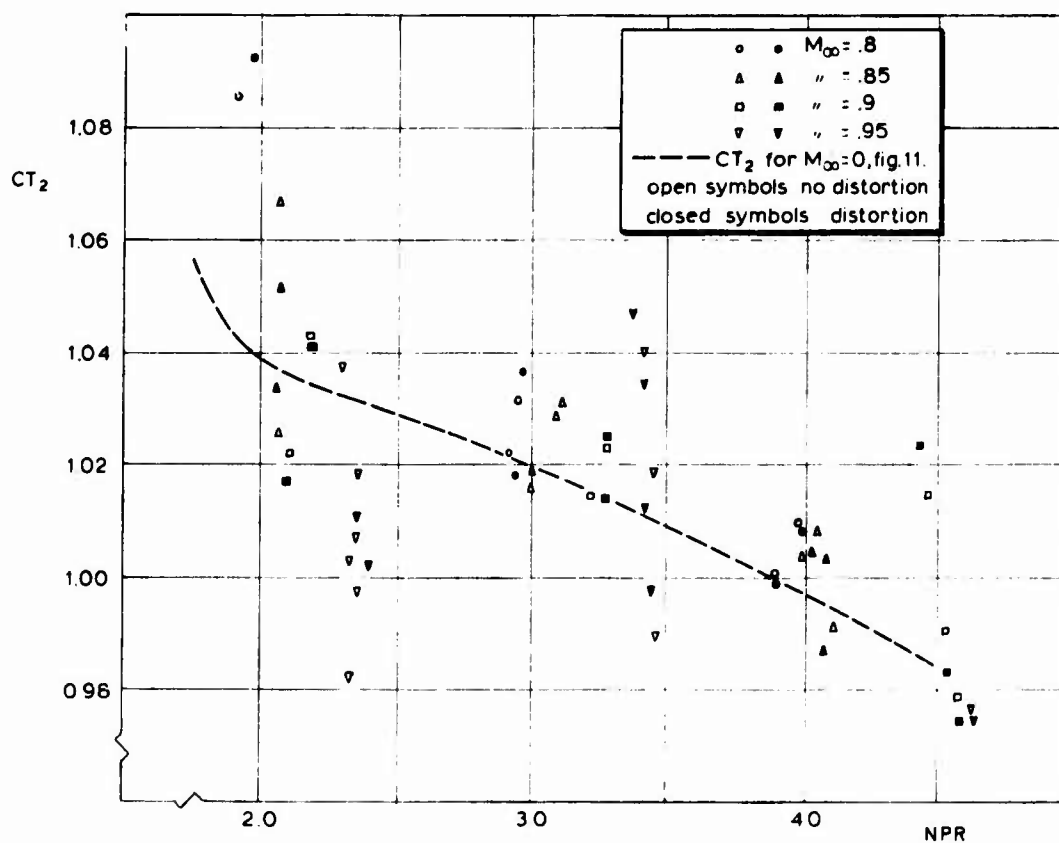


Fig.10 Static pressure in jet pipe near nozzle exit plane vs. pressure ratio

Fig.11 Thrust coefficients vs. NPR for nozzle A, hot jet, for  $M_\infty = 0$ Fig.12 Thrust coefficient vs. NPR for nozzle A, hot jet at  $M_\infty \neq 0$

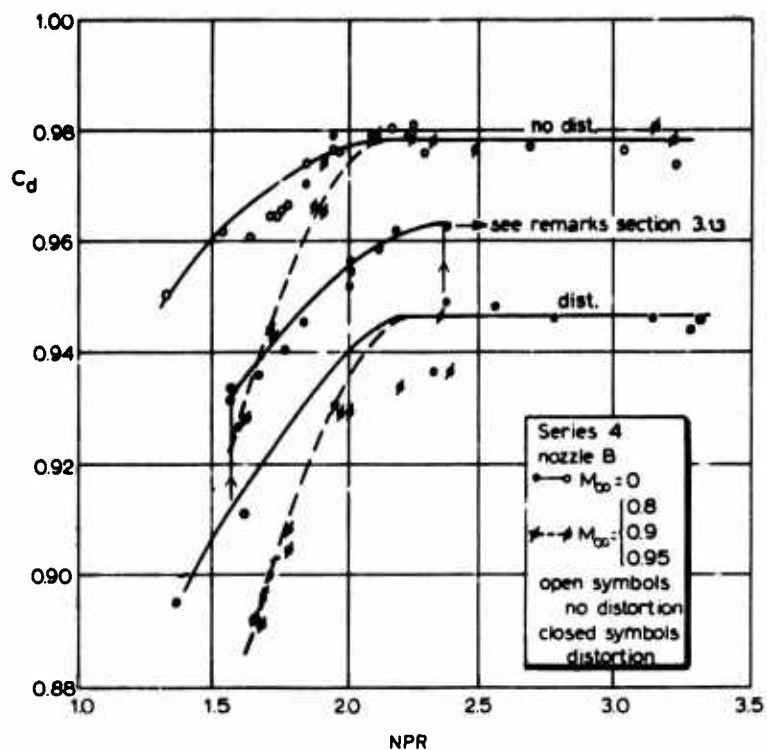


Fig.13 Discharge coefficients of nozzle B vs. NPR

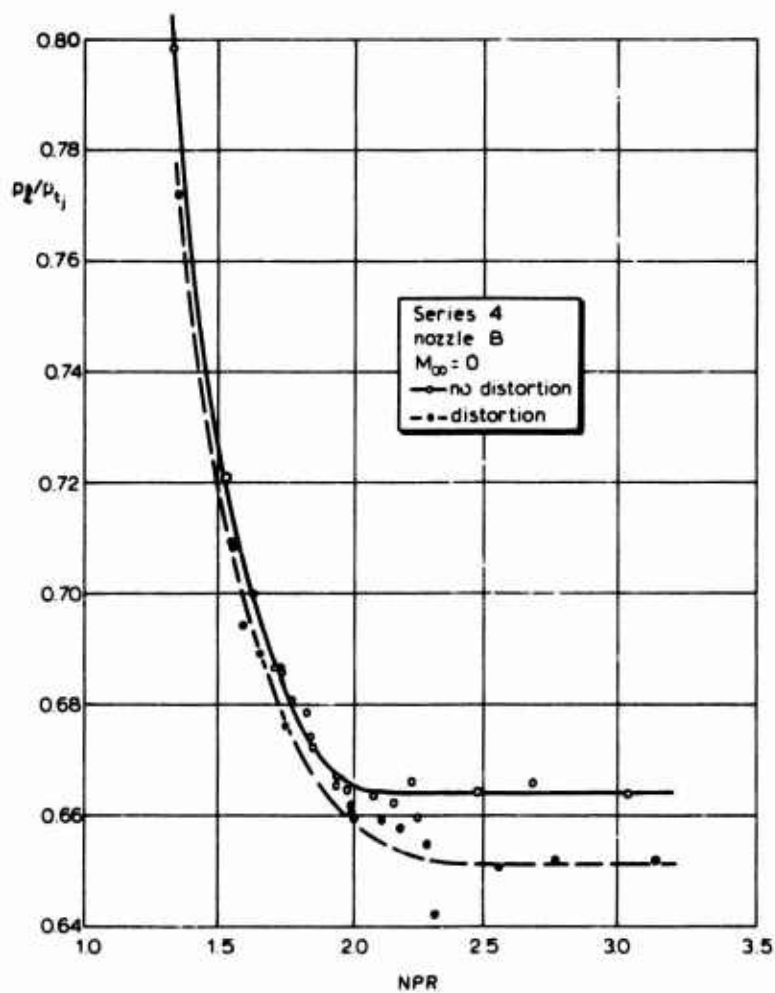


Fig.14 Ratio of static pressure near nozzle exit to jet total pressure vs. NPR for nozzle B

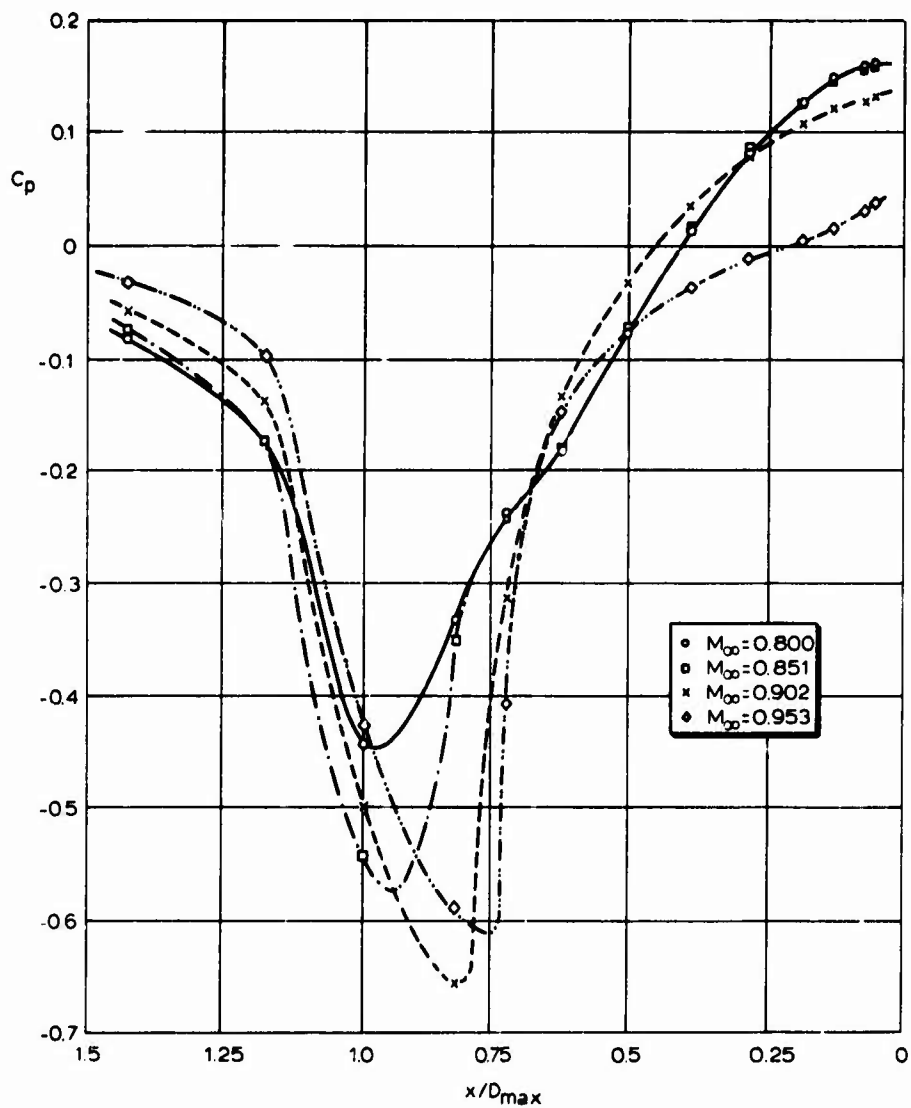
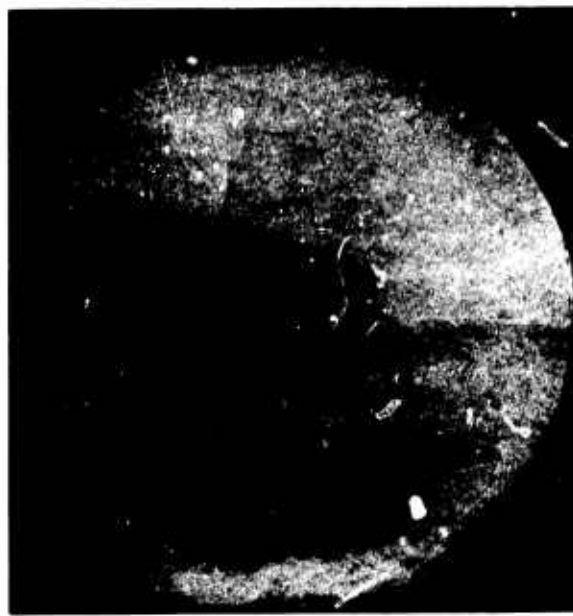


Fig.20 Mach number influence on boattail pressure distribution (nozzle A, jet off)





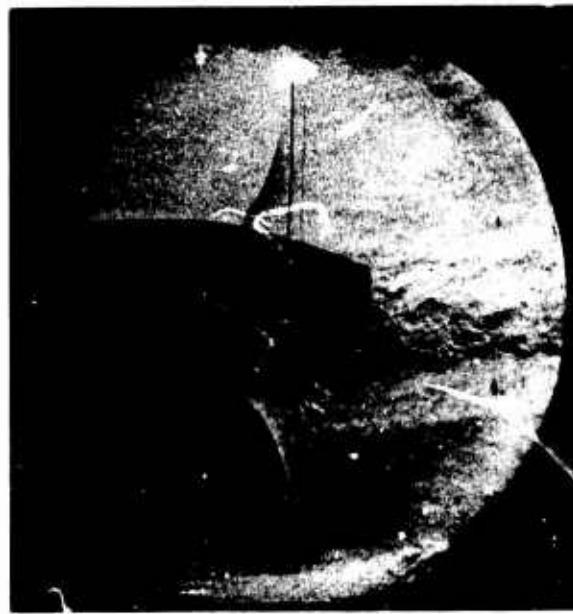
a.  $M_{\infty}=0.80$



b.  $M_{\infty}=0.85$



c.  $M_{\infty}=0.90$



d.  $M_{\infty}=0.96$

Fig.21 Schlieren photographs of the flow over the boattail (nozzle A, jet off)

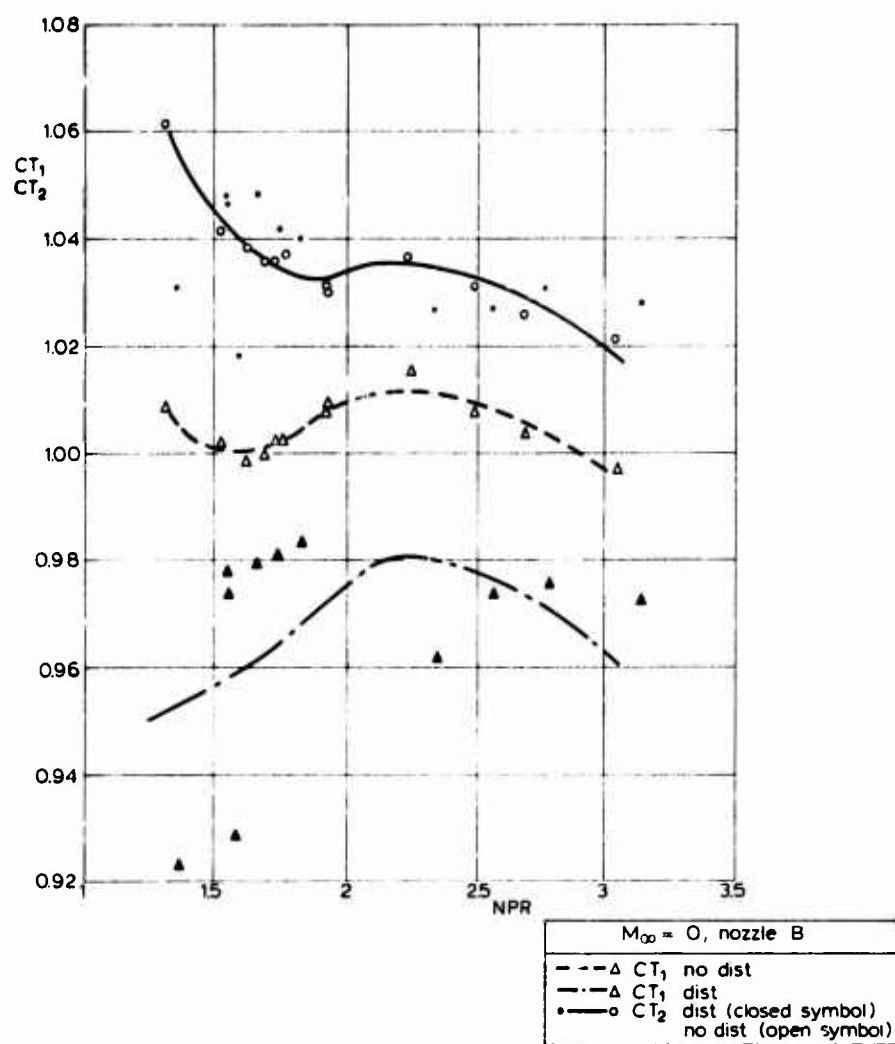
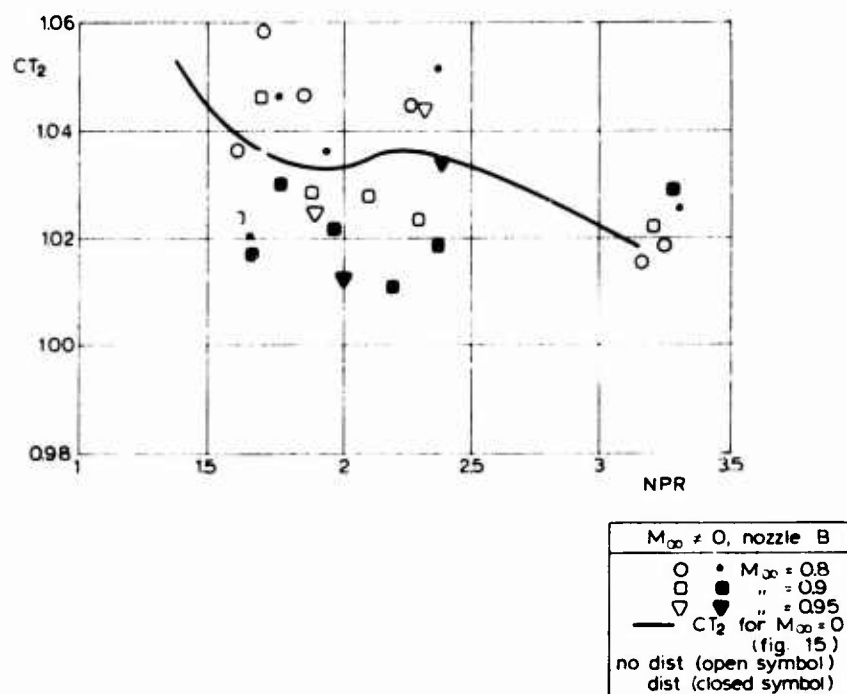


Fig.15 Thrust coefficients vs. NPR for nozzle B, hot jet

Fig.16 Thrust coefficients  $CT_2$  vs. NPR for nozzle B for  $M_\infty \neq 0$

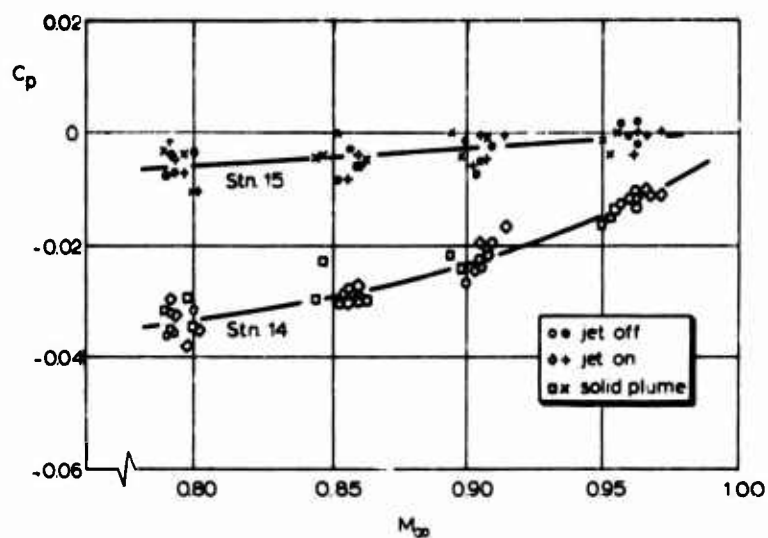


Fig.17 Upstream influence of the jet on pressures on the cylindrical part of the model

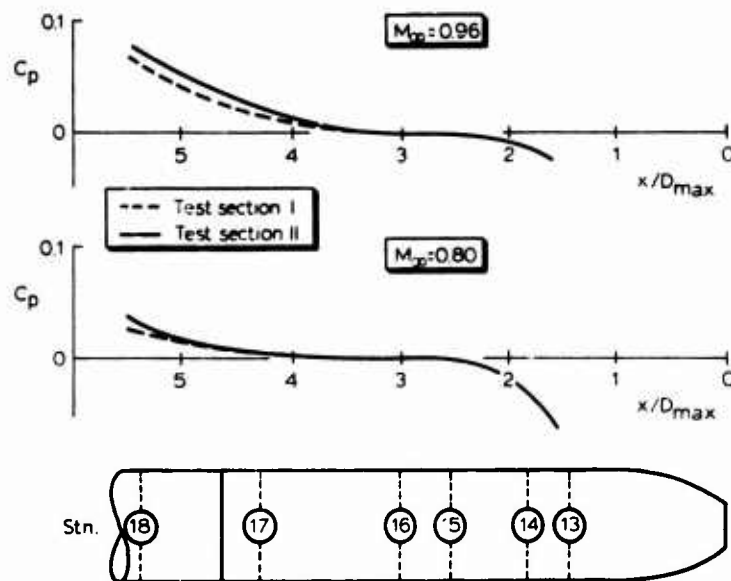


Fig.18 Effect of tunnel configuration on the axial pressure distribution along the cylindrical part of the model

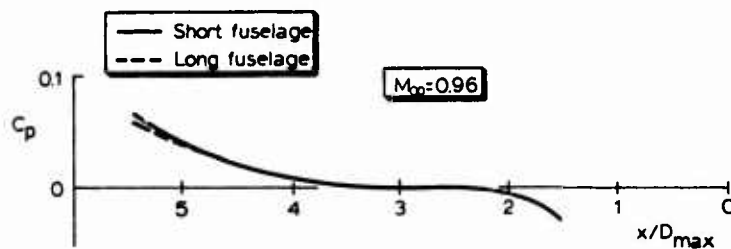


Fig.19 Effect of forebody length on the axial pressure distribution along the cylindrical part of the model

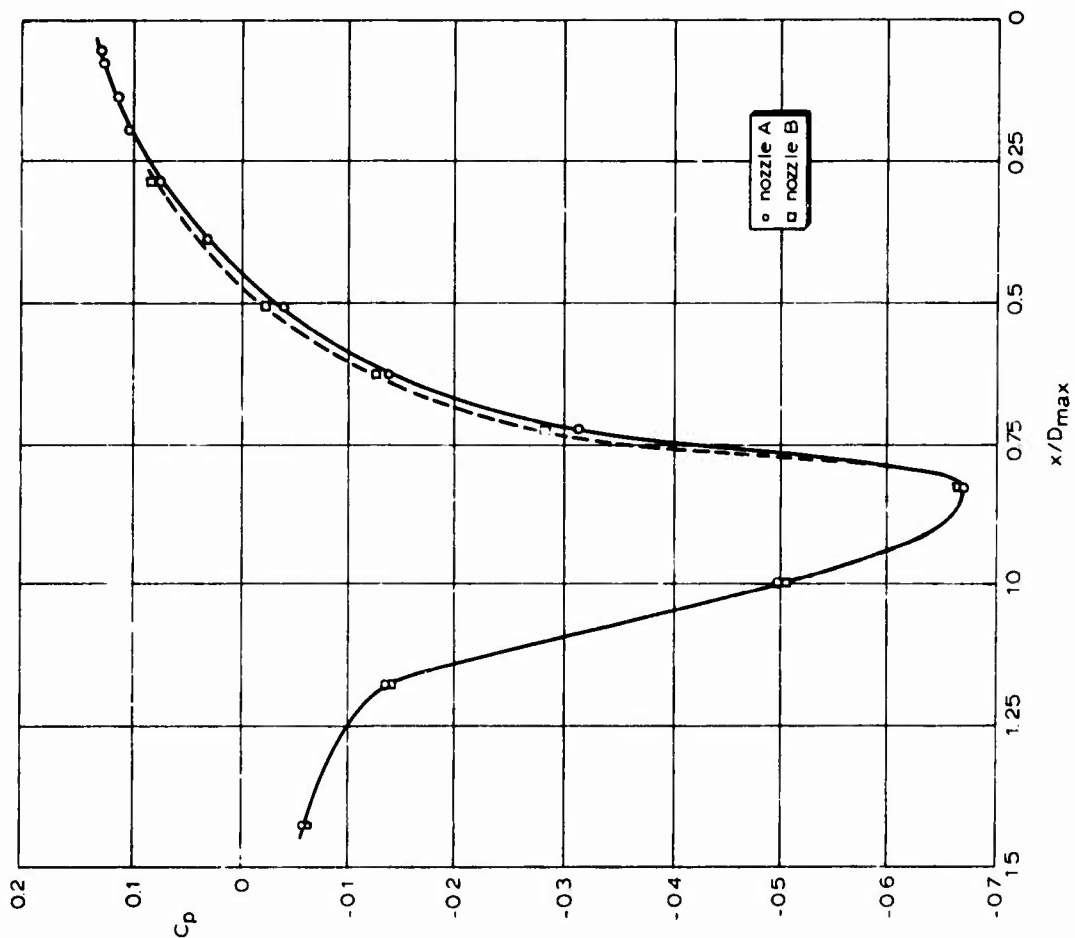


Fig.22 Comparison of boattail pressure distribution on nozzle A and nozzle B for  $M_\infty = 0.900$  (jet off)

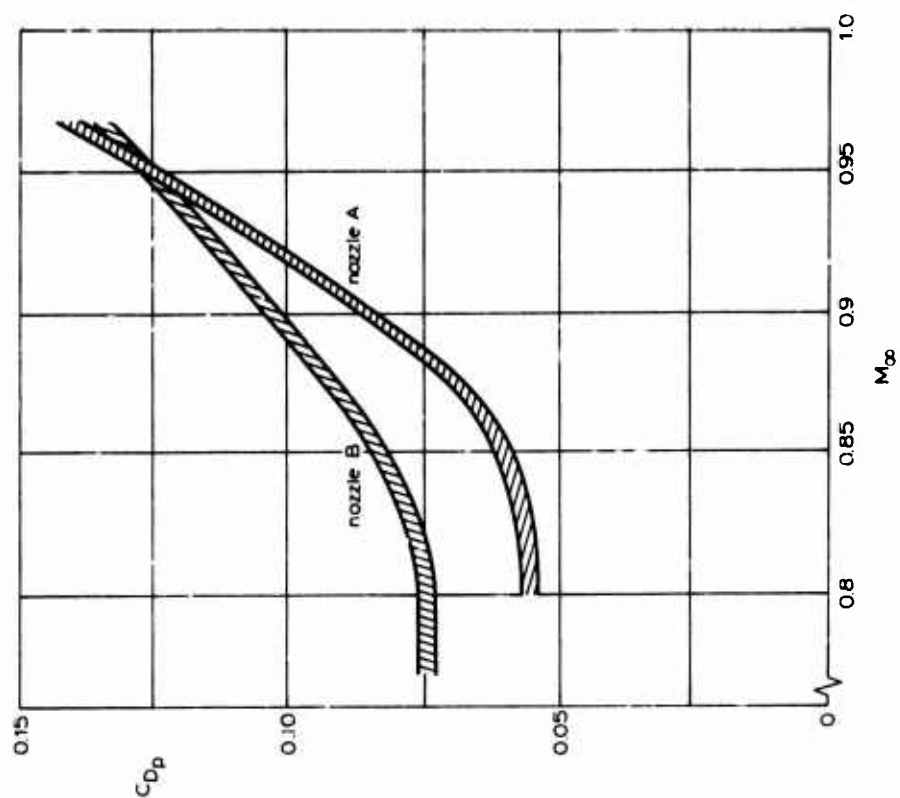


Fig.23 Boattail pressure drag coefficient as a function of Mach number (jet off)

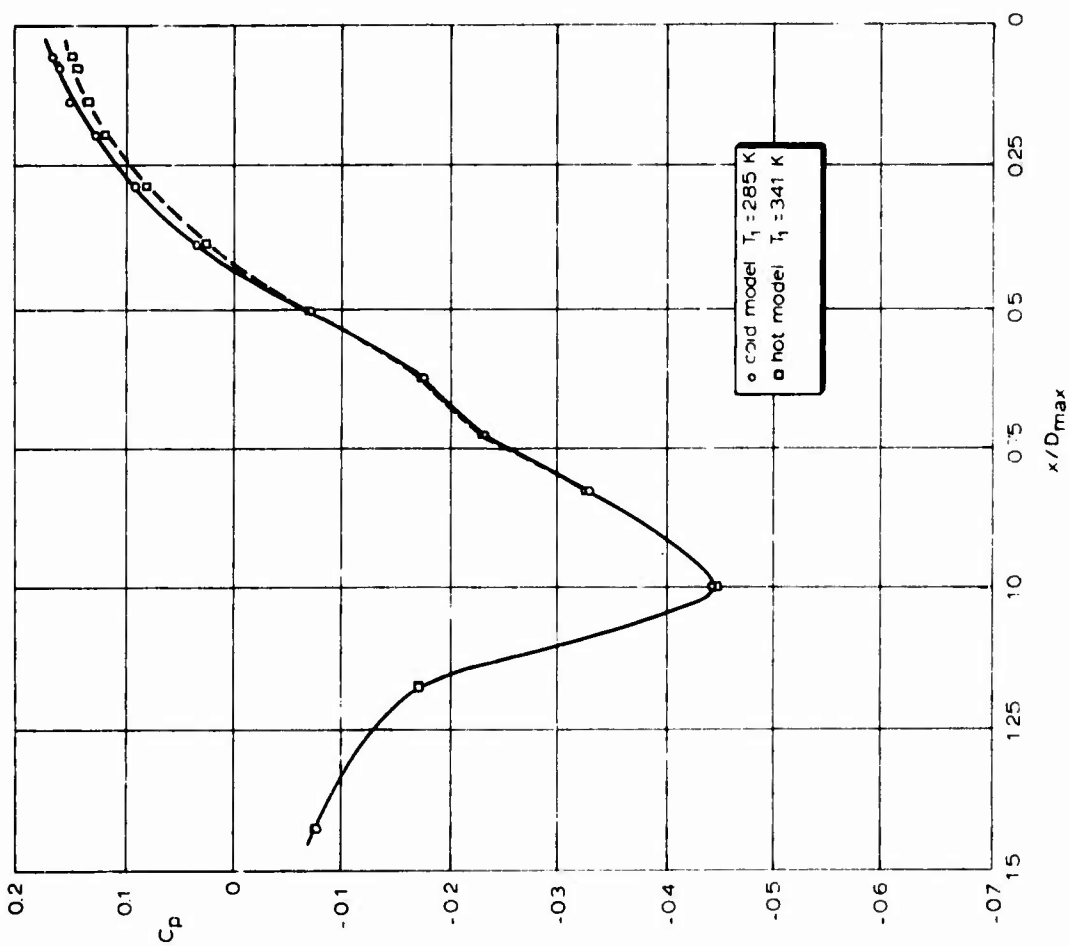


Fig. 24 Effect of model surface temperature on boattail pressure distribution  
(nozzle A, jet off,  $M_\infty = 0.80$ )

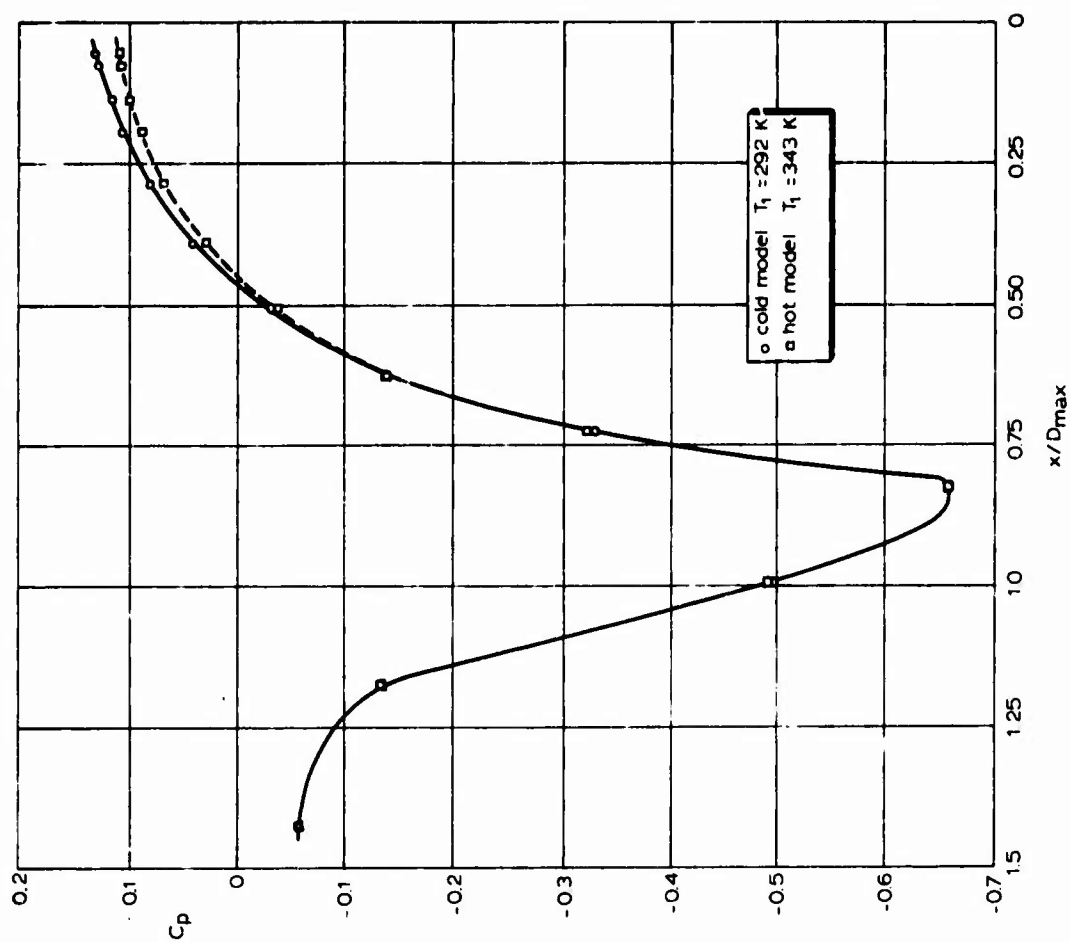


Fig. 25 Effect of model surface temperature on boattail pressure distribution  
(nozzle A, jet off,  $M_\infty = 0.90$ )

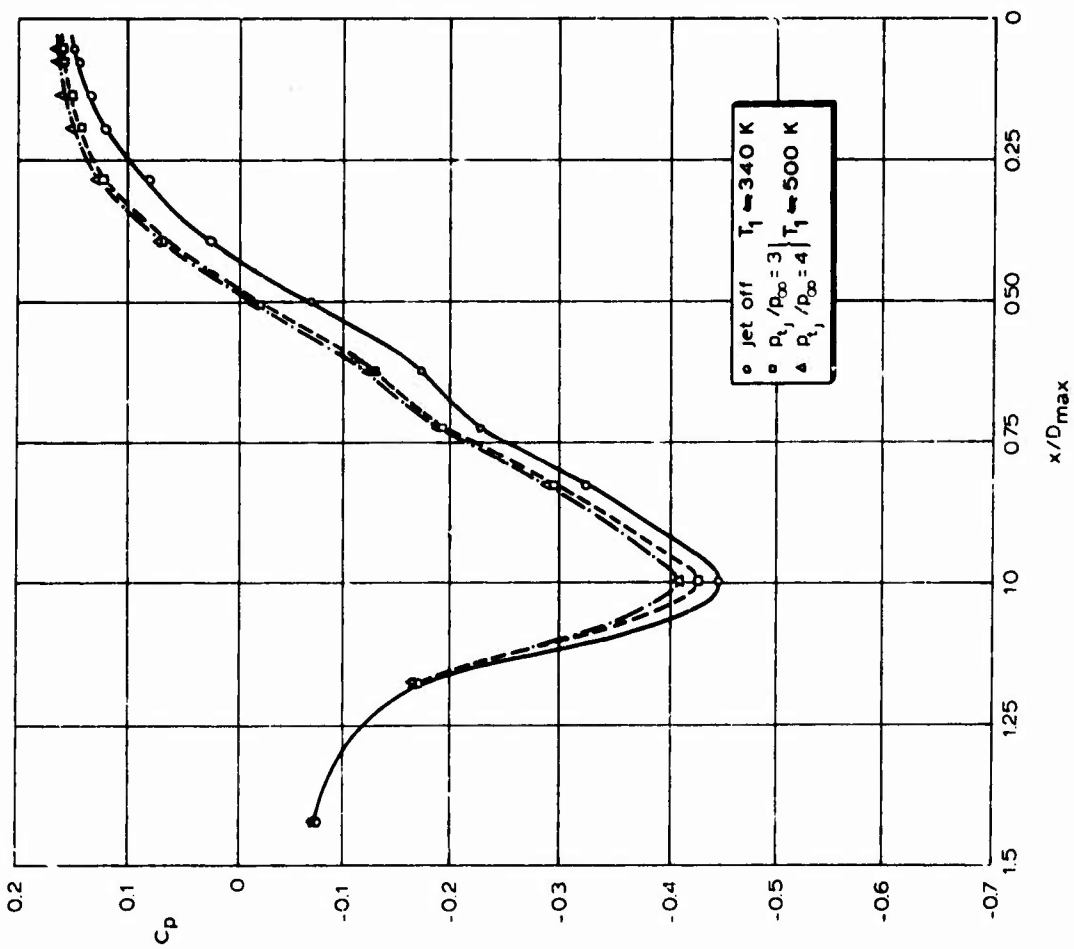


Fig. 26 Effect of nozzle pressure ratio on boattail pressure distribution at  $M_\infty = 0.800$  (nozzle A, hot jet)

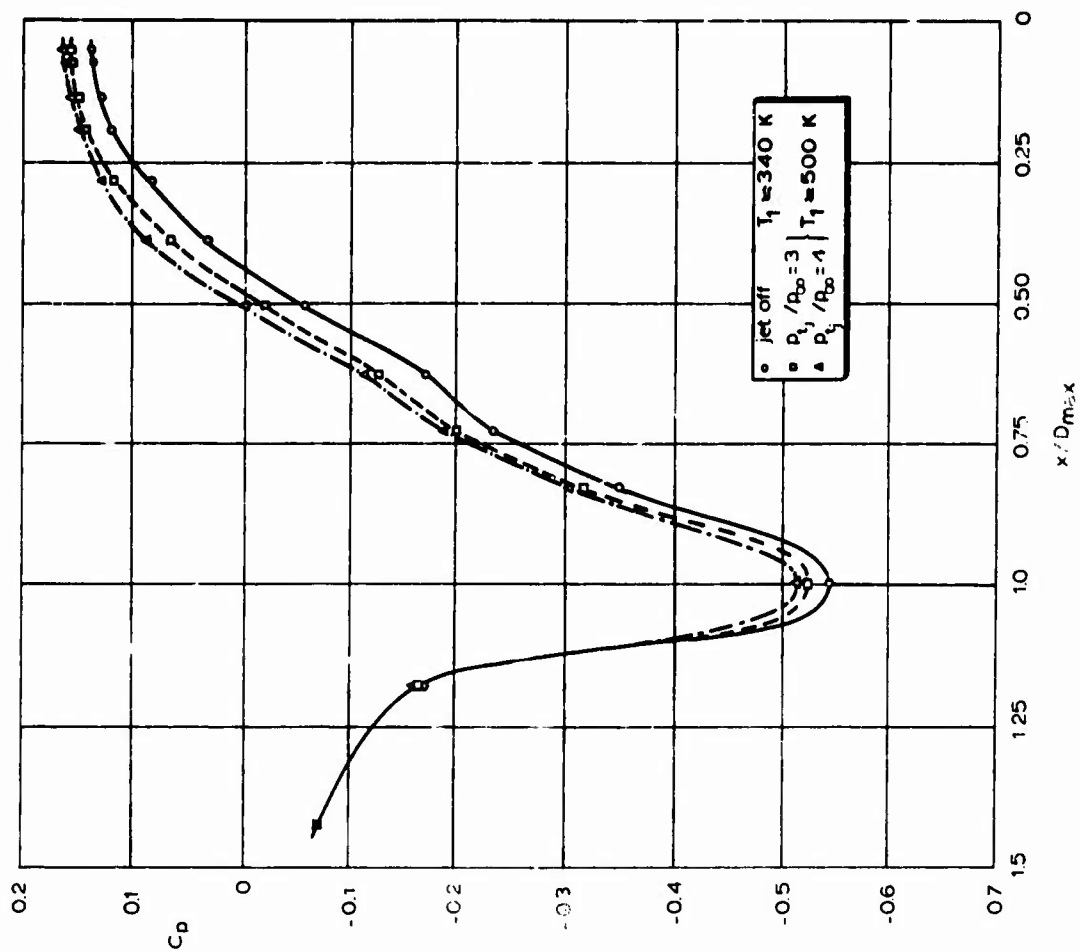


Fig. 27 Effect of nozzle pressure ratio on boattail pressure distribution at  $M_\infty = 0.850$  (nozzle A, hot jet)

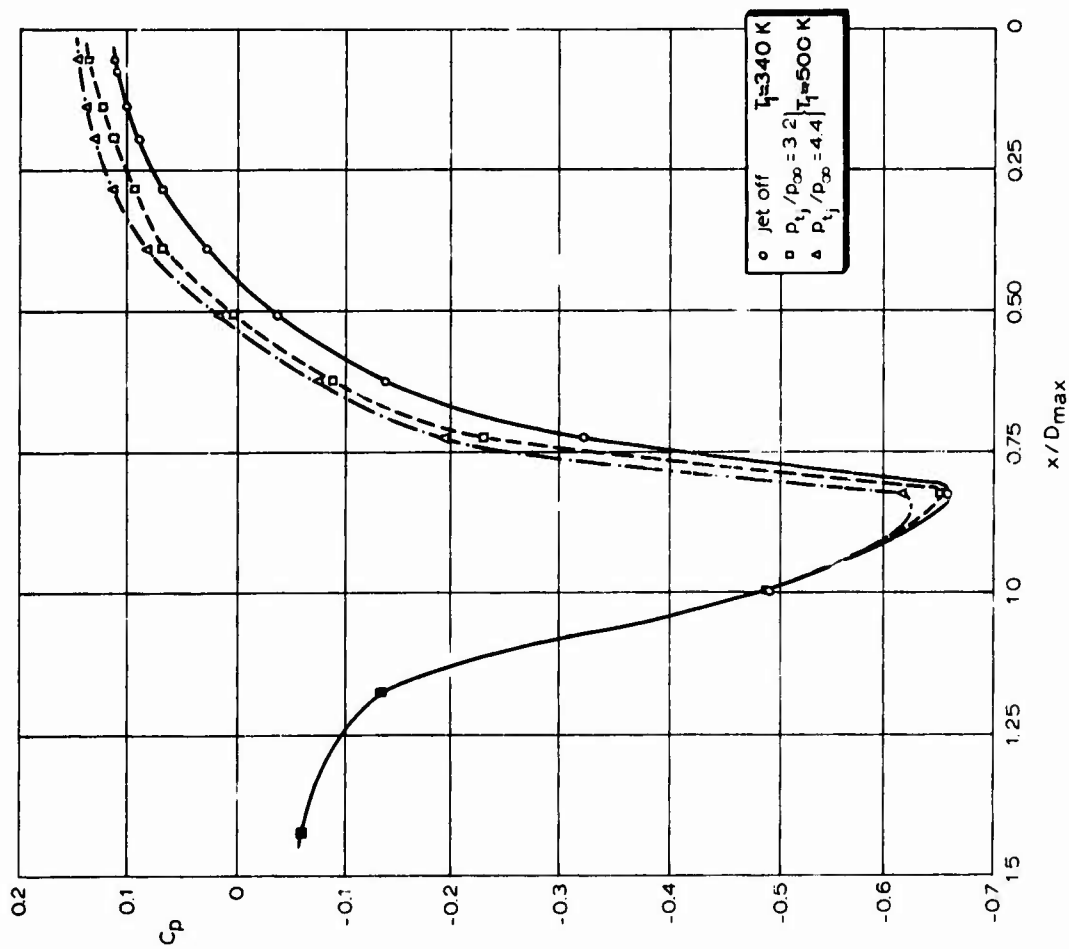


Fig.28 Effect of nozzle pressure ratio on boattail pressure distribution at  $M_\infty = 0.905$  (nozzle A, hot jet)

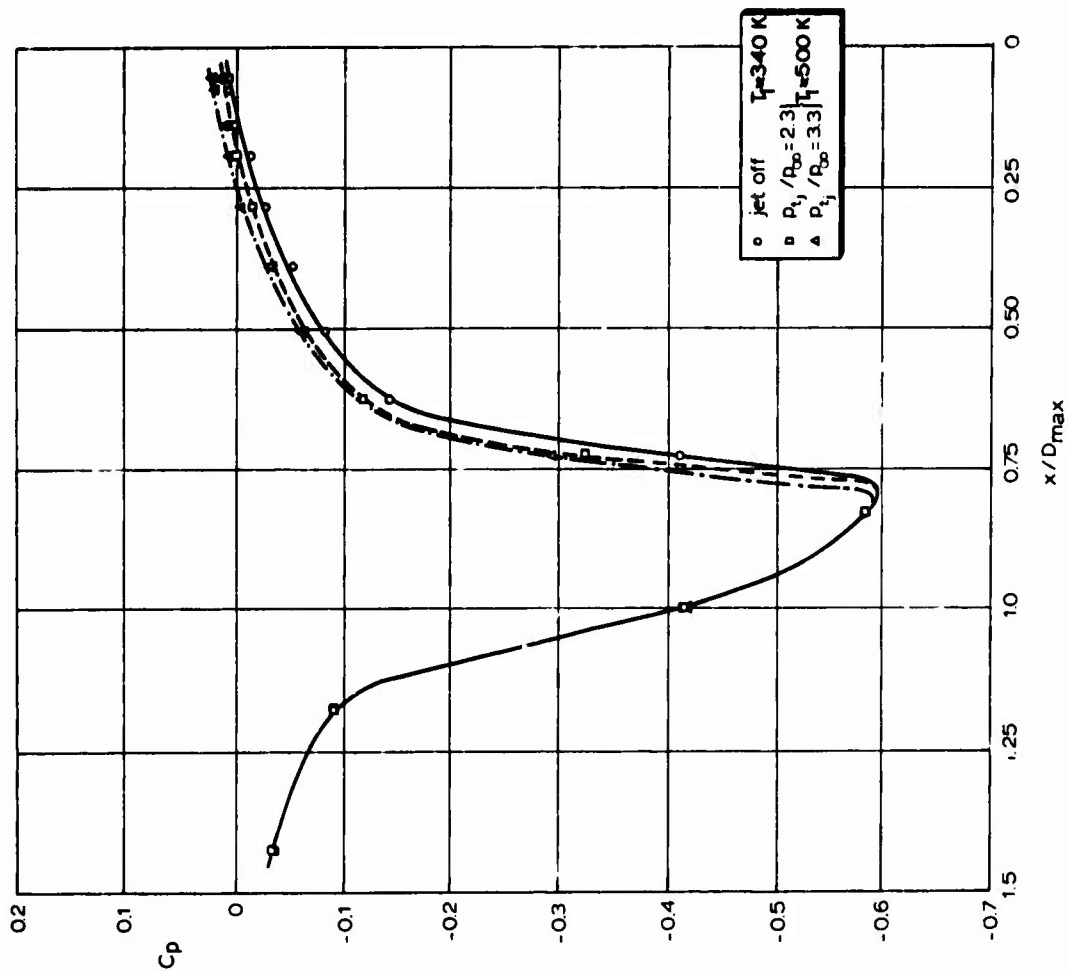


Fig.29 Effect of nozzle pressure ratio on boattail pressure distribution at  $M_\infty = 0.960$  (nozzle A, hot jet)

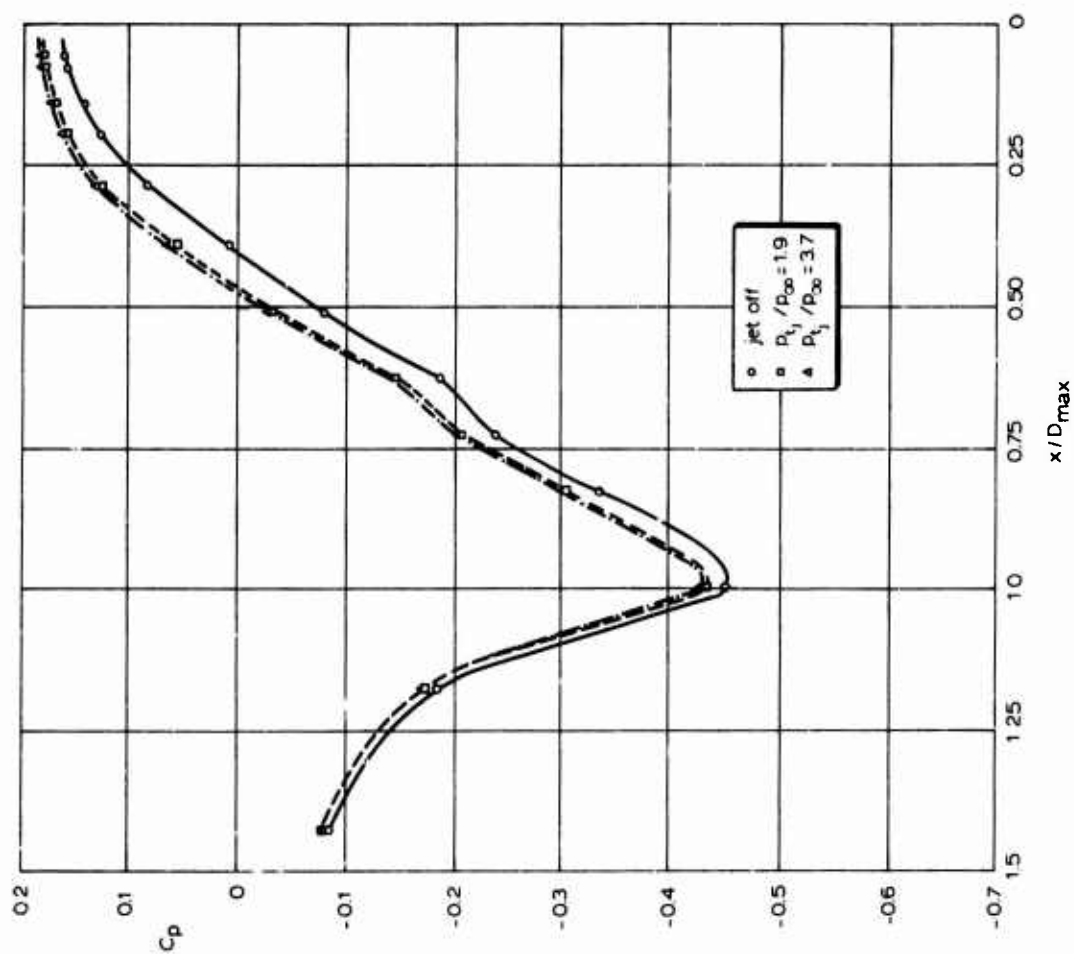


Fig.30 Effect of nozzle pressure ratio on boattail pressure distribution at  $M_\infty = 0.80$  (nozzle A, cold jet)

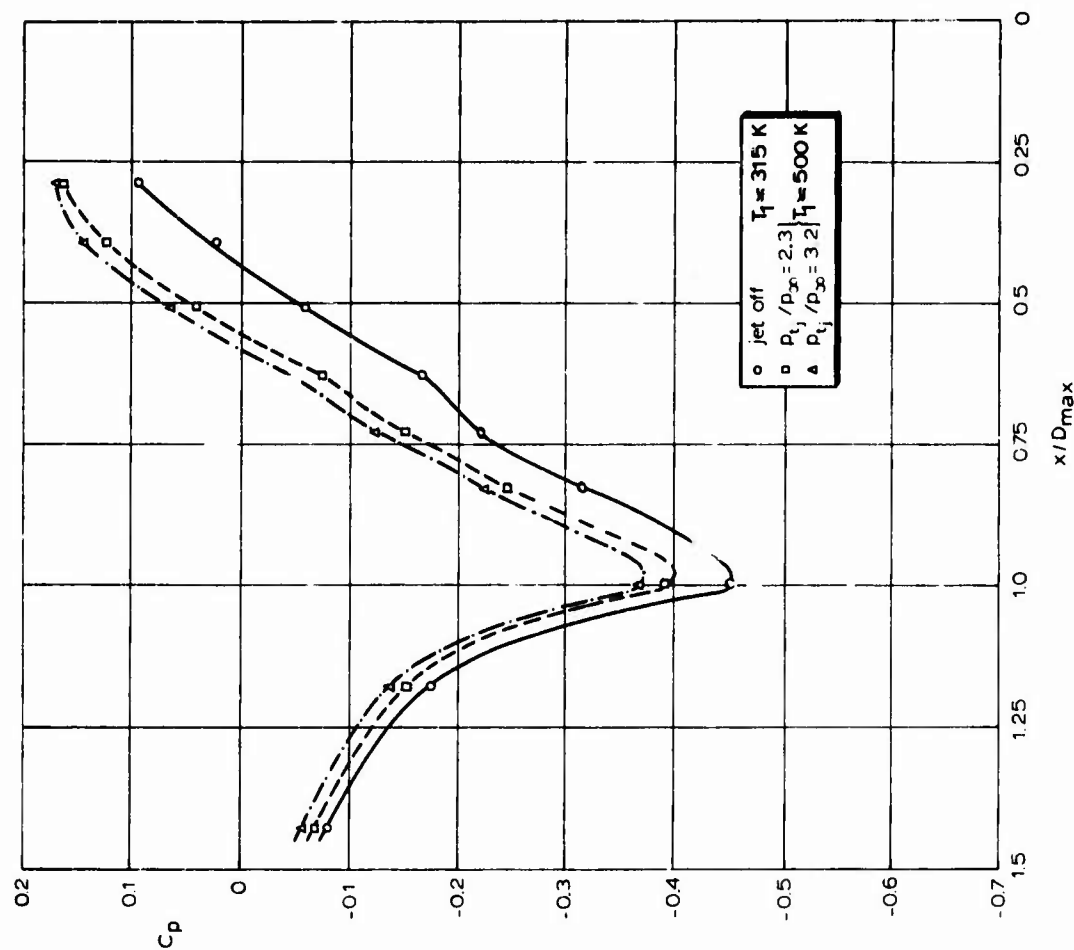


Fig.31 Effect of nozzle pressure ratio on boattail pressure distribution at  $M_\infty = 0.793$  (nozzle B)



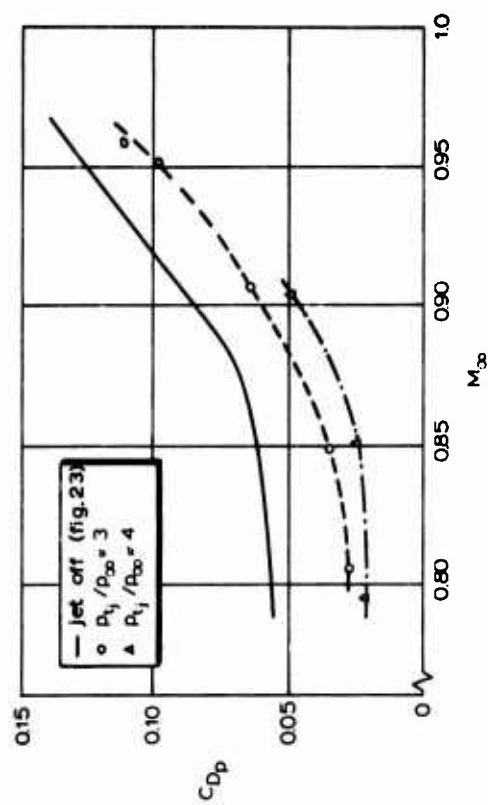


Fig. 33 The effect of nozzle pressure ratio on boattail pressure drag  
(hot jet, nozzle A)

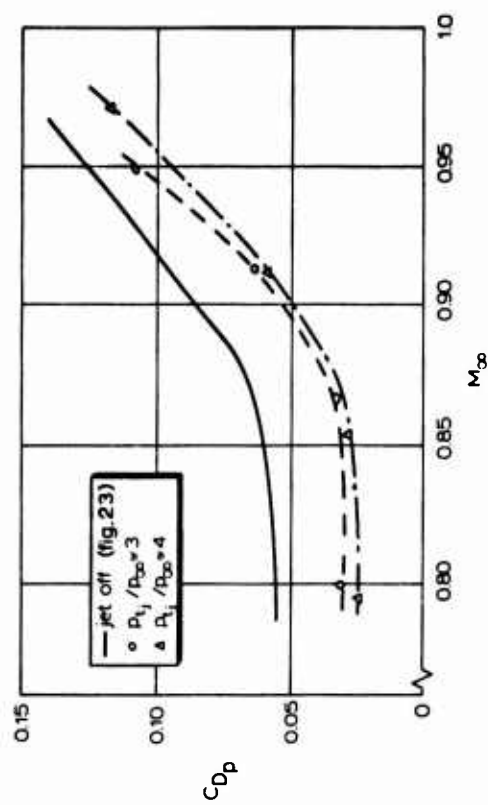


Fig. 34 The effect of nozzle pressure ratio on boattail pressure drag  
(cold jet, nozzle A)

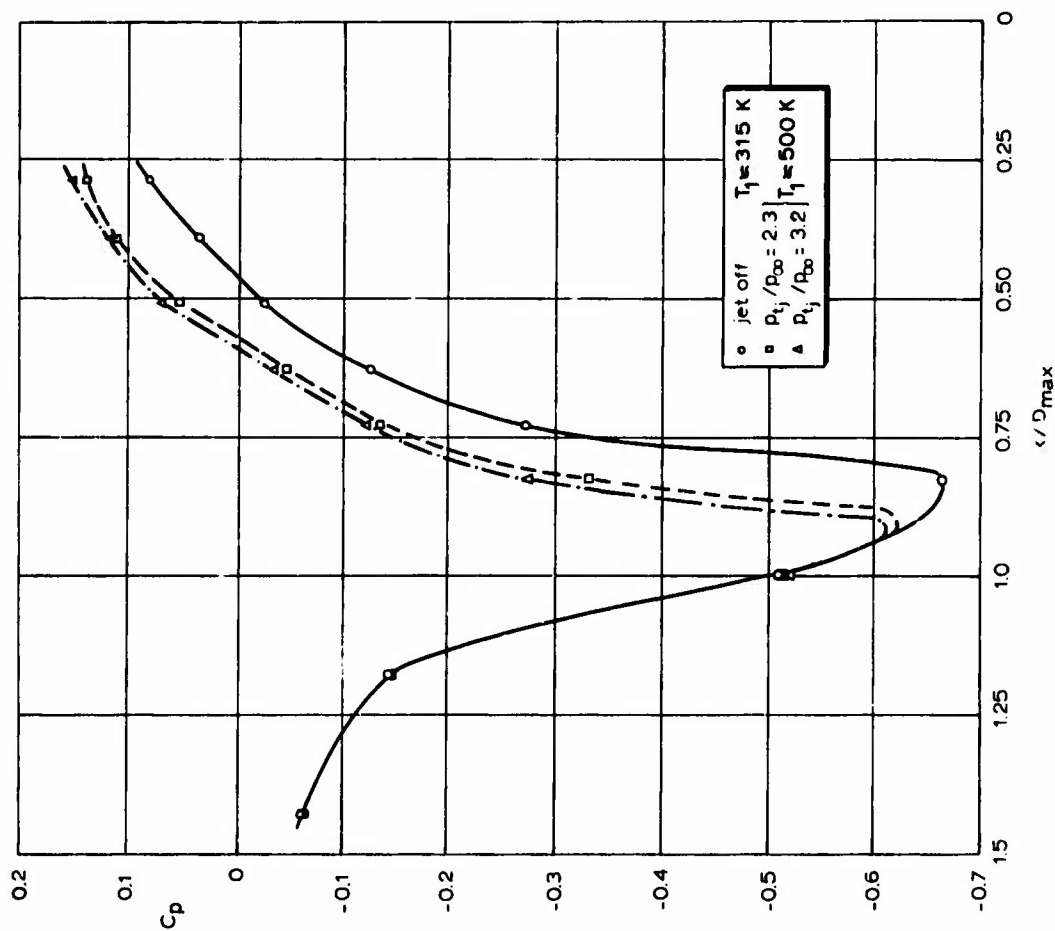


Fig. 32 Effect of nozzle pressure ratio on boattail pressure distribution at  
 $M_\infty = 0.890$  (nozzle B)

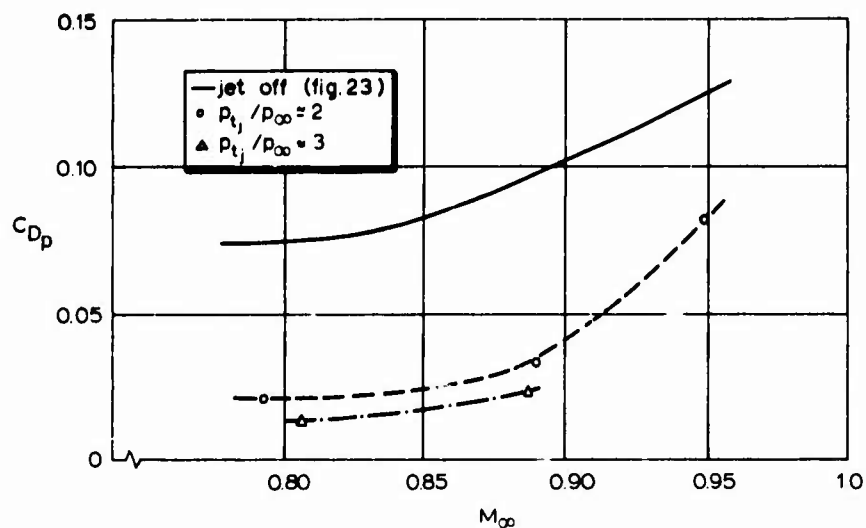


Fig.35 The effect of nozzle pressure ratio on boattail pressure drag (hot jet, nozzle B)

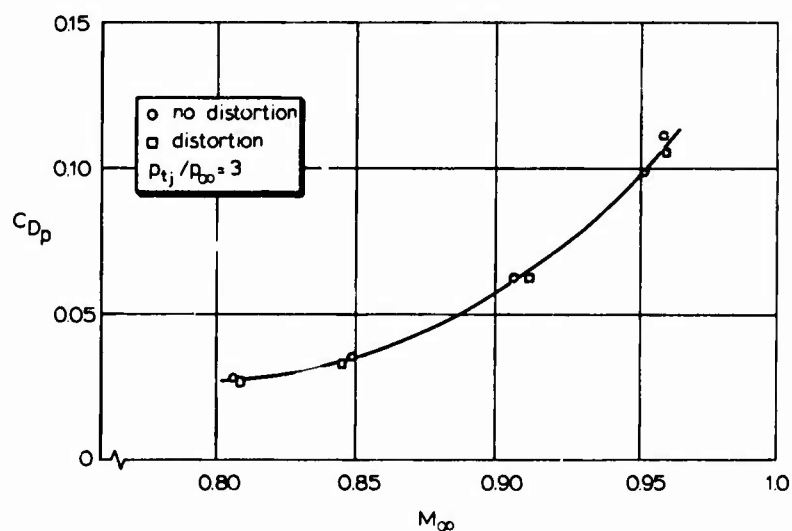


Fig.36 The effect of jet distortion on boattail pressure drag (hot jet, nozzle A)

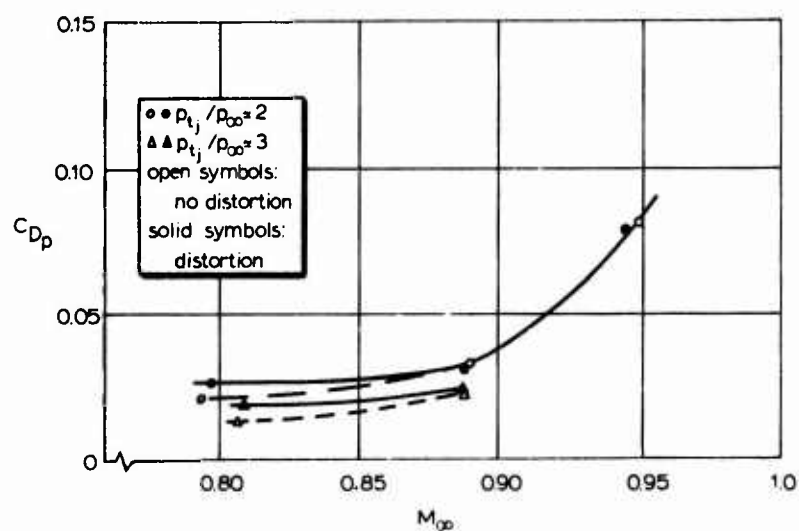


Fig.37 The effect of jet distortion on boattail pressure drag (hot jet, nozzle B)

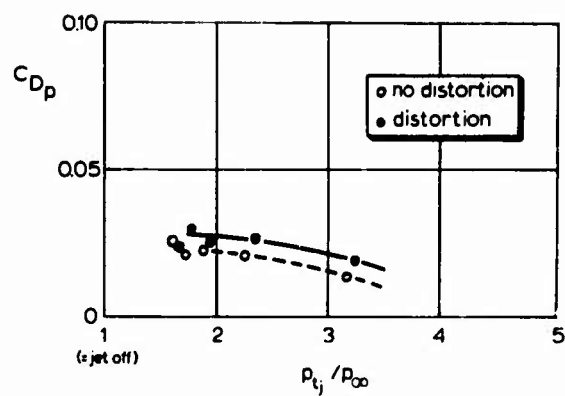


Fig.38 The effect of jet distortion on boattail pressure drag for  $M_{\infty} = 0.80$  (hot jet, nozzle B)

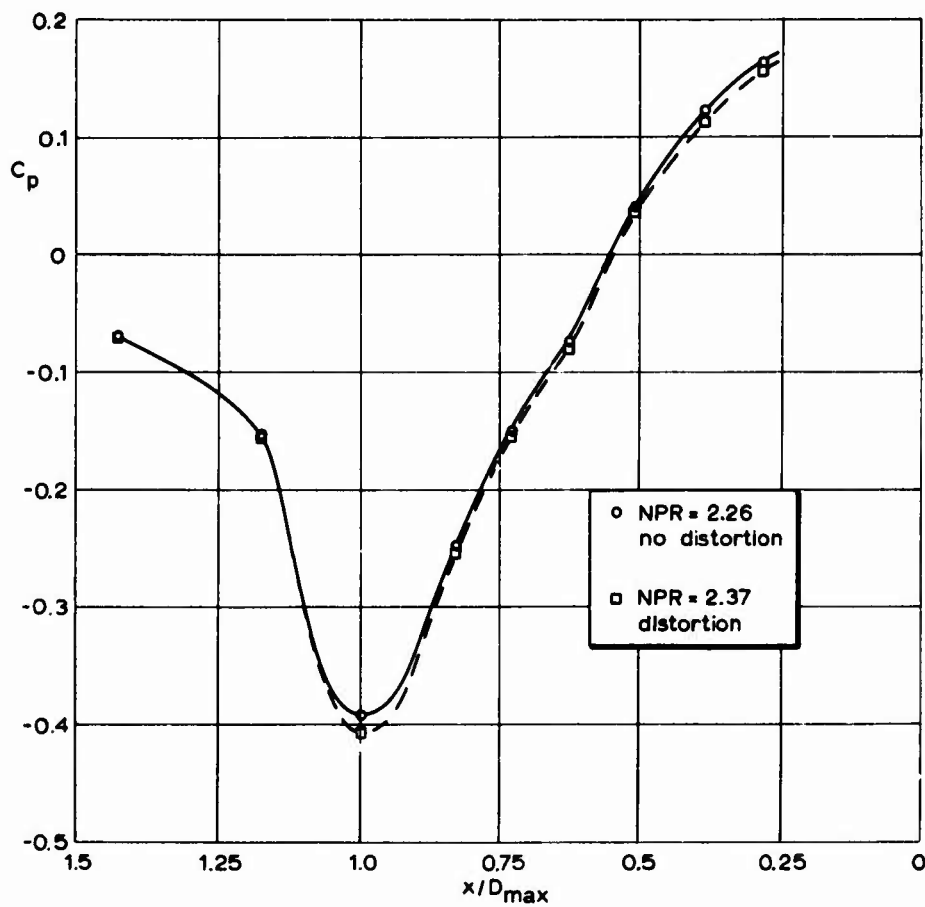


Fig.39 Effect of jet distortion on boattail pressure distribution at  $M_{\infty} = 0.80$  (nozzle B)

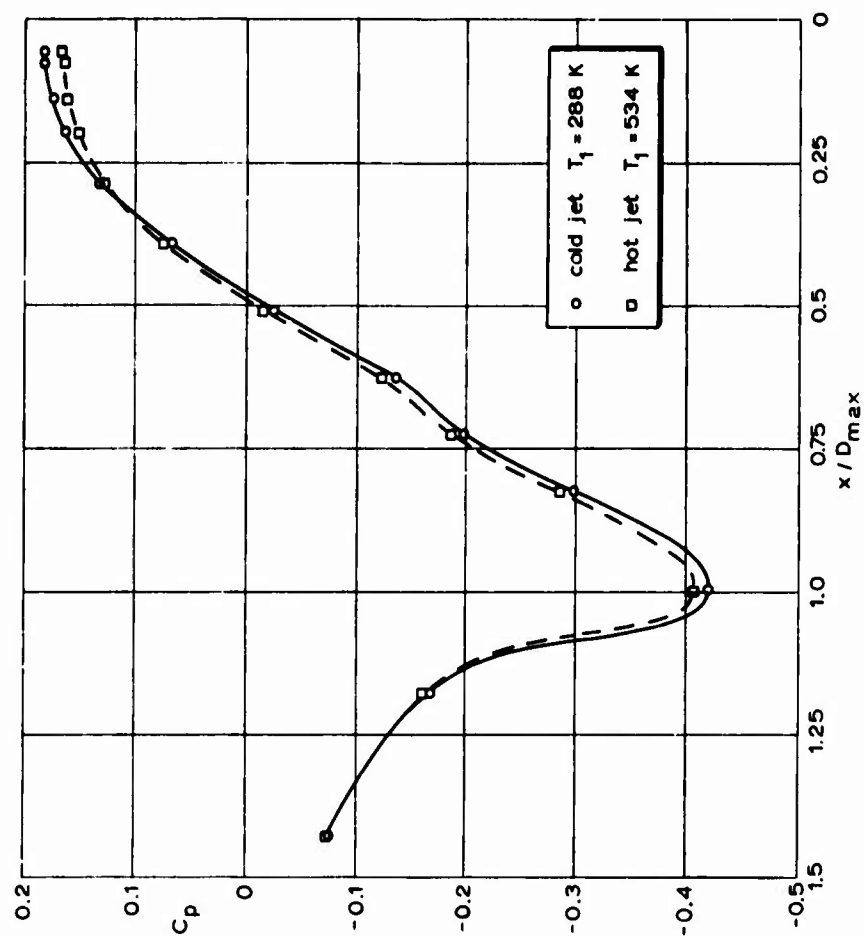


Fig. 41 Effect of jet temperature on boattail pressure distribution at  $M_\infty = 0.80$  and  $NPR \approx 4$  (nozzle A)

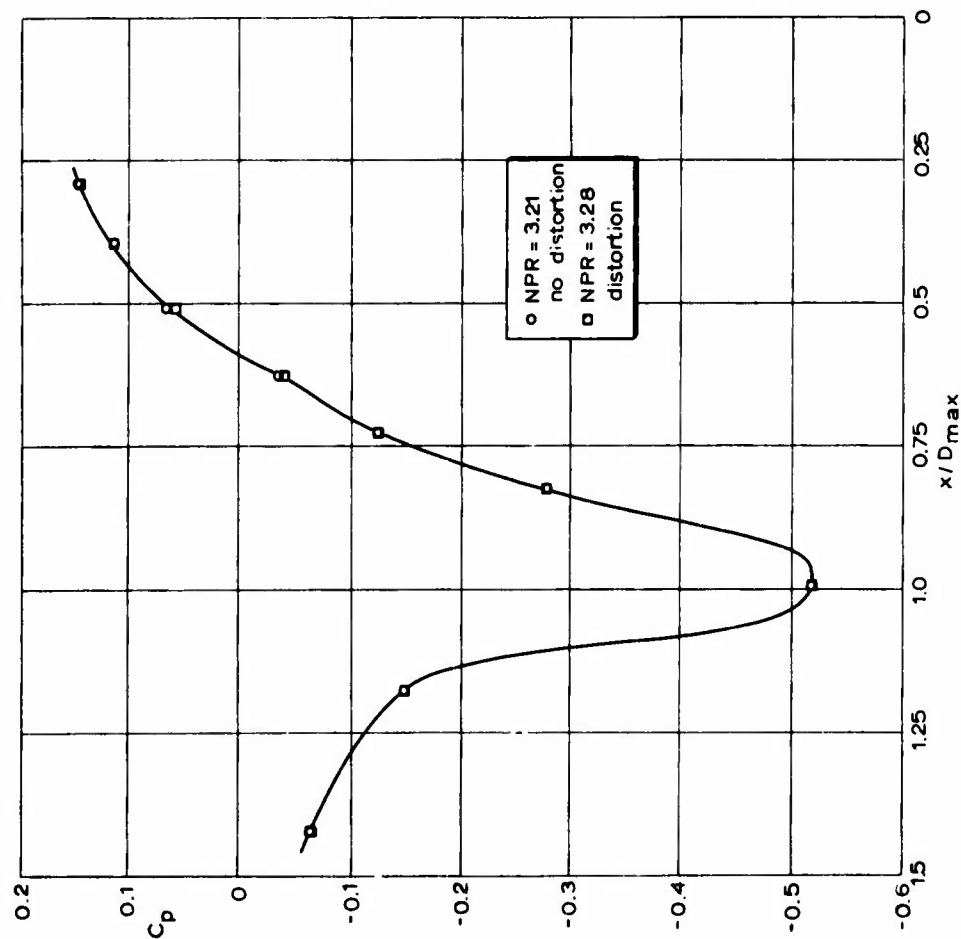


Fig. 40 Effect of jet distortion on boattail pressure distribution at  $M_\infty = 0.887$  (nozzle B)

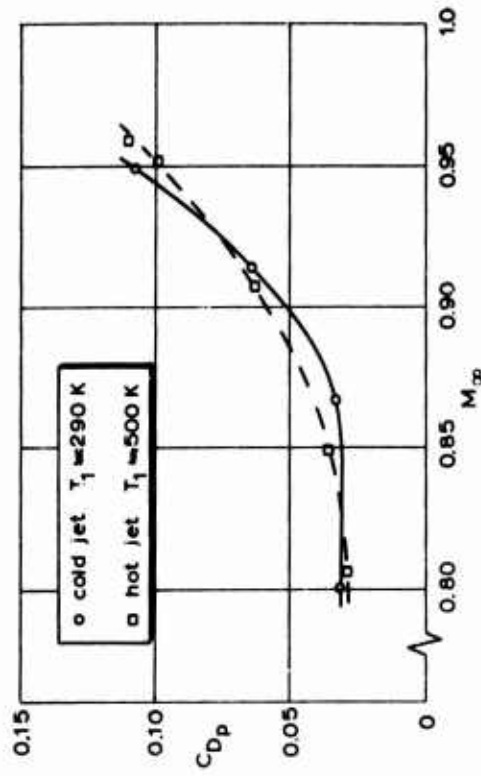


Fig. 43 Comparison of boattail pressure drag for hot and cold jets with  $NPR \approx 3$  (nozzle A)

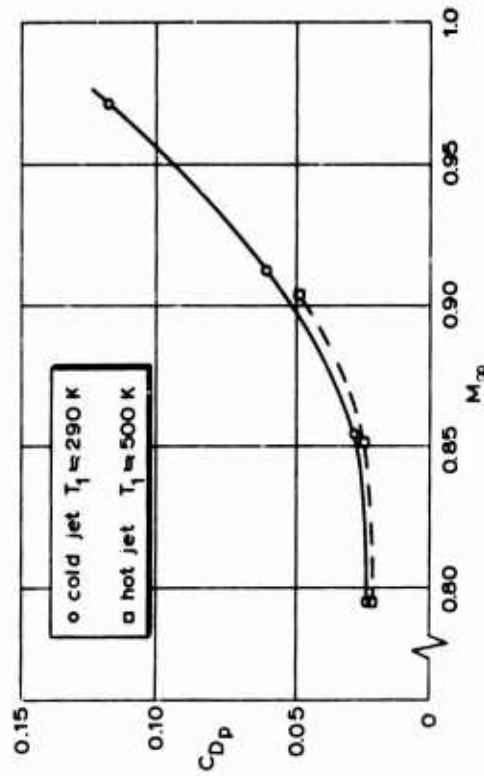


Fig. 44 Comparison of boattail pressure drag for hot and cold jets with  $NPR \approx 4$  (nozzle A)

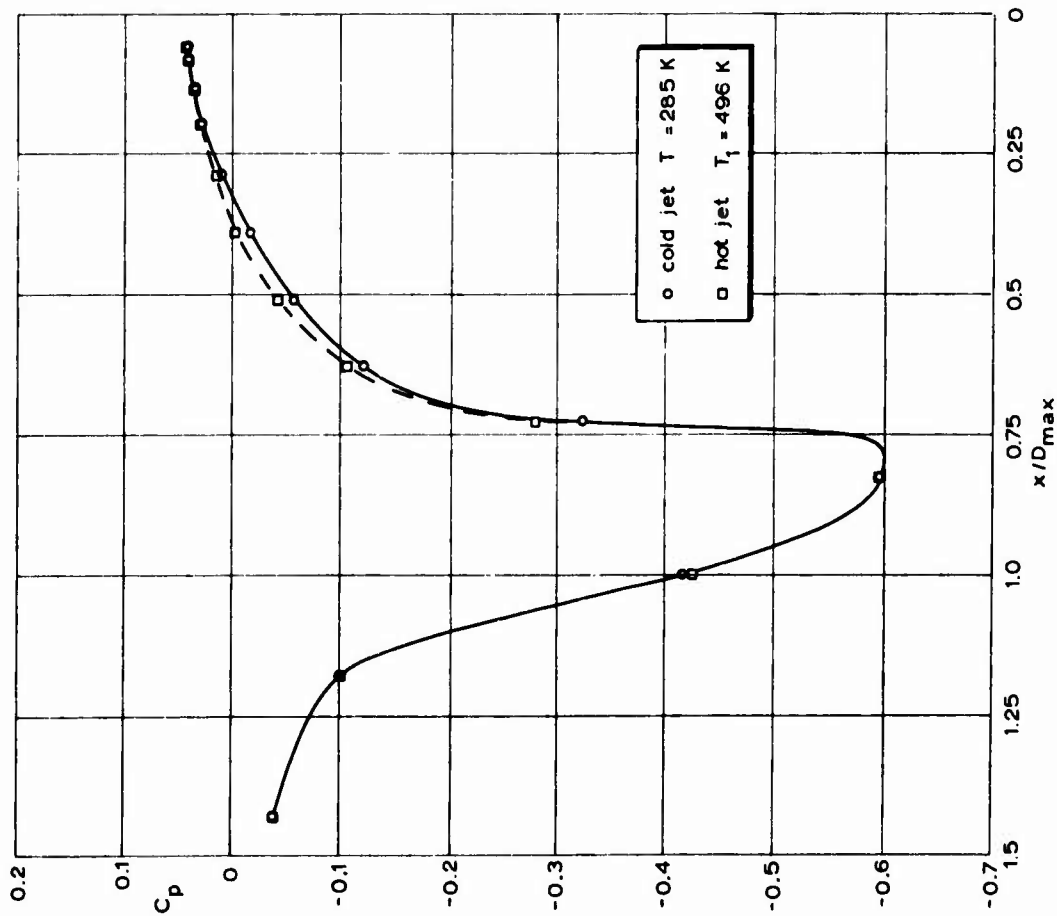


Fig. 42 Effect of jet temperature on boattail pressure distribution at  $M_\infty = 0.95$  and  $NPR \approx 3$  (nozzle A)

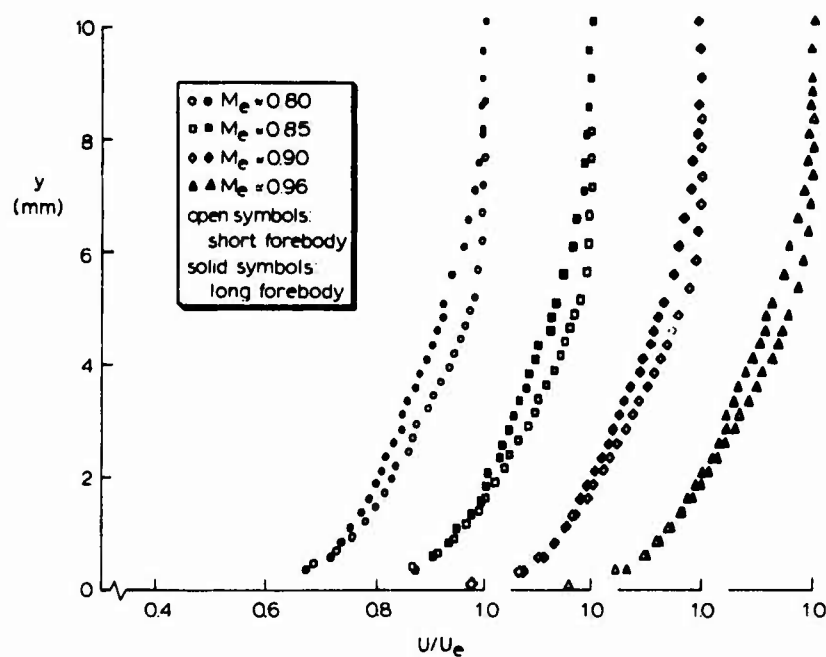


Fig.45 Boundary layer velocity profiles at the test Mach numbers for both long and short forebodies measured at  $x/D_{\max} = 2.91$

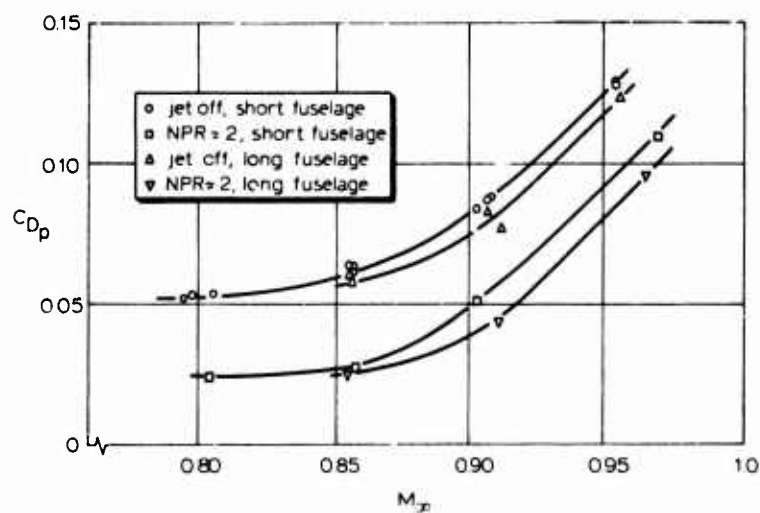


Fig.46 The effect of fuselage length on boattail pressure drag. (Nozzle A, hot jet, test section I)

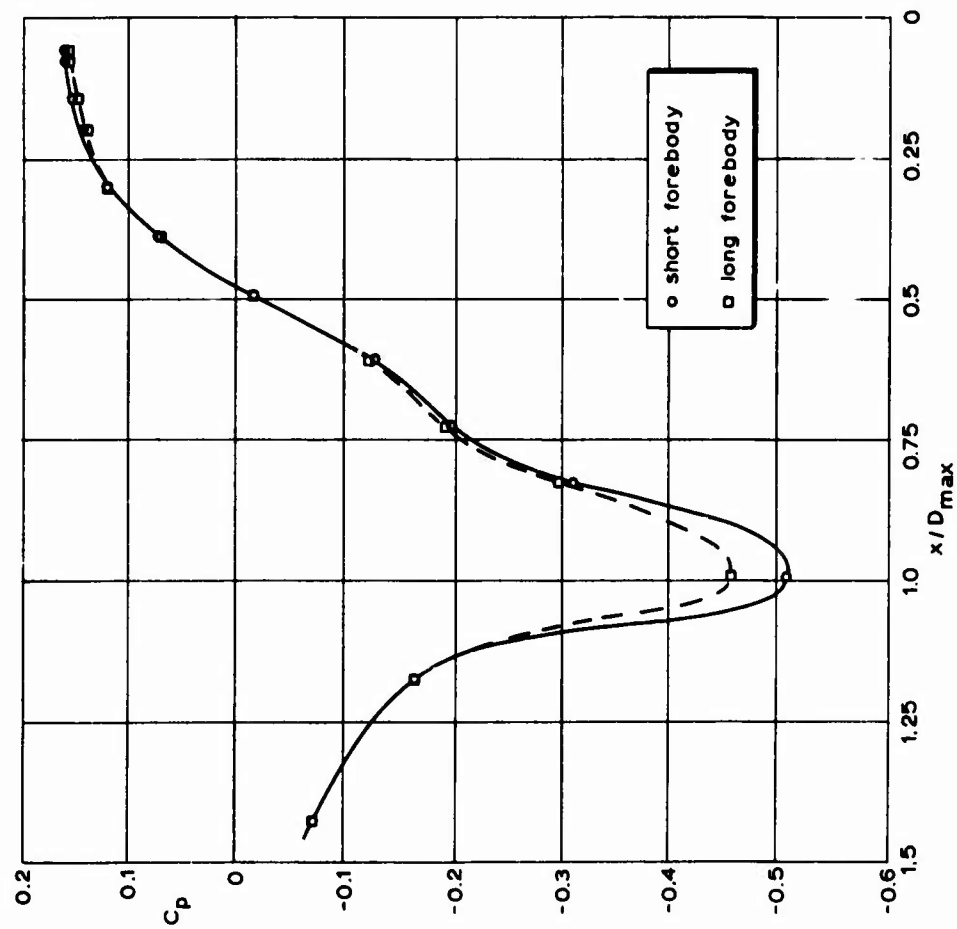


Fig.47 Effect of forebody length on boattail pressure distribution at  $M_\infty = 0.85$  (nozzle A,  $NPR \approx 2$ )

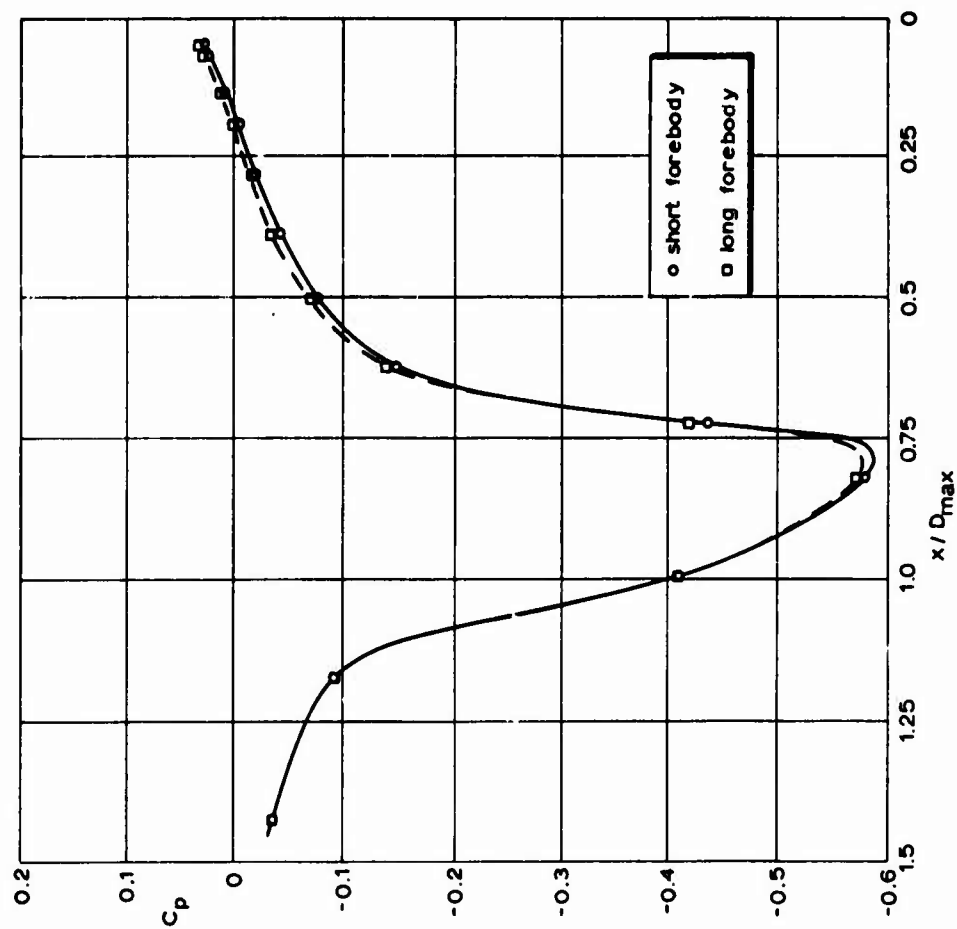


Fig.48 Effect of forebody length on boattail pressure distribution at  $M_\infty = 0.96$  (nozzle A, jet off)

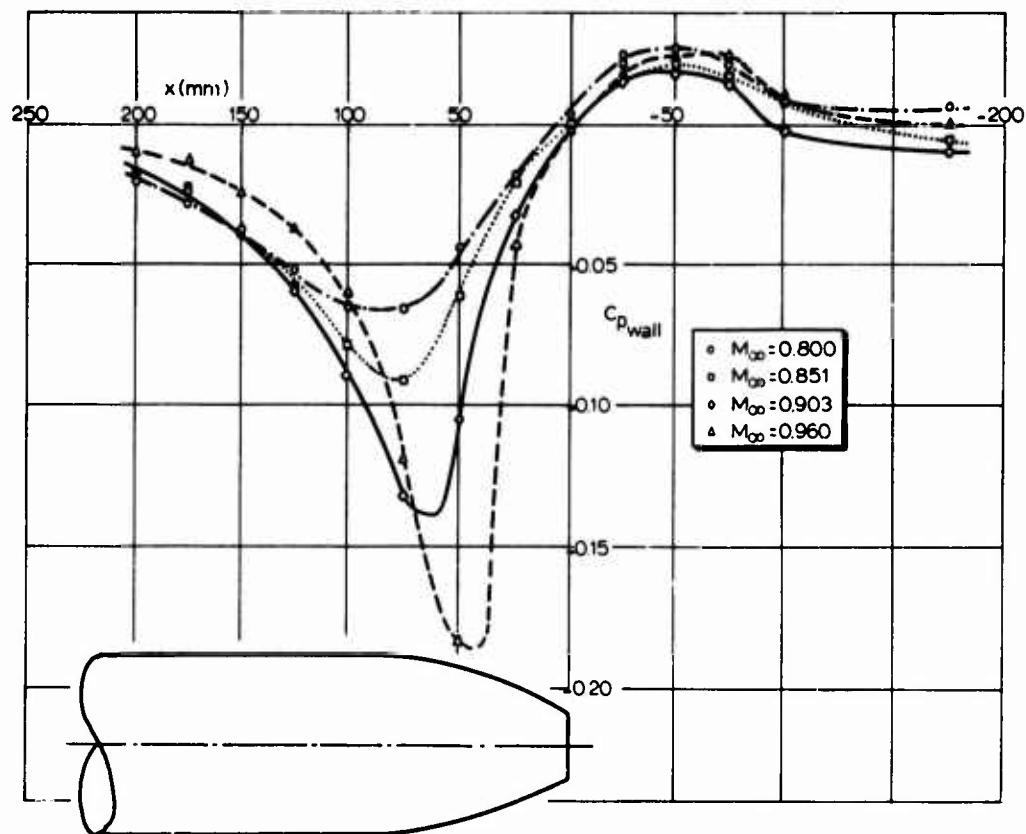


Fig.49 Mach number influence on tunnel side wall static pressure distribution  
(top and bottom wall 11.1% open, jet off)

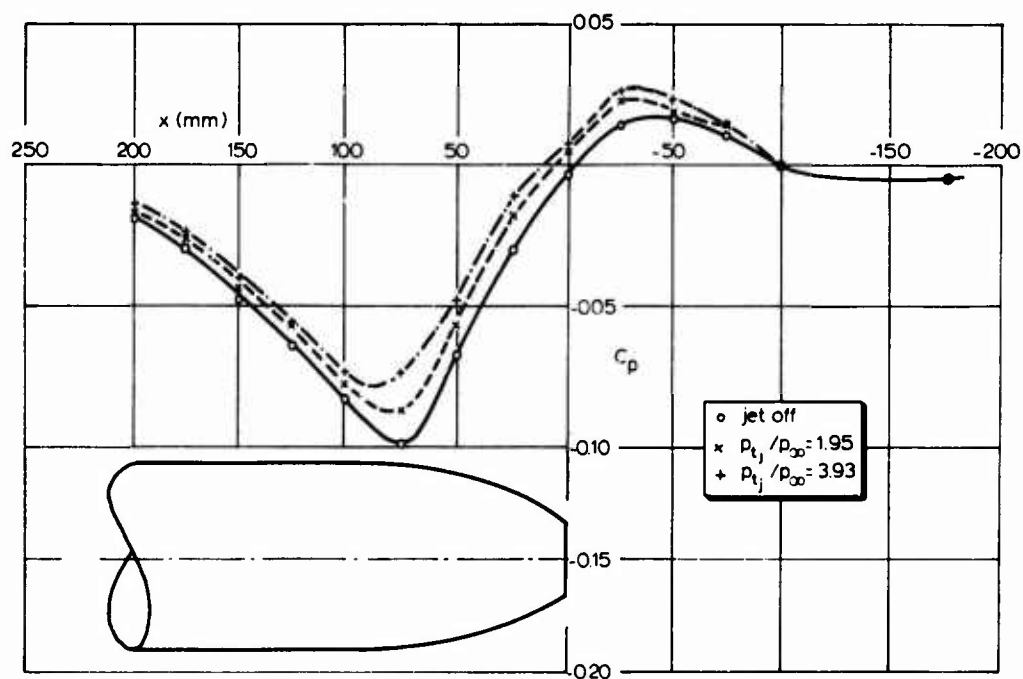


Fig.50 The effect of nozzle pressure ratio on tunnel wall static pressure distribution at  $M_{\infty} = 0.85$   
(nozzle A, cold jet)



# EFFECTS OF VARYING REYNOLDS NUMBER AND BOUNDARY LAYER DISPLACEMENT THICKNESS ON THE EXTERNAL FLOW OVER NOZZLE BOATTAILS

by

Dr.D.Zonars, James A.Laughrey, Douglas L.Bowers  
Air Force Flight Dynamics Laboratory Wright-Patterson AFB, Ohio USA

## SUMMARY

Data for the 10°, 15°, and 25° AGARD nozzle boattails presented in this paper are from those test facilities in which the Reynolds number was varied at constant Mach number or where the boundary layer was varied by blowing or changing the length of the model. Evaluation and discussion of the data concentrates on the trends in pressure drag and static pressure distributions when the external flow conditions (specifically Reynolds number and/or boundary layer displacement thickness) are altered over the Mach number range of 0.8 through 0.95.

In general (for  $M_\infty \leq 0.90$ ) when the Reynolds number was increased or the boundary layer displacement thickness was decreased, the static pressures decreased at the beginning of the boattail (flow expansion region) and increased near the nozzle exit (flow recompression region). The pressure drags associated with these changes in the pressure distributions varied only slightly at 0.8 Mach number, but increased measurably at 0.9 Mach number. Increasing the Reynolds number or decreasing the displacement thickness at a Mach number of 0.95 changed the flow such that the expansion was greater and the recompression was less resulting in a significant increase in pressure drag. The flow separated just downstream of the shoulder on the 25° boattail for all Mach numbers investigated and a change in Reynolds number or displacement thickness did not noticeably influence the point at which the flow separated although there was some variation on the level of pressure in the separated zone. Analytical procedures using "viscous-inviscid strong interaction" techniques were applied which verified the trends observed in the experimental pressure data for the boattails without extensive flow separation.

## 1. INTRODUCTION

One of the objectives of the AGARD Research Project on "Improved Nozzle Testing Techniques in Transonic Flow" is to understand more fully the effects on turbine engine exhaust nozzle external flow and related boattail drag when full scale external flow Reynolds number and boundary layer properties are not duplicated.

The Reynolds number based on a characteristic geometric dimension and the boundary layer properties (profile, upstream history, etc.) must be duplicated to obtain flow similarity on a sub scale model versus a full scale flight test. Thus if a one-tenth scale model is used in a wind tunnel facility, the unit Reynolds number should be ten times the flight unit Reynolds number to maintain the same total value, based on a selected characteristic dimension. In most wind tunnels the full scale Reynolds number and boundary layer properties are not duplicated, so it becomes important to understand the trends with Reynolds number variations in order to extrapolate flight performance of the nozzle, and to develop analytical procedures which can be applied at full scale conditions to predict installed nozzle performance. Thus the proper simulation, measurement, and interpretation of Reynolds number effects on nozzle boattails in transonic flow is an important element in improving test techniques. To approach this problem from several aspects, participants in the AGARD study varied Reynolds number and external flow properties in various ways. One method was to vary the tunnel stagnation pressure which effectively alters the Reynolds number the model external boundary layer profile at the same external Mach number. Another way of changing the boundary layer properties of the flow over the nozzle boattail was to inject additional air in the boundary layer tangential to the model surface upstream of the shoulder of the nozzle boattail. The boundary layer thickness was also varied by changing the length of the model nacelle to which the nozzle was attached.

The nozzle afterbodies investigated during this study were the AGARD contours described in References 2 to 9 that were tested in several different facilities to address several test technique problems in transonic flow. The results presented in this paper are from those facilities where Reynolds number could be varied at constant Mach number

or where the boundary layer thickness was varied by either boundary layer blowing or changing the length of the model. The boundary layer displacement thickness divided by model maximum diameter is the flow parameter used to correlate the data and determine trends (pressure drag and static pressure coefficient distribution) obtained by the various procedures, since all methods effectively change the boundary layer displacement thickness ahead of the nozzle boattail.

This paper concentrates on the trends in pressure drag and static pressure distribution when the external flow conditions are altered for Mach numbers of 0.8 through 0.95. A comparison of data obtained in different facilities or on different models is made only if the model (nacelle pod and nozzle boattail) being considered is the same or is geometrically scaled. Most of the data presented are for the AGARD 15° boattail nozzle contour; however, some drag and pressure distribution trends are given for the 10° and 25° boattails. Nozzle pressure ratio was held constant at a representative value for turbine engines for the comparisons.

Also included in the paper is a limited comparison of experimental and analytically determined pressure distributions for selected flow conditions on the 10° and 15° boattail nozzles. The analysis used is a viscous-inviscid strong interaction procedure developed by Bower<sup>1</sup> wherein the viscous flow properties are calculated by an integral theory for the compressible turbulent boundary layer that takes into account separated flow regions.

The authors of this paper would like to acknowledge the efforts of Dr. W. W. Bower of McDonnell Aircraft Company, St. Louis, Missouri, in the theoretical analysis, Mr. Lawrence L. Galigher of AEDC (ARO), Captain Robert Lock and Mr. Phillip Everling of AFFDL for their support in data analysis, and Mr. G. K. Richey of AFFDL for his review and suggestions. Also, the efforts of Mr. L. R. Harper of Rolls Royce, Ltd. in supplying data on the effects of mass injection on boundary layer development are gratefully acknowledged.

## 2. TEST FACILITIES AND MODELS

Data presented in this paper was obtained in various AGARD facilities<sup>2-9</sup>. As stated in the introduction, only the data which represents variations in Reynolds number ( $Re$ ) or boundary layer displacement thickness ( $\delta^*$ ) is discussed. United States data for the AGARD project "Improved Nozzle Testing Techniques in Transonic Flow",<sup>2</sup> was obtained in the Arnold Engineering Development Center (AEDC) 16 Foot Propulsion Wind Tunnel, Tullahoma, Tennessee, the 16 Foot Transonic Wind Tunnel at NASA Langley Research Center, Langley Air Force Base, Virginia, and the Lockheed-Georgia (USA) Compressible Flow Facility (CFF), Marietta, Georgia. Data from the NASA Langley facility were not used in this paper since the wind tunnel Reynolds number of model boundary layer properties were not varied at a particular Mach number. The data from this tunnel<sup>3</sup> is certainly valuable for other parts of the entire AGARD study. The AEDC PWT 16T facility is a continuous flow, closed circuit wind tunnel and has porous walls in the 16 Ft x 16 Ft x 40 Ft test section with a Mach number range of 0.2 to 1.6. The AEDC AGARD nozzle models were strut mounted to the tunnel floor (Fig. 1) and were instrumented with external static pressure orifices and boundary layer rakes. Overall model length was 146.934 inches (373.21 cm) and the maximum diameter was 9.86 inches (25.04 cm). This model is referred to in this paper as the "full scale" AEDC model. In a related investigation supporting the AGARD study, another model was built which is approximately one-sixth scale of the full scale AEDC model (15° boattail only). This model was tested in the same 16 foot wind tunnel and the 20 inch (50.8 cm) by 28 inch (71.12 cm) Lockheed-Georgia Compressible Flow Facility (CFF). The AEDC sub scale model was mounted on a sting supported strut (see Figure 2) in the AEDC 16T tunnel and on a floor strut in the Compressible Flow Facility. Primary instrumentation was external static pressure orifices on the nozzle boattail. The model length is 22.247 inches (56.51 cm) and the maximum diameter is 1.54 inches (3.91 cm). The unit Reynolds numbers ( $Re/ft$ ) was varied on both full scale and sub scale models from  $1.0 \times 10^6$  to  $6.0 \times 10^6$  at AEDC and from  $6. \times 10^6$  to  $50. \times 10^6$  in the CFF. The AEDC full scale model included the 10, 15, and 25 degree AGARD contours. All AEDC models simulated the exhaust plume with 530° R high pressure air.

Additional data<sup>4</sup> for the AGARD contours at 0.8 Mach number was provided by the Air Force Aerospace Research Laboratory at Wright-Patterson Air Force Base, Ohio, USA. The 30 inch (76.2 cm) long, 3 inch (7.62 cm) maximum diameter model was sting mounted from the rear with a cylindrical sting and was also tested in the Lockheed-Georgia Compressible Flow Facility (CFF). The unit Reynolds number ( $Re/ft$ ) range was  $6.0 \times 10^6$  to  $50.0 \times 10^6$ . Primary instrumentation was external static pressure orifices.

Data used in this paper from the United Kingdom was obtained in the open circuit ejector driven wind tunnel at the Rolls Royce Limited (RR) Bristol Engine Division. All three AGARD boattail shapes (10, 15, and 25 degree contours) were forward-sting mounted in the slotted octagonal test section<sup>5,6</sup>. The model maximum diameter was 101.6 mm. The boattail approach boundary layer was changed by blowing high pressure air tangential to the sting surface approximately 462.88 mm ahead of the boattail exit. Tunnel Reynolds number was approximately  $1.2 \times 10^4$  per mm. Instrumentation consisted primarily of external static pressure orifices on the nozzle boattail, external boundary layer rakes, a jet total pressure rake, and tunnel wall static pressures.

Data used in this paper for the AGARD 15° contour from France was obtained from the ONERA studies<sup>7</sup> which used an open circuit wind tunnel with the model mounted on a forward sting. The tunnel test section was rectangular (800 x 900 mm) with perforated top and bottom walls. The model maximum diameter was 80 mm.

The sting boundary layer was changed by the tangential blowing of high pressure air. The two blowing locations used were 286 mm ( $S_1$ ) and 628 mm ( $S_2$ ) ahead of the nozzle exit. The throat height of the blowing slot was varied from 0.5 to 1.5 mm. Instrumentation included internal and external static pressure orifices and total pressure rakes.

From the Netherlands, data for the AGARD 15° contour was provided by NLR<sup>5</sup> from tests in a 270 mm square slotted transonic test section of a continuous flow wind tunnel. The model had a maximum diameter of 80 mm and was mounted by two side struts and braced by two wires. The test section static pressure was adjusted to 1 atmosphere for all test conditions. The model jet flow was provided by liquid hydrogen peroxide. Instrumentation was a single component thrust balance, external static pressure orifices, sting boundary layer probes, and internal total pressure measurements. The boundary layer thickness just upstream of the boattail was changed by increasing the length of the model forebody ahead of the support struts by 350 mm.

The German participants in the AGARD study (MBB and DFVLR) conducted tests on the 10° AGARD boattail<sup>6</sup> but there were no variations in Reynolds number or boundary layer displacement thickness. This data will not be used for the discussions in this paper.

### 3. DISCUSSION OF EXPERIMENTAL DATA

This section of the paper will discuss the Reynolds number and/or boundary layer displacement thickness effects which were obtained during the AGARD study by three different techniques. One technique was to vary tunnel test conditions which varies the unit Reynolds number while maintaining Mach number constant. The other two techniques of varying boundary layer displacement thickness were injection of high pressure air upstream of the nozzle boattail or changing the length of the model while maintaining the same wind tunnel test conditions. The format of the data presentation in this section is to discuss first the details of the flow field at a given Mach number and for a given boattail shape as Reynolds number and/or displacement thickness is varied. The effect of the Reynolds number or displacement thickness changes on the flow field will then be discussed in terms of the drag determined by a pressure-area integration of the pressure distributions on the model. The AEDC data, which varied unit Reynolds number is examined first. Data from RR, ONERA and NLR will then be reviewed and consistent trends in the data from the various facilities will be discussed.

An indication of the effect of a Reynolds number change or displacement thickness variation on the flow over the AGARD boattail shapes may be observed by examining the changes in the static pressure and the projected area as a function of length along the boattail. This general relationship is shown in Figure 3 (see Appendix for explanation of the terms). On the initial part of the boattail, there is an expansion as the flow begins to turn around the shoulder of the boattail. The negative pressure coefficient region downstream of the shoulder combined with the aft facing projected area of the boattail contribute to the total pressure force acting on the boattail. As the flow continues over the external boattail surface, it begins to recompress toward positive  $C_p$  values as the flow turns back to the horizontal stream direction. In the recompression region the product of a positive  $C_p$  with an aft facing projected area is a contribution to thrust on the boattail. The relative areas of thrust and drag production for a typical condition at  $M = 0.9$  using measured pressure distributions from the AEDC facility on the three AGARD boattail shapes are shown on Figure 4. It is important to consider the contribution of both the static pressure and area changes to the total nozzle boattail force. The total projected area ( $A_p$ ) is the same for all three boattails. The relative levels of the thrust and drag contributions are affected by the viscous-inviscid interaction associated with a change in Reynolds number or a change in the boundary layer displacement thickness upstream of the nozzle boattail surface and how the boattail projected area varies in the axial direction.

#### AEDC (US) DATA

Data was obtained for all three AGARD contours (10, 15, and 25 degree boattails) at Mach numbers of 0.6, 0.8, 0.9, 0.95, 1.1, and 1.5. The unit Reynolds number was varied from  $1.0 \times 10^6$  to  $5.0 \times 10^6$  per foot which corresponds to Reynolds numbers of  $12.0 \times 10^6$  and  $60.0 \times 10^6$  based on a total model length of approximately 12 feet. Although nozzle pressure ratio ( $P_{Tj}/P_\infty$ ) was varied from jet off to pressure ratios of approximately 20, the analysis will concentrate on a nozzle pressure ratio of approximately 3.0, which is representative of the nozzle exit conditions for a fairly low bypass turbo-fan engine. Only data at Mach numbers of 0.8, 0.9 and 0.95 will be discussed in this paper. Reference 2 contains data at all Mach number which were tested. A recent calibration at various Reynolds numbers of the AEDC 16T tunnel indicates that the levels of  $C_p$  presented in this paper may be shifted slightly. The calibration change results only in a slight change in  $p_\infty$  and thus the relative pressure distribution behaviour with various Reynolds numbers does not change substantially from that described herein.

The pressure distribution over the 15° boattail at Mach number 0.8, nozzle pressure ratio of approximately 3.0, and a variation in Reynolds number from  $1.0 \times 10^6$  to  $5.0 \times 10^6$  per foot is shown on Figure 5. As Reynolds number increases there is a decrease in the boundary layer displacement thickness approaching the nozzle boattail. The data shows an increased expansion on the shoulder near  $X/D_{MAX} = 1.0$ , and increased recompression on the aft part of the nozzle boattail. Increased expansion near the shoulder tends to increase overall nozzle drag; increased

recompression on the aft boattail surface tends to decrease drag (increase thrust) on this part of the boattail and reduce overall drag of the nozzle model. These offsetting trends of pressure distribution on the contribution to the total boattail pressure force tend to give only a slight increase of nozzle boattail pressure drag with increasing Reynolds number at this Mach number.

Data for the 15° AGARD boattail at 0.9 Mach number is shown on Fig.6. As Reynolds number increases (displacement thickness decreasing) there is an increase in expansion at  $X/D_{MAX} = 0.9$  near the shoulder, with a slight shift downstream of the point of minimum pressure. There is generally increased recompression with increasing  $Re$  on the aft part of the boattail; particularly at  $Re = 5.0 \times 10^6$ /ft. At intermediate Reynolds numbers of 1.75 and 2.5 million per foot there is little change in the recompression region but an increase in expansion near the shoulder, which tends to increase total drag relative to the  $1.0 \times 10^6$  per foot case. At a  $Re$  of  $5.0 \times 10^6$  per foot the effect of the increased recompression is favorable and results in a slight decrease in boattail pressure drag coefficient.

As is shown on Figure 7, the pressure distribution trends are somewhat different at a Mach number of 0.95. Here, as Reynolds number increases, or as boundary layer displacement thickness decreases, there is very little change in pressure distribution (no increased expansion) on the shoulder of the boattail and a decrease in pressure in the recompression region except for the flow condition where  $Re$  is  $5.0 \times 10^6$ /ft. This tends to increase drag on the boattail surface at increased Reynolds number. However the corresponding drag coefficient at  $Re = 5.0 \times 10^6$ /ft is approximately equivalent to the 2.5 million per foot flow drag coefficient. At Mach number 0.95 there is a weak shock on the boattail surface at  $X/D_{MAX} \approx 0.8$  (observed from Schlieren). The shock-boundary layer interaction undoubtedly becomes more pronounced as the unit Reynolds number is increased (increase in tunnel stagnation pressure).

An example of the flow on the 10° AGARD boattail shape is shown on Figure 8 for a Mach number of 0.9, a nozzle pressure ratio 3.0 and over a range of Reynolds number. The effect of increasing Reynolds number (decreasing displacement thickness) appears to be primarily in the recompression region of the boattail surface with a small influence on the flow at the shoulder region. The increased recompression on a small projected area results in a slight decrease in pressure drag for the boattail while the small influence at the expansion region with a larger projected area contributes to a slight increase in boattail drag coefficient as Reynolds number is increased. As shown in Figure 8, this is generally verified by the pressure area integrations for this case, although the variations are rather small.

For the 25° AGARD boattail shape, data is shown in Figure 9 at  $M = 0.95$ . As Reynolds number increases from  $1.0 \times 10^6$  to  $5.0 \times 10^6$  per foot, there is an increased expansion near the shoulder and a decrease in pressure in the recompression zone on the aft surface of the boattail, which both contribute to an increase in drag. Since the flow in the boattail is almost entirely separated, the pressure is nearly constant on the boattail surface from  $X/D_{MAX} = 0.55$  to the nozzle exit. There is a slight effect of Reynolds number on the pressure level in this region, with the effect being that as Reynolds number increases the pressure coefficient is slightly more negative. The total contribution of the pressure force is a drag since the static surface pressures are never greater than the free stream pressure. As shown on Figure 10, there is a somewhat conflicting trend of drag with Reynolds number and points out the rather unique quality of the viscous-inviscid interaction for a particular boattail geometry and flow condition. At a Reynolds number of 1.75 million there is a decrease in pressure near the shoulder of the boattail. This contributes to an increase in drag at this Reynolds number. As the Reynolds number is increased further to  $2.5 \times 10^6$ /ft there is somewhat less expansion on the shoulder resulting in a slight decrease in drag. At a  $Re$  of  $5.0 \times 10^6$ /ft the flow has less recompression near the nozzle exit contributing to a slight increase in drag. The behaviour in the recompression region for this model is similar at Mach 0.95 and shows a slight decrease in the  $C_p$  level as Reynolds number is increased. All of the data on the 25° boattail indicates that most of the flow on the boattail surface just downstream of the shoulder is separated. There is strong evidence of a shock associated with the separation on this model and the effect of Reynolds number variation is to slightly alter the viscous-inviscid interaction. The point at which flow separation occurs does not appear to change significantly as Reynolds number is changed although there is some influence on the level of pressure in this separated zone as the external flow conditions are varied.

A summary of the variation in pressure drag on all three AGARD boattails is shown in Figures 11, 12, and 13 for Mach numbers of 0.8, 0.9, and 0.95 and illustrates the general trends discussed above.

Changing the Reynolds number by changing total flow conditions (tunnel stagnation pressure) as was done in the case of the AEDC tests of the AGARD models has the following influence on the viscous-inviscid interaction:

- (a) At Mach 0.8, there are somewhat offsetting trends in the pressure distributions. That is, as Reynolds number increases (displacement thickness decreases) there is increased expansion over the shoulder contributing to drag, and increased recompression on the aft part of the boattail contributing to reduced drag. The net effect is a slight increase in drag with Reynolds number.
- (b) At Mach 0.9, the trend is toward very little change of the pressure in the aft recompression region, and an increased expansion near the shoulder of the boattail, resulting in a slight increase in drag with Reynolds number.
- (c) At Mach 0.95, the trend is toward a very small change in the pressure distribution in the expansion region near the shoulder, but a decrease in pressure in the recompressions region contributing to an increase in drag at this Mach number as Reynolds number is increased.

Although the mechanisms of the viscous-inviscid interaction are slightly different for the three Mach numbers, the trend is toward a slight increase in pressure drag with increased Reynolds number for the 10° and 15° boattails. At the highest Reynolds numbers in some cases, there is a slight decrease in pressure drag as a result of increased recompression. For the 25° boattail, results are sometimes conflicting but show a trend of increased pressure drag as the Reynolds number is increased from  $1.0 \times 10^6$ /ft followed by a slight decrease and then increase at the higher Reynolds numbers. The important point is that the boundary layer displacement thickness is being influenced by Reynolds number (i.e. a decrease in displacement thickness with an increase in Reynolds number) which results in an alteration of the inviscid flow streamlines as Reynolds number is changed. Then, depending upon the basic shape of the boattail, the pressure distribution may be altered in a favorable or unfavorable manner (decrease or increase in drag).

#### AEDC 15° Boattail sub scale model data

The 15° AGARD boattail configuration was also constructed in a sub scale model approximately 1/6 scale of the exhaust nozzle pod arrangement discussed above. This model is 22 inches (55.88 cm) in length, and was run at AEDC at the same tunnel test conditions as the larger model. The Reynolds numbers based on model length varies from approximately  $2.0 \times 10^6$  to  $10.0 \times 10^6$  as unit Reynolds number varies from  $1.0 \times 10^6$  to  $5.0 \times 10^6$  per foot. The Reynolds number based on length of the larger model is between  $12.0 \times 10^6$  and  $60.0 \times 10^6$ . Blockage, based on the cross-sectional area of the model, plus its support system is approximately 0.11 percent in the AEDC 16 foot tunnel. The sub scale model also underwent tests at the Lockheed-Georgia Compressible Flow Facility, which is a blow-down wind tunnel capable of a Reynolds number based on length of  $120.0 \times 10^6$ . This data from AEDC and the high Reynolds number facility, makes it possible to examine Reynolds number effects on the same model over a very wide range of Reynolds numbers.

Pressure distributions on the 15° sub scale model at 0.8 Mach number are shown in Figures (14a) and (14b). In the expansion region, the sub scale data in both the AEDC 16 Foot Wind Tunnel (14a) and the Compressible Flow Facility (14b) show essentially the same behaviour as the larger model. The CFF data in the recompression region shows increased pressure with increased Reynolds number. The sub scale data in the 16 Foot Wind Tunnel, however, shows decreased pressure with increased Reynolds number. Pressure data is not available on this model near the exit of the boattail since the installation of pressure instrumentation in this region on the smaller scale model was very difficult. A comparison of the pressure drag on the sub scale model with the pressure drag on the full scale model where the pressure distribution is truncated at  $X/D_{MAX} = 0.2$  is shown in the lower part of Figures 14(a) and 14(b). It is important to note that the trend of pressure drag with Reynolds number based on total model length is continuous and smooth between the small scale and large scale model at Mach 0.8.

The pressure distribution and pressure drag on the sub scale model are shown on Figures 15(a) and 15(b) for a Mach number of 0.9. All tests show similar trends in the expansion region. In the recompression region however, the 16 Foot wind tunnel data for the sub scale model again shows decreasing pressure with increasing Reynolds number. Variation of pressure drag with Reynolds number based on a truncation of the "full scale" data is shown on Figures 15(a) and 15(b) and indicates a very good correlation between the pressure drag on the sub scale model and pressure drag on the larger model. Figure 16 compares the actual pressure distribution for the sub scale and larger model at a comparable Reynolds number based on total model length. As can be seen from Figure 16, there is very good agreement of the pressure distributions for the different models and test arrangements.

Data was also taken on the sub scale model at 0.95 Mach number, and is shown in Figures 17(a) and 17(b). At this Mach number, there is a substantial difference in pressure distribution of the aft part of the boattail between the sub scale and "full scale" models. Pressure coefficients for the sub scale and "full scale" models are comparable in the expansion region. However, there are significant differences upstream of the boattail shoulder. The lower pressure in the recompression region results in a large pressure drag at Reynolds number based on model length of slightly less than  $10.0 \times 10^6$  as shown on the figure. This data is being examined further to determine the effect at this particular Mach number. As stated previously, the interaction between the external flow and the boundary layer of the model is very sensitive to location of shock waves in transonic flow and the rate of change of displacement thickness with distance. In general, the sub scale data seems to substantiate the trends observed on the larger scale model with variations in Reynolds number.

#### High Reynolds number (ARL) data

In a related study sponsored by the Air Force Aeronautical Research Laboratory (ARL), the AGARD boattail shapes were tested in the high Reynolds number Lockheed-Georgia Compressible Flow Facility (CFF) at 0.8 Mach number. With this facility, variations of Reynolds number based on length of up to  $127.0 \times 10^6$  are possible with this model which was 30 inches (76.2 cm) in length. The model was sting mounted from the rear with a cylindrical plume being used as the sting. This technique has been used by many investigators and corresponds to a nozzle pressure ratio for a convergent nozzle where exit static pressure equals ambient static pressure. Variation of the pressure distributions for the 15° boattail contour at three different Reynolds numbers is shown on Figure 18. At 0.8 Mach number, the data indicates a similar variation of pressure distribution to the AEDC data. As Reynolds number based on model length is increased from  $15.0 \times 10^6$  to  $127.0 \times 10^6$  there is an increase in expansion near the shoulder and an increase in pressure level on the recompression surface near the nozzle exit. Comparison



of the pressure distribution on this boattail in the Compressible Flow Facility with the "full scale" data from AEDC is shown in Figure 19. There is good agreement between the AEDC model, which has a flowing jet, and the ARL model which uses a solid cylindrical plume to simulate the jet efflux. Data taken over the wider range of Reynolds number on this model appears to validate the interpretation of the AEDC data. That is, at a Mach number of 0.8, increasing Reynolds number (or decreasing boundary layer displacement thickness) results in increased expansion near the shoulder of the boattail and increased recompression on the aft portion of the boattail.

The pressure distributions on the ARL model for the 10° and 25° AGARD contours at Mach number 0.8 is presented in Figures 20 and 21 respectively. With increasing Reynolds number for the 10° model the pressure drag decreases slightly. The higher Reynolds number pressure data indicates slightly more expansion but a significantly higher recompression. These combined effects produce a lower pressure drag coefficient for the higher Reynolds number flow condition. Increasing the Reynolds number on the 25° model (Fig. 21), alters the pressure distribution such that the pressure drag coefficient is decreased. While the pressures are comparable in the recompression region, the lower Reynolds number flow has lower pressures in the expansion region and correspondingly more pressure drag than for high Reynolds number. The trends for both the 10° and 15° small scale contours tested in the Compressible Flow Facility correspond to the AEDC data at the 0.8 Mach number flow condition.

#### Rolls Royce (UK) data

Both the United Kingdom through Rolls Royce, Ltd. (RR) Bristol Engine Division, and France through ONERA, conducted wind tunnel studies of the effect of boundary layer injection on nozzle boattail flow<sup>5,6, and 7</sup>. Boundary layer injection effectively simulates an increase in the Reynolds number of the flow by decreasing the boundary layer displacement thickness. Although the mechanisms for changing displacement thickness are different, the change in pressure distributions on the boattail is about the same. A comparison of the pressure distributions for the natural boundary layer (no blowing) and the blown boundary layer is shown on Figure 22 for the RR test of the 15° boattail at 0.8 Mach number. Displacement thickness for the natural boundary layer is 2.0 mm measured just upstream of the nozzle boattail shoulder while displacement thickness for the blown boundary layer is 0.98 mm at the same station. The decreased displacement thickness, which is equivalent to an increase in Reynolds number, shows an increased expansion near the shoulder and increased compression on the aft surface of the boattail. These two effects are essentially off-setting so that the pressure drag remains unchanged at 0.8 Mach number. In Figure 23 a comparison is made of the pressure distributions on the 15° boattail for the natural and blown boundary layer at a Mach number of 0.91. The thinner boundary layer associated with flow injection results in an increased expansion near the shoulder but very little change on the flow in the recompression zone. The difference in pressure distribution near the shoulder contributes to a substantial increase in pressure drag for this model. The data shown on Figure 24 indicates that at a Mach number of 0.95, with and without blowing, the major change in pressure distribution occurs in the aft region of the nozzle (recompression zone). With the thinner boundary layer (blowing) the flow recompresses to a lower pressure. This was observed at 0.95 Mach number on other models tested during this investigation and is most likely related to the boundary layer interaction with the shock wave which is present on the model at  $X/D_{MAX}$  approximately 0.75. The lower pressures in the recompression zone result in an increase in pressure drag at 0.95 Mach number. The effect of displacement thickness changes by boundary layer blowing on the AGARD 25° boattail is shown on Figures 25 and 26. Although the flow is separated just downstream of the boattail shoulder, the effect of boundary displacement thickness variations is still evident. For the natural boundary layer condition the flow recompresses more than the blown boundary layer case, which is consistent with the associated changes in unit Reynolds number. The two different boundary layer thicknesses result in flow separation at slightly different boattail locations with a resultant difference of the pressure level in the region of separated flow. A summary of the variation of the pressure drag with Mach number for the natural and blown boundary layer flow conditions is given on Figure 27 which indicates that there generally is an increase in pressure drag for the thinner boundary layer. This could be off-set in some cases by reduced friction drag associated with the thinner boundary layer but in most cases the variation in pressure drag will predominate, resulting in an increase in total drag of the boattail with the thinner boundary layer.

It is concluded, in the case of the RR data, that the variation of displacement thickness on the viscous-inviscid interaction on the AGARD boattails is similar in character to the effect of a variation of Reynolds number which was observed on the AEDC "full scale" and sub scale models. For a wind tunnel which cannot vary Reynolds number, the technique of varying displacement thickness to simulate a change in Reynolds number may be a valuable test to investigate nozzle shapes in the transonic regime.

#### ONERA (France) data

Boundary layer displacement thickness was also varied in tests conducted in the ONERA facility on the 15° boattail by using mass injection at a location well upstream of the shoulder of the boattail. In addition to the natural boundary layer, the boundary layer profile was varied by using two throat heights in the injection channel. These are referred to on the figures as  $e = 0.5$  (millimeters) and  $e = 1.5$  (millimeters). At the higher injection rates associated with  $e = 1.5$  there is a greater reduction in the displacement thickness. Results from these tests in which the boundary layer had recovered to a typical turbulent boundary layer profile at the measurement station just upstream of the nozzle shoulder were used to assess the effect of displacement thickness variation on nozzle boattail pressure and drag coefficients. Results from the ONERA test at 0.8 Mach number of the 15° boattail are shown on

Figure 28. Decreasing displacement thickness by mass injection produces increased expansion at the shoulder and increased compression on the aft surface of the boattail, similar to the results observed in the RR test of the blown versus natural boundary layer. This results in a slight change in pressure drag with the decreased boundary layer thickness ( $e = 1.5$ ). At Mach number 0.9 (Fig.29) similar trends to that observed with increasing Reynolds number are shown with the reduced displacement thickness associated with boundary layer injection. That is, at  $M = 0.9$  there is little change of the flow on the boattail in the aft recompression region, but an increased expansion near the shoulder which results in an increased pressure drag. For a Mach number of 0.95 (Fig.30) the pressure level in the recompression region decreases when the displacement thickness decreases. This is the same trend observed in the AEDC and RR data, verifying the nature of the viscous-inviscid interaction. A summary of the pressure drag variation with Mach number for the ONERA 15° boattail at various displacement thickness conditions is shown in Figure 31 and in general shows the same trends observed from the AEDC and RR data.

In summary, injecting air into the boundary layer ahead of the boattail shoulder and thus decreasing displacement thickness is very similar to an increase in unit Reynolds number. The general trend, subsonically, for the 10° and 15° AGARD boattails is greater expansion at the boattail shoulder and greater recompression at the boattail exit for the thinner blown boundary layer. The 25° AGARD contour for the thinner boundary layer cases has greater flow expansion over the boattail shoulder and not as much recompression at the boattail exit.

#### NLR (Netherlands) data

Another method of varying displacement thickness entering the boattail region is to change the length of the forebody. This procedure was used at NLR<sup>8</sup> in the Netherlands to assess the effect of different external conditions on the nozzle boattail. Two lengths of forebody were investigated; one which was 850 mm in length and the other which was 1200 mm in length. Boundary layer profile measurements were obtained only at jet off conditions for the NLR tests. Values of  $\delta^*/D_M$  of 0.0124, 0.0136, and 0.0143 were determined for the model with the short forebody at Mach numbers of 0.85, 0.90, and 0.95 respectively. With the long forebody installed and at the same respective Mach numbers, the values of  $\delta^*/D_M$  were 0.0157, 0.0162, and 0.0171. For a turbulent boundary layer, where the displacement thickness varies approximately with the 1/5 power of the change in Reynolds number, this change in model length results in about a 7% calculated change in displacement thickness upstream of the boattail. Data from the NLR facility on the 15° AGARD boattail shape at Mach number 0.9 is shown in Figure 32. The effect of a decreased  $\delta^*$  just upstream of the shoulder of the boattail is to increase the expansion near the shoulder, but with no significant change on the pressure in the recompression region. This is similar to trends observed at 0.9 Mach number with variations in unit Reynolds number or variations in displacement thickness due to injection. The increased expansion near the shoulder results in an increased pressure drag for this condition. Data shown in Figures 33 and 34 for Mach numbers of 0.855 and 0.965 respectively, indicate that there is some influence of the change in displacement thickness on the pressure distributions. However, the variations are rather small and this is reflected in the small changes in the drag coefficients. In general, the trends seem to validate the character of the viscous-inviscid interaction at these Mach number which has been observed previously. At 0.965 Mach number, the primary effect of the decreased displacement thickness (short fuselage) is to decrease the pressure in the recompression region. A summary of the pressure drag variation versus Mach number for the long and the short forebody is shown in Figure 35 and indicates a slight increase in pressure drag with the thinner displacement thickness of the short forebody.

#### 4. ANALYSIS OF THE VISCOUS-INVISCID INTERACTION

The experimental data obtained under this AGARD investigation indicates that changing Reynolds number and/or displacement thickness alters the viscous-inviscid interaction of the flow over the nozzle boattail. Trends with Reynolds number may be discerned, but cannot be expected to hold for other model geometries or other upstream boundary layer conditions. There seems to be a rather unique quality to the interaction between the boundary layer and the inviscid flow which must be considered for a given model or nozzle shape. The primary benefit of examining variations with Reynolds number from the experimental data is to gain an understanding of the interaction between the boundary layer and the inviscid flow to guide development of analysis procedures that can be used to predict the viscous-inviscid interaction at higher Reynolds numbers.

This section briefly describes an analytical procedure which has been used to help validate the trends observed in the experimental data and to provide additional insight into the nature of this rather complex interaction. Although this method compares favorably with the trends observed from the AGARD model data, there is a need for improved analytical procedures, particularly if shock waves are present on the external surface of the boattail.

Bower<sup>1</sup> has developed a "viscous-inviscid strong interaction theory" which is capable of predicting the pressure distribution over axisymmetric bodies in transonic flow with a supersonic exhaust plume. The procedure is unique in that it can successfully handle a region of separated flow. The separated flow regions are analyzed through a two layer integral technique similar to reference 11, but modified for turbulent compressible boundary layers. The analysis as applied to exhaust nozzles assumes the total flow field is composed of three component flow fields, namely the outer inviscid flow, the inner viscous flow, and the supersonic exhaust plume. The shape of the exhaust plume is computed by the Method of Characteristics, with the inviscid flow field calculated as in reference 10.

The pressure distribution over the body is calculated by iterating on the boundary layer displacement thickness until an effective body contour is determined which produces the same pressure distribution from both the inviscid flow procedure and an inverse boundary layer procedure. Figure 36 shows that when a conventional, weak interaction theory is used, which combines a standard integral boundary layer analysis with an inviscid procedure such as that of reference 10, the boundary layer displacement thickness diverges on the first iteration, making further analysis impossible. This situation occurs because separation is predicted based on the initial inviscid pressure distribution. This pressure distribution is never felt by the flow as it goes over the boattail. The strong-interaction theory gives results typically as shown on Figure 36 which shows a boundary layer thickening near the boattail exit and its effect on the converged pressure distribution.

Figures 37 to 39 compare the strong interaction theory with experimental data from AEDC tests of the "full scale" 10° and 15° AGARD boattail configurations at 0.8 Mach number. The theory predicts the essential character of the viscous-inviscid interaction discussed in Section 3.0 and compares very favorably with the actual level of  $C_p$ , particularly for the 10° boattail. For the 15° boattail, the theory predicts somewhat higher  $C_p$  values in the aft recompression region of the boattail, which may be related to nozzle plume effects. Comparing Figures 38 and 39, the theory predicts an alteration of the viscous-inviscid flow interaction for the two different Reynolds numbers. There is better agreement between theory and data at unit Reynolds number of  $1.0 \times 10^6$  per foot.

The theoretical prediction of Reynolds number effect on pressure distribution for the 15° boattail is shown on Figures 40 ( $M = 0.9$ ) and 41 ( $M = 0.8$ ). Figure 40 shows that, as Reynolds number is increased, there is increased expansion near the shoulder with a decreased  $\delta^*$ . This is the same trend shown by the experimental data, except that experimentally this behaviour occurred at 0.8 Mach number. Similar results are shown on Figure 41 except that the interaction in the expansion region near the shoulder does not change substantially with increased Reynolds number. The theory is definitely showing that there is an interaction between the boundary layer and the inviscid flow and that as Reynolds number increases,  $\delta^*$  is reduced as expected, but also changes in the slope  $d\delta^*/dx$  occur at critical points on the model which influence the pressure distribution.

The application of the strong interaction theory to the AGARD contours was made with no modifications of the parameters in the integral boundary layer technique. Further refinement of the analysis could yield improved results for the 15° boattail.

## 5. SUMMARY AND CONCLUSIONS

Data obtained in support of the AGARD research program on "Improved Nozzle Testing Techniques in Transonic Flow" has provided valuable information concerning exhaust nozzle boattail performance. In particular, the Reynolds number variations from tests at AEDC and the boundary layer variations from test data obtained at RR, ONERA, and NLR have yielded similar nozzle boattail performance trends as the displacement thickness of the boundary layer approaching the nozzle boattail shoulder was changed. In general, the experimental data indicates the following trends for the AGARD 10° and 15° contours:

- (a) At a Mach number of 0.8, increasing Reynolds number or decreasing  $\delta^*$  increases the expansion at the boattail shoulder and the recompression at the boattail exit. These effects tend to be compensating and the pressure drag increases only slightly.
- (b) At 0.9 Mach number, increasing Reynolds number or decreasing  $\delta^*$  produces only small changes in the recompression region but increases the expansion near the boattail shoulder. These combined effects yield an increased pressure drag.
- (c) Increasing the Reynolds number or decreasing  $\delta^*$  at a Mach number of 0.95 alters the flow such that expansion is greater and recompression is less resulting again in a higher nozzle pressure drag.

For the 25° boattail contour, the data indicates that the flow on the surface is separated just downstream of the shoulder. There is evidence of a shock associated with this separation, and changing the Reynolds number influences this viscous-inviscid interaction. The point at which flow separation occurs does not appear to change significantly as Reynolds number is changed although there is some variation on the level of pressure in the separated zone.

Analytical procedures using "viscous-inviscid strong interaction" techniques were applied which verified the trends in the experimental pressure data and yield comparable results to the experiments for boattails without extensive flow separation. Further efforts are required to refine the analytical procedures and extend them to cases with strong shock-boundary layer interactions.

From the data and analysis presented in this paper, it is clear that the effect of Reynolds number or boundary layer displacement thickness variations on the transonic flow over a given nozzle shape must be addressed in terms of a rather complicated interaction of the viscous and inviscid flow, which may under certain conditions include the presence of shock waves. Changing Reynolds number or  $\delta^*$  alters the basic interaction between the viscous and inviscid flow which under certain conditions may result in an increase in drag, while at other conditions it may result



in a decrease in drag. Some of the data (e.g. AEDC subscale) indicates that other factors, such as model mounting techniques, tunnel wall and blockage effects, might also influence the magnitude of the pressure data and the absolute value of the drag coefficients.

## REFERENCES

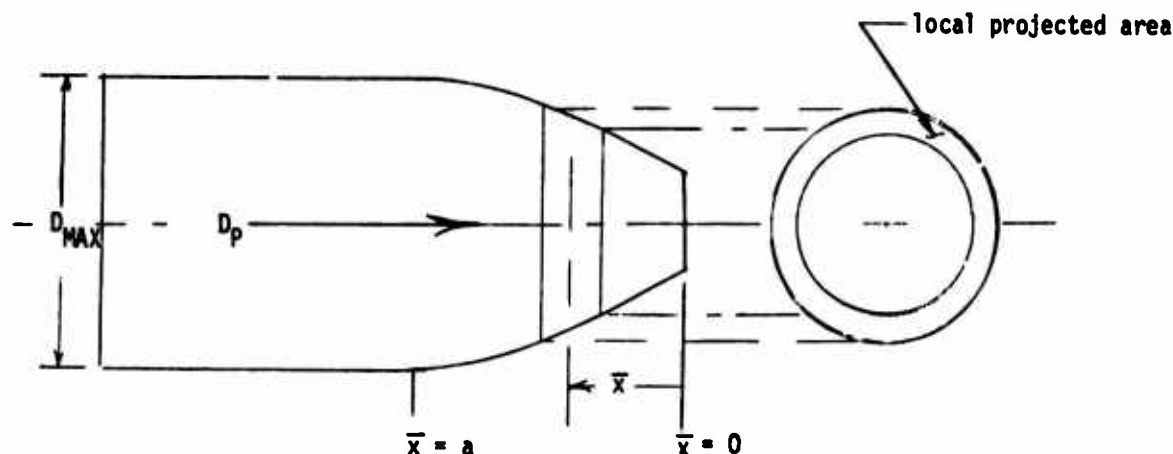
1. Bower, W.W. *An Analytical Procedure for the Calculation of Attached and Separated Subsonic Diffuser Flows*, to be presented at AIAA/SAE 10th Propulsion Specialists Conference, San Diego, California, October 1974.
2. — *Arnold Engineering Development Center, AGARD NAB Study (Phase I) In The Propulsion Wind Tunnel (16T), Test Plan — TF 337, February 1974.*
3. NASA, Langley *Improved Nozzle Testing Techniques In Transonic Flow*, Unpublished data, November 1973.
4. Dansby, T *Reynolds Number Effects On The Boattail Characteristics of A Simulated Nozzle At A Mach Number of 0.8*, ARL-TR-74-0120, June 1974.
5. Deer, D.J. *Results Of Tests On Single Afterbody Nozzles Defined By AGARD*, Rolls Royce (1971) Limited, Bristol Engine Division Report PPE 67, March 1974.
6. Harper, L.R. *The Influence of Boundary Layer Thickness On Nozzle Afterbody Pressure Drag*, Rolls Royce (1971) Limited, Bristol Engine Division Report PPE 69, April 1974.
7. — *ONERA, Improved Nozzle Testing in Transonic Flow*, Data Transmittal, March 1974.
8. — *NLR, Improved Nozzle Testing Techniques in Transonic Flow Preliminary Results of NLR Contribution to AGARD ad hoc Study*, National Aerospace Laboratory Report AV-74-02, May 1974.
9. Riedel, H.  
Emunds, H. *Preliminary Report On AGARD Research Project : 'Improved Nozzle Testing Techniques In Transonic Flow'*, DFVLR, Porz-Wahn, May 1974.
10. Krupp, J.A.  
Murman, E.M. *Computation of Transonic Flows Past Lifting Airfoils and Slender Bodies*, AIAA Journal, Vol.10, No.7, pp 880-886, July 1972.
11. Klineberg, J.M.  
Steger, J.L. *Calculation of Separated Flows at Subsonic and Transonic Speeds*, Third International Conference on Numerical Methods in Fluid Dynamics, Paris, France, July 1972.

## APPENDIX

## DERIVATION OF PRESSURE DRAG FORMULAS

The pressure drag ( $D_p$ ) of a nozzle boattail is the net force due to a local free-stream pressure difference ( $P_L - P_\infty$ ) that acts on the total projected area ( $A_p$ ) is simply the change in cross-sectional area of the boattail length, hence;

$$D_p = - \int_A (P_L - P_\infty) dA_L = - \int_{\bar{x}=0}^a (P_L - P_\infty) \frac{dA_L}{d\bar{x}} d\bar{x}$$



where  $\bar{x} = \frac{x}{D_{MAX}}$  and the subscript L denotes local conditions on the boattail. The pressure difference is related to the pressure coefficient, i.e.

$$C_{pL} = (P_L - P_\infty) / q_\infty$$

thus the pressure drag can be expressed in terms of  $C_{pL}$

$$D_p = - \int_{\bar{x}=0}^a C_{pL} q_\infty \frac{dA_L}{d\bar{x}} d\bar{x}$$

The pressure drag coefficient is defined as:

$$C_{Dp} = \frac{D_p}{q_\infty A_{Ref}}$$

which in terms of  $C_{pL}$  becomes

$$C_{Dp} = - \int_{\bar{x}=0}^a C_{pL} d(A_L / A_{Ref}) d\bar{x} \quad \text{where } A_{Ref} = \frac{(\pi D_{MAX}^2)}{4}$$

The local projected area (non-dimensionalized by reference area) associated with the local pressure coefficient can be defined as:

$$A_{pL} = \frac{d(A_L / A_{Ref})}{d\bar{x}}$$

and the local pressure drag coefficient associated with this local projected area is then defined as:

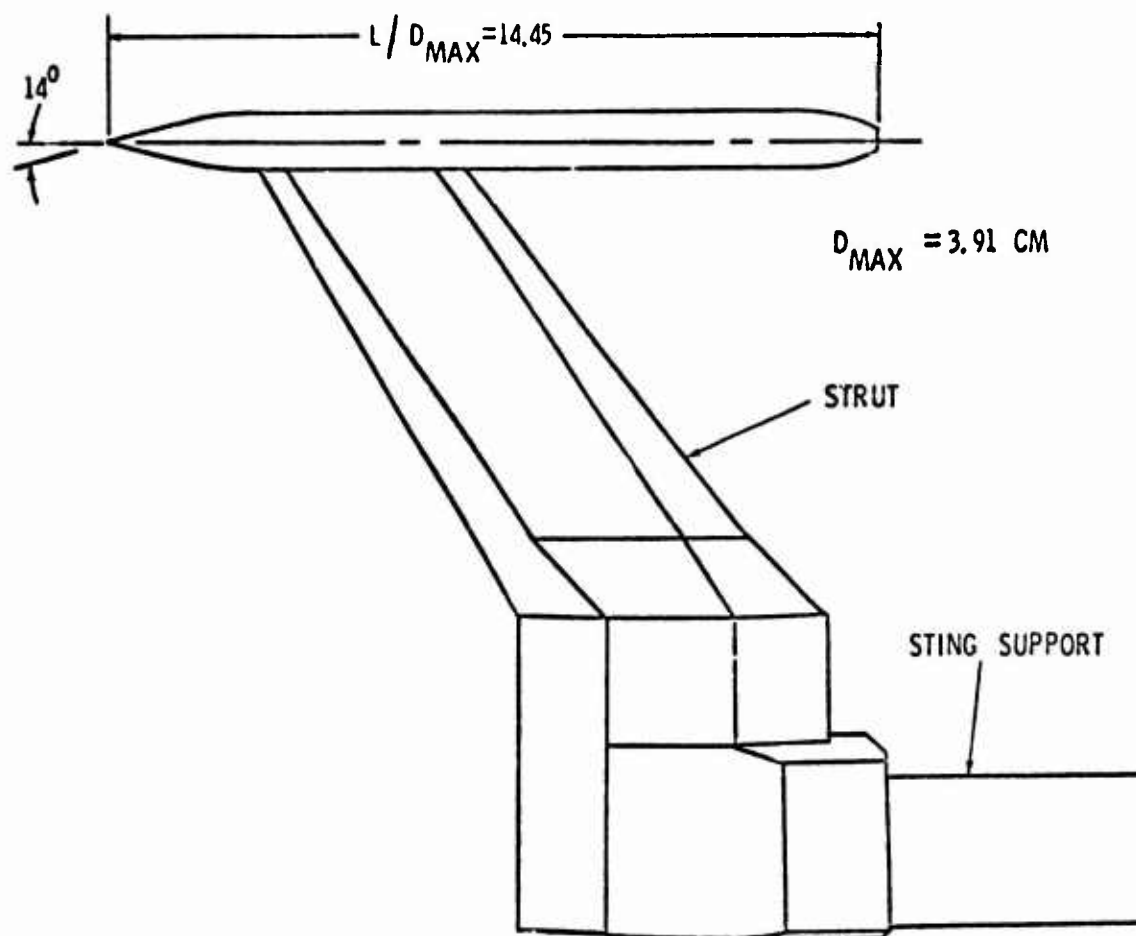
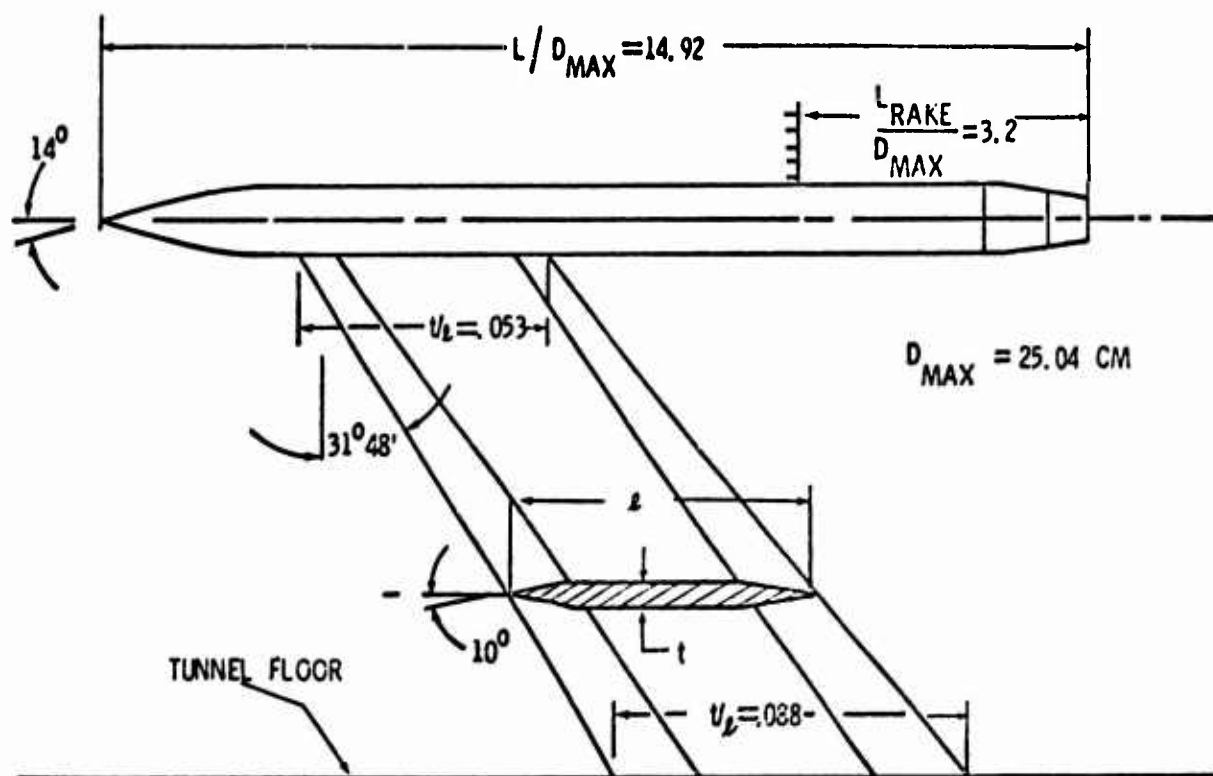
$$C_{DpL} = C_{pL} \cdot A_{pL} = C_{pL} \frac{d(A_L / A_{Ref})}{d\bar{x}}$$

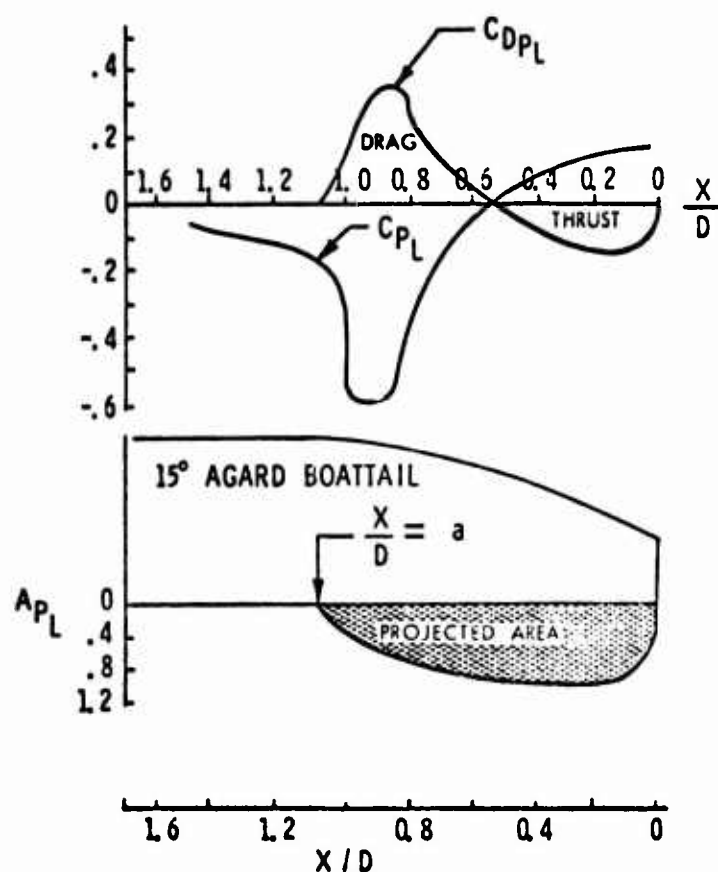
These are the parameters shown in Figures 3 and 4. The total pressure drag coefficient then becomes:

$$C_{Dp} = - \int_{\bar{x}=0}^a C_{DpL} d\bar{x}$$

Likewise the total projected area (non-dimensionalized by reference area) is given by:

$$A_p = \int_{\bar{x}=0}^{\bar{x}^*} A_{pL} \cdot d\bar{x}$$





$$\begin{aligned} M &= 0.9 \\ Re &= 2.5 \times 10^6 / \text{FT} \\ NPR &= 3 \end{aligned}$$

$$C_{DP} = - \int_0^a C_{DP_L} \cdot d\left(\frac{X}{D}\right)$$

$$C_{DP_L} = C_{P_L} \cdot A_{P_L}$$

$$A_P = \int_0^a A_{P_L} \cdot d\left(\frac{X}{D}\right)$$

Fig.3 Pressure distribution/projected area relation

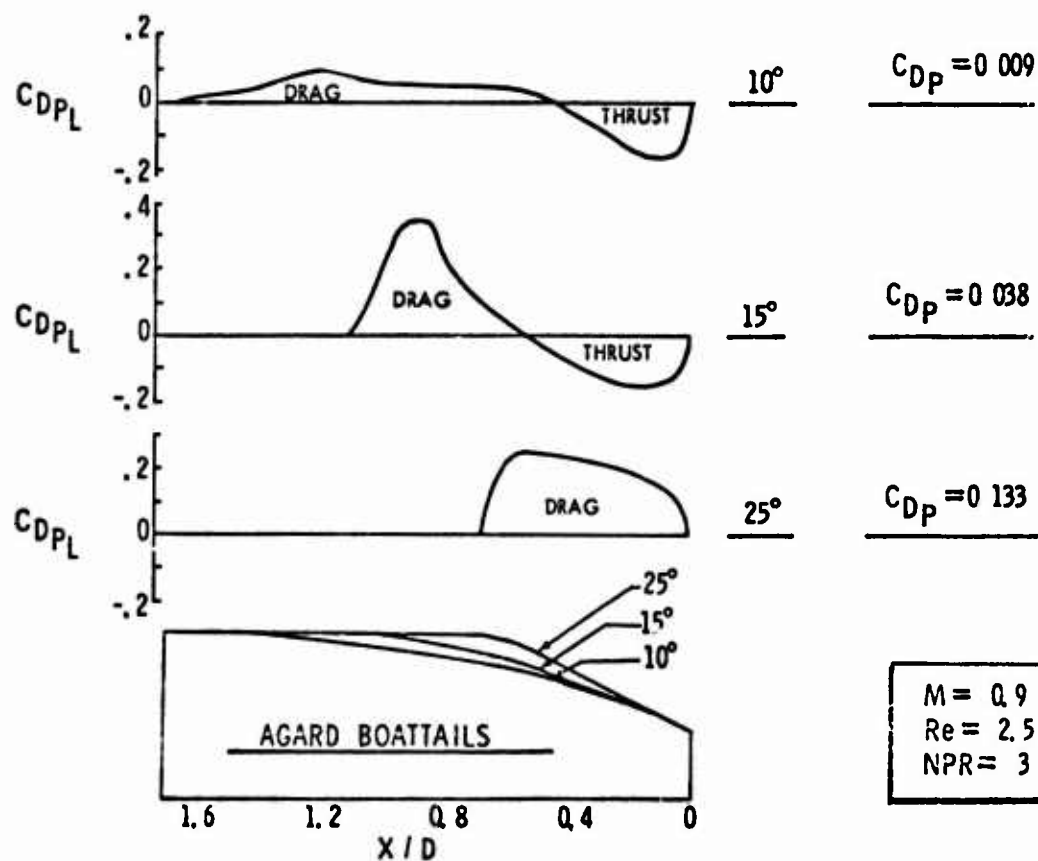


Fig.4 Relative areas of thrust and drag for AGARD contours

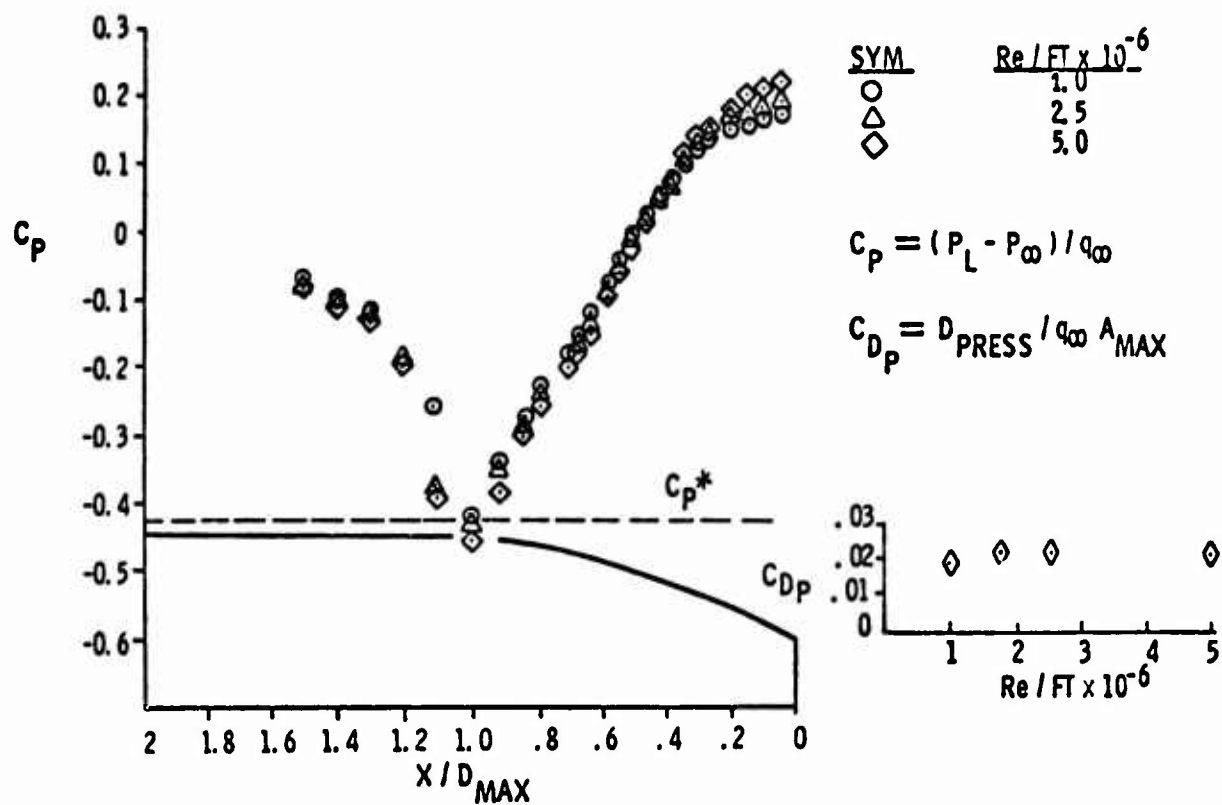


Fig.5 Reynolds No. variation, AEDC 15° boattail, M = .8

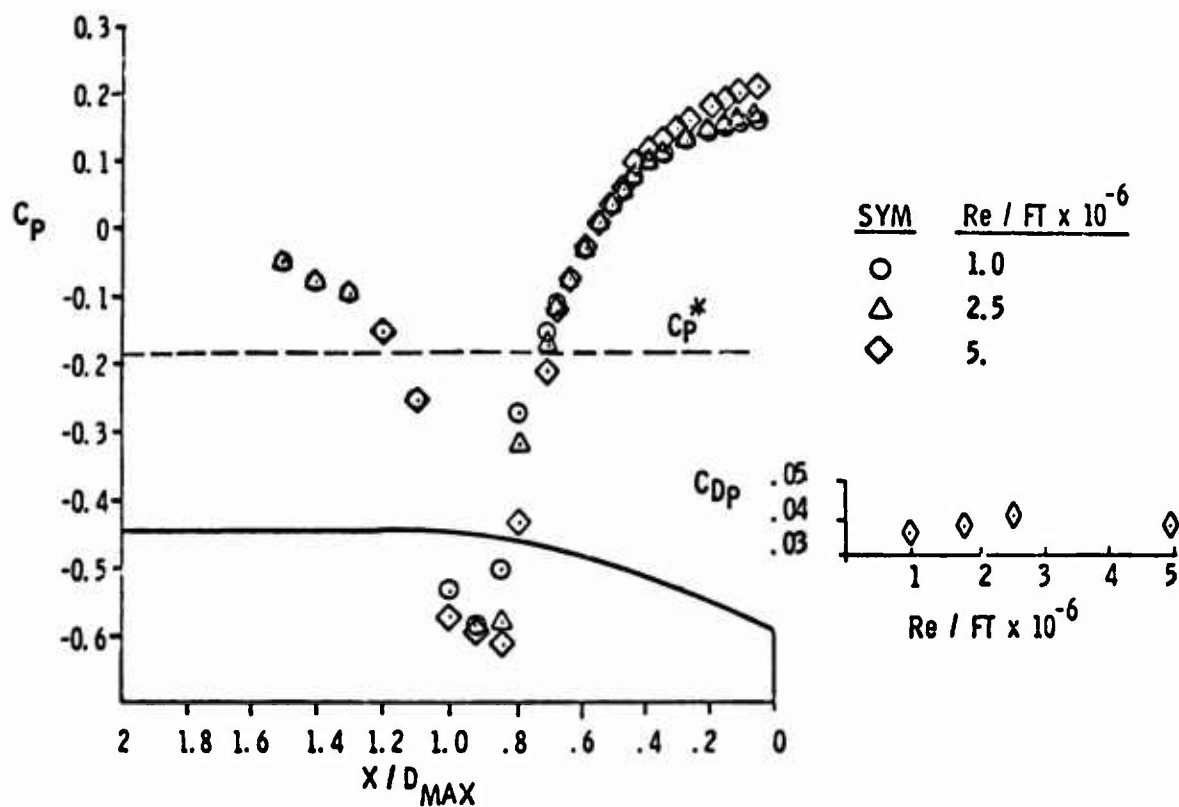
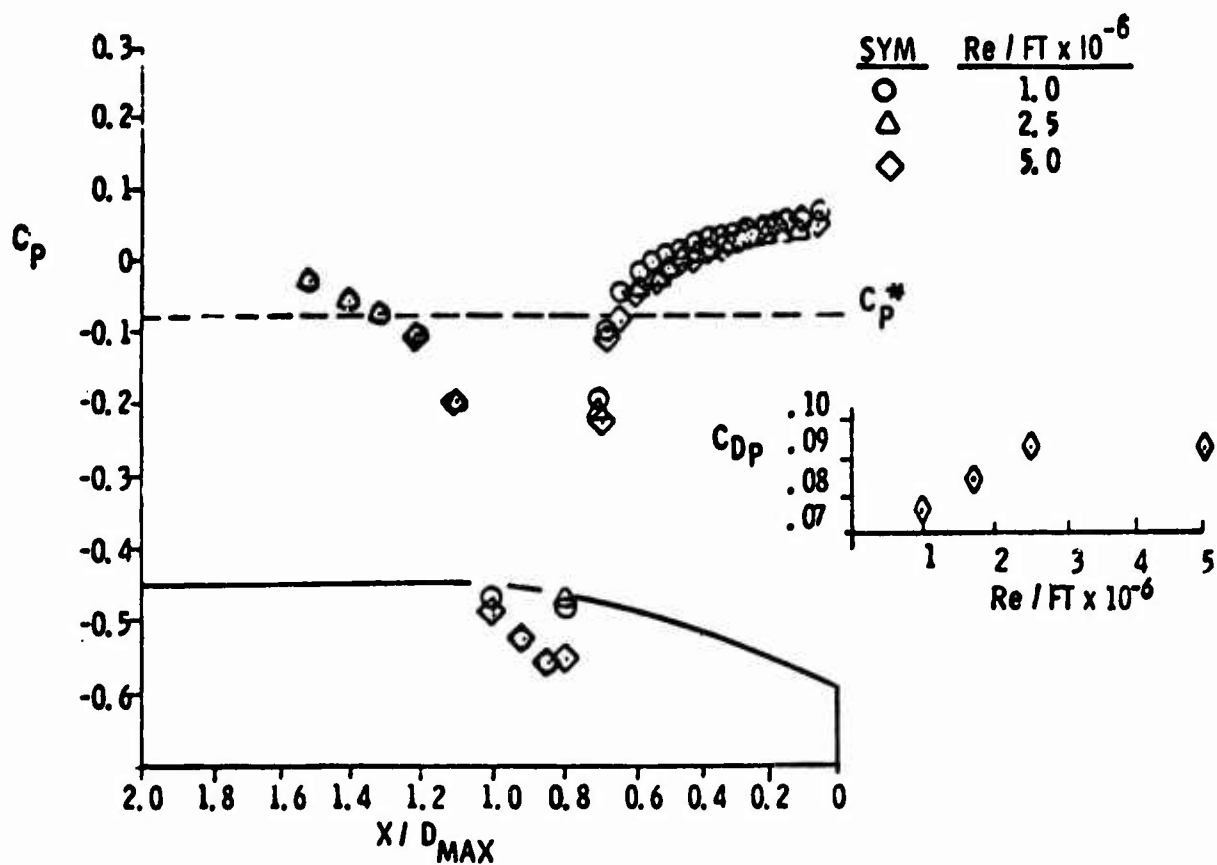
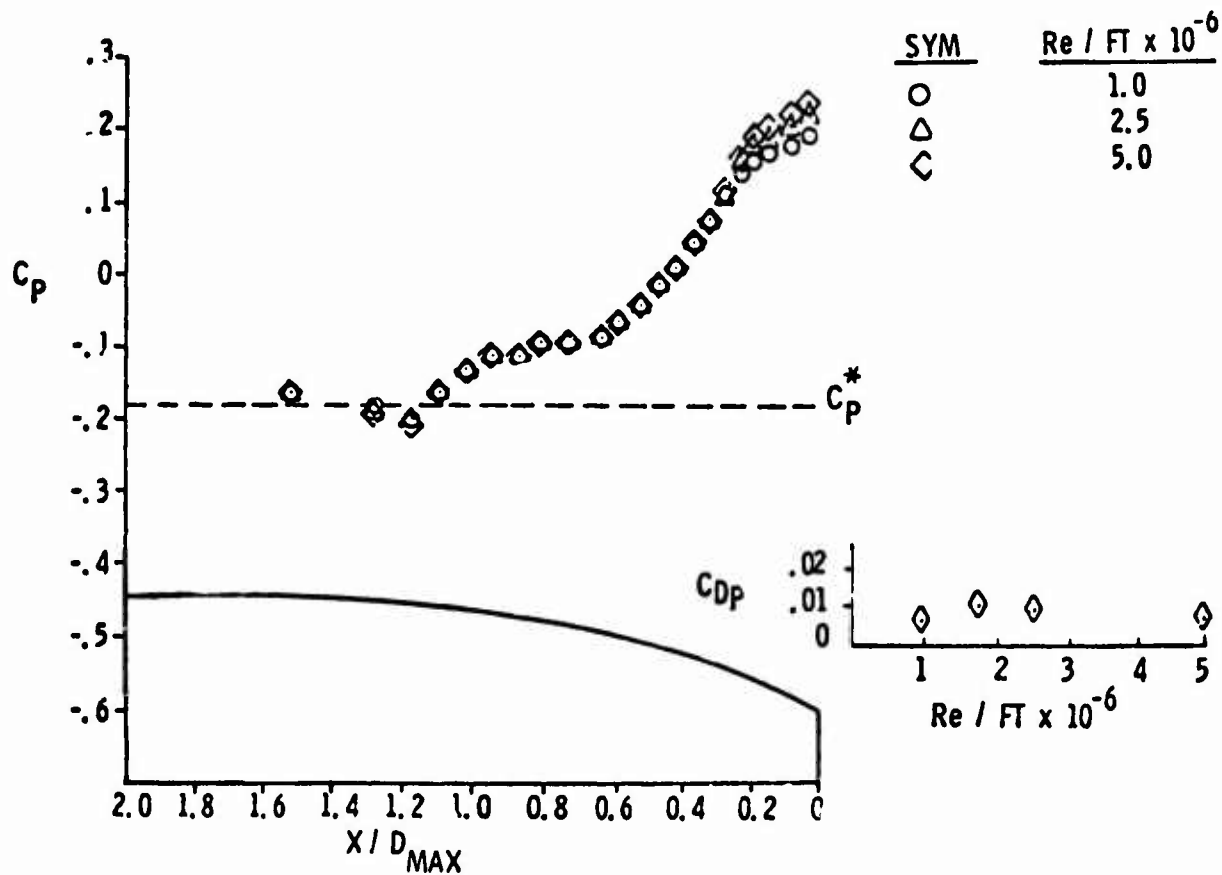
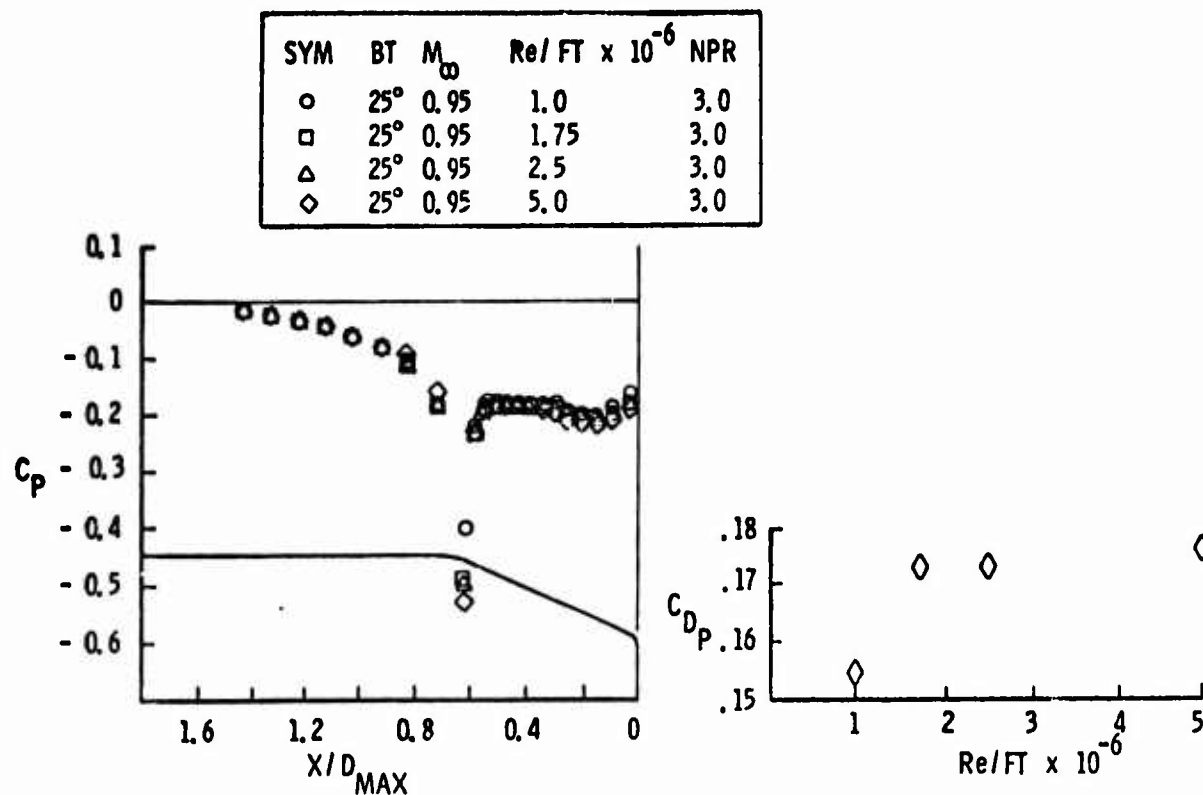
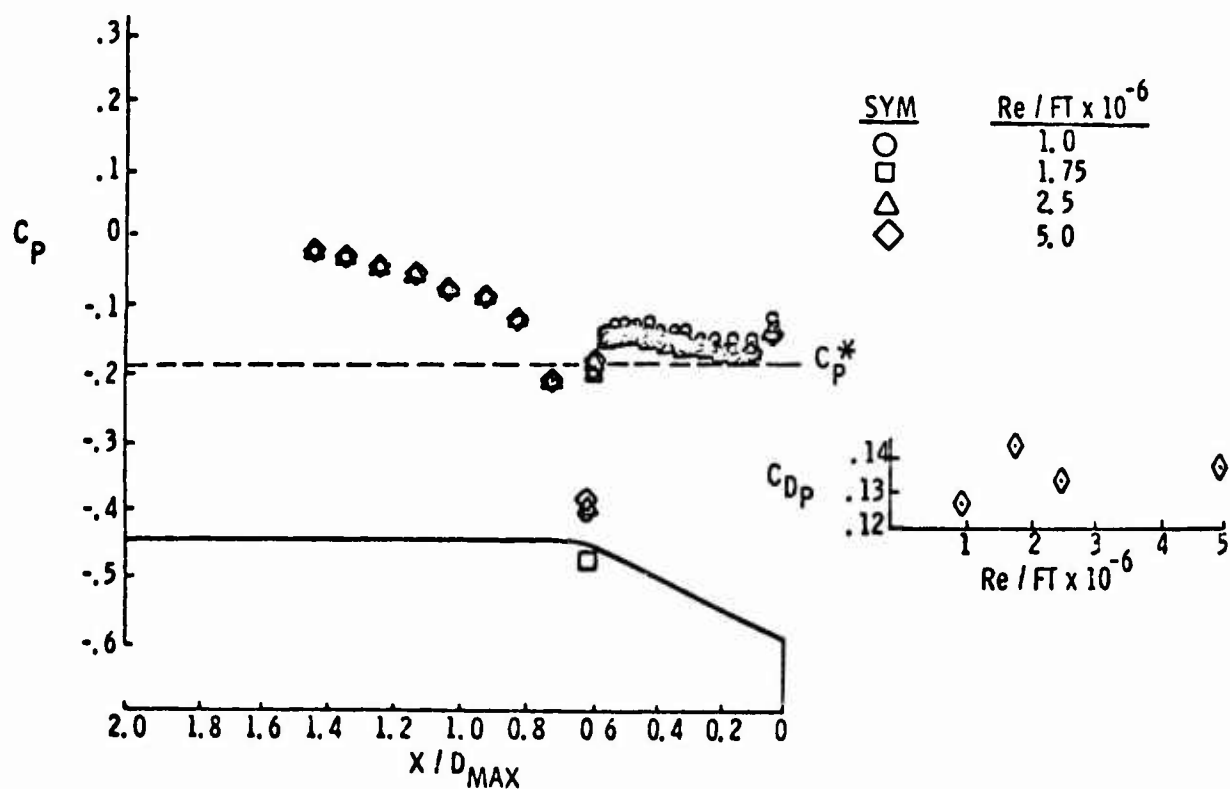


Fig.6 Reynolds No. variation, AEDC 15° boattail, M = .9

Fig.7 Reynolds No. variation, AEDC 15° boattail,  $M = .95$ Fig.8 Reynolds No. variation, AEDC 10° boattail,  $M = .9$

Fig.9 Reynolds No. variation, AEDC 25° boattail,  $M = .95$ Fig.10 Reynolds No. variation, AEDC 25° boattail,  $M = .9$



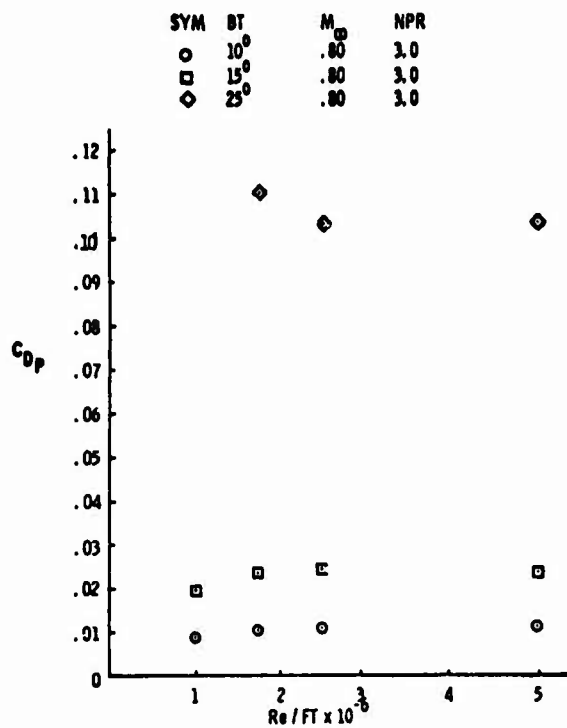


Fig. 11 Pressure drag summary with Reynolds No.  
AEDC 10°, 15°, 25° boattails  $M = .8$

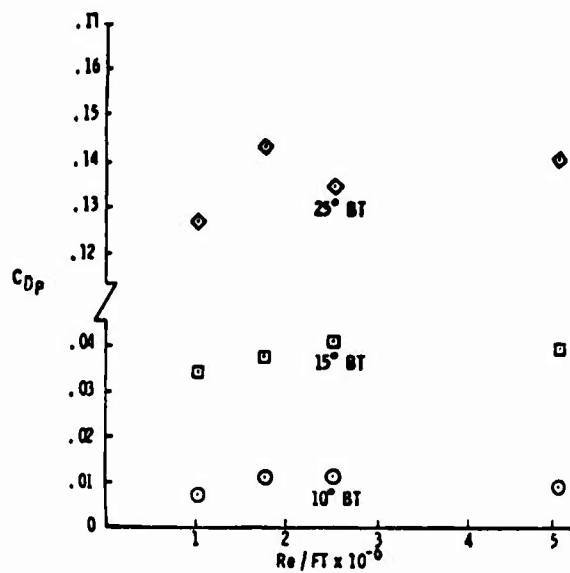


Fig. 12 Pressure drag summary with Reynolds No.  
AEDC 10°, 15°, 25° boattails,  $M = .9$

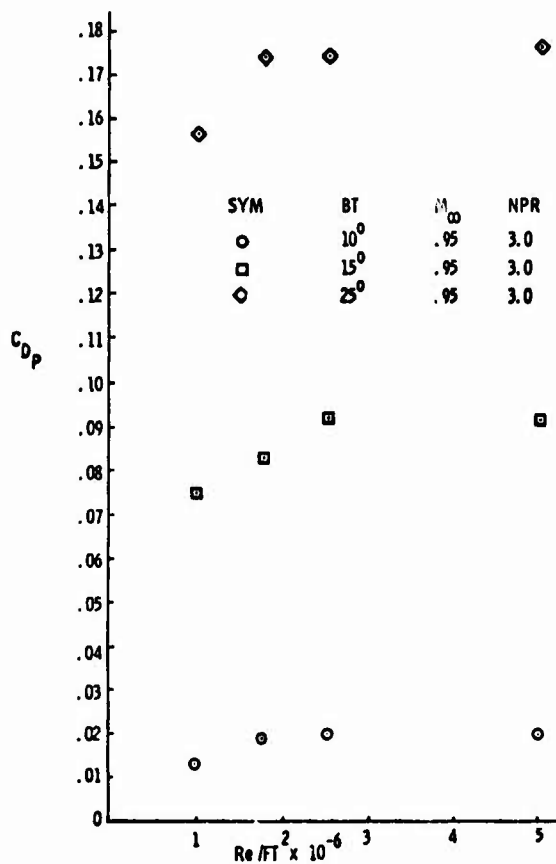
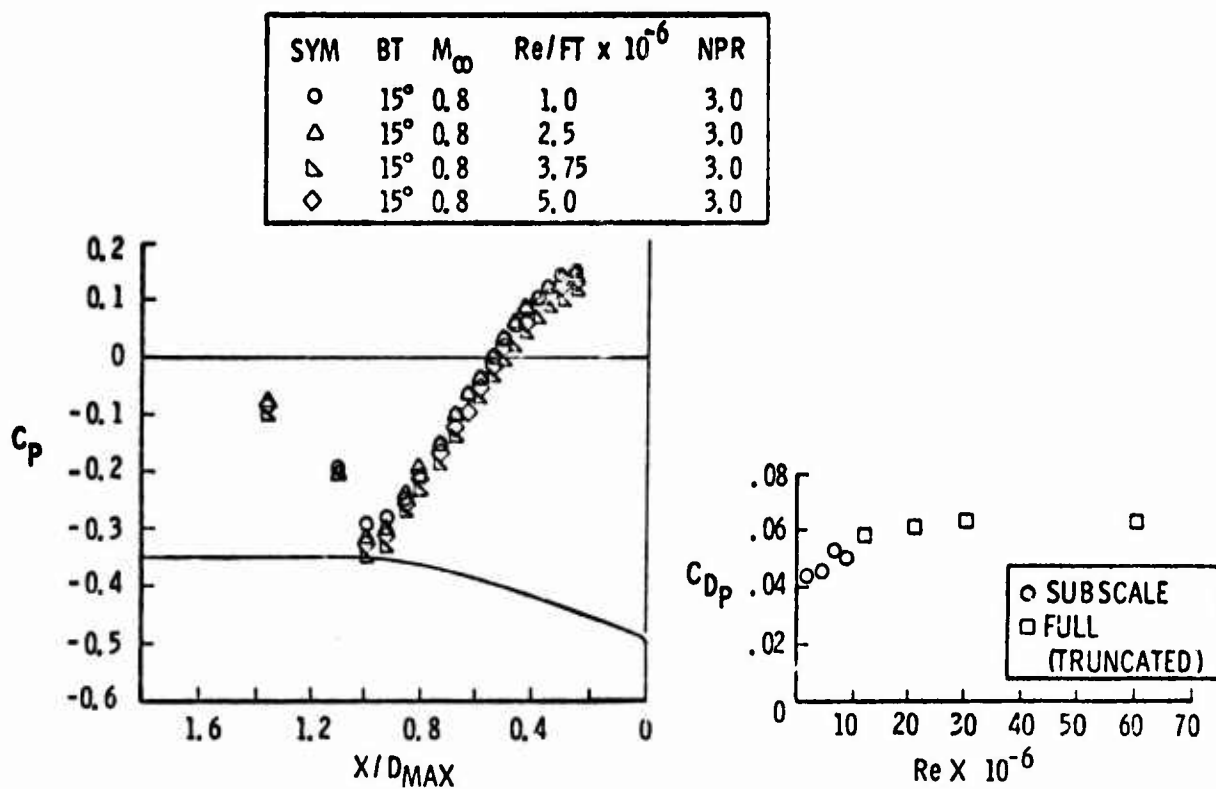
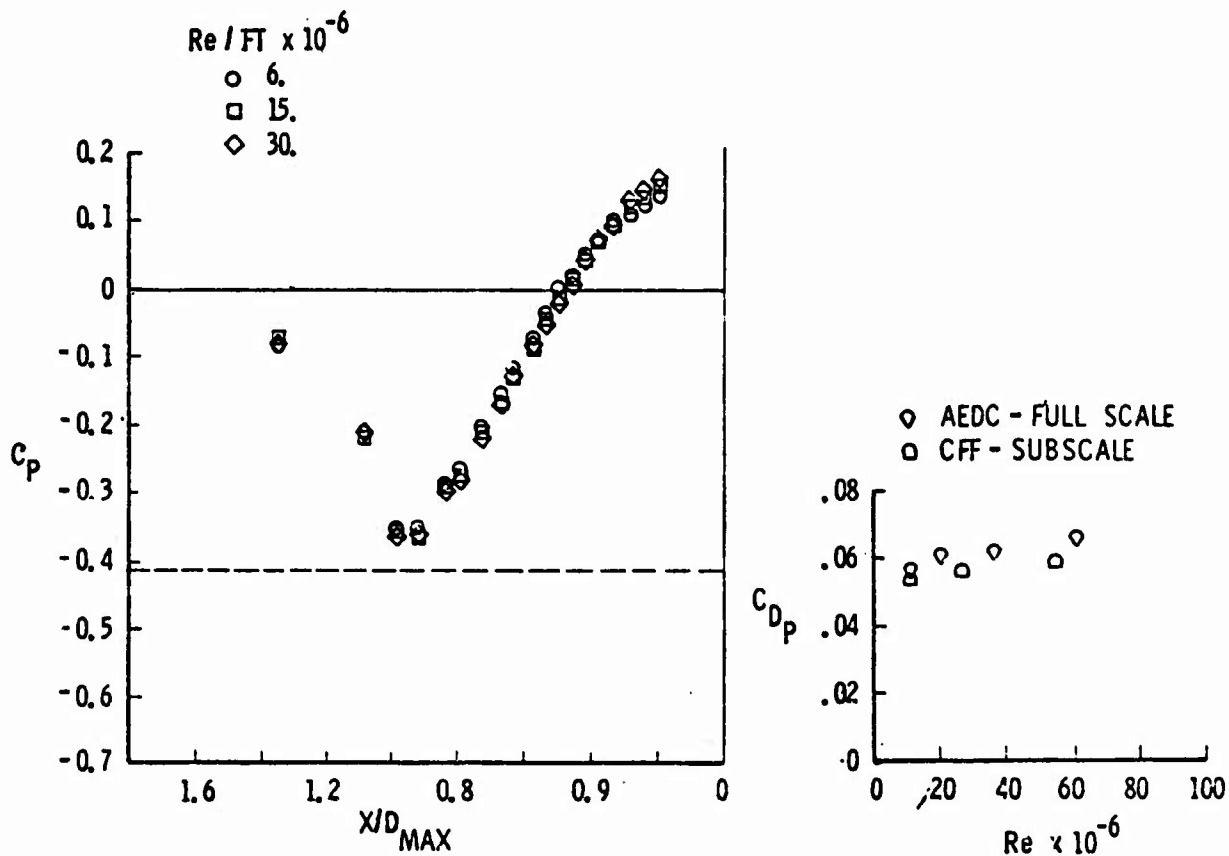
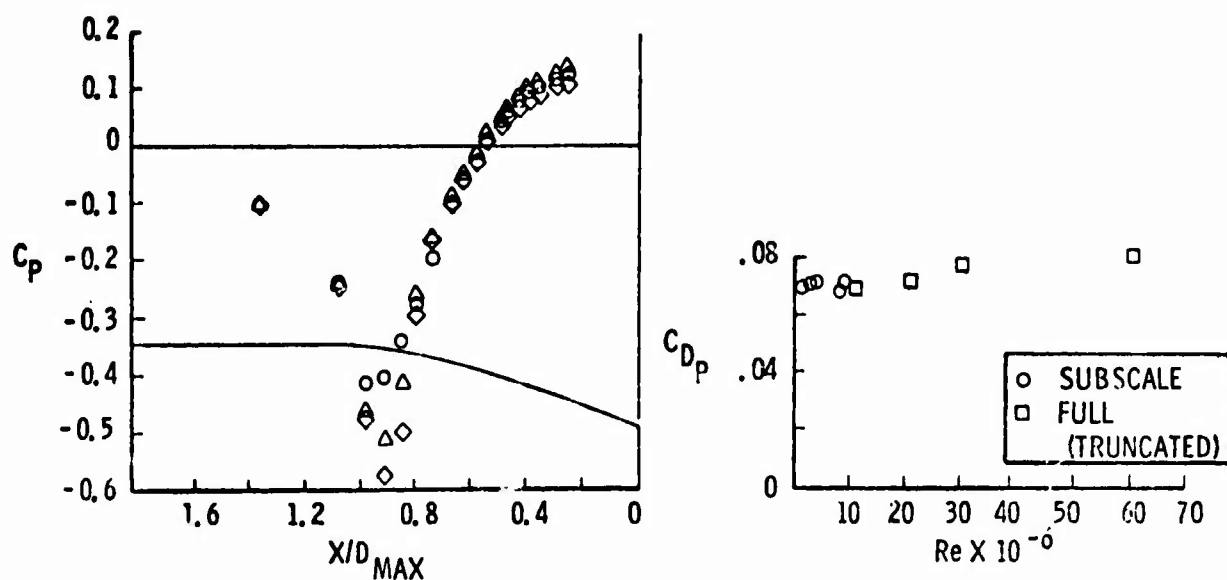
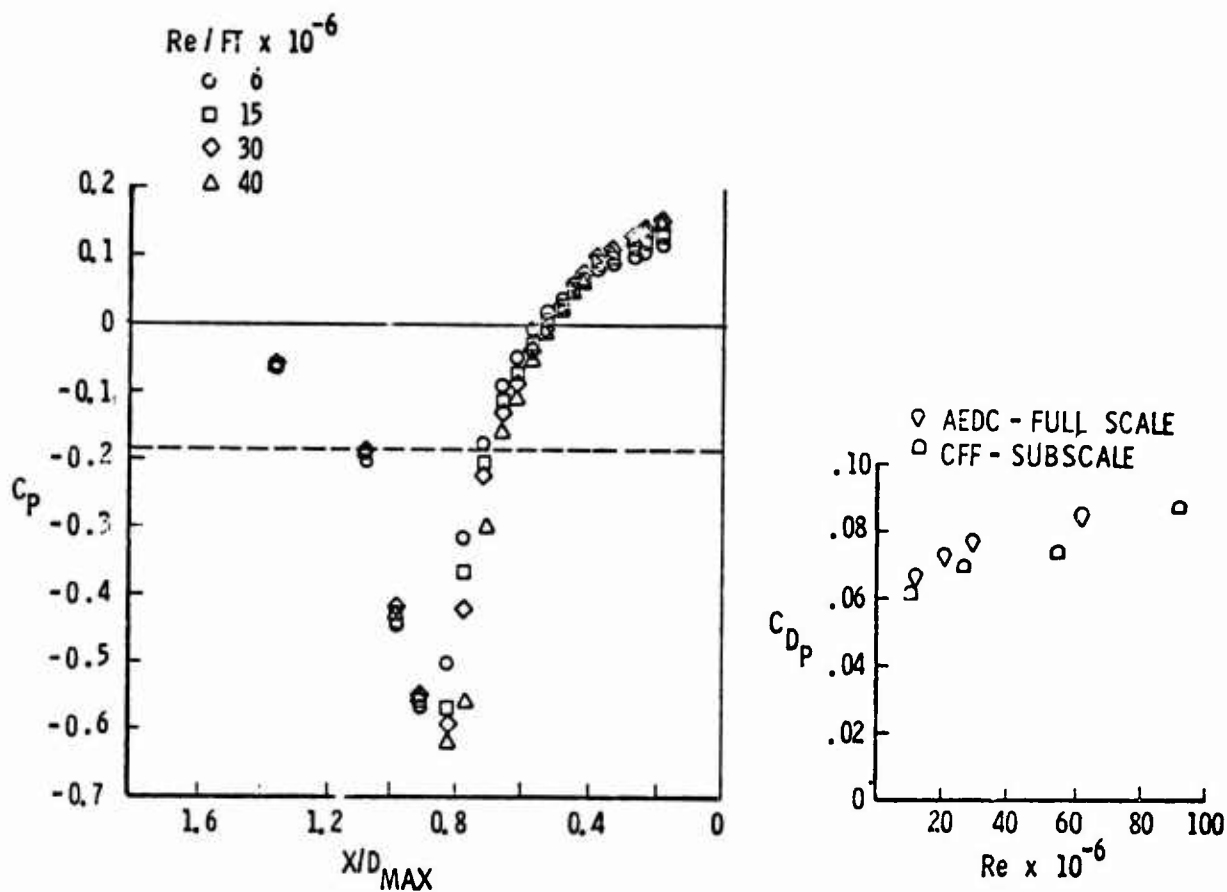
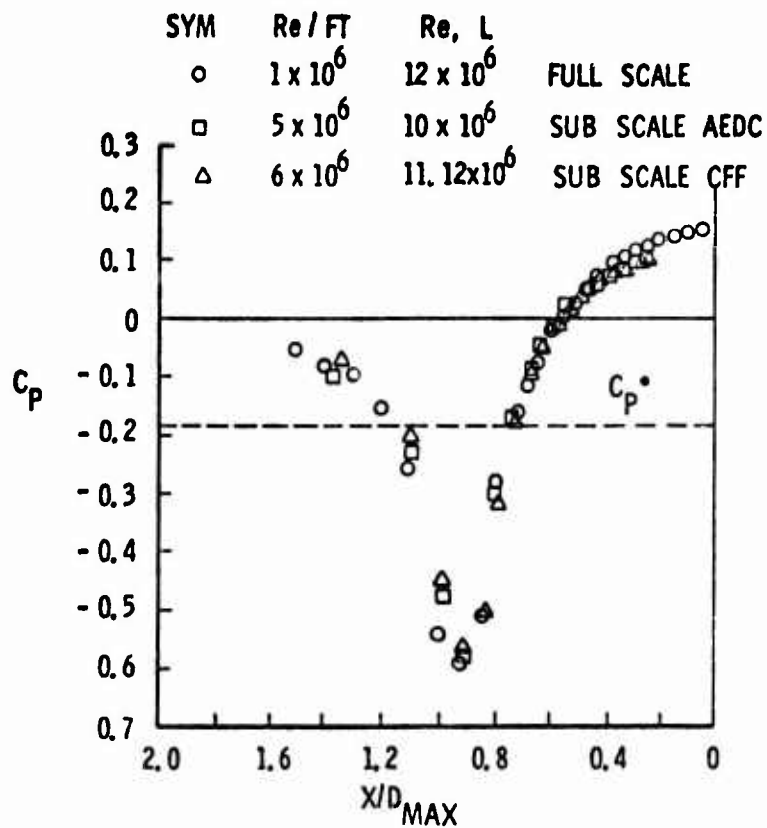
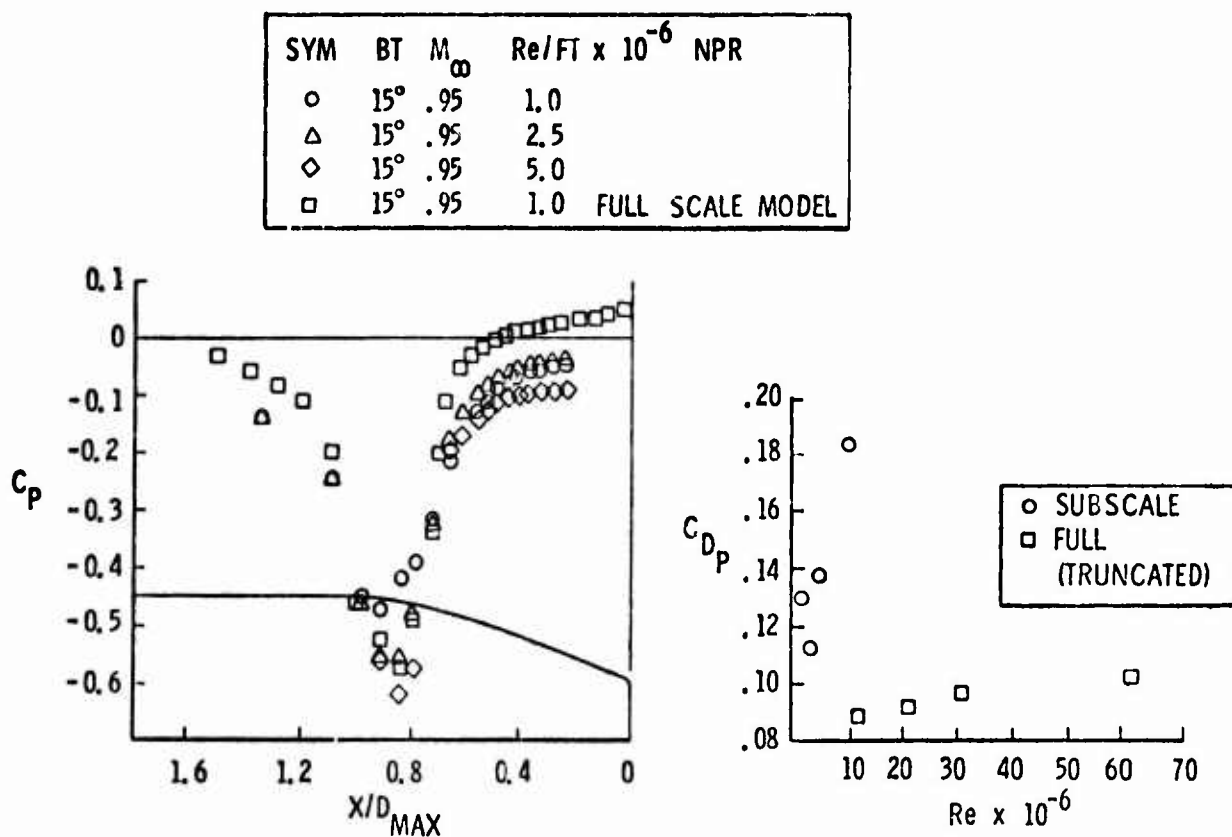


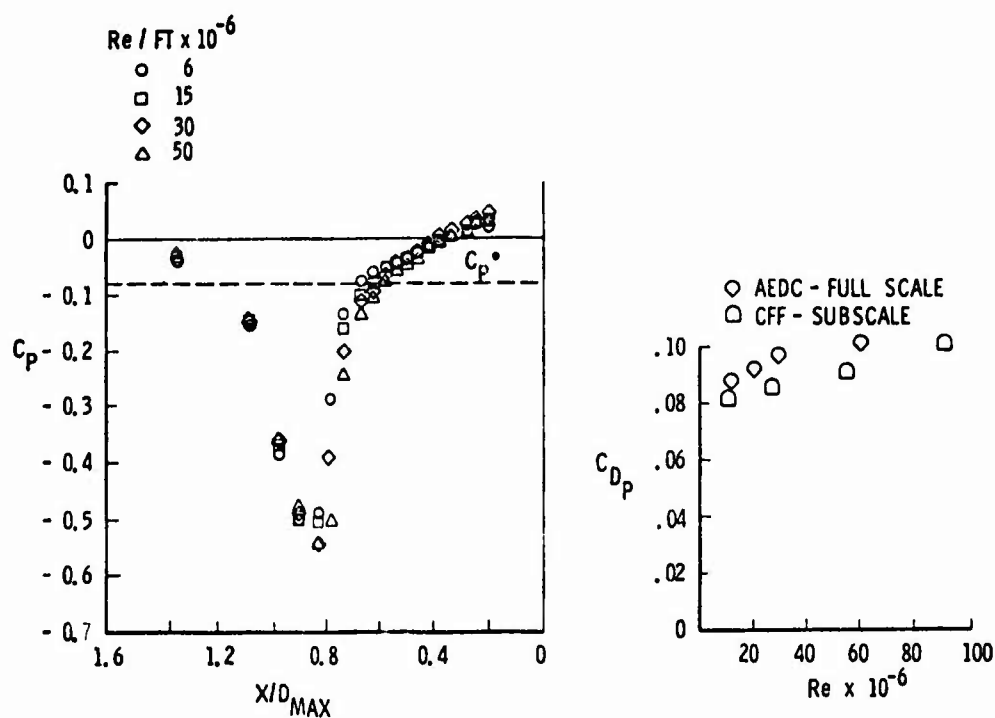
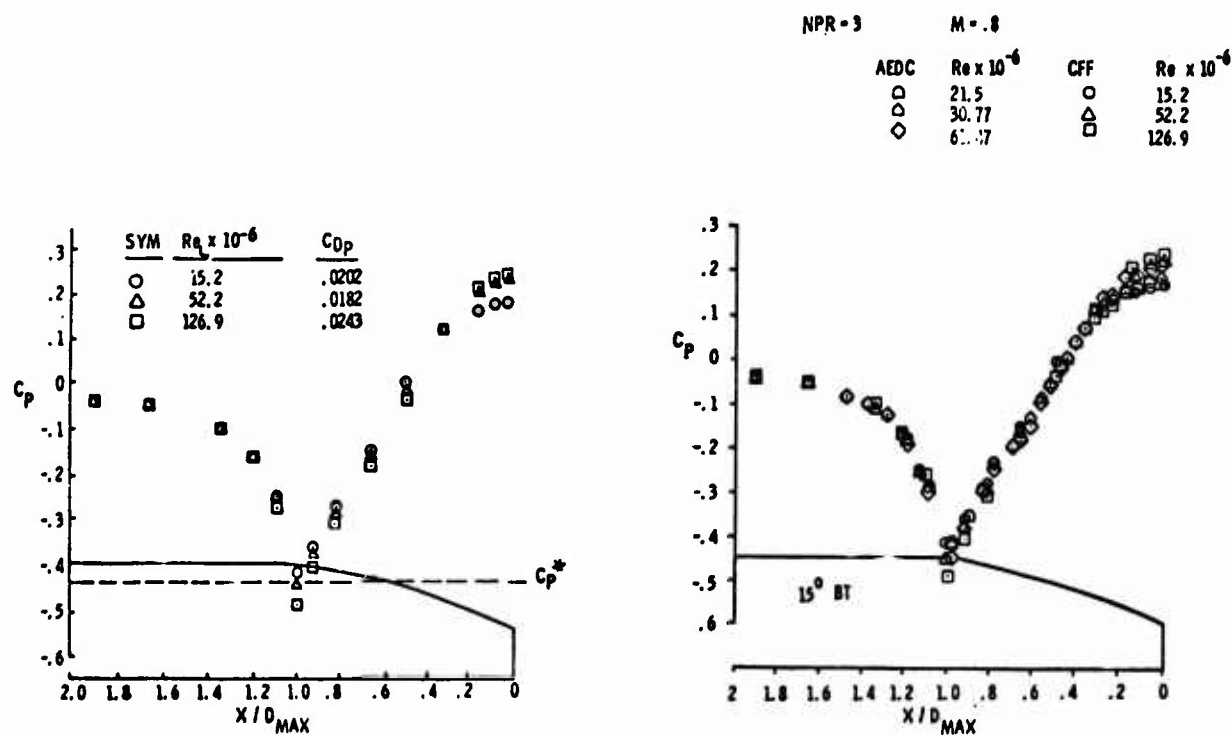
Fig. 13 Pressure drag summary with Reynolds No.  
AEDC 10°, 15°, 25° boattails,  $M = .95$

Fig.14(a) Reynolds No. variation, AEDC 15° subscale boattail,  $M = .8$ Fig.14(b) Reynolds No. variation, AEDC 15° subscale boattail,  $M = .8$

SYM	BT	M <sub>∞</sub>	Re/FT x 10 <sup>-6</sup>	NPR
○	15°	0.9	1.0	3.0
△	15°	0.9	2.5	3.0
◇	15°	0.9	5.0	3.0

Fig.15(a) Reynolds No. variation, AEDC 15° subscale boattail,  $M = .9$ Fig.15(b) Reynolds No. variation, CFF 15° subscale boattail  $M = .9$

Fig.16 Pressure distribution comparison, AEDC full scale and subscale 15° boattail,  $M = 0.9$ Fig.17(a) Reynolds No. variation, AEDC 15° subscale boattail,  $M = .95$

Fig.17(b) Reynolds No. variation, CFF 15° subscale boattail,  $M = .95$ Fig.18 Reynolds No. variation ARL 15° boattail,  $M = .8$ Fig.19 Reynolds No. variation AEDC and ARL 15° boattail,  $M = .8$

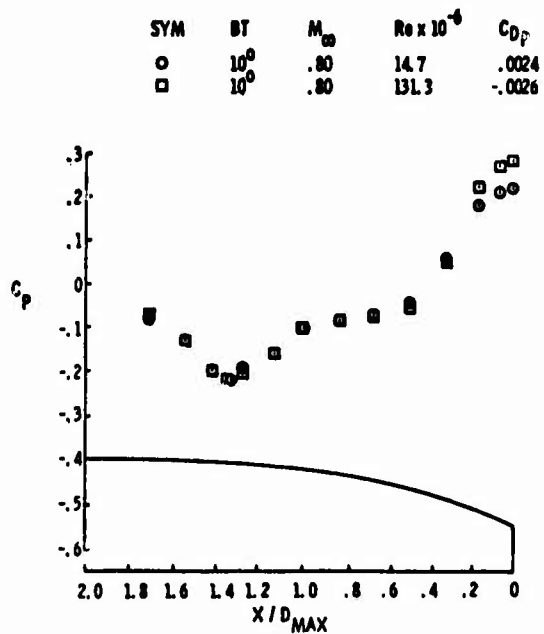


Fig.20 Reynolds No. variation ARL  $10^\circ$  boattail,  $M = .8$

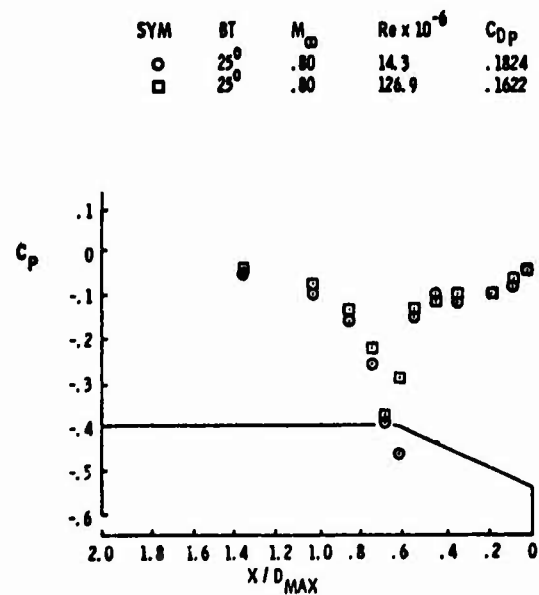


Fig.21 Reynolds No. variation ARL  $25^\circ$  boattail,  $M = .8$

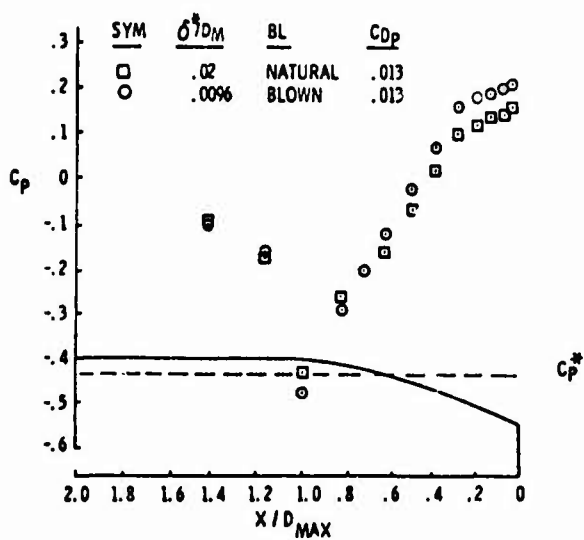


Fig.22 Displacement thickness variation RR  $15^\circ$  boattail,  $M = .8$

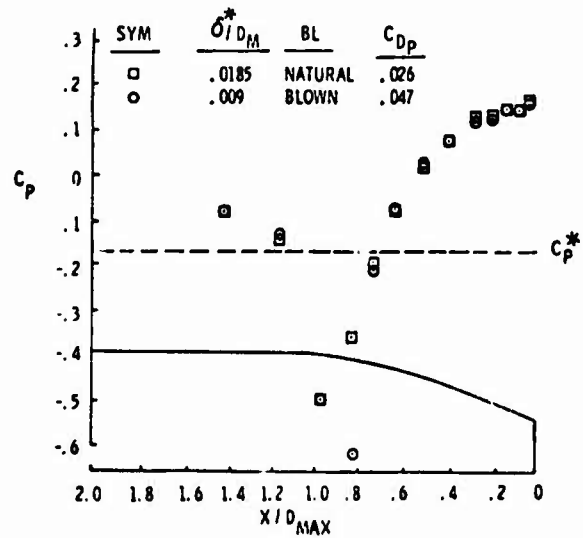


Fig.23 Displacement thickness variation RR  $15^\circ$  boattail,  $M = .91$

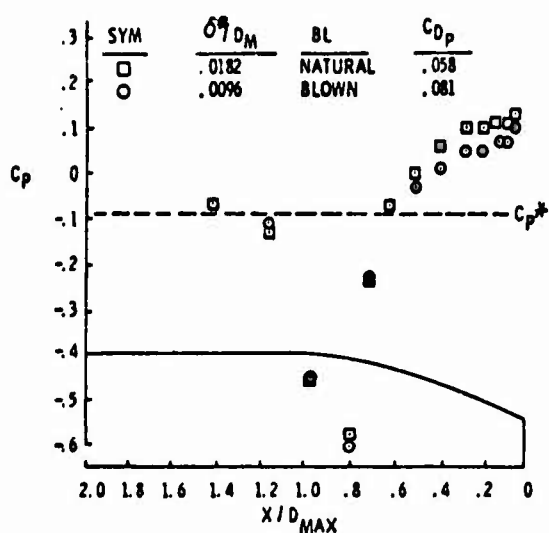


Fig.24 Displacement thickness variation RR 15° boattail,  $M = .95$

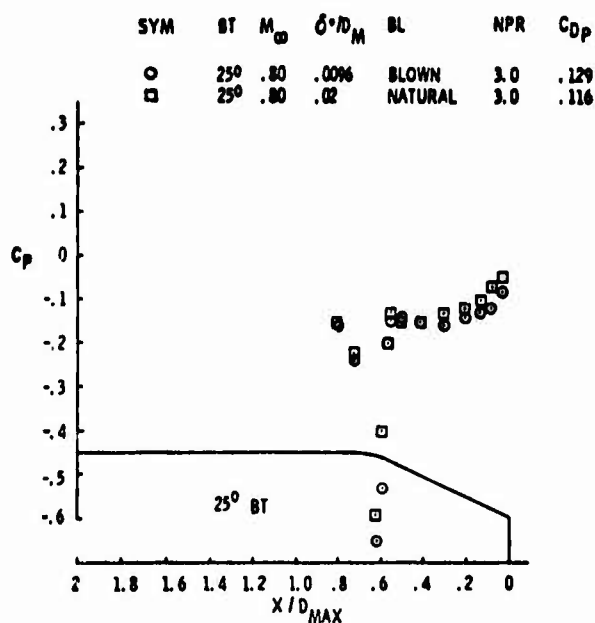


Fig.25 Displacement thickness variation RR 25° boattail,  $M = .8$

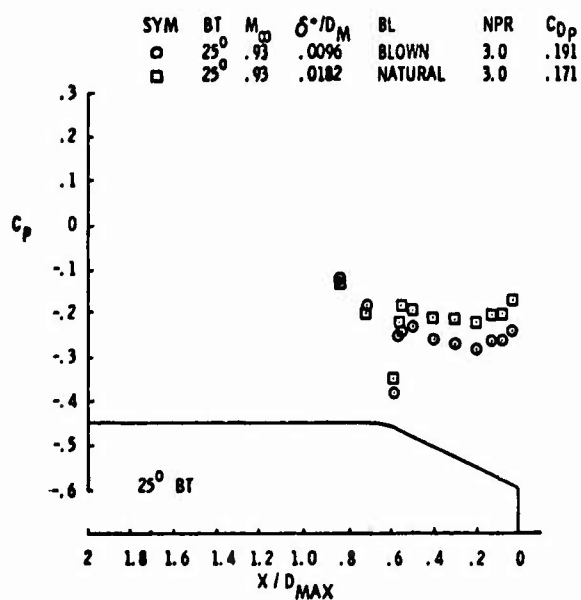


Fig.26 Displacement thickness variation RR 25° boattail,  $M = .93$

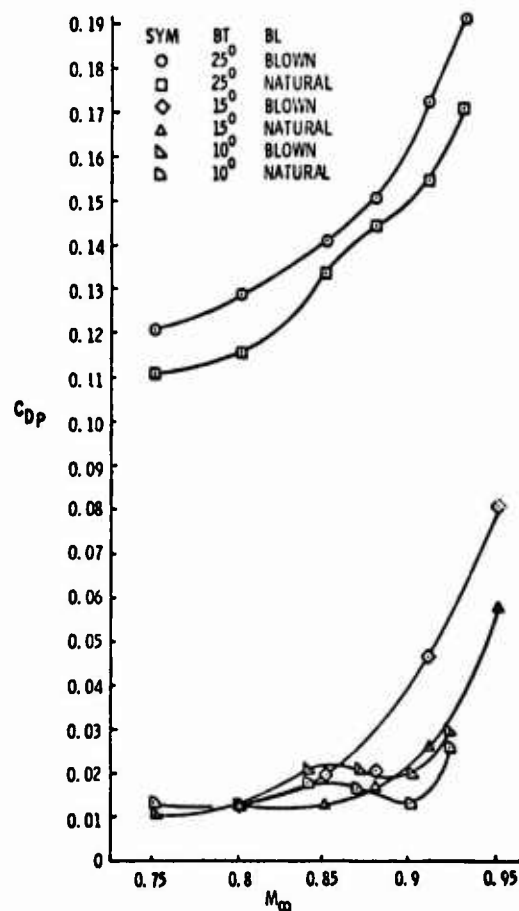


Fig.27 Pressure drag summary RR 10°, 15°, 25° boattail

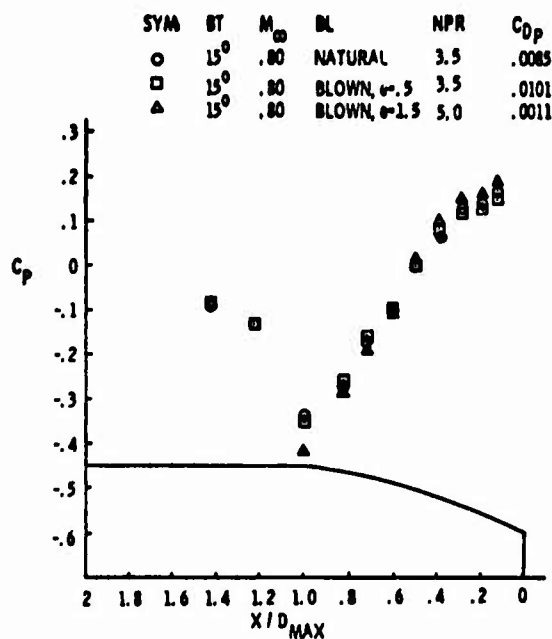


Fig.28 Displacement thickness variation ONERA 15° boattail,  $M = .8$

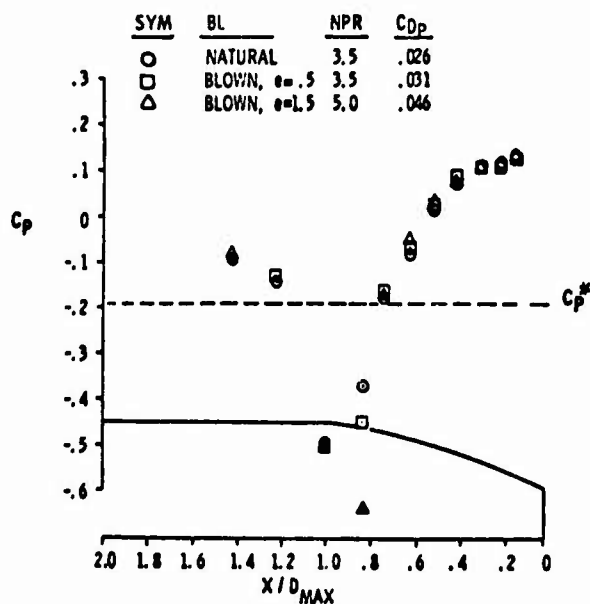


Fig.29 Displacement thickness variation ONERA 15° boattail,  $M = .9$

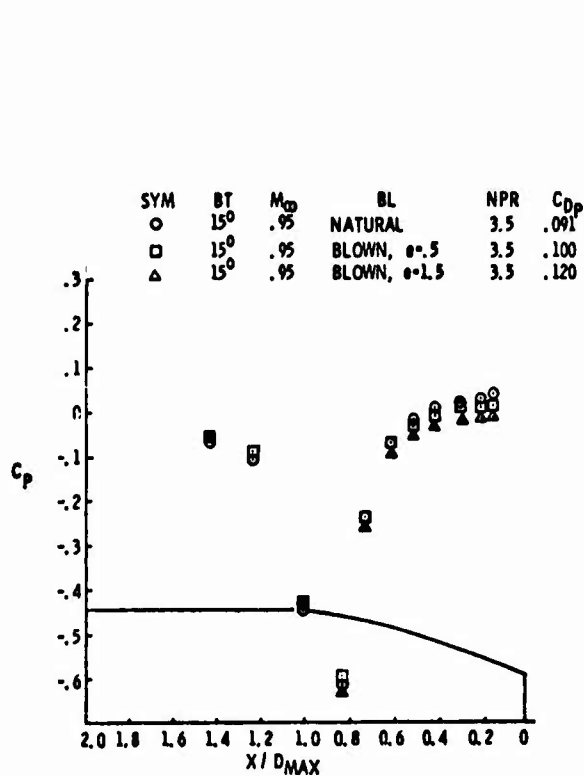


Fig.30 Displacement thickness variation ONERA 15° boattail,  $M = .95$

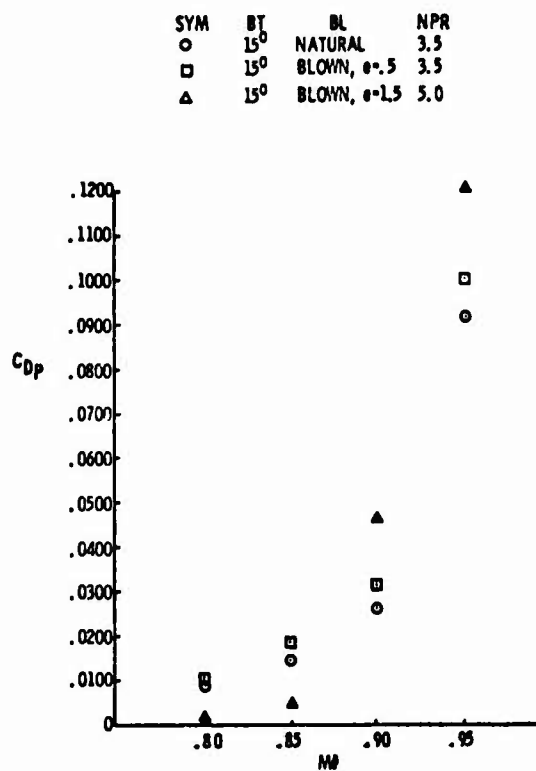


Fig.31 Pressure drag summary ONERA 15° boattail



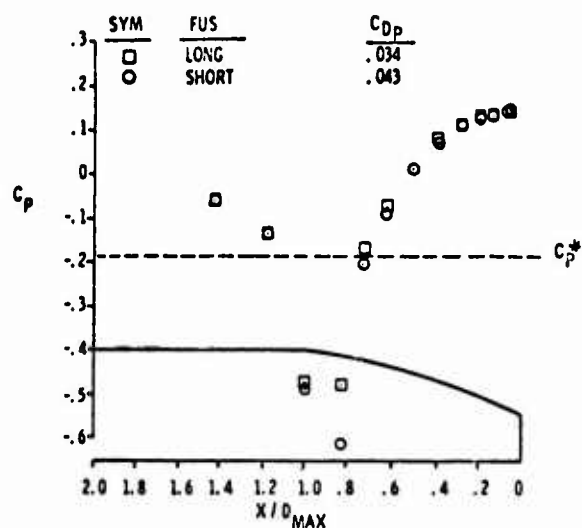


Fig.32 Displacement thickness variation NLR 15° boattail,  $M = .9$

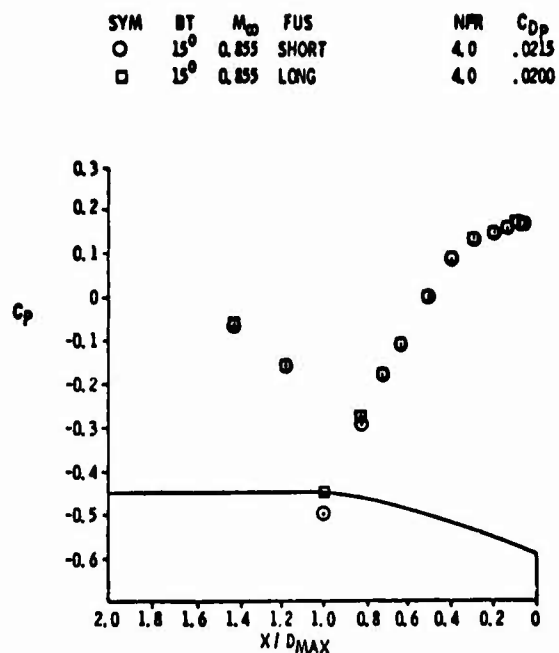


Fig.33 Displacement thickness variation NLR 15° boattail,  $M = .855$

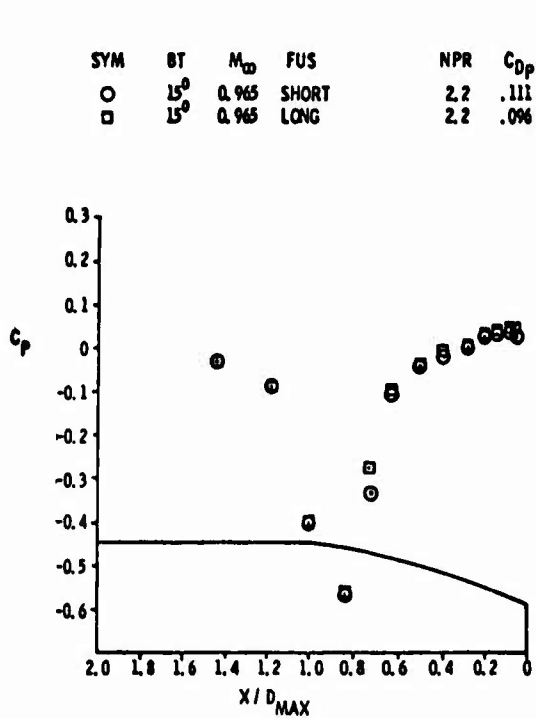


Fig.34 Displacement thickness variation NLR 15° boattail,  $M = .965$

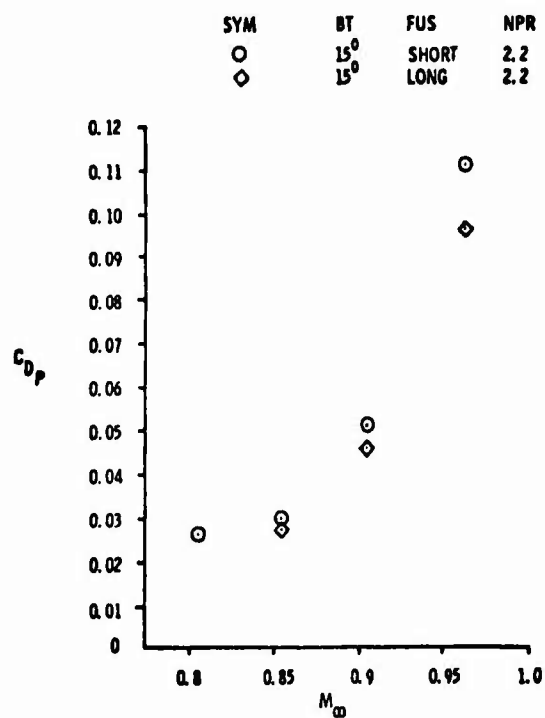


Fig.35 Pressure drag summary NLR 15° boattail

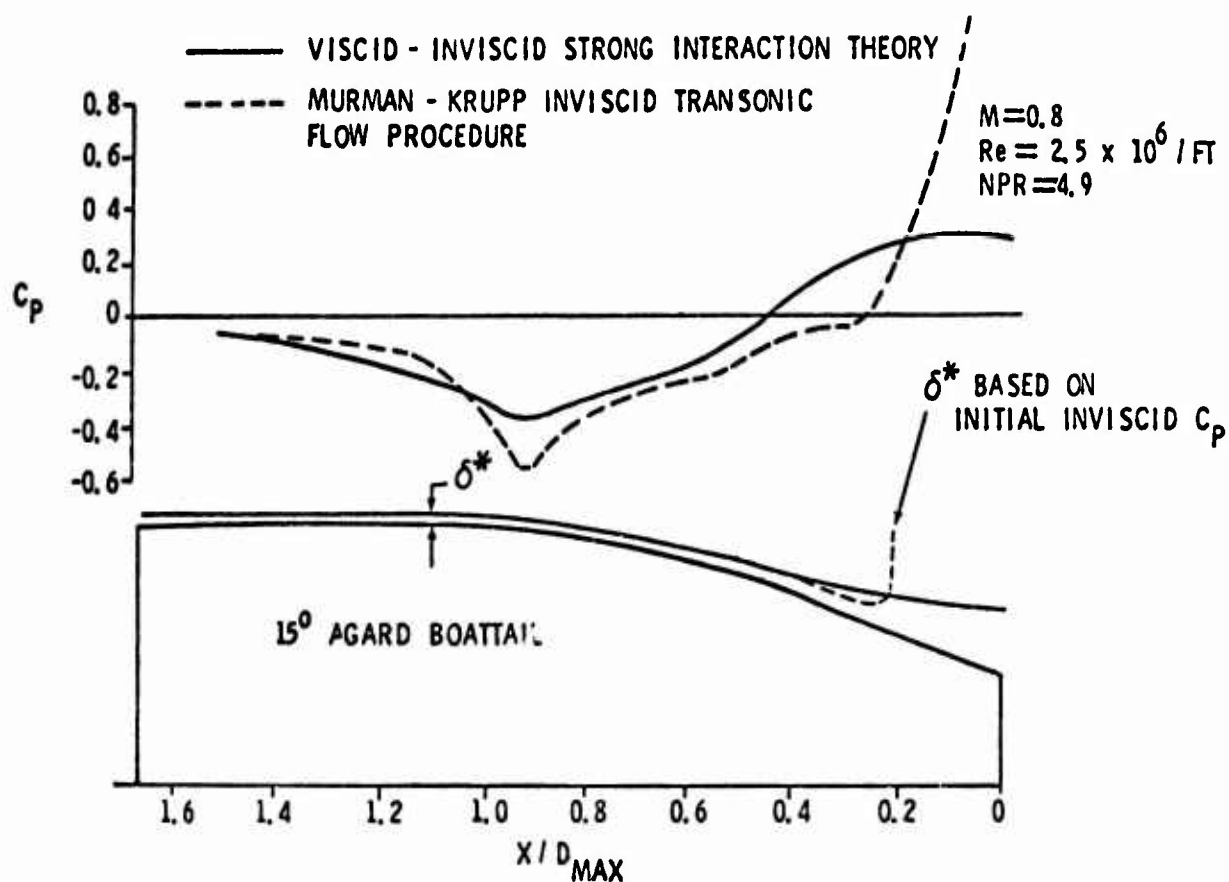


Fig.36 Comparison of theoretical pressure distributions

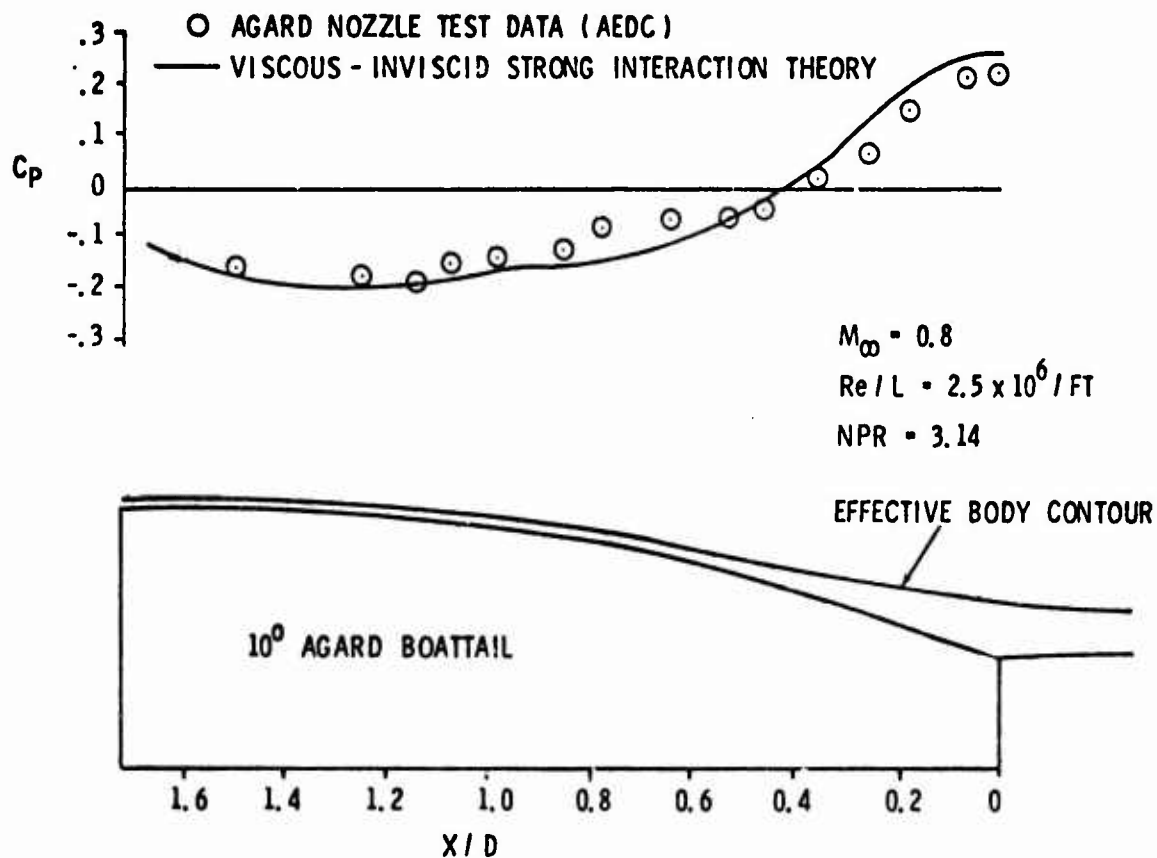


Fig.37 Comparison of measured and analytical pressure distributions

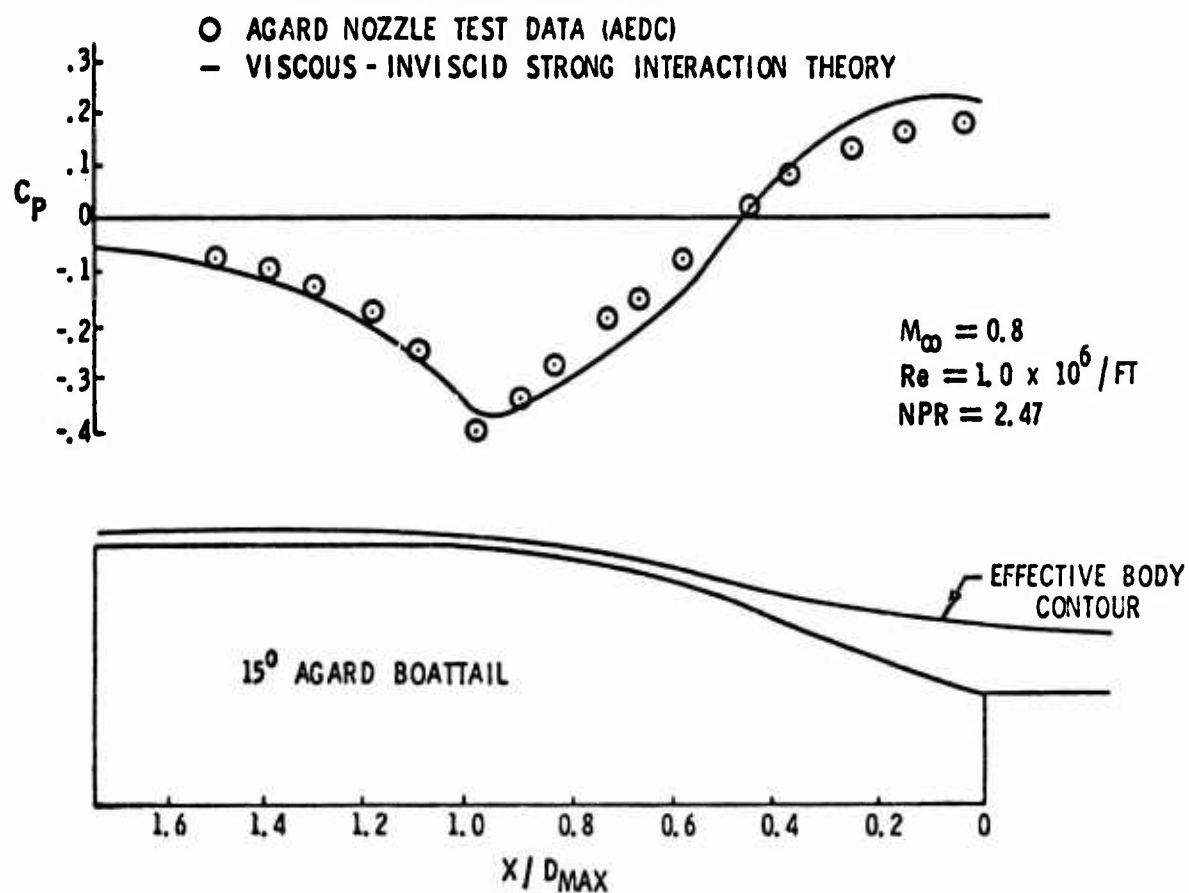


Fig.38 Comparison of measured and analytical pressure distributions

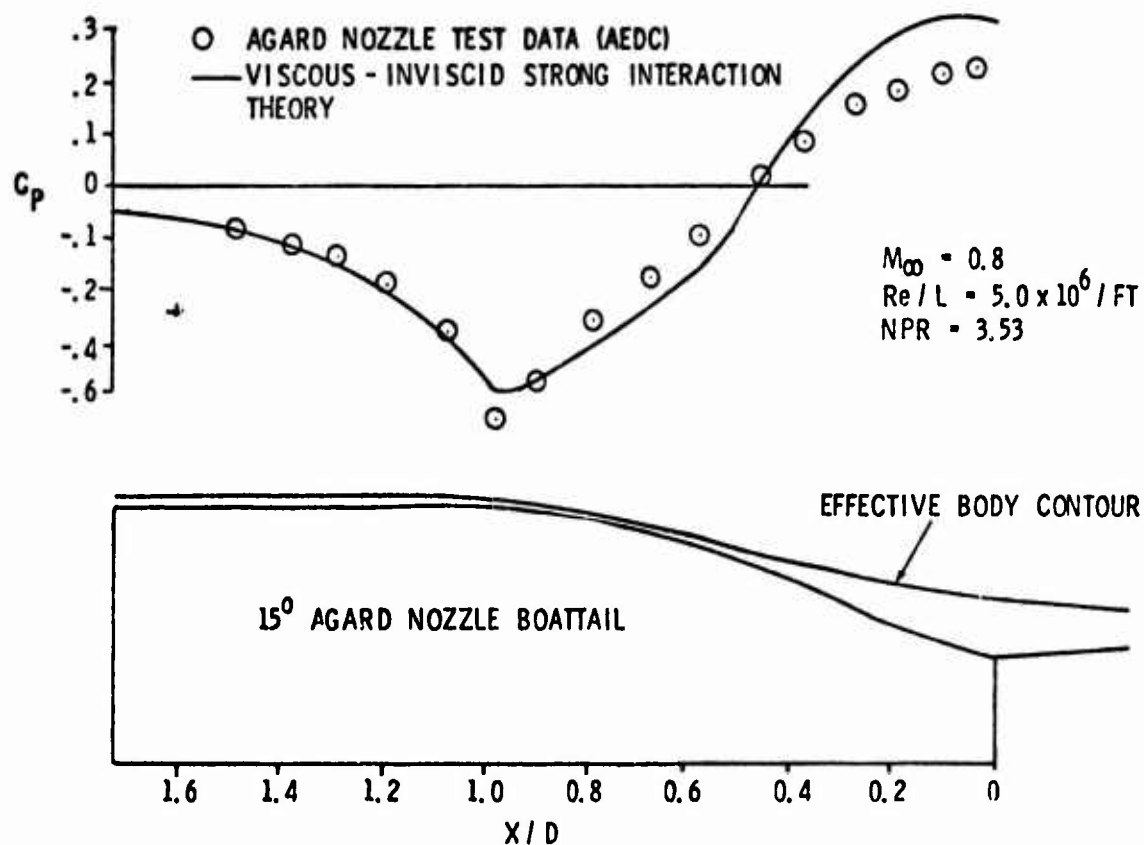


Fig.39 Comparison of measured and analytical pressure distributions

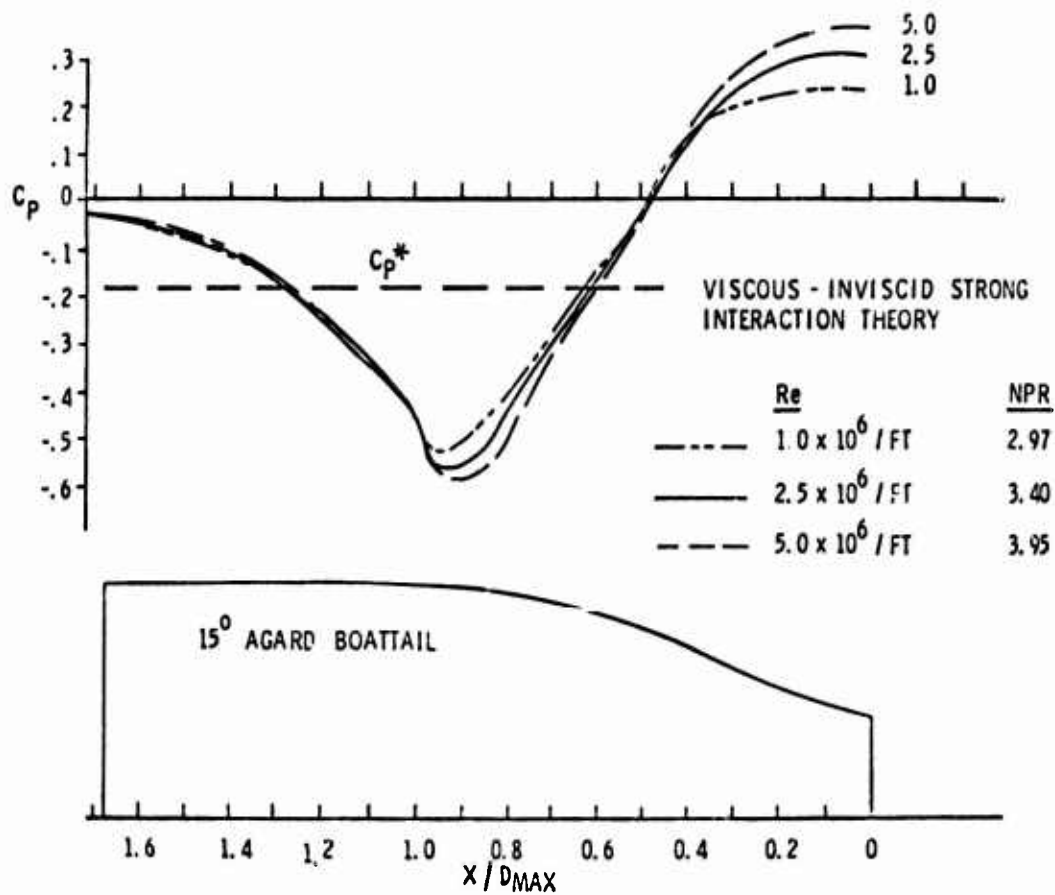
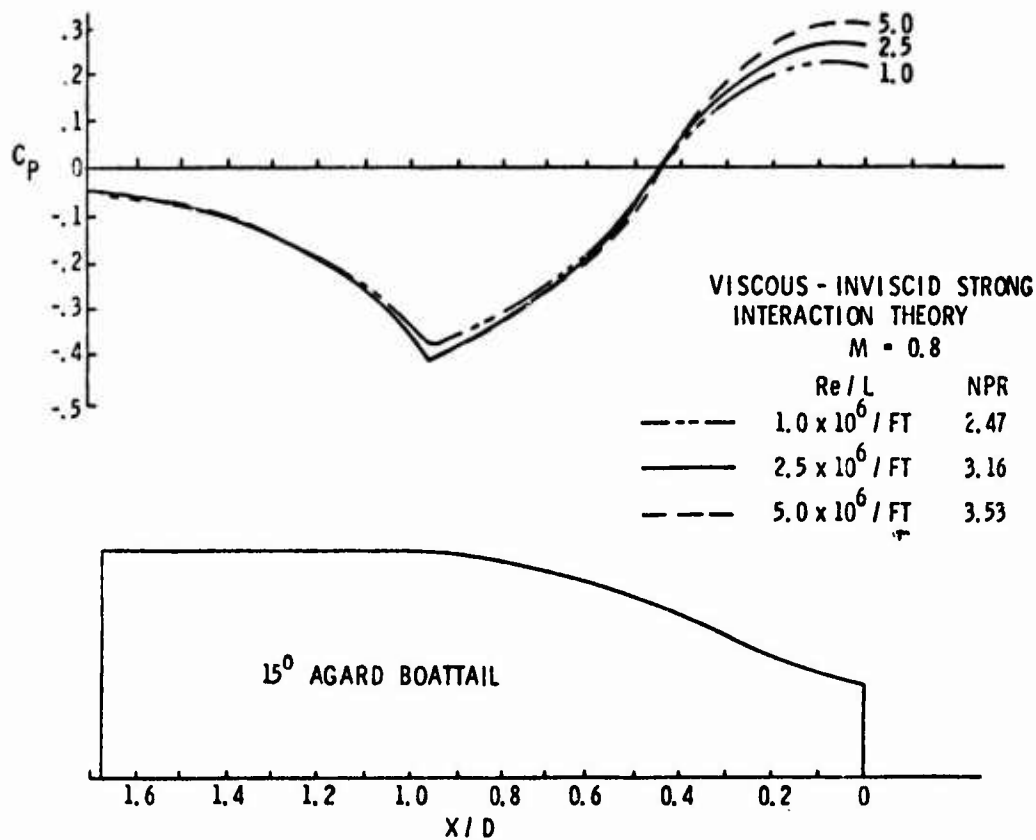
Fig.40 Reynolds No. variation,  $M = 0.9$ 

Fig.41 Reynolds No. variation

## DESCRIPTION OF THE AGARD NOZZLE AFTERBODY EXPERIMENTS CONDUCTED BY THE ARNOLD ENGINEERING DEVELOPMENT CENTER

by

L.L.Galigher, F.M.Jackson and C.E.Robinson  
AEDC, Tennessee, USA

### INTRODUCTION

A comprehensive test program was conducted at the Propulsion Wind Tunnel Facility of the Arnold Engineering Center (AEDC), Arnold Air Force Station, Tennessee, USA, and Lockheed Georgia Compressible Flow Facility, Marietta, Georgia, USA, in partial support of the AGARD research project on "Improved Nozzle Testing Techniques in Transonic Flow". Program emphasis was directed toward evaluation of Reynolds number and exhaust plume temperature effects on nozzle afterbody pressure drag. Reynolds number effects were obtained by varying both model scale and wind tunnel pressure level. At AEDC, Ethylene<sup>®</sup>/air combustor, installed in the nozzle flow tube, was used to provide hot exhaust products which very closely duplicate the exhaust products of JP-4 burned in air. Ignition was accomplished by injecting a small quantity of tri-ethyl borane (a pyrophoric fuel) into the combustor flameholder. Nozzle afterbody pressure drag, determined from pressure integration, was obtained at freestream Mach numbers of 0.6, 0.8, 0.9, 0.95, 1.1, and 1.5. Reynolds number (based on model length) and nozzle total pressure-to-free-stream static pressure ratio was varied from  $2 \times 10^6$  to  $62 \times 10^6$  and from jet-off to a maximum of 22, respectively, depending upon the free-stream Mach number. Fuel/air ratio was varied from 0 to 0.05, which corresponds to an exhaust plume total temperature range from 306°K to approximately 1889°K. Model angle of attack was zero degrees at all test conditions.

To evaluate the effect of test section wall porosity on the performance of transonic wind tunnels the walls were modified for wall porosities of 2 and 4 percent in addition to the normal 6 percent, through the Mach number range from 0.6 to 0.95.

### TEST FACILITY – AEDC 16T PWT

#### General Description

The PWT 16 Ft Transonic Wind Tunnel is a continuous-flow closed circuit tunnel which can be operated at Mach numbers from 0.2 to 1.6. The tunnel has a test section 40 ft (12.19 m) long and 16 ft (4.88 m) square with 6 percent porosity walls. The test section side walls can be either converged or diverged 1°. The general arrangement of the test section and the perforated wall geometry is shown in Figure 1.

Tunnel 16T is a variable density tunnel which is operated within a stagnation pressure range of 120 psfa to a maximum of 4000 psfa ( $5.75 \times 10^3$  Newton/m<sup>2</sup> to  $1.92 \times 10^5$  Newton/m<sup>2</sup>), depending upon the Mach number. The stagnation temperature can be varied from a minimum of about 27°C, dependent upon available cooling water temperature, to a maximum of 72°C.

The Tunnel 16T main compressor is a constant speed, three stage, axial flow compressor with variable stator blades. The compressor drive system consists of four motors with a power rating of  $1.61 \times 10^8$  watts.

Supersonic Mach numbers are generated by a flexible, two-dimensional Laval nozzle. Test section flow removal is required to prevent tunnel choking in the transonic range. Although the tunnel is equipped with diffuser flaps, an auxiliary compressor system (PES) is utilized for necessary plenum suction. The PES consists of ten compressors which are driven by motors with a total power rating of  $1.34 \times 10^8$  watts. The PES is also utilized for tunnel pressure level control. Additional details with regard to Tunnel 16T and its capabilities are presented in Reference 1.

#### Tunnel Operating Procedures

Various Mach numbers in Tunnel 16T are established by regulation of compressor speed, pressure ratio, nozzle contour, and the plenum pressure. Mach numbers below 0.55 are obtained by operating the compressor drive motors subsynchronously. Auxiliary flow removal is utilized at Mach numbers above 0.75 and supersonic nozzle contours are utilized at  $M > 1.05$ .

During conduct of tests, the stagnation pressure and temperature can be held within  $\pm 5$  psf ( $\pm 2.39 \times 10^3$  Newton/m<sup>2</sup>) and  $\pm 1^\circ$  F, respectively. The Mach number is determined from previous tunnel calibrations as a function of test section wall angle and measured plenum and stagnation pressures. The Mach number is normally controlled within  $\pm 0.002$ .

### Tunnel Calibration

The calibration of the 16T Tunnel is based on the measured pressure differential across the test section walls at various operating conditions. As a matter of procedure, a plenum chamber Mach number equivalent is defined based on plenum chamber and stagnation pressure environments. The calibration can therefore be expressed as a function of the difference between the free stream and plenum chamber Mach numbers. These data, for all possible tunnel operating conditions, are incorporated into the on-line data reduction routine for each test program. During testing, the plenum chamber Mach number is determined from current measurements and is used to compute the free-stream Mach number. Both centerline and wall static pressure distributions have been obtained during tunnel calibrations. Comparisons of such data show good agreement, such that with proper procedures either may be utilized to define the tunnel calibration.

For the special tunnel calibration conducted in support of the AGARD study, a 6.5-in (16.51 cm) diameter static pressure pipe was used to obtain the centerline Mach number distributions from tunnel station -5.8 ft to 48.2 ft (-1.77 meters to 14.69 meters). The pipe included a total of 75 static orifices. The calibration installation is illustrated in Figure 1.

During the calibration, centerline Mach number distributions were obtained for wall porosities of 2, 4, and 6 percent at Mach numbers from 0.5 to 1.6. Corks were utilized to modify the wall porosity from the normal 6-percent configuration. The effects of Mach number, porosity, test section pressure ratio, and test section wall angle upon the centerline Mach number distributions were determined at a stagnation pressure of 1600 psfa ( $7.66 \times 10^4$  Newton/m<sup>2</sup>). Limited data were also obtained to indicate the effects of Reynolds number on the tunnel calibration.

Although the tunnel was calibrated at various porosities, all of the AGARD nozzle afterbody testing at AEDC was conducted with a porosity of 6.0 percent. Typical Tunnel 16T calibration data at porosity of 6.0 percent are presented in References 2 and 3. It is noted that the centerline Mach number distributions obtained during the special calibration at a porosity of 6.0 percent compared well with those obtained during previous calibrations. Variation of test variables, including porosity, had no significant effect upon the distributions for the test regime over which the AGARD models were tested.

With regard to the tunnel Mach number calibration, the special calibration data at 1600 psfa ( $7.66 \times 10^4$  Newton/m<sup>2</sup>) and a zero test section wall angle agreed within  $\pm 0.001$  with the Reference 2 calibration. The tunnel calibration data (at  $M = 0.6$  and  $0.8$ ) indicates that the free-stream Mach number increases slightly with increasing Reynolds number. For the range of Reynolds numbers covered during the AGARD nozzle afterbody test program, the special calibration agrees with Reference 2 Mach numbers within  $\pm 0.0025$ . Because this agreement was within the data precision and repeatability and since only limited calibration data at various Reynolds numbers was available, the Reference 2 calibration was used to conduct the AGARD tests.

Following the conduct of the AGARD tests, analysis of the data revealed that some trends in model afterbody drag with Reynolds number could possibly be attributed to the tunnel calibration. The errors attributed to use of the Reference 2 calibration and neglecting the effects of Reynolds number on  $M_\infty$ ,  $P_\infty$ , and  $Q_\infty$  were less than 0.4, 0.2, and 0.6 percent, respectively. These small errors are about the same order of magnitude as errors associated with instrumentation precision. For most test programs in the AEDC/PWT wind tunnels, such errors are not significant. However, for testing of bodies such as those used in the AGARD program, the error in static pressure can induce an error in afterbody drag as high as 15 percent at the highest Reynolds number. As a consequence of these results, an additional Tunnel 16T calibration was conducted with Reynolds number as a primary variable. Results of this calibration are presently being applied to data obtained from prior tests to determine if there are any changes in the nozzle drag trends with Reynolds number.

### TEST FACILITY - LOCKHEED GEORGIA COMPRESSIBLE FLOW FACILITY

The Compressible Flow Facility (CFF) is a blowdown transonic wind tunnel with a test section that has a 20 in (50.8 cm)  $\times$  28 in (71.12 cm) cross-section and is 72 in (182.88 cm) long. The facility is capable of unit Reynolds numbers from 6 to  $50 \times 10^6$  Re/Ft ( $19.7$  to  $164.0 \times 10^6$  Re/M). The perforated walls, with 60 degree inclined holes, can be varied from 0 to 10 percent porosity. Flow from the 13,000 cubic foot (368.12 m<sup>3</sup>) storage vessels passes through a contraction/nozzle to accelerate the flow approaching the test section. Both the rectangular test section and the diffuser flap are enclosed in the plenum chamber. A variable diffuser with a re-entry flap section and an adjustable second throat provides Mach number control in the subsonic and transonic speed ranges. A fixed diffuser directs the flow from the variable diffuser to the exhaust stack.

Figure 2 shows the model installed in the CFF. A description of the model is included in the next section. Test section Mach number was set by measuring wall static pressures upstream of the model using a tunnel empty calibration. The tunnel stagnation and test section wall static pressures were measured with transducers with an accuracy of 0.05 percent. The scanivalves used to measure external model pressures had an accuracy of 0.25 percent.

## AGARD TEST PROGRAM -- AEDC

### Test Article Description

An existing axisymmetric pod model was modified to satisfy requirements for both cold and hot exhaust testing with the three AGARD external afterbody configurations with boattail angles of 10, 15, and 25 degrees. The model had a length of 12.25 ft (374 cm) a maximum diameter of 9.86 in (25.04 cm) and a 14 degree half-angle conical nose. A boundary-layer trip consisting of 0.055 in (0.14 cm) diameter steel spheres spot-welded to a trip ring at a circumferential spacing of four sphere diameters was located 1-ft (30.48 cm) aft of the cone vortex. The model was mounted on a tapered strut with an average aft sweep angle of 35 degrees. The strut thickness-to-chord ratio varied from 0.053 at the model to 0.088 at the tunnel floor. The maximum cross-sectional area of the model/strut arrangement was equivalent to 0.88 percent of the wind tunnel test section cross-sectional area. A sketch of the model is presented in Figure 3.

High pressure air was used to simulate the nozzle exhaust for the cold-flow portion of testing. For the hot-flow portion of testing, high pressure air was used as an oxidizer for the combustion of Ethylene®. Water cooling requirements for the hot-flow nozzle and combustor liner resulted in decreasing the nozzle exit diameter from 3.982 (10.11 cm) to 3.228 in (8.2 cm). Therefore, the nozzle base area was equivalent to 6.52 percent of the model maximum cross-sectional area for the hot-flow nozzle as compared to 0.93 percent for the cold-flow nozzle. Both nozzle configurations were convergent nozzles. All nozzles had approximately 102 static pressure orifices mounted on their external surface.

A 0.1514 sub-scale model of the existing, large-scale, cold-flow model with the 15 degree boattail configuration was fabricated to investigate the effects on aftbody drag caused by tunnel wall porosity variations and by varying unit Reynolds number. The sub-scale model support strut was also a scale model of the large-scale support strut. Primary instrumentation consisted of 21 surface-mounted static pressure orifices which were installed on the nozzle boattail to provide a more precise pressure-integrated drag value. The sub-scale model was tested in the AEDC 16T tunnel and the Lockheed Georgia CFF.

### Experimental Procedure and Sample Results -- AEDC

The data acquisition procedure consisted of (1) setting desired free-stream Mach number based on tunnel calibrations and Reynolds number, (2) varying nozzle total pressure-to-free-stream static pressure ratio (NPR) from jet-off to a maximum of 22, depending on the Mach number, and (3) setting, if required, a desired fuel/air ratio. Nozzle pressure ratio surveys for the hot flow model were conducted primarily at constant fuel/air ratios of 0, 0.015, 0.025, and 0.040; which correspond to nozzle exhaust total temperatures of approximately 550°R, 1550°R, 2150°R, and 2900°R, respectively. Two data reduction techniques were employed to calculate nozzle boattail pressure-integrated drag; one was based on all of the boattail surface pressure measurements and the other based on individual rows of pressure measurements along the nozzle boattail.

Results are presented in the form of (1) pressure coefficient as a function of model station, and (2) nozzle boattail pressure drag coefficient as a function of nozzle total pressure-to-free-stream static pressure ratio. Drag coefficient was normalized with free-stream dynamic pressure and maximum cross-sectional area based on a model diameter of 9.86 in (25.04 cm). Sample data results are presented in Figures 4 and 5, and more thoroughly discussed elsewhere in this report.

## REFERENCES

1. — Test Facilities Handbook (Tenth Edition). *Propulsion Wind Tunnel Facility, Vol.4*. Arnold Engineering Development Center, Arnold Air Force Station, Tennessee.
2. Gunn, J.A. *Check Calibration of the AEDC 16-Ft Transonic Tunnel*. AEDC-TR-66-80, May 1966.
3. Jackson, F.M. *Supplemental Calibration Results for the AEDC Propulsion Wind Tunnel (16T)*. AEDC-TR-70-163, August 1970.

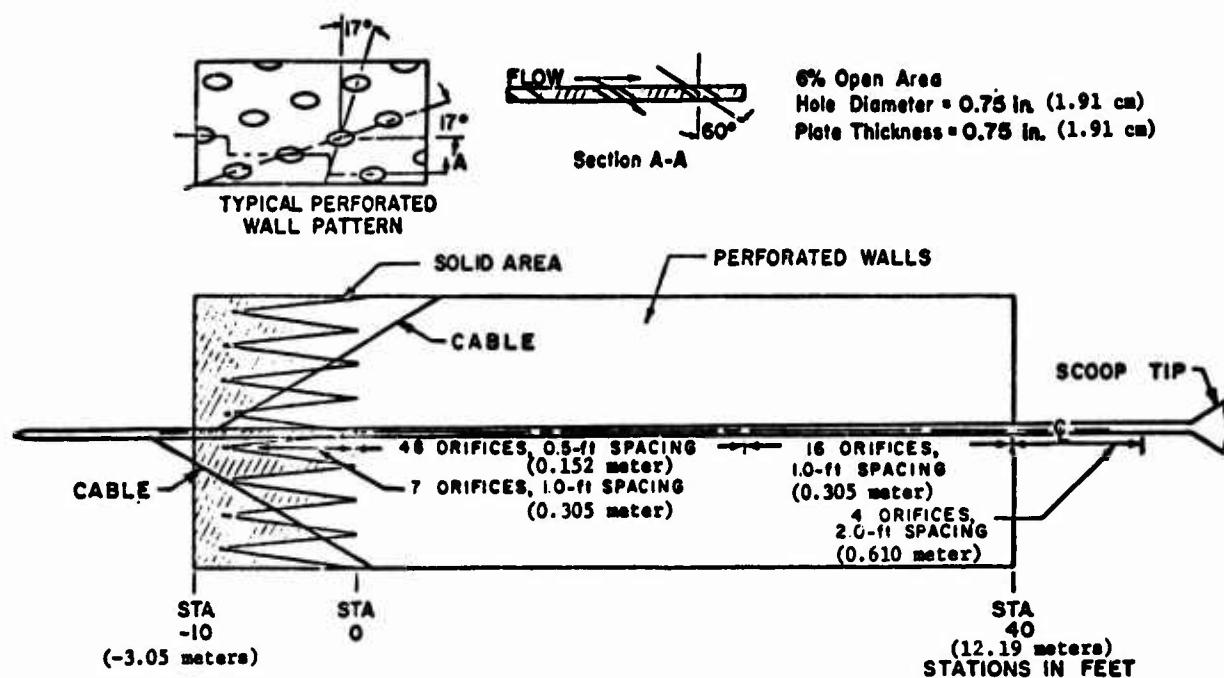


Fig.1 Schematic of the test section and centerline pipe installation

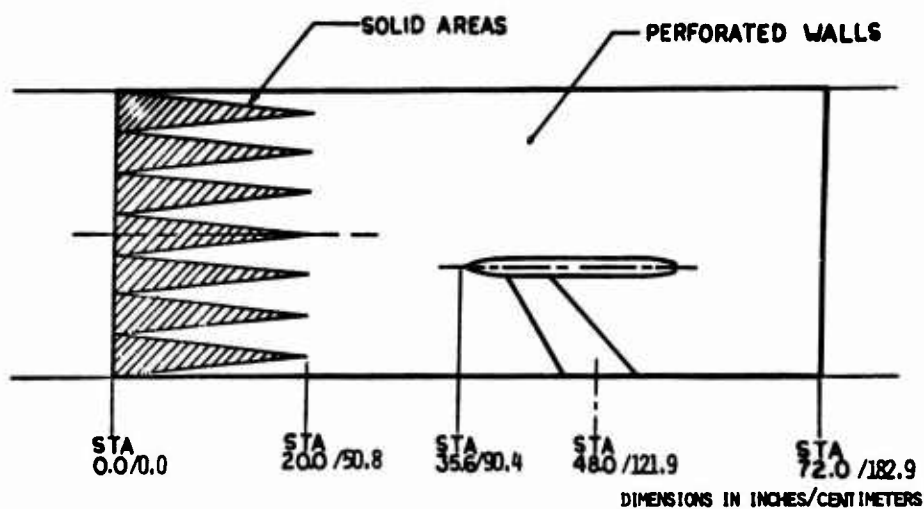
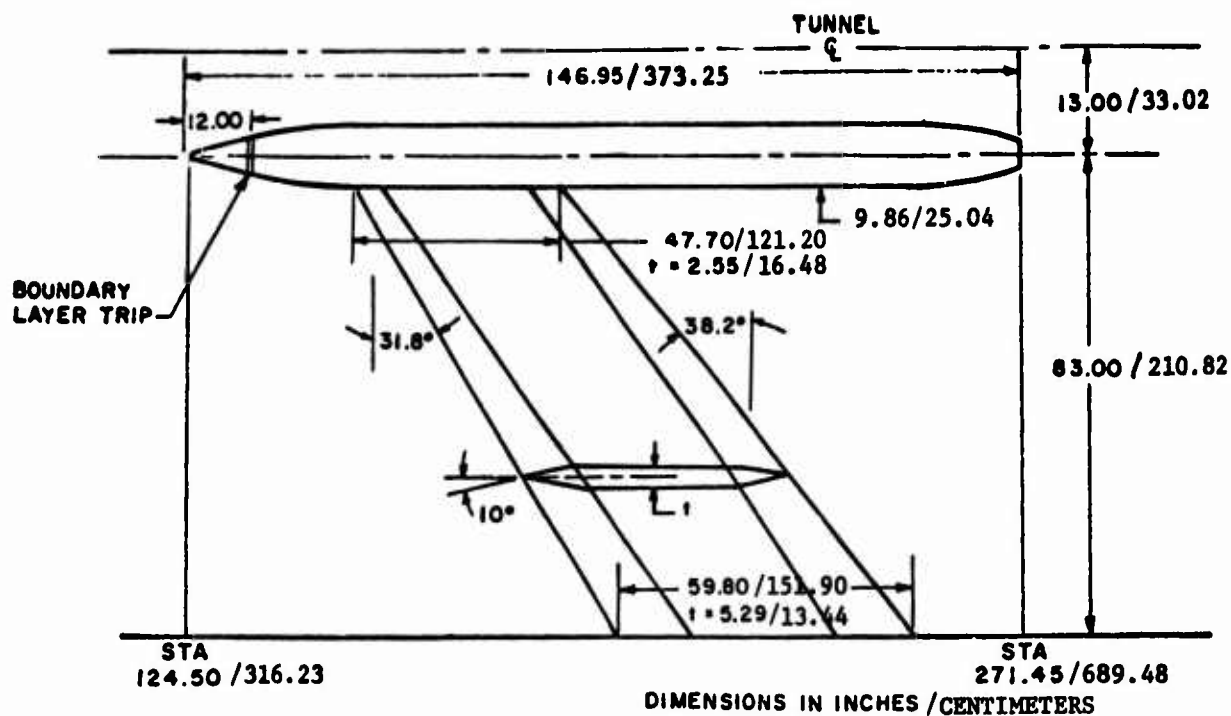


Fig.2 Sub-scale model installed in CFF





**Fig.3 Basic model dimensions and location in test section**

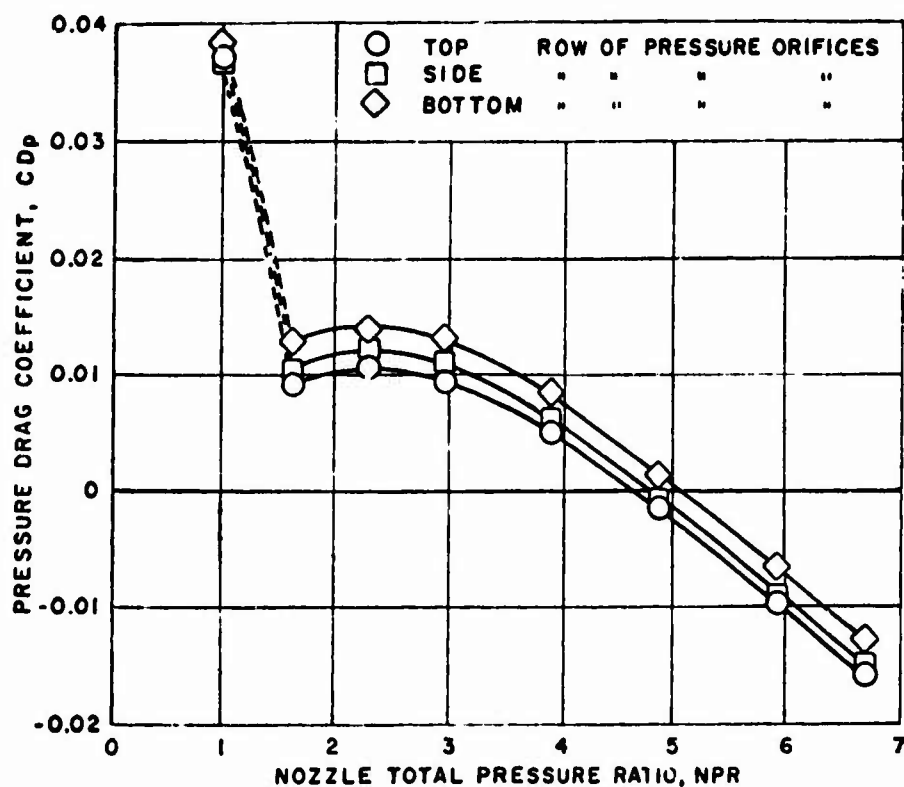


Fig.4 Flow asymmetry effects on  $10^\circ$  boattail, Mach = 0.9

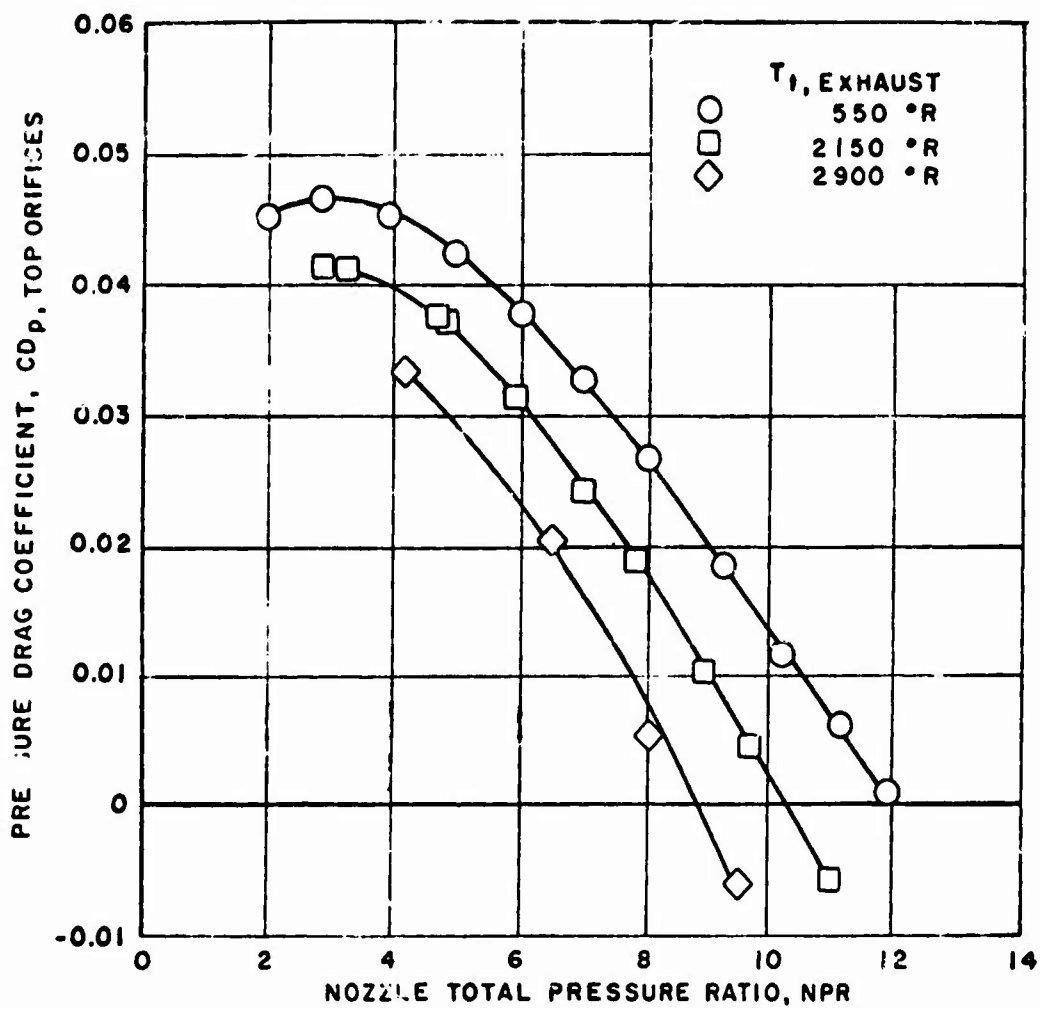


Fig.5 Nozzle exhaust temperature effects on 15° boattail, Mach = 0.9

# CONTRIBUTION OF THE NATIONAL AERONAUTICS AND SPACE ADMINISTRATION LANGLEY RESEARCH CENTER

by

William B. Compton, III and Jack F. Runckel  
Langley Research Center, Hampton, Va., USA

## 1. INTRODUCTION

A special international effort has been organized by the Propulsion and Energetics Panel of AGARD to improve nozzle testing techniques in transonic flow. The program is designed to demonstrate the influence of the experimental apparatus on test results, and to determine the importance of the parameters to be simulated. As a result of the effort, three nozzles were designed and tested on single nacelle models in wind tunnels of several nations belonging to the North Atlantic Treaty Organization.

As part of the contribution of the United States of America to the program, all three of these nozzles were investigated in the Langley 16-foot transonic wind tunnel at the National Aeronautics and Space Administration's Langley Research Center. Langley Research Center also contributed theoretical calculations of the jet plume boundary and afterbody pressures. The calculations were obtained using an iterative solution which combined the inviscid Douglas Neumann method<sup>1</sup> for the external flow with the method of characteristics for the flow in the jet plume. For the investigation, the nozzles were mounted on a single nacelle model 15.24 centimeters in diameter and 162.56 centimeters long. Tests were made at free stream Mach number from 0.4 to 1.2, and at Reynolds numbers per meter from 7.38 million to 13.78 million depending on the Mach number. Four types of data were recorded: afterbody pressure data, afterbody force data, model boundary layer data, and tunnel wall pressure data. The ratio of jet total pressure to free stream static pressure ranged up to 8.5. A brief description of the wind tunnel, model, and test procedure follows.

## 2. WIND TUNNEL

The Langley 16-foot transonic tunnel is a single-return atmospheric wind tunnel with a slotted transonic test section. The Mach number is continuously variable from 0.20 to 1.30. An exterior view of the facility is shown in Figure 1 and a schematic diagram in Figure 2.

The test section, which extends from tunnel station 39.77 meters to station 41.76 meters is an octagonal cylinder vented to a surrounding plenum through slots at the corners of the octagon. Air is removed from the plenum by an exhaustor to obtain Mach numbers of 1.05 or greater. The slots at the corners of the test section walls are shaped for a minimum axial gradient of Mach number in the test section. The test section walls are diverged up to  $0^\circ 45'$  to further minimize the axial Mach number and pressure gradient. The predetermined wall divergence setting is a function of Mach number and dew point.

Extensive calibrations of the test section have been made using a center line probe and wall flat pressure measurements. At the worst conditions, the average test section axial Mach number gradient is less than  $\pm 0.0016$  per meter. This gives an axial pressure gradient normalized by the free-stream total pressure of 0.0010 per meter. There is generally very good agreement between the center line and wall Mach number distributions except where the curvature of the wall between the test section and diffuser causes the local Mach number on the wall to exceed the center line Mach number. Measurements have been made of the length of run of laminar flow on a highly polished  $10^\circ$  cone. These measurements (see Reference 2) indicate that longer runs of laminar flow were obtained in the Langley 16-foot transonic tunnel than in the other wind tunnels investigated. A long run of laminar flow indicates a low level of airstream turbulence.

The basic wind tunnel reference measurements are airstream stagnation pressure and temperature, and plenum static pressure. Test section airstream Mach number is a calibrated function of airstream stagnation pressure and plenum static pressure. The absolute error of the calibration is believed to be no more than  $\Delta M_\infty = \pm 0.005$ . For more information on the tunnel, see Reference 3 which presents a detailed description of the tunnel, the tunnel calibration, and the tunnel equipment.

### 3. MODEL

The three AGARD nozzles were tested on a single nacelle model with an ogive nose. The model was 15.24 centimeters in diameter and 162.56 centimeters long with the nozzles installed. The model was supported from the nose by a sting-strut arrangement which positioned the center line of the model on the center line of the tunnel. A photograph of the model installed in the tunnel is presented in Figure 3. Figure 4 shows a detailed sketch of the model and support system. The double cross-hatched portion of the model aft of the metric break at station 67.31 is supported by the strain gage balance.

Room temperature air, which was used for the jet exhaust, is introduced into the metric portion of the model through eight sonic nozzles equally spaced radially around a central core. The two flow smoothing plates have a lattice-work of sharp edged holes drilled in an equilateral triangular pattern. The jet total temperature and pressure were obtained from a rake. No jet exit total pressure profiles were measured, however the jet total pressure profiles at the rake are uniform (see Figure 5). Figure 6 presents cross-sectional area distributions of the model and support system. The blockage of the model and support system was 0.148 percent of the test section cross-sectional area.

### 4. TEST PROCEDURE

At the Langley 16-foot transonic tunnel, afterbody pressure data, afterbody force data, and model boundary layer and tunnel wall pressure data were measured. Separate tunnel runs were made for the three groups of data. During a tunnel run, the free stream Mach number was set and held constant while data were recorded at several discrete values of jet pressure ratio. Data were taken at the highest Mach numbers first, and then at progressively lower Mach numbers to keep the variation in the tunnel stagnation temperature small. Pressures on the model and wind tunnel wall were measured with individual strain gage pressure transducers calibrated to an accuracy of  $\pm 0.75$  percent of the capacity of the gage. Temperatures were measured with iron-constantan swaged wire thermocouples which had an accuracy of  $\pm 0.6$  Kelvin. Wind tunnel parameters were measured with the standard tunnel instrumentation described in Reference 3.

Since the Langley 16-foot transonic wind tunnel is an atmospheric tunnel, the values of the tunnel free-stream parameters are a function of the atmospheric conditions. Thus the free-stream Reynolds number varied during the investigation. Figure 7 presents the band of Reynolds numbers encountered. Reference 4 indicates that for this band width, at subsonic speeds the effect of Reynolds number on afterbody pressures and drag should be very small.

Afterbody pressures were measured at the recommended locations. Figure 8 presents pressure coefficients for both the top, bottom, and side rows of afterbody pressure orifices for the  $15^\circ$  boattailed nozzle. The support strut creates a narrow wake at the bottom of the model in which there is a decrement in total pressure. The top row of pressures are considered to be the row least affected by the strut.

The boundary layer on the model surface was measured with a rake at model station 123.18 at radial locations of  $0^\circ$  (top),  $180^\circ$  (bottom), and  $247.5^\circ$ . The  $15^\circ$  boattailed nozzle was installed on the model when these measurements were made. Boundary layer profiles are presented in Figure 9. The boundary layer on the bottom of the model is slightly thicker and has a different shape than the top and side boundary layers. The top boundary layer changed very little with Mach number; also, the boundary layer was not significantly affected by changing the jet pressure ratio. At a free-stream Mach number of 0.90, the boundary layer displacement thickness and momentum thickness on top of the model were respectively .012 and .009 times the model maximum diameter.

When the force balance data was being recorded, only the pressure instrumentation necessary to the proper interpretation of this data was retained. Therefore, restraints across the balance were kept to a minimum. Figure 10 presents a plot of nozzle discharge coefficient and thrust normalized by ideal thrust versus jet total pressure ratio. The data is for static conditions, zero free-stream Mach number. The measured thrust is close to the calculated theoretical ideal convergent nozzle thrust.

Static pressures were measured on the tunnel test section wall at a radial location of  $225^\circ$  looking upstream. Tunnel wall Mach numbers were computed from these pressures and the tunnel total pressure. During the AGARD nozzle test, the accuracy of the wall pressures based on gage accuracy was  $\pm 293$  newtons/meter<sup>2</sup> which resulted in a wall Mach number accuracy of approximately  $\pm 0.005$ . In addition, the condition of the tunnel wall orifices was poor (chipped paint near the orifices, etc.). Differences between these tunnel wall Mach numbers with the model installed, and those with the tunnel empty, are shown in Figure 11. No pressure signature of the model on the wall can be discerned at subsonic speeds, and most of the data lies within the free-stream Mach number accuracy band which is also  $\Delta M_\infty = \pm 0.005$ . Therefore tunnel wall effects on the model pressure and force measurements should be insignificant at subsonic speeds. At a free-stream Mach number of 1.2, disturbances emanating from the model nose appear on the wall between tunnel stations 41.15 meters and 42.06 meters. Boundary-reflected-disturbance lengths measured in the Langley 16-foot transonic tunnel indicate that these disturbances should be reflected far behind the model.

## 5. REFERENCES

1. Hess, J.L.  
Smith, A.M.O.      *Calculation of Potential Flow About Arbitrary Bodies*. Volume 8 of Progress in Aeronautical Sciences, D.Kücheman, et al eds. Pergamon Press, pp.1-138, 1967.
2. Dougherty, N.S., Jr  
Stienle, Frank W., Jr      *Transition Reynolds Number Comparisons in Several Major Transonic Tunnels*. AIAA Paper No. 74-627, July 1974.
3. Corson, Blake W., Jr  
Runckel, Jack F.  
Igoe, William B.      *Calibration of the Langley 16-foot Transonic Tunnel with Test Section Air Removal*. NASA TR R-423, August 1974.
4. Reubush, David E.      *The Effects of Reynolds Number on Boattail Drag*. AIAA Paper No. 75-63, presented at the AIAA 13th Aerospace Sciences Meeting, January 20-23, 1975.

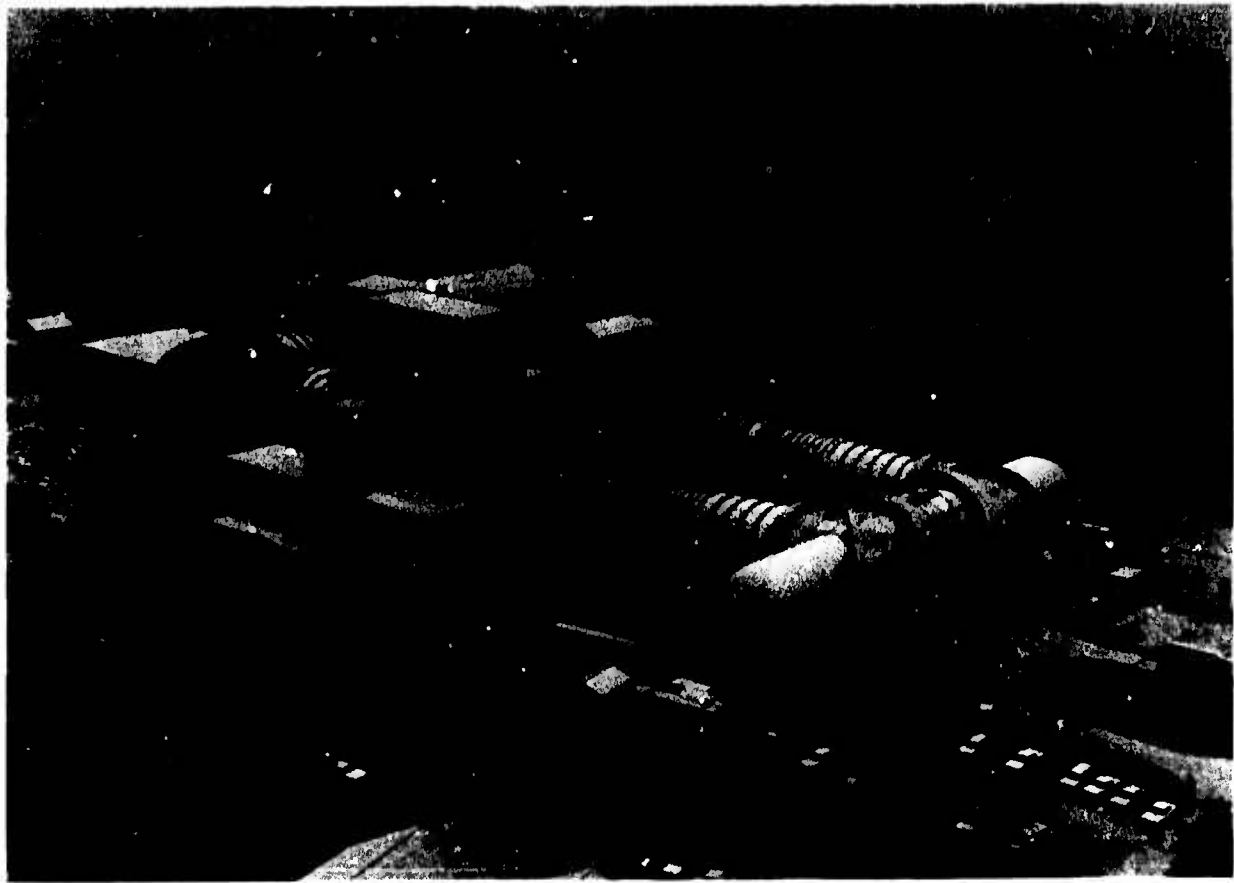


Fig.1 The 16-foot transonic wind tunnel at NASA Langley Research Center, Hampton, Virginia, United States of America

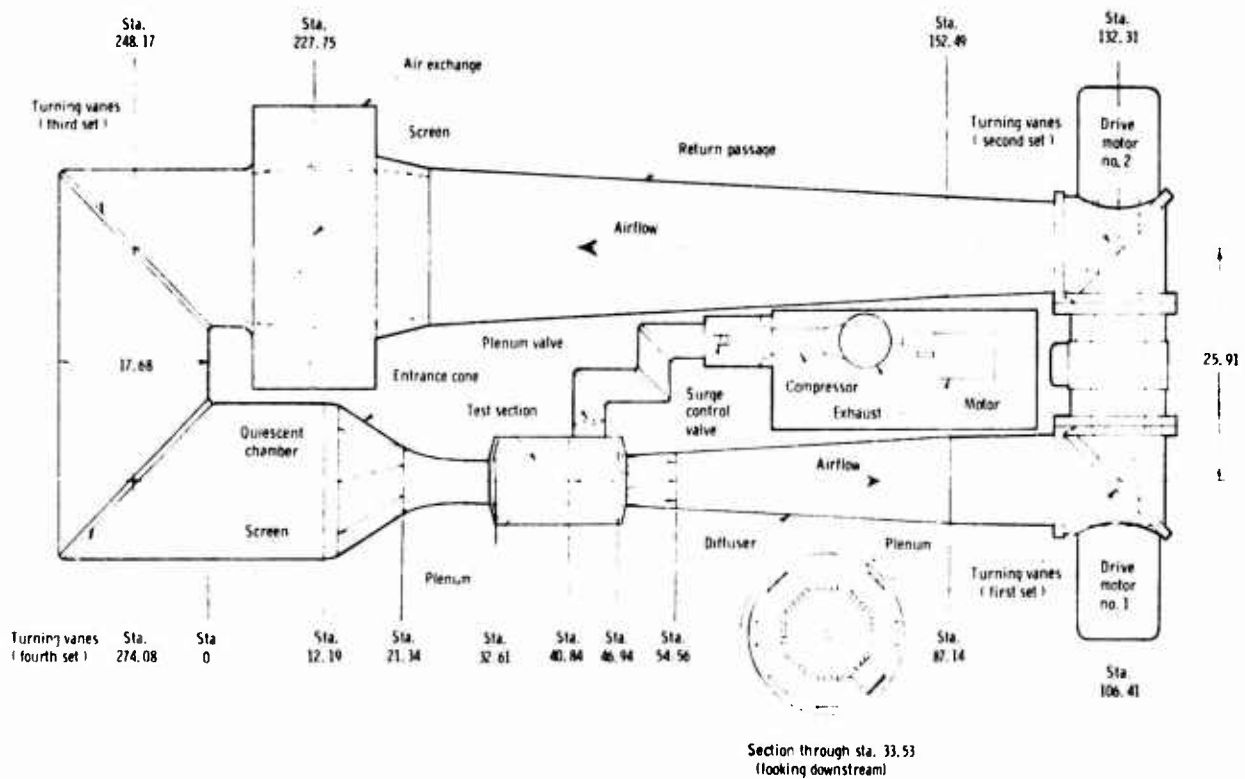


Fig.2 Arrangement of the Langley 16-foot transonic wind tunnel. (All dimensions are in meters)



Fig.3 Photograph of NASA-Langley Research Center model installed in the Langley 16-foot transonic wind tunnel

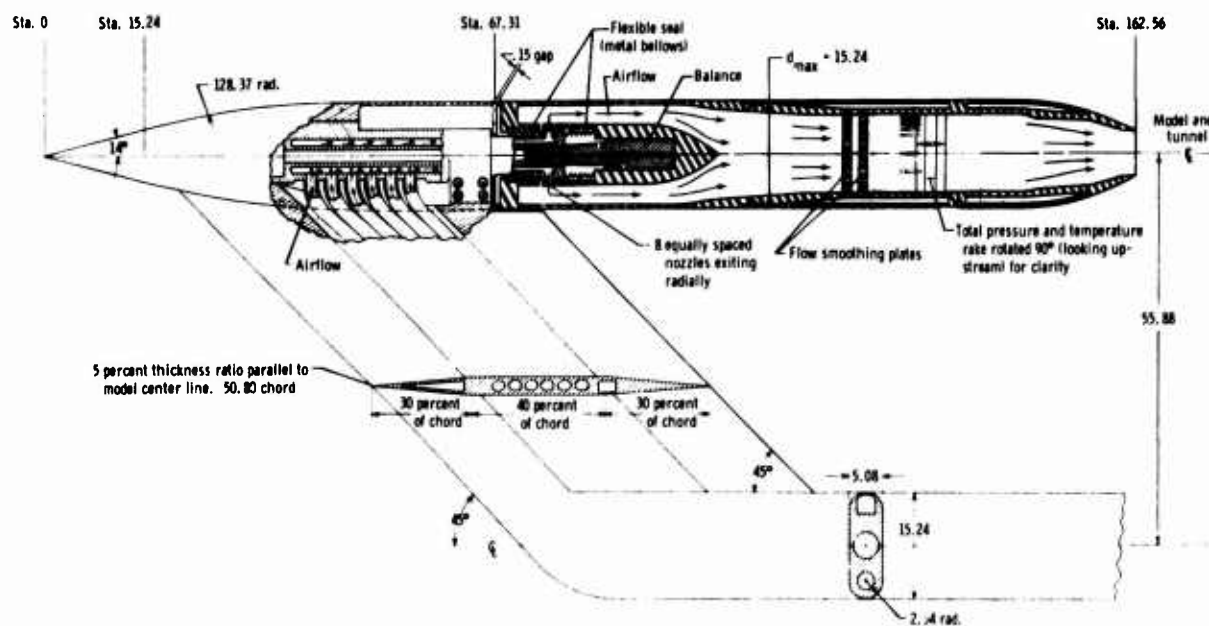


Fig.4 Sketch of the NASA-Langley Research Center model.  
(All dimensions are in centimeters unless otherwise noted)

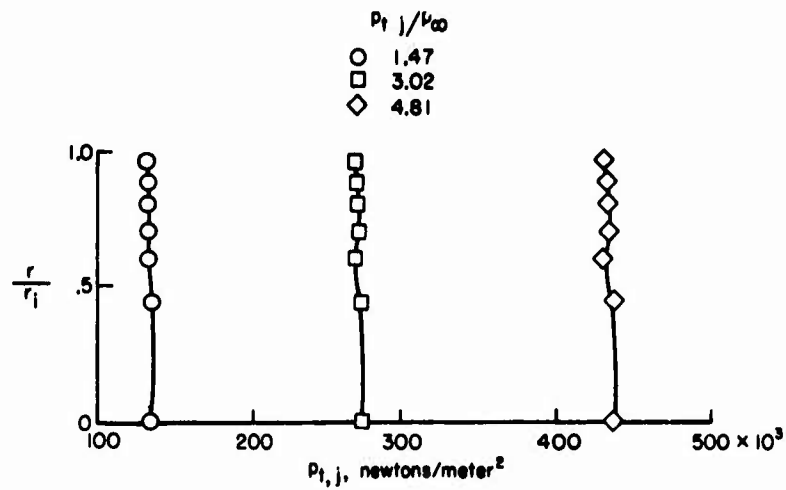


Fig.5 Jet internal total pressure profiles for the NASA-Langley Research Center model.  
(The profiles were measured at the internal rake location.  $M_{\infty} = 0$ )

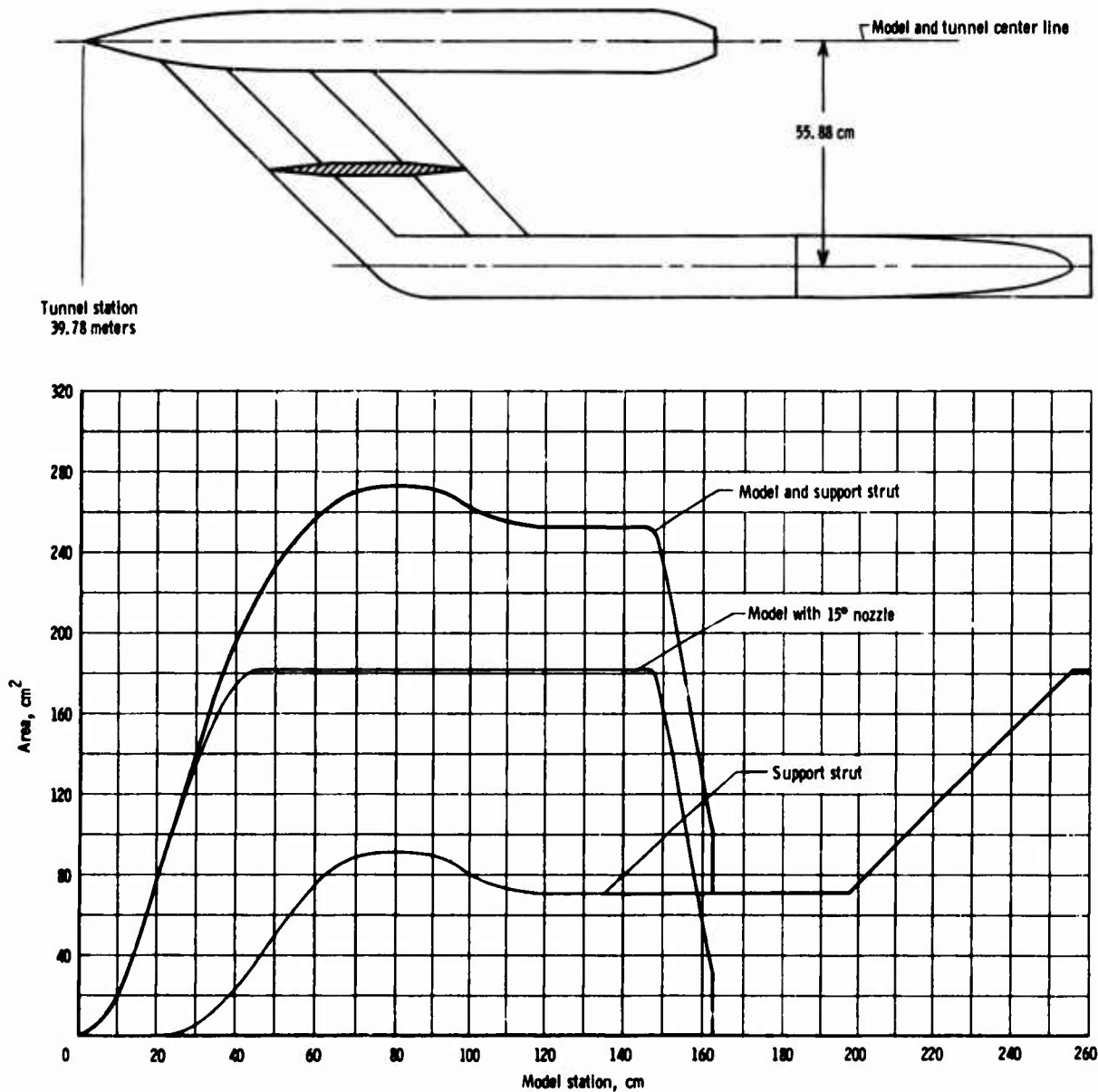


Fig.6 Cross-sectional area distributions of the NASA-Langley Research Center model and support.  
(The 15° AGARD nozzle is installed)



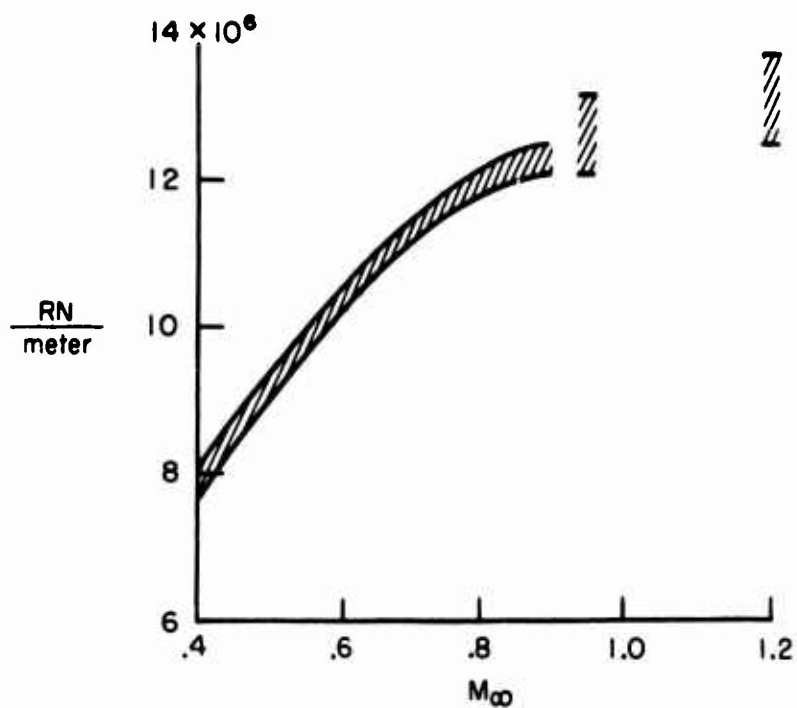


Fig.7 Band of free-stream Reynolds numbers per meter encountered during the NASA-Langley Research Center investigation

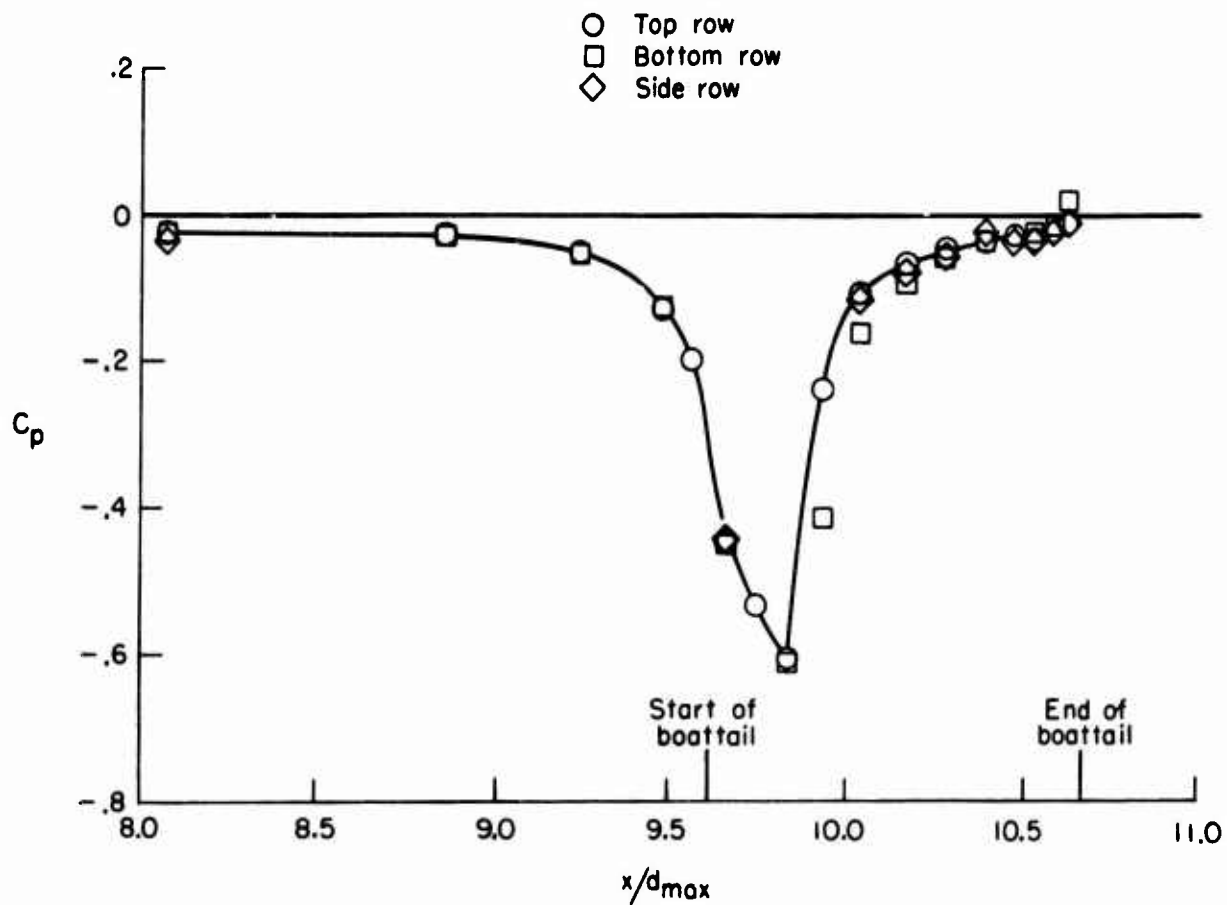


Fig.8 Afterbody pressure coefficient distributions on the NASA-Langley Research Center model with the 15° AGARD nozzle installed. ( $M_\infty = 0.95$ ,  $p_{t,j}/p_\infty = 3.0$ )

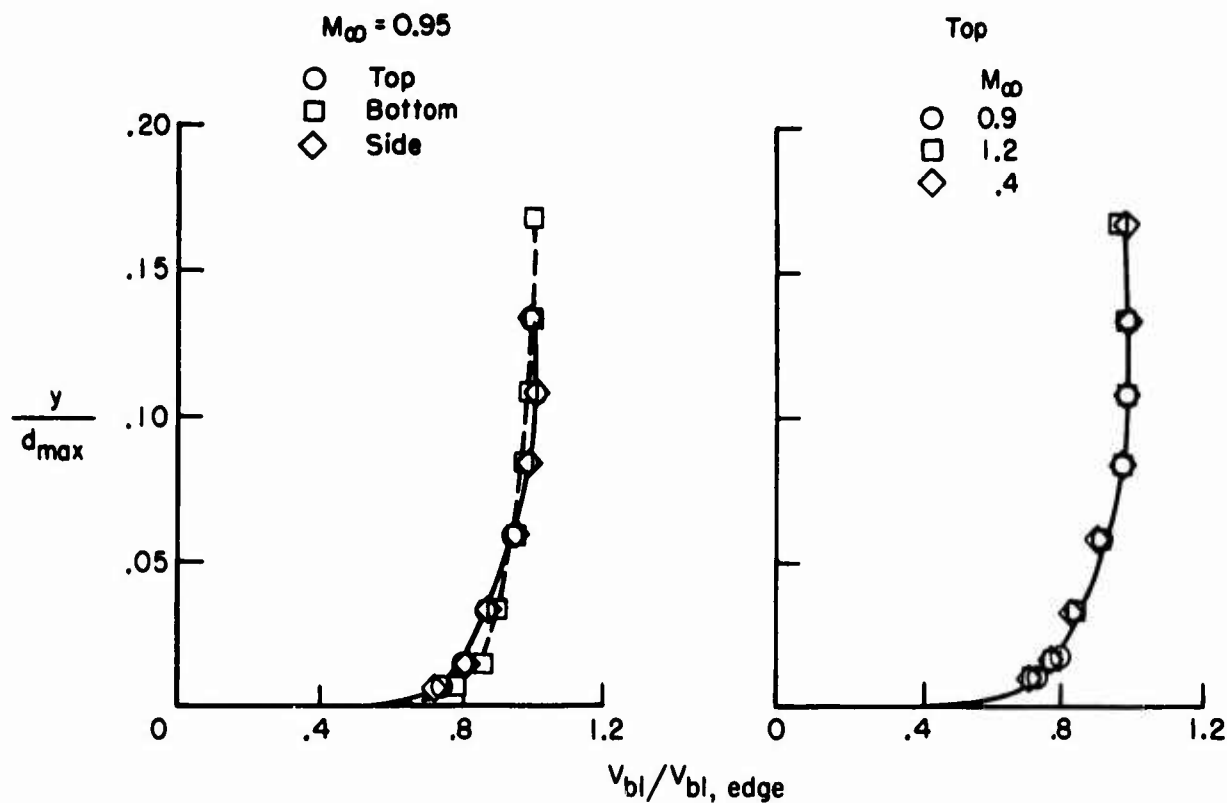


Fig.9 Boundary layer profiles for the NASA-Langley Research Center model with the 15° AGARD nozzle installed. (The profiles were measured at model station 123.18,  $p_{t,j}/p_\infty = 3.0$ )

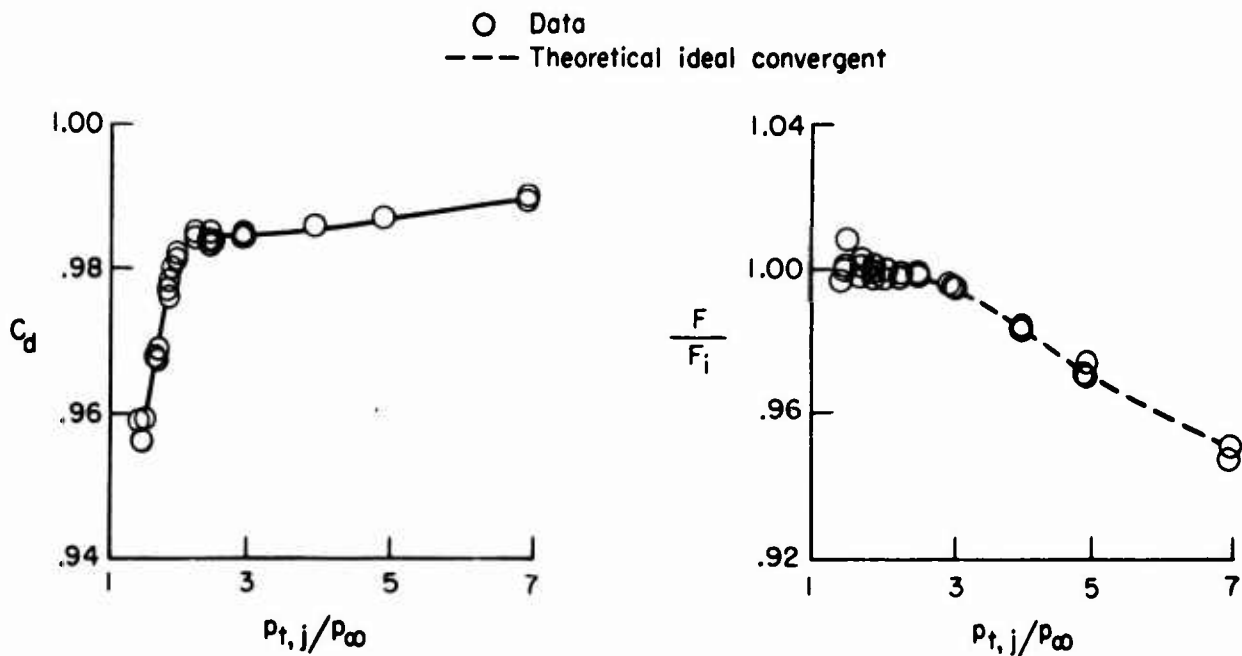


Fig.10 Discharge coefficient and thrust normalized by ideal thrust for the 10° AGARD nozzle installed on the NASA-Langley Research Center model. ( $M_\infty = 0$ )

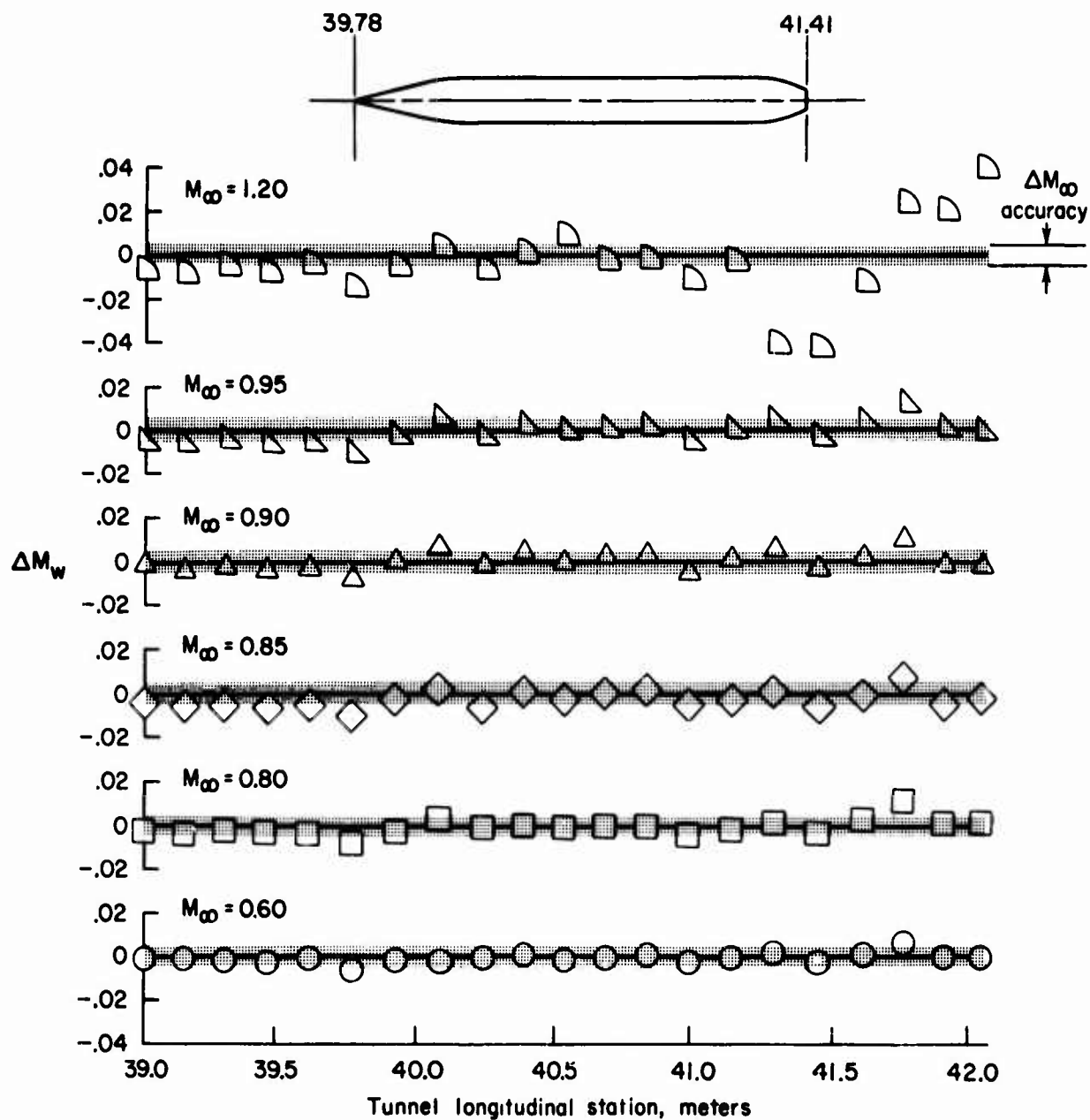


Fig. 11 Incremental Mach number measured on the Langley 16-foot transonic tunnel wall.  
 ( $\Delta M_w = M_{w, \text{model installed}} - M_{w, \text{tunnel empty}}$ ; measurements were taken at a radial location of  $225^\circ$  looking upstream)

**PART II**

**CRITICAL ANALYSIS**

**OF EFFECTS OF**

**PARAMETERS**

# THE INFLUENCE OF MODEL EXTERNAL GEOMETRY

by

L.R. Harper and W.J. Lewis  
Rolls-Royce (1971) Limited (Bristol Engine Division)

## SUMMARY

The results of tests carried out under the AGARD (PEP) collaborative programme are discussed in terms of the influence of model external geometry. Three aspects are considered; (i) the variation of drag and drag rise Mach number, which are shown to correlate with boattail chord angle. (ii) the sensitivity of drag measurement to boundary layer thickness, where an increase in thickness is found to decrease the effective body curvature. (iii) tunnel interference, which is found to have no measureable effect on pressure drag for blockages between 0.2% and 7%, although high blockages introduce difficulties in definition of tunnel static pressure.

The overall conclusion is that results obtained in the various facilities are in good agreement and the techniques in current use are generally satisfactory, at least up to about Mach 0.95, although correct simulation of boundary layer thickness is sometimes necessary.

## NOTATION

A	cross sectional area
$C_D$	pressure drag coefficient $\frac{\int C_p dA}{A_{max}}$
$C_p$	pressure coefficient $\frac{p_{local} - p_{\infty}}{\frac{1}{2} \gamma P_{\infty} M_{\infty}^2}$
D	diameter
M	Mach number
P	total pressure
p	static pressure
Re	Reynolds number
X	distance from nozzle exit plane
$\delta_{0.95}$	boundary layer height at which velocity is 95% of free-stream velocity.

## Subscripts

$\infty$	in free-stream
max	at model maximum diameter
j	in jet at nozzle exit
dr	drag rise

## 1. INTRODUCTION

Earlier papers in this series have described the tests carried out by several organisations of the three single nozzle axisymmetric afterbodies whose profiles are compared in Fig.1. The results of these tests are discussed here in terms of the influence of model external geometry. For the purposes of this paper model geometry will be taken to refer only to the afterbody since the influence of forebody geometry and the interaction between forebody and afterbody is discussed separately.

The aim of the present exercise is to improve the capability of accurate drag measurement. The way in which tunnel or technique imperfections affect the accuracy of drag measurement may vary with the type of afterbody shape being tested so the first objective has been to relate the drag characteristics of the models to their geometry. This has been done by use of a simple shape parameter so that a correlation could be obtained which used data from a wide range of sources in addition to the present tests and so that the results should be fairly general.

One of the ways in which the model test environment often differs from that experienced in flight is that the boundary layer on the model may be unrepresentatively thick. The way in which the drag of the three afterbodies varied with boundary layer thickness has been examined, using data from tests in which the boundary layer was blown, with the aim of assessing the influence of model geometry on the sensitivity of drag to boundary layer thickness. The results of this exercise should be of assistance in deciding whether correct boundary layer simulation is necessary in any particular test application.

Considerations of cost and other practical limitations often lead to afterbody models being tested at considerably higher model/tunnel blockages than are usually recommended. The present series of tests of similar models in a wide range of facilities has provided the opportunity to assess whether high blockage tests are valid and what are their limitations.

## 2. THE INFLUENCE OF MODEL GEOMETRY ON DRAG

Although the drag of three dimensional bodies cannot, in general, be predicted with high confidence there are rules by which estimates can be made for reasonably simple classes of afterbody shape. One such rule is that drag increases and drag rise Mach number falls as the body is made less slender. Various parameters are available to define "slenderness", for axisymmetric bodies the boattail chord angle is convenient.

Drag coefficient at Mach numbers below drag rise and drag rise Mach number are plotted against boattail chord angle in Fig.2 using results from the tests of the three AGARD models together with data from a wide range of geometries tested elsewhere. While it is recognised that drag is also dependent on other features of the afterbody shape such as final boattail angle, maximum curvature and nozzle exit area to maximum cross sectional area ratio, it can be seen that these correlation bands are in fact quite narrow and can be used at least for preliminary estimates of drag characteristics for this class of afterbody. This type of estimate may be useful in deciding whether or not it would be necessary to represent a realistically thin boundary layer in any particular model test programme since it will be shown in the next section that boundary layer thickness is of greater importance near and above the drag rise Mach number.

## 3. THE INFLUENCE OF MODEL GEOMETRY ON SENSITIVITY TO BOUNDARY LAYER THICKNESS

The question of whether it is necessary to represent a realistically scaled boundary layer thickness is of considerable practical importance. In many model test arrangements the afterbody is supported on a long sting, while even when the model is strut mounted it frequently has an unrepresentatively long forebody. In addition Reynolds number is usually significantly lower than at full scale. As a result in most model tests the boundary layer is two or three times as thick as the equivalent flight value. There are methods whereby the boundary layer thickness can be reduced by blowing or by suction, but these involve considerable complication of the test arrangement. Therefore it is worth determining how significant is the effect of boundary layer thickness on drag and whether, at least for certain classes of geometry or ranges of test conditions, it is possible to measure drag to adequate accuracy without boundary layer control.

The effect of boundary layer thickness has been examined at Rolls-Royce, and in a similar programme at ONERA, in tests of an afterbody mounted on a long support sting where the boundary layer thickness could be reduced by blowing. Pressure distributions on the three models with and without blowing are plotted in Fig.3. The effect of a thick boundary layer can be seen to be to reduce the rate of flow deflection over the afterbody so that below drag rise (Figures 3(a) and (b)) both the peak suction and the maximum recompression are reduced. It is found that these two effects nearly cancel so that there is little change in drag in this regime. Above the drag rise Mach number (Figures 3(c) and (d)) the peak suction is again reduced and this now causes the supersonic expansion and recompression losses to be less severe so that a higher recompression level is reached at the end of the afterbody. Therefore at this condition a thick boundary layer causes a significant reduction of drag.

These effects are clearly shown for the three AGARD afterbodies in Figure 4 where it can be seen that up to the drag rise Mach number changes in boundary layer thickness caused little change in drag but at higher Mach numbers the drag coefficient was increased by about 0.01 when the boundary layer was blown.

When making the decision whether it is necessary to represent a realistically thin boundary layer the first step is to determine whether one is going to be attempting to make measurements in the drag rise regime. Correlations such as those in the first part of this paper might be helpful here. If the answer is yes then the next question is

just how accurate must these measurements be. The results presented here have shown that reducing the 95% boundary layer thickness from the typical model test value of 10% of body diameter to 3%, which is more typical of flight conditions, caused an increase of drag coefficient of about 0.01 for each of the three model geometries.

A note of caution is needed regarding the extent to which flight conditions are simulated by use of a blown model support sting. Although blowing reduces the thickness of the model boundary layer the unit Reynolds number in the test environment remains unchanged so that the Reynolds number based on boundary layer momentum thickness is made even smaller relative to the flight value. In a marginally separating situation, as described for example in Reference 1, it is found that decrease of Reynolds number increases the extent of separation and so increases drag. Therefore there appears to be a risk that in some cases reduction of boundary layer thickness to the equivalent flight value could cause the drag measured on the model to be considerably higher than in flight.

It seems clear that when dealing with an afterbody where the flow is likely to be marginally separating the test environment should simulate the full scale viscous flow conditions as closely as possible.

#### 4. THE INFLUENCE OF BLOCKAGE ON TUNNEL INTERFERENCE

The significance of tunnel interference has long been a source of considerable anxiety to those engaged in afterbody drag measurement. In the field of whole aircraft model testing blockages not exceeding a few tenths of a percent are usually recommended and in some cases, of course, large wind tunnels are available for afterbody tests. However in many cases cost considerations lead to the use of rather small tunnels and the need to be able to represent quite fine mechanical details on the model, together with the usual desire to maintain as high a Reynolds number as possible, result in a relatively large model. As a result tests frequently are carried out at blockages of seven percent. The programme of tests of the AGARD models in a wide range of test facilities has provided an unusually good opportunity of assessing whether high blockage tests are valid and what are their limitations.

Figure 5 shows the drag of the 15° boattail as measured in a number of wind tunnels with blockages ranging from 0.2% to 7%. While there is some scatter in these results, particularly at higher Mach numbers, the agreement is generally quite good and there seems to be no distinct trend of variation of drag or drag rise Mach number with blockage. The indication of these results is that for the facilities and test conditions considered tunnel interference has not been significant. As a further confirmation Figure 6 compares the pressure distributions measured on the 15° boattail in the various facilities. Apart from some variation in the pressure close to the end of the boattail, which does not seem to be related to blockage, the various sets of data are seen to be in very close agreement. Similarly close agreement has been found throughout the Mach number range and in the distribution measured on the 10° and 25° boattails.

As well as the experimental data Figure 6 includes a distribution calculated for the 15° model in an infinite stream using an inviscid incompressible analysis procedure<sup>2</sup>. This is seen to correspond quite closely with the experimental results apart from an exaggerated perturbation part-way down the boattail and near the end of the boattail where the analysis predicts a very high recompression which in reality is terminated by viscous effects. This analysis was also used to predict the pressure distribution in an infinite stream along a surface corresponding to the position of the tunnel wall in the Rolls-Royce tests. These distributions are compared with the experimental measurements in Figure 7 where it can be seen that the measured pressures on the tunnel wall near the afterbody location vary a great deal more than would the pressure field in the same region in an infinite stream. This large variation in tunnel wall static pressure provides the main difficulty in accurate drag measurement in high blockage tunnels, that of specifying the correct tunnel static pressure to be used as the datum against which the pressure coefficients and pressure drag are referred. Large absolute errors can easily arise if the reference pressure is measured in a region influenced by the model pressure field. In the Rolls-Royce tests the tunnel static datum pressure has been taken as the mean of three statics, as indicated in Figure 7 which are considered to be downstream of the tunnel entry effects but upstream of the afterbody field.

#### 5. CONCLUSIONS

The results of model tests of three axisymmetric afterbodies in a number of different wind tunnels have been examined in terms of the influence of model external geometry.

The variation of drag with afterbody geometry has been shown to be in accord with the trend for drag to increase and drag rise Mach number to decrease as the body is made less slender. It is found that drag and drag rise Mach number can be correlated quite well with boattail chord angle for a wide range of afterbody geometries in addition to those tested in this exercise.

Increase of boundary layer thickness has been shown to decrease the effective curvature of the afterbody. At speeds below the drag rise Mach number for any particular geometry this modifies the afterbody pressure distribution but has little effect on the pressure drag. Above the drag rise Mach number drag coefficients measured with a boundary layer thickness typical of model test conditions were about 0.01 lower than when the boundary layer

thickness was reduced to a value typical of flight conditions.

Comparison of results obtained in various wind tunnels covering blockage ratios from 0.2% to 7% failed to show any discernable effect of tunnel interference at least for Mach numbers up to about 0.9 to 0.95. At high blockages static pressure varies considerably along the tunnel wall and it becomes crucial to select a reference static pressure which is substantially free from the influence of the afterbody pressure field.

The overall conclusion is that results obtained in the various facilities are in good agreement and the techniques of afterbody drag measurement in current use are generally satisfactory although correct simulation of boundary layer thickness is sometimes necessary.

## 6. SOURCES OF DATA

The results presented in this paper have been taken from various contributions to the AGARD collaborative programme, particularly those from Rolls-Royce (1971) Ltd., U.K.; Air Force Flight Dynamics Laboratory (WPAFB), U.S.A., O.N.E.R.A., France, and National Aerospace Laboratory (NLR), the Netherlands.

## 7. REFERENCES

1. Bowditch, D.N. *Inlet-engine-nozzle wind tunnel test techniques*. Inlets and Nozzles for Aerospace Engines. AGARD CP-91-71 Paper 7, 1971.
2. Mason, J.G. *Flow Synthesis by Singularities, Two-dimensional and Axisymmetric Problems*. Rolls-Royce (1971) Ltd., D.E.D. Report IAR 99801 April 1968.



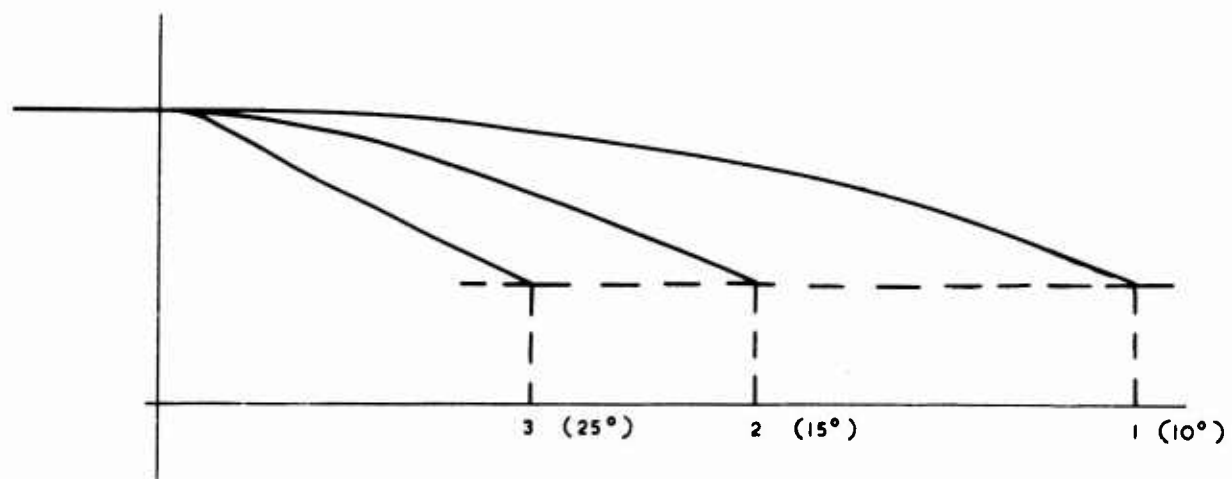


Fig.1 Comparison of the AGARD afterbody profiles

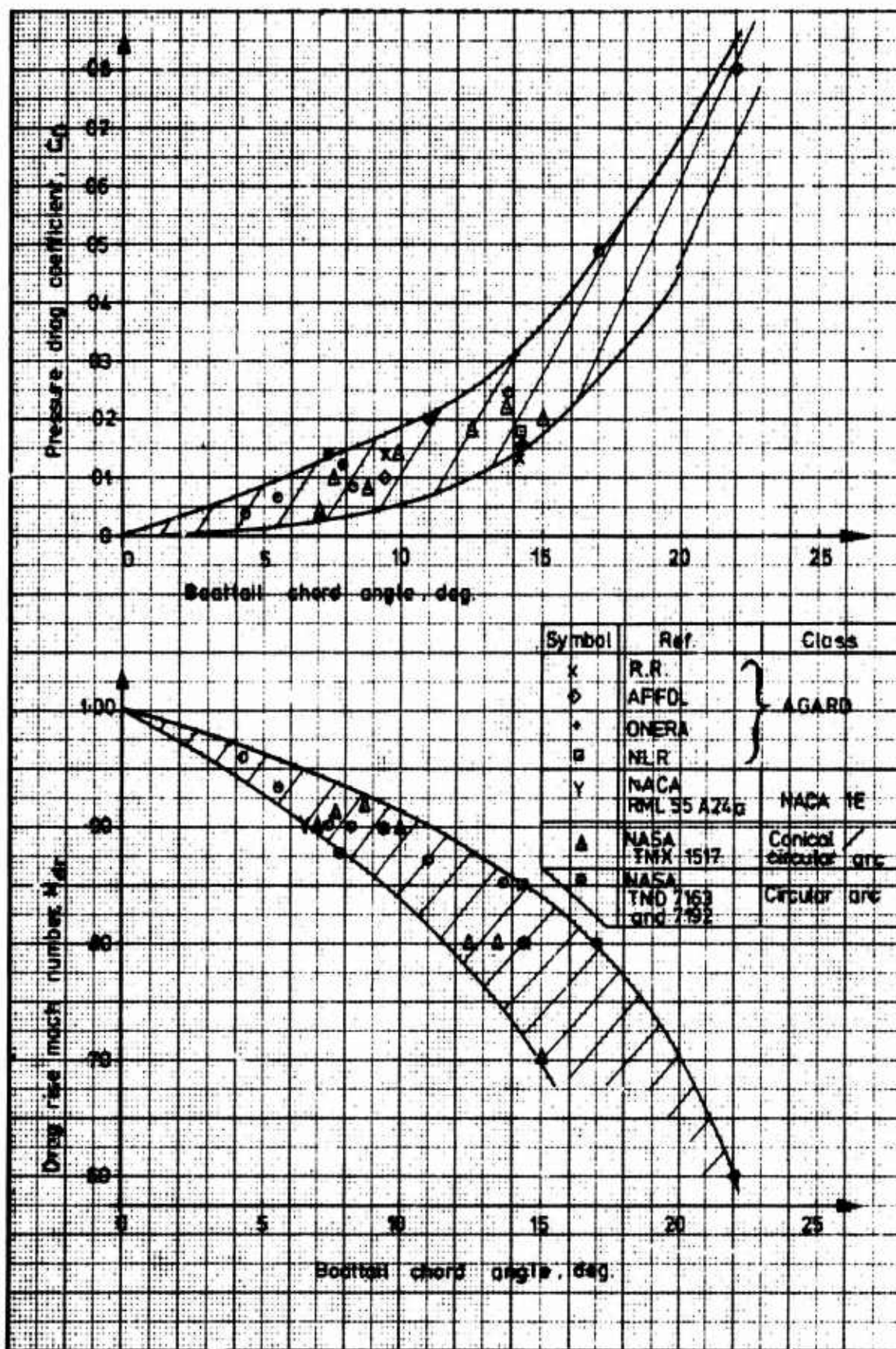
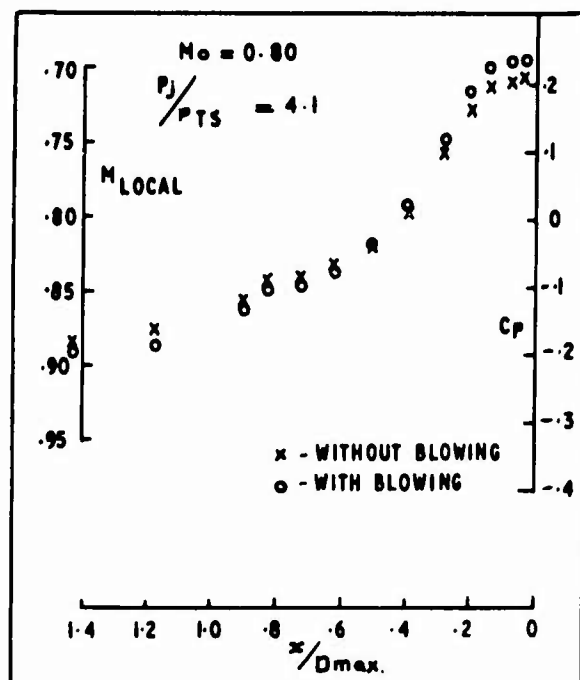
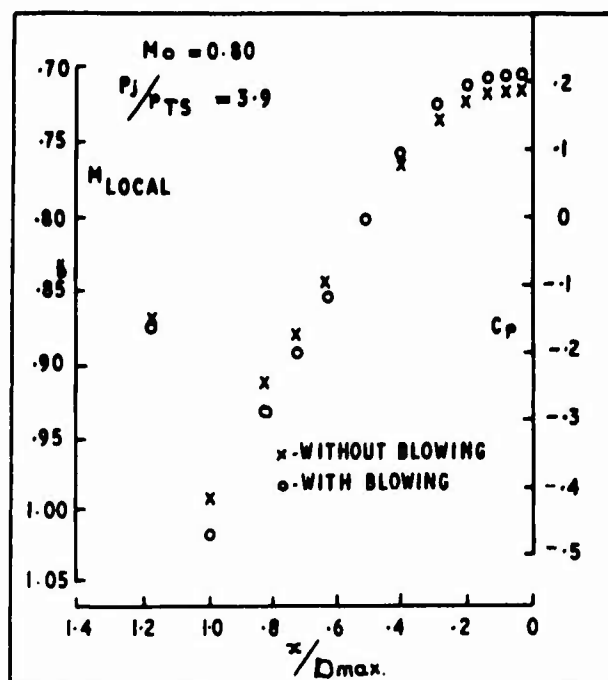


Fig.2 Correlation of subsonic drag coefficient and drag rise Mach number with boattail chord angle for axisymmetric afterbodies without annular bases at nozzle pressure ratios near 3:1

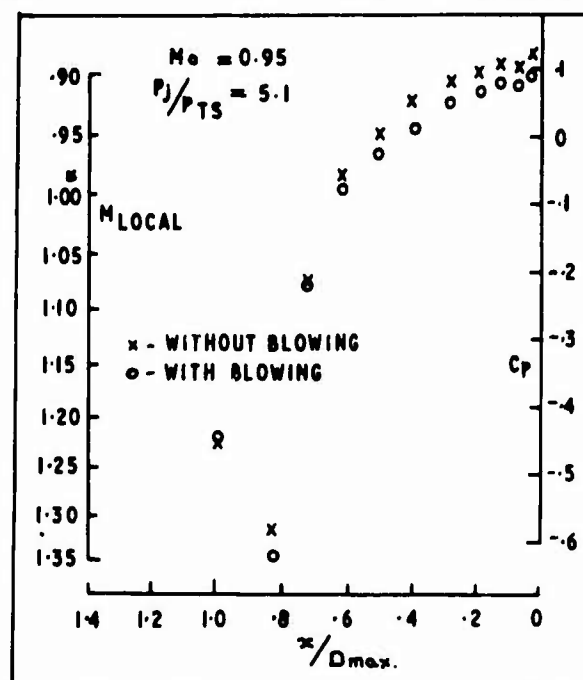
(a) R.R. TESTS OF AGARD 10° BOATTAIL.



(b) R.R. TESTS OF AGARD 15° BOATTAIL.



(c) R.R. TESTS OF AGARD 15° BOATTAIL.



(d) R.R. TESTS OF AGARD 25° BOATTAIL.

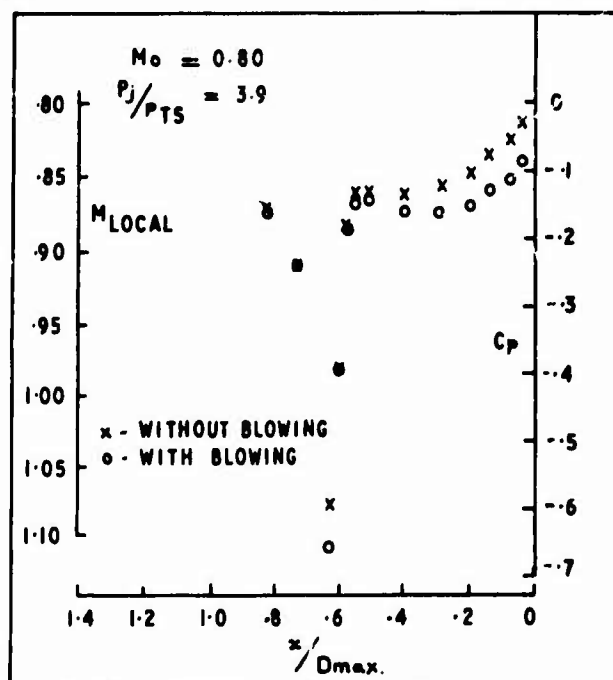


Fig.3 Effect of boundary layer blowing

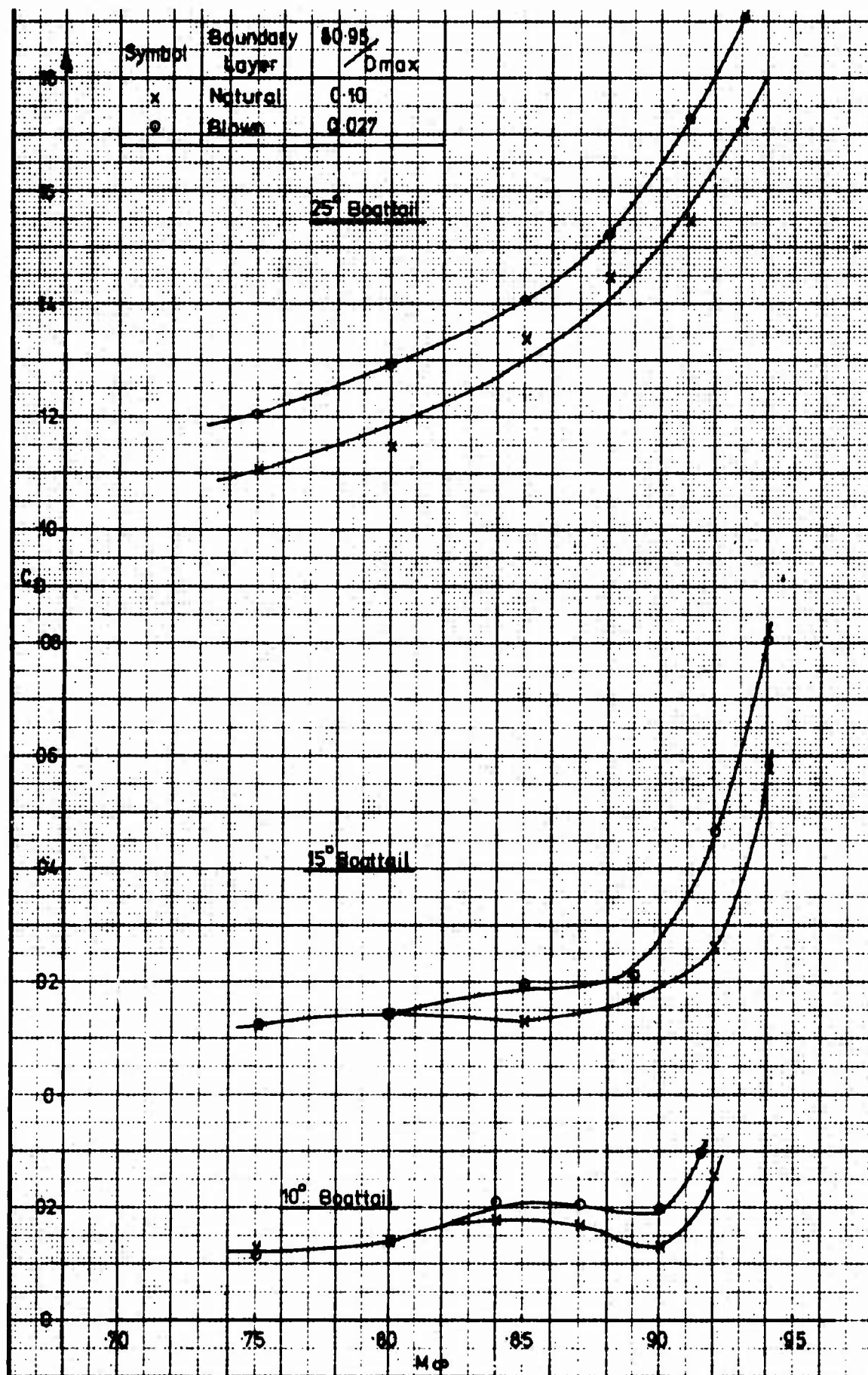


Fig.4 Variation of pressure drag with boundary layer thickness  $P_j/p_\infty = 3.0$

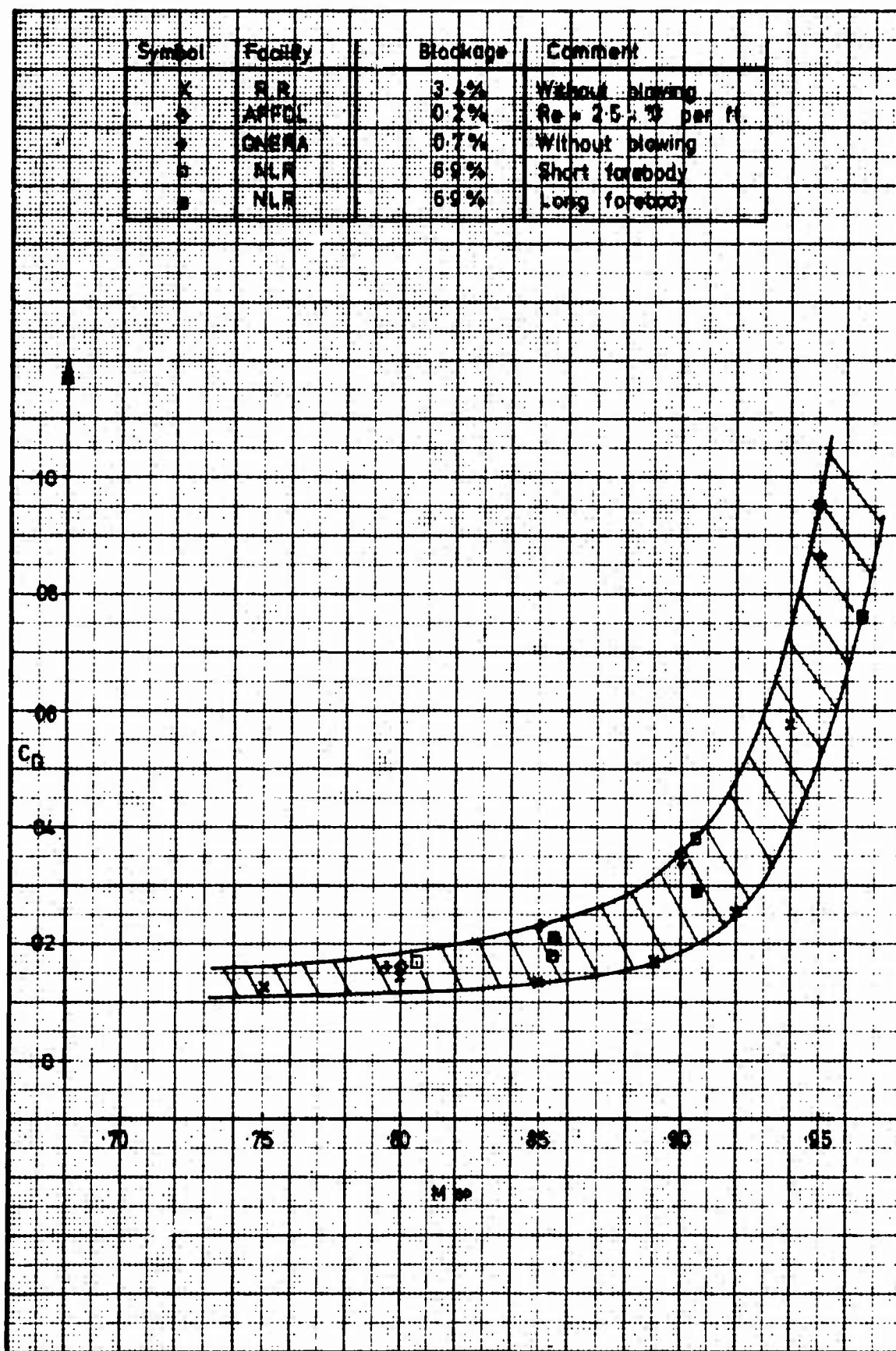


Fig.5 Comparison of drag coefficient of the AGARD 15° boattail measured in various wind tunnels at  $P_j/p_\infty \sim 3.0$

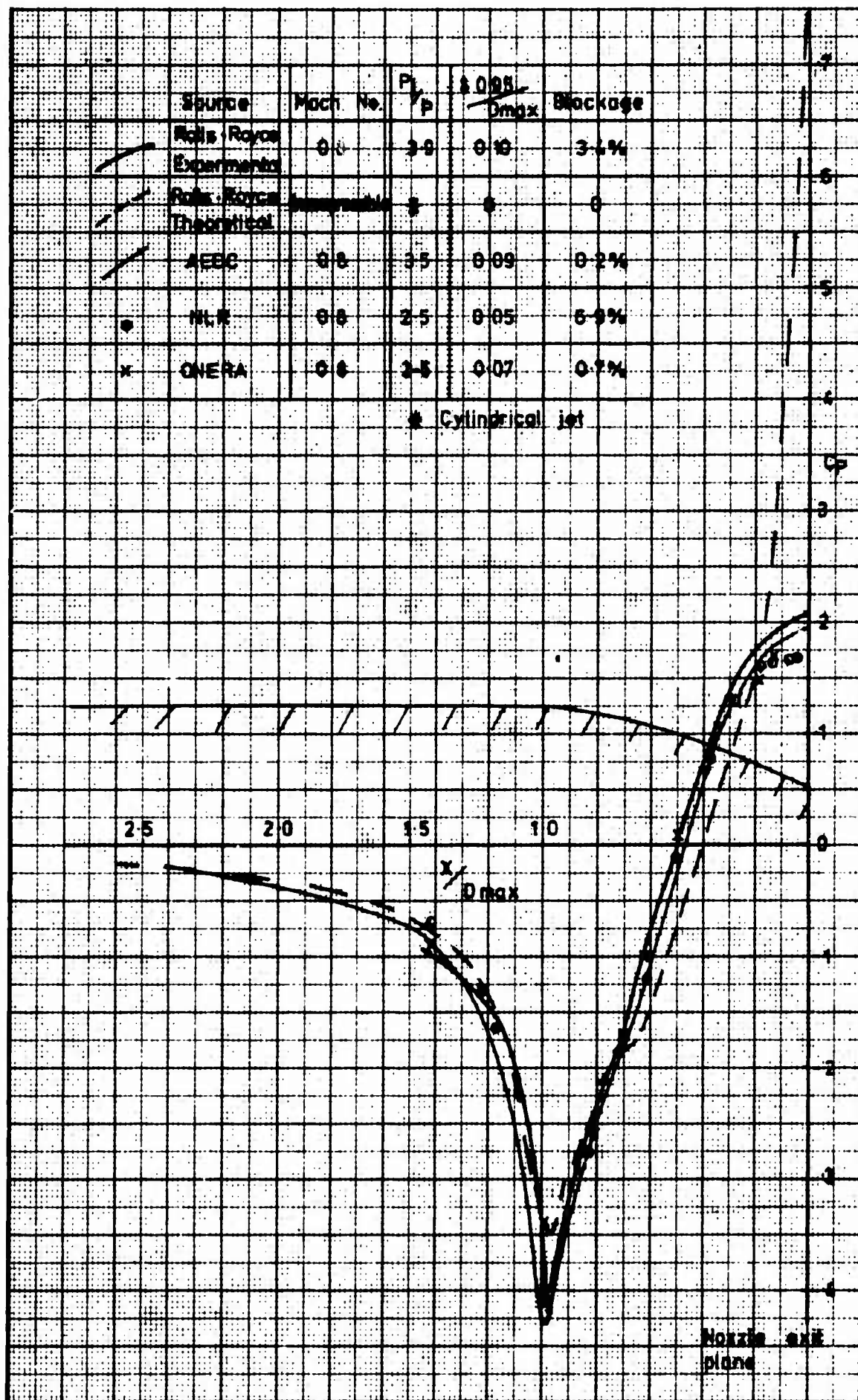


Fig.6 Pressure distribution on AGARD 15° boattail



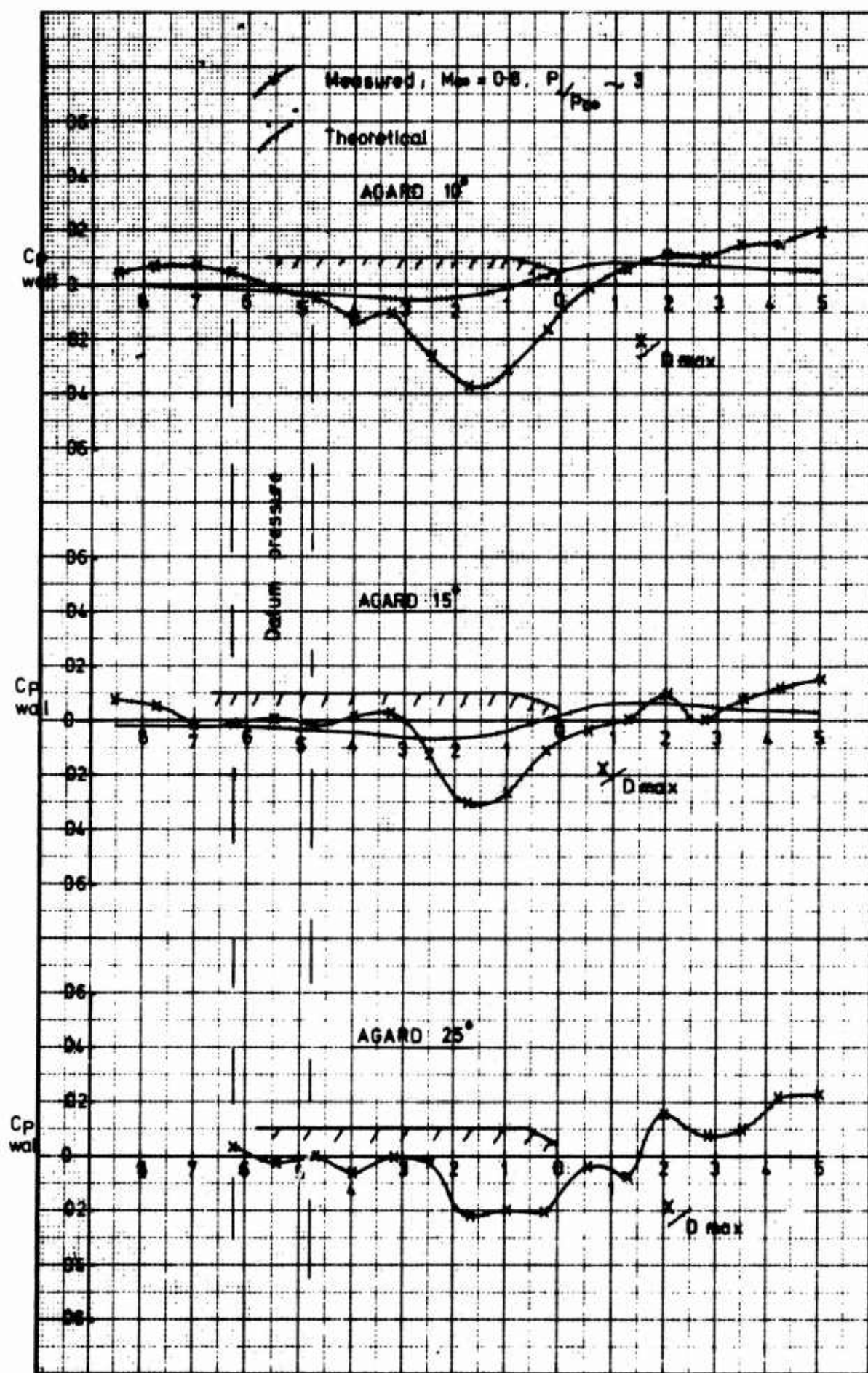


Fig.7 Tunnel wall static pressure distributions

# INFLUENCE DU TAUX DE DETENTE DU JET SUR LES COEFFICIENTS DE PERFORMANCE D'UN ARRIERE-CORPS MONOFLUX AGARD DE MACH 0,60 A MACH 0,95.

par Bernard MECHIN\* et Jean-Marie HARDY\*\*

## Résumé

Dans le cadre de l'étude entreprise par l'AGARD, la synthèse des résultats expérimentaux relatifs à l'influence des conditions génératrices du jet sur la traînée des différents arrières-corps est présentée. L'influence du taux de détente sur les pressions de rétreint et les décollements de la couche limite est analysée. Cette étude est effectuée pour différentes épaisseurs de couche limite, certains montages permettant le contrôle de celle-ci par un soufflage tangentiel.

## INFLUENCE OF THE JET PRESSURE RATIO ON THE PERFORMANCE OF AN AGARD SINGLE FLOW AFTERBODY IN THE 0.60-0.95 MACH RANGE

## Summary

Within the scope of an AGARD study, the synthesis of the experimental data concerning the effect of jet stagnation conditions on the drag of various afterbodies is presented. Jet pressure ratio effect on boattail pressure and on boundary layer separation is analysed. This study is made for several values of the boundary layer thickness, taking into account the fact that some test rigs make its control possible by means of tangential blowing.

## Notations

- $M_\infty$  : nombre de Mach de l'écoulement externe à l'infini amont  
 $p_\infty$  : pression statique de l'écoulement externe à l'infini amont  
 $p_j$  : pression génératrice du flux interne de la tuyère  
 $p_j/p_\infty$  : taux de détente  
 $p$  : pression externe sur le rétreint.  
 $C_p$  : coefficient de pression sur le rétreint

$$C_p = \frac{p - p_\infty}{\frac{\gamma}{2} p_\infty M_\infty^2}$$

$C_{DP}$  : coefficient de traînée de pression

$Re_{D_{MAX}}$  : nombre de Reynolds de l'écoulement externe rapporté au diamètre  $D_{MAX}$  du maître couple.

## 1. Introduction

Un programme d'études sur les techniques d'essai d'arrière-corps de révolution en écoulement transsonique a été proposé par l'AGARD aux différents organismes de recherche des pays membres de ce groupe : NASA et AEDC aux USA, Rolls-Royce (BED) en Grande-Bretagne, NLR aux Pays-Bas, DFVLR en Allemagne et ONERA en France. Chacun de ces organismes a réalisé la totalité ou une partie seulement du programme initial ; les essais ainsi effectués dans les différentes souffleries transsoniques donnent la possibilité de caractériser les différentes techniques utilisées et de mieux comprendre le rôle joué par les divers paramètres entrant en ligne de compte, aussi bien ceux qui sont liés au fonctionnement de l'arrière corps (taux de détente, température du jet, distorsions du jet, nombre de Mach) que ceux qui sont inhérents au montage et à la soufflerie utilisée : couche limite, montage sur mât latéral ou en dard amont, nombre de Reynolds de l'écoulement externe, obstruction de la veine.

La synthèse présentée dans ce document ne concerne que l'influence du taux de détente sur les coefficients caractéristiques de l'arrière-corps : coefficient de pression, coefficient de traînée. L'influence des autres paramètres fondamentaux (nombre de Mach, nombre de Reynolds, couche limite ...) est étudiée par ailleurs par les autres participants au programme d'études et fait l'objet de documents de synthèse particuliers.

\*Ingénieur de Recherche à l'ONERA.

\*\* Chef du Service Tuyères à la SNECMA.



## 2. Montages d'essai

2.1 - Les montages d'essai utilisés sont décrits en détail dans les références [1 à 6]. Ils appartiennent à deux catégories :

. Les montages sur mâts latéraux (AEDC, NASA, NLR) où la maquette se trouve placée à l'extrémité aval d'un fuseau muni d'une ogive à l'amont, l'ensemble du montage se trouvant ainsi dans la veine.

. Les montages en dard amont (ONERA, Rolls Royce, DFVLR) où la maquette est disposée à l'extrémité aval d'un dard dont l'origine se trouve dans la chambre de tranquillisation. Les montages de ce type sont d'ailleurs munis d'un dispositif de soufflage tangentiel de la couche limite.

Les schémas d'ensemble de ces montages sont représentés sur les figures 1 à 6.

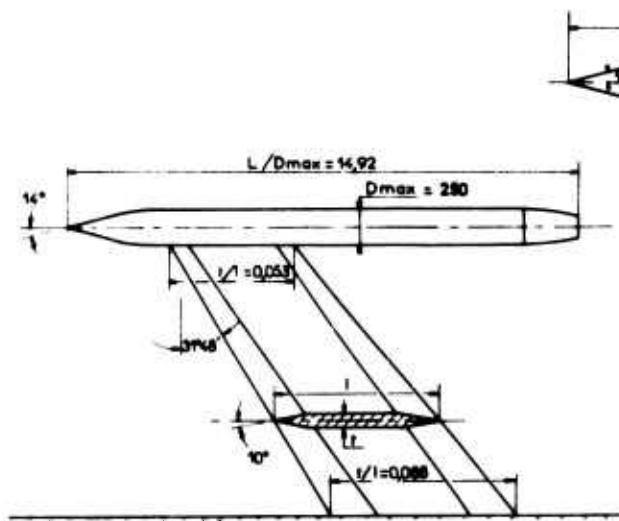
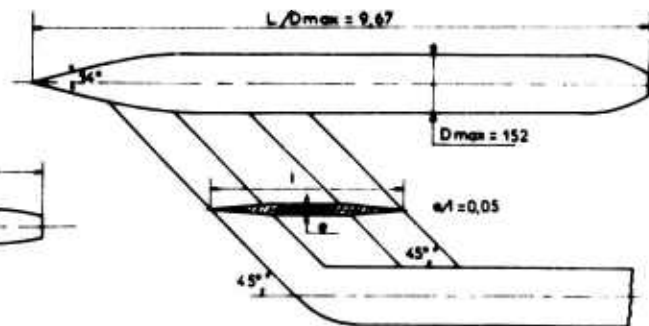


Fig. 1 - Montage AEDC (USA).



SOUFFLERIE DE 16 F1 LANGLEY

Fig. 2 - Montage NASA (USA).

Fig. 3 - Montage NLR (NL).

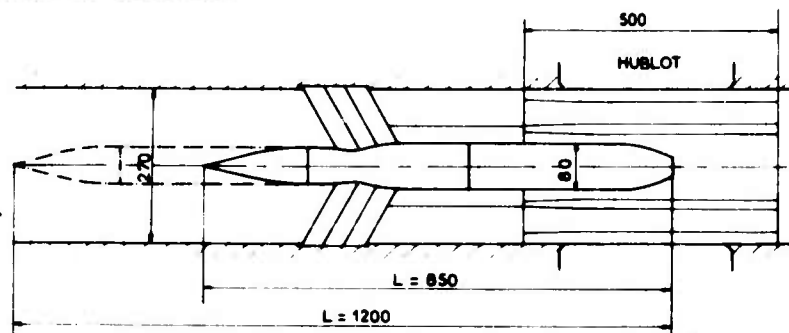


Fig. 4 - Montage ONERA (France).

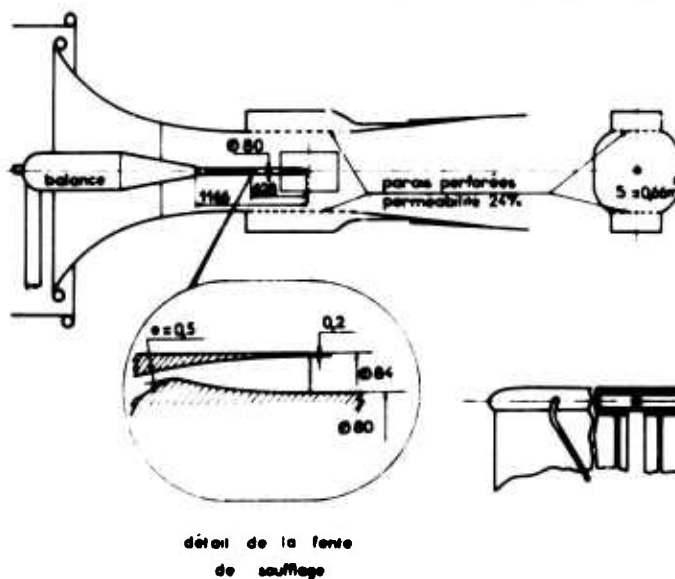
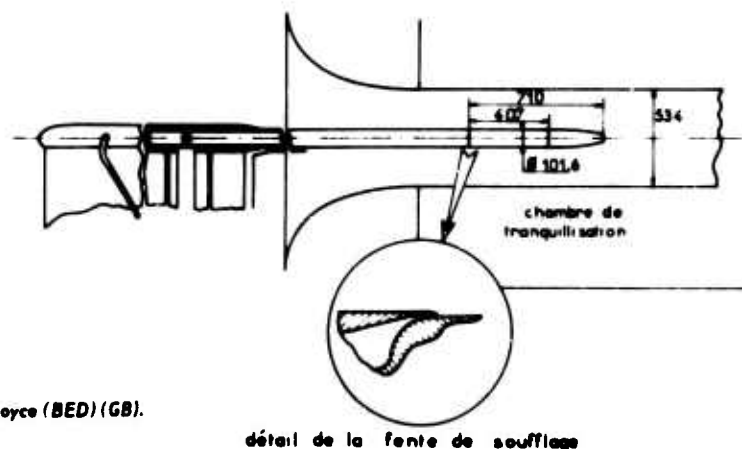


Fig. 5 - Montage Rolls-Royce (BED) (GB).



Les trois types de maquettes utilisés sont schématisés sur la figure 7.

Fig. 6 - Montage DFVLR.

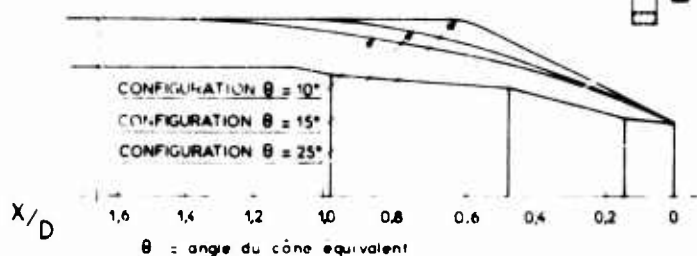


Fig. 7 - Schema des trois maquettes utilisées.

## 2.2 - Couches limites

Les couches limites mesurées sur les montages à des nombres de Mach de 0,6 et 0,9 sont représentées sur les figures 8 et 9. L'effet du soufflage tangential de la couche limite observé sur les montages Rolls-Royce et ONERA est de réduire sensiblement les épaisseurs caractéristiques de la couche limite tout en conservant un profil de vitesses régulier. Ce dispositif permet donc de contrôler efficacement la couche limite et de compenser ainsi un épaississement de celle-ci dû à la grande longueur du montage. Les dissymétries observées pour les couches limites du montage ONERA ont récemment été considérablement réduites par une amélioration des carénages du montage dans sa partie amont.

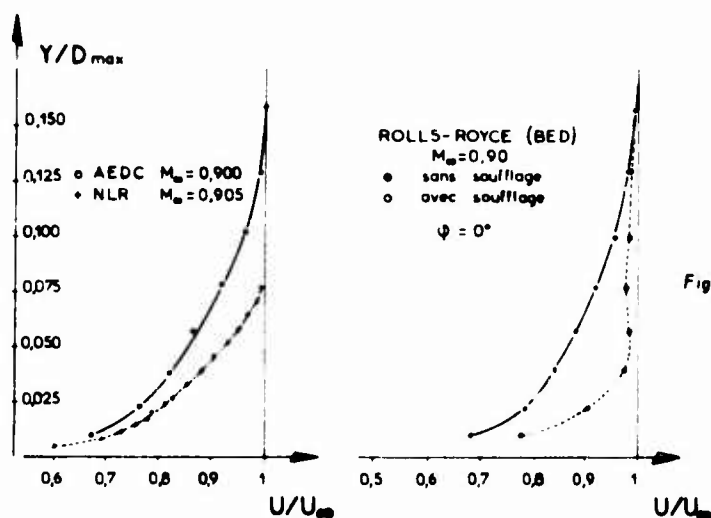
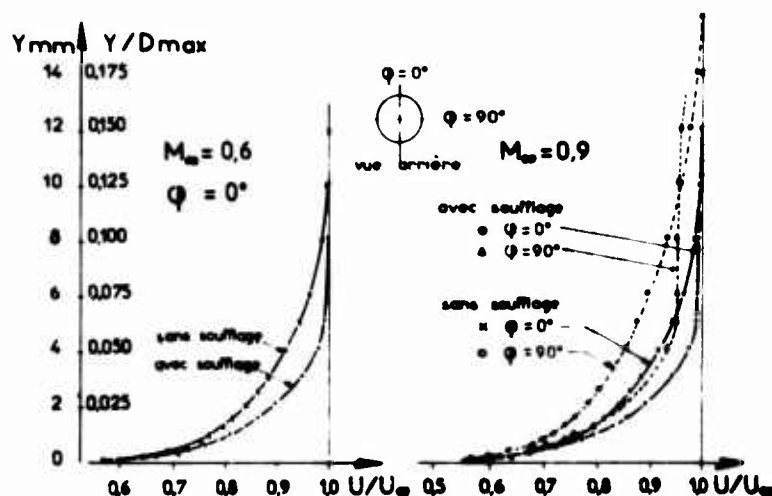


Fig. 8 - Couche limite (AEDC, NLR, Rolls-Royce).

Fig. 9 - Couche limite (ONERA).



### 3. Comparaison des résultats

Sur les figures 10 et 11 sont représentées les variations du coefficient de pression  $C_p$  sur la tuyère  $15^\circ$  obtenues par les différents organismes pour les nombres de Mach 0,80 et 0,95 et pour un taux de détente moyen compris entre 2,5 et 3. A Mach 0,8, les points obtenus se regroupent sur une courbe unique. Toutefois dans les essais NLR la détente est moins prononcée et la recompression retardée par rapport aux autres essais, ce qui peut s'expliquer par la forte valeur du taux d'obstruction (7 %). Ces essais sont par ailleurs effectués en gaz chaud ( $T_i = 630^\circ\text{K}$ ).

A Mach 0,95 l'apparition d'un choc et d'un décollement de caractère instable provoque de légères différences à la fois au niveau de la position du choc et de la répartition de pression dans la zone décollée.

L'influence du taux de détente sur les coefficients de pression reste comparable entre tous les essais. C'est le seul point qui est analysé dans cette note, l'influence des conditions particulières d'essai devant être examinée par ailleurs.

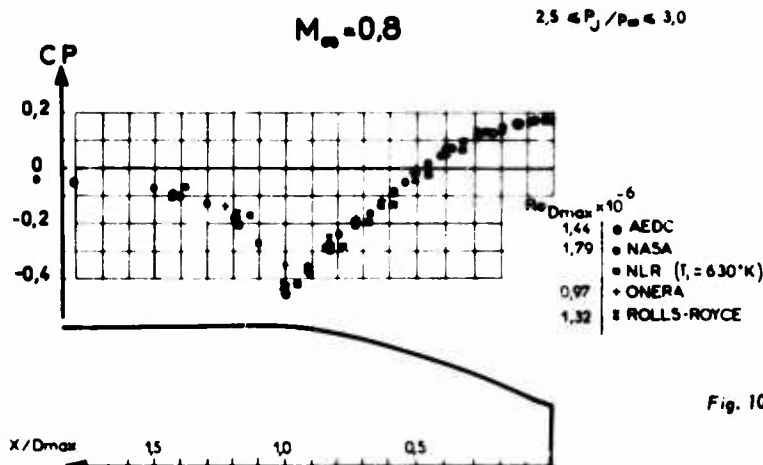


Fig. 10 - Coefficient  $C_p$  sur tuyère  $15^\circ$  (AGARD).

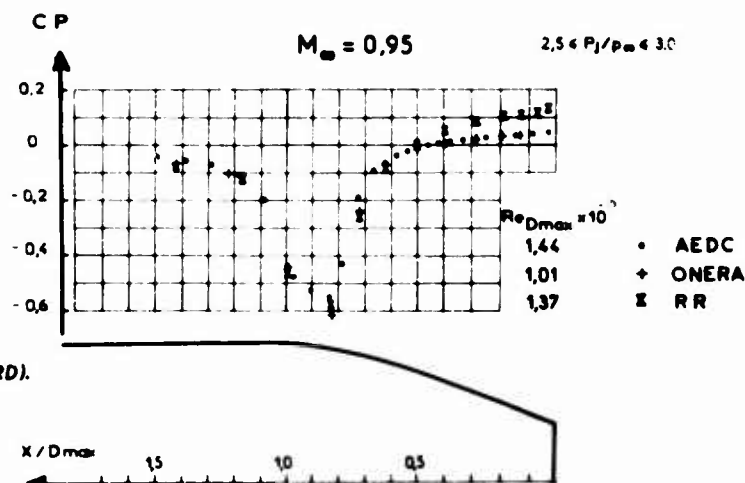


Fig. 11 - Coefficient  $C_p$  sur tuyère  $15^\circ$  (AGARD).

### 4. Influence du taux de détente sur le coefficient de pression

Parmi les résultats disponibles, nous avons retenu principalement ceux obtenus par l'AEDC sur les trois maquettes  $10^\circ$ ,  $15^\circ$  et  $25^\circ$  car ils ont été effectués pour une large gamme de taux de détente ( $P_1/p_\infty$  compris entre 1 et 12) avec des maquettes disposant de très nombreuses prises de pression. Les résultats utilisés pour chacune des tuyères à des nombres de Mach de 0,60, 0,80 et 0,95 sont regroupés sur les figures 12 à 15 (essais ONERA fig. 12, essais AEDC fig. 13 à 15).

#### 4.1. Tuyères $10^\circ$ et $15^\circ$ (fig. 12 à 14)

- L'effet du taux de détente sur le coefficient de pression  $C_p$  est d'accroître sensiblement le niveau de la recompression lorsque le taux de détente augmente, ceci par effet potentiel dû à la présence du jet, tant qu'il n'y a pas décollement de la couche limite. Cet effet n'est sensible que dans la zone où le gradient  $dC_p/dx$  est positif.

- Cet effet est d'autant plus intense que le nombre de Mach extérieur est élevé. Vers l'extrémité du rétreint l'accroissement du taux de recompression est annulé :

- soit par effet d'entraînement qui accélère l'écoulement proche (explication valable dans tous les cas sauf dans celui de la tuyère  $15^\circ$  à  $M_\infty = 0,95$ ). Des sondages de l'écoulement au voisinage de la paroi seraient nécessaires pour confirmer cette hypothèse ;

soit par une tendance au décollement de la couche limite. Il semble toutefois que ce phénomène soit davantage lié à l'apparition d'un choc comme le montre le ralentissement de la recompression au pied du choc sur le rétreint 10° à  $M_\infty = 0,95$ . Sur le rétreint 15°, au même nombre de Mach, le décollement, qui part du choc, reste établi sur tout le rétreint.

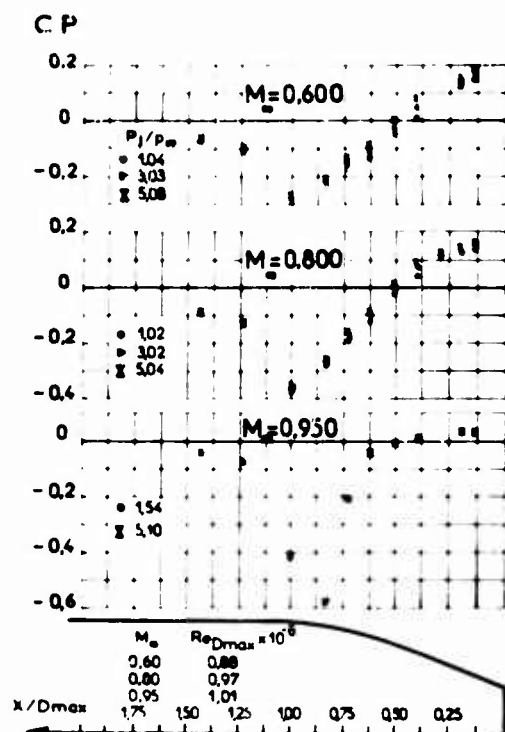


Fig. 12 - Tuya 15° (ONERA).

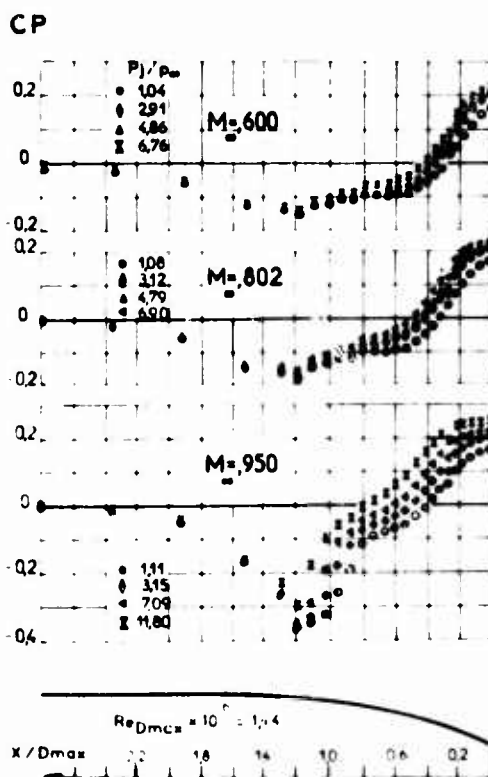


Fig. 13 - Tuya 10° (AEDC).

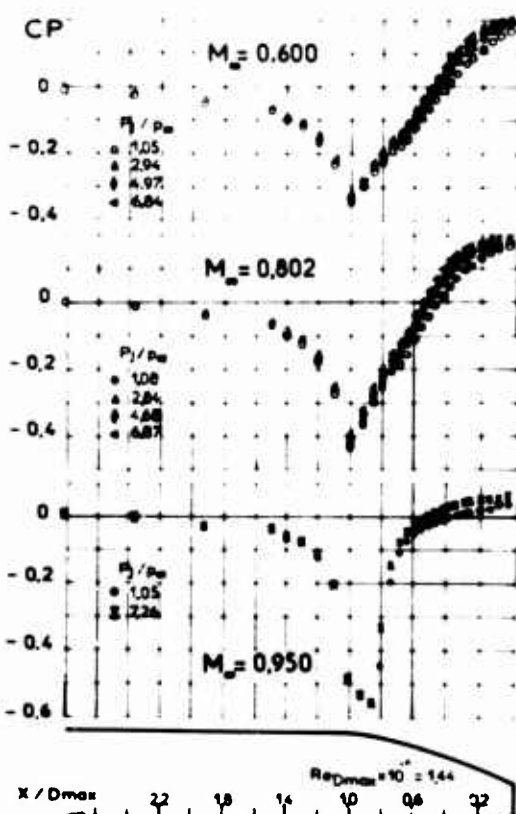


Fig. 14 - Tuya 15° (AEDC).

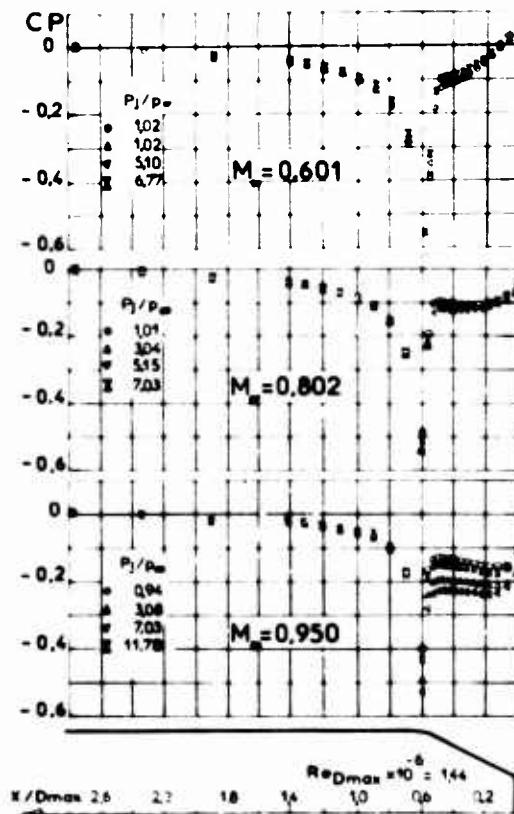


Fig. 15 - Tuya 25° (AEDC).

#### 4.2. Tuyère 25° (fig. 15)

- La très grande courbure en début de rétrojet fait apparaître un choc droit, même à Mach 0,6. Pour ce nombre de Mach, le choc est suivi d'une recompression régulière dont le niveau dépend du taux de détente.

- Dès que  $M_\infty = 0,80$ , il apparaît en aval du choc un profil de pression plat caractéristique d'un écoulement décollé.

- A Mach 0,95 le niveau de recompression est inférieur à celui obtenu à Mach 0,80 et passe par un minimum pour un taux de détente voisin de 7. Cette évolution peut s'expliquer par un échange entre l'effet de jet sur l'écoulement potentiel et l'effet d'entraînement prépondérant aux faibles taux de détente, en raison de l'étendue de la zone de mélange. Ces hypothèses demanderaient également à être vérifiées par des sondages de l'écoulement en particulier en aval du plan de sortie.

#### 5. Influence du taux de détente sur le coefficient de traînée de pression

Le coefficient de traînée de pression  $C_{DP}$  est calculé par intégration de la répartition de pression sur l'arrière-corps considéré. La précision obtenue dépend étroitement du nombre de prises de pression disponibles pour la mesure. A ce titre les essais AEDC paraissent les plus précis eu égard au grand nombre de prises de pression installées.

L'évolution de ce coefficient de traînée, en fonction du taux de détente, est représentée pour chaque tuyère et pour des nombres de Mach de 0,80, 0,90 et 0,95 sur les figures 16 à 24.

L'analyse de ces résultats permet de préciser et de confirmer les observations déjà faites précédemment pour l'évolution des coefficients  $C_p$ .

##### 5.1. Tuyères 10° et 15° - Figures 16 à 21.

Comme pour les coefficients  $C_p$ , le coefficient de traînée  $C_{DP}$  diminue de façon importante lorsque l'on passe de la configuration sans jet à un taux de détente de 2. Cet effet est d'autant plus marqué que l'angle de carène est plus faible.

La traînée reste ensuite sensiblement constante entre  $P_j/p_\infty = 2$  et  $P_j/p_\infty = 4$  puis décroît régulièrement lorsque le taux de détente croît. Elle devient négative pour une valeur suffisamment élevée du taux de détente.

Sur les figures 19 et 21 sont représentées également les variations de  $C_{DP}$  obtenu pour la tuyère 15° avec les montages Rolla-Royce et ONERA avec et sans soufflage de la couche limite. A Mach 0,8 (fig. 19) la valeur de  $C_{DP}$  obtenu avec et sans soufflage sont très voisines entre elles, à la dispersion des mesures près. A Mach 0,95 (fig. 21) le soufflage augmente le  $C_{DP}$ . La forte dispersion des résultats entre les différentes souffleries traduit la répercussion sur le  $C_{DP}$  de petites différences notamment sur la position du choc dont l'existence a été signalée précédemment. Ces différences sont tributaires d'effets d'obstruction de veine et de couche limites variables suivant les montages.

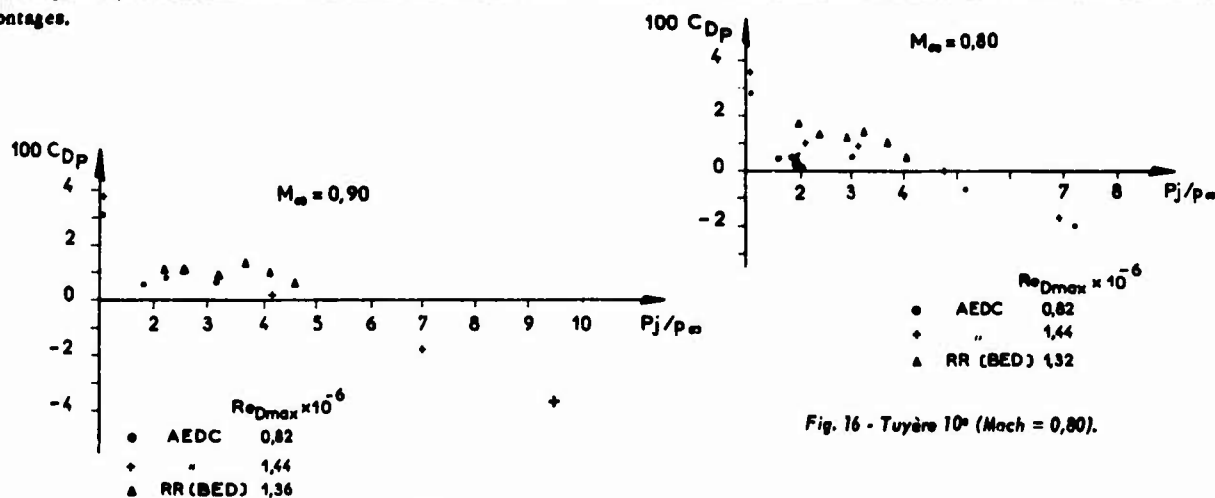


Fig. 16 - Tuyère 10° (Mach = 0,80).

Fig. 17 - Tuyère 10° (Mach = 0,90).

EVOLUTION DU COEFFICIENT  $C_{DP}$   
EN FONCTION DE  $P_j/p_\infty$ .

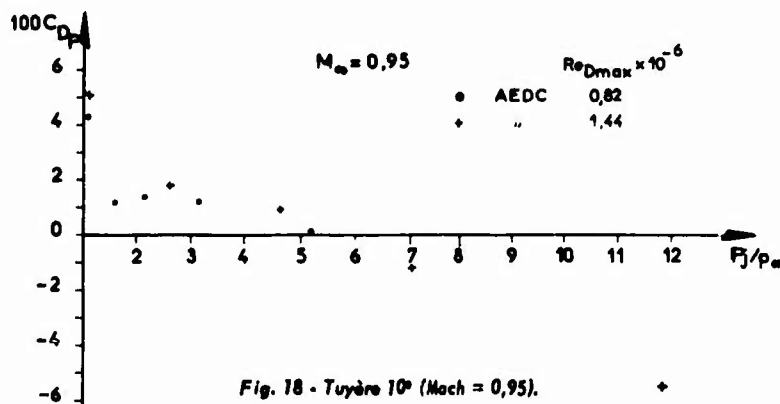


Fig. 18 - Tuyère 10° (Mach = 0,95).

Fig. 19 - Tuyère 15° (Mach = 0,80).

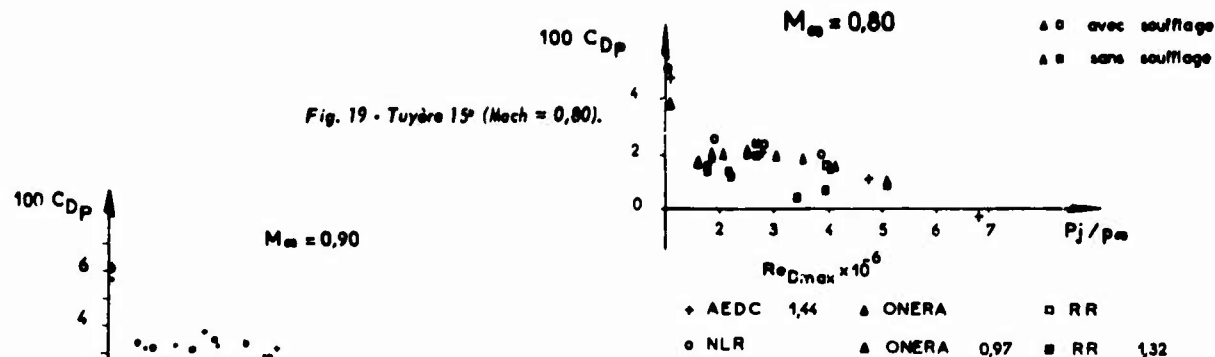
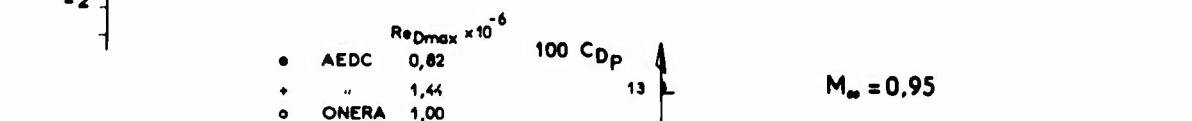


Fig. 20 - Tuyère 15° (Mach = 0,90).



## 5.2 - Tuyère 25° (fig. 22 à 24)

Pour cette tuyère dont l'angle de carène est beaucoup plus important, l'évolution est différente : la traînée commence par croître avec le taux de détente, atteint un maximum pour une valeur du taux de détente croissante avec le Mach, puis décroît régulièrement. S'il y a quelques différences dans les niveaux absolus de  $C_{Dp}$ , l'évolution de ce coefficient en fonction du taux de détente est commune aux différents essais.

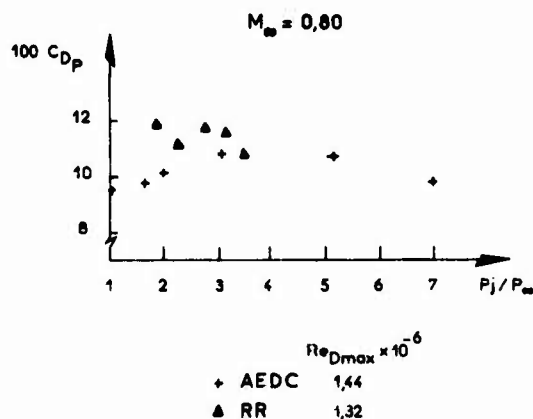


Fig. 22 - Tuyère 25° (Mach = 0,80).

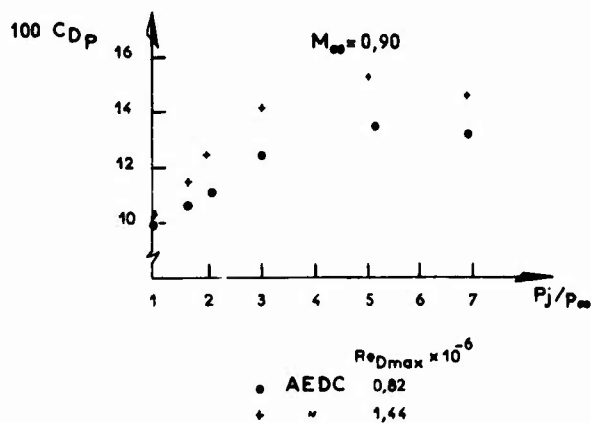


Fig. 23 - Tuyère 25° (Mach = 0,90).

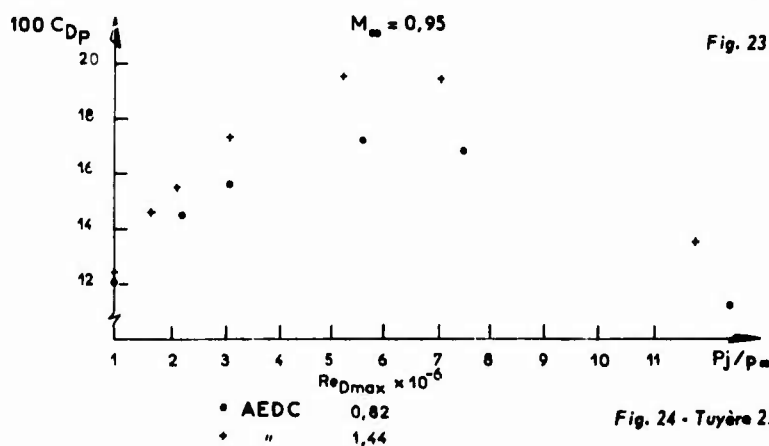


Fig. 24 - Tuyère 25° (Mach = 0,95).

## 6. Conclusions

Quelques tendances générales peuvent être dégagées des essais effectués dans différentes installations concernant l'influence du taux de détente de jet sur l'écoulement externe autour d'un arrière-corps.

1) Les conditions particulières des différentes installations font apparaître de faibles écarts sur les valeurs absolues des coefficients mesurés, mais ne modifient pas l'évolution de ces grandeurs en fonction du taux de détente.

2) L'effet du taux de détente sur le coefficient de pression  $C_p$  est surtout sensible lorsque le jet commence à s'établir.

3) Le taux de détente n'a d'effet que sur la partie de l'arrière-corps formant rétreint, et n'affecte pas la répartition des pressions en amont du choc qui apparaît aux nombres de Mach suffisamment élevés : le choc est légèrement modifié en intensité, ce qui se traduit par des écarts visibles de traînée.

4) Dans le cas d'un écoulement non décollé sur le rétreint, une augmentation du taux de détente tend à augmenter la recompression.

5) Dans le cas d'un écoulement décollé en aval du choc le niveau de pression de la zone décollée commence par décroître quand  $P_j/p_\infty$  croît, puis augmente à partir d'un certain niveau, assez élevé, du taux de détente.

Des hypothèses ont été formulées pour expliquer les différentes tendances. Leur discussion qui pourrait être un prolongement normal de cette étude, nécessiterait une analyse plus approfondie de l'écoulement par des sondages des régions proches de la sortie du jet, et éventuellement par l'introduction de tuyères convergentes et divergentes permettant, parallèlement aux essais en gaz chaud, de faire varier les conditions d'entraînement et de recollement sur la frontière du jet.

## Références

- [1] Improved nozzle testing techniques in transonic flow. Preliminary results of NLR contribution to AGARD Ad Hoc Study. NLR-AH-74-002 (mai 1974).
- [2] DEER D.J. - Results of tests on single afterbody nozzles. Defined by AGARD. Rolls Royce (BED) PPE 67 (mars 1974).
- [3] HARPER L.R. - The influence of boundary layer thickness on nozzle afterbody pressure drag. Rolls Royce (BED) PPE 69 (avril 1974).
- [4] United states data for "Improved nozzle testing techniques in transonic flow". AGARD Ad Hoc Study (3 mai 1974).
- [5] MECHIN B. - Etude expérimentale de la tuyère étalon AGARD ( $\beta = 15^\circ$ ) à la soufflerie S3 de Chalais de l'ONERA. Note à paraître.
- [6] RIEDEL H., EMUNDS H. - Preliminary report on AGARD research project "Improved nozzle testing techniques in transonic flow. DFVLR - Porz-Wahn - Institut Für Angewandte Gasdynamik (mars 1974).

# INFLUENCE OF JLT PARAMETERS: NOZZLE THRUST AND DISCHARGE COEFFICIENTS

by

C.C.Groothoff  
National Aerospace Laboratory, NLR,  
The Netherlands

## SUMMARY

Internal flow and nozzle characteristics were analysed as part of the program coordinated by the AGARD ad hoc study group. All available data were used in a comparison of the nozzle discharge and thrust coefficients and jet pipe wall static pressures of similar model configurations. It was found necessary to take into account the distortion of the total pressure profiles in the jet pipe. The mass flow averaged total pressure was used in the calculations. The distortion coefficient DCM proved to be a useful tool in the comparison of the mass flow averaged total pressure with the 1-D isentropical total pressure, derived from mass flow, temperature and static pressure.

The discharge coefficients that were found in the range of nozzle pressure ratios of about 1.3 to 12 were in good agreement. For the specified nozzle A the discharge coefficient  $C_d = .986$ . For this nozzle configuration with a contraction ratio of 3.24 hardly any influence on  $C_d$  of jet medium or distortion was found. External air flow did influence  $C_d$ , mainly through the boattail overpressure near the nozzle lip. The thrust coefficients were found to be difficult to compare, one set of data however shows an unexplained higher level (about 1 - 2%). Nozzle B (contraction ratio 1.62) showed more influence of distortion in the jet flow. The values for the choked nozzle discharge coefficients were  $C_d = .978$  (no dist.) and  $C_d = .946$  (dist.). Distortion was also found to influence the wall static pressures in the jet pipe. The distortion coefficient DCM enabled comparison of the results of the various institutes which cooperated in the program.

## LIST OF SYMBOLS

A	area, $m^2$
$A_n$	geometric exhaust area, corrected for nozzle wall temperature, $m^2$
B	factor in Equation (5), Section 3
$C_t$	static pressure coefficient, $\frac{p - p_\infty}{q_\infty}$
$C_d$	nozzle discharge coefficient, see list of definitions
CT	nozzle thrust coefficient, see list of definitions
$c^*$	specific velocity, m/s
$D_{max}$	maximum model diameter, mm
DCM	distortion coefficient, Section 3
F	thrust, N
i	number of $i^{th}$ concentric jet pipe area
k	factor in Equation (5), Section 3
$M_\infty$	free stream Mach number
$\dot{m}$	mass flow, kg/s
NPR	nozzle pressure ratio $p_{t_j}/p_\infty$



## II-C2

$n$	total number of equal concentric jet pipe areas
$p$	pressure, $N/m^2$
$q_{\infty}$	free stream dynamic pressure $\frac{1}{2}\gamma p_{\infty} M_{\infty}^2$ , $N/m^2$
$Re_{D_n}$	nozzle Reynolds number $\left(\frac{UD}{\nu}\right)_n$
$R$	gas constant $\frac{m^2}{s^2 K}$
$r$	distance from model centreline, mm
$T$	temperature, K
$U$	velocity, m/s
$x$	distance from exit of nozzle A, upstream is positive, m
$\alpha$	nozzle convergence half angle, degrees
$\beta$	mixing parameter of Reference 10
$\gamma$	ratio of specific heats
$\nu$	viscosity, $m^2/s$
$\rho$	density, $kg/m^3$

### Subscripts

av	average
CL	on centreline
ex	external near nozzle exit plane $x/D_{max} = .056$ (nozzle A) or $= .27$ (nozzle B)
f	flat, according to 1 - D isentropical calculation
i	index
id	ideal
j	jet
jp	jet pipe
l	internal near nozzle lip at $x/D_{max} = .063$ (nozzle A) or $= .204$ (nozzle B)
meas	measured
n	nozzle
t	total
1, 2, 3	different definitions of CT
$\infty$	free stream
*	critical throat condition

### LIST OF DEFINITIONS

$$C_d \quad \text{nozzle discharge coefficient} = \frac{\dot{m}}{\dot{m}_{id}}$$

$$\text{For supercritical pressure ratios } C_d = \frac{c^* \cdot \dot{m}}{p_{tj} \cdot A_n} \quad \text{where the specific velocity}$$

$$c^* = \frac{1}{\gamma} \sqrt{\frac{\gamma R T_{tj}}{\left(\frac{2}{\gamma+1}\right)^{(\gamma+1)/(\gamma-1)}}$$

$$\text{For subcritical pressure ratios } C_d = \frac{\dot{m}}{p_{\infty} A_n} \sqrt{\frac{\gamma-1}{2\gamma} \frac{R T_{tj}}{\left(\frac{p_{tj}}{p_{\infty}}\right)^{(\gamma-1)/\gamma} \left[\left(\frac{p_{tj}}{p_{\infty}}\right)^{(\gamma-1)/\gamma} - 1\right]}}$$

$CT_0$	thrust coefficient as used in Reference 7 $CT_0 = CT_2 + \frac{\text{pressure drag}}{F_{id_2}}$ (upstream force is positive)
$CT_1$ $CT_2$ $CT_3$	thrust coefficients $= \frac{F_{\text{meas}}}{F_{id(1,2 \text{ or } 3)}}$ The ideal thrust $F_{id}$ 1, 2, or 3 is based on - 1: actual $p_{t_j}$ and $A_n$ , derived is $\dot{m}_{id}$ - 2: actual $p_{t_j}$ and $\dot{m}$ , derived is $A_n \cdot C_d$ - 3: actual $\dot{m}$ and $A_n$ , derived is $p_{t_j}$ with suffices 1, 2 or 3 omitted, the used equation for the maximum attainable thrust after complete expansion to the ambient pressure is $F_{id} = \dot{m} \sqrt{\frac{2\gamma}{\gamma-1} RT_{t_j} \left[ 1 - \left( \frac{p_{\infty}}{p_{t_j}} \right)^{(\gamma-1)/\gamma} \right]}$ $CT_1 = CT_2 \times C_d$
$F_{\text{meas}}$	measured thrust force = measured balance force - pressure drag - friction - gap pressure correction (upstream force is positive)
nozzle A	exhaust nozzle defined by AGARD coordinates, contraction ratio 3.24, see Table I
nozzle B	exhaust nozzle with contraction ratio 1.62, see Table I

## 1. INTRODUCTION

The AGARD ad hoc study group PEP/04 on "Improved Nozzle Testing Techniques in Transonic Flow" has been formed to investigate the relevant parameters which affect the performance of nozzle and afterbodies at transonic speeds. Several institutes coordinated their research in this project, mostly using essentially the same afterbody and nozzle configurations. Comparison of the results of analogous experiments would yield a frame of reference, while the special topics that were investigated by the different institutes would extend the range of parameters.

Several groups, cooperating in this program, have accepted to compile and discuss the results, each concentrating on one topic of relevance in the afterbody nozzle performance testing. The part that discusses the influences of jet parameters on the afterbody and nozzle performance was shared between DFVLR (Germany) and NLR (the Netherlands). These groups agreed that DFVLR would concentrate on the external boattail pressure distribution while NLR would deal with internal nozzle phenomena. This report is the NLR contribution to the data analysis and complementary to the DFVLR report.

The internal jet pipe flow and nozzle characteristics constitute an important area in the assessment of jet engine performance.

The nozzle discharge coefficient affects the exhaust total pressure and hence the thermodynamic cycle of the engine, while the engine gross thrust is proportional to the nozzle thrust coefficient.

The flow in the jet pipe of real jet engines, particularly at afterburning, and also of turbofan engines, is not homogeneous. Generally, the total pressure and total temperature are non-uniform (distorted), the flow may contain swirl and the turbulence level is usually high. The degree, to which these inhomogeneities affect the nozzle characteristics, depends on the nozzle geometry, contraction ratio of the nozzle and the external flow field in which the jet exhausts. In this analysis only the influence of jet flow total pressure distortion could be included, as swirl or turbulence have not been investigated in this program.

In order to establish the nozzle characteristics, the primary jet parameter, i.e. the jet total pressure, must be defined. In a distorted flow this requires a special approach.

The tested conical convergent nozzle configurations (except of Reference 2) constituted a simplified representation of an actual exhaust system of a non-afterburning engine (nozzle A) and of an afterburning engine (nozzle B). Nozzle B is also representative for a fan engine nozzle as regards to the contraction ratio. The model of Reference 2 simulated to a larger degree the exhaust system of an actual engine nacelle.

The measuring and flow definition station at the entry of the jet pipe may be considered to coincide with the engine end face, generally constituting the split line between the responsibility of the engine manufacturer and the airframe designer.

This report discusses the influence of some jet, nozzle and external flow parameters on the internal nozzle characteristics and jet pipe pressures, as compiled from the results, gathered by the different participants in this program. Some of the data that have been received are published elsewhere in this AGARDograph (References 1, 2, 3), others (References 4, 5, 6, 7, 12) were made available as preliminary results or in private communication.

## 2. INVESTIGATED NOZZLES AND PARAMETERS

### 2.1 Nozzle Geometry

Although the investigation of the different study groups have been performed using essentially the same nozzle and jet pipe configuration, some differences are noted. In Table I and Figure 1 the dimensionless jet pipe and nozzle shapes are given. In Table II the nozzle size is given along with other parameters. It may be noted that the location of the static pressure orifices in the jet pipe, of the thermocouple and of the total pressure rake were specified in this program (Table I). Most configurations essentially conformed to this specification.

Nozzle A is the standard nozzle according to AGARD specifications. Nozzle B has a twice as large nozzle area and was derived from nozzle A with a  $15^\circ$  boattail angle by "cutting off" an appropriate length and fairing the exhaust inner contour with a straight cone into the jet pipe. This resulted in a nozzle convergence half-angle of  $4^\circ$  vs.  $7^\circ$  for nozzle A. Nozzle B can therefore be considered as the opened, reheat, position of nozzle A in case the nozzle is supposed to be a convergent conical iris nozzle. The dimensionless contours of the nozzles of References 5 and 7 are only slightly different from nozzle A and will be considered to be the same.

The model assembly of Reference 2 simulated the engine nacelle of the HFB 320-CJ610 jet engine, incorporating a hot primary jet and a cold secondary jet. The tests with this nozzle however have been focussed more on external effects, impeding comparison of the internal characteristics of this nozzle with the others.

The boattail and nozzle external contours will not be discussed here, as these will be related to the internal phenomena mainly through the external nozzle lip pressure  $p_{ex}$ . This pressure will be taken into account when the effect of ambient airflow is discussed.

### 2.2 Jet Parameters

In Table II a survey is given of the relevant jet parameters and dimensions of the models that were used.

The data which could be used in the present analysis on internal phenomena were scarce, because most results dealt with external nozzle phenomena such as afterbody pressure distribution and afterbody drag. From the supplied data results could be deduced concerning the following jet flow parameters: nozzle pressure ratio, total pressure distortion, jet medium, Reynolds number and axial static pressure distribution.

Main emphasis in the data analysis will be on NPR and total pressure distortion, both closely connected to the flow delivered from the engine. The use of the different jet simulation media as listed in Table II gives an indication how internal nozzle characteristics are affected if the engine combustion gases are simulated with an other gas, for example by cold air as is often done in wind tunnel tests. Other jet parameters such as turbulence, swirl and temperature distortion may also be of relevance for assessing the performance of nozzles, but have not been considered in the program. Nozzle leakage and lip edge curvature will also affect nozzle performance (Reference 8 and 9 respectively) but are not considered either. The data that were available and could be used for a comparison of the nozzle characteristics and jet pipe total pressure determination are surveyed in Table III. More details of the experimental facilities, models and instrumentation used by the different research groups, can be found elsewhere in this AGARDograph.

## 3. DETERMINATION OF THE JET TOTAL PRESSURE

For the determination of the nozzle characteristics knowledge of the jet total pressure is essential. It had been proposed by the AGARD study group that in this test program if possible the jet total pressure should be derived from the measured mass flow, static pressure and gas temperature in the jet pipe. In a jet flow with a total pressure profile distortion however, the determination of a valid mean jet total pressure from these parameters poses some special problems.

The average  $p_t$  that must be determined should be a characteristic property of the jet flow, i.e. it must be independent of the axial location where the measurements are made. It must not change its value, except due to viscous losses, if the cross sectional area of the jet pipe is changed.

The area averaged jet total pressure will not satisfy this requirement. During expansion the cross section area of a stream tube with a higher total pressure will decrease less than that of a stream tube with a lower total pressure. This means that the area averaged total pressure of a distorted flow will increase in a contraction. However per stream tube the mass flow and the total pressure remain the same in a contraction. Hence the total pressure mass

averaged over all stream tubes will remain constant and might therefore be a proper means of averaging, at least superior to area averaging.

In Part I of this AGARDograph a method is described (Ref.3) to derive the mass flow averaged total pressure for distorted velocity profiles, if the mass flow distribution, the mass flow, the static pressure and the temperature in the jet pipe are known. The description method defines the mass flow averaged jet total pressure as:

$$p_{tj} = \sum_{i=1}^n p_{ti} \left( \frac{\Delta \dot{m}}{\dot{m}} \right)_i \quad (1)$$

where

$$p_{ti} = p_{jp} \left\{ \frac{1}{2} + \frac{1}{2} \sqrt{1 + \left( \frac{\Delta \dot{m}}{\dot{m}} \right)_i^2 \frac{\dot{m}^2 R T_{tj} 2(\gamma-1)}{\left( \frac{A_{jp}}{n} \right)^2 p_{jp} \gamma}} \right\}^{(\gamma)/(\gamma-1)} \quad (2)$$

Knowledge of the mass flow distribution  $\left( \frac{\Delta \dot{m}}{\dot{m}} \right)_i$  can be obtained by measuring the total pressures with a rake during a run (Refs 1, 5) or by preliminary tests (Refs 3, 4, 6). In Figure 2 the mass flow distributions in the jet pipe are given as derived from the different sources. It was found that these distributions for each test set-up and model were fairly constant. An example of accompanying total pressure profiles is given in Figure 3.

If the total pressures are calculated according to the mass averaging procedure, for distorted flows it is found that these values are different from the values obtained from a one-dimensional isentropic calculation that assumed the profile to be flat. This is illustrated for the simplified example as shown in Figure 4. If in case I (flat)  $\Delta \dot{m}_1 = \Delta \dot{m}_2$ , and in case II (distortion)  $\Delta \dot{m}_1 = .5 \Delta \dot{m}_2$  ( $\Delta \dot{m}_1 + \Delta \dot{m}_2 = \text{constant}$ ), then Equations (1) and (2) yield  $p_{tj} = 2.06 \times 10^5 \text{ N/m}^2$  (case I) and  $p_{tj} = 2.08 \times 10^5 \text{ N/m}^2$  (case II). Hence a correction of 1% would be necessary on a 1-D isentropically derived  $p_{tj}$  to obtain the mass flow averaged  $p_{tj}$ , if distortion is present. It can also be seen that any distortion will lead to an increase in the ratio of total to static pressure in the jet pipe.

The parameter to describe the distortion in the jet pipe mass flow distribution used here is the DCM, the distortion coefficient, mass flow averaged. Based on the presence of the factor  $\left( \frac{\Delta \dot{m}}{\dot{m}} \right)_i^2$  in Equation (2), it is defined as

$$\text{DCM} = n \sum_{i=1}^n \left( \frac{\Delta \dot{m}}{\dot{m}} \right)_i^2 - 1 \quad (3)$$

or more general

$$\text{DCM} = \frac{A}{\dot{m}^2} \int \rho^2 U^2 dA - 1. \quad (4)$$

For low subsonic Mach numbers in the jet pipe flow it can be shown that a relation exists between DCM and the correction that is necessary to obtain the mass averaged  $p_{tj}$  from  $p_{tjr}$ :

$$p_{tj} = p_{tjr} \left( 1 + \text{DCM} \frac{kB}{1+B} \right) \quad (5)$$

where

$$k = \frac{n^2 \sum_{i=1}^n \left( \frac{\Delta \dot{m}}{\dot{m}} \right)_i^3 - 1}{n \sum_{i=1}^n \left( \frac{\Delta \dot{m}}{\dot{m}} \right)_i^2 - 1} \quad \text{and} \quad B = \frac{\dot{m}^2 R T_{tj}}{2 p_{jp}^2 A_{jp}^2}$$

It can be deduced that the factor  $k$  has a value of 3 if the surplusses and deficits of the mass flow distribution balance as compared to the average value. If the mass flow distribution profile is very peaky, for instance if in

Figure 4  $\frac{A_1}{A_2} = .5$  and  $\frac{\Delta \dot{m}_1}{\Delta \dot{m}_2} = 1.5$ , the factor  $k$  is somewhat different from 3, in this case  $k = 3.4$ . The factor  $B$  primarily depends on the effective contraction ratio  $A_{jp}/A^*$ .

Figure 5 illustrates the described relation between  $p_{tj}$ ,  $p_{tjr}$  and DCM. Data of 5 AFDC (air) and 5 NLR (decomposed  $\text{H}_2\text{O}_2$ ) test runs with nozzle A were used to determine the ratio  $\frac{p_{tj}}{p_{tjr}}$  for the distortion profiles of

Figure 2. It is found that the data points are close to the lines representing Equation (5) with  $k = 3$  and B derived from the test data. The sonic throat area  $A^*$ , which is used in the parameter  $\frac{A_{jp}}{A^*}$ , is related to  $p_{tjr}$ .

Only the NLR distortion profile shows some discrepancy, with respect to  $k = 3$ . Here  $k$  is approximately 3.3 due to the peaky mass flow distribution profile.

For nozzle B with a contraction ratio  $A_{jp}/A_n = 1.62$  the ratio  $\frac{p_{tj}}{p_{tjr}}$  is much larger. For a choked nozzle,  $\frac{p_{tj}}{p_{tjr}} = 1.141$  for a DCM = .338. Equation (5) with  $k = 3$  would yield a less precise correction due to the higher jet pipe Mach number (for the given example  $\frac{p_{tj}}{p_{tjr}} = 1.116$ , see insert of Figure 5).

It may be noted that for low subsonic Mach numbers in the jet pipe the distortion coefficient DCM is related to the mixing parameters  $\beta$  in Reference 10, i.e.  $\beta = \text{DCM} + 1$ .

In the following sections the jet total pressures  $p_{tj}$  are expressed as the mass flow averaged values, using either the calculation method of Reference 3 or Figure 5.

#### 4. NOZZLE DISCHARGE COEFFICIENTS

##### 4.1 General Remarks on Data Presentation

The definition of the nozzle discharge coefficient used here is  $\frac{\dot{m}}{\dot{m}_{id}}$ , not  $\frac{A^*}{A_n}$  as is sometimes preferred. For supercritical nozzle pressure ratios these definitions would give the same results, for subcritical NPR's the results diverge.

As discussed in Section 3, it is necessary to take into account the jet pipe flow distortion in the calculation of  $p_{tj}$  and hence of the discharge coefficients. Reference 5 gives a series of discharge coefficients which were derived from  $\dot{m}_{meas}$ ,  $p_{jp}$  and  $T_j$  according to the proposal of the AGARD study group. In order to compare these data with the results of other groups, they were recalculated taking into account the appropriate mass flow distribution of Figure 2. This resulted in approximately 1.3% increase of the jet total pressure. This is in agreement with Figure 5, for DCM = .19.

The jet pipe total pressure profile of Reference 6 was almost flat (DCM  $\approx$  .01) and a correction of less than .1% would be required, according to Figure 5.

The modification in the results due to the new definitions of  $C_d$  and  $p_{tj}$  are illustrated in Figure 6. This figure shows the results of a recalculation of  $C_d$  vs. NPR for a given set of data points of Reference 5.

Figure 7 shows the nozzle discharge coefficients from References 3, 5 and 6 for nozzle A, while Figure 8 shows  $C_d$  vs. NPR for nozzle B from Reference 3. The shift in the results for "distortion" in Figure 8 for  $1.6 < \text{NPR} < 2.2$  requires some reservedness towards the absolute values of these data.

##### 4.2 Choked Nozzle Pressure Ratio

For two-dimensional nozzles Reference 11 gives a method to derive the choked nozzle pressure ratios. For a nozzle with a convergence half angle  $\alpha$  this yields

$\alpha = 7^\circ$	$\gamma = 1.4$ (air)	choked NPR = 2.42
	$\gamma = 1.3$ ( $\text{H}_2\text{O}_2$ decomposed)	choked NPR = 2.31
$\alpha = 4^\circ$	$\gamma = 1.3$ ( $\text{H}_2\text{O}_2$ decomposed)	choked NPR = 2.13

Axisymmetric nozzles show a slightly larger choked NPR than two-dimensional nozzles with the same convergence angles. Hence for nozzles A and B the choked NPR were expected to be slightly larger than the values mentioned above. The test results do not disagree with these theoretical results, slightly lower values may be possible too.

The values of the discharge coefficients for increasing NPR very gradually approach the choked  $C_d$  value. Hence for the determination of the choked  $C_d$  no large inaccuracy will be introduced if data are included for NPR's slightly lower than the choked value. For nozzle A the data with  $\text{NPR} > 2.2$  were used, for nozzle B the data with  $\text{NPR} > 2.1$ .

For both nozzles it could not be determined with certainty whether distortion in the jet pipe flow affected the nozzle choking pressure ratio.

### 4.3 Choked Discharge Coefficient, No Distortion

Although some convex distorted pressure profile is present in the jet pipe flow of Reference 5 (Fig.3), these results are included in this group of data. For nozzle A the following choked nozzle discharge coefficients were derived for  $NPR > 2.2$  (see Figure 7), the tolerances indicating the standard deviations,

ONERA	52 runs, air	$C_d = .9858 \pm \text{approx. } .0005$
NLR (no dist.)	21 runs, air	$C_d = .986 \pm .004$
NLR (no dist.)	36 runs, decomposed $H_2O_2$	$C_d = .988 \pm .004$
AEDC	29 runs, air	$C_d = .986 \pm .004$

For nozzle B, the choked discharge coefficient for  $NPR > 2.1$  was (Fig.8)

$$C_d = .978 \pm .002 .$$

A prediction derived from Reference 11 would yield for nozzle A,  $C_d = .987$  and for nozzle B,  $C_d$  slightly below .99. For nozzle A this value agrees well with the results, though the discharge coefficient of nozzle B averages one per cent lower. This may be caused by the slight amount of distortion that still exists in the jet pipe flow even in the "no distortion" condition (Fig.3) and by the influence of the step in the wall of the duct on the internal boundary layer. Due to this step the boundary layer will thicken appreciably due to the local high Mach number and besides the boundary layer will diminish only slightly in the small contraction to the nozzle exit.

The data of ONERA show a substantial greater accuracy than the other data. This is the result of the great care that was taken in the mass flow measurement, by means of a plenum chamber and a sonic throat, and measuring pressure levels and temperatures very accurately by special techniques. In the other tests sharp edge orifice and venturi flowmeter are used. However the ONERA measurements were taken at  $M_\infty = 0$  only. The NLR results for tunnel off and on combined, gave greater scatter ( $\pm .004$ ) than for tunnel off ( $\pm .002$ ).

The jet medium ( $H_2O_2$  decomposition products or air) does not appear to significantly affect the discharge coefficient of nozzle A. The same is found for the influence of changing nozzle Reynolds number. This is in agreement with Reference 12, where data are presented for  $C_d$  vs. throat Reynolds number which ranged from  $.5 \times 10^6$  to  $7.3 \times 10^6$ .

### 4.4 Effects of Distortion on Choked Discharge Coefficient

For nozzle A the choked nozzle discharge coefficient in the case of distortion (Fig.7) is:

$$NLR \text{ (dist.) } 36 \text{ runs, decomposed } H_2O_2 \quad C_d = .986 \pm .005 .$$

The effect of distortion is insignificant for this nozzle, for all runs with  $NPR > 2.2$  (Ref.3)

$$C_d \text{ (dist.)} - C_d \text{ (no dist.)} = - .002 \pm .004 .$$

This result is not surprising if it is remembered from Figure 3 that with distortion the total pressure profile is still rather uniform both in the tail pipe and in the exit plane. For nozzle B distortion in the jet pipe flow had more effect

$$\begin{aligned} NLR \text{ (dist.) } 12 \text{ runs} \quad C_d &= .946 \pm .010 \\ \text{and} \\ C_d \text{ (dist.)} - C_d \text{ (no dist.)} &= -.032 \pm .008 \end{aligned}$$

This tendency must be caused by the increased curvature of the sonic line at the nozzle exit due to the "hollow" velocity profile.

From the fact that for nozzle A the marked hollow distortion profile hardly changed the discharge coefficient, it can be concluded that the less distorted convex velocity profile of the jet pipe flow of Reference 5, would hardly alter the  $C_d$  value. However if in the tests of Reference 5 the nozzle had a lower contraction ratio, such as nozzle B, the convex velocity profile would have caused  $C_d$  to increase, because the sonic line would be straighter and would move towards the geometric exit plane. In Reference 9 analogous results for low contraction ratio nozzles are discussed, although in that paper the presented  $C_d$ 's for distorted flows (hollow and convex) were derived for area averaged total pressures. A correction for the mass averaged  $p_{t_j}$  would slightly decrease the presented discharge coefficients.

### 4.5 Effects on Discharge Coefficients for Unchoked Nozzles

Figures 6, 7 and 8 show the discharge coefficients of nozzles A and B also in the region of unchoked nozzle pressure ratios. The  $C_d$ 's increase with  $NPR$  until the choked condition is attained.

The curves for  $C_d$  vs. NPR are different if external flow is present. Figure 7 shows the results for nozzle A, where the influence of  $M_\infty$  is clear. For  $M_\infty = .6 - .9$  the external pressure at the nozzle lip  $p_{ex}$  is higher than the free stream static pressure  $p_\infty$ ,  $C_{p_{ex}} \approx +.15$ , while at  $M_\infty = .95$  this overpressure has almost disappeared.

Due to this overpressure the effective NPR,  $\frac{p_t}{p_{ex}}$ , will be lower than the normally used NPR,  $\frac{p_t}{p_\infty}$ , and also  $C_d$  will be different. Figure 9 incorporates the correction for the boattail overpressure  $p_{ex}$  for nozzle A. It may be seen that this correction alone is insufficient to explain the differences in  $C_d$  for  $M_\infty \neq 0$  and  $M_\infty = 0$ , though the gross effect of external flow is explained. The final vena contracta of the jet flow is also affected by the momentum of the external flow. The scatter in the data does not allow to distinguish the differences at various Mach numbers.

For nozzle B the effect of distortion can be established for unchoked NPR. In case of a hollow profile in the jet pipe, it is indicated that the discharge coefficient decreases more rapidly with decreasing NPR than for a less distorted profile (Fig.8). For a convex profile a different tendency may occur.

## 5. NOZZLE THRUST COEFFICIENTS

Information concerning the thrust characteristics was available from two sources, ONERA (which used a special thrust rig in the tunnel settling chamber) and NLR (where an internal thrust balance was mounted inside the model). In both cases the balances measure nozzle gross thrust minus afterbody drag. The used thrust coefficients were defined differently. A comparison of the definitions gives

$$CT_0 (\text{ONERA}) = CT_2 + \frac{\text{pressure drag}}{F_{id2}} (\text{NLR}) .$$

Figure 10 shows the average lines for the thrust coefficients  $CT_1$  and  $CT_2$  for nozzle A at  $M_\infty = 0$  from Reference 3. It would have been expected from the studies of Reference 11 that for  $\text{NPR} \approx 1.9$  the thrust coefficient would have been approximately  $CT_1 \approx 1.005$  (for this NPR the coefficient from Reference 11,  $\eta_{abs} \equiv CT_1$ ). Even after very extensive calibration the about 1.5% higher values of  $CT_1$  and consequently of  $CT_2$  could not be explained.

The results for  $M_\infty \neq 0$  show a large scatter for the data of Reference 3, which was attributed to the inaccuracies introduced by the pressure force correction, particularly in the gap pressure force correction at the split line. These data however show the same trend as for  $M_\infty = 0$ . In Figure 11 the results of ONERA and the data for  $M_\infty \neq 0$  (for test Section 2, see Reference 3) of NLR are presented. The NLR data were recalculated to include the boattail drag component for direct comparison. In the ONERA tests the afterbody pressure drag could be affected by boundary layer blowing. Both conditions, "blowing" and "without blowing" are included in the figure.

Both at the lowest Mach numbers and at the higher NPR's, when the pressure drag is much less than the thrust force, the NLR data are 1 to 2% in excess of the ONERA data. This conforms with the unexplained high value of  $CT_2$  at  $M_\infty = 0$  for the NLR data. At lower NPR and at high Mach numbers the thrust force is relatively less important and differences in afterbody drag are more pronounced.

For nozzle B similar trends for the thrust coefficients as for nozzle A are found (Ref.3). Figure 12 shows that the influence of distortion is especially marked in the thrust coefficient  $CT_1$  (-3 to -5%), due to the influence of the change in  $C_d$ . The thrust coefficient  $CT_2$  had the least tendency to change due to distortion (0 to -1%), while  $CT_3$  increased significantly (about + 2%) when the jet total pressure profile was distorted.

## 6. JET PIPE INTERNAL STATIC PRESSURES

### 6.1 General

Some interesting features of the nozzle characteristics are reflected in the static pressures in the jet pipe. In Section 3 the influence of the jet pipe velocity profile distortion on the jet total pressure was discussed, with the related effect on the ratio of static pressure to jet total pressure. In this section some attention is given both to the static pressure distribution in down-stream direction along the jet pipe wall and to the internal static wall pressure close to the nozzle lip.

### 6.2 Wall Static Pressure Distribution in the Jet Pipe

Figure 13 shows the static pressure distribution along the jet pipe wall for nozzle A at a nozzle pressure ratio of about 3, for 6 series of data from various groups.



For this nozzle at choked NPR the ratio  $\frac{A_{jp}}{A^*} = 3.3$  and consequently  $\frac{p_{jp}}{p_{tj}} = .978$  or  $p_{tj} = p_{jp} (1.0225)$ . From Equation (2) in Section 3 for low subsonic velocities in the jet pipe the following approximation can be derived:

$$p_{tj} = p_{jp} (1 + B) . \quad (6)$$

With Equation (5) this expression yields

$$\frac{p_{jp}}{p_{tj}} = \frac{1}{1 + B(1 + k \text{ DCM})} \quad (7)$$

(for "balanced" total pressure distortion profiles  $k = 3$ , Section 3). The relation between DCM and  $\frac{p_{jp}}{p_{tj}}$  in the cylindrical part of the jet pipe, with  $B = .0225$  and  $k = 3$ , is included in Figure 13. It is shown that for flows which exhibit a rather undistorted velocity profile indeed  $\text{DCM} < .1$ , with exception of the data of ONERA which would be expected to show less distortion. The data of Rolls Royce, as included in Figure 13, are related to the  $1 - D$  calculated  $p_{tj}$ . Hence in the cylindrical part  $\frac{p_{jp}}{p_{tj}} \left( \text{here} = \frac{p_{jp}}{p_{tj}} \right) = .978$  is expected.

Because stream tubes with a higher total pressure contract less during expansion than with a lower total pressure, in the case of distortion the DCM will tend to decrease in a convergent channel. The effects of a decreasing DCM and a decreasing cross sectional area act in opposite direction on the average static pressure in a cross section. For "distortion" in nozzle A this is seen to result in an approximately constant static pressure between  $\frac{x}{D_{\max}} = .6$  and .85.

In the downstream part of the nozzle the difference between the static wall pressures for flows with and without distortion disappears. For nozzle B this difference remains up to the nozzle exit (Fig.14). The exit total pressures as presented in Figure 5 of Reference 3, are in agreement with these observations. Nozzle A shows hardly any distortion in the exit plane while for nozzle B the profile still is clearly concave.

In the cylindrical part of the jet pipe of nozzle B the static pressure tends to increase slightly towards the exit (Fig.14), which indicates that the "hollow" distortion decreases downstream due to mixing and wall friction. This increase is also observed in the mixing tubes of constant area ejectors.

In the wall static pressure distributions of both nozzle A and B some exceptional pressures are found near the deflection points of the wall. For some series of data the static pressures are high, while for other tests the static pressures are low at seemingly the same location. As the deflection points cause local flow acceleration as well as stagnation, the pressures are very sensitive to the exact location of the orifices and to the condition of the jet pipe wall boundary layer (separation). It may be noted that the pressures at  $\frac{x}{D_{\max}} = 1.025$  and at .505 show relatively low values for all NLR test series with respect to the other data.

### 6.3 Wall Static Pressures Close to the Exit Plane

Although the difference in the wall static pressures in the jet pipe flows with and without distortion may have disappeared for nozzle A in the downstream direction, an influence of the external flow is found in the level of the wall static pressure  $p_l$  close to the nozzle exit plane for unchoked conditions, Figure 15. A correction can be made by replacing  $p_{\infty}$  by the external boattail overpressure at the nozzle exit plane  $p_{ex}$  for the cases  $M_{\infty} \neq 0$ . This effective nozzle pressure ratio  $p_l/p_{ex}$  better correlates the data points for the ratio  $\frac{p_l}{p_{tj}}$ . This finding is in agreement with the similar corrections for the discharge coefficient (Fig.9).

As was shown in Figure 14 for nozzle B the wall static pressure  $p_l$  at the nozzle lip still is influenced by the initial degree of distortion in the jet pipe flow. Figure 16 shows this more clearly for a range of NPR. Ideally such data could yield the experimental choking NPR, even with distortion. Unfortunately Figure 16 shows that due to the scatter in the data the choked nozzle pressure ratio cannot be determined with greater confidence than from the data for the discharge coefficients, Figure 8.

## 7. CONCLUSIONS

- The jet pipe total pressure profiles in most test series of the participating groups showed some distortion. The jet total pressure, which is the prime jet parameter, was derived from a mass averaging procedure.



This enabled comparison of the results of the various groups. The distortion coefficient DCM proved to be a useful tool to obtain mass flow averaged total pressures from one-dimensionally isentropically derived total pressures.

- The choked discharge coefficients for the nozzle A (contraction ratio 3.24) were in agreement for all test series:  $C_d = .986$ . The jet medium, jet total pressure distortion or throat Reynolds number did not significantly affect the discharge coefficient. For nozzle B (contraction ratio 1.62) the influence of distortion was more marked, choked  $C_d$  (no distortion) = .978  
 $C_d$  (distortion) = .946.

The effects of external airstream on the nozzle discharge coefficients resulted in lower values for  $C_d$  in the case of unchoked NPR's. The accuracy of the data, derived from test series incorporating a special test set-up for mass flow measurement by means of a plenum chamber, a sonic throat and highly accurate pressure and temperature instrumentation, was appreciably greater than from other test series where a sharp edge orifice and a venturi flow meter were used.

- The thrust coefficients were compared for two sets of data. One set showed at  $M_\infty = 0$  values 1 to 2% larger than expected. This same difference existed for higher NPR's between the two sets of data for  $M_\infty = 0$ , when the boattail pressure drag was included in the comparison of thrust minus drag forces. The thrust coefficient, based on measured jet total pressure and actual mass flow, showed relatively little effect from distortion.
- In the jet pipe wall static pressure distribution the effect of distortion in the jet pipe total pressure profile could clearly be seen for all nozzles. The differences in wall static pressures between "distortion" and "no distortion" disappeared downstream for nozzles with a high contraction ratio. The difference was found to be present up to the wall static pressure close to the nozzle exit plane for low contraction ratio nozzles.
- It was found that including the jet pipe total pressure distortion profiles in the calculation of the jet total pressure and derived coefficients was the key to obtaining comparable results for the various test series. Neglecting distortion would have caused large discrepancies in the obtained values of nozzle coefficients.

## 8. REFERENCES

1. Emunds, H.  
Riedel, H. *Improved Nozzle Testing Techniques at Transonic Speeds.* Contribution of the Institut für Angewandte Gasdynamik of the DFVLR, Porz-Wahn. This AGARDograph, part 1.
2. Dissen, H.  
Zacharias, A. *An Experimental Study of the Influence of the Jet Parameters on the Afterbody Drag of a Jet Engine Nacelle Model.* This AGARDograph, part 1.
3. Rozendal, D.  
Groothoff, C.C.  
Derksen, W.B.G. *Improved Nozzle Testing Techniques in Transonic Flow.* Results of NLR contribution to AGARD ad hoc study. This AGARDograph, part 1.
4. Deer, D.J. *Results of Tests on Single Afterbody Nozzles Defined by AGARD,* Rolls Royce PPE 67, March 1974.
5. - *Data package of AFDC, Results with 15° Boattail Model,* July 1974.
6. - *Data package of ONERA, Results of Tests with 15° Boattail Model,* February 1974.
7. - *Data package of ONERA, Results of Tests with 15° Boattail Model,* additional data, June 1974.
8. Carriere, P. *Problème d'Adaptation de Tuyères,* AGARD CP 34, pt.2, September 1968.
9. Wehofer, S.  
Matz, R.J. *Turbine Engine Exhaust Nozzle Performance,* AIAA Paper No.73-1302, November 1973.
10. Bevilaqua, P.M. *Evaluation of Hypermixing for Thrust Augmenting Ejectors,* J.Aircraft, Vol.11, No 6, June 1974.
11. Hardy, J.M.  
Dutouquet, L. *Etude de l'écoulement dans un éjecteur transonique.* L'Aeronautique et l'Astronautique, No.47, 1974.
12. - *United States data for Improved Nozzle Testing Techniques in Transonic Flow,* AGARD ad hoc study, 3 May, 1974.

TABLE I

**Jet Pipe, Internal Nozzle Shapes and Specified Location  
of Instrumentation**

Nozzle A						Nozzle B	
References 1, 3, 4		Reference 7		Reference 5		Reference 3	
$x/D_{\max}$	$r/D_{\max}$	$x/D_{\max}$	$r/D_{\max}$	$x/D_{\max}$	$r/D_{\max}$	$x/D_{\max}$	$r/D_{\max}$
1.513	.366	1.513	.362	1.513	.366	1.513	.366
1.124	.366	1.045	.362	1.126	.366	1.124	.366
1.014	.343	1.014	.343	1.016	.343	1.014	.343
.516	.314	.516	.314	.517	.314	.516	.314
						.212	.287
.179	.226	.176	.226	.179	.227		
0	.2035	0	.202		.202		
contraction ratio							
		3.24		3.22		3.28	
convergence half angle		7°		7.6°		8.1°	
						1.62	
						4°	

**Specified Location of Static Pressure Orifices**

$\frac{x}{D_{\max}}$	Angle Orientation			
	45°	135°	225°	315°
.435	x		x	
.505	x		x	
.545	x		x	
.635	x		x	
.745	x		x	
.845	x		x	
1.025	x		x	
1.265	x		x	
1.385	x		x	
1.515	x	x	x	x
1.705	x		x	

Total pressure rake at  $\frac{x}{D_{\max}} = 1.515$

Thermocouples at  $\frac{x}{D_{\max}} = 1.315$

**TABLE II**  
**Survey of Parameters**

<i>Reference</i>	<i>1</i>	<i>2</i>	<i>3</i>	<i>4</i>	<i>5, 12</i>	<i>6, 7</i>
nozzle	A	Special	A + B	A	A	A
$D_{\max}$ , mm	67	100	80	101.6	250	80
jet medium:	air	air comb. gases	air $H_2O_2$	air	air	air
NPR	1 - 6.6	1 - 3	1 - 4.5	1.9 - 5	1 - 12	1 - 5
$\gamma$	1.40	1.40, -	1.40 + 1.30	1.40	1.40	1.40
R	287	287, -	287, 390	287	287	287
$T_{tj}$	285	290, 790	290, 630	--	310	--
$M_{\infty}$	0, .5 - .95	.2 - .6	0, .8 - .95	0, .75 - .95	0, .6 - .95	0, .6 - .95
DCM	.001	--	.02, .34	.08	.19	.01
$Re_{D_n}$ (max)	$2.8 \times 10^6$		$2.2 \times 10^6$	$1.7 \times 10^6$	$7.3 \times 10^6$	$2.0 \times 10^6$

**TABLE III**  
**Survey of Available Data for the Determination of Nozzle  
and Jet Pipe Characteristics**

<i>Reference</i>	<i>1</i>	<i>2</i>	<i>3</i>	<i>4</i>	<i>5</i>	<i>6, 7</i>
$p_{tjp}$ profile, radial	x	--	x	x	x	x
$C_d$ , $M_{\infty} = 0$	--	--	x	--	--	x
$M_{\infty} \neq 0$	--	--	x	--	x	--
CT, $M_{\infty} = 0$	--	--	x	--	--	--
$M_{\infty} \neq 0$	--	--	x	--	--	x
$p_{jp}$ distribution (axial)	x	--	x	x	--	x

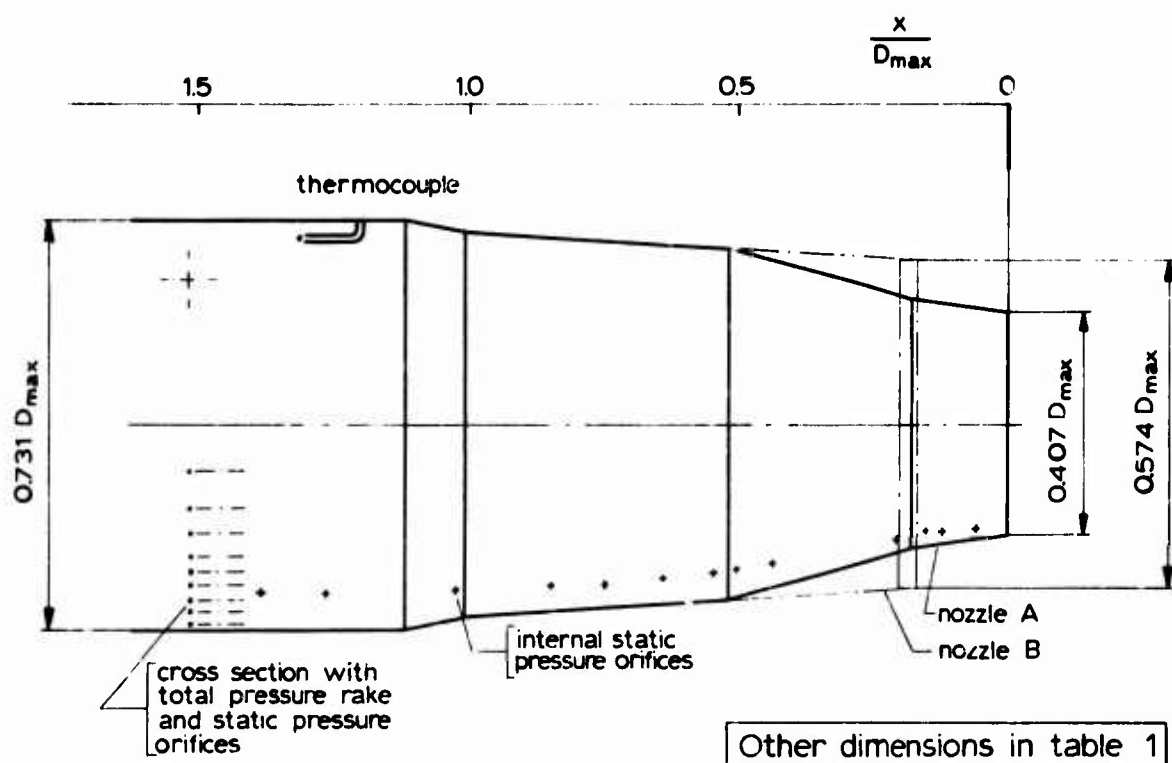


Fig.1 Jet pipe and nozzle contour and location of instrumentation

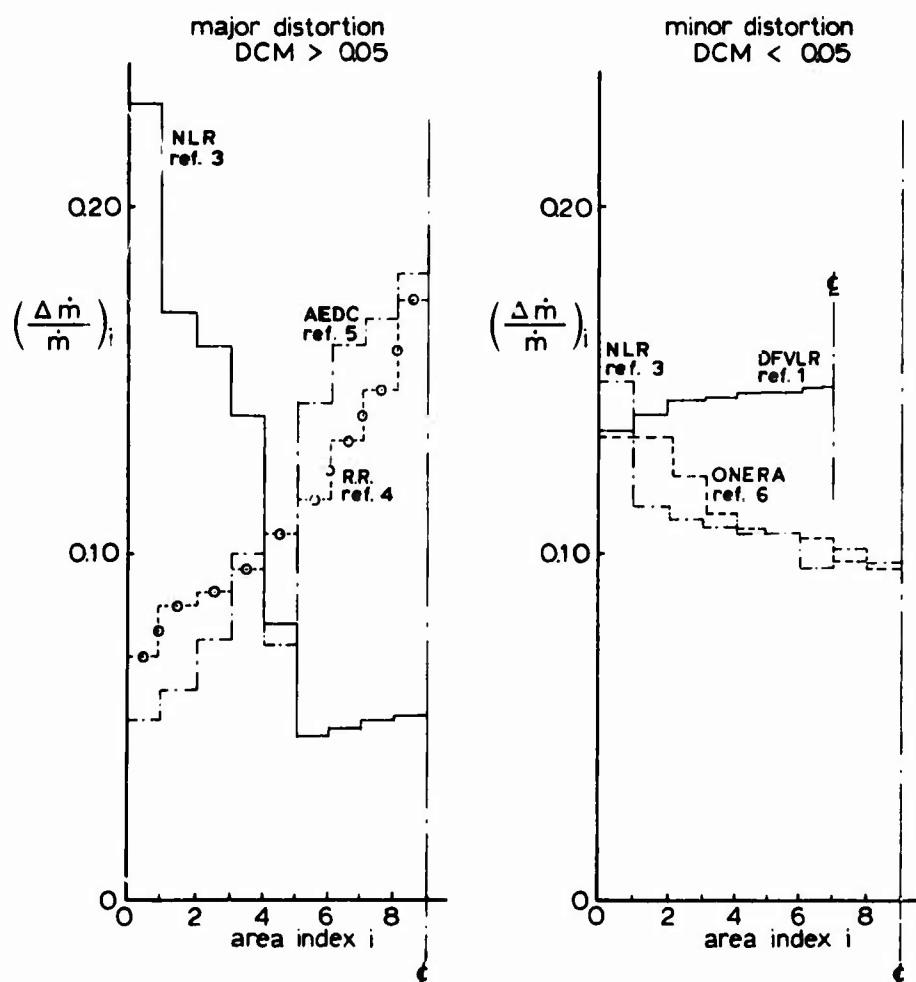


Fig.2 Standardized mass flow distribution in the jet pipe, nozzle A and nozzle B

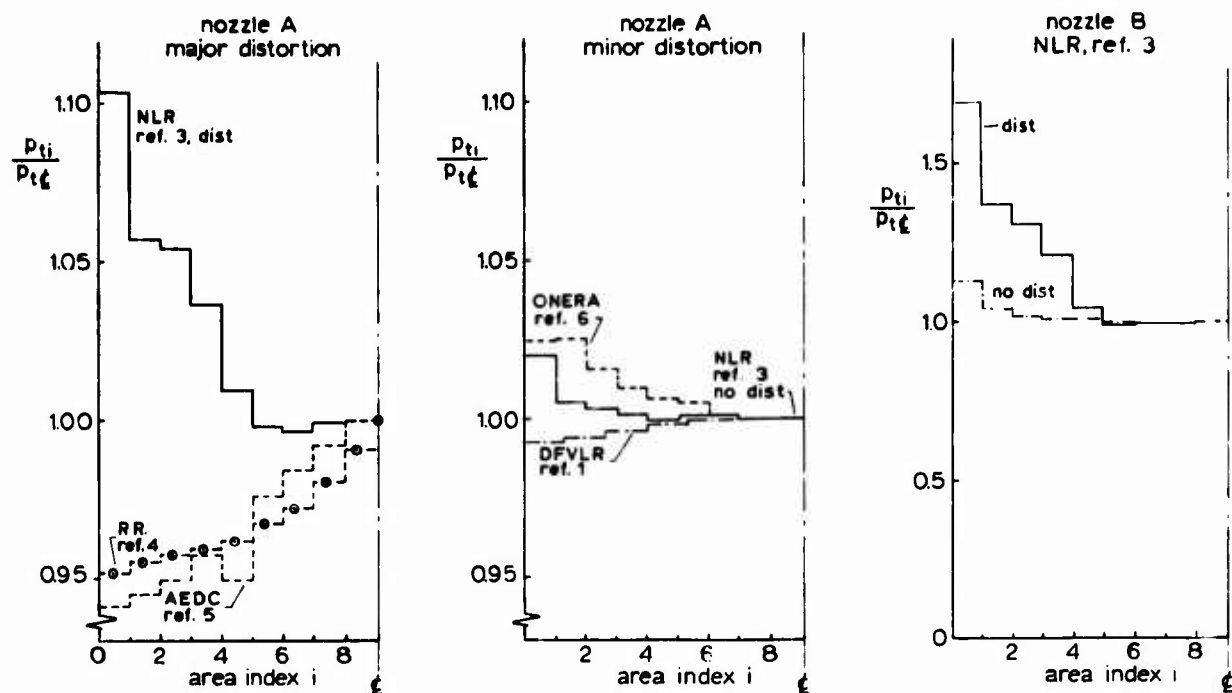


Fig.3 Jet pipe total pressure profiles in nozzle A and nozzle B

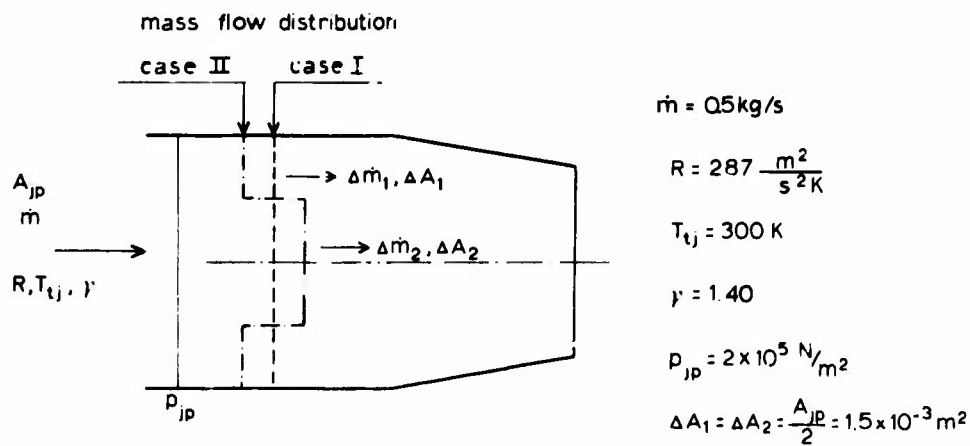


Fig.4 Flow in a jet pipe with and without distortion of the mass flow distribution

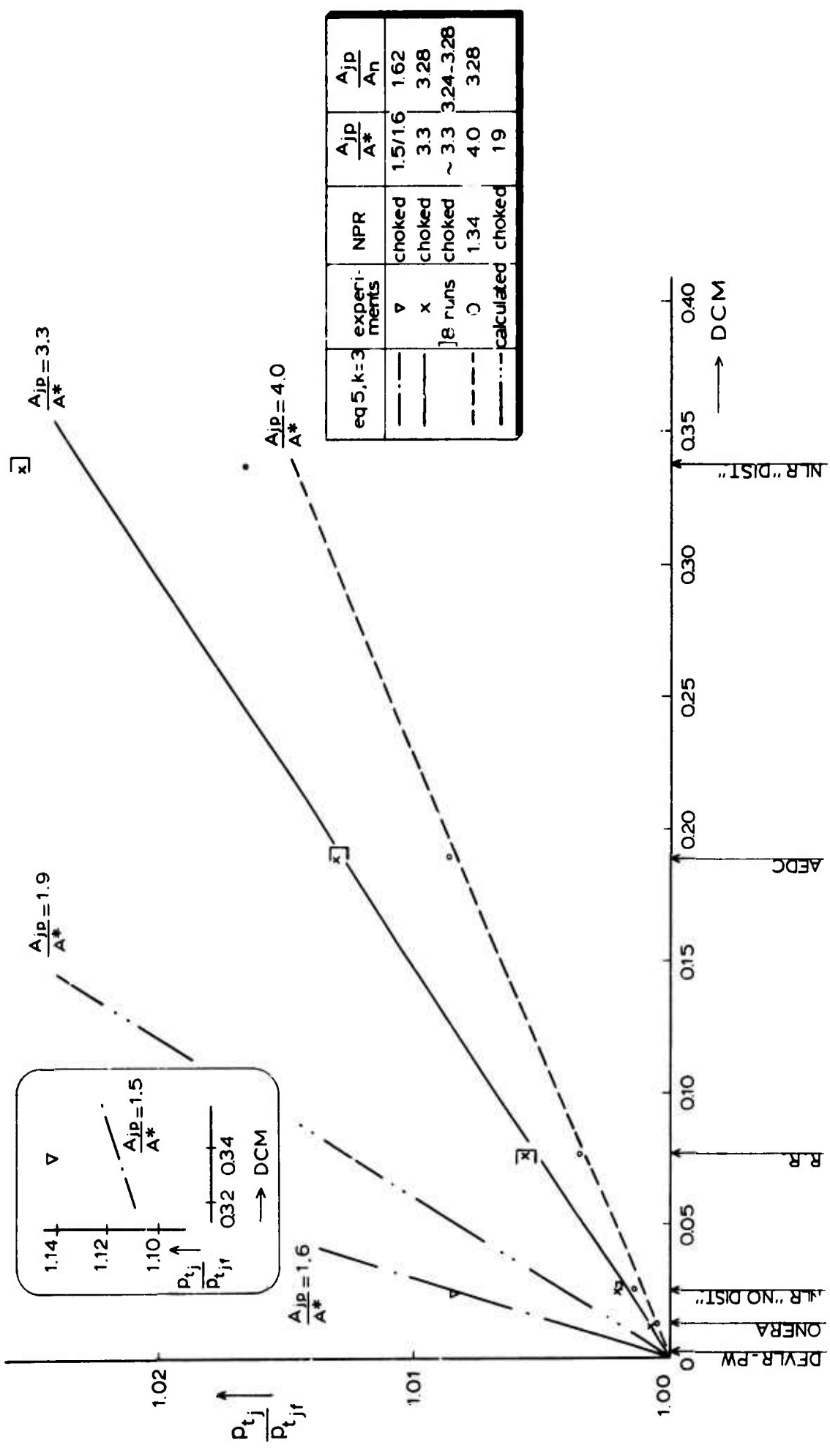


Fig.5 Modification of total pressure with distortion coefficient

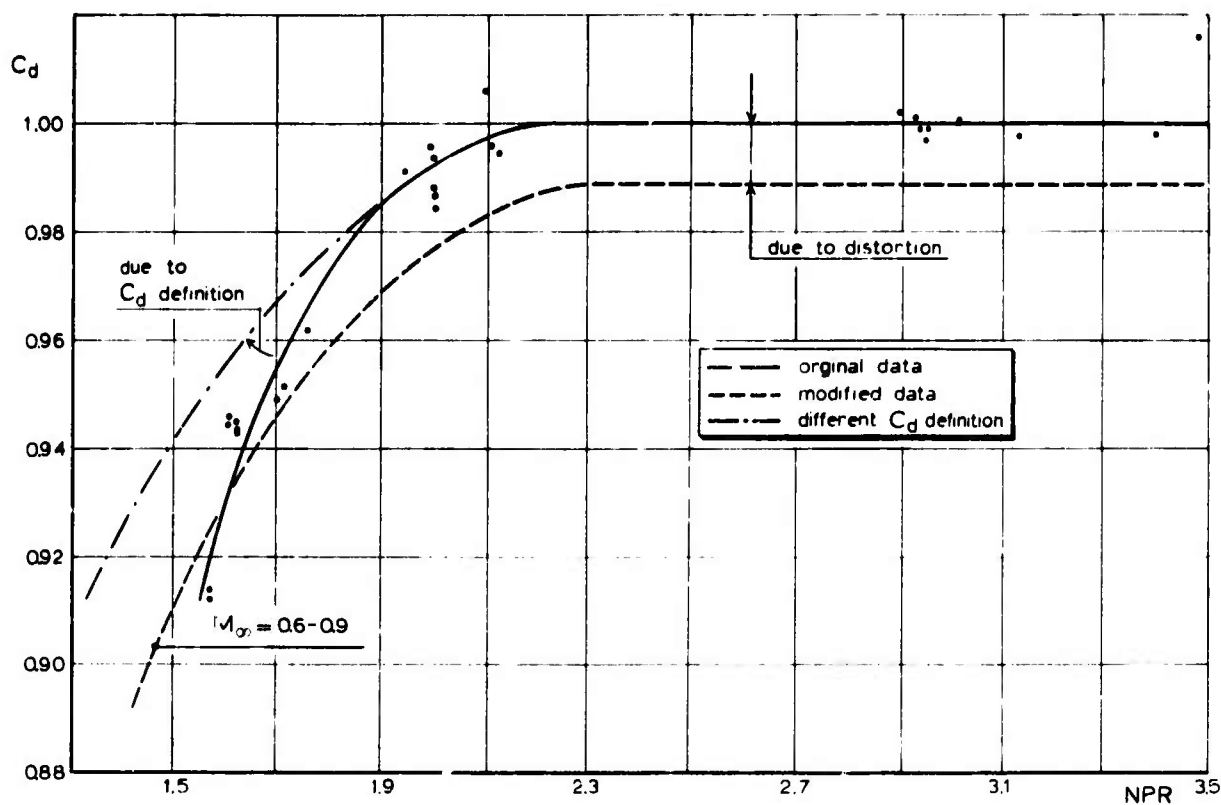
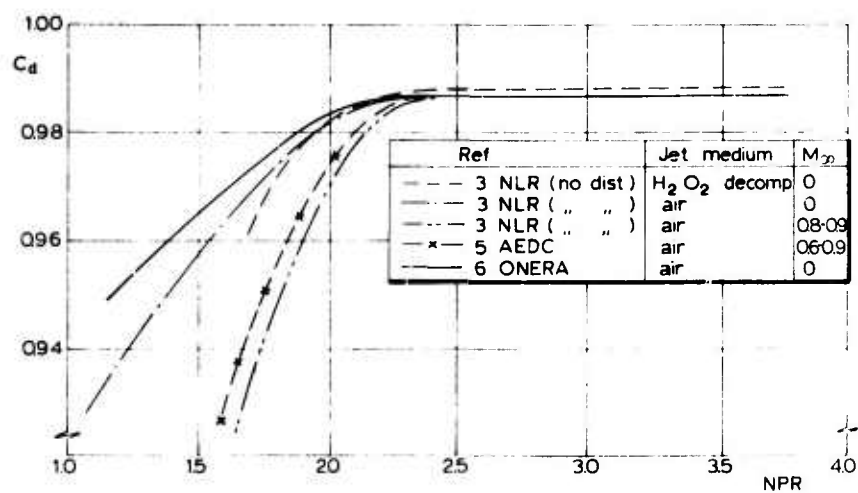
Fig.6 Modification of discharge coefficient due to distortion and definition of  $C_d$ 

Fig.7 Nozzle discharge coefficients for nozzle A

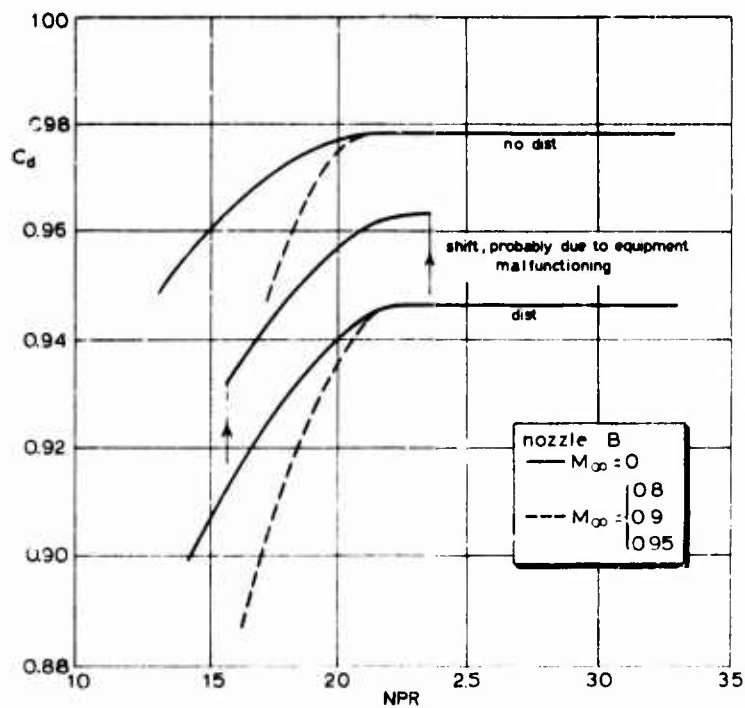
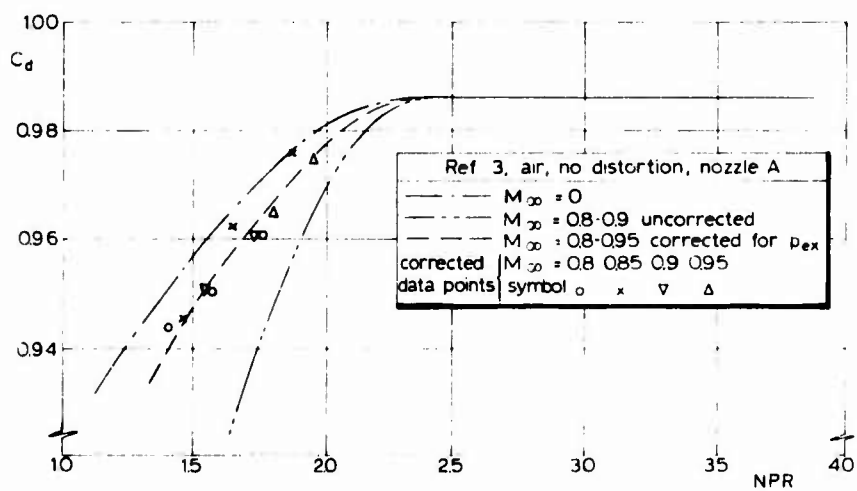


Fig.8 Discharge coefficients of nozzle B vs. NPR, NLR data

Fig.9 Effect of external flow on unchoked discharge coefficient.  
Correction due to external nozzle pressure



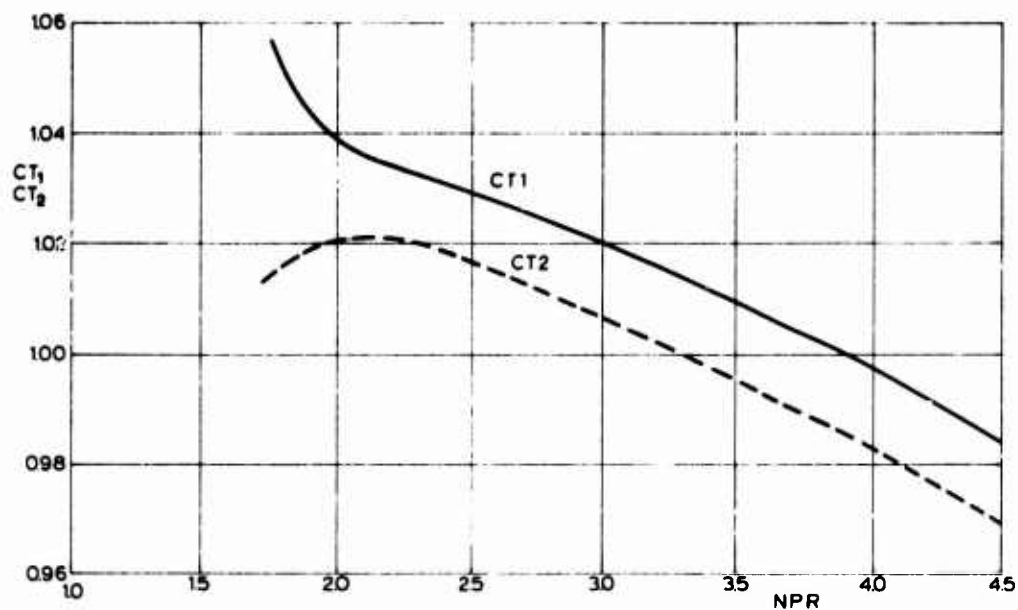


Fig.10 Thrust coefficients vs. NPR for nozzle A, hot jet, for  $M_{\infty} = 0$

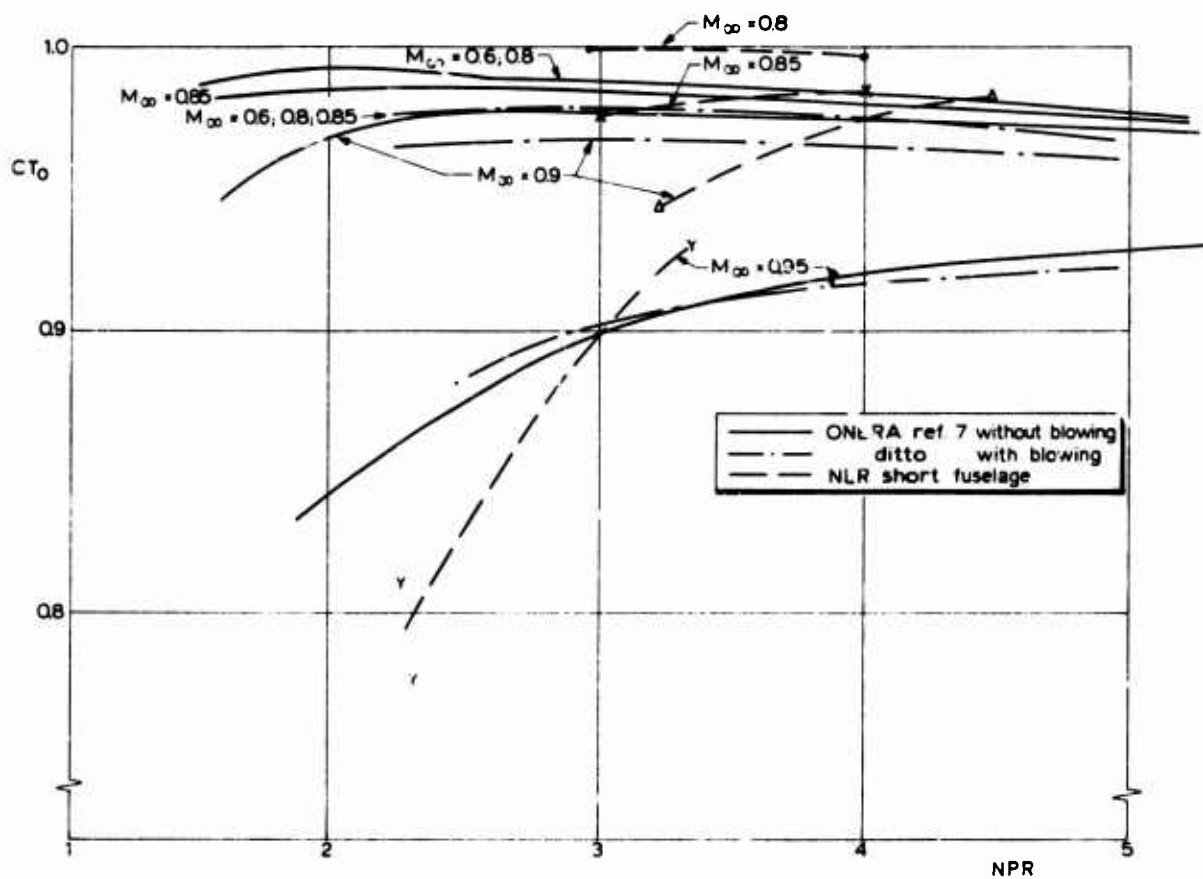


Fig.11 Thrust coefficients for  $M_{\infty} \neq 0$

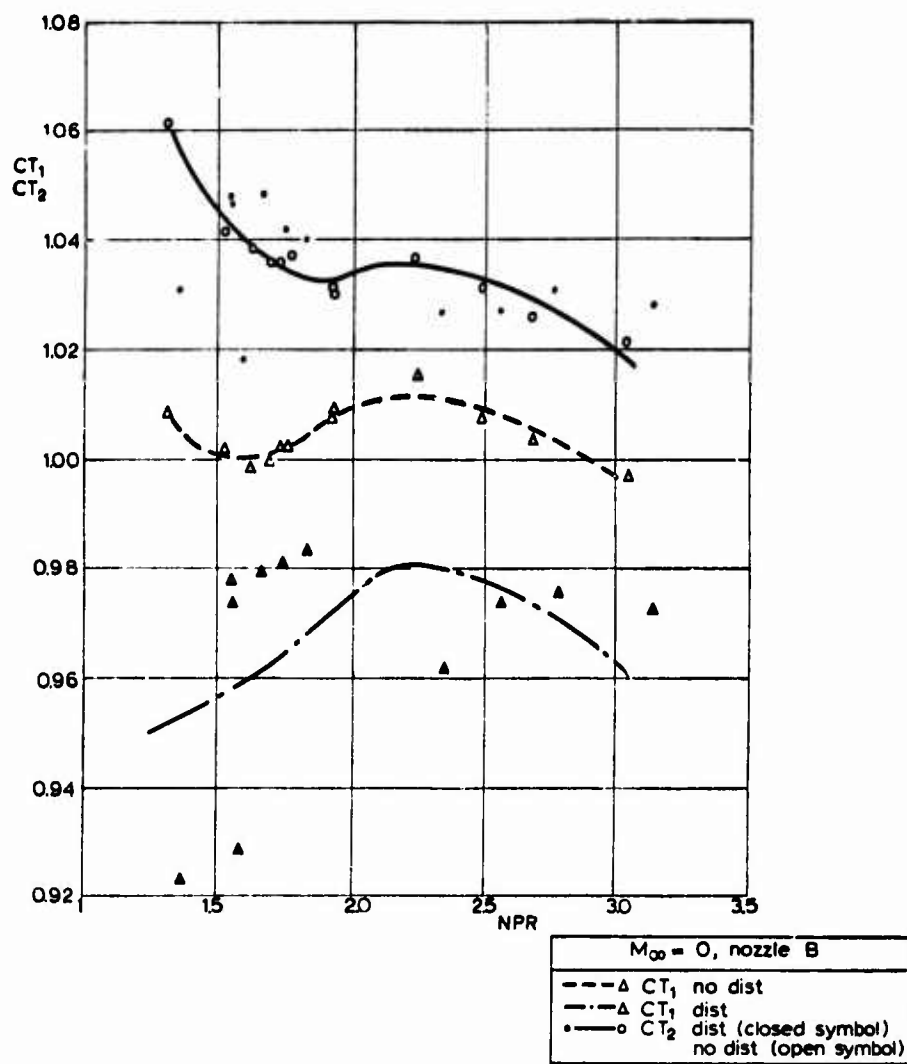


Fig.12 Thrust coefficients vs. NPR for nozzle B, hot jet

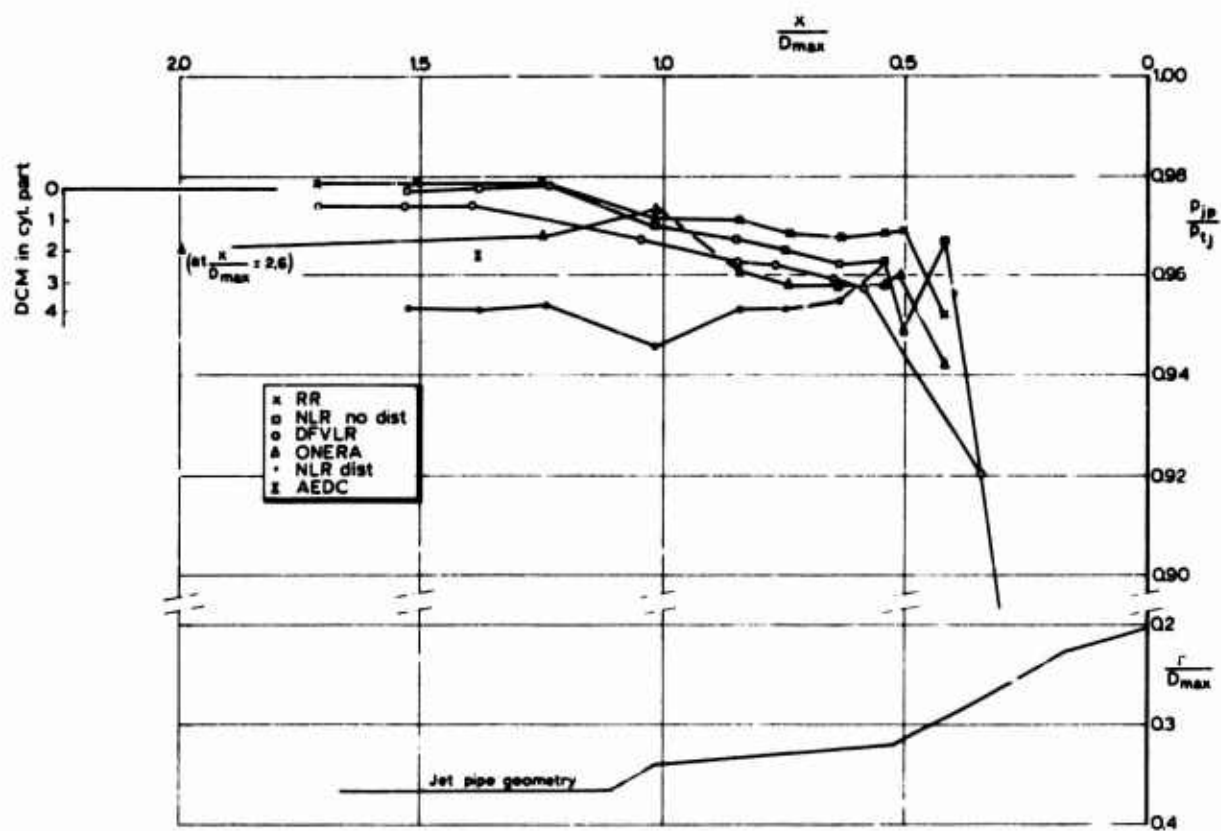


Fig.13 Static wall pressure distribution in the jet pipe of nozzle A for  $NPR \approx 3$

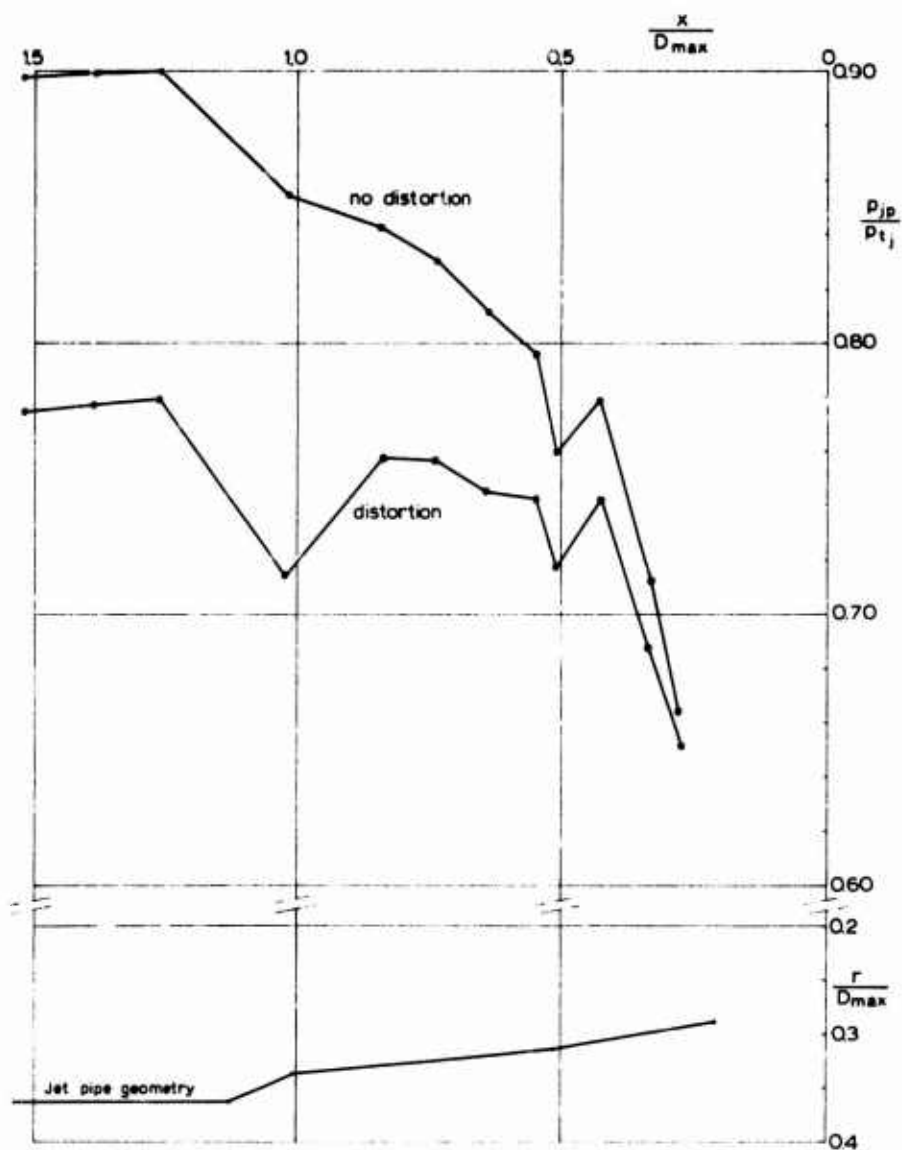


Fig.14 Static wall pressure distribution in the jet pipe of nozzle B for  $NPR \approx 3$  (Ref.3)

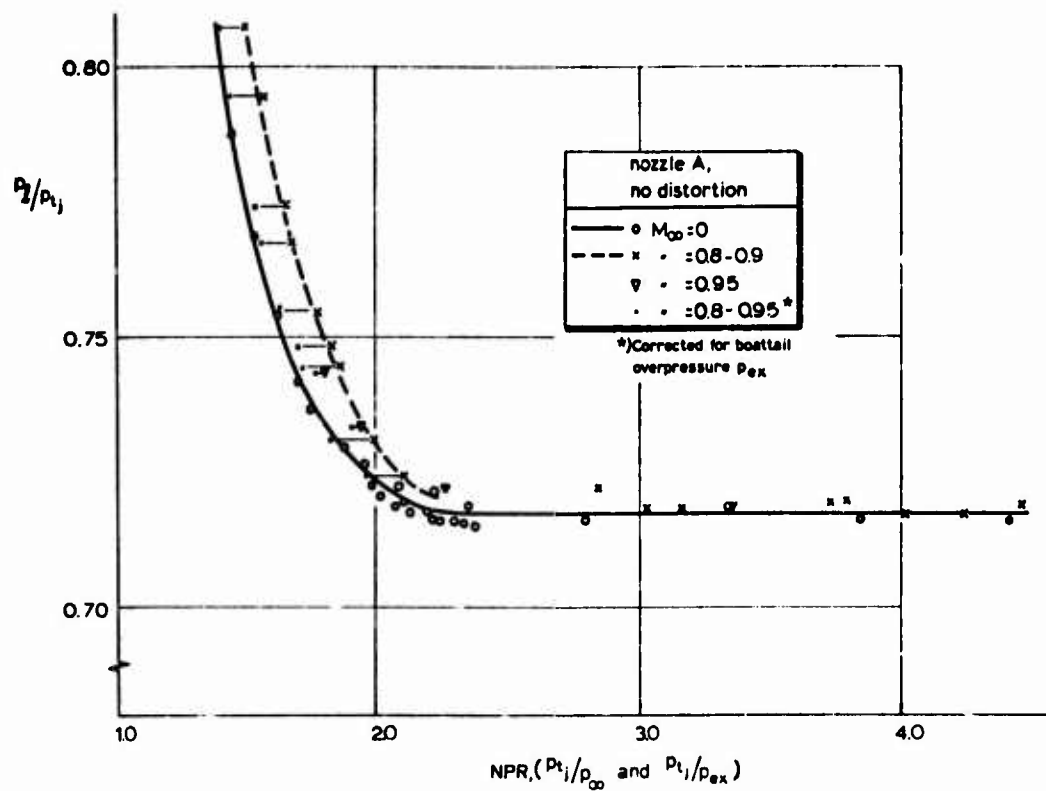


Fig.15 Static wall pressure in jet pipe near nozzle exit plane vs. pressure ratio for nozzle A (Ref.3)

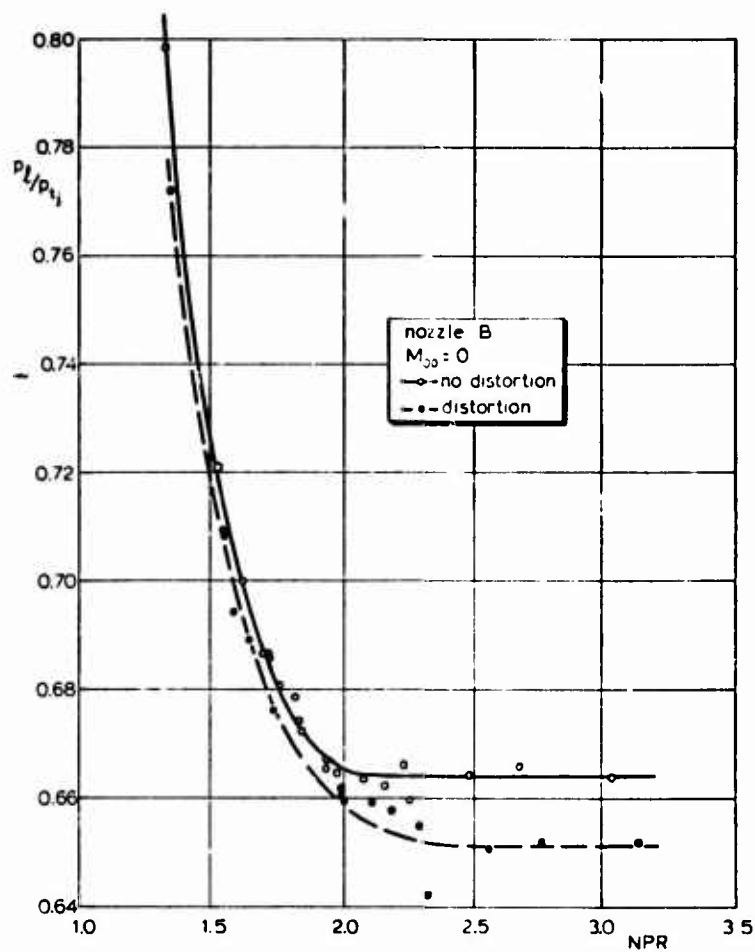


Fig.16 Ratio of static pressure near nozzle exit to jet total pressure vs. NPR for nozzle B (Ref.3)

**INFLUENCE OF JET PARAMETERS:  
BOATTAIL PRESSURE DISTRIBUTION AND PRESSURE DRAG**  
Evaluation of preliminary results contributed by the  
participants in the AGARD ad-hoc study

Edited by

H.Dissen, H.Emunds, H.Riedel and A.Zacharias  
DFVLR-Institut für Antriebssysteme, Braunschweig  
DFVLR-Institut für Angewandte Gasdynamik, Porz-Wahn

**SUMMARY**

Within the framework of the AGARD ad-hoc study: "Improved Nozzle Testing Techniques in Transonic Flow" preliminary results are presented of the influence of the jet parameters on the boattail pressure distribution and on the boattail pressure drag with reference to the AGARD models and a model of the HFB 320 engine nacelle. The jet parameters investigated were the jet temperature, the wake and jet mixing, the internal nozzle configuration, and the jet distortion. Concerning the influence of jet temperature two contrasting effects were observed. These differences may be due to different surface temperatures and base areas of the models tested. Further investigations as regards these temperature effects seem to be necessary. Very little information has become available on wake and jet mixing, so that in this area further research is also needed. No effect was observed for changes of the internal nozzle geometry and of the jet distortion.

**LIST OF SYMBOLS**

$A_{MAX}$	maximum cross-sectional area, $m^2$
$C_{DP} = D_p / (q_\infty \cdot A_{MAX})$	boattail pressure drag coefficient
$C_p = (p - p_\infty) / q_\infty$	boattail surface static pressure coefficient
$d$	nozzle exit diameter, $m$
$D_{MAX}$	maximum model diameter, $m$
$D_p$	boattail pressure drag, $N$
$L_{D_{MAX}}$	boattail length, $m$
$M_\infty$	free stream Mach number
$NPR = p_{tj} / p_\infty$	nozzle pressure ratio
$p$	pressure, $N/m^2$
$q_\infty = \frac{\gamma}{2} M_\infty^2 p_\infty$	free stream dynamic pressure, $N/m^2$
$Re_{D_{MAX}} = (\rho_\infty \cdot U_\infty \cdot D_{MAX}) / \mu_\infty$	free stream Reynolds number based on maximum model diameter
$t$	temperature, $^\circ C$
$T$	temperature, $K$
$U$	velocity in x-direction, $m/s$
$U_\infty$	free stream velocity, $m/s$
$X, Y$	Cartesian co-ordinates
$\rho_\infty$	free stream density, $kg/m^3$
$\mu_\infty$	free stream molecular viscosity, $kg/(ms)$

*Subscripts*

$\infty$	free stream
j	jet
t	total
W	wall

**1. INTRODUCTION**

The paper deals with the influence of the jet parameters on the boattail surface static pressure distribution and pressure drag in transonic flow with particular reference to the AGARD models and a model of the HFB 320 engine nacelle. The latter model was investigated in addition to the AGARD models in view of the intended full scale flight testing of this engine nacelle by the DFVLR. The jet parameters encompass

- (a) Jet temperature
- (b) Wake and jet mixing
- (c) Internal nozzle configuration
- (d) Jet distortion

The effects of the above parameters are discussed by mainly referring to the boattail surface static pressure distributions and in some cases to the boattail pressure drag coefficient. Since, because of the wall interference and installation effects, the flow parameters investigated cannot be considered in isolation of the testing facilities used, the main characteristics of the wind tunnel facilities, including data on the test set-up and blockage, are presented in Figure 1. A survey of the various models tested by Group members to date together with some fundamental geometric parameters is displayed in Figure 2. In this connection a comparison of the external and internal model contours of the AGARD models with HFB 320 engine nacelle model is shown in Figure 3. The flow parameters investigated by Groups members up to the time of writing are summarized in Figure 4. For the present paper the information and data have been obtained from References 1-4.

**2. EFFECT OF JET TEMPERATURE**

Data on the effect of the jet temperature are available from three sources. These are the NLR (NL), where the AGARD model with the 15° boattail angle was tested, the AEDC (USA) (AGARD model with 15° and 25° boattail angle), and the DFVLR (GER 2). In the case of the latter the model of the HFB 320 engine nacelle was tested, and the hot propulsive jet was produced by combustion of jet fuel JP 4 with compressed air in a combustion chamber outside the model. The jet temperature could be controlled by varying the fuel mass flow. At the NLR the hot jet was obtained by decompression of liquid hydrogen peroxide in a gas generator situated inside the model.

With reference to the results, Figure 5 shows the boundary layer velocity and total temperature profiles at the maximum diameter of the HFB 320 engine nacelle for cold and hot propulsive jets ( $T_{ij} = 290$  K and 790 K respectively) and for the free stream Mach number  $M_\infty = 0.45$ . From the above measurements it is evident that, as result of the heat conduction within the model for the hot jet condition, the surface temperature of the model exceeded the static temperature of the free stream, entailing a heat transfer from the model to the free stream. This gives rise to a more turbulent shape of the velocity profile, the influence being equivalent to the effect produced by boundary layer blowing. The DFVLR measurements cover free stream Mach numbers up to  $M_\infty = 0.6$ , while NLR results are only available for the condition of jet off. Thus, the velocity profiles obtained by the NLR, and which are displayed in Figure 6, can only give an insight into the effect of high subsonic free stream Mach numbers on the shape of the velocity profile. No boundary layer velocity and temperature profiles are available for the AEDC tests.

Surface temperature distributions for the model of the HFB 320 engine nacelle and  $M_\infty = 0.45$  are presented in Figure 7. For the hot jet the wavy trend of the curves is caused by the structural layout of the model of the engine nacelle, since at the attachment points of the model to the jet pipe the heat flux to the outer surface is intensified in comparison with the more insulated intermediate portions of the nacelle. The slight streamwise rise in the surface temperature is also a result of the heat conduction within the model, if the jet discharging from the nozzle is hot. In the case of the blown boundary layer a shift of the curves to a higher temperature level is observed because the air injected into the boundary layer was at a higher temperature (340 K) than the wind tunnel air (280 K). No surface temperature distributions are available from other sources.

Boattail static pressure distributions on the model of the HFB 320 engine nacelle for cold and hot propulsive jets and  $M_\infty = 0.45$  and 0.6 are plotted in Figures 8 and 9. It is evident that with the hot propulsive jet a general reduction of the boattail surface static pressure is associated. As already indicated, the heat transfer from

the HFB 320 engine model to the free stream leads to a shape of the boundary layer velocity profile comparable to that of a blown boundary layer. Consequently, in regions of surface curvature a larger centrifugal force is established in the shear flow layer, so that, as long as the surface curvature is convex outwards, the boattail surface static pressure coefficient is decreased. In the vicinity of the nozzle exit, where the flow curvature necessarily becomes concave outwards, a rise in the surface static pressure coefficient is to be expected. Such trend is, however, not observed. There may exist several reasons for this discrepancy. Firstly, in the rear portion of the boattail the velocity may have changed shape from that measured at the maximum diameter of the model of the HFB 320 engine nacelle. Secondly, the entrainment of fluid from the free stream by the propulsive jet may have increased in the hot jet case compared with the cold jet case. Both these factors could lead to a reduction of the static pressure coefficient in the rear portion of the boattail. On the other hand it is known that at a given nozzle pressure ratio a hot jet possesses a larger initial jet plume angle than a cold jet. The displacement effect of a hot jet would thus be more pronounced than for a cold jet and lead to a higher static pressure coefficient at the rear end of the boattail. However, within the framework of the present AGARD investigation the initial jet plume angle has not yet been measured by the DFVLR. Similarly, no results concerning the magnitude of the flow entrainment are available. Therefore, at this stage no conclusive evidence exists as regards the relative importance of any of the above factors. No doubt further research has to be undertaken in this field. Of interest in connection with the above are the NLR results of the effect of boattail surface temperature on the boattail pressure distribution of the AGARD model with  $15^\circ$  boattail angle. The results, shown in Figures 10 and 11 for the jet-off case, display a trend similar to that observed for the HFB 320 engine nacelle model of the DFVLR for the jet-on condition. A detailed discussion of these NLR results is included in the NLR contribution to the AGARDograph. In contrast the AEDC results for the AGARD model with  $15^\circ$  boattail angle, which are displayed in Figures 12 and 13, indicate that the surface static pressure coefficient grows with increasing jet temperature. No information is available on the surface temperature of the model of the AEDC tests. However, what is known is that there was a significant difference in the base area of the AE model used for the hot jet tests compared with that for the cold jet tests. This obviously creates problems in the interpretation of the results.

The boattail pressure drag coefficient for the model of the HFB 320 engine nacelle is shown in Figure 14 for the cases of a cold and a hot propulsive jet ( $T_{ij} = 290$  K and  $790$  K respectively) and the free stream Mach number range  $0.2 \leq M_\infty \leq 0.6$ . The corresponding results for the NLR-AGARD model with  $15^\circ$  boattail angle and  $T_{ij} = 287$  K and  $630$  K are plotted for  $0.8 \leq M_\infty \leq 0.969$  in the same figure.

The results reveal opposite trends for the  $C_D$  distribution for these two models. Here again too many parameters like free stream Mach number range, NPR, surface temperature, and model geometry are not comparable to allow a conclusion to be reached.

### 3. EFFECT OF WAKE AND JET MIXING

A propulsive jet discharging from a nozzle at the tail end of an afterbody has basically two effects on the surrounding flow field and therefore on the aircraft. Firstly, the jet acts like a solid body in eliminating the wake and displacing the external flow, and, secondly, it entrains fluid from the surrounding medium. The displacement effect, especially in the case of an underexpanded propulsive jet, causes a pressure rise at the tail end of the afterbody because of the associated concave curvature in the outward direction to the model axis. In contrast, the entrainment of the jet accelerates fluid particles of the external flow in the neighbourhood of the nozzle exit and, thus, leads to a static pressure reduction. Only limited data have become available on the wake and jet mixing. Therefore, this subject will be discussed by referring to the boattail static pressure distributions on the  $10^\circ$  boattail angle AGARD model tested by the DFVLR (GER 1) at  $M_\infty = 0.95$ , and which are displayed in Figure 15. On turning the jet flow on, the displacement effect overshadows the influence of the entrainment, since the pressure coefficient in the vicinity of the rear and of the afterbody is increased for  $NPR > 1$ . The NPR range 1.2-3.0 covers the regime of subsonic ( $M_j = 0.5$ ) to sonic nozzle flow and slight underexpansion ( $p_j/p_\infty = 1.5$ ). For this nozzle flow regime the changes in the entrainment and displacement effects are balanced in such a way that with increasing displacement effects ( $NPR > 1.89$ ) no significant variation in the pressure distribution occurs.

Evidence in support of this is found in Figure 16, showing the boattail static pressure distributions on the model of the HFB engine nacelle for a cold propulsive jet as  $M_\infty = 0.6$ . For  $NPR = 3$  the displacement begins to dominate as result of the establishment of a well defined jet plume, and the static pressure coefficient in the rear portion of the boattail is continuously increased as the NPR becomes larger. This is confirmed, for example, by the AEDC results displayed in Figure 17. The above holds true for attached flow and cases of slight or moderately strong separation. For strongly separated flow in the tail end portion of the boattail the opposite trend may occur. Details are discussed in Reference 4.

### 4. EFFECT OF INTERNAL NOZZLE CONFIGURATION

Concerning the effect of the internal nozzle configuration, data are only available for the HFB 320 engine nacelle model. The contours of two different nozzles tested are shown in Figure 3. It was found that the boattail static pressure distributions obtained with the AGARD and DFVLR nozzles did not differ significantly. The results displayed in Figure 18 are typical.



played in Figure 18 are typical. These represent data obtained by the DFVLR (GER 2) and correspond to  $NPR = 1.89$ ,  $M_\infty = 0.45$ , and a cold propulsive jet.

## 5. EFFECTS OF JET DISTORTION

The effect of jet distortion was investigated by the NLR and the DFVLR (GER 2). The method of producing the jet distortion adopted by the NLR was to make use of pneumatically operated device for disturbing the flow inside the jet pipe. The DFVLR investigation centred on the model of the HFB 320 engine nacelle. Jet distortion in this case was produced by coaxial secondary air injection round the circumference of the propulsive jet. The results of Figure 19, which show the boattail surface static pressure distribution on the NLR AGARD model with  $15^\circ$  boattail angle for a hot propulsive jet and  $M_\infty = 0.966$ , indicate that the distortion of the propulsive jet produces no significant effect on the static pressure distribution. This holds true for the  $NPR$  range  $2.0 \leq NPR \leq 4.0$  and  $0.8 \leq M_\infty \leq 0.966$ . Further details are contained in the NLR-contribution to the AGARDograph. DFVLR results for the model of the HFB 320 engine nacelle confirm the absence of any marked effect of the jet distortion on the boattail static pressure distribution.

## 6. REFERENCES

1. Dissen, H.  
Zacharias, A. *An experimental study of the influence of the jet parameters on the afterbody drag of a jet engine nacelle scale model.* DFVLR contribution to AGARD Ad-Hoc Study: *Improved Nozzle Testing Techniques in Transonic Flow.* DFVLR Braunschweig, Institut für Antriebssysteme, December 1974.
2. — *Improved Nozzle Testing Techniques in Transonic Flow.* Preliminary results of NLR contribution to AGARD ad-hoc study (AV-74-02) and subsequent results.
3. — *Status of U.S. Participation in AGARD Ad-Hoc Study: Improved Nozzle Testing Techniques in Transonic Flow.* Air Force Flight Dynamics Laboratory (AFFDL) Air Force Arnold Engr. Devel. Center (AEDC) NASA/Langley, March 1974 and November 1974.
4. Emunds, H.  
Riedel, H. *Improved Nozzle Testing Techniques in Transonic Flow.* Contribution of the Institut für Angewandte Gasdynamik of the DFVLR, Porz-Wahn, December 1974.

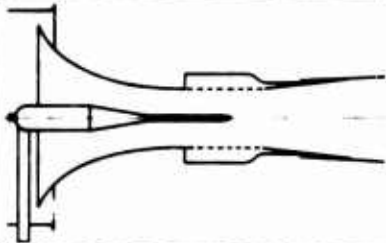
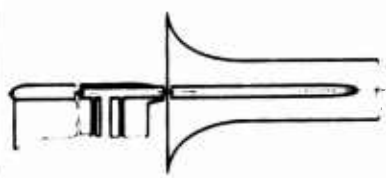
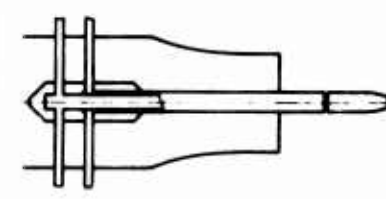
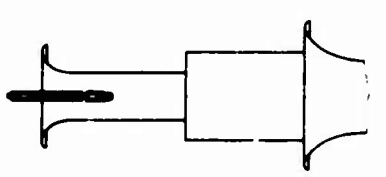
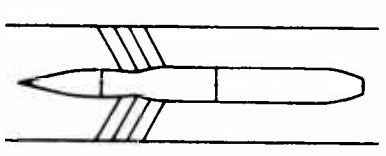
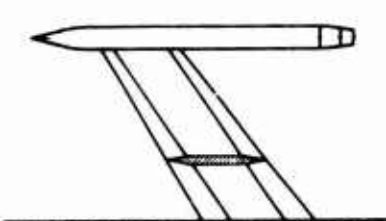
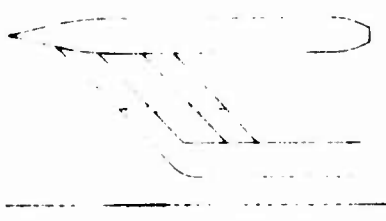
		test set-up	wind tunnel	$M_m$	blockage
F			800x900 mm <sup>2</sup> test section with perforated top and bottom walls	0,6 - 0,95	0,8%-1,8%
GB			534 mm (across flats) octagonal, slotted test section	0,75-0,92	4%
GER	1		340 mm dia open, ver- tical free jet test section	0,5 - 0,95	~ 0
	2		500 mm dia closed test section	0,2 - 0,6	4%
NL			270x270 mm <sup>2</sup> test section with slotted top and bottom walls	0,8-0,965	7%
USA	A E D C		4875 mm (16ft) per- forated test section	0,6 - 1,5	0,2%
	N A S A		4875 mm (16ft) test section	0,4 - 1,2	0,37%

Fig.1 Main characteristics of the wind tunnel facilities




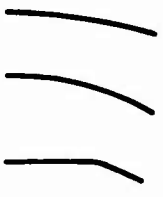




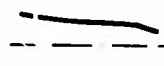



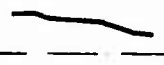


	model configuration		boattail angle 	D <sub>MAX</sub> mm	d/D <sub>MAX</sub>	L/D <sub>MAX</sub>
	boattail	Nozzle				
F			10° 15° 25°	80, 100, 120	0,407	1,050
GB			10° 15° 25°	101,6	0,407	1,775 1,150 0,725
GER1			10° 15° 25°	67	0,407	1,6578 1,0909 0,6268
GER2			8° 15° 25°	96,3	0,418	2,2
NL			10° 15° 25°	80		
USA AEDC			10° 15° 25°	250		1,674
USA NASA			10° 15° 25°	152		

Fig.2 Main characteristics of the models

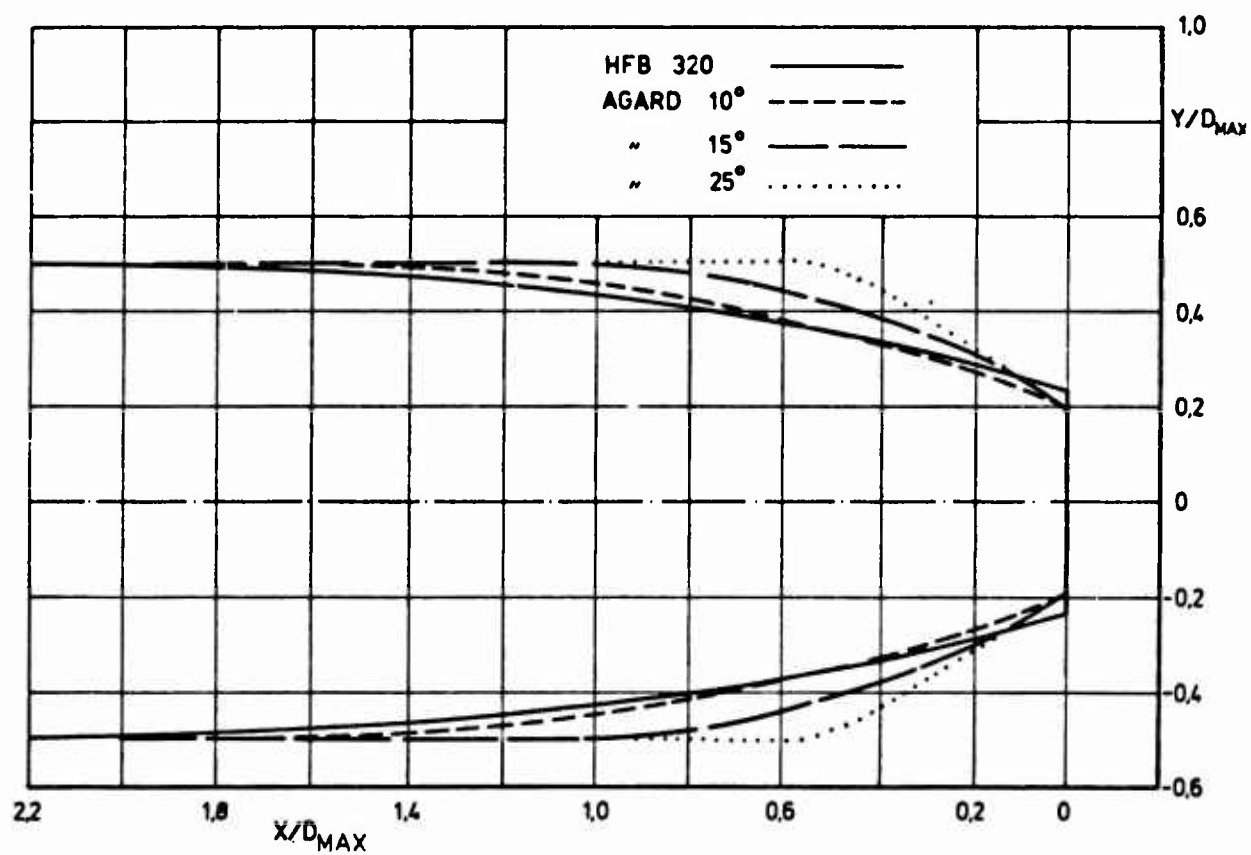
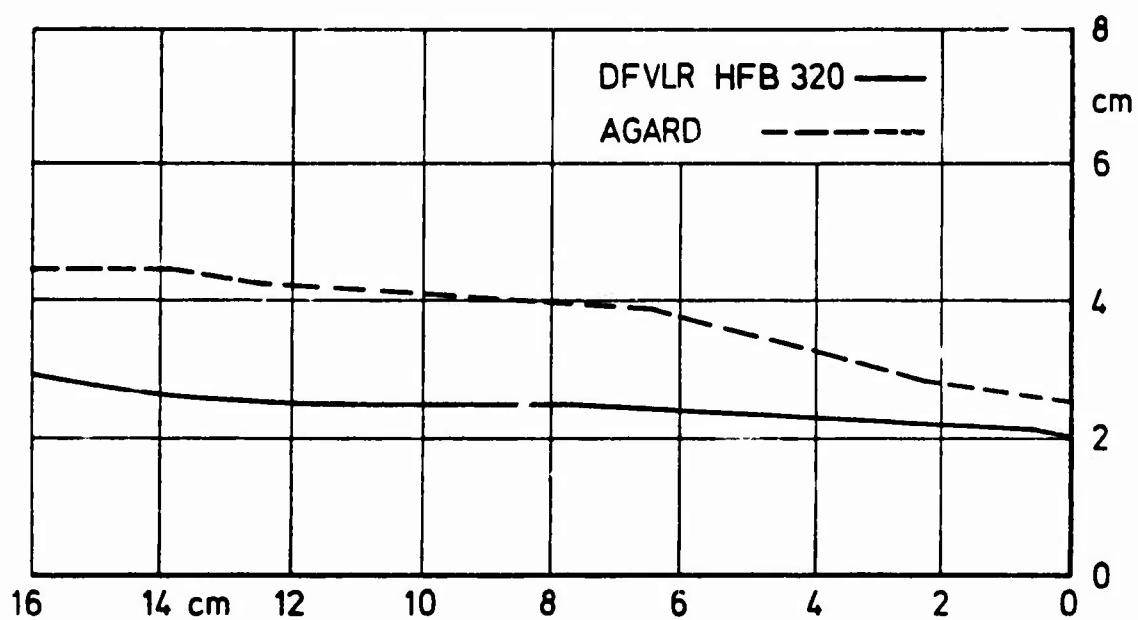


Fig.3 Comparison of the internal and external model contours of the AGARD models with the HFB 320 engine nacelle model

	F	GB	GER1	GER 2	NL	USA AEDC	USA NASA
NPR	1.0 ..... 5.15	1.86 ..... 4.7	1.0 ..... 6.63	1.0 ..... 3.0	1.0 ..... 4.5	1.0 ..... 12	1.0 ..... 10
$T_{tj}$				290 - 790 K	(290)-630 K	320 - 1500K	
Boundary Layer	●	●		●	●	●	
Re-Number *						●	
Distortion				●	●		

\*at constant Ma - Number

Fig.4 Survey of the flow parameters investigated

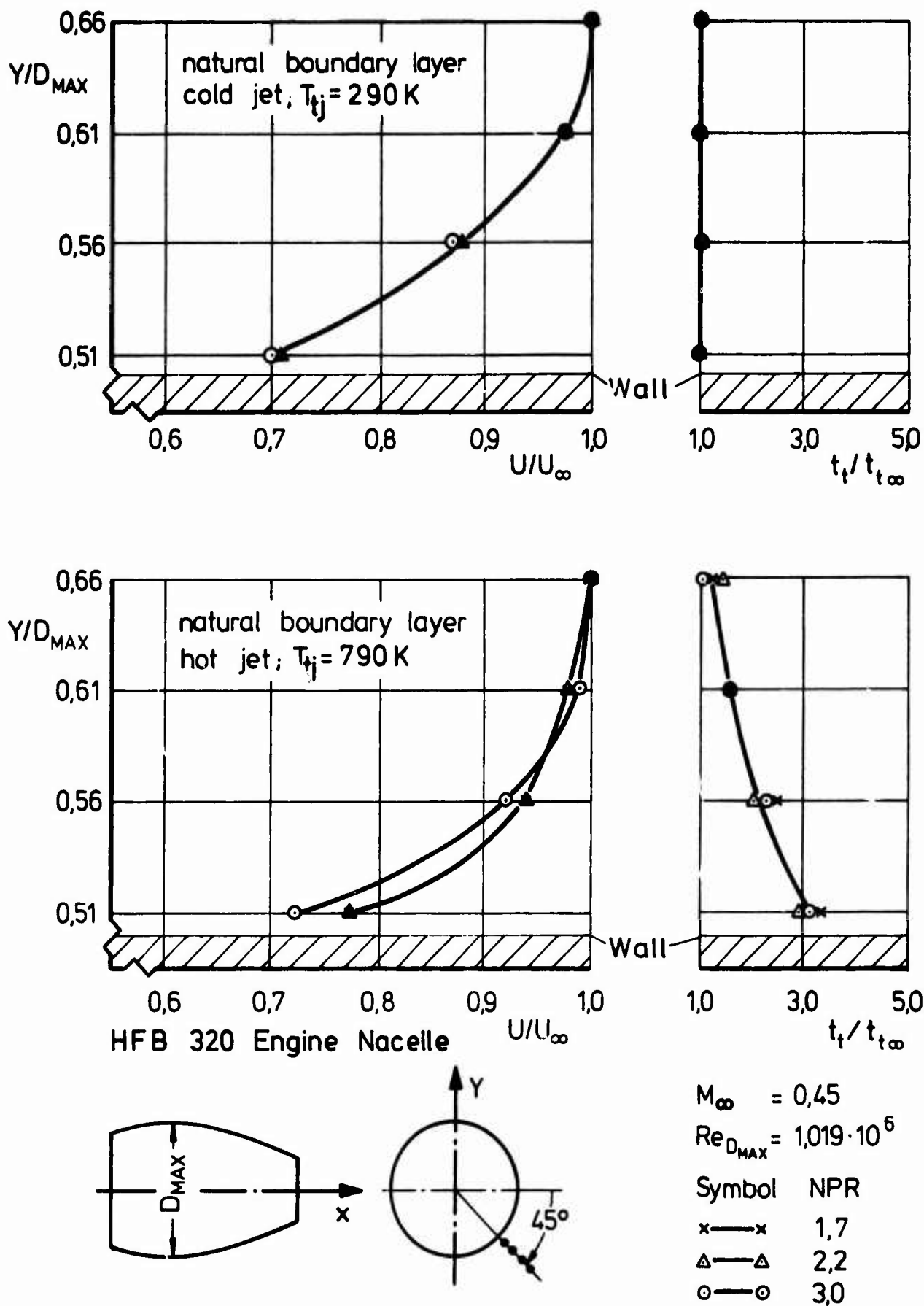


Fig.5 Boundary layer velocity and total temperature profiles at the maximum diameter of HFB 320 engine nacelle model for cold and hot propulsive jets ( $M_\infty = 0.45$ )

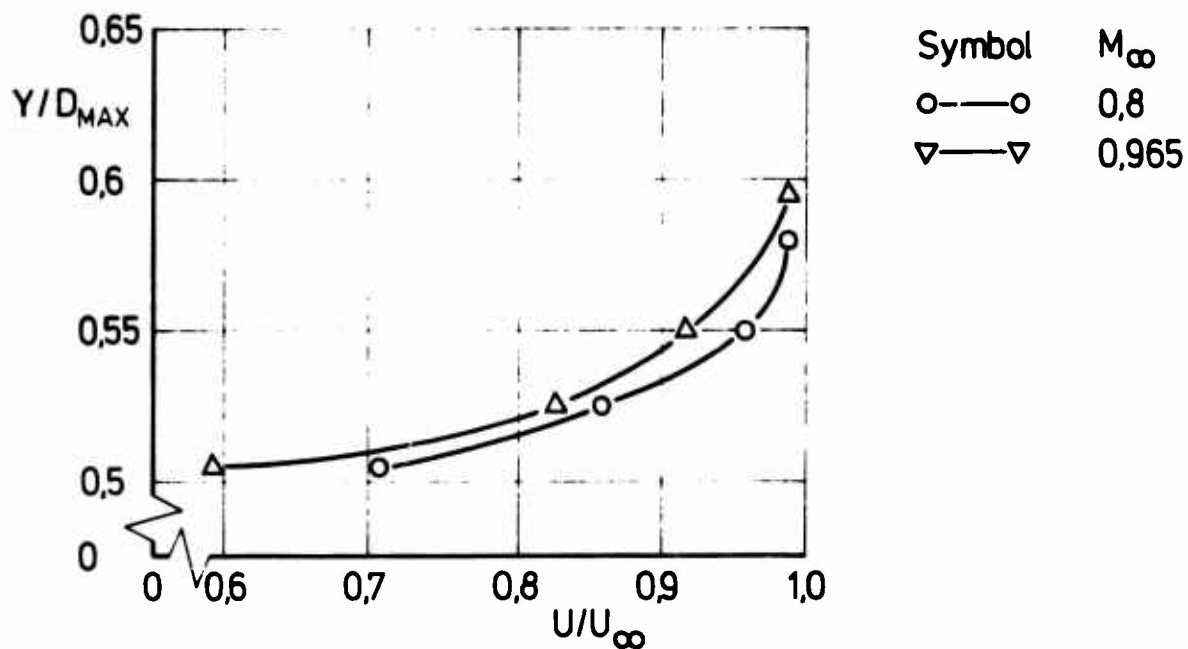
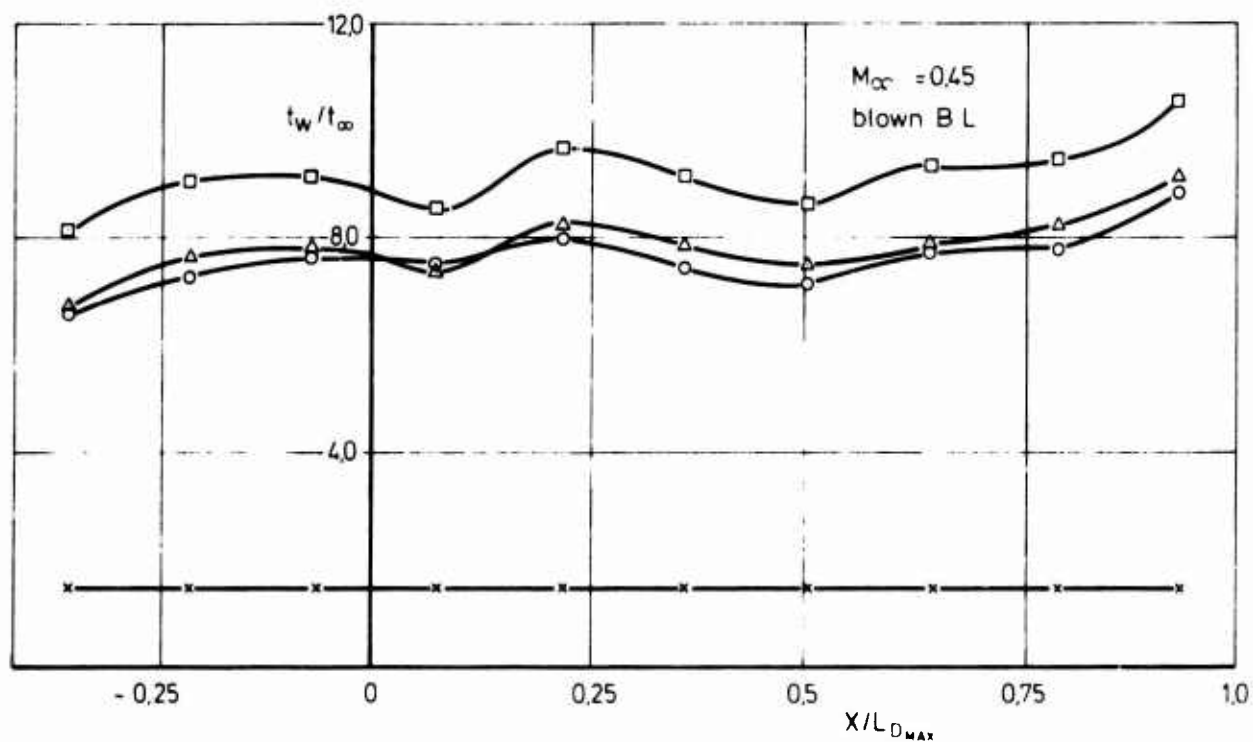
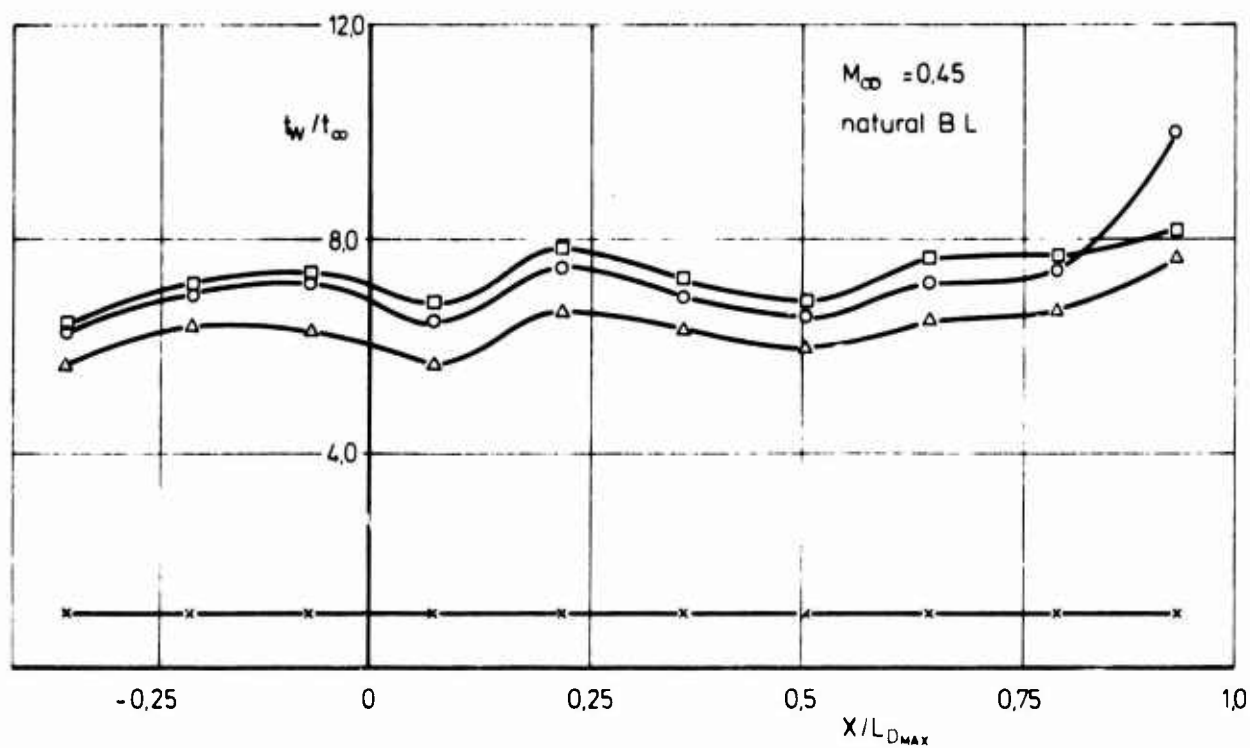


Fig.6 Boundary layer velocity profiles for the NLR 15° AGARD model measured at a position of 2.91 diameters upstream the jet exit plane at  $M_{\infty} = 0.8$  and 0.965



Symbol	NPR	
x x	1.7; 2.2, 3.0	cold jet
Δ Δ	1.7	hot jet
□ □	2.2	
○ ○	3.0	

Fig.7 Static temperature distributions on the boattail of HFB 320 CJ 610 jet engine nacelle model for cold and hot jets and natural and blown boundary layers at  $M_\infty = 0.45$



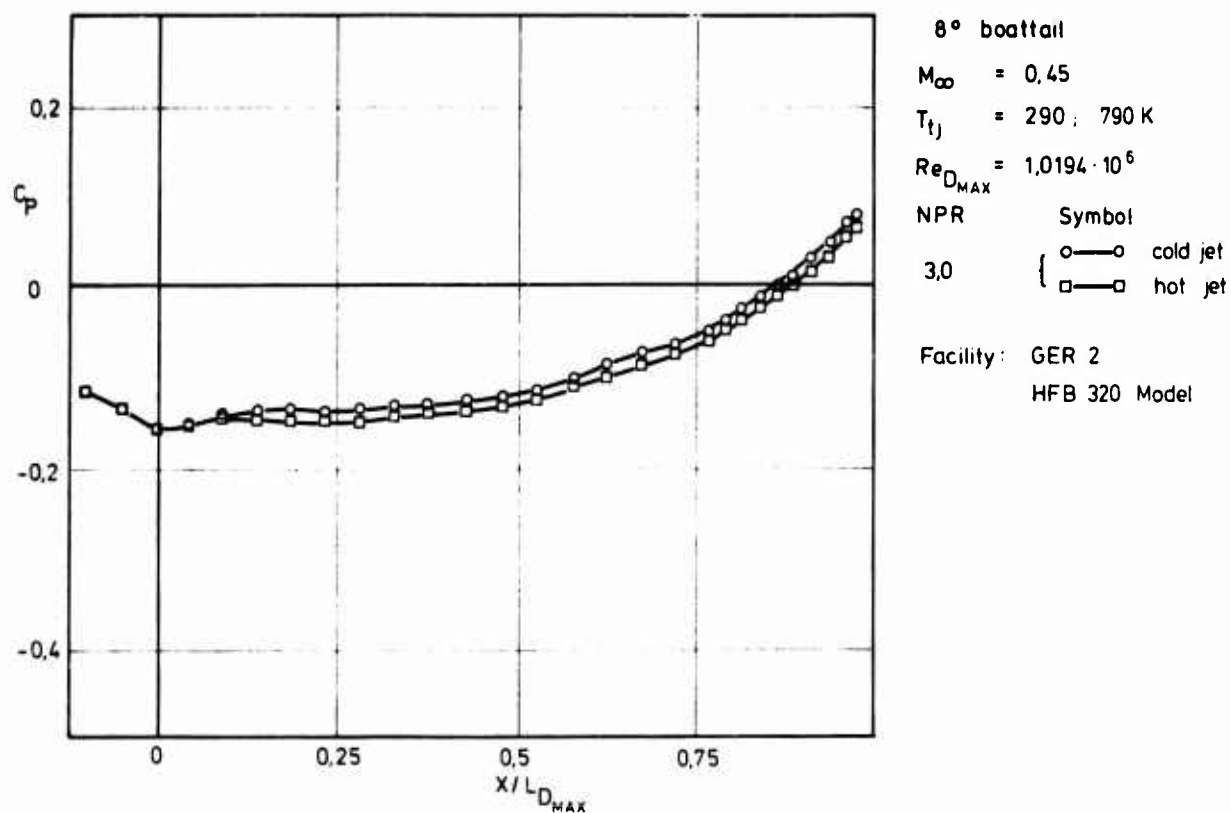


Fig.8 Boattail static pressure distributions on HFB 320 engine nacelle model for cold and hot propulsive jets at  $M_\infty = 0.45$

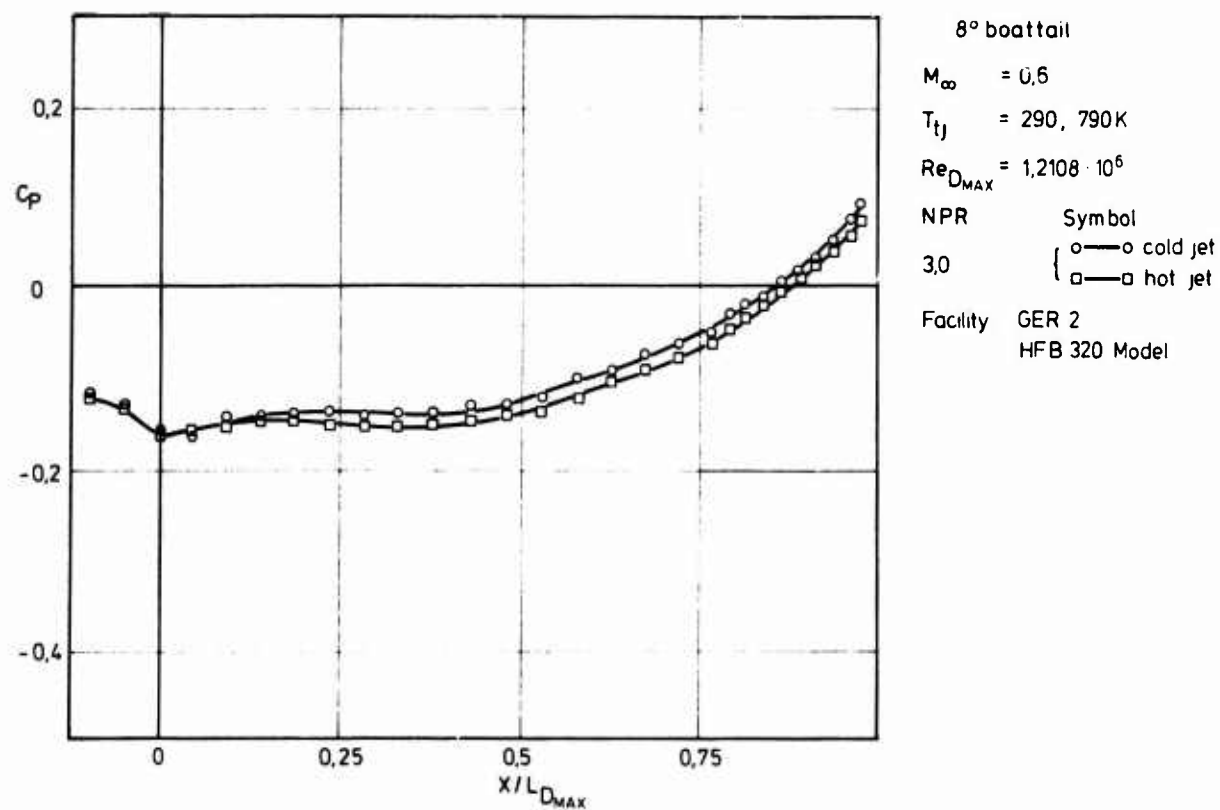


Fig.9 Boattail static pressure distributions on HFB 320 engine nacelle model for cold and hot propulsive jet at  $M_\infty = 0.6$

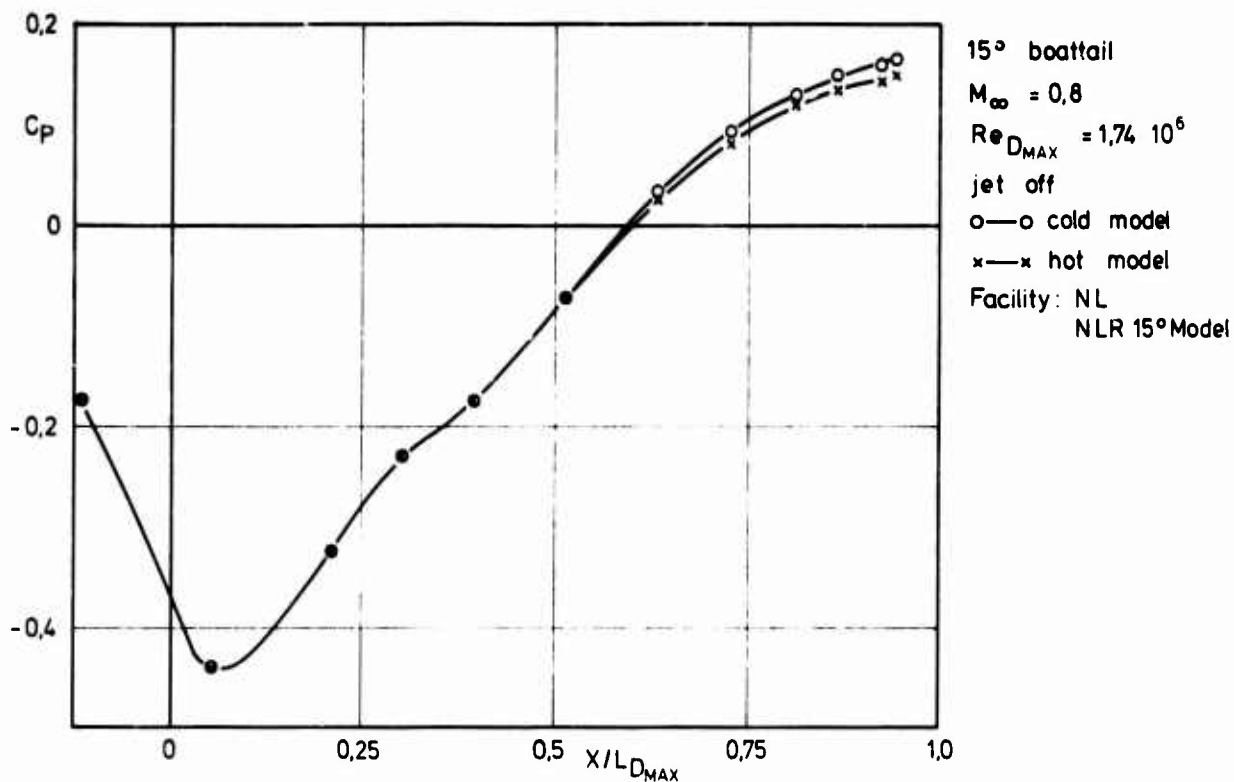


Fig.10 Effect of boattail surface temperature on boattail pressure distribution

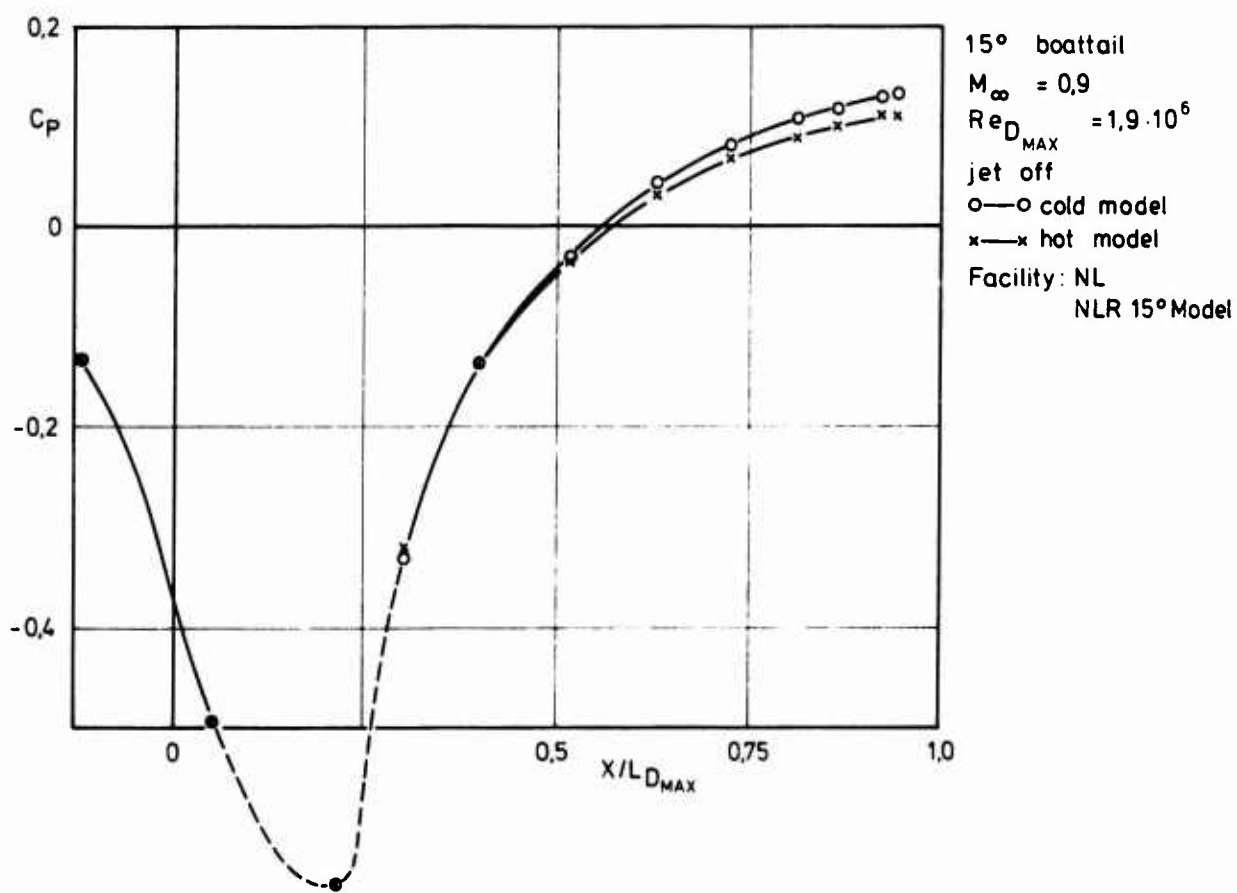


Fig.11 Effect of boattail surface temperature on boattail pressure distribution

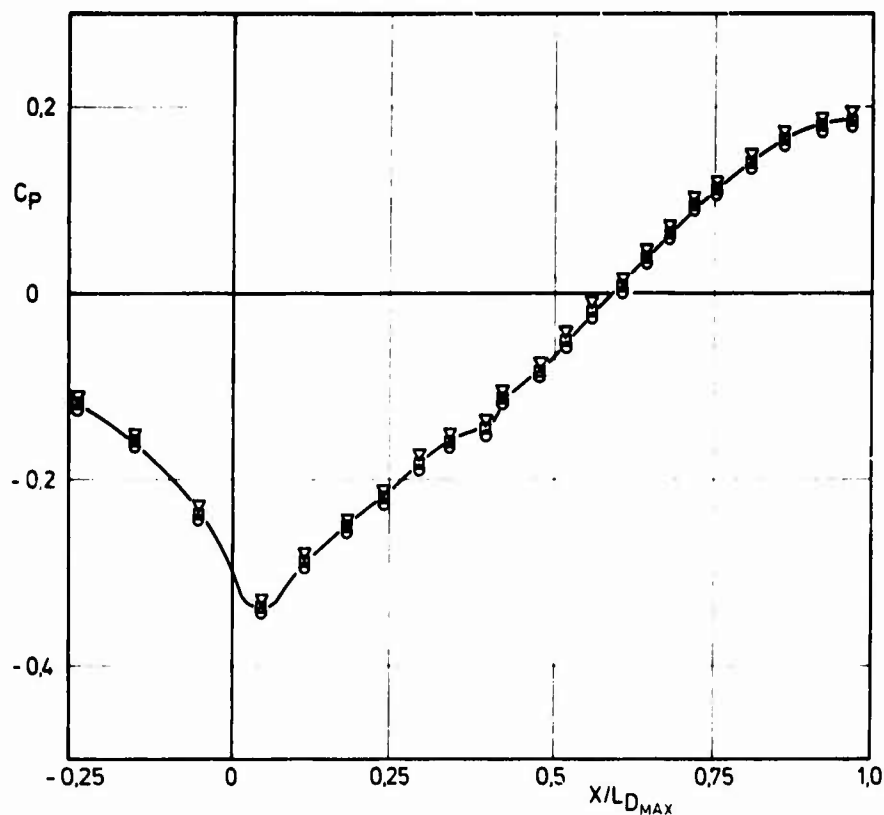


Fig.12 Boattail static pressure distributions on the AEDC 15° boattail model for different jet temperatures at  $M_\infty = 0,6$

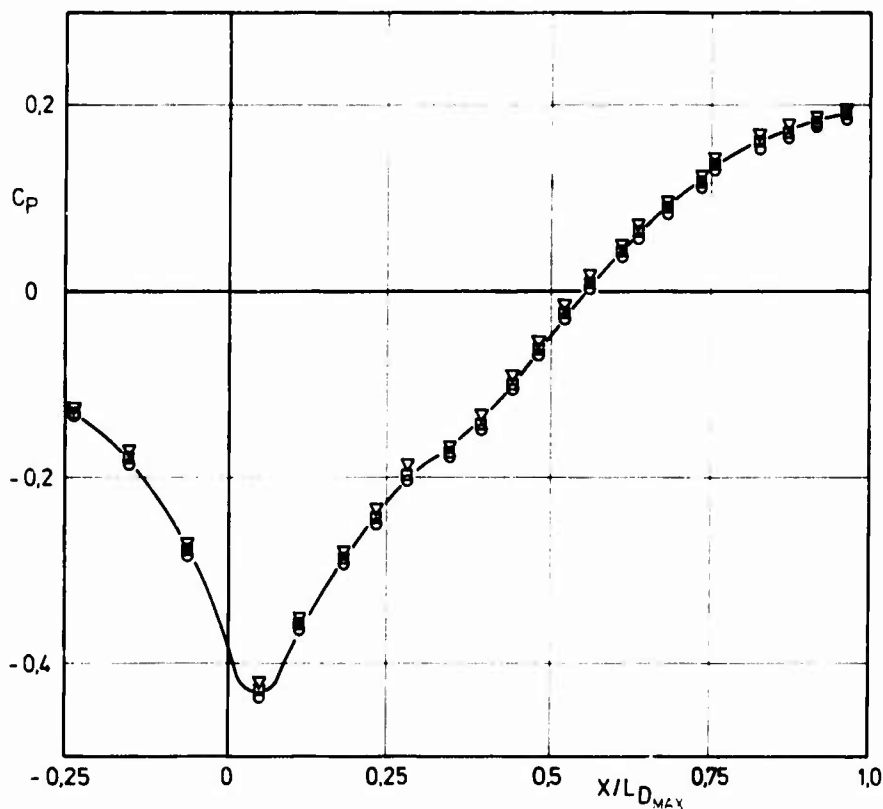


Fig.13 Boattail static pressure distributions on the AEDC 15° boattail model for different jet temperatures at  $M_\infty = 0,8$

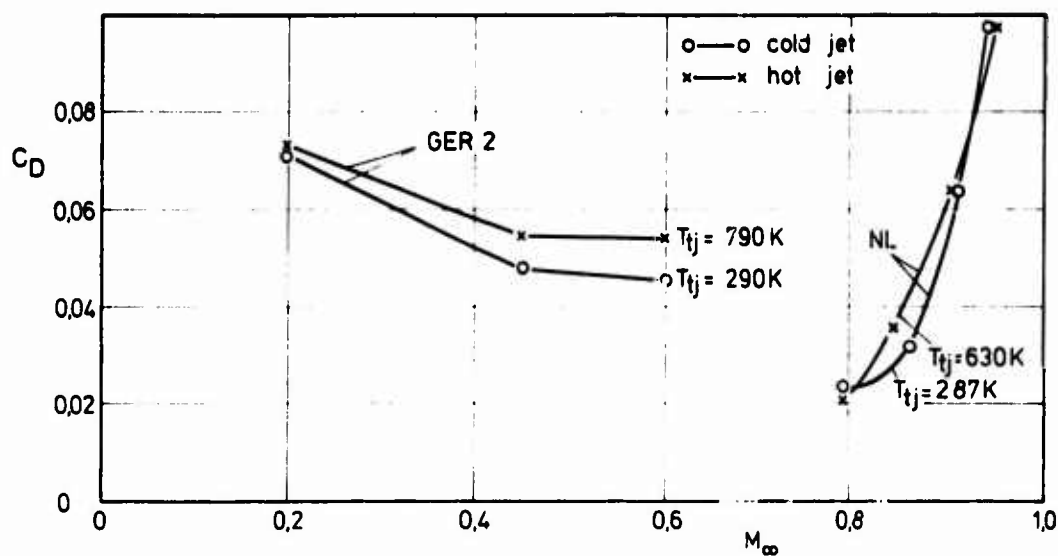


Fig. 14 Boattail pressure drag coefficient for HFB 320 engine nacelle and for AGARD model (NLR 15° boattail) for cold and hot jets at different free stream Mach numbers

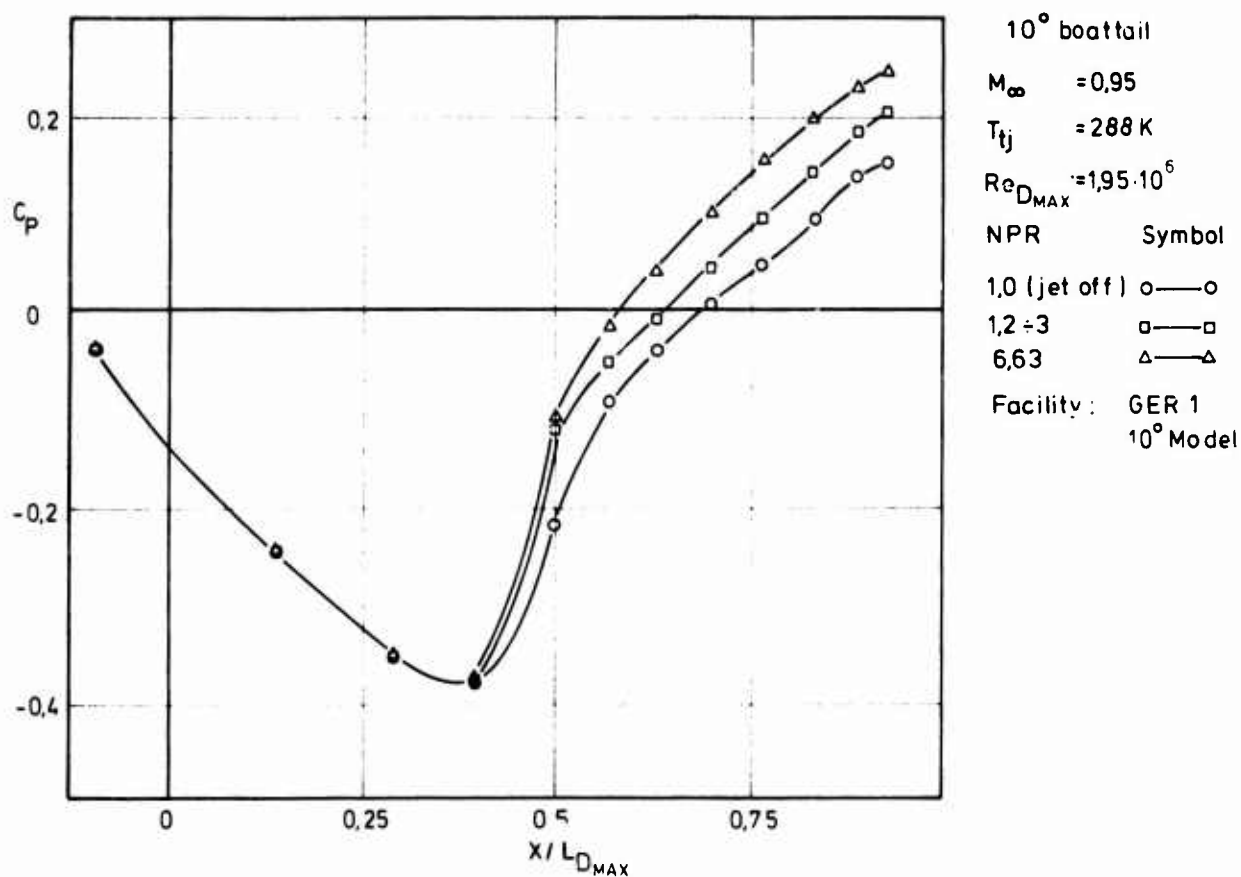


Fig. 15 Boattail static pressure distributions on AGARD model with 10° boattail angle for cold propulsive jet at  $M_\infty = 0.95$

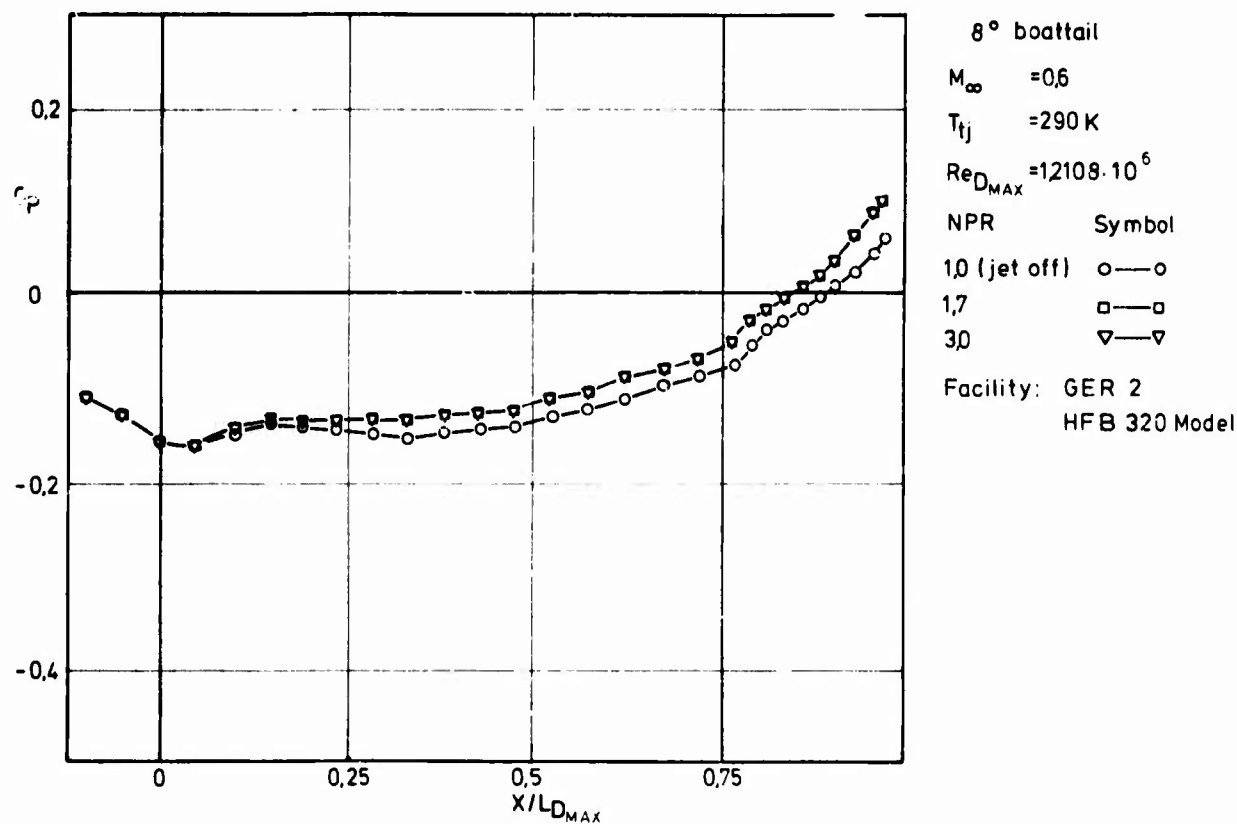


Fig.16 Boattail static pressure distributions on HFB 320 engine nacelle model for cold propulsive jet at  $M_\infty = 0.6$

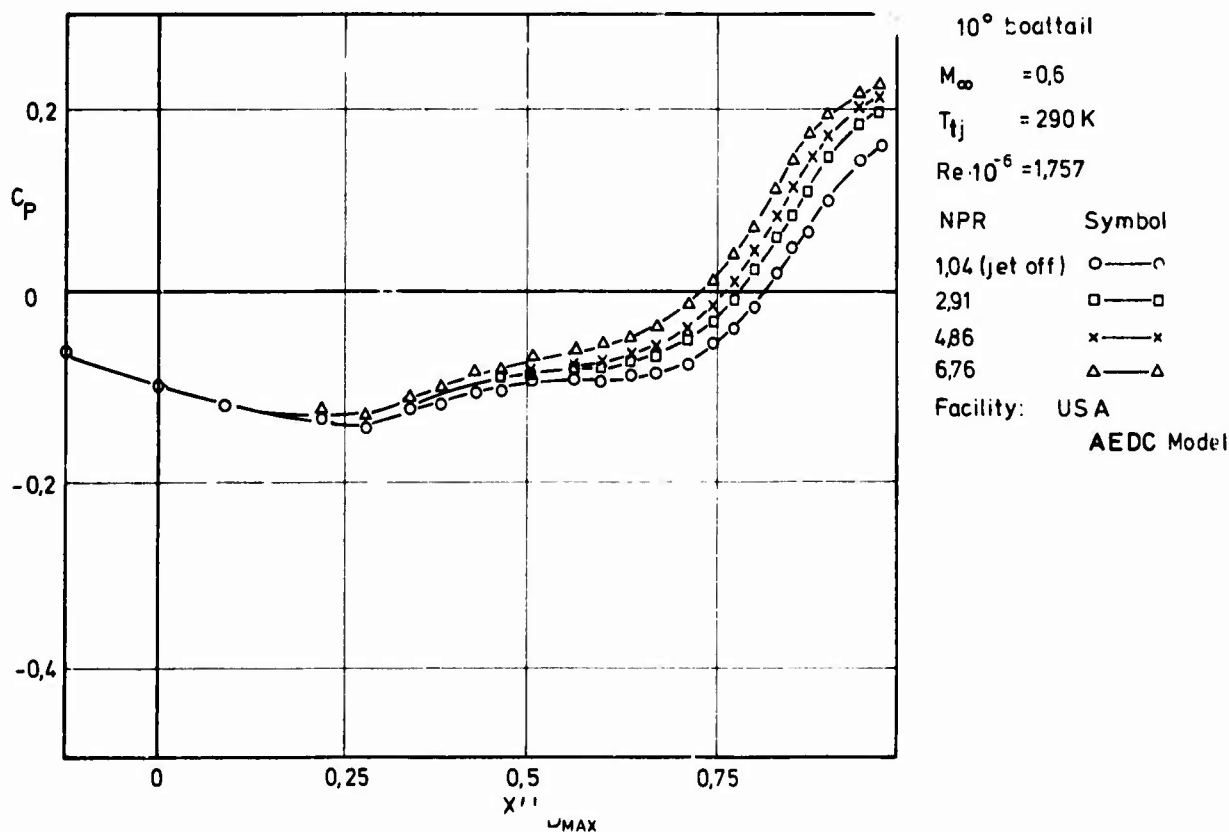


Fig.17 Boattail static pressure distributions on AGARD model with 10° boattail angle for cold propulsive jet at  $M_\infty = 0.6$

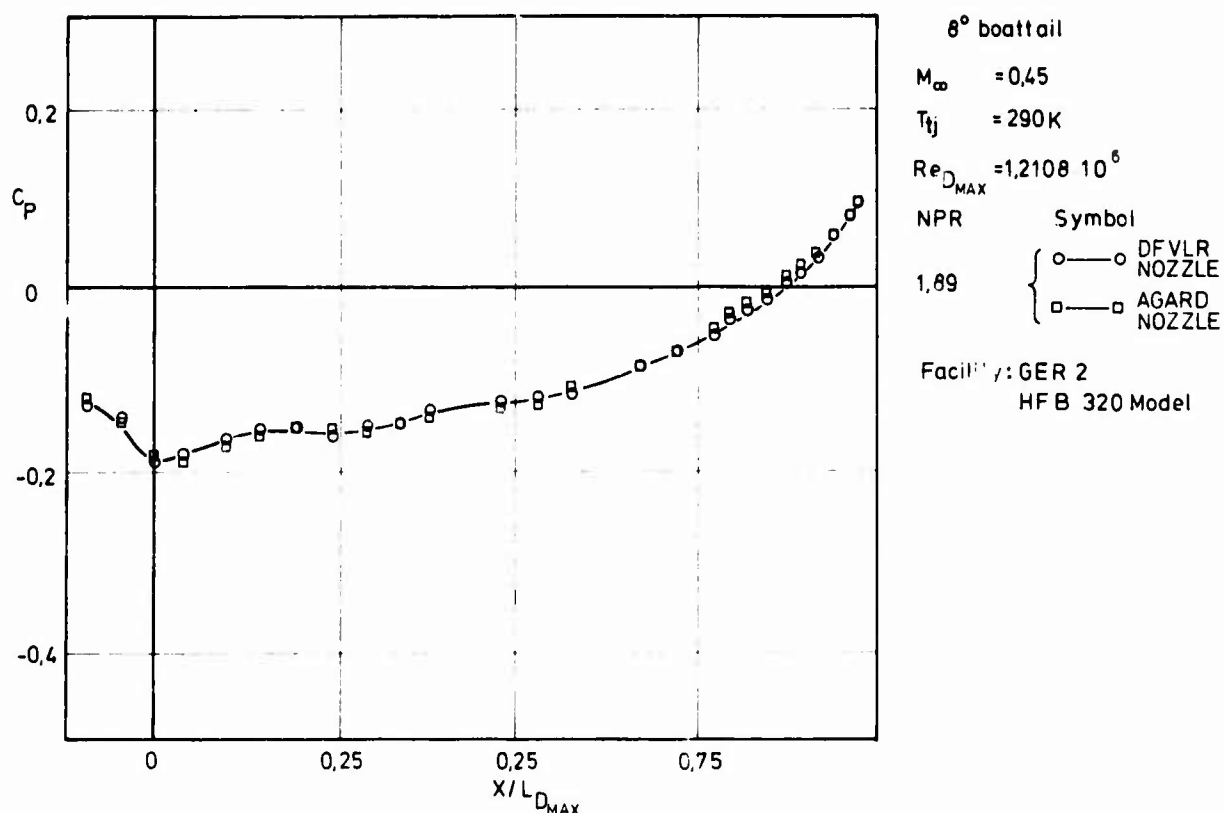


Fig.18 Boattail static pressure distributions on HFB 320 engine nacelle model for cold propulsive jet at  $M_\infty = 0.45$

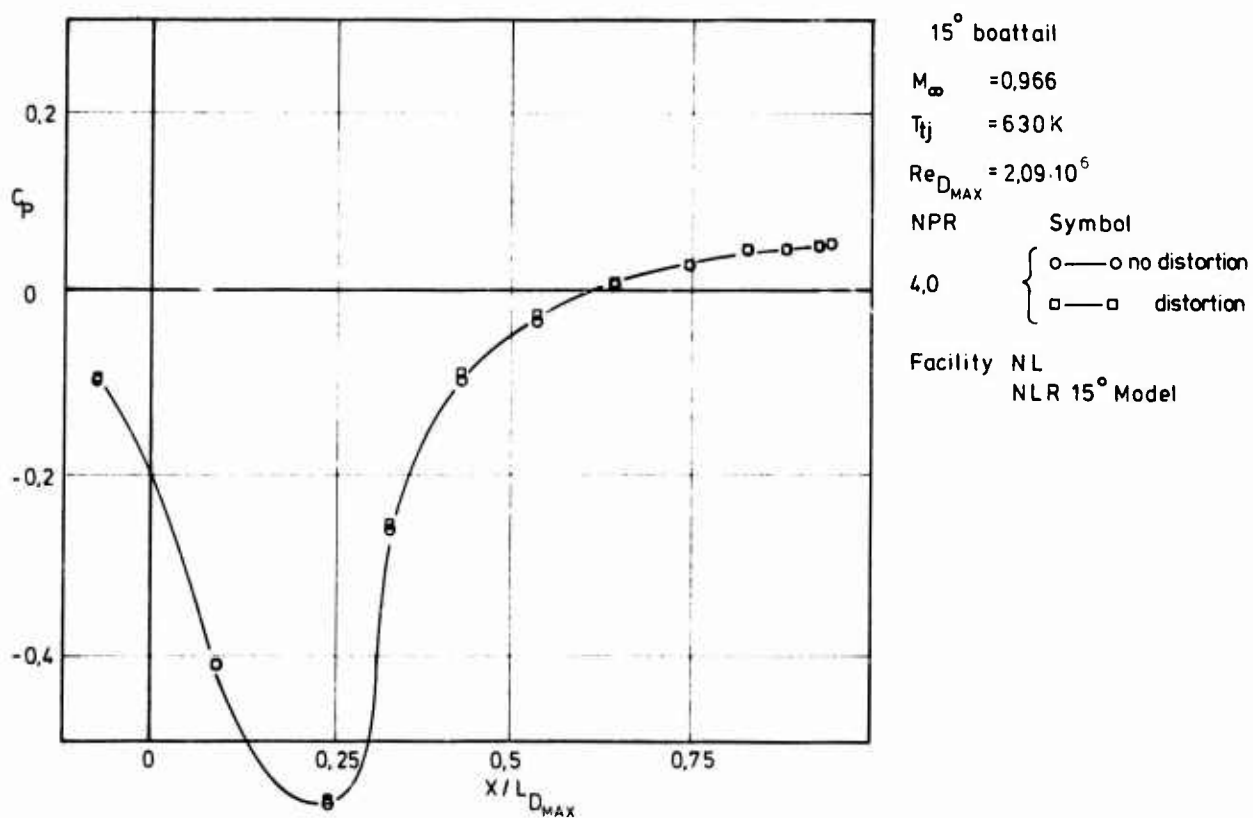


Fig.19 Boattail static pressure distributions on AGARD model with 15° boattail angle at  $M_\infty = 0.966$

## DATA VARIANCE DUE TO DIFFERENT TESTING TECHNIQUES

by

J.A. Laughrey and G.K. Richey

Aerospace Engineers, U.S. Air Force Flight Dynamics Laboratory

Antonio Ferri

Astor Professor of Aerospace Sciences, New York University, USA.

### 1. INTRODUCTION

A comparison of the boattail pressure distributions from data presented in other sections of this report shows that there is a significant variance in the data obtained in the various facilities, particularly at 0.9 and 0.95 Mach numbers. The analysis is concentrated on the 15° AGARD boattail tested in the 0.8 to 0.95 Mach number range. Differences in model support, model scale, tunnel blockage, tunnel buoyancy, wall type and porosity, and determination of tunnel reference flow conditions are examined in an attempt to understand the disagreement in the data. Model and wall static pressure distributions from various facilities are analyzed to try to isolate the reasons for these differences and to determine if there is a significant effect on the flow over the nozzle boattail. An indication of possible wall interference is obtained by comparing the measured wall static pressure distributions to those determined analytically with a far field boundary condition corresponding to free flight conditions.

### 2. TEST FACILITIES AND MODEL ARRANGEMENTS

A brief description of each facility and model arrangement used to test the 15° AGARD boattail is given in Figure 1. Further details may be found in the first section of this AGARDograph. In all, six different facilities were used with eight different model arrangements. The first two facility/model arrangements shown in Figure 1 were both in the AEDC 16T Propulsion Wind Tunnel with the difference being in the size and mounting arrangement of the model. The compressible flow facility (CFF) at Lockheed-Georgia Company (USA) was used for the next two facility/model arrangements. The subscale model is the same one tested previously in the AEDC 16T tunnel while the other model, tested in the CFF (ARL model), had the same relative boattail ordinates as the subscale model but had a larger diameter, a smaller fineness ratio ( $L/D_{MAX}$ ), and was supported by a sting which simulates the exhaust jet. In the NASA facility the model was supported by the sting-strut arrangement as shown. In the NLR facility, the nozzle model was installed in the tunnel using struts on the forebody, while in the ONERA and RR facilities the model was mounted on the end of a sting. In the NLR and RR facilities static pressures on the body surface or on the wall upstream of the boattail were used to set the test section Mach number. For the AEDC, NASA, and ONERA facilities, the test conditions (Mach number  $M_\infty$  and static pressure  $-P_\infty$ ) were established by measuring the test section plenum and tunnel stagnation pressures and using appropriate tunnel calibration data. Test conditions were established in a similar manner in the CFF; however, an averaged wall static pressure (one on each wall), ahead of the model location was used instead of test section plenum pressure as a reference static pressure. Figure 1 also provides other summary information pertinent to the discussion in this section.

### 3. BASIC COMPARISON OF BOATTAIL STATIC PRESSURE DISTRIBUTIONS

A comparison of the pressure coefficient ( $C_p$ ) distributions measured on the 15° boattail by the top row of pressure orifices for five different facilities is shown on Figures 2(a) through 2(d). At a Mach number of 0.8 (Figure 2(a)) there appears to be very little variation in the  $C_p$  distribution ahead of the boattail. However, in the expansion region over the shoulder and the recompression region near the nozzle exit there is a variance in the  $C_p$ 's of approximately 0.05. In the shoulder region the RR data gives the highest  $C_p$  while the NASA data indicates more expansion (lowest  $C_p$ ). Near the exit the flow over the RR model recompressed to the lowest values. In general, the data is considered to be in good agreement at 0.8 Mach number.

Data on Figure 2(b) at 0.9 Mach number indicates that there is very little difference in the flow over the shoulder (expansion region) for the various sets of data. More instrumentation might have revealed a variance in shock position. The flows recompress to different levels near the nozzle exit with a variation in  $C_p$  of approximately 0.06 compared to an average  $C_p$  of 0.13. At a Mach number of approximately 0.95 (Figure 2(c)) the data in the expansion region is similar for all the facilities; however, there is a significant variance in the recompression region (0.16 in  $C_p$ ). At both 0.9 and 0.95 Mach number, the data indicates that flow over the NASA model recompressed to the lowest

pressure, AEDC and RR models recompressed to the highest pressures with NLR and ONERA in between these data. The data at 0.95 Mach number for the RR model must be questioned due to the fact that, according to the facility description elsewhere in this report, there is "visible water vapor" in the test section above about 0.9 Mach number. Apparently this has a very strong influence on the recompression region.

An appreciation of the importance of these differences in the pressure data from the different facilities can be gained by determining the changes in pressure drag associated with the variations in the pressure distributions. Nozzle pressure drag coefficients ( $C_{Dp} = D_p/q_\infty A_{MAX}$ ), determined from data corresponding to that shown on Figure 2(a) ( $M_\infty = 0.80$ ), varied from 0.010 to 0.026. In terms of aircraft drag these values range from 0.0006 to 0.0016 (approximately 2% to 5% of total aircraft drag) for a typical single engine fighter aircraft with a fuselage area to wing area ratio ( $A_{MAX}/S_w$ ) of 0.06. A more significant variation is observed at a Mach number of 0.90 where the nozzle pressure drag determined from the various facilities ranged from 0.017 to 0.065 or from 0.0010 to 0.0039 when referenced to aircraft wing area. These latter values would be approximately 3% to 12% of total aircraft drag at a Mach number of 0.9. The variation in drag determined at a Mach number of 0.95 would undoubtedly be much greater due to the larger difference in the pressure data shown in Figure 2(c).

The AEDC data shown in Figures 2(a) through 2(c) were obtained at a unit Reynolds number of  $2.5 \times 10^6/\text{ft}$  ( $8.2 \times 10^6/\text{meter}$ ). From Reynolds number excursions made in the AEDC tunnel, cross plots of the pressure data were made and compared to other facilities data at about the same characteristic Reynolds number. The characteristic Reynolds number  $Re_{\delta^*}$  chosen for this comparison was based on the boundary layer displacement thickness ( $\delta^*$ ) approaching the shoulder of the nozzle boattail. An example of this comparison is shown in Figure 2(d) for 0.9 Mach number where it is seen that there is still about the same variation in the data as in Figure 2(b). Thus it appears that some effect (or effects) other than Reynolds number is creating the more significant differences in the flow that were observed. However, this does not rule out the fact that the state of the boundary layer ahead of the boattail can have a definite influence on the flow over the boattail. Another section in this AGARDograph discusses this aspect in some detail. In the following sections, some of the "other" effects which might give rise to variances of the recompression region pressure distribution are discussed.

Pressure distributions on the 10 and 25 degree boattails tested in three different facilities are shown on Figures 2(e) and 2(f) respectively. There is very little difference in the distributions for the 10° boattail; however, the flow separated at a higher pressure level on the 25° boattail in the AEDC tunnel. The following discussion on comparison of data between facilities concentrates on the 15° boattail as it was tested in all of the facilities.

#### 4. MODEL SUPPORT AND TESTING TECHNIQUE INFLUENCE

##### 4.1 Support Interference and Flow Asymmetry

In general the flow around the AGARD models, tested at zero angle of attack, should be symmetric unless there is some influence on the flow of a support mechanism or the basic flow in the wind tunnel test section is nonuniform. Asymmetrical flow on the boattail, possibly due to the effects of support interference, can be observed in the static pressure distributions measured along and circumferentially around the model, and in the boundary layer (total pressure) measurements upstream of the boattail. As discussed earlier in this report, (the NASA contribution by Compton and Runckel) the boundary layer measurements on the strut supported NASA model indicated that the boundary layer on the bottom of the model was slightly thicker with a somewhat fuller profile than the boundary layer on the top and side. This characteristic is likely caused by mixing in the wake downstream of the strut. Static pressure distributions obtained during the same series of tests (without the boundary layer rakes installed) also give an indication of some flow asymmetry around the model (see Figure 3). Comparison of the  $C_p$  distributions at 0°, 180°, and 270° on the 15° boattail at a Mach number of 0.9, indicates a greater expansion at the shoulder and more recompression near the nozzle exit at the 180° peripheral location than on the top (0°). This trend seems to be consistent with an increased effective Reynolds number associated with a fuller upstream boundary layer profile and a smaller displacement thickness. Flow asymmetry can result in small variations in pressure drag depending on which row of pressures is used to calculate the drag. An example of this is given in the description of the AEDC contribution by Galigher and Jackson to the AGARD nozzle study. For the 10° boattail at 0.9 Mach number and a nozzle pressure ratio of 3.0, the pressure drag coefficient determined for the top row of static pressures was 0.009 compared to a value of 0.013 calculated for the bottom row. Equivalent aircraft drag coefficients (referenced to wing area) would be 0.0005 and 0.0008 respectively, which is approximately 1% to 3% of total drag for a typical single engine aircraft. Thus, if the model is at zero angle of attack, flow asymmetry due to the NASA or AEDC strut arrangements is small and does not significantly affect the comparison with data from the other AGARD tests of the 15° boattail.

In addition to an alteration of the viscous flow on the model surface by the strut wake, which is a local effect, a sting-strut area distribution can produce pressure waves and blockage effects which can be transmitted to the model in subsonic/transonic flow. This type of strut (or sting) interference can have a significant influence on the flow over the boattail at high subsonic Mach numbers. It is believed that such an influence appears in the data shown on Figures 4(a) through 4(c), which compares the  $C_p$  distributions for the full scale model at AEDC and the subscale model at CFF (same relative strut arrangement, as shown in Figure 1) with the subscale model at AEDC which has



a sting-strut arrangement. Figure 4(d) is a photograph of the subscale model arrangement in AEDC. Note that the rapid area change of the support mechanism is at a tunnel location slightly upstream of the boattail on the model. As the Mach number increases from 0.8 (Figure 4(a)) to 0.95 (Figure 4(c)), there is a substantial variance (lower  $C_p$ ) with the strut-sting mounted model, compared to the models supported only by the strut. The full scale AEDC and subscale CFF model data agree at all Mach numbers and with a CFF tunnel porosity of 6%. Although there is a difference in blockage as well as a different strut arrangement, it is believed that strut interference is the predominant effect. Figure 4(c) shows that there is a substantial expansion of the flow upstream of the shoulder for the subscale model in the AEDC facility, which gives a higher local Mach number approaching the expansion region at  $X/D_{MAX} \cong 3$ . This higher Mach number apparently increases the shock strength at  $X/D_{MAX} \cong 1.0$  and causes the flow to separate at a lower pressure than for the other model arrangements.

An analysis of the sub-scale mounting arrangement was conducted to determine if the pressure gradient observed upstream of the shoulder could be caused by the sting-strut support system. First the area distribution of the sting-strut combination was equated to an equivalent body of revolution; then the pressure distribution at a distance away from this equivalent body corresponding to where the nozzle model would be located was computed using the transonic analysis techniques<sup>1</sup>. Results of this analysis are shown at 0.95 Mach number in Figure 4(e) where it can be seen that the support produces an expansion upstream of the shoulder. Although the absolute value of the calculated  $C_p$ 's are somewhat higher than those measured experimentally, it is an indication that the gradient on the cylindrical portion of the model ahead of the boattail could be caused by sting-strut interference. Similar calculations performed on the NASA sting-strut arrangement indicated a very slight influence on the flow over the model upstream of the shoulder, compared to the effect observed on the subscale model in the AEDC tunnel.

Other indications of flow asymmetry around the model were observed in both the RR and the ONERA tunnels. The RR data indicated a fuller boundary layer profile on the bottom ( $\theta = 180^\circ$ ) of the model than on the top or side for all Mach numbers tested<sup>2</sup>. Data from the ONERA<sup>3</sup> tests shows variations in the boundary layer profile measured at four locations around the model ( $\theta = 0^\circ, 90^\circ, 180^\circ$ , and  $270^\circ$ ). The profiles at  $90^\circ$  and  $270^\circ$  (near the solid wind tunnel walls) were different from the profiles measured at  $0^\circ$  and  $180^\circ$  (near the perforated walls). These differences could be created by the dissimilar walls, or could possibly be due to model misalignment or model-sting support interference.

## 5. WALL POROSITY EFFECTS

Another factor that can influence the flow over the model when testing in the transonic regime is the test section wall porosity. Porous walls are used to help develop uniform flow along the test section transonically and reduce shock reflections at supersonic speeds. In tests conducted at the compressible flow facility with the AEDC subscale model and the ARL model, the test section porosity was varied by sliding the walls which changed the area of the holes. The test results indicate a significant influence of porosity on the  $C_p$  distributions for the  $15^\circ$  boattail at 0.9 and 0.95 Mach number as the porosity was changed from 2% to 6%. There was negligible effect of porosity changes below 0.9 Mach number. The change in the  $C_p$  distributions at 0.9 Mach number for 2% and 4% porosity is shown on Figure 5. As the porosity increases, the absolute level of the pressure increased (increasing  $C_p$ 's) upstream of the shoulder and in the recompression region near the nozzle exit. As shown in Figure 4(b) (0.9 Mach number), the 6% porosity data correlates well with data from the AEDC tunnel which has 6% porosity. Similar trends with increasing porosity were observed on the ARL model in the same facility<sup>4</sup>. The compressible flow facility may exhibit somewhat stronger trends with porosity than other facilities since there is a large pressure difference across the porous walls. Many transonic tunnels operate with a very small pressure difference between the test section and the surrounding plenum.

## 6. MODEL-WALL FLOW INTERACTIONS

In several of the experiments, static pressure along the wall were measured as well as the pressure levels on the surface of the model. These pressure distributions can give some indication of a possible interaction between the wind tunnel wall flow and the flow over the model by comparing the experimental wall pressure distribution with that predicted at the wall location, but with a far field boundary condition corresponding to free flight. The calculated pressure distribution obtained at a distance away from the model equivalent to the wall location being analyzed is considered to be free of wall interference. If the measured wall pressures are significantly different from the predicted values, there may be some influence of the model wall interaction on the boattail flow. Wall static pressure measurements were obtained in the NLR, RR, ONERA, and NASA facilities and will be discussed in that order which represents a decreasing ratio of maximum model to wind tunnel cross-sectional area (normally called the "blockage factor" for strut supported models).

When considering the blockage factor/area ratio in the NLR and RR wind tunnels it should be kept in mind that the AGARD nozzle tests were conducted using these facilities like an "annular" wind tunnel. That is, the Mach number was set by either a static pressure on the cylindrical portion of the model (NLR) or by the static pressures on the tunnel wall opposite the cylindrical portion of the model (RR). This experimental technique does not produce a blockage in the usual sense, where a model is introduced into a wind tunnel flow which is set at a particular

Mach number using the plenum pressure as a reference. In the NLR and RR test technique used for the AGARD tests, there is a rapid area change near the exit of the model, producing expansion and compression waves which are transmitted to the wall and may in turn be reflected back to the model; in transonic flow, these pressure disturbances are transmitted in a generally lateral direction.

Data obtained in the NLR facility at Mach numbers of 0.8, 0.85, 0.90, 0.96 are shown in Figures 6(a) through 6(d). As the free stream Mach number increases, the  $C_p$  on the wall at a tunnel location corresponding to the nozzle boattail shoulder becomes more negative. This indicates a higher Mach number on the wall than the reference Mach number. The data at 0.96 Mach number (Figure 6(d)) indicates that the flow is supersonic ( $C_p < C_p^*$ ) across the test section, from the model to the wall. This is an indication of a rather strong interaction between the wall and the model at this condition. From the data on Figure 6(b) it can be observed that there is a slight change in the wall pressures between jet on and jet off, indicating that the nozzle jet plume changes what could be considered the effective body in the test section.

As stated previously, a better indication of wall-model interaction can be obtained by comparing the measured wall pressures with those predicted using a far field boundary condition corresponding to free flight ( $C_p = 0$ ), at the reference Mach number. The predicted wall pressures were computed in two different ways. In the first method a direct calculation of the flow field around the body is performed which gives the pressure distribution on the model surface and at the wall location. This type calculation was made using procedures developed by Calarese<sup>5</sup> and by Krupp and Murman<sup>1</sup>. Figure 7(a) compares the model surface pressure distributions calculated by these methods with the experimental data from AEDC at 0.9 Mach number. The theoretical pressure coefficients are slightly higher than experiment in the recompression region. In the second method of predicting the wall pressures, the experimental body pressure distribution is prescribed as a boundary condition and the wall pressure is then calculated with a far field boundary condition corresponding to free flight using a modified Murman and Cole analysis technique<sup>6</sup>.

Figure 7(b) compares the predicted wall pressure distributions (free flight condition) with the experimental data in the NLR facility at 0.9 Mach number. The increment between the theoretical and experimental distributions is assumed to be a measure of the wall interaction effect. Although there is some disagreement in the various theoretical results, the experimental data shows a substantially lower (more negative)  $C_p$  on the wall, which would indicate that the flow at this location ( $R_{WALL}/D_{MAX} = 1.68$ ) is at a somewhat higher Mach number than if the wall was not present. The radius  $R_{WALL}$  is the distance from the model center line to the test section wall. If the Mach number near the body is also increased, due to the presence of the wall, the boattail would be expected to have less recompression, which is the usual trend of the boattail flow field with increased Mach number. In this case, it might be more appropriate to compare the NLR data at 0.9 Mach number with data from another facility (with reduced wall interaction) at a somewhat higher Mach number.

Model and wall static pressure data were obtained in the Rolls Royce (RR) facility where the "blockage factor" is 3.6% with the 15° AGARD boattail model installed. The experimental pressure distributions on the model and at the wall ( $R_{WALL}/D_{MAX} = 2.67$ ) are shown in Figures 8(a) and 8(b) for 0.91 and 0.95 Mach number respectively. The wall pressure distribution is similar to that observed in the NLR facility but the absolute value of the  $C_p$ 's are considerably reduced, consistent with the wall being farther away from the model. This result is verified by the theoretical prediction of the wall pressures shown in Figure 9. All the theoretical curves are in essential agreement and indicate that there is a slight increment between the theoretical wall pressures (free flight boundary) and the measured wall pressures. The result using the method of Krupp and Murman<sup>1</sup> predicts a somewhat larger model-wall flow interaction than the other approaches. The effect of this interaction on the nozzle boattail flow would be expected to be similar to that for the NLR data, but less severe. The tunnel reference pressure is an average of three static pressures on the wall approximately five body diameters upstream of the nozzle exit and any influence of the model on the flow at the wall could possibly have some effect on these pressures.

Predicted and wall pressure coefficients measured during tests of the AGARD 15° boattail model at 0.9 Mach number in the ONERA facility are shown on Figure 10. The results shown are for the model with the smallest diameter ( $D_{MAX} = 80$  mm) which gives an equivalent "blockage factor" of 0.7%. The tunnel wall is at  $R_{WALL}/D_{MAX} = 5.27$ . Although there is a significant difference between the theoretical wall pressures computed with a free flight boundary and the measured wall pressures, which could be interpreted as a wall interaction, the measured wall pressure distribution appears to have a shape associated more with a pressure gradient in the wind tunnel. Comparing this wall pressure distribution with that observed in Figures 7 and 8, it is noted that the wall  $C_p$  does not return to zero downstream of the nozzle exit in the ONERA facility as it does in the NLR and RR wind tunnels. From the measured pressure distributions, it appears that the flow on the cylindrical part of the model is at a slightly higher Mach number than the reference Mach number. The reference pressure used to determine the free stream conditions is measured in the plenum of the ONERA tunnel; it is assumed that this measured pressure is compared to calibration information to establish the test section reference flow conditions ( $M_\infty$  and  $P_\infty$ ). If the wind tunnel has a pressure gradient, a more realistic comparison of analytical and measured wall pressures would be to consider, as the measured wall pressure, the difference with and without the model installed. The distribution of wall pressure downstream of the model, shown in Figure 10, indicates that the flow downstream of the model may be adversely affecting the flow over the boattail of the model. This effect is discussed later under "Diffuser and Back-Pressure Effects". Another indication of a model-wall flow interaction was observed from the results of the

ONERA investigation in which three models with different maximum diameters ( $15^\circ$  boattail nozzle) were tested at various Mach numbers. The pressure distributions on the nozzle did not vary much over the shoulder (expansion region) as  $D_{MAX}$  was increased from 80 mm to 120 mm, however, near the nozzle exit there was less flow recompression. This was particularly evident at a Mach number of 0.95 and is an indication that the local Mach number ahead of the boattail is increasing with increasing diameter; this would have the effect of reducing the pressures in the recompression region.

Model and wall static pressure data shown on Figures 11(a) and 11(b) was obtained in the NASA facility at 0.9 and 0.95 Mach number with the  $15^\circ$  boattail model installed. The absolute level of the wall static pressure coefficients at the wall is very small, indicating that the wall-model interaction is negligible in this facility ( $R_{WALL}/D_{MAX} = 14.4$ ). This was verified by the analytical techniques which predicted a maximum wall  $C_p$  of 0.002 at 0.9 Mach number, due to the presence of the body. The variation of the wall pressure data presented in Figures 11(a) and 11(b) is within the accuracy of the pressure instrumentation used. In the NASA facility the test section Mach number and free stream pressure ( $P_\infty$ ) are determined from a tunnel empty calibration and measured values (during the test) of stagnation pressure and plenum static pressure.

Although wall pressure measurements were not made in the AEDC facility, theoretical predictions indicate that the wall pressure coefficient would not exceed 0.002. Thus it is felt that the larger tunnels used in the AGARD study, with blockage factors of less than one percent, have very little wall-model interaction. However, other test technique variables or a combination of unknown effects may contribute to discrepancies in the measured nozzle pressure distributions.

## 7. BACK PRESSURE AND DIFFUSER EFFECTS

The above analysis of the results from the various facilities accounts for some of the differences observed in the data, but it is still not entirely clear why there exists large differences in the pressure distributions near the nozzle exit (recompression region), especially at Mach numbers of 0.9 and 0.95. An explanation of part of this discrepancy is that the local flow conditions over the boattails are not similar between facilities even when test section reference conditions ( $M_\infty$  and  $P_\infty$ ) are supposedly the same. There are undoubtedly several reasons for the local flows being dissimilar including support type, tunnel blockage, tunnel buoyancy, etc. Tunnel buoyancy has not been addressed directly in the discussion so far other than noting that there was a possible pressure gradient in some of the test sections (e.g. the ONERA facility).

An analysis of the pressure data obtained along the tunnel walls and on the model in several of the facilities indicates there might be an influence on the flow over the model of a pressure gradient in the test section (tunnel buoyancy) or of the close proximity of the diffuser back pressure to the end of the model. An analysis of the information shown on Figure 12 gives some indication of what might be causing some of the differences in the data. The Mach number distribution along the test section and into the diffuser for the four facilities indicates the magnitude of any pressure gradient and of course any model-wall flow interaction. As can be seen from the data in Figure 12, the local Mach number distribution along the wall in the ONERA tunnel indicates a rather significant increasing pressure gradient in the test section prior to the flow entering the diffuser. There was insufficient data from the NLR facility to establish a trend. The data shown on Figure 12 for NLR is undoubtedly being influenced by the flow over the model. The data from the RR facility indicates an increasing pressure gradient as the flow approaches the diffuser.

For the NASA facility, data from the AGARD tests along with data obtained during the tunnel calibration was used to gain some insight into the behaviour of the flow through the tunnel test section and into the diffuser. As discussed previously, the presence of the model in the test section had very little influence on the wall pressure distributions; any pressure gradient observed is there with and without the model present. As shown on Figure 12, the Mach number distributions along the wall of the diffuser in the NASA facility indicate that the flow first expands and then recompresses. However, data obtained along the center line (obtained during tunnel calibration) indicates only a flow deceleration (recompression) as the flow enters the diffuser. Of note here is the proximity of the nozzle exit to the diffuser for the NASA model arrangement.

The Krupp and Murman analytical technique cited previously<sup>1</sup> was used to analyze the possible effects on the flow over the boattail of a pressure distribution downstream of the nozzle exit similar to that observed in the NASA facility. This was accomplished by inputting the experimental back pressure distribution as a boundary condition. The inviscid flow analysis indicated an increase in the pressure level of the flow over the simulated plume and boattail. A similar analysis performed to assess the effect of the sting flare arrangement in the NASA facility also indicated a very slight ( $\Delta C_p = 0.002$ ) increase in the pressure in the flow field near the nozzle exit. The experimental data obtained on the NASA model indicates that the flow possibly separated at a lower pressure than on the models in the facilities. It is felt that the diffuser back pressure could create a more adverse pressure gradient for the boattail flow to negotiate in the recompression region, thereby causing the flow to separate at a lower pressure. A similar effect in the RR and ONERA facilities could explain some of the differences observed in the data at Mach numbers 0.9 and 0.95. The experimental results appear to indicate that the diffuser back pressure has less effect on the flow over the models in the facilities where the nozzle exit is further from the diffuser (see Figures 2(b))

and 2(c)). This would be especially true in the AEDC facility where the model nozzle exit is over 20 model diameters upstream of the diffuser entrance.

## 8. FINENESS RATIO AND TUNNEL TURBULENCE EFFECTS

Also investigated as a possible explanation of part of the differences was the influence of model length on the results obtained in the NASA facility. The inviscid flow was calculated over two bodies that differed only in length. One body had a fineness ratio of 14.9 (AEDC model) while the other had the fineness ratio of the NASA model ( $L/D_{MAX} = 10.7$ ). At a Mach number of 0.9 the results indicate that the local Mach number ahead of the boattail would be higher on the model with the lower fineness ratio. This would in turn indicate a stronger shock-boundary layer interaction and the possibility of the flow separating at a lower pressure.

It has been shown (e.g. see Reference 7) that the degree of freestream turbulence or noise in a tunnel can influence the flow over a model. As reported in<sup>8</sup>, the majority of investigations in this area have concentrated on the effect of tunnel turbulence or noise on the transition from laminar to turbulent flow in the boundary layer. According to the results presented in Reference 7, the NASA facility has a very low turbulence level through the transonic Mach number range. This could influence the flow over the model boattail in such a way that the flow separates at a lower pressure than it would on the same model located in a flow field that has more freestream turbulence. In general, with increased turbulence and mixing in the boundary layer there is a tendency for the flow to remain attached longer in an adverse pressure gradient. The information presented in References 9 and 10 gives some indication of how tunnel freestream turbulence or noise might influence the boundary layer flow on a boattail model; however, there needs to be a more thorough investigation of how tunnel turbulence or noise can effect flow separation on a model such as those investigated during the AGARD study.

## 9. SUMMARY

Experimental data on the AGARD 15° boattail shape from six facilities using eight different model arrangements, obtained under the cooperative AGARD investigation, has been analyzed in an attempt to isolate the causes of observed variances in the pressure distribution on this axisymmetric model. Although the test data was not originally obtained to determine specific transonic test technique effects, it is believed that a comparative analysis of the results has provided valuable insight into the influence of model installation, support arrangements and test procedures. In many cases, further experimental and analytical research is needed before these effects can be fully understood and quantified for an accurate assessment of their influence on aircraft and missile performance in the transonic speed regime.

Based on the rather limited comparative analysis of data on one of the AGARD nozzle configurations, the following general observations are drawn:

- (a) In the transonic flow regime, it is extremely important to accurately determine the true Mach number and reference pressure. A very small change in these parameters can have a significant effect on the boattail flow. Comparison of data from one facility to another must be very carefully based on the same reference conditions. These reference conditions may be influenced by the model itself, tunnel calibration variations with flow parameters including Reynolds number, or by atmospheric conditions such as water vapor content.
- (b) Model support systems can cause a local effect on the boattail flow by interaction of the strut or sting flow with the flow on the model. For the model arrangements used in the AGARD study, this effect is primarily manifested in a flow asymmetry over the boattail which may result in a slight increase in pressure drag on the aft portion of the model. Flow asymmetry does not seem to be responsible for a significant part of the overall variance observed in the data. However, model support systems can, under certain circumstances, alter either the flow field approaching the boattail or the flow field downstream of the model in a way that the flow separation point (present on most nozzle configurations in transonic flow) is changed dramatically. Thus one must be concerned about the pressure field created by the support system if there is any possibility that these flow fields can interact with the test article.
- (c) In transonic flow, disturbances from the model and the wall are transmitted in a nearly lateral direction across the flow field between the two surfaces. Even in the absence of flow restriction (blockage) by the model, the model and wall flow fields can interact to alter the flow over the boattail. Data from the various AGARD facilities indicate that this interaction decreases rapidly as the non-dimensional distance from the model centerline to the tunnel wall ( $R_{WA} / D_{MAX}$ ) increases from 1.68 to 14.4. For the boattail shape tested, the model wall interaction appears to place the aft portion of the boattail in a higher Mach number flow field than indicated by the reference conditions. The true measure of the interaction should be based on the increment between the measured wall pressures and those computed at the wall surface with a far field boundary condition corresponding to free flight. Thus the theoretical analyses are used to put the experimental results into proper perspective. It seems obvious then, that improved transonic test techniques and improved theoretical analyses must be developed together.

- (d) The flow field downstream of the model can also be very important in determining the flow over the boattail, particularly in the recompression region. If the facility produces a pressure gradient, even without the model in the wind tunnel, which alters the point of separation on the boattail, there can be a significant change in the pressure distribution in the recompression region. Analysis of data from various facilities where the location of the wind tunnel diffuser varied between 2.3 and 6.1 model diameters from the exit of the nozzle model indicates that some the variance observed in the pressure distributions could be caused by an increased back pressure which may move the separation point upstream on the model. If this occurs, reduced pressures in the recompression zone would be expected.

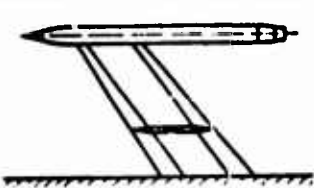
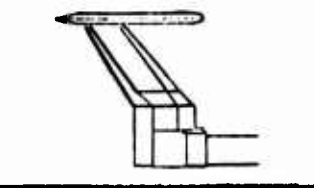
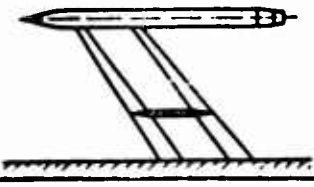
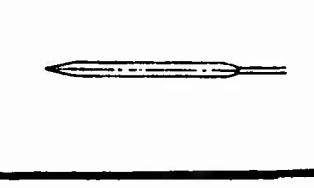
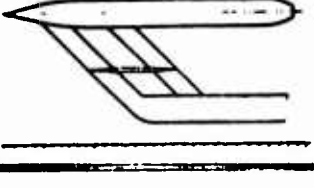
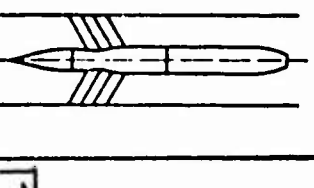
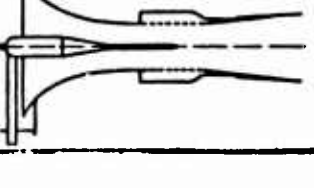
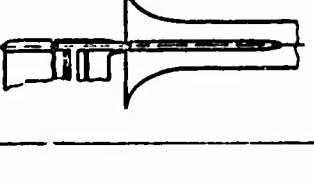
It is felt that further experimental and analytical research is necessary to fully understand the influence of transonic test technique variations on the data obtained, but the AGARD study has made a substantial contribution to gaining insight into some of these effects.

## ACKNOWLEDGEMENT

The authors of this section would like to acknowledge and thank Dr.W.Calarese and Mr.J.L.Mace of the U.S. Air Force Flight Dynamics Laboratory (AFFDL), and Dr.S.Panunzio of New York University for their efforts in the theoretical calculations of model surface and wall pressure distributions. The assistance of Mr.D.L.Bowers of AFFDL in the experimental data correlation is gratefully acknowledged.

## 10. REFERENCES

1. Krupp, J.A.  
Murman, E.M.      *The Numerical Calculation of Steady Transonic Flows Past Thin Lifting Airfoils and Slender Bodies*, AIAA Paper No.71-566, AIAA 4th Fluid and Plasma Dynamics Conference, Palo Alto, California, June 1971.
2. Deer, D.J.      *Results of Tests on Single Afterbody Nozzles Refined by AGARD*, Rolls Royce Report PPE 67, March 1974.
3.      Unpublished Results of ONERA Tests of AGARD Nozzles,,1974.
4. Dansby, T.      *Reynolds Number Effects on the Boattail Characteristics of a Simulated Nacelle at a Mach Number of 0.8*, Aerospace Research Laboratories (USA), Report ARL TR 74-0120, October 1974.
5. Calarese, W.      *Analytical Investigation of Transonic Viscous-Inviscid Interaction on Axisymmetric Boattailed Bodies With Jet Effects*, AF Flight Dynamics Laboratory (USA), Report, AFFDL TM 75-33-FX, January 1975.
6. Wang, H.C.  
Srokowski, A.      *Flowfield Determination for Axially Symmetric Configurations at Transonic Speeds*, New York University (USA), Report NYU-AA-73-11, June 1973.
7. Dougherty, N.S.Jr.  
Steinle, F.W.Jr.      *Transition Reynolds Number Comparisons in Several Major Transonic Tunnels*, AIAA Paper No.74-627, AIAA 8th Aerodynamic Testing Conference, Bethesda, Maryland, July 1974.
8.      *A Review of Current Research Aimed at the Design and Operation of Large Wind Tunnels*, AGARD Report No.68, March 1974.
9. McDonald, H  
Fish, R.W.      *Practical Calculations of Transitional Boundary Layers*, AGARDograph No.164, December 1972, pp 29-54.
10. Huffman, G.D.  
Zimmerman, P.R.  
Bennett, W.A.      *The Effect of Free-Stream Turbulence Level on Turbulent Boundary Layer Behaviour*, AGARDograph No.164, December 1972, pp.89-116.

FACILITY	MODEL ARRANGEMENT	TEST SECTION	BLOCKAGE *(OF AREA RATIO)	D <sub>MAX</sub> (mm)	L <sub>BODY</sub> D <sub>MAX</sub>
USA  AEDC (FULL SCALE MODEL)		4877 X 4877 mm PERFORATED WALLS 6% POROSITY	0.88%	250.4	14.92
USA  AEDC (SUBSCALE MODEL)		4877 X 4877 mm PERFORATED WALLS 6% POROSITY	0.02% + STING	39.1	14.45
USA  CFF (SUBSCALE MODEL)		508 X 711 mm PERFORATED WALLS 0-10% POROSITY	1.41%	39.1	14.45
USA  CFF (ARL MODEL)		508 X 711 mm PERFORATED WALLS 0-10% POROSITY	1.26%	76.2	10.0
USA  NASA		4877 mm (ACROSS FLATS) OCTAGONAL SLOTTED WALLS 4% POROSITY	0.148%	152.4	10.67
NETHERLANDS  NLR		270 X 270 mm SLOTTED TOP AND BOTTOM WALLS 11% POROSITY	7.0%	80	10.63 15.0
FRANCE  ONERA		800 X 900 mm PERFORATED TOP AND BOTTOM WALLS 24% POROSITY	*0.007 0.011 0.016	80 100 120	- - -
UNITED KINGDOM  RR		534 mm (ACROSS FLATS) OCTAGONAL SLOTTED WALLS 11% POROSITY	*0.034	101.6	-

\*RATIO OF MODEL AREA TO TUNNEL AREA

Fig.1 Facility/model arrangements



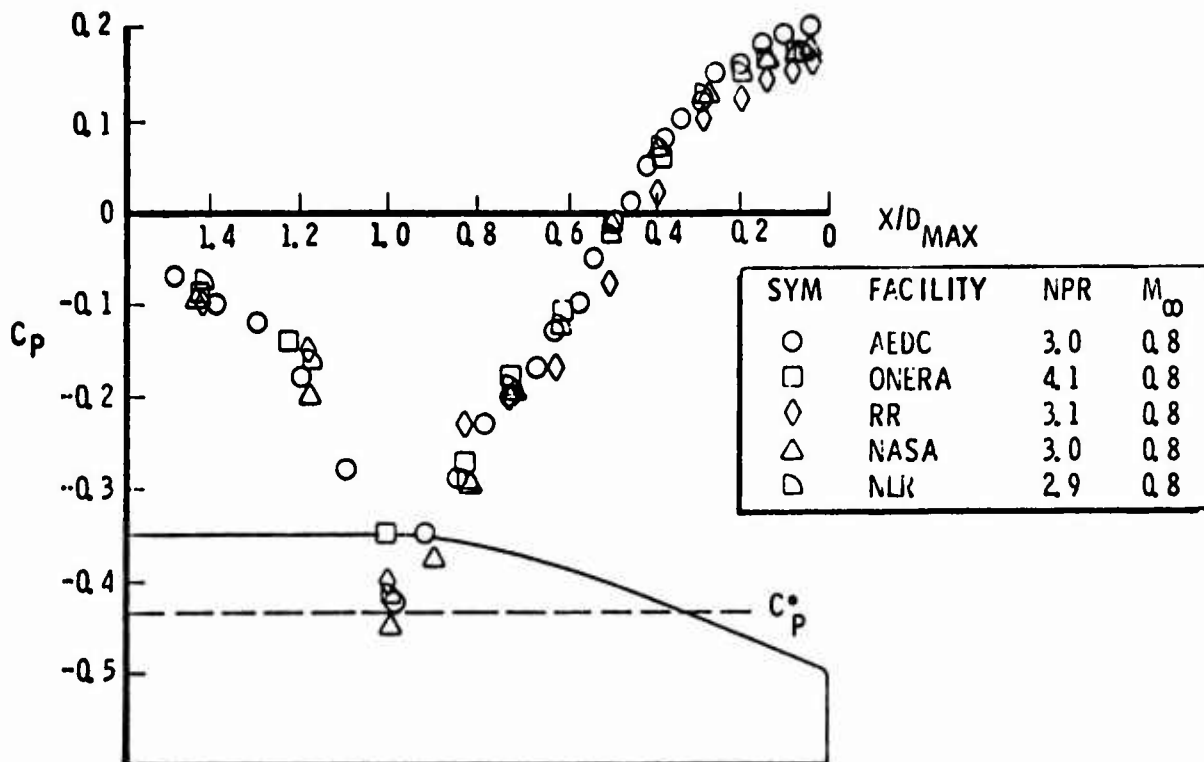


Fig.2(a) Model surface pressure distributions in different facilities  
15° boattail,  $M_\infty = 0.80$

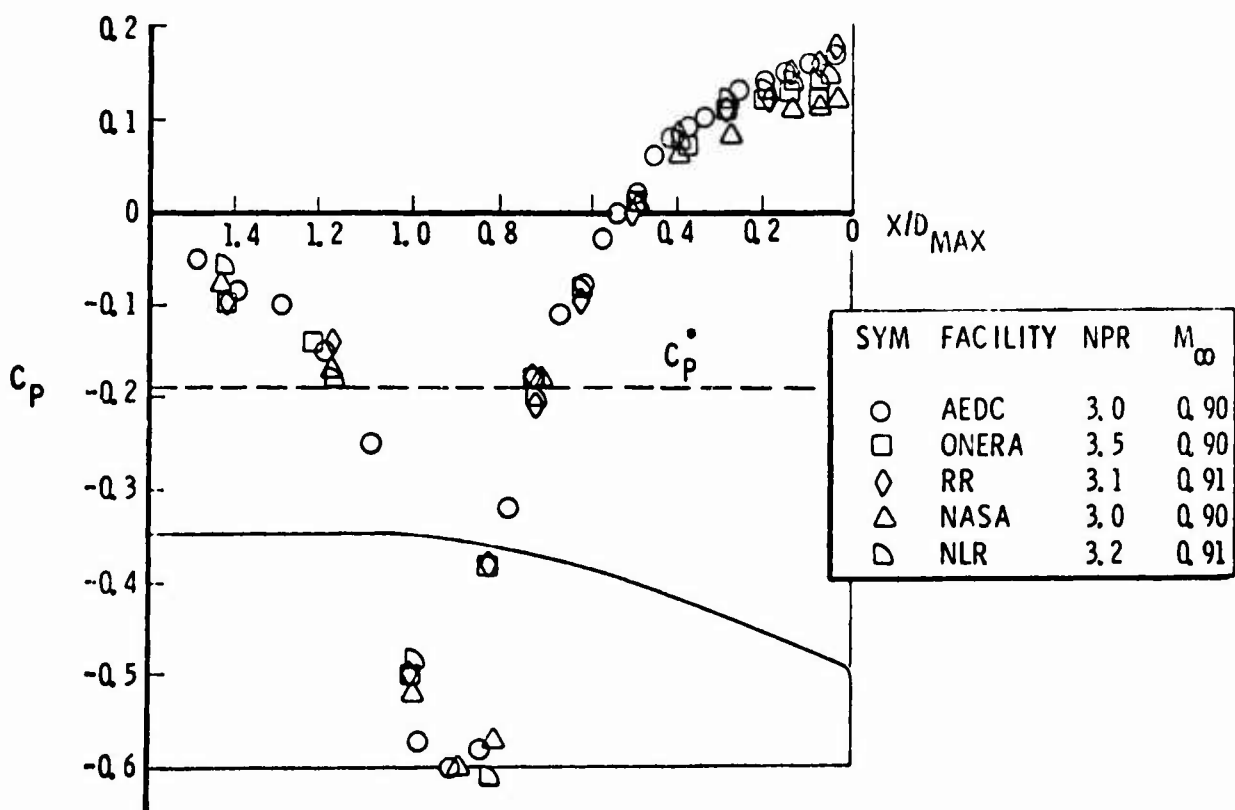


Fig.2(b) Model surface pressure distributions in different facilities  
15° boattail,  $M_\infty = 0.90$  to  $0.91$

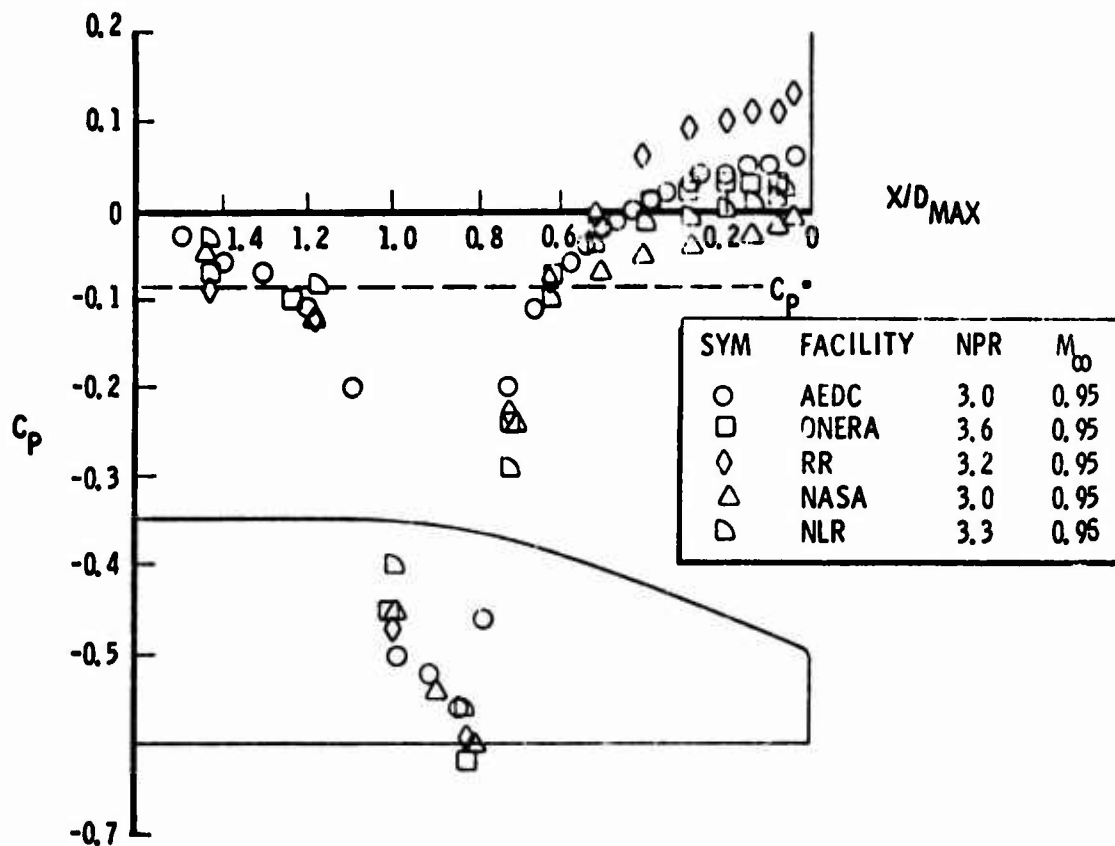


Fig.2(c) Model surface pressure distributions in different facilities  
 $15^\circ$  boattail,  $M_\infty = 0.95$  to  $0.96$

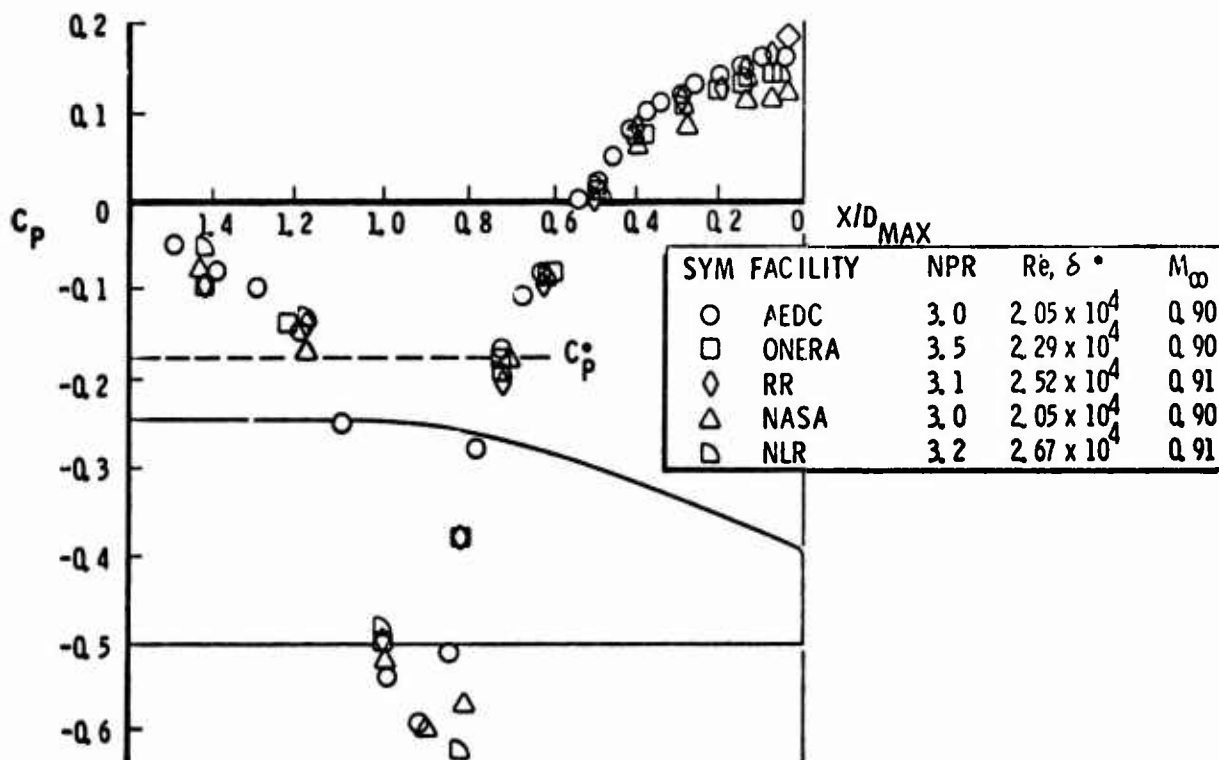


Fig.2(d) Model surface pressure distributions in different facilities  
 $15^\circ$  boattail,  $Re_{\delta^*} = 2.05 \times 10^4$  to  $2.67 \times 10^4$



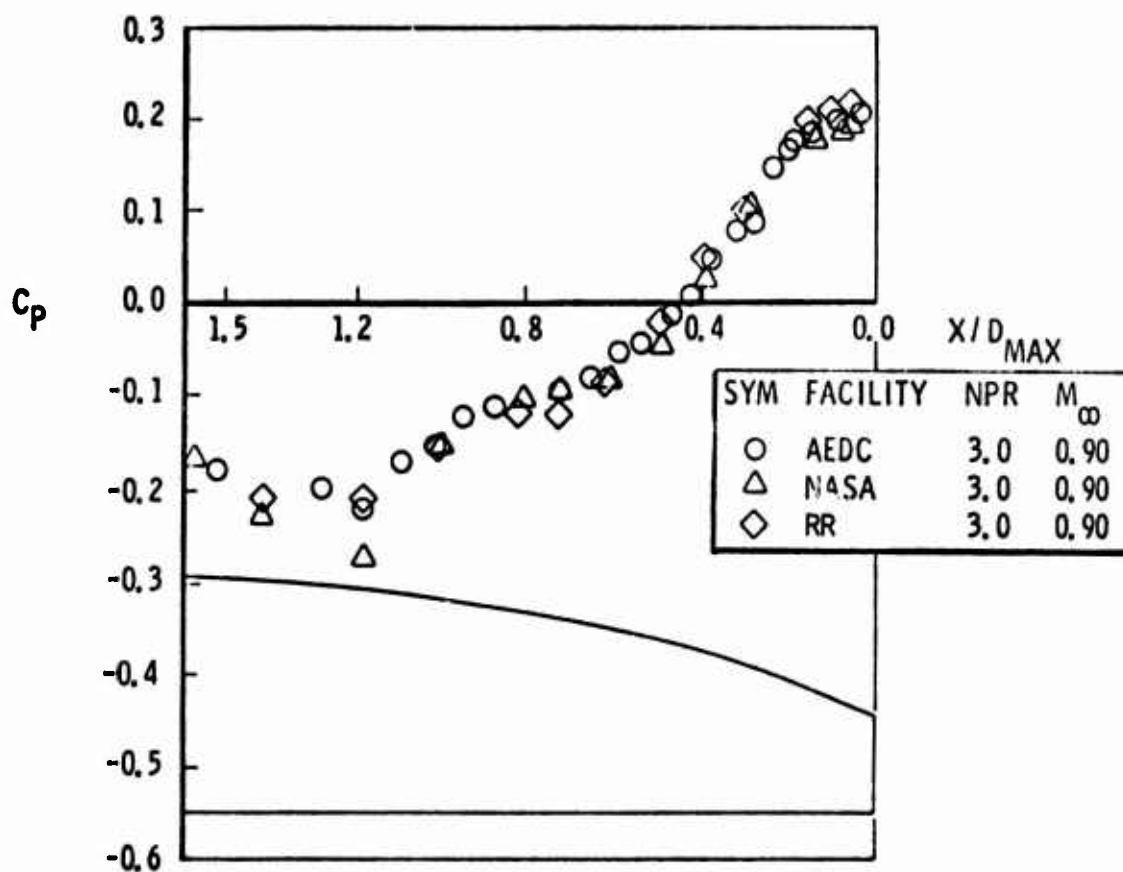


Fig.2(e) Model surface pressure distributions in different facilities  
 $10^\circ$  boattail,  $M_\infty = 0.90$

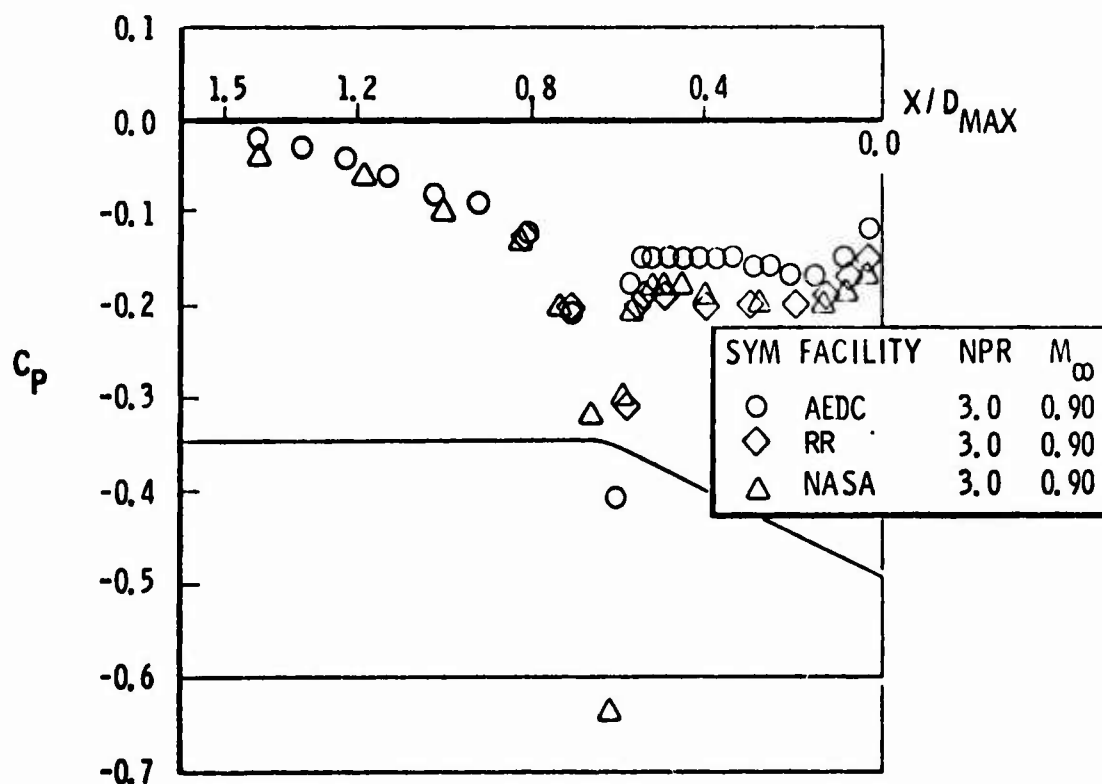


Fig.2(f) Model surface pressure distributions in different facilities -  $25^\circ$  boattail,  $M_\infty = 0.90$

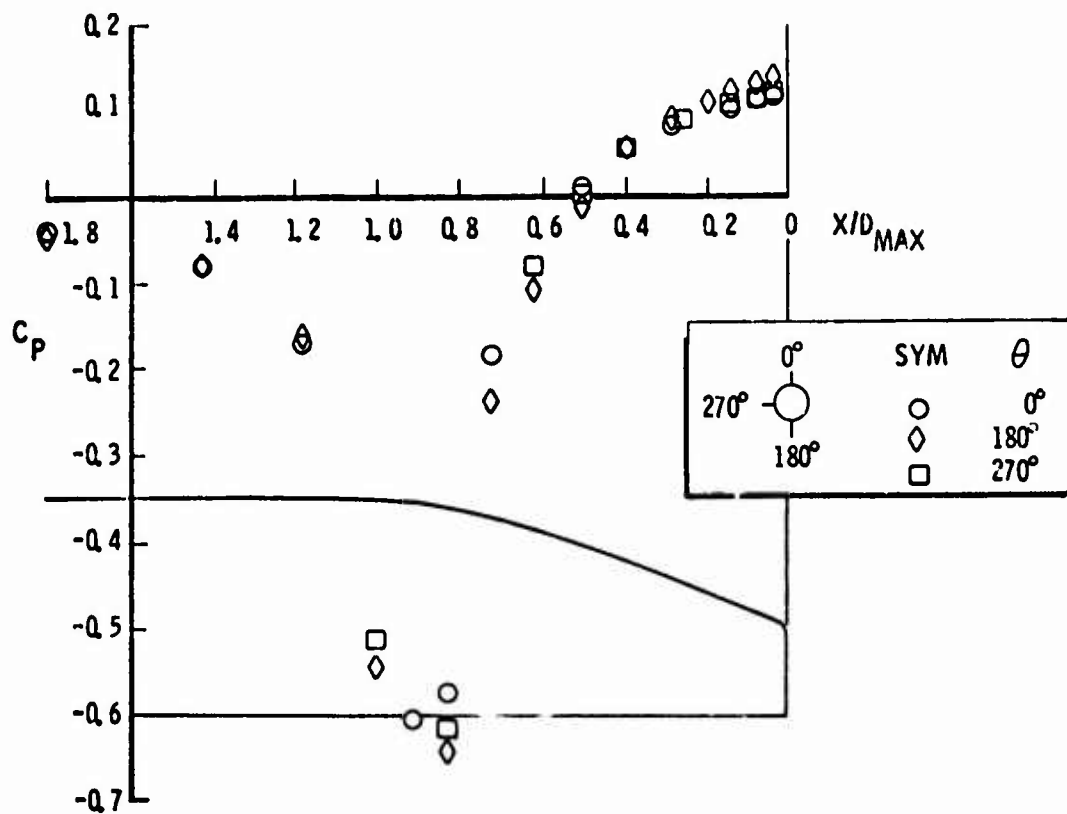


Fig.3 Asymmetric flow effects NASA facility, 15° boattail, NPR = 3.0,  $M_\infty = 0.90$

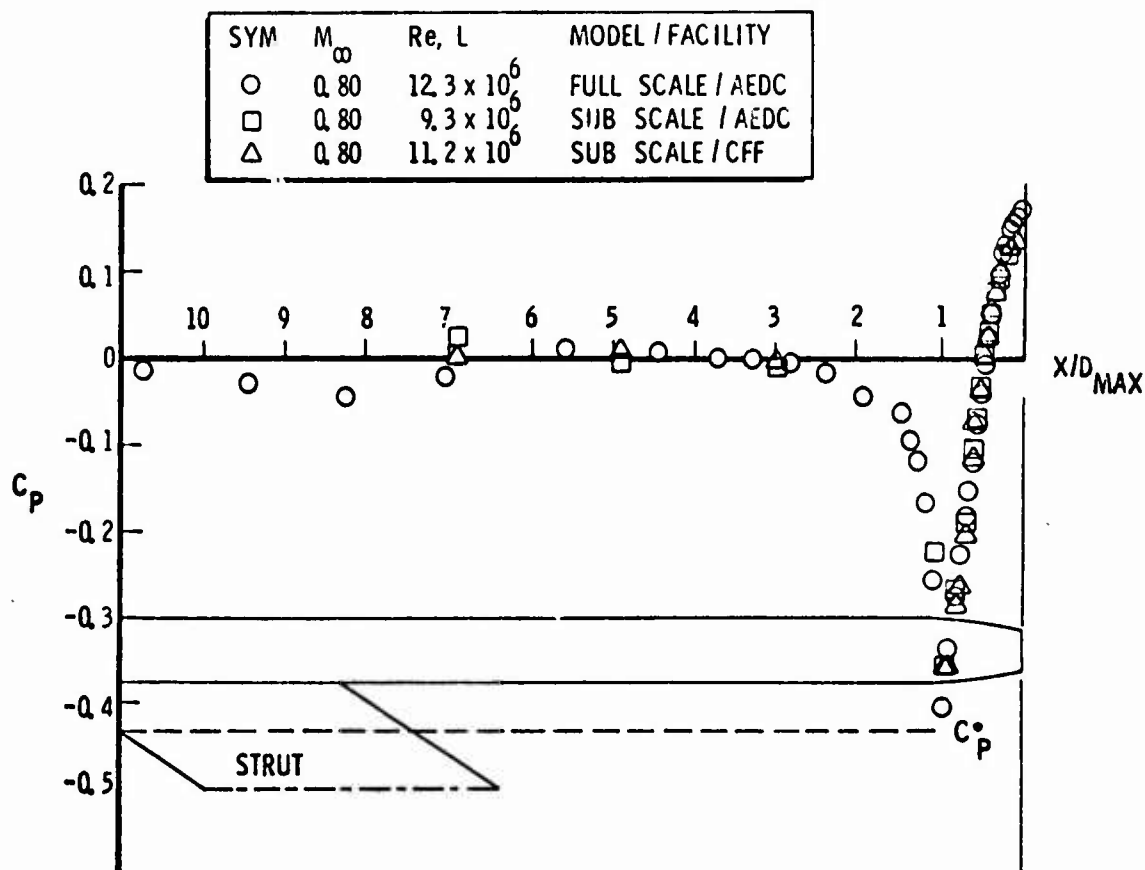


Fig.4(a) Surface pressure distributions on AEDC full scale and subscale models 15° boattail, NPR = 3.0,  $M_\infty = 0.80$

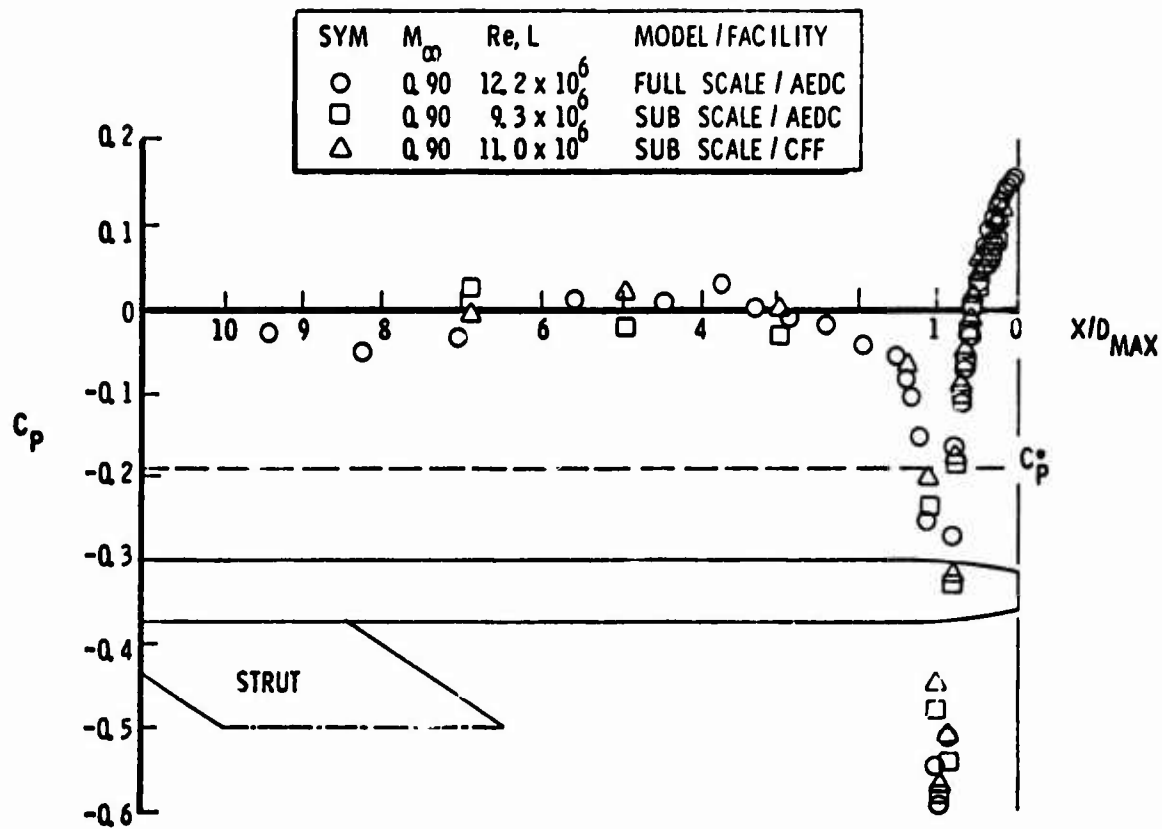


Fig.4(b) Surface pressure distributions on AEDC full scale and subscale models  
15° boattail, NPR = 3.0,  $M_\infty = 0.90$

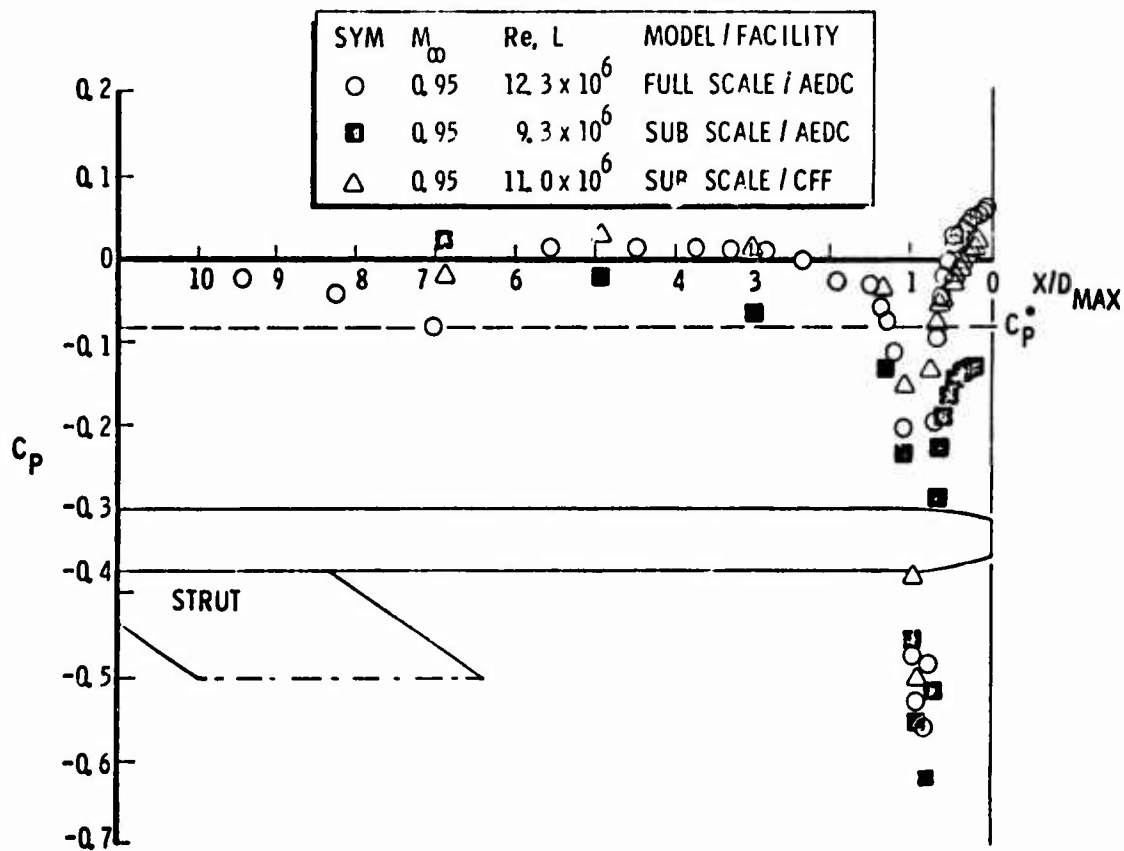


Fig.4(c) Surface pressure distributions on AEDC full scale and subscale models,  
15° boattail, NPR = 3.0,  $M_\infty = 0.95$

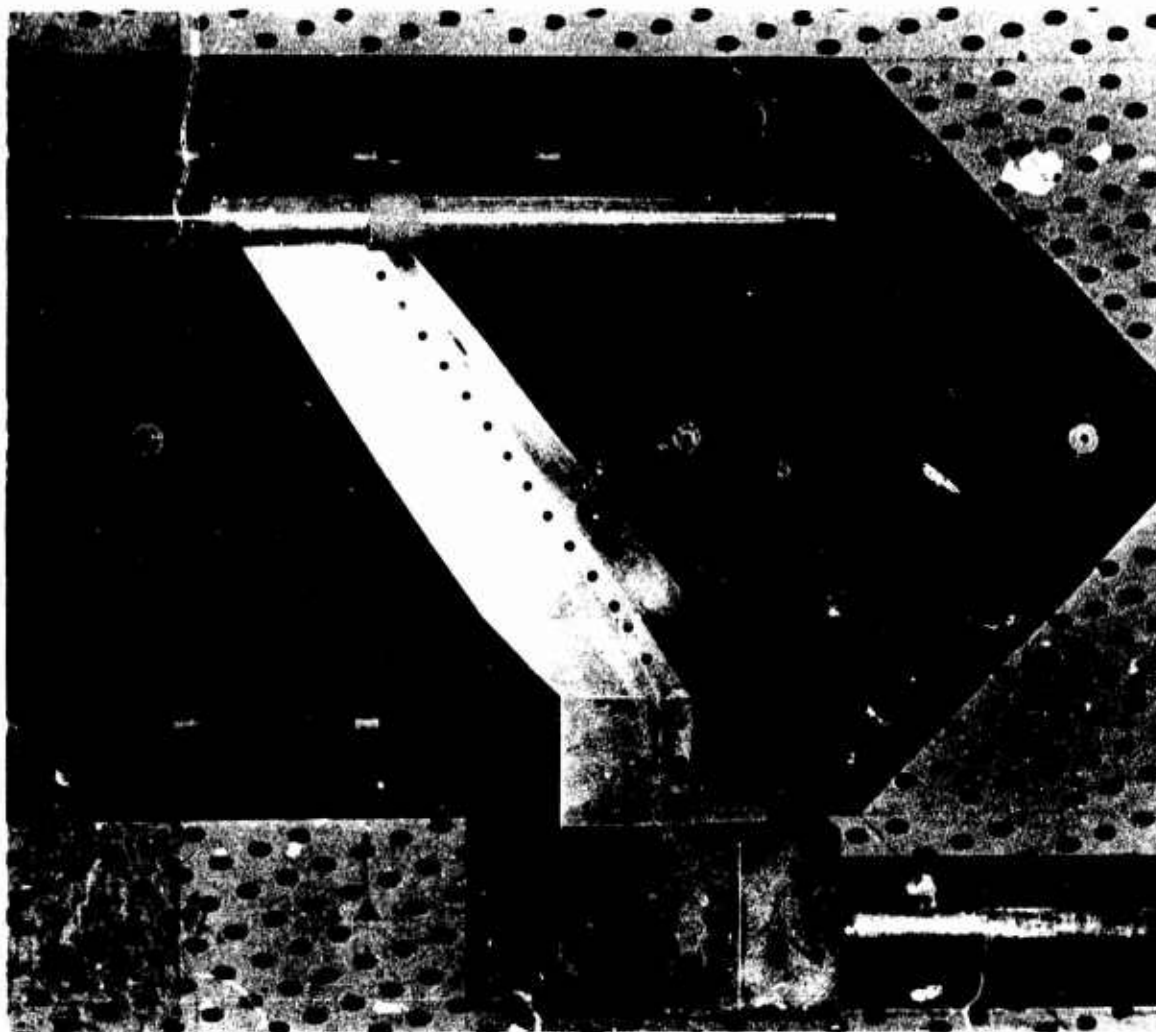


Fig.4(d) Photograph of subscale model installed in AEDC 16T tunnel

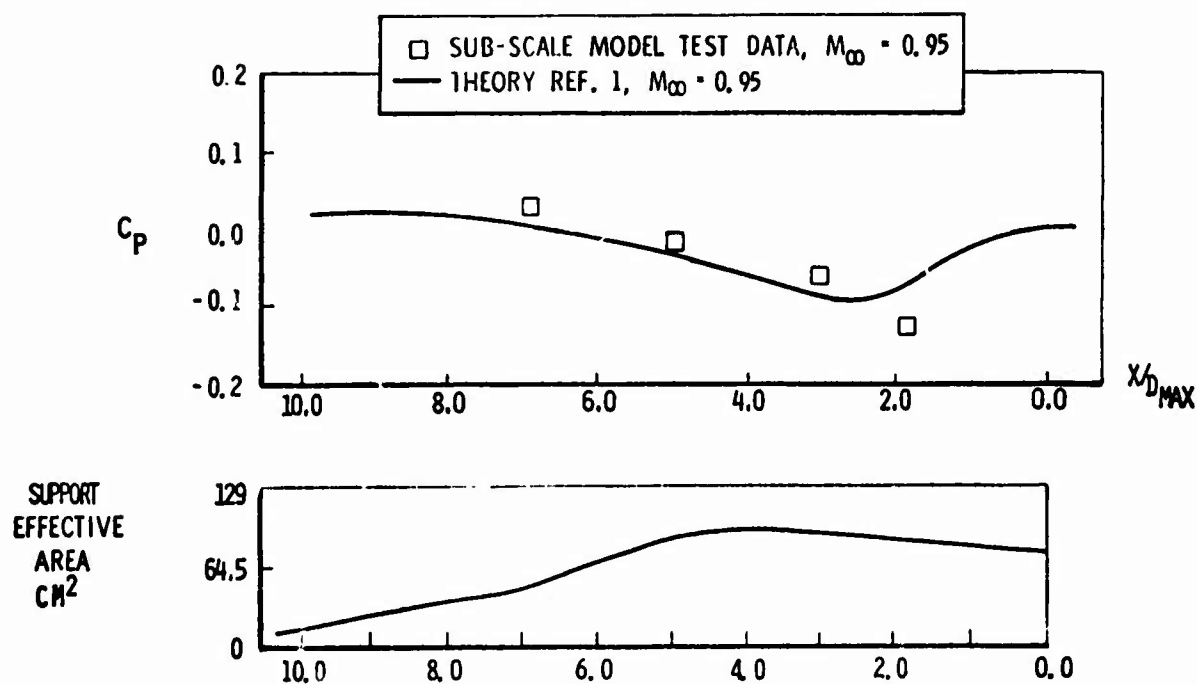


Fig.4(e) Calculated and measured  $C_p$  at  $M_\infty = 0.95$  due to sting-strut interference  
AEDC subscale model

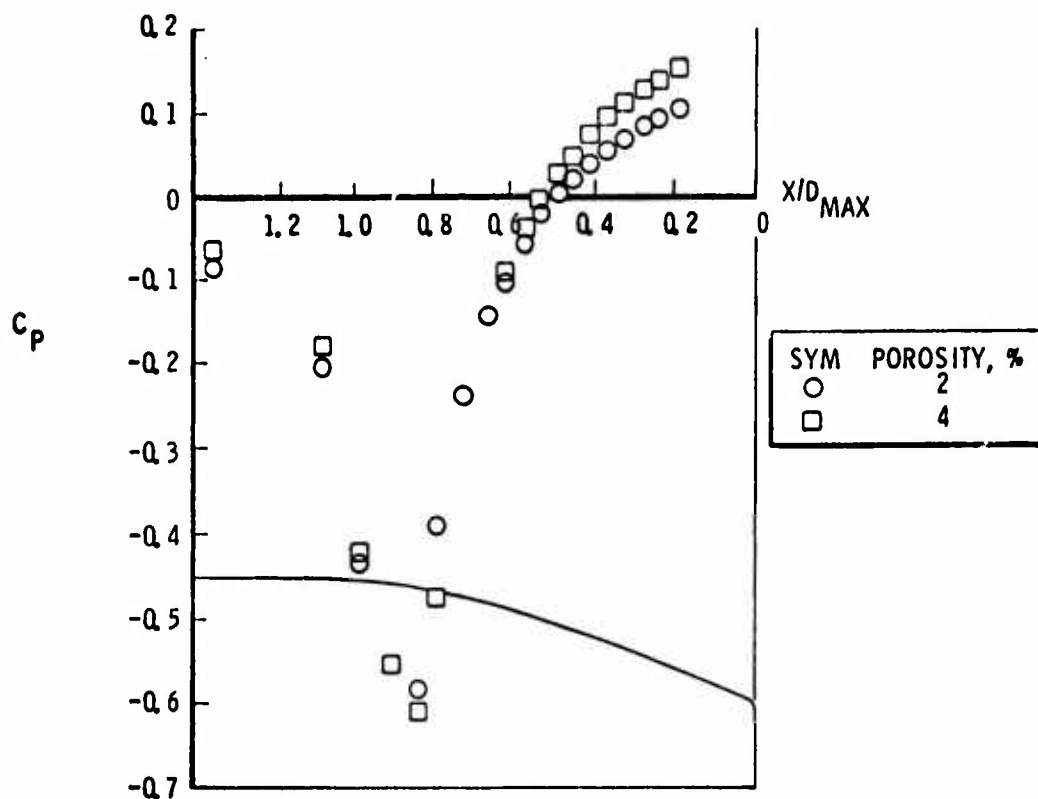


Fig.5 Surface pressure distributions on the AEDC subscale model in the CFF for two porosities  
 $15^\circ$  boattail,  $NPR = 3.0$ ,  $R_e L = 55.6 \times 10^6$ ,  $M_\infty = 0.90$

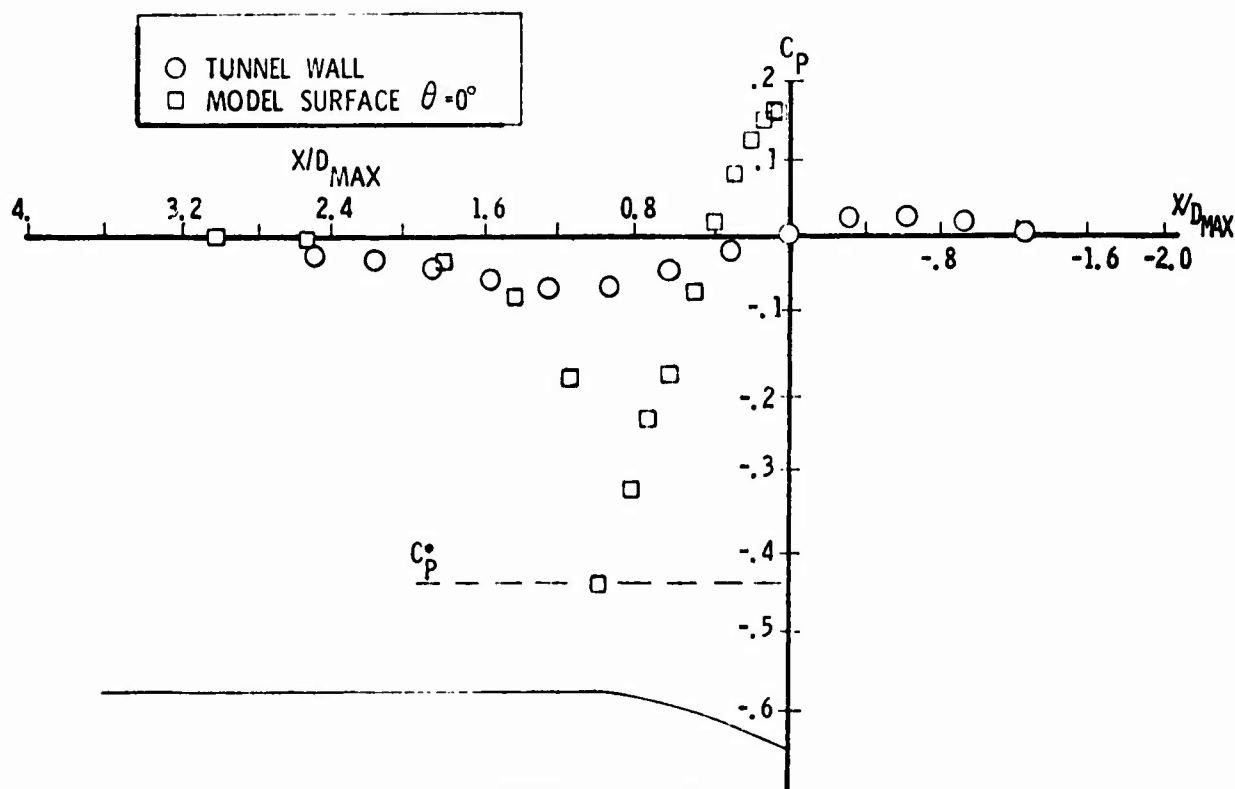


Fig.6(a) Model surface and tunnel wall pressure distributions in the NLR facility  
 $15^\circ$  boattail,  $M_\infty = 0.80$ , jet off,  $R_{WALL}/D_{MAX} = 1.68$

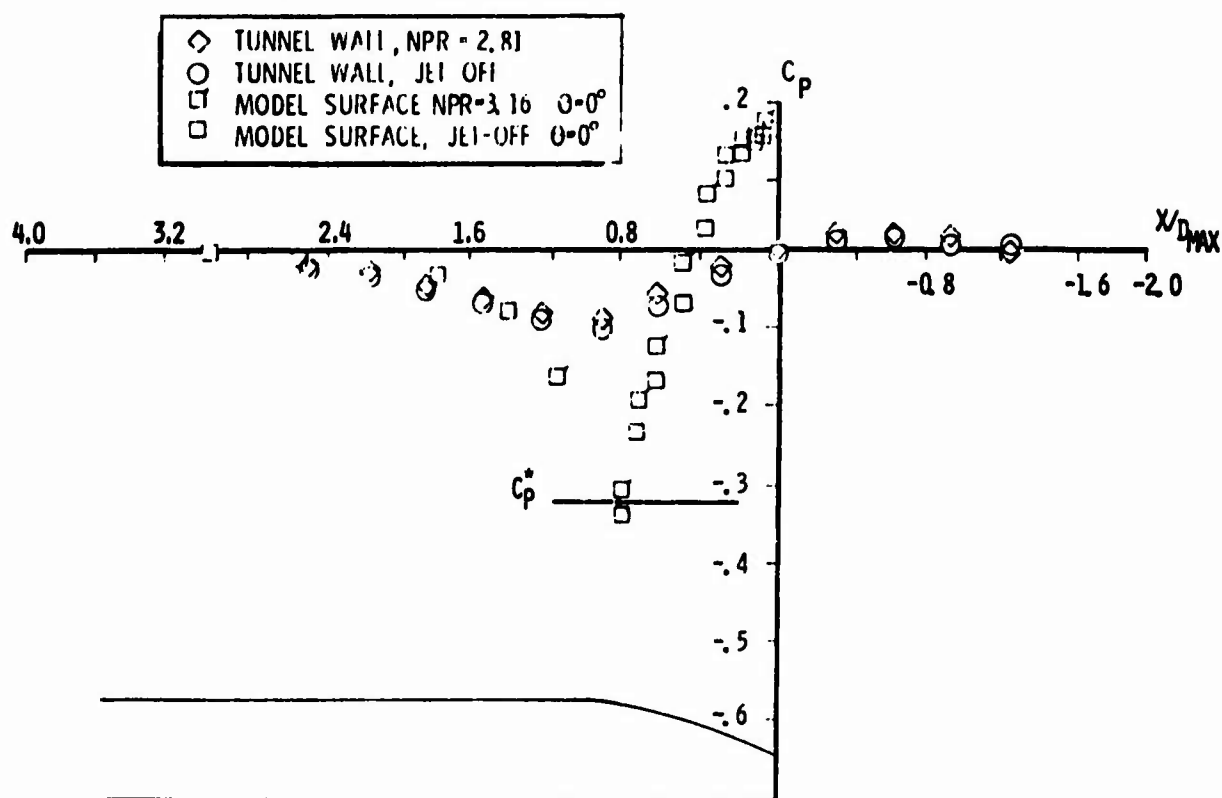


Fig.6(b) Model surface and tunnel wall pressure distributions in the NLR facility  
 $15^\circ$  boattail,  $M_\infty = 0.85$ , jet off & NPR = 3.16,  $R_{WALL}/D_{MAX} = 1.68$

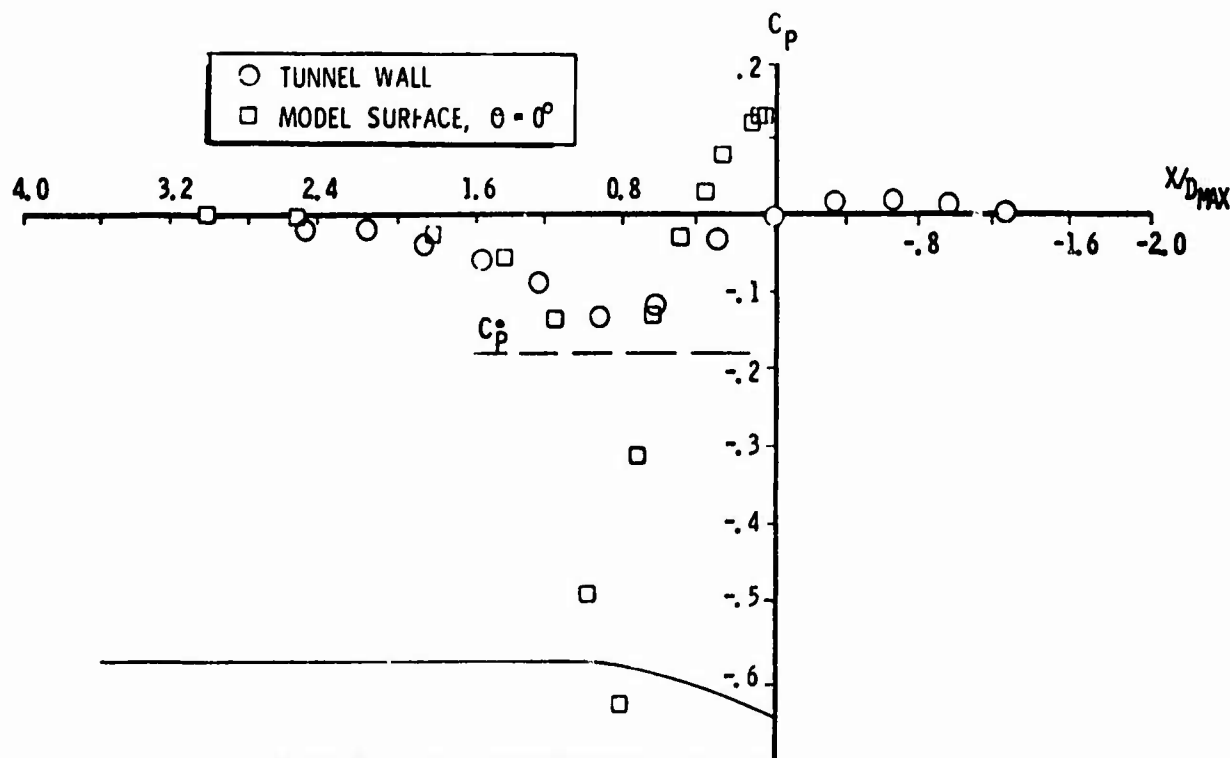


Fig.6(c) Model surface and tunnel wall pressure distributions in the NLR facility  
 $15^\circ$  boattail,  $M_\infty = 0.90$ , jet off,  $R_{WALL}/D_{MAX} = 1.68$

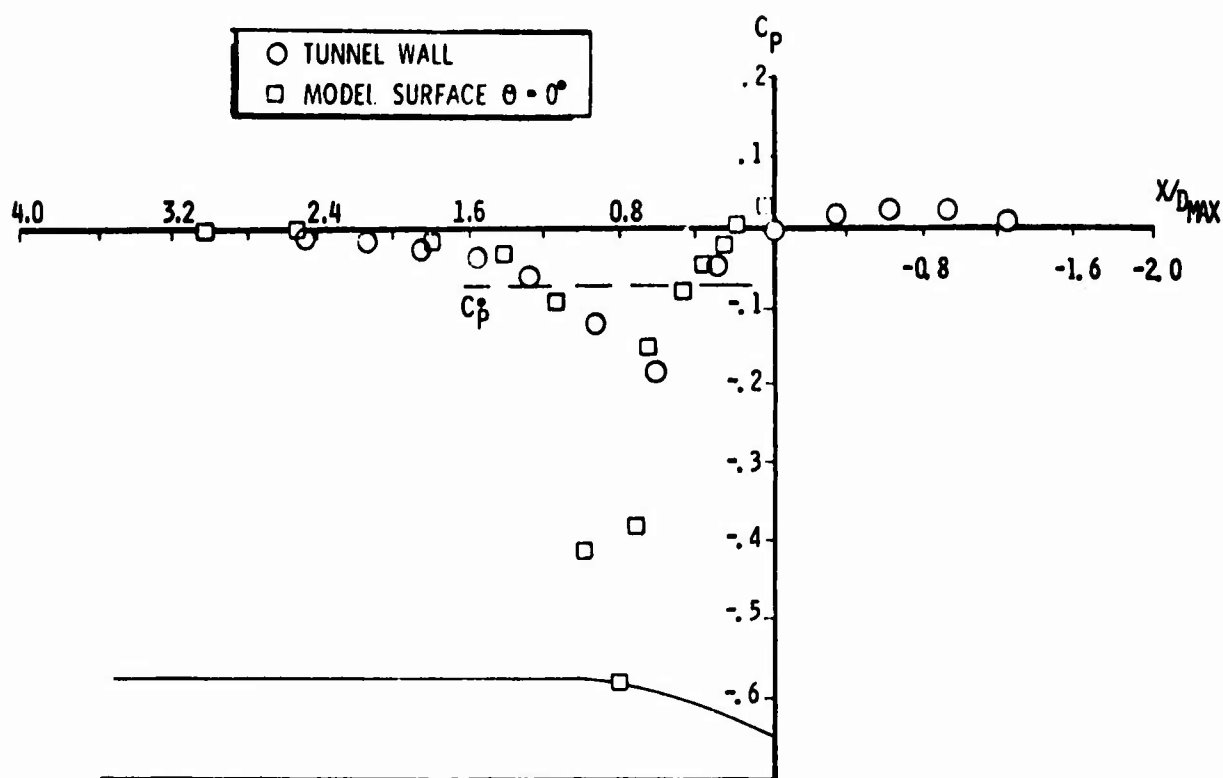


Fig.6(d) Model surface and tunnel wall pressure distributions in the NLR facility  
 $15^\circ$  boattail,  $M_\infty = 0.96$ , jet off,  $R_{WALL}/D_{MAX} = 1.68$

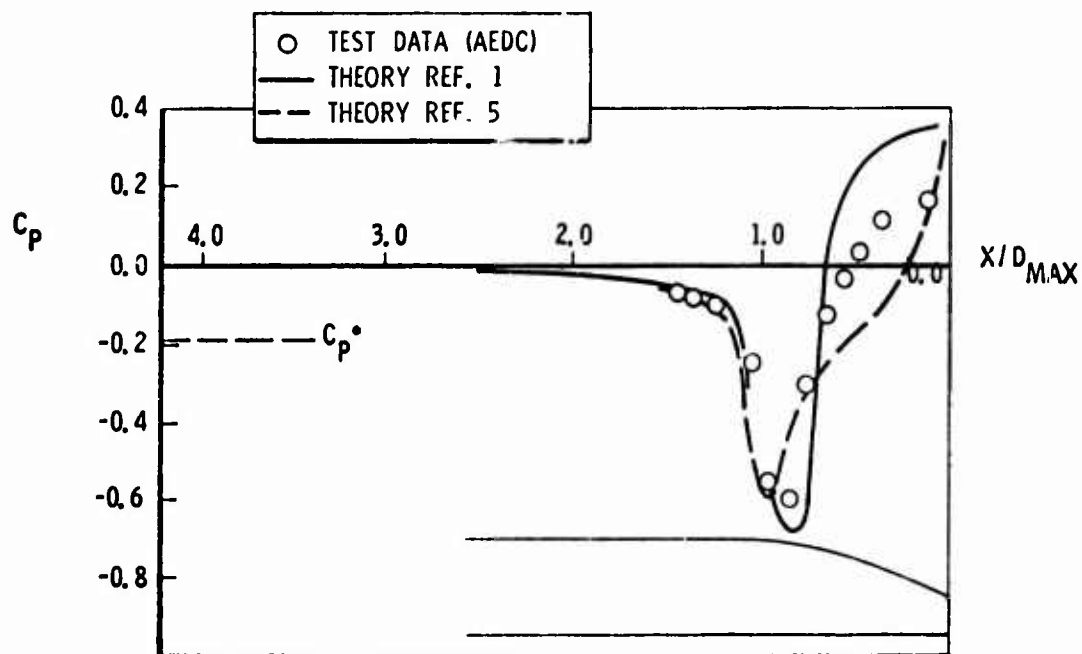


Fig.7(a) Comparison of predicted body pressures to experimental data,  
 $15^\circ$  boattail,  $M_\infty = 0.90$

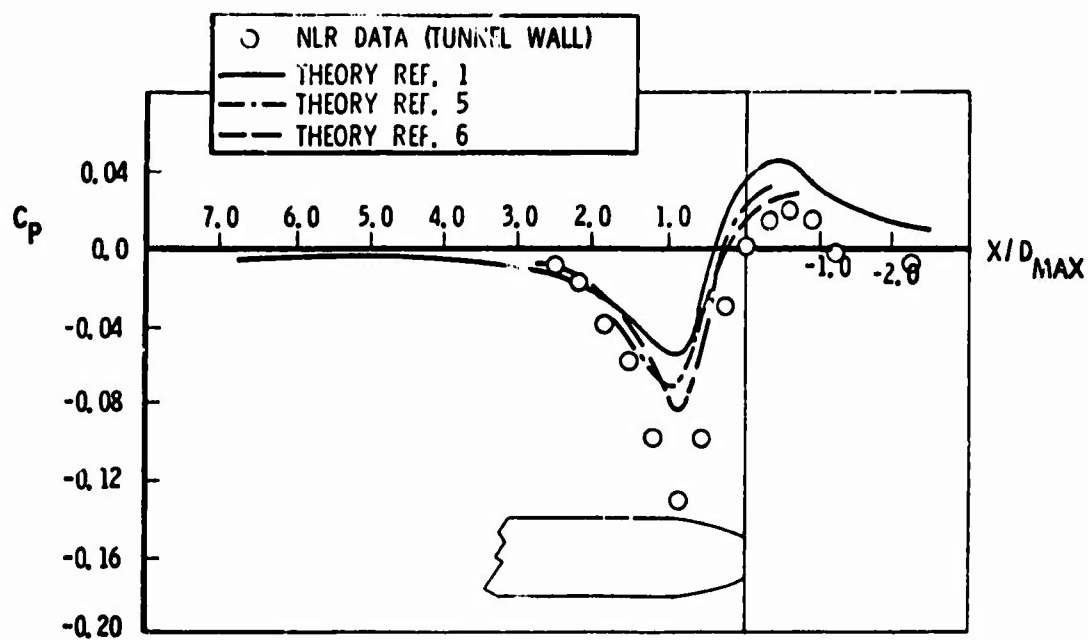


Fig.7(b) Calculated and measured wall pressure distributions for the NLR facility,  
 $M_\infty = 0.90$ ,  $R_{WALL}/D_{MAX} = 1.68$

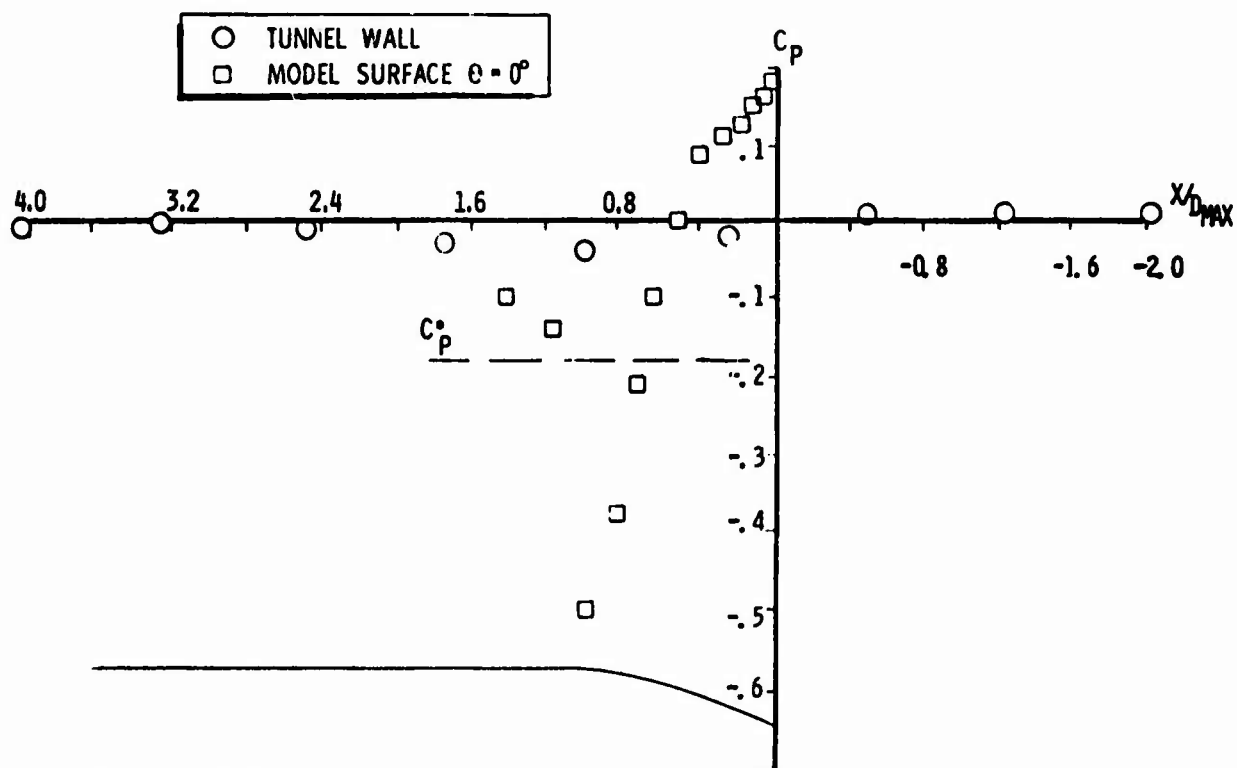


Fig.8(a) Model surface and tunnel wall pressure distributions in the RR facility,  
 $15^\circ$  boattail,  $M_\infty = 0.91$ ,  $R_{WALL}/D_{MAX} = 2.67$



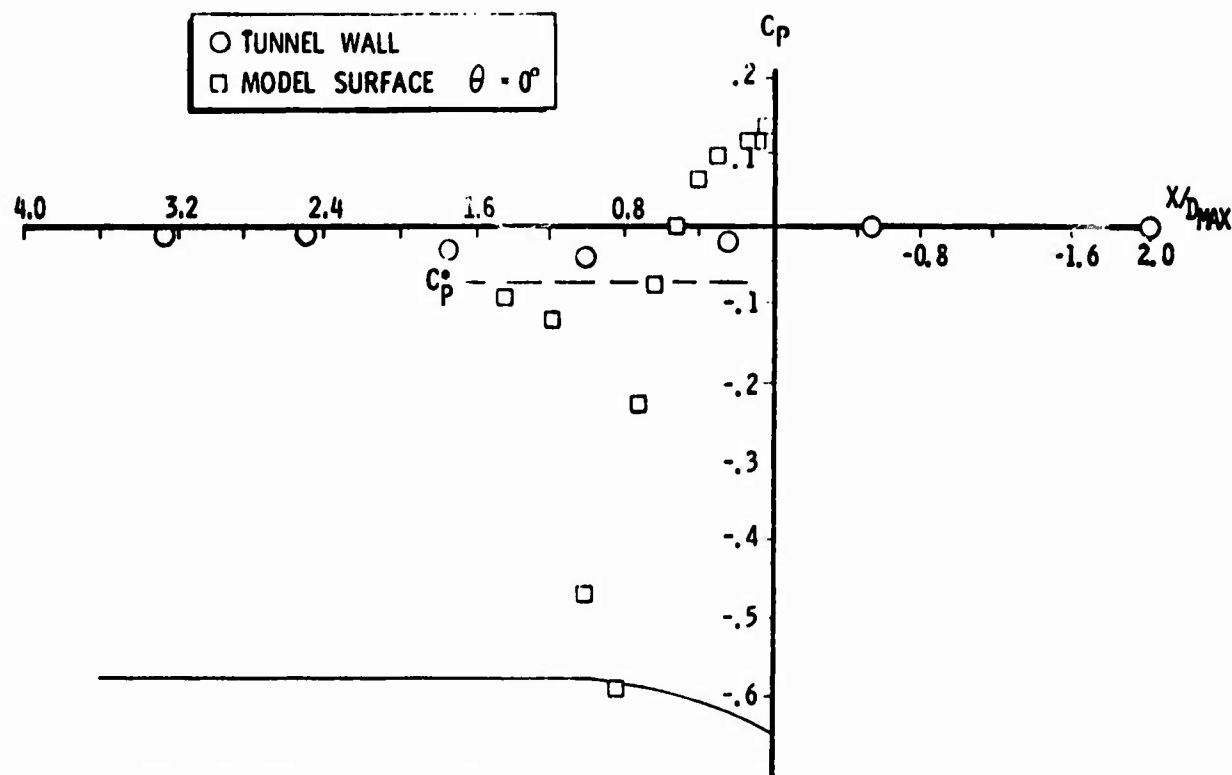


Fig.8(b) Model surface and tunnel wall pressure distributions in the RR facility,  
 $15^\circ$  boattail,  $M_\infty = 0.95$ ,  $R_{WALL}/D_{MAX} = 2.67$

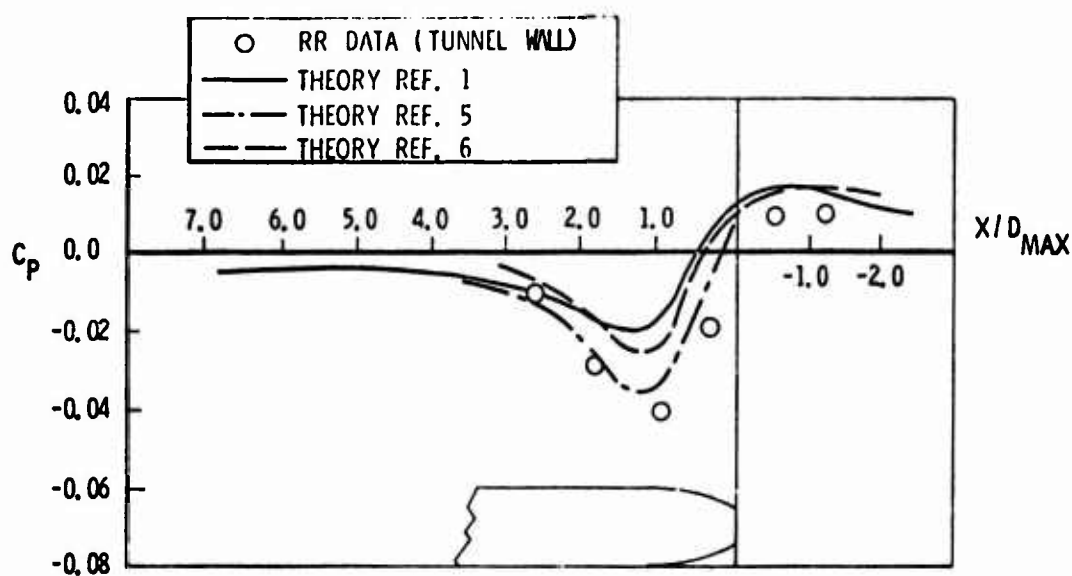


Fig.9 Calculated and measured wall pressure distributions for the RR facility,  
 $M_\infty = 0.91$ ,  $R_{WALL}/D_{MAX} = 2.67$

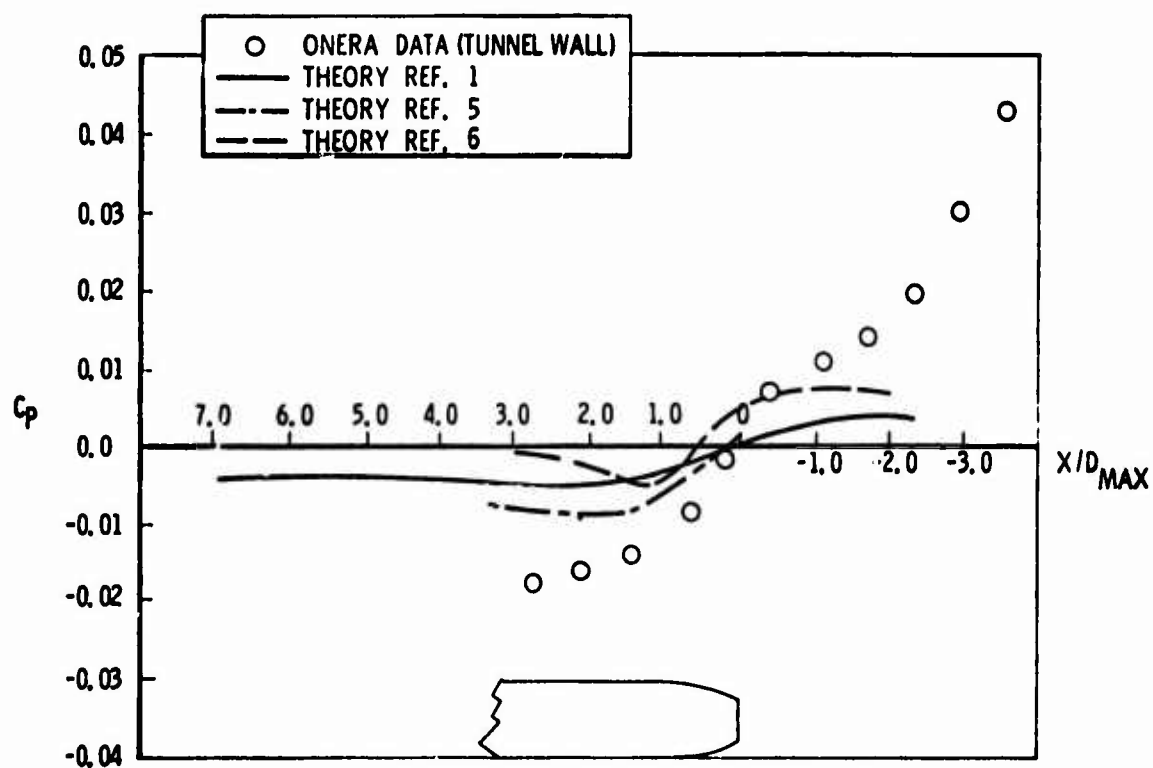


Fig.10 Calculated and measured wall pressure distributions for the ONERA facility,  
 $M_\infty = 0.90$ ,  $R_{WALL} D_{MAX} = 5.27$

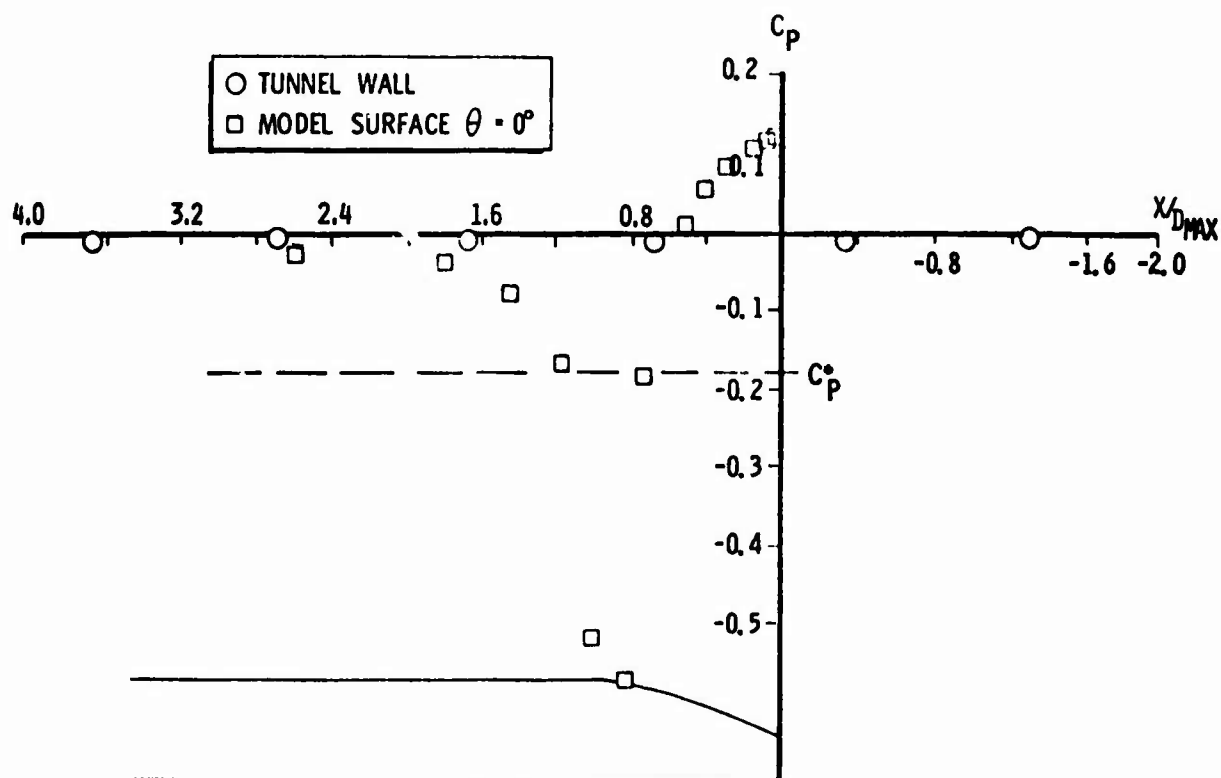


Fig.11(a) Model surface and tunnel wall pressure distributions in the NASA facility  
 $15^\circ$  boattail,  $M_\infty = 0.90$ ,  $R_{WALL}/D_{MAX} = 14.4$

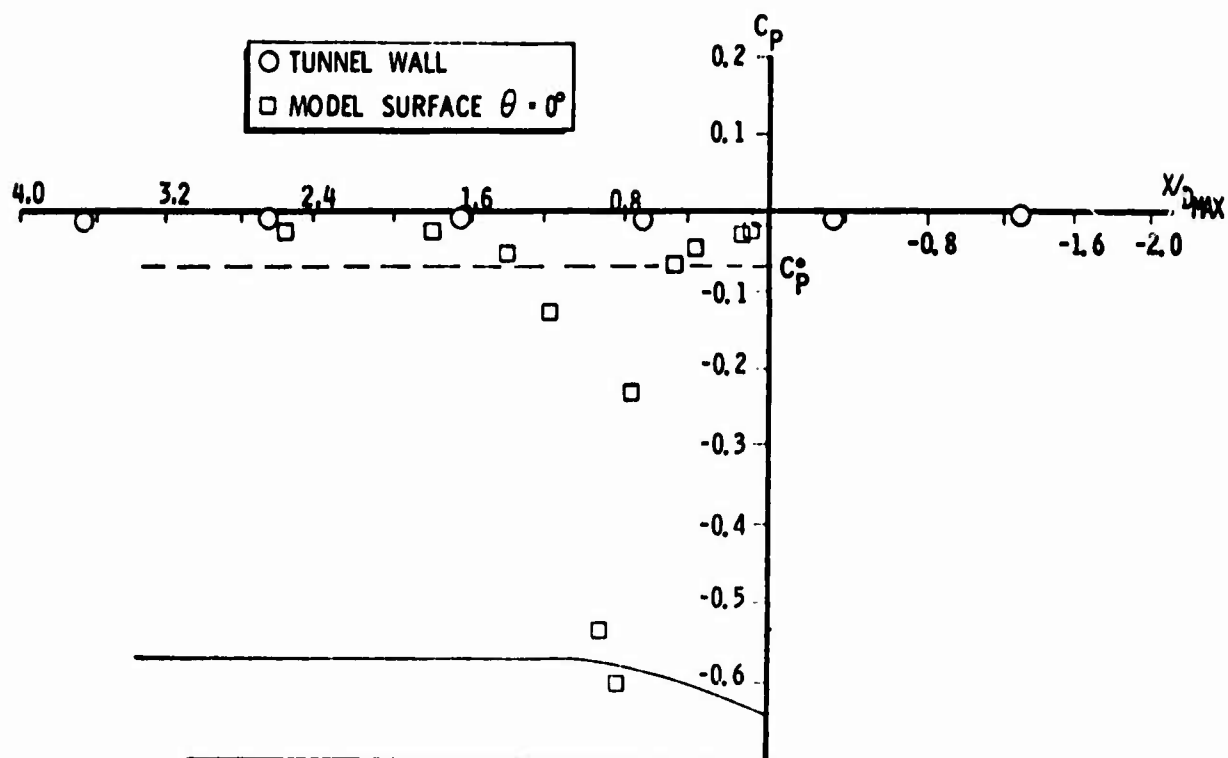


Fig.11(b) Model surface and tunnel wall pressure distributions in the NASA facility  
 $15^\circ$  boattail,  $M_\infty = 0.95$ ,  $R_{WALL}/D_{MAX} = 14.4$

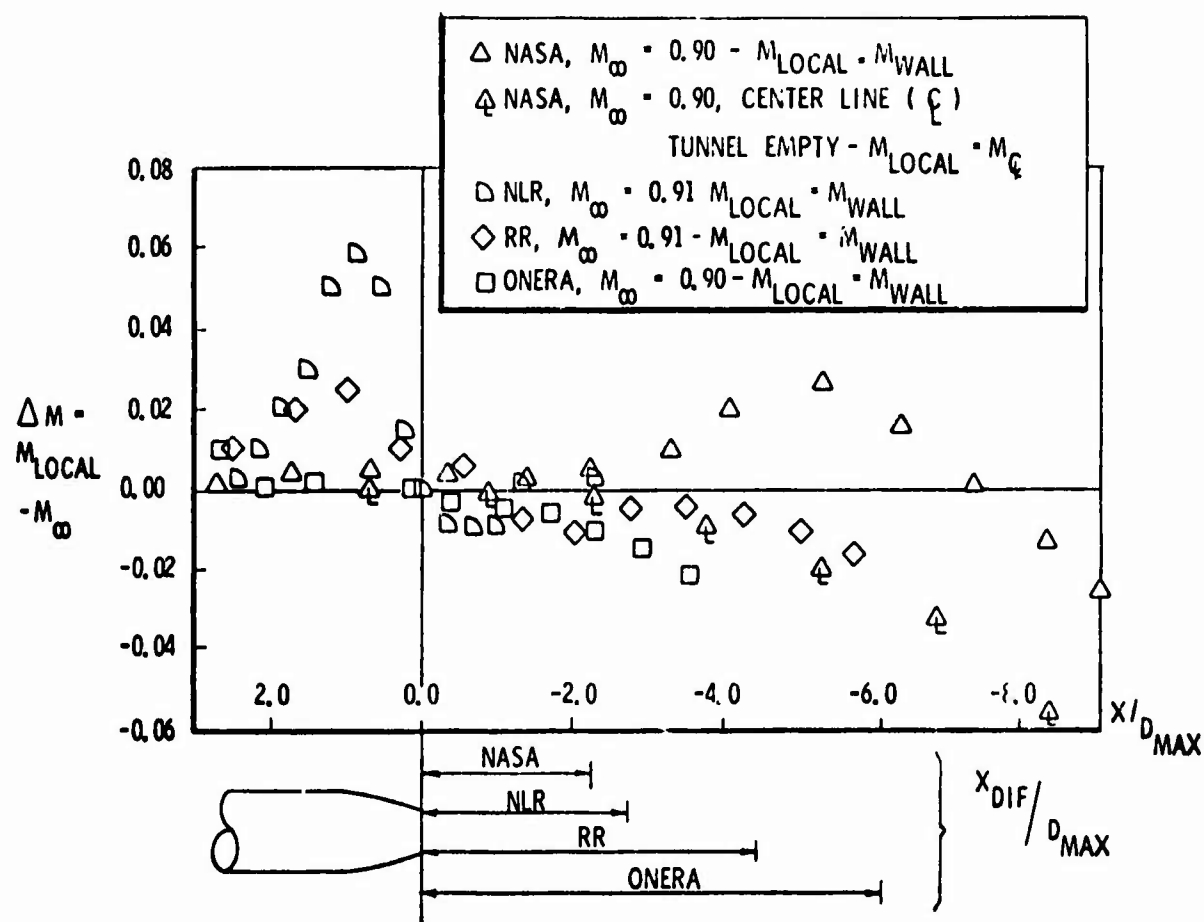


Fig.12 Mach number distributions in four facilities:  
 $X_{DIF}/D_{MAX}$  = distance from nozzle exit to diffuser

# FORE- AND AFTBODY FLOW FIELD INTERACTION WITH CONSIDERATION OF REYNOLDS NUMBER EFFECTS

Felix Aulehla and Geert Besigk

Messerschmitt-Bölkow-Blohm GmbH  
Unternehmensbereich Flugzeuge  
D 8 München 80  
Postfach 801160  
W. Germany

## SUMMARY

Recent aftbody drag results obtained from different transonic wind tunnel measurements showed such large increases in aftbody pressure drag with increasing Reynolds number that extrapolation to full scale became questionable. The present paper tries to clarify this unexpected Reynolds number effect with the aim of contributing to improved testing techniques.

An analysis of a wind tunnel investigation at Mach number 0,8 on a series of axisymmetric bodies showed as main result that varying Reynolds number produced in the wind tunnel opposite changes in pressure drag on fore- and aftbody, respectively. It is explained that this result probably was caused by small deviations in free stream static pressure to which part-models are by an order of magnitude more sensitive than complete models. Therefore, unless a wind tunnel is calibrated to considerably better standards than usual it is recommended to take into account the compensating effects on the forebody; the buoyancy corrections due to pressure gradients, however, have to be considered in addition. In the present measurements the changes of the mean wall pressures seemed to correlate with the corresponding changes on the model and were used as a correction term.

Finally it is pointed out that modifications in aftbody geometry affect forebody drag. Results from the commonly used aftbody test rigs with forebodies fixed to the ground therefore need appropriate corrections.

## LIST OF SYMBOLS

A	Cross-section of body	$q_0$	Free stream dynamic pressure, $0,5\rho_0 V_0^2$
$A_{\max}$	Maximum cross-section of body	R	Radius of body
$C_D$	Drag coefficient, referred to maximum body cross-section area, $D/q_0 A_{\max}$	Re	Reynolds No., based on length of body; $Re_1$ = lowest, $Re_3$ = highest value tested
$C_{DF}$	Friction drag coefficient	S	Wetted surface
$C_{DP}$	Pressure drag coefficient	$V_0$	Free stream velocity
$C'_{DP}$	$(2\pi/A_{\max}) \int_{R=0}^R C_P R dR$	x	Axial distance from model nose
$C_{DT}$	Total drag coefficient, $C_{DP} + C_{DF}$	$(x/L)_N$	Relative axial distance from boattail shoulder
$C_{DT0\%}$	$C_{DT}$ of profile with zero thickness	$\beta_C$	Boattail chord angle
$C_P$	Pressure coefficient, $(P - P_0)/q_0$	$\beta_T$	Boattail terminal angle
$\bar{C}_P$	Mean value of $C_P$	$\delta^*$	Boundary layer displacement thickness
$\bar{\bar{C}}_P$	Mean value of $\bar{C}_P$ from all test runs	SUBSCRIPTS AND ABBREVIATIONS	
$\Delta C_P$	Difference in $C_P$ relative to intermediate Reynolds number $Re_2$ , $C_P Re - C_P Re_2$ , except fig. 13		
$\overline{\Delta C_P}$	Mean value of $\Delta C_P$ over $0 \leq x/L \leq 1,0$	AB	Aftbody
D	Drag	CB	Complete body, AB + FB
$\Delta D$	Drag difference	FB	Forebody
L	Ideal length of body (beyond sting intersection, to $R = 0$ )	HB	Halfbody, AB or FB
$M_0$	Free stream Mach number	i	internal
		W/T	Wind tunnel
		$\phi$	Diameter
		$\infty$	True free stream conditions

## 1. INTRODUCTION

The correlation of wind tunnel results obtained from small scale models with full scale flight measurements is an old problem in drag determination since the real flight Reynolds numbers can be very seldom achieved. In the past, therefore, one attempted to build models as big as possible and also to cover large Reynolds number ranges. This led to the construction of huge wind tunnels and, for the high densities and Reynolds numbers respectively, to enormous installed power levels. In order to raise the accuracy of measurement, one also tried to weigh only a minimum of wetted surfaces when making force measurements, i.e. it was attempted not to weigh the complete model but only a part of it. When measuring aftbody drag, therefore, the forebody and also the wing and tailplanes were fixed to the ground.

The Reynolds number investigations which were conducted in these facilities (wind tunnel plus test rig) did not always lead to the hoped for clarification of the Reynolds number influence. On the contrary, some of these measurements produced such unexpected results that fundamental doubts arose about their validity. This paper attempts to clarify some of these dubious Reynolds number effects and also to illustrate basic interrelations, thereby contributing to a better drag synthesis as well as to an improved testing technique.

## 2. UNEXPECTED REYNOLDS NUMBER INFLUENCE

Aftbody drag levels recently measured with different models in different tunnels showed an increase in aftbody pressure drag coefficient with increasing Reynolds number (fig. 1). Adding friction reduces this increase but does not eliminate it. However, a decreasing tendency had been expected similar to the trend of the fully turbulent flat plate or similar to profile drag coefficients of slender airfoils (compare e.g. profile drag values computed by Squire and Young, ref. 1). The rapid rise of aftbody drag coefficient with Reynolds number makes it questionable whether these data can be extrapolated to full scale. Even when, as widely practised, one uses only differences in drag from wind tunnel measurements, the problem regarding the drag difference between aftbody No. 1 and No. 3 remains essentially the same, because curves 1 and 3 are not parallel to each other.

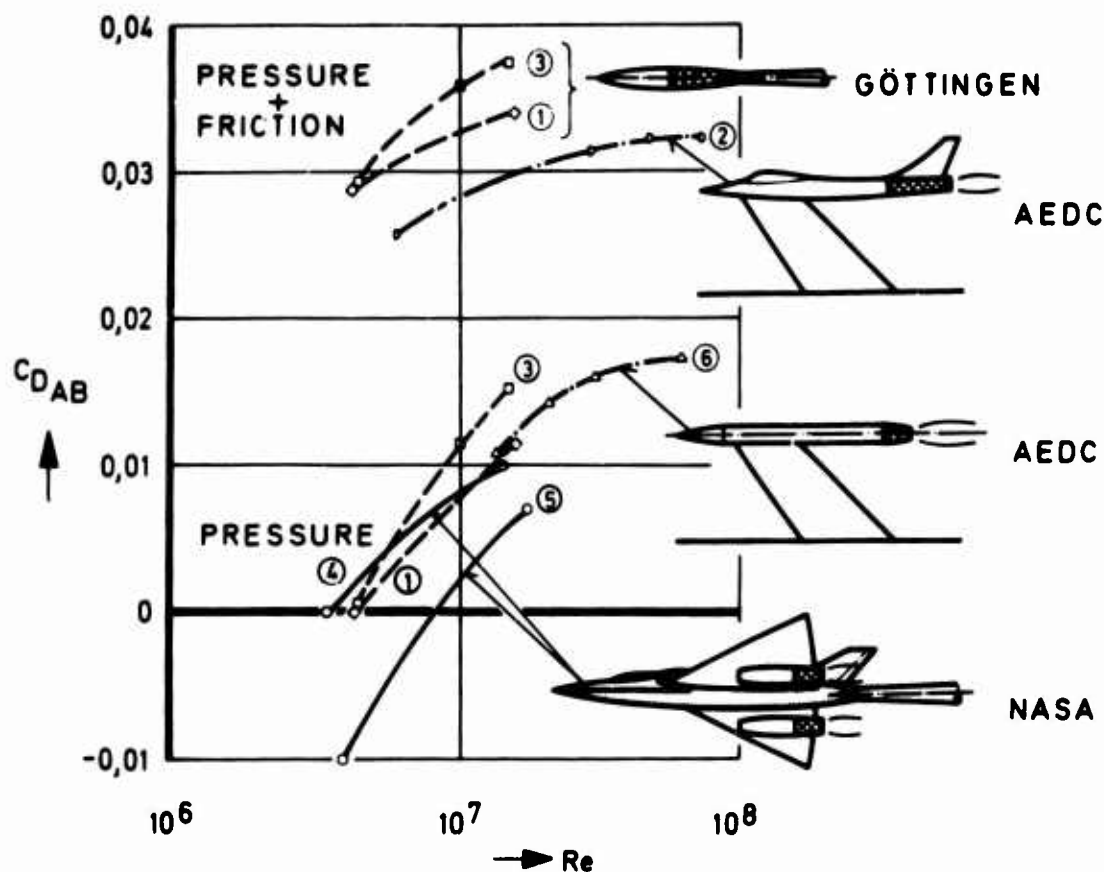


Fig. 1 Reynolds number effect on aftbody drag

Curve No.	$M_0$	$\frac{P_{T1}}{P_0}$		Ref.
1 3	$\left. \begin{array}{l} 0,8 \\ 0,8 \end{array} \right\}$	-	AB 1 } axisym. body AB 3 }	2 3
2	0,9	3	twin jet fighter	4
4 5	$\left. \begin{array}{l} 0,6 \\ 0,9 \end{array} \right\}$	?	J-85 nacelle on F-160, $\theta_T = 16^\circ$	5
6	0,6	3	axisym. body, $\theta_C = 10^\circ$	6

Fig. 2 Model configurations

Curves 4 and 5 have been obtained with two wind tunnel models of the F-106 with underwing installed J-85 nacelles in the 8 ft. x 6 ft. supersonic wind tunnel of NASA Lewis (ref. 5). Both curves apply to the  $16^\circ$  boattail nozzle; the nozzles with steeper boattailing showed a greater increase in drag with Reynolds number.

The variation of Reynolds number was achieved in these investigations by altering the density, except with the NASA tests in which two models of different sizes were used: the smaller model had a scale of 0,05, the larger model, which was a half model, a scale of 0,22. The method of drag determination was not identical: in the Göttingen tests, the total drag (pressure + friction) of the complete, i.e. undivided fuselage was obtained from an internal strain gauge balance. The longitudinal pressure distribution was also measured in one row on the upper side of the body. Several pressure tapings at corresponding locations on the lower side were used as an additional check of the incidence being zero. In the AEDC tests, curve 2, only the twin jet aftbody was attached to the balance, leaving forebody and tailplanes fixed to the ground, whereas curve 6 was obtained from a mere pressure plotting.

In reference 13 the measured total aftbody drag of a twin jet fighter configuration is reported (fig. 3). The tests were conducted as force measurements in the 16 ft transonic wind tunnel of AEDC. The increase of the total aftbody drag coefficient with increasing Reynolds number is very similar to that shown on fig. 1; the level, however, is rather low. Since in these tests the metric break was rather far downstream of the maximum cross-section (at  $0,8 A_{max}$ , trailing edge of wing) the recompression predominates and thus produced this low aftbody drag level. This explanation is in agreement with fig. 7a where it will be shown that depending on the definition of the forward end of the aftbody (location of split line) also negative total drag values will result. Perhaps the greatest concern regarding Reynolds number effects on aftbody drag, has arisen in recent years from the fact that identical configurations gave an increasing trend when measured in the wind tunnel whereas the corresponding flight tests clearly showed the opposite, decreasing drag trend with Reynolds number (ref. 5 and 17). In an attempt to explain these unexpected test results an experimental investigation on a series of axisymmetric fuselages was reanalysed and is reported in the following.

Curves 1 and 3 in fig. 1 stem from wind tunnel measurements conducted by MBB in the 1m x 1m transonic tunnel of DFVLR Göttingen without jet and with different boattail angles (ref. 2 and 16).

Curve 2 was obtained with a strut mounted twin jet fighter model tested by the Air Force Flight Dynamics Laboratory in the 16 ft. transonic tunnel of the Arnold Engineering Development Center (ref. 4).

Curve 6 also results from an AFFDL test in the same AEDC transonic wind tunnel. Here, a single jet model with a cylindrical midbody was used.

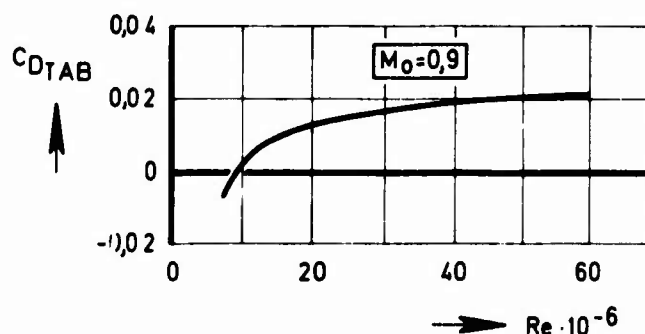


Fig. 3 Measured total aftbody drag of a twin jet configuration

## 3. GÖTTINGEN MEASUREMENTS

## 3.1. Test Series, Wind Tunnel and Models

In 1971/72 two test series (No. 1 and 2) were conducted by MBB in the 1 m x 1 m transonic wind tunnel of DFVLR Göttingen. The measurements consisted of pressure plotting and force measurements of the complete body as described in the preceding chapter. Fig. 4 shows the sting mounted model installed in the tunnel. The rectangular test section has four perforated walls, two of which can be rotated from  $+1^\circ$  to  $-2^\circ$ . The perforation consists of inclined holes yielding an open-area ratio of 6 %.

Pressurizing or evacuating the tunnel allowed a variation of the Reynolds number by the factor 4 (ref. 11). All pressure differences were measured by a standard pressure pick-up, which was calibrated against a Betz-manometer ( $\pm 0,1$  mm H<sub>2</sub>O). The pressure level in the tunnel, however, could be determined only to  $\pm 0,1$  mm Hg accurate which is still better than the usual accuracy ( $\pm 0,01$  inch Hg). The models were bodies of revolution with a common forebody and five interchangeable aftbodies, referred to in fig. 1, curves No. 1 and 3. The body contours are defined in Fig. 5



Fig. 4 Model installed in the transonic tunnel

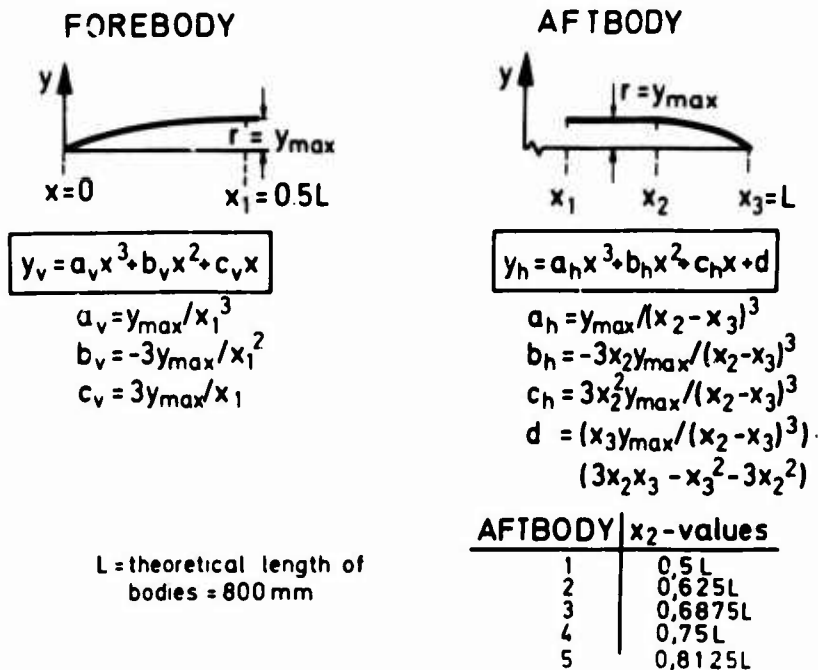


Fig. 5 Model contour

The model with aftbody No. 1 had no cylindrical midbody; thus fore- and aftbody had the same contours. The cross-section distributions and the wetted surfaces are shown in Fig. 6.

In order to confirm the main results deduced from the first two test series additional measurements were conducted in 1974 in close cooperation with DFVLR-AVA Göttingen, Institut für Strömungsmechanik, which was responsible for the experimental side.

In these additional measurements, referred to as test series 3 and 4, the wind tunnel wall pressures were recorded as well as the forebody drag of bodies No. 1 and 3. The forebody drag was obtained by means of an internal strain gauge balance which was designed for a maximum load of 5 kp and could discriminate 1 to 2 p. For the measurement of the forebody drag the models were modified, i.e. the forebody was attached to the balance and the aftbodies No. 1 and 3 were fixed to the sting (non-metric). Between fore- and aftbody there was a knife edge gap of 0,3 mm. Due to the movement of the balance this gap was reduced under maximum load only by 0,075 mm. The gap between the end of the aftbody and the sting was sealed.

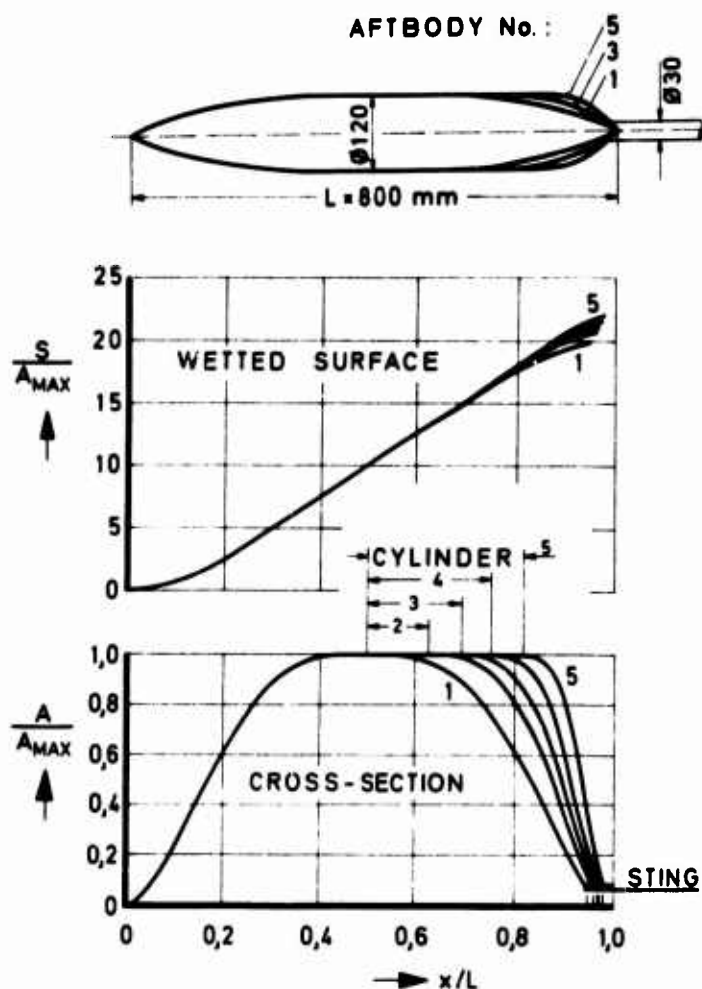


Fig. 6 Model geometry

The wind tunnel wall pressures were recorded from 24 pressure tapings installed in one row on the centre line of the upper wall of the test section at  $-0,3 < x/L < 1,1$ . In test series 2 and 4, which were almost exclusively used for the presented results, boundary layer transition was triggered by a carborundum roughness strip which extended from  $x/L = 0,05$  to  $0,0575$ . The grain size was  $0,15$  mm. Test series 1 and 3 had different transitions.

### 3.2. Results

In aftbody force testing the metric boattail of the model occasionally is subdivided into the portion of the airframe manufacturer as well as into the portion of the engine manufacturer (protruding nozzle). The drag of the nozzle "N" is then measured either against the jet pipe or relative to the boattail "B", fig. 7 (The interface B/N in this figure is at  $x/L = 0,90$ ).

If during a wind tunnel measurement the Reynolds number is varied by changing the tunnel total pressure, subdividing the model causes particular difficulties because the drag values of the model portions nozzle, boattail, midbody and forebody vary differently with Reynolds number, thus further complicating the synthesis of the aircraft drag (fig. 7a).

The total aftbody drag coefficient for a different configuration with a metric break at  $0,8$  of  $A_{max}$  is reproduced here from fig. 3 and shows qualitative agreement. Fig. 7a represents the results as obtained from the wind tunnel by force measurement and pressure plotting of the complete body No. 3 when only the first (standard) correction for the internal pressure is applied to the balance readings. Fig. 7b shows on the other hand the drag variations as expected by the authors: a forebody drag decrease which is almost completely due to the decrease in friction drag, i.e. a practically constant forebody pressure drag. As a consequence, the aftbody total drag decreases with Reynolds number similarly as the friction drag.



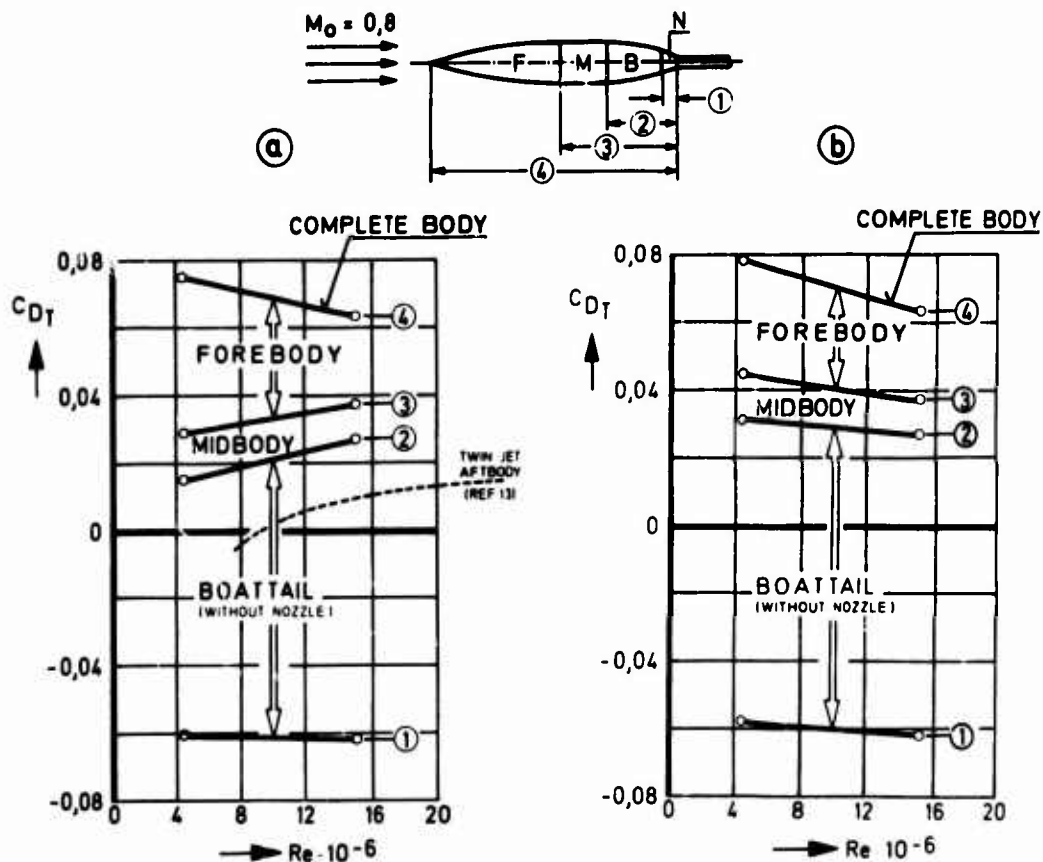


Fig. 7 Reynolds number effect on body subdivisions

It will be shown in the following how the trends in fig. 7a were obtained and also how the differences between measured and expected Reynolds number trends might be explained and corrected respectively. In fig. 8 the uncorrected pressure distribution of body No. 3 is plotted. Increasing the Reynolds number lowered the pressures on both, the forebody and the aftbody.

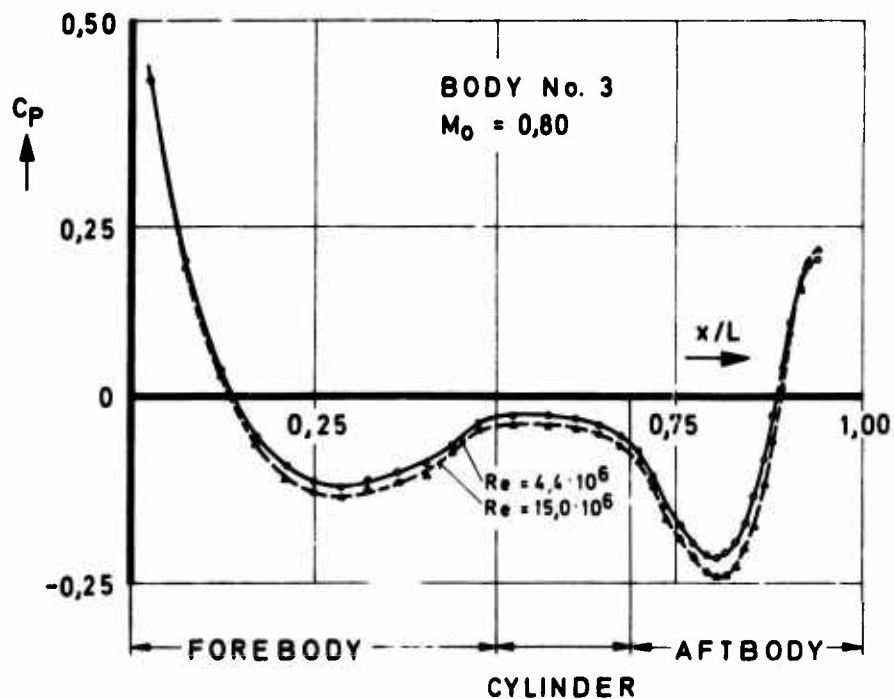


Fig. 8 Reynolds number effect on pressure distribution

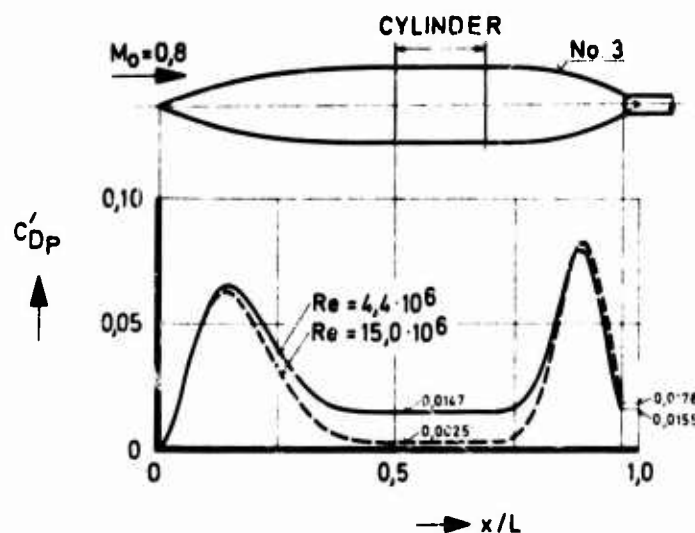


Fig. 9 Reynolds number effect on pressure drag

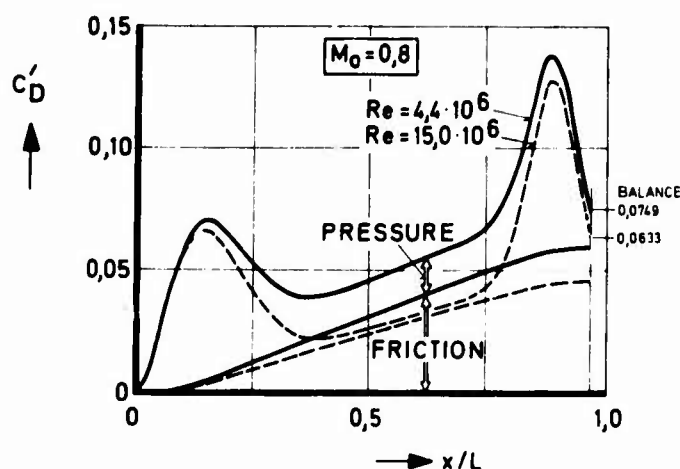


Fig. 10 Reynolds number effect on pressure and friction drag

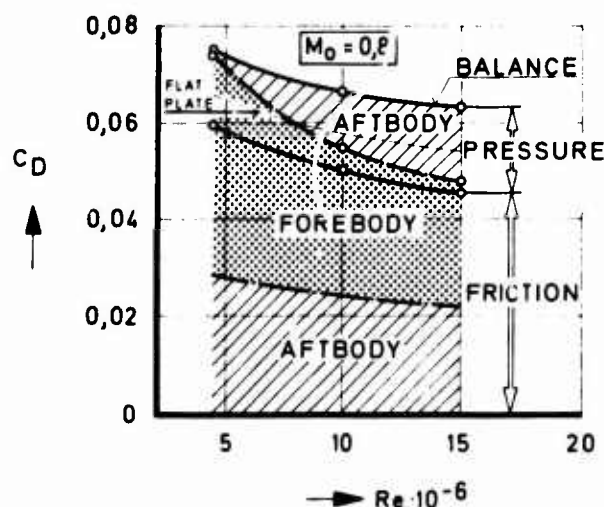


Fig. 11 Reynolds number effect on pressure and friction drag of fore- and aftbody No. 3

Integrating the pressure distributions in fig. 8 from the nose of the body ( $x=0$ ) up to an arbitrary limit of integration  $x$  yields the running sum of the pressure drag coefficient  $C'_{DP}$  in fig. 9. This coefficient enables one to read off the pressure drag not only of the complete body but of body portions as well, which is done by taking the difference of the  $C'_{DP}$  at the beginning and the end of the portion.

Increasing the Reynolds number as in the example of fig. 9 results in a reduction of the forebody pressure drag coefficient from 0,0147 to 0,0025, i.e. by 83 %. This corresponds to about 16 % of the total drag of the complete body. On the aftbody this Reynolds number influence is reversed: at the lower Reynolds number the pressure drag is about equal to zero. At the larger Re-number, however, the afterbody pressure drag coefficient is read off as  $0,0178 - 0,0025 = 0,0153$ . Thus, increasing the Reynolds number causes here a rise in aftbody drag by a factor of 19, which is still 20 % of the total drag of the complete body. Adding friction to the pressure drags of fig. 9 gives fig. 10. The friction drag of the complete body was obtained from the difference between the drag from the balance minus the integrated pressure distribution. The distribution of that friction drag over the body length was theoretically determined (ref. 9).

The individual drag components for the forebody ( $x/L = 0,5$ ) and for the complete body ( $x/L = 1,0$ ) can be taken from fig. 10. These drag components are plotted in fig. 11 for the three measured Reynolds numbers: the pressure drags of both aftbody and forebody change considerably with Reynolds number while the sum of these two components remains almost constant. The friction drag of the fully turbulent flat plate is also shown for comparison; this friction is above the "measured" friction by 11 % at the low Reynolds number and 18,5 % at the high Reynolds number.

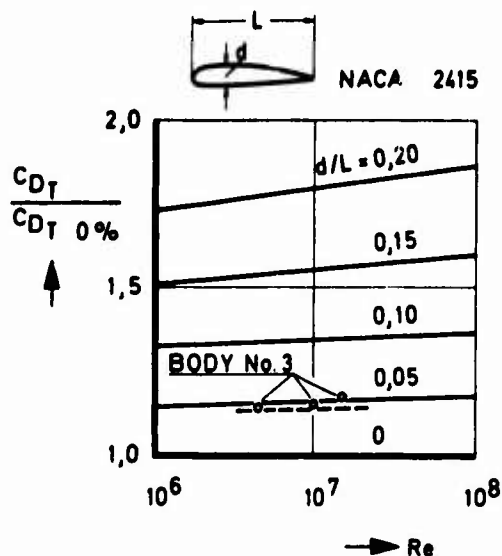


Fig. 12 Increase of relative profile drag with Reynolds number

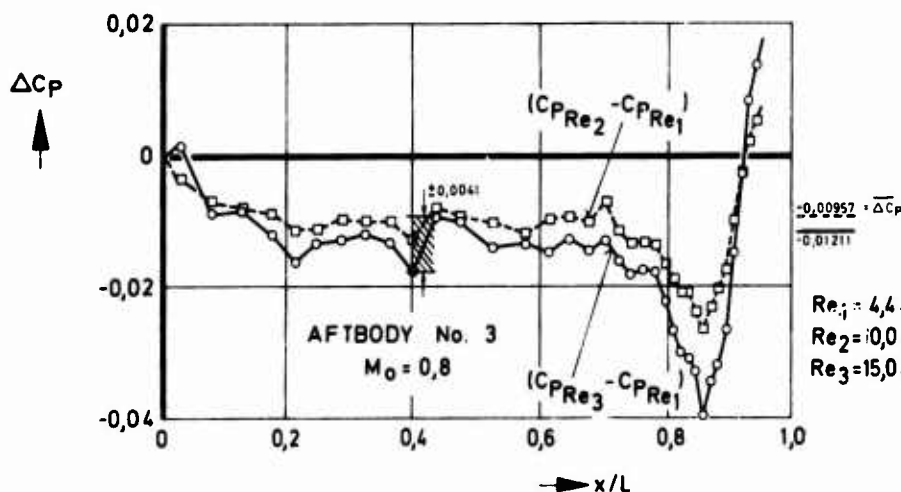


Fig. 13 Change in body pressure distribution

### 3.3. Systematic Errors

The test results reported so far do not include any flight data, but stem exclusively from transonic wind tunnels with ventilated test sections. It was suspected, therefore, that the Reynolds number effects shown in the preceding chapters might have been caused by systematic errors related to the wind tunnel itself. To investigate this possibility, let us first consider the pressure changes on the model, fig. 13. Increasing the Reynolds number caused here an almost constant pressure drop over the greater part of the body. Besides this constant pressure drop, increasing Reynolds number also increased the expansion and the recompression on the boattail. Later it will be shown that similar effects were found in a flight test, however, of opposite sign as far as the constant pressure shift is concerned. The random scatter of the differences in the individual pressure coefficients  $\Delta C_p$  lies at  $M_0 = 0.8$  well within a band of  $\pm 0.0041$  (maximum error). Preferably, these  $\Delta C_p$  are not quoted relative to the lowest Reynolds number  $Re_1$  but to the intermediate one,  $Re_2$ . The maximum error reduces thereby to  $\pm 0.0025$  (compare also fig. 18 in ref. 14).

The probable value of the integrated pressure differences i.e. of the incremental pressure drag coefficient  $\Delta C_{DP}$  can then be quoted for those conditions with a precision of about  $\pm 0.001$  (mean error). The good precision in  $\Delta C_p$  is also reflected in fig. 8 where the original curves i.e. the  $C_p$ -distributions are plotted. This mean error refers only to the recording and integration of the model pressure

As a further comparison the profile drags computed in ref. 1 for the incompressible, fully turbulent case were considered and were divided in each case by the drag of the profile of zero thickness (flat plate), fig. 12. It is seen that the profile drag of slender profiles lies above the value of the flat plate by an almost constant factor in the Reynolds number range under consideration. In this context it should be remembered that the flat plate skin friction is reduced to 50 % when the Reynolds number is raised from  $10^6$  to  $10^8$ . The total drag of the complete body No. 3 measured at  $M_0 = 0.8$  was also divided by the friction drag of the fully turbulent flat plate and plotted in the same diagram. To allow for the difference between two-dimensional and three-dimensional bodies the ordinates of the curve for  $d/L = 0.15$  were reduced to 25 % in a first approximation (compare ref. 10) and plotted as dashed line in the same figure. There is fair agreement between this dashed line and the total drag of body No. 3 having also a relative thickness of 15 %. If only the pressure drag instead of the total drag is referred to the flat plate friction, then a quite similar trend with Reynolds number is found.

The pressure drag of the complete body, therefore, seems to be about correct. However, whether the aft- and forebody pressure drags are correct remains still unclear. This question will be critically reviewed in the next chapter.

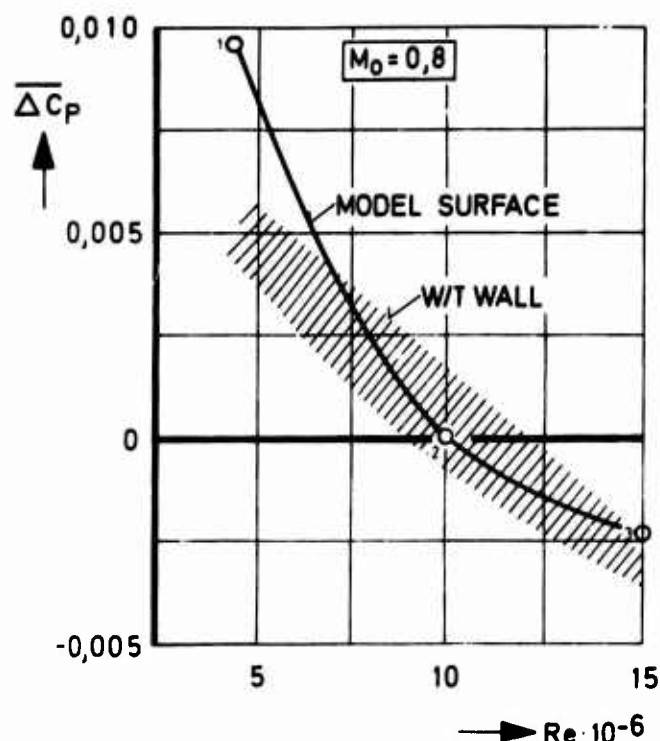


Fig. 14 Comparison of averaged changes in pressure coefficients on model and tunnel wall

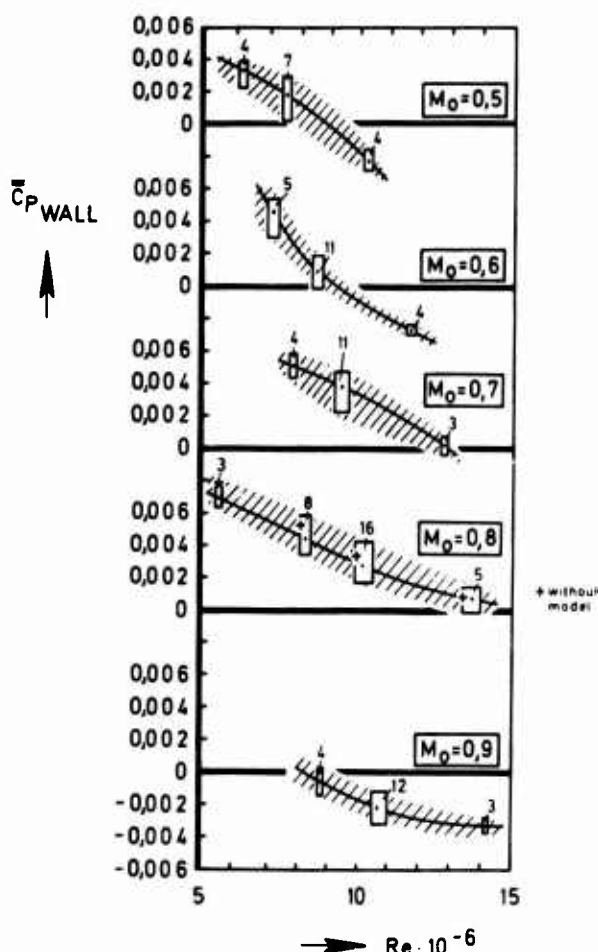


Fig. 15 Mean wall pressure coefficients

coefficients, to surface imperfections etc. It does not take into account any (systematic) errors in the assessment of the true free stream conditions as well as errors due to the incorrect simulation of the free flight flow field by the wind tunnel. Therefore, the total errors are expected to be larger by an order of magnitude as will be shown in the following.

In this context one should recall that for slender bodies having a pressure drag coefficient of about 0,01 the error in the integrated  $C_p$ -distribution has to be smaller than 0,001 if the pressure drag is to be determined within an accuracy of 10 % which requires that the error  $\Delta M_0$  must be below 0,0005 (!) at subsonic speeds.

The mean values  $\overline{\Delta C_p}$  from fig. 13 were plotted in fig. 14 versus Reynolds number and are compared with the corresponding mean values obtained from the upper tunnel test section wall (hatched band, taken from fig. 15): at the higher Reynolds numbers there is good agreement between the pressure changes on the model and those on the wall. This agreement led to the hypothesis that the measured Reynolds number effects were caused only to a minor degree by true Reynolds number effects, but primarily by undetected deviations of the free stream static pressure from its nominal value as will be discussed in more detail in the following chapters.

At the lower Reynolds numbers the agreement is not so good. It should be noted, however, that the wall pressure measurements were conducted in test series 3 and 4, while the model surface pressures were obtained from pressure plotting body No. 3 in test series 2. The only simultaneous measurements of wall pressures and body drag were made in the forebody force tests (series 3 and 4).

In fig. 15 the wall pressures recorded during all runs of test series 3 and 4 have been included. The pressure readings from all 24 pressure tapings were averaged arithmetically for each individual run to give one value of  $\overline{C_p}$  wall per run. The numbers at each bar indicate how many runs at each Mach and Reynolds number were conducted (repeatability). Within each bar, these repeats were arithmetically averaged a second time to give  $\overline{C_p}$  wall shown as dots and solid curves respectively. The scatter is shown by the hatched band which is about 0,003 wide. For those tests in which the wall pressures were recorded simultaneously with the model force measurements, this band width is of little importance since the model results were corrected in each run to their corresponding mean wall pressure.

Comparing the cross symbols (empty tunnel) with the solid curve at  $M_0 = 0,8$  it can be seen that the blockage of these models of 1,13 % had little or no effect on the averaged wall pressures. This is in agreement with the general rule that up to  $M_0 = 0,85$  a blockage of 0,75 % does not greatly affect the mean free stream static pressure.

In fig. 16 the same data are plotted against Mach number. The curves show a wave shape while their dependence on Reynolds number in the foregoing figure was an almost linear decrease. These two different trends are reflected in the forebody force measurements shown in the following diagrams.

The upper two curves in fig. 17 show the total drag coefficient of the forebody with aftbody No. 1 and 3 respectively as a function of Reynolds number. The internal pressures were corrected to free stream static pressure as a standard practice. The friction drag coefficient of the forebody, assumed to be equal for both bodies, was obtained by two different methods and plotted as dotted lines: the upper curve represents flat plate skin friction, laminar up to the transition strip (at  $x/L = 5\%$ ), the lower one was taken from fig. 11 (2nd Test Series) and is described there.

The difference between the total forebody drag (standard correction) and the skin friction drag is the forebody pressure drag which shows, plotted as coefficient, the same decreasing trend as on fig. 11. Thus the two entirely different measurement techniques (half/complete body) gave fairly good agreement. If, however, the balance readings are not only corrected for the internal pressure but also for the wall pressures, then this decrease of the pressure drag coefficient with Reynolds number disappears almost completely, especially for body No. 3. In the lower part of this figure, the wall pressure coefficients are shown which were simultaneously measured and used for the correction. Since for these models the maximum cross section equals the "base" area  $A_i$  to be used for the correction of the internal pressure, the "fully" corrected forebody drag coefficient is obtained as

$$C_{D_{T \text{ corr}}} = C_{D_{T \text{ balance}}} + (C_{P_i} - C_{P_{\text{wall}}})$$

which implies that the averaged wall pressure is equal to the effective free stream static pressure. If this supposition is correct, then the fully corrected curves give the true effect of aftbody geometry on forebody drag.

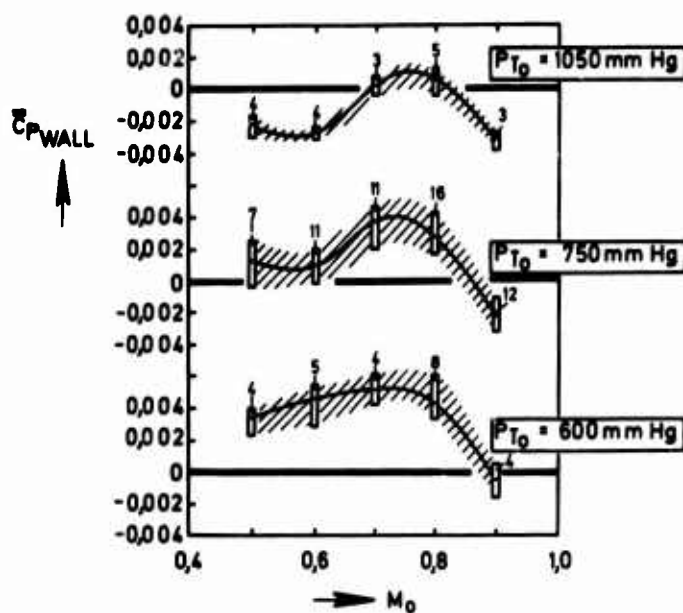


Fig. 16 Mean wall pressure coefficients

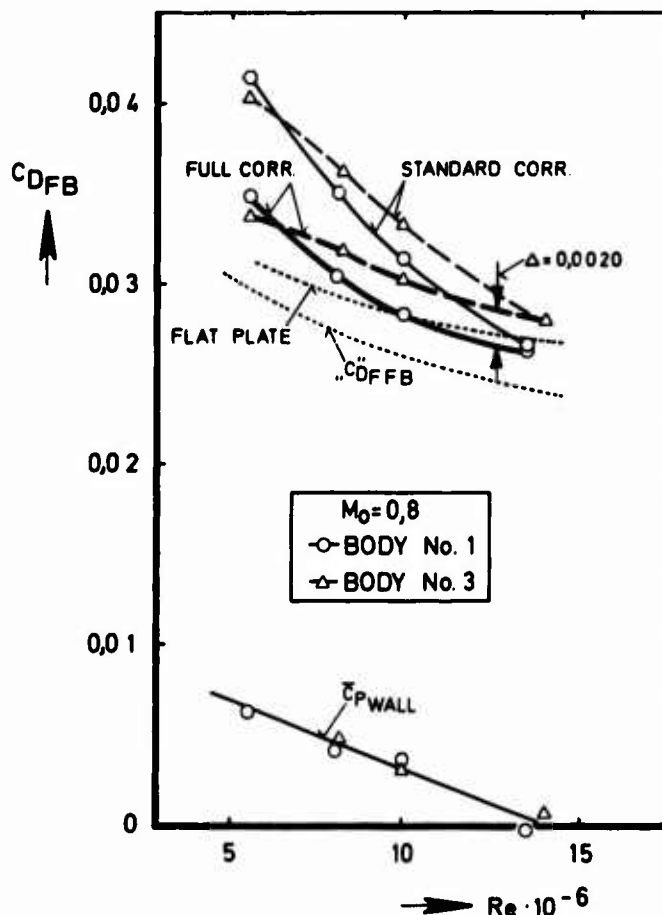


Fig. 17  $P_o$  correction at different Reynolds numbers

This difference in forebody drag decreases with decreasing Reynolds numbers similarly as the difference in aftbody drag shown in fig. 1 for body No. 1 and 3. Steeper boattailing thus raises both forebody and aftbody drag by a similar amount. At the largest Reynolds number tested, this increase in drag is 0,0020 which agrees with the computed value of 0,0022 obtained by the MBB-Panel method (see fig.27).

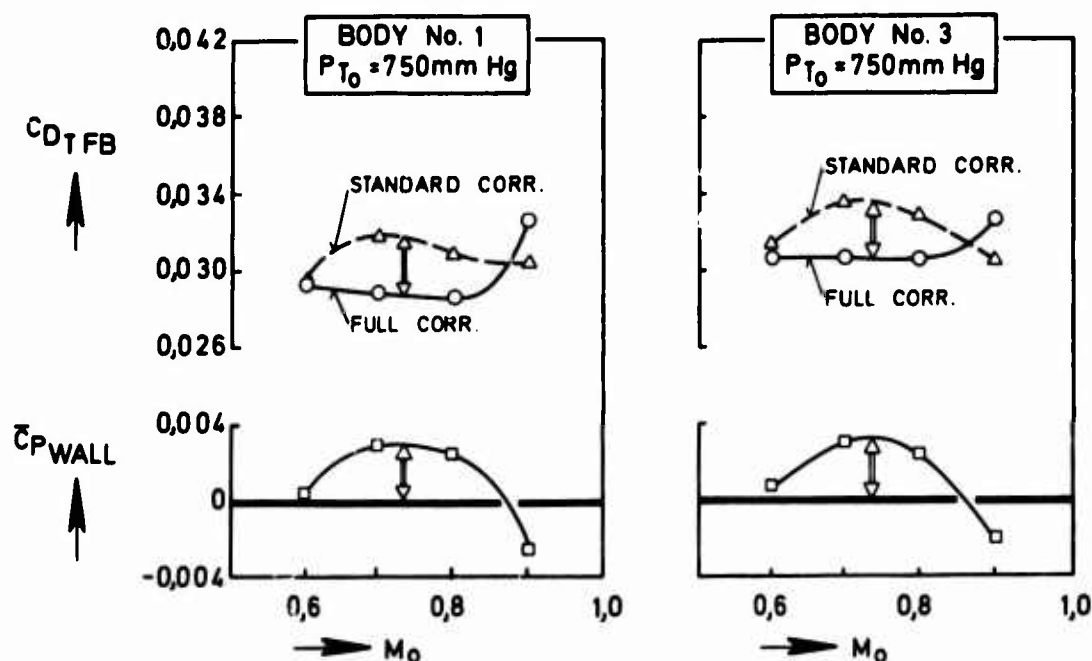


Fig. 18  $P_0$ -correction at different Mach numbers

The Mach number dependence of the forebody drag is shown on figure 18 for a constant tunnel total pressure. Here again, applying the  $C_{p\text{ wall}}$  correction, does change the shape of the upper curve (standard correction) to a more familiar one (full correction), and thereby underlines its usefulness, which, of course, does not prove that the free stream static pressure was exactly equal to the mean wall pressure. On the other hand it is expected that for small tunnel blockages the changes of these two pressures are similar when Reynolds and Mach number are varied. Therefore, the drag levels may still be slightly wrong, the drag trends with Reynolds and Mach number, however, are probably correct. In this context it should be noted that complete bodies are much less sensitive to changes in static pressure and, therefore, produce straighter curves with only the standard correction applied because the  $P_0$ -correction has only a small contribution to complete bodies (small sting diameter) as will be discussed in the next chapter.

#### 4. SENSITIVITY CONSIDERATIONS AT SUBSONIC SPEEDS

##### 4.1. Conversion to True Tunnel Static Pressure

In the preceding chapter it was supposed that the nominal free stream static pressure  $P_0$  was affected by a systematic error. Assuming that everything else (e.g. balance, total pressure) was correct, the measured quantities can then be corrected merely by converting them to the true reference conditions  $M_\infty$ ,  $P_\infty$ ,  $q_\infty$ . If e.g. force measurements are made on complete bodies having a rear sting and an internal pressure  $P_i$  the corrected drag coefficient then becomes

$$(1) \quad C_{D_{T\infty}} = \left[ C_{D_{T\text{ balance}}} + (C_{P_i} - C_{P_\infty}) A_i / A_{\text{max}} \right] q_0 / q_\infty$$

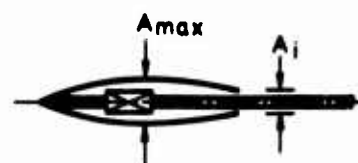
where:  $C_{D_{T\text{ balance}}}$  = total drag coefficient without internal pressure correction, referred to  $q_0$

$$C_{P_i} = (P_i - P_o)/q_o$$

$$C_{P_\infty} = (P_\infty - P_o)/q_o$$

$$q_o/q_\infty = (1 + S_q C_{P_\infty})^{-1}$$

$$S_q = \frac{\Delta q}{q_o} / C_{P_\infty}$$

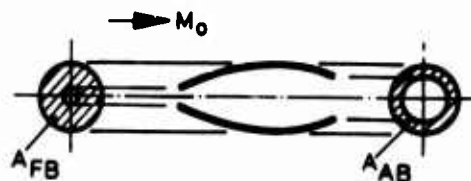


In a more generalized form, valid for force measurements and for pressure plotting on complete or part bodies equation (1) reduces to

$$(2) \quad C_{D_\infty} = [C_{D_o} - C_{P_\infty} (A_{FB} - A_{AB}) / A_{max}] q_o / q_\infty$$

where  $A_{FB}$  and  $A_{AB}$  are the projected (outer) body surfaces

$$\text{and } C_{D_o} = C_{D_{T \text{ balance}}} + C_{P_i} \cdot A_i / A_{max}$$



Since  $S_q = -0,680$  at  $M_o = 0,8$  (see table below) and usually  $-0,008 < C_{P_\infty} < 0,008$  the ratio  $q_o/q_\infty = 1$  and may therefore be neglected. For the forebody correction in fig. 17 and 18 equation (2) then reduces to

$$(3) \quad \Delta C_D = C_{D_\infty} - C_{D_o} = - C_{P_\infty}$$

$$(A_{FB} = A_{max}, A_{AB} = 0)$$

#### 4.2. General Relations

For the above corrections the following sensitivities are valid:

$M_o =$	0,5	0,6	0,7	0,8	0,9	1,0
$S_M = \frac{\Delta M}{M_o} / C_{P_\infty} =$	-0,525	-0,536	-0,549	-0,564	-0,581	-0,600
$S_{Re} = \frac{\Delta Re}{Re_o} / C_{P_\infty} =$	-0,414	-0,376	-0,332	-0,281	-0,224	-0,161
$S_P = \frac{\Delta P}{P_o} / C_{P_\infty} =$	0,175	0,252	0,343	0,448	0,567	0,700
$S_q = \frac{\Delta q}{q_o} / C_{P_\infty} =$	-0,875	-0,820	-0,755	-0,680	-0,595	-0,500

where  $\Delta = ( )_\infty - ( )_o$  and  $C_{P_\infty} = (P_\infty - P_o)/q_o$

Table 1 Sensitivities

#### 4.3. Sensitivity of Complete and Half Bodies to $P_o$ -Errors at $M_o = 0,8$

Assuming that the tunnel static pressure can be determined by a standard balanced beam manometer to 0,01 inch Hg precise then for a tunnel total pressure of 760 mm Hg the relative error in the free stream static pressure is  $\Delta P/P_o = 5,1 \cdot 10^{-4}$  or, expressed as pressure coefficient

$$C_{P_\infty} = \Delta P / P_o \cdot S_P^{-1} = 5,1 \cdot 10^{-4} \cdot 0,448^{-1} = 11,4 \cdot 10^{-4}$$

Usually this error is considered as "absolute" minimum for the above free stream conditions. Fig. 15 showed that in the Göttingen tests the wall pressures varied systematically by a 7 times larger amount, i.e. in the range  $-4 \cdot 10^{-4} < C_{P_{wall}} < 30 \cdot 10^{-4}$ . Assuming that the true free stream static pressure  $P_\infty$  varied accordingly i.e.  $C_{P_\infty}$  varied by the same amount and in the same direction, then for these two cases (manometer/wall pressures) the resulting errors in complete and half body are obtained from equation (2) and shown in table 2.

$$\Delta C_D = C_{DT\infty} - C_{DT0}$$

$$C_{DT\text{ CB}} = 2 C_{DT\text{ FB}} = 0,06$$

			COMPLETE BODY ( $A_{FB} - A_{AB}$ ) / $A_{\max} = 1/14$		FOREBODY $A_{AB} = 0, A_{FB} = A_{\max}$	
			$\Delta C_D \cdot 10^4$	$\frac{\Delta C_D}{C_{DT\text{ CB}}}$	$\Delta C_D \cdot 10^4$	$\frac{\Delta C_D}{C_{DT\text{ FB}}}$
assumed errors						
mano- meter	$\Delta P = 0,01 \text{ inch Hg}$	$P_{T0} = 1,5 \text{ atm}$	0,5	0,09 %	7	2,5 %
		$P_{T0} = 0,5 \text{ atm}$	1,6	0,27 %	23	7,6 %
wall	$C_{P\infty} = C_{P_{\text{wall}}} = -4 \cdot 10^{-4}$	$P_{T0} = 1,5 \text{ atm}$	+0,3	+0,05 %	+4	+1,3 %
	$C_{P\infty} = C_{P_{\text{wall}}} = -80 \cdot 10^{-4}$	$P_{T0} = 0,5 \text{ atm}$	-5,7	-0,95 %	-80	-27,0 %

Table 2 Errors in Drag for Complete and Half Bodies

Table 2 illustrates clearly how 3 assumed values for the error in  $P_0$  contribute differently to the (yet unknown) total error of the result depending on whether complete or half bodies are tested: In our example the relative errors in forebody drag increased by a factor of 28. This factor may reduce noticeably if the total error is considered, i.e. if also other types of errors are included and particularly so if these are large. In aftbody testing this situation is only slightly better (only slightly reduced projected area, higher pressure drag) and stays essentially the same as for the forebody.

As mentioned earlier, the large projected internal area is responsible for the high sensitivity of part model testing towards deviations in free stream static pressure. The magnitude of this internal pressure correction is shown on fig. 19. It is worth mentioning that the uncorrected forebody drag curves, i.e. without internal and wall corrections, were much more linear when plotted against Mach number than the dashed curves in fig. 18. Thus the uncorrected half body drag showed a similarly low sensitivity as the uncorrected drag of the complete body. Therefore, it is primarily by applying the internal (standard) correction that these large relative errors of 27 % at the low Reynolds number and 10 % at the intermediate Reynolds number (750 mm Hg) respectively are introduced. If part model testing is done by pressure plotting and not by force measurement there is no "internal" correction; the absolute error  $\Delta C_D$ , however, stays the same (same open loop of integration).

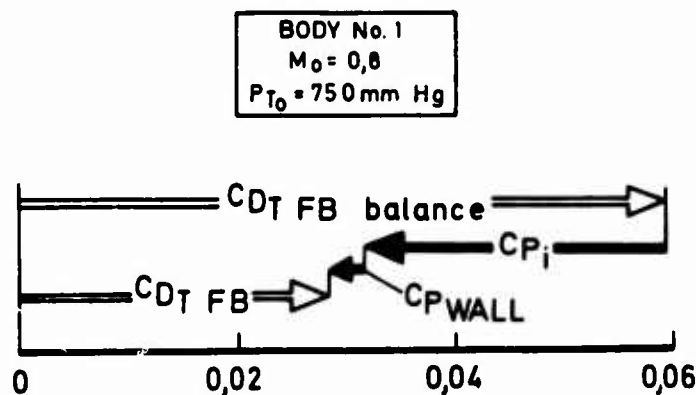


Fig. 19 Magnitude of internal pressure correction



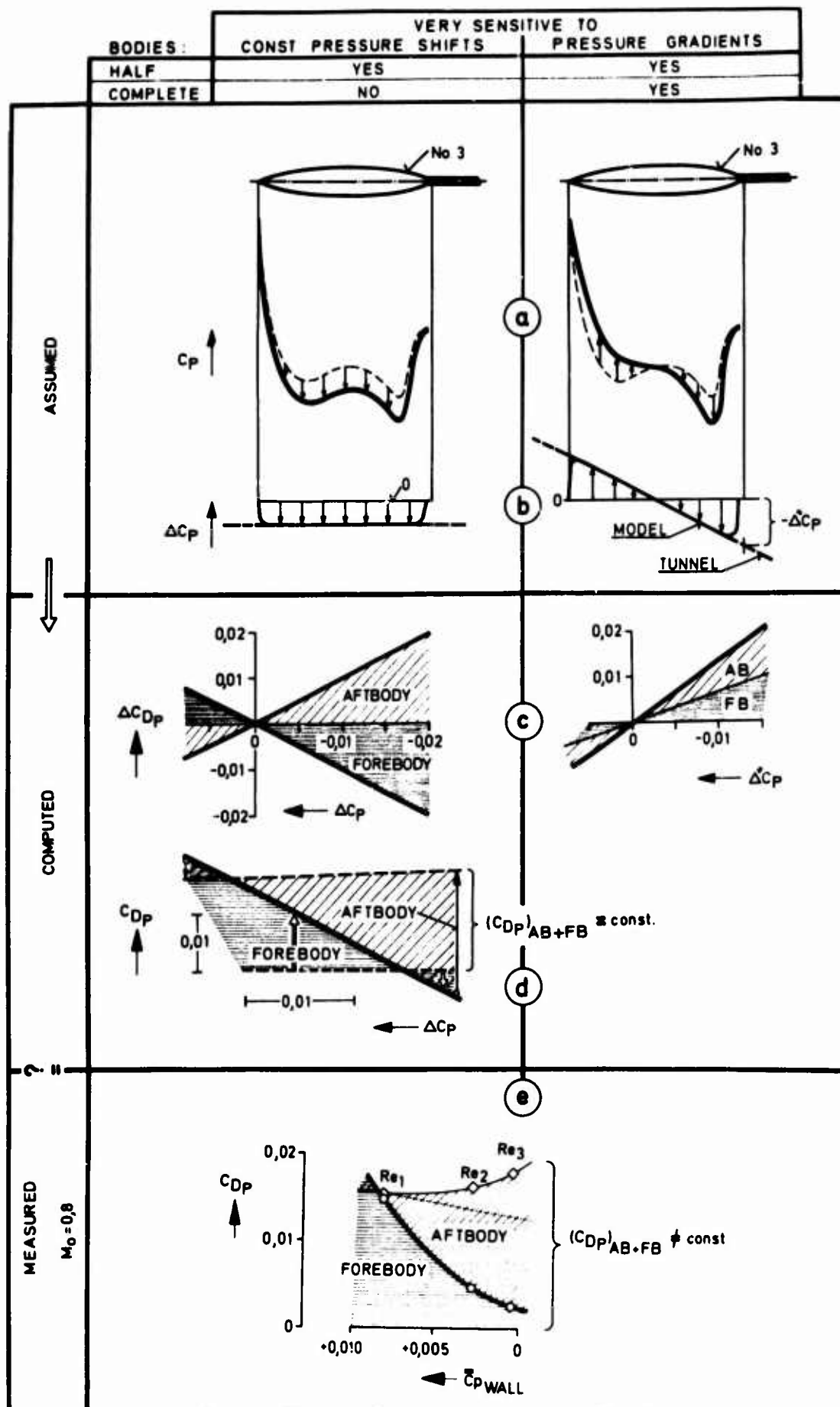


Fig. 20 Changes in drag due to deviations from nominal static pressure

So far only constant pressure shifts have been discussed while there may be a number of additional flow irregularities, e. g. a pressure gradient along the test section. Fig. 20 tries to illustrate these two sources of error and their effect on testing complete and half bodies respectively: in the left half of the figure a constant pressure shift was assumed, whereas the right half shows a pressure gradient (fig. 22a and b). With these assumed deviations the aft- and forebody pressure drag changes for model No. 3 were computed (fig. 22c and d). The pressure gradient, in the right half of this figure, affects both forebody and aftbody in the same sense resulting in an even steeper increase in pressure drag for the complete body amounting to  $\Delta C_{DP} / \Delta C_P^* = 1.35$ . The constant pressure shift on the other hand, changes forebody and aftbody pressure drag almost by the same amount, however, in an opposite sense whereby the sum of these two drag changes cancel each other virtually completely (small sting diameter). So far only drag changes have been discussed. If, however, a value for the pressure drag of the complete body is assumed, say 0.016 (dashed line) then a deviation  $\Delta C_P$  greater than 0.016 will cause a change in pressure drag of the half body, i.e. of the fore- and aftbody respectively, which is greater than the pressure drag of the complete body itself. In other words, in aftbody drag testing where the forebody is not taken into account, the measured aftbody (pressure) drag will attain arbitrarily great values, depending on the free stream underpressure (deviation from nominal). If, however, the complete body is measured then this high sensitivity towards constant deviations in free stream static pressure disappears (compare also table 2). In fig. 20e the measured pressure drags of fore- and aftbody are plotted, this time, however, not against Reynolds number, but against the mean values of the incremental wall pressure coefficients  $\bar{C}_{P_{wall}}$  shown in fig. 15. (Dotted line in fig. 20e corresponds to decrease in friction coeff.)

Comparing measured with computed values it would appear that at least as far as the pressure drags of the half bodies are concerned, the changes in these pressure drags were not so much caused by true Reynolds number effects but primarily by deviations in the free stream static pressure. As far as the complete body is concerned, the slight increase in pressure drag with Reynolds number shown in fig. 20e is probably a result of a longitudinal pressure gradient which varied with tunnel Reynolds number (right half of fig. 20). An inspection of the tunnel wall pressure distribution did in fact reveal a pressure gradient which varied systematically with tunnel total pressure and volumetric blockage ratio.

Looking at fig. 20e, no matter for what Reynolds number and  $\bar{C}_{P_{wall}}$  respectively, it is not clear what exact proportion of the pressure drag of the complete body can be assigned to the fore- and aftbody drag components. If the true free stream pressure had been achieved at  $\bar{C}_{P_{wall}} = 0$ , then virtually all of the pressure drag is on the aftbody leaving only 12 % for the forebody. If, in addition, one tried to correct the measured "Reynolds" number trend for halfbodies, one could think of applying the pressure changes on the wall to the model. In doing so a forebody pressure drag is obtained which is almost independent of Reynolds number at the higher tunnel densities. At the lower values there is some disagreement between pressure changes on the model and those on the wall, as mentioned earlier. It should be noted, however, that much better agreement had been found for different test series which are not presented here.

## 5. EFFECT OF DISPLACEMENT THICKNESS

It is clear that varying Reynolds number causes a corresponding change in boundary layer displacement thickness which in turn alters the pressure drag. The question remains open, however, as to the sign and magnitude of this change, i.e. whether a variation in  $\delta^*$  could be the only or main cause for the presented Reynolds number effects. To check the order of magnitude rather than trying to answer this question exactly, a very simple hypothetical flow model was considered. Fig. 21 shows an ellipsoid of revolution with a displaced geometrically similar surface. The distance between these two surfaces is defined as hypothetical boundary layer displacement thickness  $\Delta R$  and is compared with the displacement thickness  $\delta^*$  of the fully turbulent flat plate boundary layer in figure 22.

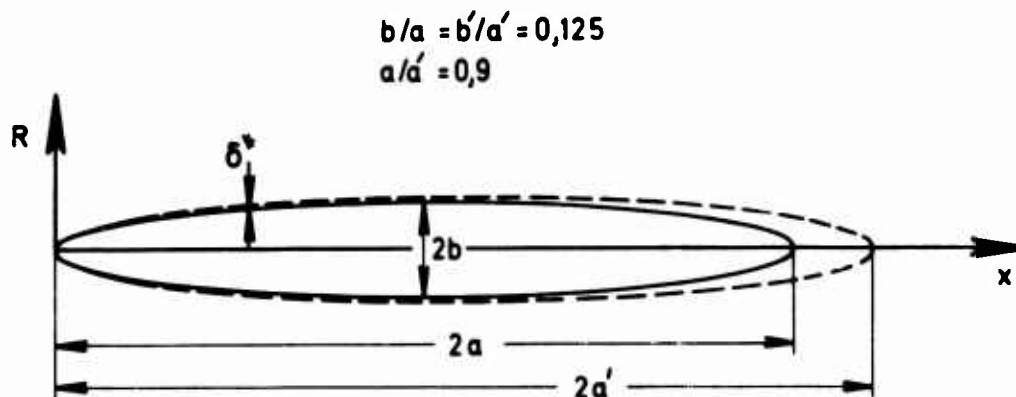


Fig. 21 Hypothetical flow model

A Reynolds number of 2.06 million corresponds to a displacement ratio  $a/a' = 0.98$  (fig. 21 shows a 5 times bigger displacement). In most practical applications the Reynolds numbers are above two million resulting in an even smaller displacement. This is simply to illustrate how thin the boundary layer displacement thickness is on the forebody. Therefore, increasing the Reynolds number from 1 million to 10 or even 100 million has little effect on the forebody pressure drag as shown on fig. 23. This diagram was obtained by projecting the exact pressure distribution on the displaced surface orthogonally onto the basic ellipsoid for subsequent pressure integration.

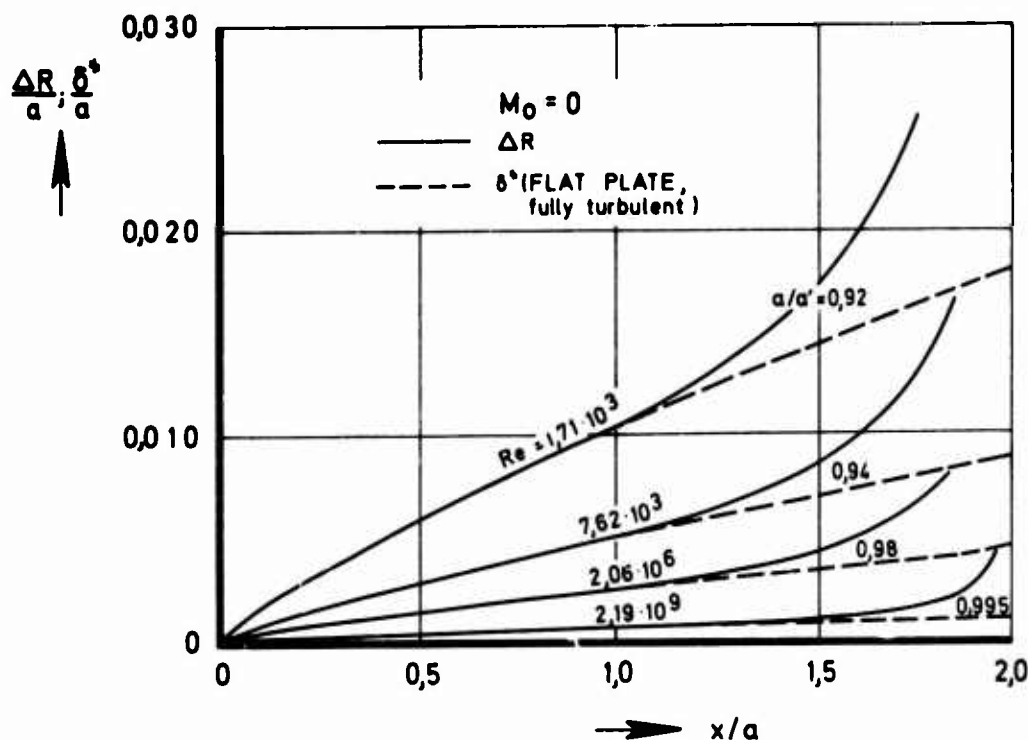


Fig. 22 Boundary layer displacement thickness and distance of displaced surfaces

For the example of the Götting measurements in which the Reynolds number was increased from 5 to 15 million, fig. 23 gives a change in computed forebody pressure drag coefficient of approximately  $2 \cdot 10^{-4}$  which is about hundred times smaller than the measured decrease of  $1.5 \cdot 10^{-2}$ . Therefore, the change in displacement thickness can by no means explain the changes in forebody pressure drag measured in the Götting tunnel even when taking into account that bodies No. 1 and 3 were not ellipsoids. The absolute values  $C_{DP\ FB}$  from the hypothetical flow model may not be correct due to the unrepresentative aftbody flow field. The main purpose, however, was to show that  $C_{DP\ FB}$  is small and changes little when Reynolds number is varied. In fig. 23 the measured forebody pressure drag of an ellipsoid of revolution with  $b/a = 0.125$  is also shown for comparison. The pressure drag was obtained by pressure integration. The measurement was conducted in a different tunnel at  $M_0 = 0.8$  and a total pressure of one atmosphere. The relative large scatter of  $\pm 2.4 \cdot 10^{-3}$  is due to the manufacturing quality which was for this early model not as refined as for the present bodies No. 1 to 5.

The aftbody pressure drag coefficient is read off as difference between  $C_{DP\ CB}$  computed according to DATCOM and  $C_{DP\ FB}$  obtained from the flow model. If these two curves are correct then  $C_{DP\ AB}$  should decrease in the Reynolds number range tested by a small amount (0.002). The uncorrected, measured pressure drag coefficient in fig. 11, however, rose by 0.015. If the wall corrections are applied or if the forebody is taken into account, this discrepancy is largely eliminated leaving then only a small increase which probably was caused by a pressure gradient as mentioned above.

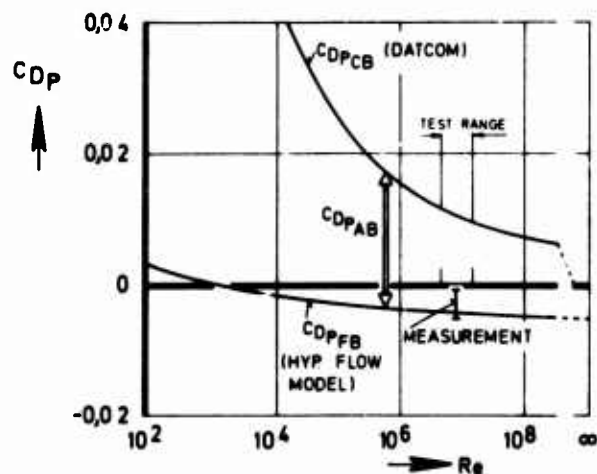


Fig. 23 Decrease of pressure drag with Reynolds number

## 6. COMPARISON WINDTUNNEL / FLIGHT DATA

So far only Reynolds number trends obtained from wind tunnels have been discussed. NASA Lewis tested the same configuration in the wind tunnel and in flight. In disagreement to the windtunnel measurements the flight tests produced a clear decreasing aftbody pressure drag with Reynolds number, fig. 24E (ref. 17). In contrast thereto, the aftbody pressure drag variation of body No. 3 is shown in fig. 24 D as typical example of the corresponding aftbody pressure drag trends obtained in wind tunnels (see also fig. 1). A difference in drag level must be expected because of the different configurations; the difference in trends, however, was questioned in the preceding chapters: curve 1 corresponds to the windtunnel results as measured while curve 2 includes a correction for the deviation in free stream static pressure (assumption  $\bar{C}_{p\text{ wall}} = 0$ ). This corrected curve still shows an increasing trend.

If on the other hand one accepts the argument from the preceding chapter that the pressure drag coefficient of the forebody must be virtually constant in the small Reynolds number range tested then the same forebody  $P_0$ -correction applied to the aftbody gives an almost constant aftbody pressure drag, curve 3. The remaining slight increase is probably due to a varying buoyancy pressure gradient as indicated by the increasing pressure drag of the complete body shown in fig. 20 e. The rather strong decrease of the flight data relative to the flat plate skin friction coefficient, fig. 24E, might be explained by the fact that variable amounts of separated flow were present in those tests.

Comparing the pressure distributions from windtunnel and flight tests, fig. 24A and 24B show that an increase in Reynolds number lowered the surface pressures in the windtunnel (dotted line) while in the flight tests a corresponding increase was found. The stronger recompression at the higher Reynolds number is apparent in both cases. This again points towards a uniform error in free stream static pressure: for example, increasing the  $C_p$ -distribution for the lower Reynolds number in fig. 24B (solid line) by a constant value of  $C_p$  between 0,05 and 0,07 would suffice to obtain qualitative agreement between wind tunnel and flight results. Since similar  $C_p$ -shifts as in fig. 24A were also found in different windtunnel investigations, e.g. fig. 5 in ref. 18 one might expect that these trends were caused at least to some extent by windtunnel wall interference. This will be discussed in the following chapter.

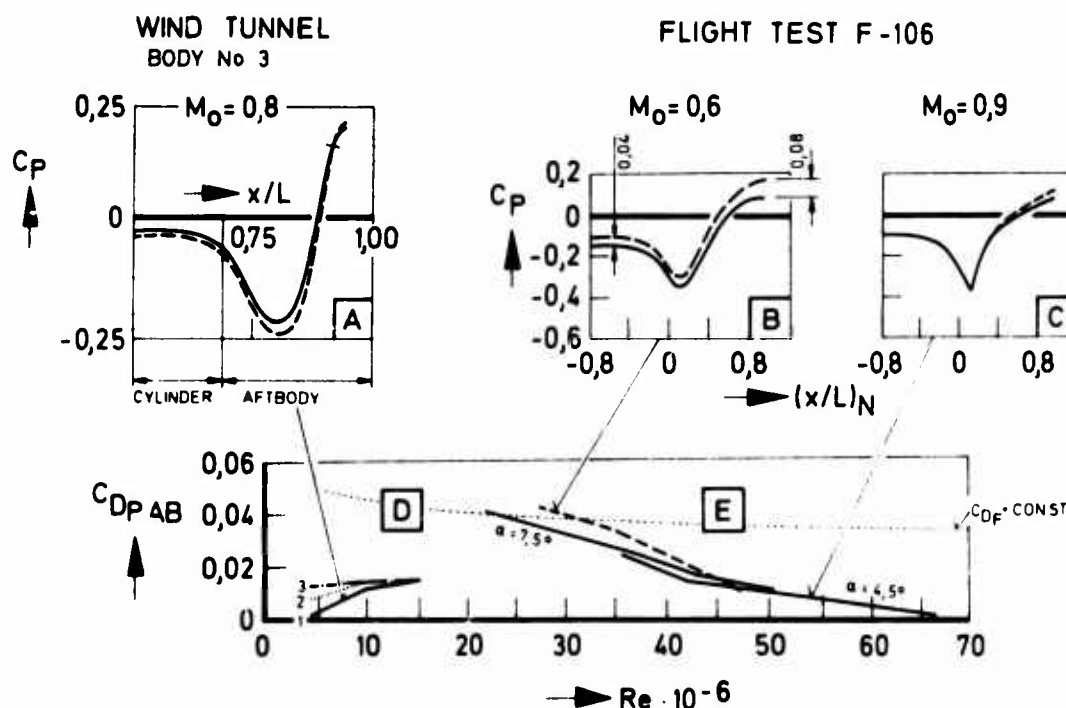


Fig. 24 Aftbody pressure drag from wind tunnel and flight test

## 7. WIND TUNNEL WALL INTERFERENCE

It was questioned whether the criterion  $\bar{C}_{p\text{ wall}} = 0$  is permissible and whether one should not rather stick to the standard procedure of empty tunnel centre line calibration and apply the appropriate blockage corrections. This method has proven its feasibility in many types of testing. However, it is obvious that for most transonic wind tunnels the calibrations available today do not meet the high accuracies required for the very sensitive part-model testing techniques.

Blockage will give  $\Delta V_0$  or  $\Delta M_0$  corrections to the indicated plenum Mach number. This must be allowed for in the evaluation of  $P_0$ , independently of any empty tunnel/plenum relationship. Also for porous walls a gradient  $dP_0/dx$  exists which cannot be detected during empty-tunnel calibrations because it is produced by the presence of the model itself. Computed blockage corrections for a doublet in a rectangular wind tunnel with four perforated walls are shown in fig. 25 (compare ref. 15): for various wall parameters  $\beta K$  different  $\Delta M_0$ -corrections result. For  $\beta K \approx 2, 5$  and sufficiently small models this disturbance velocity disappears whilst  $dP_0/dx$  remains finite. Drag measurements on long slender models will therefore require significant corrections. A calculation for the body of revolution shown in the figure indicates a buoyancy correction of  $\Delta C_D \approx 0,01$  at  $M_0 = 0,85$ , with considerably larger values at higher Mach numbers (model blockage 1 %, uniform wall open-area ratio of 22 %).

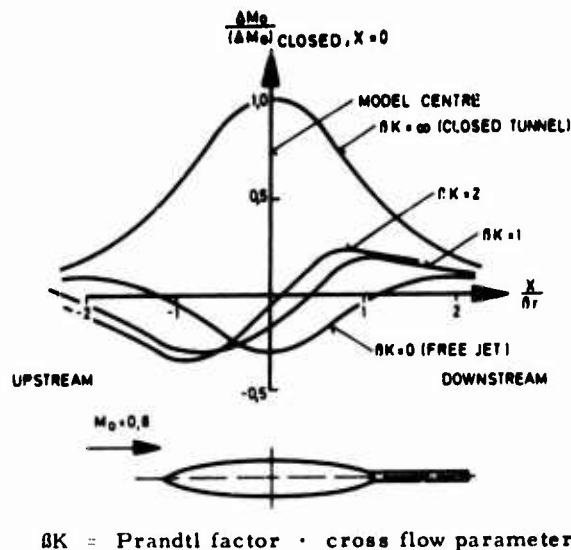


Fig. 25 Disturbance Mach number distribution on tunnel centre line

A blockage of 1 %, therefore, seems almost too large for accurate drag measurements particularly at transonic speeds, although of course for comparative work 1 % might be acceptable as long as the buoyancy corrections are applied to each body area distribution separately. If identical models are tested at different tunnel total pressures the cross-flow characteristics of the wall will change as well as the longitudinal pressure gradients (see also para. 4, p. 15).

Therefrom it is concluded that Reynolds number testing of this type in a variable Reynolds number tunnel has to be very sophisticated and probably requires knowledge of wall characteristics versus Reynolds number to an order of accuracy better than currently understood. This inability of present tunnels to simulate the free flight flow field correctly indicates that for sensitive pressure drag measurements considerably improved testing techniques are required. These requirements may lead to new features like fully variable porosity, controlled suction and to on-line computed tunnel flow fields using the monitored wall pressures and model geometries as input for semiempirical model corrections (ref. 21, 22, 23).

In the Göttingen tests reported in the preceding chapters the mean wall pressures were used in a very simple way to detect deviations in free stream static pressure. Such a method could be used with the tunnel empty or with calibration model installed to monitor the original wind tunnel calibration, which often is not repeated for years, and might have been invalidated due to tunnel changes. In the particular tests with the bodies of revolution the centre line calibration was no longer up to the required standard. Therefore, the best one can probably do in such conditions is to look at the relationship change of ( $C_p$  plenum -  $C_p$  wall ref) with Reynolds number. If there is a significant change then the Reynolds number trends may be corrected by this relationship - no absolute values can be used without at least a point relationship with the centreline static pressure and its change with Reynolds number. Preferably this reference  $C_p$  wall should be obtained at some distance upstream of the model.

#### 7. TAKING INTO ACCOUNT THE FOREBODY\*

The variation of aftbody shape naturally leads to the largest changes in pressure distribution on the rear body; on the forebody there are at the same time only minor changes in pressure distribution. In wind tunnel measurements with forebodies fixed to the ground

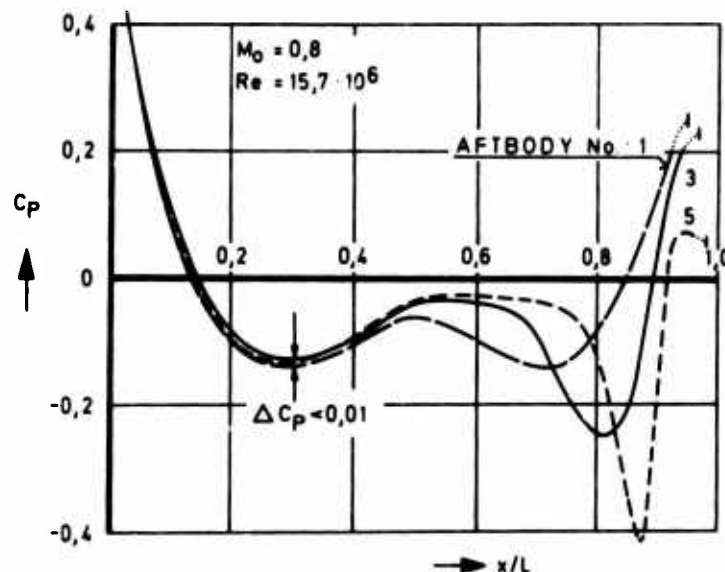


Fig. 26 Effect of aftbody geometry on forebody pressure distribution

\* See comment by Professor Ferri on page II-F23

the surface pressures near the split station forebody/afterbody are therefore in practice often taken as a criterion for a possible upstream influence: if the change of these pressure coefficients is sufficiently small, e.g.  $\Delta C_p$  smaller than 0,01, then no noteworthy changes in forebody drag are expected. In the measurements discussed in the following a slender boattail (No. 1) was replaced by a steeper one (No. 3). Due to this alteration the surface pressure coefficients at the split station changed only by  $\Delta C_p = 0,02$ ; on the greater part of the forebody ( $x/L \leq 0,45$ ) these changes were even below  $\Delta C_p = 0,01$  (fig. 26). The forebody pressure drag, however, increased at the same time by 0,0020. This amounts to 3,5 % of the total drag (pressure + friction) of the complete body. For the testing technique it follows therefrom that optimizing the afterbody drag by measuring the afterbody alone does not yield valid results, except if appropriate computed corrections are applied to the forebody drag. That is, by omitting such corrections one may succeed in merely transferring the drag problem to the forward end (compare ref. 7, p. 4 - 3) and in an incorrect overall aircraft drag synthesis.

An example of such a computed correction is shown in fig. 27. The MBB Subsonic Panel Method (ref. 8) was used for this end neglecting viscosity effects. Checking this computing method against exact solutions it has been found that the absolute drag coefficients may be in error by a few thousands, the difference  $\Delta C_{DP}$ , however, seemed to be by an order of magnitude more accurate. Therefore, the changes in forebody drag coefficients  $\Delta C_D = 0,0022$  in fig. 27 were considered to be correct.

To quantitatively confirm this upstream influence, test series 3 and 4 were conducted in which the forebody was attached to a sensitive drag balance and afterbodies 1 and 3 respectively were non-metric. The result is shown in fig. 28. At  $M_0 = 0,8$  the difference in forebody drag coefficients was found to be 0,0020 which is in very good agreement with the computed difference. The data points in fig. 28 are identical to those shown in fig. 18 with the "full" correction applied. Although only three subsonic Mach numbers were tested, the linear portions of the curves reflect little random scatter.

A further example of upstream influence is shown in fig. 29 for an ellipsoid of revolution having an infinitely long sting of constant cross-section. The forebody pressure drag of that ellipsoid has been computed as a function of sting diameter. To apply this result from this very simplified case to practical afterbody testing, let us assume that in a trade-off study on afterbody optimization one accepts larger amounts of separated flow and the corresponding higher drag in favour of a reduced structural weight (as for instance with short convergent or short Con Di-Iris nozzles). Let us moreover assume that the wake displaces the external flow field similarly as the sting does, then this modified afterbody flow field causes in turn a reduced suction i.e. an increase in pressure drag on the forebody as shown on fig. 29 in principle. A similar situation exists for attached flows if e.g. slender Con Di-nozzles of very different exit diameters and nozzle pressure ratios are tested (reheat on/off; oversized reference

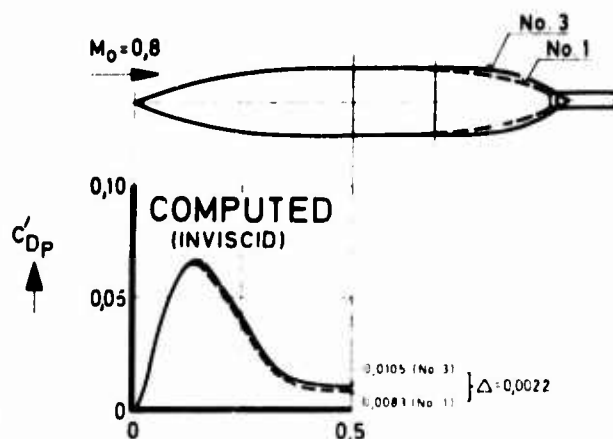


Fig. 27 Effect of aftbody geometry on forebody pressure drag

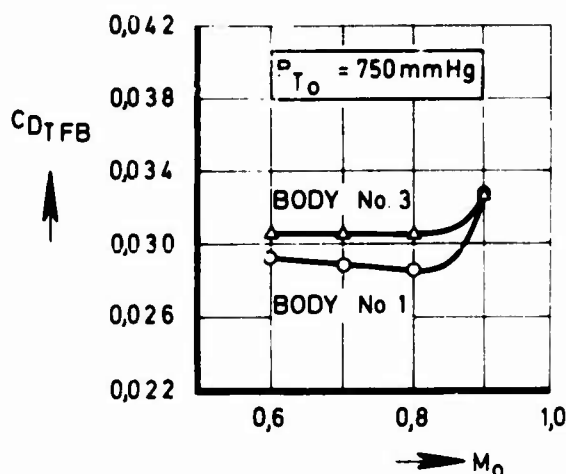


Fig. 28 Effect of aftbody geometry on forebody drag

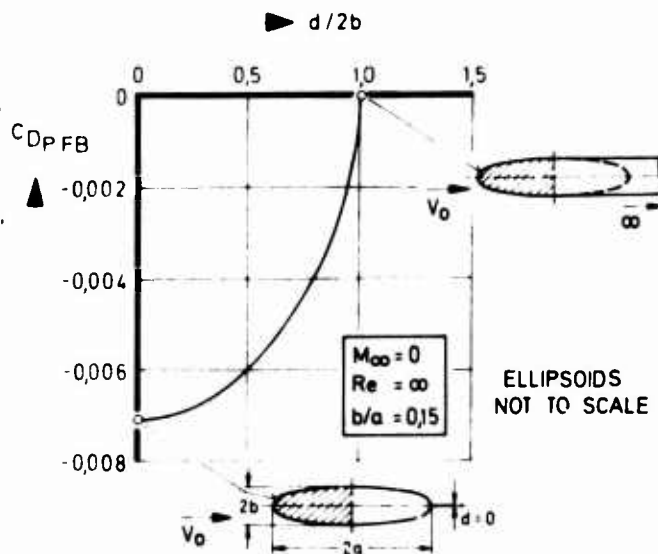


Fig. 29 Effect of sting diameter on forebody pressure drag

nozzles from sting mounted complete models etc.) In aftbody testing with non-metric forebodies these upstream influences are quite often overlooked. This, however, is acceptable as long as the measurements need not be very accurate. Typical errors for such relatively short isolated fuselages are about 1 % to 2 % of the total drag of the complete fuselage at subsonic Mach numbers.

Fig. 30 shows such an upstream influence measured on a wind tunnel model of a twin jet fighter configuration at  $M_0 = 0,7$  (ref. 19). The pressures along the top outboard quadrant of the engine nacelle are seen to rise when the nozzle is moved into the maximum reheat position. At the metric break this pressure rise corresponds to a

$\Delta C_p = 0,017$ . Depending on the attenuation rate of these pressure differences on the forebody, different drag changes occur on the non-metric part: if  $\Delta C_p$  approaches linearly zero near the maximum cross-section then the fuselage forebody drag is reduced by  $\Delta C_D = 0,002$ . If, on the other hand,  $\Delta C_p$  approaches zero only at the nose of the fuselage, which is more probable then the forebody fuselage drag is increased by  $\Delta C_D = 0,003$ . The corresponding drag changes on the wing must be accounted for in addition.

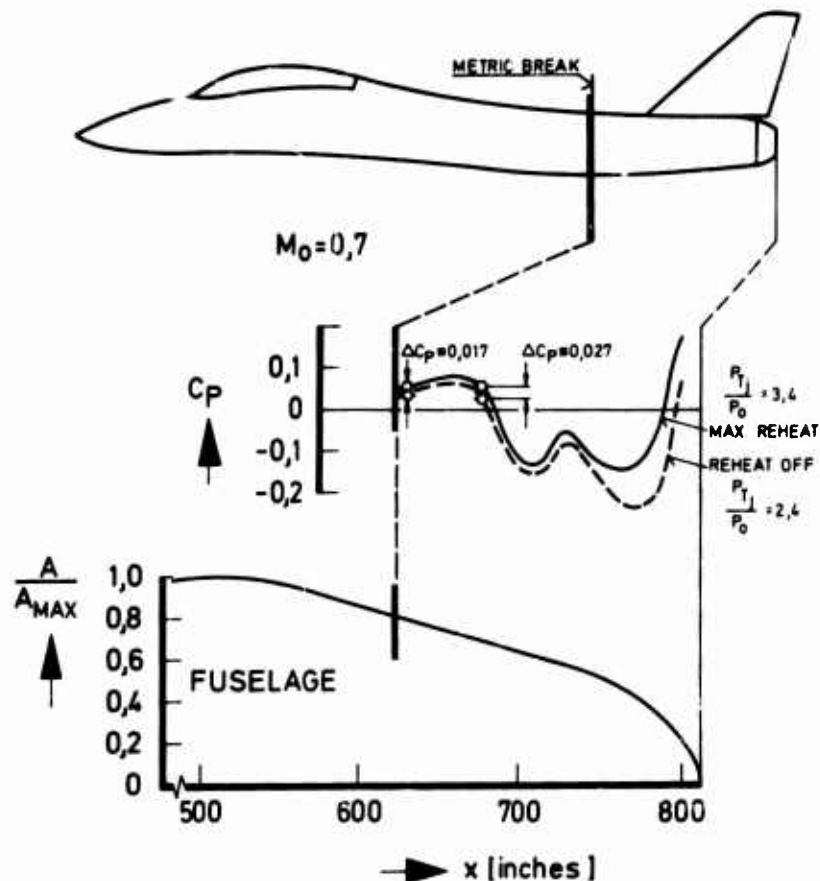


Fig. 30 Effect of nozzle position on pressure distribution

## 8. CONCLUDING REMARKS

A Reynolds number investigation, conducted with small scale axisymmetric bodies in a transonic wind tunnel, was analysed with the aim of explaining some of the unexpected Reynolds number effects measured recently by MBB and others. It is expected that most of the conclusions drawn in this paper will also apply to those wind tunnels which produced similar Reynolds number results. To confirm this supposition, similar measurements on wind tunnel wall  $C_p$ -distribution and other data on wall crossflow characteristics as well as their correlation with the tunnel centre line pressures are necessary for all such tests. Those statements which do not apply to Reynolds number effects but to aftbody testing in general, like sensitivities of half bodies and interrelation of forebody/aftbody flow fields, should hold. The main results and conclusions are summarised below.

### 8.1. Fore and Aftbody Flow Field Interaction

At subsonic speeds there is a clear interrelation between the flow field of the aftbody and that of the forebody. Correct aftbody testing, particularly aftbody testing pertaining to given aircraft configurations, therefore requires provision of a representative forebody and, at least to some extent, also of the wing flow fields (downstream influence). If, on a test rig, the forebody and the wing are not attached to the balance, then the drag changes on these non-metric model portions should be accounted for by measured or computed corrections (upstream influence).

### 8.2. Sensitivity and Accuracy

Half bodies, i.e. aftbodies or forebodies are an order of magnitude more sensitive to small deviations in free stream static pressure than complete bodies. This applies to both pressure integration and force measurement. As the pressure drag coefficient of a half body is directly proportional to the mean pressure coefficient on the body surface, the mean error in the integrated pressure coefficients should not be greater than  $\pm 0,001$  if the pressure drag of the complete body is to be determined with an accuracy of  $\pm 7$  to  $10$  % (slender body, no separation).



This is a possible measuring accuracy as was shown for the integrated model pressures (random errors). Some of the systematic errors, however, were considerably larger: at the lowest Reynolds number tested, a uniform deviation of the effective free stream static pressure from its nominal value by 0,8 % of the free stream dynamic pressure, caused an error of 27 % in total forebody drag. For the complete body, however, the corresponding error amounts to less than 1 %.

### 8.3. Wind Tunnel Calibration and Interference

Since the change of the mean wall pressures correlated with the corresponding changes on the model, it is assumed that the free stream static pressure varied accordingly, i.e. the measured Reynolds number trends were not so much caused by true Reynolds number effects but primarily by small deviations in free stream static pressure. The planned high accuracy recalibration of the tunnel centre line pressures should confirm or reject this assumption. In the meantime, one could by-pass this problem by testing complete bodies rather than half bodies, in order to make use of the compensating effects on the forebody.

The influence of Reynolds number on blockage corrections and on pressure gradients respectively, suggests that drag measurements in a variable Reynolds number tunnel need to be very sophisticated and probably require knowledge of wall characteristics versus Reynolds number to an order of accuracy better than currently understood.

### 8.4. Correlation with Other Results

An almost identical rise in aftbody drag with Reynolds number has been found in the AEDC and NASA tests shown in fig. 1. As a first step towards clarification, one could, therefore, assume that the causes were the same. With the NASA tests, Reynolds number was not varied by changing the density but by varying the model size resulting in different blockages. The results discussed in this paper showed how sensitive aftbody pressure drag is to altered crossflow conditions at the wind tunnel wall. Therefore, the same aftbody shape, tested as half body either in different wind tunnels or in the same tunnel with a different blockage, will give very different aftbody drag values.

### 8.5. True Reynolds Number Trends

The analysis presented here made it plausible that the strong drag increase, shown in fig. 1, was most likely caused by systematic errors related to the wind tunnel itself. Also, the tunnel wall interference was indicated as a possible source of the remaining discrepancy between wind tunnel and flight data. Therefore, it would appear that only the first step towards correct drag testing in variable Reynolds number tunnels has been achieved.

## 9. REFERENCES

- 1 H. B. Squire, A. D. Young      The calculation of the profile drag of aerofoils  
ARC RM 1838 (1938), also in ref. 12, chapter XXV
- 2 G. Besigk      Halbempirische Theorie zur Bestimmung des Heckwiderstandes  
MBB-Report UFE 628/1-70, March 1971
- 3 G. Besigk      Influence of Reynolds number on Drag Evaluation  
MBB-Report UFE 1078, 1974 (Test Series No. 1)
- 4 P. Antonatos, L. E. Surber, J. A. Laughrey, D. J. Stava      Assessment of the Influence of Inlet and Aftbody/Nozzle  
Performance on Total Aircraft Drag  
AGARD-CP-124(15), 1973
- 5 R. Chamberlin, B. J. Blaha      Flight and Wind Tunnel Investigation of the Effects of Reynolds  
Number on Installed Boattail Drag at Subsonic Speeds  
AIAA Paper No. 73-139, 1973
- 6 G. K. Richey      Preliminary data of the AGARD Ad Hoc Study "Improved Nozzle  
Testing Techniques in Transonic Flow"  
AFFDL, March 1974
- 7 F. Aulehla, K. Lotter      Nozzle/Airframe Interference and Integration  
AGARD-LS-53, 4 (pages 4-1 to 4-25), 1972
- 8 N. Bretthausen, W. Kraus      Das MBE-Unterschall-Panel-Verfahren. Teil 1: Das  
Verdrängungsproblem ohne Auftrieb in kompressibler Strömung  
MBB-Report UFE 632-70, 1970
- 9 J. G. Rotta      Fortran IV-Rechenprogramm für Grenzschichten bei  
kompressiblen ebenen und achsensymmetrischen Strömungen  
AVA-Bericht No. 68R 03 (1968)



- 10 N. Scholz      Über eine rationelle Berechnung des Strömungswiderstandes schlanker Körper mit beliebig rauher Oberfläche  
Jb. Schiffbautechn. Ges. 45, 244-259 (1951) also in ref. 12, chapt. XXV
- 11 H. Ludwig, W. Lorenz-Meyer, W. Schneider      Der transsonische Windkanal der aerodynamischen Versuchsanstalt Göttingen  
Jahrbuch 1966 der WGLR
- 12 H. Schlichting      Grenzschicht-Theorie  
Verlag C. Braun, Karlsruhe (1964)
- 13 E. R. Glasgow      Integrated Airframe-Nozzle Performance for Designing Twin-Engine Fighters  
Journal of Aircraft, Vol. 11, No. 6, June 1974, pp. 354-362
- 14 F. Aulehla, G. Besigk      Reynolds Number Effects on Fore- and Aftbody Pressure Drag  
AGARD-CPP-150 (12), 1974
- 15 C. F. Lo, R. H. Oliver      Boundary Interference in a Rectangular Wind Tunnel with Perforated Walls (final report)  
AEDC-TR-70-67, April 1970
- 16 G. Besigk      Einfluß der Heckgeometrie auf den Vorkörperwiderstand, Kraftmessung an Rotationskörpern bei Mach-Zahlen von 0.6 bis 0.9  
To appear as MBB-Report UFE 1169 (test series No. 3 and 4)
- 17 R. Chamberlin      Flight Reynolds Number Effects on a Fighter-Type, Circular-Arc -  $19^\circ$  Conic Boattail Nozzle at Subsonic Speeds  
NASA TM X-3121, October 74
- 18 D. Zonars, J. A. Laughrey, D. L. Bowers      Effects of Varying Reynolds Number and Boundary Layer Displacement Thickness on the External Flow over Nozzle Boattails  
Paper presented at AGARD Specialists Meeting on Airframe/Propulsion Interference, Rome, September 74
- 19 W. C. Schnell      F-14A Installed Nozzle Performance  
AIAA Paper No. 74-1099, presented at AIAA/SAE 10th Propulsion Conference, San Diego, Cal., October 74
- 20      USAF Stability and Control DATCOM  
AFFDL, Wright Patterson Air Force Base  
Revised edition August 1968
- 21 C. F. Lo      Wind-Tunnel Wall Interference Reduction by Streamwise Porosity Distribution  
AIAA Journal, Vol. 10, No. 4, April 1972, pp. 547 - 550
- 22 A. Ferri, P. Baronti      A Method for Transonic Wind-Tunnel Corrections  
AIAA Journal, Vol. 11, No. 1, January 1973, pp. 63 - 66
- 23 W. R. Sears      Self-Correcting Wind Tunnels  
Aeronautical Journal, February/March 74, pp. 80 - 89

## ACKNOWLEDGEMENT

This work was sponsored by the German Ministry of Defense, RüFo 4. The authors gratefully acknowledge the co-operation of Dr. Lorenz-Meyer, DFVLR Göttingen and in particular the valuable advice of E. C. Carter, Aircraft Research Association Ltd., Bedford.

Comment by Professor Ferri on

**FORE- AND AFTBODY FLOW FIELD INTERACTION  
WITH CONSIDERATION OF REYNOLDS NUMBER EFFECTS**

One of the important parameters to be considered in nozzle testing techniques is the interaction between the front part of the vehicle and the nozzle flow. For example, the effect of the Reynolds number in the region of the nozzle cannot be analyzed separately from the effect of the Reynolds number in the front part of the nozzle in view of the fact that if we consider the effect on the pressure as a displacement thickness effect, this effect in the two parts could be of opposite sign. In addition, in practical experiments, it is extremely difficult to represent correctly the air intake in all its details, including boundary layer scoops, boundary layer bleeding, etc.

In the limited program of the experiment, the Ad Hoc Group was unable to perform the tests on this type of interference directly related to the AGARD nozzle. However, the Messerschmitt-Bolkow-Blohm research group involved in these types of problems was in a position to perform analyses and experiments that could generate some important information on the points mentioned above. On this basis, it was decided to incorporate the following work as a part of the report of the Ad Hoc Group even if some of the configurations involved are not directly representative of the AGARD configuration. Many of the results presented in this section bear important information on the problem discussed.

Antonio Ferri

## CONCLUDING REMARKS

by

Antonio Ferri

The research in improved nozzle testing techniques in transonic flow has been organized by an Ad Hoc Committee of the Propulsion and Energetics Panel with close cooperation of the Fluid Dynamics Panel. Several NATO research groups have effectively cooperated in this effort.

The first phase of the effort was mainly directed to determining the effects of several parameters which influence the nozzle characteristics, specifically, the external parameters such as:

- boundary layer characteristics
- details of geometry
- tunnel interference
- testing techniques

and internal parameters such as:

- nozzle pressure ratio
- jet stagnation temperature
- jet flow distribution

It was already known that several of the parameters described affect the characteristics of the nozzle. This investigation, performed by different laboratories, has been limited to an axially symmetric problem. The investigation contributes substantially because it gives quantitative information on these effects. Of particular value are the data on boundary layer effects and jet temperature effects, because they indicate the strong importance of the boundary layer properties on the flow, and of the nozzle wall temperature. These results, combined with the data on interaction between the front part and the rear part of the body, permit us to imply that tests of a three-dimensional type could be strongly influenced by the small modification of pressure distribution and boundary layer properties upstream of the nozzle. In addition, these results tend to indicate that the presence of heat transfer and leakage from the nozzle could have an important effect on the performances.

The results related to wall interference and testing techniques are of particular importance. Such results show that substantial effects are present due to wall interference and model support. The data indicates that some of these effects could be reduced by a combination of analysis and experimental data.

The effects of the internal flow distribution are also important even if the configuration selected for the internal shape tends to minimize the influence of these effects. More detailed conclusions may be presented in a separate report. However, a general conclusion can be made here. The problem of testing nozzles and engine installations, especially for three-dimensional cases, is a real one and not yet resolved. The results presented permit us to also conclude that a cooperative effort of this type is a useful way to aid in improving the understanding of the problem. The Committee feels that such an effort should be continued, and recommends that a next step should be considered, if possible, under AGARD sponsorship. Possibly a special panel, sponsored either by PEP and FDP, or a separate temporary special panel should be formed.

More detailed conclusions and recommendations may be published as a separate Technical Evaluation Report.

REPORT DOCUMENTATION PAGE			
1. Recipient's Reference	2. Originator's Reference AGARD-AG-208	3. Further Reference	4. Security Classification of Document UNCLASSIFIED
5. Originator	Advisory Group for Aerospace Research and Development North Atlantic Treaty Organization 7 rue Ancelle, 92200 Neuilly sur Seine, France		
6. Title	Improved Nozzle Testing Techniques in Transonic Flow		
7. Presented at	the 35th Fluid Dynamics Panel Meeting in Rome, Italy, 4-10th September, 1974.		
8. Author(s) Editor A. Ferri	9. Date October 1975		
10. Author's Address	11. Pages 384		
12. Distribution Statement	This document is distributed in accordance with AGARD policies and regulations, which are outlined on the Outside Back Covers of all AGARD publications.		
13. Key words/Descriptors Transonic flow Fluid flow Nozzles	Tests Boundary layer Reynolds number Flow distribution	14. UDC 533.6.011.35:533.697.4	
15. Abstract <p>This AGARDograph describes research in the field of improved nozzle testing techniques in transonic flow which was coordinated by an ad hoc committee of the Propulsion and Energetics Panel and Fluid Dynamics Panel. Eight institutions from 5 nations participated in tests using standardized models. The report is divided into two major portions. The first describes tests conducted at each facility. The second portion consists of comparison of the test results obtained in various facilities and an analysis of the reasons for variations based on effects of boundary layer, jet temperature, fore-and-aft body interaction, wall interference, model support, Reynolds number, and internal flow distribution.</p>			